NEXT GENERATION VACUUM DEPOSITED AlO_x CLEAR BARRIER COATINGS FOR FLEXIBLE FOOD PACKAGING MATERIALS

Carolin Franziska Struller

A thesis submitted in partial fulfilment of the requirements of Manchester Metropolitan University for the degree of Doctor of Philosophy

Faculty of Science and Engineering
School of Engineering
Surface Engineering Group
in collaboration with

Bobst Manchester Ltd. and Innovia Films Ltd.

December 2013

DECLARATION

This is to certify that the material contained in this thesis has been produced by the author, has not been accepted in substance for any other degree and is not currently submitted in candidature for any other academic award.

RESTRICTION NOTE

This PhD thesis contains internal and confidential information and data of Bobst Manchester Ltd. and Innovia Films Ltd.. Release or duplication in parts or in the whole – also in digital form – without the written consent of the companies is not permitted. Furthermore, disclosure of the information to anyone other than the examination board is not authorised.

ABSTRACT

In the field of packaging, barrier layers are functional films, which can be applied to polymeric substrates with the objective of enhancing their end-use properties. In the case of food packaging applications, the packaging material is required to preserve packaged foodstuffs and protect them from a variety of environmental influences. Amongst others, the impermeability of the packaging material to substances including water vapour, oxygen and aromas is an important requirement for successful food packaging. Polymer films, vacuum coated with thin transparent barrier layers of aluminium oxide or silicon oxide, are very attractive candidates for food packaging applications due to the oxide film imparting attractive properties, including good barrier performance, transparency, microwaveability and recyclability.

In this project, aluminium oxide barrier layers were deposited onto various commodity grade BOPP films via reactive evaporation of aluminium, using a modified industrial 'boat-type' roll-to-roll metalliser. Optimisation of the deposited coating, in some cases together with potential surface modifications of the BOPP films, was the main focus of the work. The effects of different film treatments (in-line and off-line); surface properties of the polymer film, such as topography and chemistry; coating stoichiometry and thickness; as well as conversion processes; on barrier properties were investigated using a broad variety of analytical techniques. Furthermore, critical parameters for the convertibility of vacuum coated films, including coating adhesion and coating surface energy, were assessed.

This project has demonstrated that the barrier performance of aluminium oxide coated BOPP is heavily dependent on the plain film surface and the growth/nucleation conditions of the deposited film, both of which can vary to a large extent on standard packaging grade BOPP film. Whilst acceptable oxygen barrier levels were achieved on some BOPP film types, others did not match the requirements, despite investigating a wide range of coating parameters. This was found to be due to the presence of defects (permeation pathways) in the coating, which were reproduced from defects in the underlying polymer film surface. With regards to the barrier performance after aluminium oxide coating, the polymer film surface chemistry was identified as an important parameter. Barrier performance was enhanced when the surface of the BOPP film had high oxygen content and

when a high surface energy skin layer was co-extruded onto the BOPP film. Furthermore, the barrier properties could be improved by the use of BOPP shrink films as substrates; this was assumed to be due to a densification of the coating. Finally, a lower deposition pressure is also supposed to positively impact the barrier performance. Nevertheless, water vapour barrier improvement for aluminium oxide coated BOPP films was only achieved for samples that had undergone extensive ageing periods, or through the use of different polymer skin layers or via depositing coatings with reduced oxygen content, thus obtaining grey coatings that can no longer be classified as transparent. Peel tests indicated very high levels of adhesion of the aluminium oxide coating to the BOPP film, with cohesive failure taking place within the polymer, rather than adhesive failure at the coating-substrate interface. Examination of the time related change of surface energy revealed a distinct decay with ageing time, most probably due to transfer of polymeric material and film additives from the reverse side of the film onto the coating and also migration through defects in the coating. Finally, the application of acrylate under- and topcoats, as well as adhesive lamination, was found to have the capability to significantly enhance the barrier performance of the aluminium oxide coated BOPP film. In the case of acrylate undercoats, this was attributed to the change in surface chemistry, whilst for topcoats and lamination processes, the barrier properties of the acrylate/adhesive play an important role, together with a possible ‘pore filling’ effect.

ACKNOWLEDGEMENTS

This PhD thesis could not have been written without assistance and contributions from a number of fantastic people, whom I have met during the course of my PhD project.

In the first place, I would like to express my deepest gratitude to my Director of Studies, Professor Peter Kelly, for his scientific guidance, constant support and valuable advice throughout my entire PhD, and for giving me the possibility to accomplish this project. Furthermore, I'm grateful to my supervisors, Dr. Christopher Liauw and Dr. Glen West, for their continuous assistance, encouragement, enthusiasm and excellent discussions. Thank you for making this research such an amazing and enjoyable experience.

I am greatly indebted to Bobst Manchester Ltd. for partially funding this project and providing an industrial-scale trial platform, as well as for giving me the opportunity to attend various conferences and present my results. Moreover, I am truly thankful to the guys in the lab and on the shop floor at Bobst Manchester, for their help and assistance in conducting coating trials and analysing the barrier performance.

A special mention of thanks goes to Innovia Films Ltd. and my industrial supervisor Dr. Simon Read, for supporting the PhD project and giving me access to Innovia's analytical facilities. I would like to thank for the endless support from the members of the research team at Wigton, especially Christopher Walford, Craig Hollliday and Dr. Simon Malone, to name only a few. Their commitment, recommendations, fruitful discussions and help with the analytical study have been of inestimable value.

In addition, I would like to thank Dr. Steven Hinder of the University of Surrey for carrying out the XPS analysis and helping with the result evaluation, Dr. Aleksandr Mironov of the University of Manchester for performing TEM analysis and the Fraunhofer Institute for Process Engineering and Packaging for being able to use their atomic force microscope. Furthermore, I'm grateful to Dr. Vladimir Vishnyakov for his guidance in the use of the scanning electron microscope and Dr. Charles Bishop for his advice and support.

My heartfelt thanks go to Dr. Hazel Assender and Vincent Tobin of the University of Oxford for being able to use their facilities to deposit acrylate coatings, Bobst Italia Spa. for conducting industrial-scale lamination and Rory Wolf of Enercon Industries Corp. for arranging atmospheric plasma and flame treatment trials.

I would also like to thank all postgraduate students of the Surface Engineering Group for their friendship, exchange of experience and the amazing and pleasant working environment and, furthermore, all technical and analytical staff at Manchester Metropolitan University that have contributed to this research project.

I especially want to thank my family, my parents, who have always loved me unconditionally, have raised me to be the person I am today and whose good examples have taught me to work hard for the things that I aspire to achieve, and my brother and sister, for their support and encouragement.

And last but definitely not least, I would like to thank my partner Nick for his commitment, love, patience and faith in me. Without him and his support during the challenges of this research work, this project would not have been successful and this thesis could not have been written. Our interesting and crazy discussions on barrier mechanisms over romantic evening meals, including Valentine's Day, are unforgettable. This thesis is dedicated to you.

CONTENTS

LIST OF FIGURES

LIST OF TABLES

LIST OF ABBREVIATIONS AND ACRONYMS

AFM	Atomic force microscopy
AIMCAL	Association of International Metallizers, Coaters and Laminators
ALD	Atomic layer deposition
AlO_x	Aluminium oxide (stoichiometry not confirmed)
AlO_xN_y	Aluminium oxynitride (stoichiometry not confirmed))
Arb. unit	Arbitrary unit
ASTM	American Society for Testing and Materials
ATR	Attenuated total reflectance
BIF	Barrier improvement factor
BOPET	Biaxially oriented polyethylene terephthalate
BOPLA	Biaxially oriented polylactic acid
BOPP	Biaxially oriented polypropylene
CPP	Cast polypropylene
CVD	Chemical vapour deposition
DIC	Differential interference contrast
EAA	Ethylene acrylic acid
EMA	European Metallizers Association
ESCA	Electron spectroscopy for chemical analysis
EVOH	Ethylene vinyl alcohol (copolymer)
FTIR	Fourier transform infrared (spectroscopy)
GPC	Gel permeation chromatography
HAD	Hollow cathode activated deposition
IR	Infrared
ISO	International Organization for Standardization
LC-MS	Liquid chromatography – mass spectrometry
LISIM	Linear motor simultaneous stretching technology
MAD	Magnetron activated deposition

MD	Machine direction
MOPP	Monoaxially oriented polypropylene
m/z	Mass to charge ratio
OD	Optical density
OTR	Oxygen transmission rate
PACVD	Plasma assisted chemical vapour deposition
PE	Polyethylene
PECVD	Plasma enhance chemical vapour deposition
PET	Polyethylene terephthalate
PLA	Polylactic acid
PP	Polypropylene
PVD	Physical vapour deposition
PVdC	Polyvinylidene chloride
PVOH	Polyvinyl alcohol
RMS	Root mean square
SEM	Scanning electron microscopy
SIMS	Secondary ion mass spectrometry
SiO_x	Silicon oxide (stoichiometry not confirmed)
SSIMS	Static secondary ion mass spectrometry
TD	Transverse direction
TEM	Transmission electron microscopy
TOF	Time-of-flight
TPGDA	Tripropylene glycol diacrylate
UV	Ultraviolet
WVTR	Water vapour transmission rate
XPS	X-ray photo electron spectroscopy

1 INTRODUCTION

1.1 Context of research

Flexible polymer films are of great importance in many fields and modern applications, ranging from encapsulation of electronic and optical devices and solar cells to packaging of a variety of products, including foodstuffs and pharmaceutical products. Due to advantages such as low costs, ease of handling and processing, flexibility and low weight, polymer films are increasingly being used as replacements for traditional materials, such as aluminium foil or glass.

When applying flexible plastic films for packaging food, the packaging material needs to meet high standards in order to be able to preserve the packaged products. The crucial function of a package besides containment, convenience and communication is the protection of its contents. Hence, the packaging material has to maintain the quality and freshness of the food, prevent spoilage and ensure a long shelf life from production via transport and storage through to delivery to the final consumer. As most foodstuffs are very sensitive, they need to be protected from a variety of environmental influences, such as contaminants, microorganisms, mechanical damage/deformation and, furthermore, moisture and gas ingress. [1]

The impermeability of the packaging material to vapours and gases, such as water, oxygen, carbon dioxide and aromas (either going into or coming from the product), is an essential design consideration for the longevity of the packaged product and, hence, is key to successful food packaging. These characteristics are collectively termed barrier properties. However, plain polymer films do not usually act as good barrier materials, apart from barrier polymers such as ethylene vinyl alcohol copolymer (EVOH), polyvinyl alcohol (PVOH) and polyvinylidene chloride (PVdC). To achieve these features and to further enhance the end-use properties of the polymer substrates, the films are coated (vacuum coating, e.g. metals and their oxides, and atmospheric coating, e.g. PVdC) with an additional functional film; a barrier layer. Nevertheless, barrier performance depends on many factors. In the case of vacuum coated films, these include the structure and properties of the coating, the nature of the polymer substrate, the interface characteristics, the interactions between coating and substrate as well as the coating technique itself.

Polymer films vacuum coated with thin transparent inorganic barrier layers, such as aluminium or silicon oxide (usually referred to as AlO_x and SiO_x as exact stoichiometry is not generally measured), are particularly suited for food packaging, since they exhibit a combination of properties that are technologically and commercially attractive, i.e. good barrier performance, transparency (product visibility), microwaveability (microwave transparency), retortability, suitability for

metal detectors (non-conductive coating), recyclability. Furthermore, the high surface energy of the oxide coating is expected to promote adhesion and to improve printability. Nevertheless, the inherently brittle nature of the ceramic coating is a major drawback. [2, 3]

The clear barrier flexible packaging market, which is currently growing worldwide at a rate of 10 to 15 % per year [4], arouses widespread interest. Traditionally, EVOH or PVOH coextruded/coated barrier films and PVdC atmospheric coated polymer films tend to dominate the market [5-7]. EVOH and to a larger extent PVOH, however, are moisture sensitive (loss of barrier at high humidity) [6, 8], which makes them unsuitable for some foodstuffs, whilst PVdC coated polymer films have fallen into disrepute due to the possible release of dioxins upon incineration [9]. As a result, such PVdC-based films became unpopular in Japan, thus promoting the development of inorganic transparent barrier coatings [4].

AlO_x and SiO_x vacuum coated polymer films can eliminate the issues associated with PVdC and EVOH/PVOH and, additionally, offer a further advantage over conventional transparent barrier layers, in that they only require a thickness in the nanometre range, i.e. three orders of magnitude smaller than the barrier layers mentioned above, which are in the range of several microns. Despite this, they still give similar barrier properties and, hence, can provide vast economic (raw material consumption and cost) and environmental benefits.

A number of different routes exists for the production of SiO_x and AlO_x clear barrier films, including reactive evaporation of SiO with O_2, plasma enhanced chemical vapour deposition (PECVD) of organosilanes, electron beam evaporation of Al_2O_3, reactive thermal evaporation of aluminium in an O_2 atmosphere (resistively or electron beam), sputtering from an oxide or metal target (reactive sputtering) and also atomic layer deposition (ALD). According to current assessments, the reactive evaporation of aluminium using resistively heated boats appears to have the potential for the lowest cost, due to the low associated capital investment, the use of inexpensive raw materials as well as the high process speeds that can be achieved. [3, 10, 11]

During the last decades, developments towards the production of AlO_x clear barrier films using industrial ‘boat-type’ roll-to-roll metallisers have taken place [2, 3, 10, 12]. In this process, the standard aluminium metallisation process is modified by injection of oxygen into the aluminium vapour cloud, thus resulting in the deposition of a transparent aluminium oxide layer. Adapting a standard aluminium vacuum web coater for the deposition of transparent AlO_x coatings has been an aspiration for many years. A modification of this well established process will give the unique

possibility of using standard high speed coating equipment for the production of transparent barrier films at low cost. Nevertheless, optimisation and development leading to a commercially viable and fully productionised process are far from straightforward.

Considering the low profit margins within the packaging market, the associated cost of the base substrate also plays an important role. Among the billions of square metres of plastic films that are vacuum web coated per year for packaging applications, polyethylene terephthalate (PET)[a] and biaxially oriented polypropylene (BOPP) are the substrates most widely used [13]. However, BOPP base film still remains at a lower cost level than PET film, which causes it to be the material of choice regarding commodity clear barrier films.

Whilst the barrier levels obtained for PET with reactively evaporated aluminium oxide (using a 'boat-type' roll-to-roll web coater) readily fulfil the requirements for food packaging applications, BOPP films have proven to be a more difficult base material, on which to apply AlO_x. Therefore arises the need for an AlO_x clear barrier solution on BOPP film. This will be a substantial advance on the current state of the art in a scientific/technological context, not to mention the significant commercial and environmental impact.

[a] Although polyethylene terephthalate films are commonly referred to as PET films, they generally are biaxially oriented and, hence, BOPET (biaxially oriented polyethylene terephthalate) would be a more appropriate term to describe these films.

1.2 Thesis layout

This thesis is divided into nine chapters, including a bibliographical chapter (Chapter 9) that contains all references. After a general introduction to the context of the research work carried out (Chapter 1), Chapter 2 summarises the aims and objectives with respect to the trials to be conducted and investigated, the various properties to be analysed and characterised, as well as the fundamental understanding to be obtained regarding barrier mechanisms for thin vacuum deposited inorganic barrier layers on polymer films.

In Chapter 3, state of the art, the vacuum deposition process used (reactive thermal evaporation via resistively heated boats in a roll-to-roll process), its past and recent developments and its commercialisation and use are reported.

Chapter 4 provides the reader a theoretical background on the various subjects and processes that have been involved and investigated in the course of this research work. This chapter starts with a description of the structure and morphology of polypropylene and the BOPP film production process, which is followed by a general presentation of the plasma treatment process and its effects on polymer surfaces. Subsequently, physical vapour deposition processes, vacuum web coating and conversion of vacuum coated films are discussed. At the end of Chapter 4, two critical characteristics and requirements for vacuum coated polymer films, adhesion and barrier properties (both also investigated extensively in this thesis), are defined and explained in detail.

In Chapter 5, the AlO_x deposition process and deposition equipment is described and illustrated, as are the additional processes applied pre- and post- AlO_x deposition, such as off-line treatments, under- and topcoat deposition and lamination. Furthermore, this chapter also contains information on the different substrate materials used, as well as the analytical techniques and specific analytical equipment applied for the investigation. The experimental flow chart at the end of Chapter 5 sheds some light on the context of the experiments and analyses conducted.

The experimental and analytical details are followed by Chapter 6, the main chapter of this thesis, in which the results are presented and discussed in six subchapters. Thereby, the data on the uncoated polymer films is initially outlined, followed by the detailed characterisation of the AlO_x coated films. The three succeeding subchapters present and debate the results following different off-line treatments, under- and topcoat deposition and industrial scale lamination. The results obtained

for AlO_x coated polylactic acid film, a biodegradable polymer film, round off the main chapter.

Finally, the main findings and conclusions of this work are summarised in Chapter 7, whilst and outlook on possible future work is given in Chapter 8.

To end with, this thesis is completed with a list of the references and materials cited (Chapter 9) as well as an appendix containing additional information and results.

2 AIMS AND OBJECTIVES

The overall aim of this work is to develop a new generation of low-cost and high-performance AlO_x coated BOPP packaging films that will be produced at high throughput using the reactive PVD process in a standard 'boat-type' industrial roll-to-roll vacuum web coater/metalliser. Reproducible and consistent barrier performance, optical clarity, uniformity of the coated film and coating-to-substrate adhesion comparable to current AlO_x coated PET films, are essential characteristics for a successful final product. This will be achieved via completion of the following objectives:

- Construction and completion of a matrix of various process trials to be conducted at the industrial partner's site (reactive thermal evaporation);
- Assessment of coating-to-substrate adhesion strength in PET and BOPP based films;
- Investigation of the effect of pre- and post-treatment during AlO_x coating of the BOPP base film with the aim of improving coating adhesion and barrier;
- Detailed analysis/characterisation of the AlO_x coatings produced regarding stoichiometry, structure and optical transparency of the coatings;
- Establish which of the above factors have the dominant effect on barrier and adhesion properties, and how these factors may be interrelated;
- Analysis/characterisation of various BOPP base films in order to find important factors that govern the barrier properties after AlO_x coating;
- Adjustment and optimisation of the process conditions as well as the base BOPP film followed by examination of the effect of further downstream processing such as adhesive lamination on barrier;
- Application of organic smoothing layers (undercoats) prior to AlO_x deposition as well as protective polymer topcoats after AlO_x deposition and analysis of their barrier characteristics in combination with an AlO_x layer;
- Investigation of the fundamental mechanisms and reactions taking place when water vapour and also oxygen permeate through an inorganic AlO_x coated BOPP substrate, based on the analytical data obtained.

3 STATE OF THE ART

The interest in and, furthermore, work on aluminium oxide barrier coatings via reactive evaporation from resistively heated boats started in the late 1980's, with Camvac Ltd., a producer of metallised film (based in Thetford, United Kingdom, formerly Bowater/Rexam Packaging), modifying a standard industrial roll-to-roll metalliser in order to deposit transparent AlO_x coatings [14, 15]. However, the early AlO_x coated polymer films revealed insufficient barrier properties and additional humidification/conditioning was required in order to boost barrier performance to an acceptable level. Further optimisation of the process, together with the application of a proprietary plasma technique, resulted in the first commercially available AlO_x coated film of its type: 'Camclear', an AlO_x coated PET barrier film [2, 3]. Throughout the years, Camvac's AlO_x coated films enjoyed relatively little scientific publicity [16-18] and for many years, their patented process was the only industrial AlO_x coating process of its type (i.e. reactive evaporation from resistively heated boats) in operation. Today, Camvac's 'Camclear' AlO_x coated films are used and distributed by companies such as Celplast Metallized Products [19] and Dupont Teijin Films [20, 21].

In addition to Camvac, another group of researchers at the Fraunhofer Institute for Electron Beam and Plasma Technology (based in Dresden, Germany) was working on the same topic. Publications reporting their research date back to 1993 [22]. Originally starting off with electron beam evaporation [23-25], they soon saw the economic potential of reactive deposition from conventional boat evaporators [10]. Their process was developed on an experimental-scale roll coater, meeting the requirements of commercial production. The key to the Fraunhofer process is the plasma assisted deposition of AlO_x, which results in a densification of the coating thus giving better coating structure and barrier properties. A magnetron activated deposition (MAD, using a magnetron gas discharge) process [26-28] and a hollow cathode activated deposition (HAD, using a hollow cathode gas discharge with a cylindrical cathode to create a high density plasma) process [29] were the two plasma techniques applied. Further results from the Fraunhofer work have been published in several papers [30-34]. Finally, their system with an optimised, modular (i.e. with up scaling possibility) HAD unit was successfully incorporated into a metalliser from Applied Materials, a manufacturer of industrial vacuum roll coaters (based in Alzenau, Germany, formerly Leybold) [35]. Since then, the industrial process and data associated with barrier performance obtainable have been presented at various conferences [12, 36-40]. In addition to the AlO_x-HAD process, Applied Materials have also started offering a so-called AlO_x-ECON process in 2012 [40], which does not have the plasma assistance and is only recommended/marketed for PET substrates .

The Centro Tecnologie del Vuoto (based in Carsoli, Italy) reports on the reactive deposition of AlO_x barrier layers using a two-step/two-zone process on a conventional boat evaporator [41, 42]. Firstly, aluminium is evaporated in a reactive environment in order to form a partially oxidised AlO_x layer (evaporation process) and, subsequently, the coating is exposed to a reactive plasma (oxidation process). By the use of a suitable winding system, the two steps are repeated four times for the final barrier layer of approximately 20 nm thickness. Although this two-step/two-zone process was patented [43, 44], no further publications or commercialisation for the deposition of AlO_x barrier coatings followed.

Ultimet Films Ltd., a producer of metallised film (based in Attleborough, United Kingdom), have developed and trademarked their own AlO_x coated barrier film, 'CeramAlO_x', now distributed by FILMtech in North America [45].

Bobst Manchester Ltd. (formerly General Vacuum Equipment Ltd.), a manufacturer of industrial vacuum roll coaters (based in Heywood, United Kingdom), began development work on an AlO_x process in 2008 and their technology was finally fully productionised after two years, with the first machine for industrial AlO_x production being released in 2010. In contrast to the Fraunhofer AlO_x process, no expensive and sophisticated plasma densification is applied. Results of their work have now also been published and presented at relevant conferences [46-49].

As mentioned previously, there are several techniques available to produce AlO_x barrier layers. The focus of this section, however, only lies on AlO_x coatings produced via reactive evaporation using a 'boat-type' roll-to-roll metalliser.

4 THEORETICAL BACKGROUND

4.1 Biaxially oriented polypropylene film

Due to its desirable intrinsic key characteristics, such as high melting point, low density and excellent chemical resistance, polypropylene (PP) is one of the most important modern plastics. Because PP is extremely versatile and the production process, as well as the material itself, are environmentally friendly (clean efficient process, recyclability), it is used in a wide range of industrial and domestic applications as films, fibres or moulded products. [50]

4.1.1 Chemical composition, structure and morphology of polypropylene

Polypropylene (formula shown in *Figure 4-1*) is a thermoplastic polymer and consists of long, linear chains. Within the organic polymer Van der Waals forces act between the polymer chains. As PP is prepared by polymerisation of propylene (also called propene), an olefin, it belongs to the class of polymers known as polyolefins. Propylene (see *Figure 4-1*) is obtained from petrochemical resources, usually via cracking of hydrocarbons.

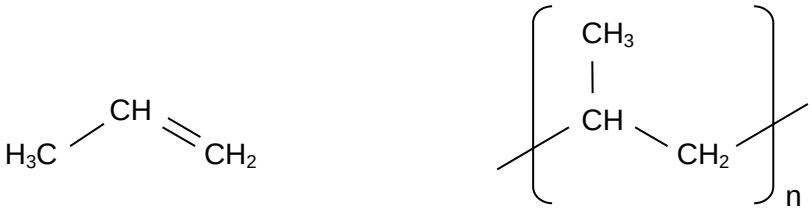

Figure 4-1: Structural formulae of propylene (left) and polypropylene (right)

The unsaturated double bond of propylene provides the basis for the polymerisation process. During the chemical polymerisation reaction, the single propylene monomers are joined together and form chain-like macromolecules (polymers) with an weight-average molecular weight of generally 2.2 x 10^5 to 7.0 x 10^5 g/mol [51]. As polypropylene features a pseudo-asymmetric carbon atom (the carbon atom bearing the methyl group) in every repeat unit, the stereochemical orientation, in which monomer is added to a growing polymer chain, is of great importance. Therefore, different types of polypropylene homopolymer (consisting of only propylene derived repeat units) can be obtained; these are distinguished according to the position of the methyl group with respect to the carbon backbone, or the variation in stereochemistry of the pseudo-asymmetric carbon atoms along the chain. Such variation is known as tactic variation and is often called tacticity (see *Figure 4-2*). [50, 52, 53]

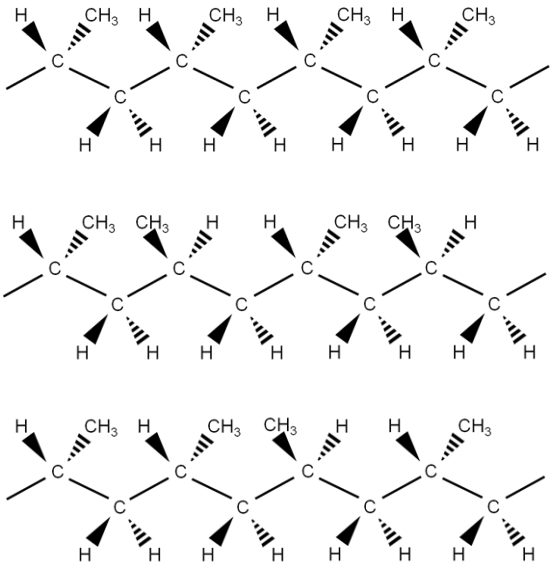

Figure 4-2: Tactic variations in PP homopolymer

Isotactic PP

The addition of propylene monomers to the end of the polymer chain in the same stereochemical orientation leads to the formation of isotactic PP. When isotactic PP is schematically represented in a planar zig-zag conformation, the constant stereochemistry of the pseudo-asymmetric carbon atom causes the methyl group to be always located on the same side of the polymer chain. However, in reality, the planar zig-zag conformation is sterically impossible due to the bulk of the methyl groups. Consequently, the polymer chains form regularly shaped 3_1 helices (a 3_1 helix has one rotation over three repeat units, see *Figure 4-3*) that can readily pack into a crystal lattice. Commercial PP homopolymer grades generally are 90 to 95 % isotactic [54]. Like other semi-crystalline thermoplastics, the basic crystal structure of isotactic PP is the lamella, which is made up of folded chains (see *Figure 4-3*). PP chains between adjacent lamellae are in amorphous state. Thus, isotactic PP is semi-crystalline with a crystalline melting point (T_m) of 160 to 166 °C (for commercial isotactic grades; ideal $T_m \approx 171$ °C) [51] and a glass transition temperature (T_g) between 0 and 10 °C [55].

Syndiotactic PP

Syndiotactic PP represents another type of stereoregularity. The methyl groups are assembled in an alternating stereochemistry along the polymer chain. When represented as a planar zig-zag, the orientation of the methyl groups alternates in and out of the carbon backbone plane. Syndiotactic PP can also adopt a helical conformation (this time a 2_1 helix) and can therefore crystallise.

Atactic PP

The propylene monomers are attached to the chain without any consistency in stereochemical arrangement. Consequently, the orientation of the methyl groups relative to the carbon backbone varies randomly. Atactic PP has low or zero crystallinity and is considered to be an amorphous polymer. It is rubbery at room temperature due to its low T_g.

Isotactic PP is normally the desired product and to achieve a high yield of this material, the polymerisation catalyst system has to be carefully considered, as they govern the tacticity and thus the degree of crystallinity. The choice of catalyst also enables control of further properties such as molecular weight, molecular weight distribution, thermal-oxidative stability, toughness, rigidity or transparency. However, the production process and its conditions also have an impact on the polymer features.

The crystalline content of PP can be precisely controlled by co- or terpolymerisation of propylene with ethylene and/or butylene. Using a living polymer system, the amount and distribution of the co/termonomers can be controlled, hence giving PP random co/terpolymers and PP block co/terpolymers. Due to the endless number of combinations and distribution of co/termonomers, a large variety of polypropylene co/terpolymers are commercially available.

After isolation from the polymerisation reactor, the PP (sometimes in powder form) is fed into an extruder for re-melting and mixing with the corresponding additives, such as stabilisers (see next section). The extrudate strands are then pelletised to manufacture commonly used PP granules. It is worth noting here that due to the tertiary hydrogen atom on the carbon atom carrying the methyl group, virgin PP reveals poor oxidative stability and without stabilisers PP would not be the commercial success we know it to be. A basic general purpose stabilisation package is always added to PP after isolation from the reactor.

As mentioned before, isotactic PP is a semi-crystalline polymer. The crystallisation process in the polymer melt during cooling is driven by the quest for a favourable low-energy conformation, which results in the formation of ordered polymer chains. The overall crystallisation process takes place in two steps, firstly the nucleation and secondly the growth of crystalline structures. Whilst the dominant morphological form of isotactic PP is the α-form, which exhibits a monoclinic unit cell, a β-form (hexagonal unit cell) and γ-form (orthorhombic unit cell) are also possible [51]. Which type of basic crystal structure (i.e. unit cell) is formed, depends on the conditions during crystallisation, such as temperature, pressure, cooling rate or flow conditions. The structural features of semi-crystalline isotactic PP are illustrated in

Figure 4-3. The polymer chains adopt a helical conformation and fold into lamella-shaped crystals, with typical lamella thicknesses around 50 to 200 Å (for the α-form) [50]. The lamellae itself (organised as fibrils) can be arranged in spherulites, which grow radially from the point of nucleation. Thereby, the polymer chain axis runs vertically to the spherulite radius, i.e. fibrils. The spherulites typically are 1 to 50 µm in size [50] and can be observed using light microscopy.

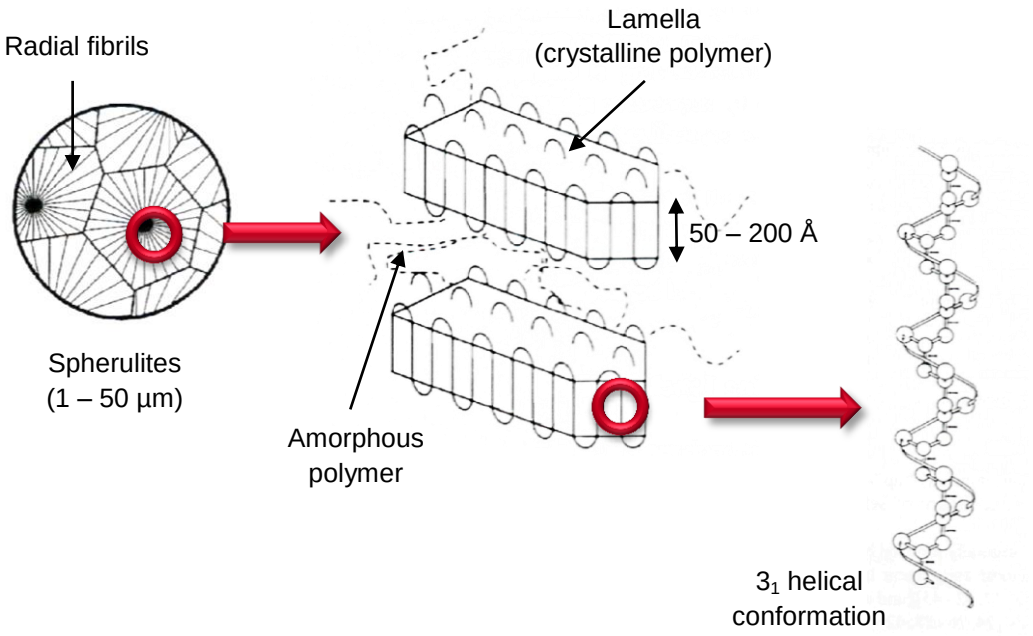

Figure 4-3: Structural features of semi-crystalline isotactic PP (adapted from reference [50])

During the orientation process for BOPP film production (refer to Chapter 4.1.2), the initial spherulitic morphology of the cast sheet (before orientation) is transformed. For sequentially oriented BOPP homopolymer films, the orientation in machine direction (MD) results in the formation of a stacked lamellae morphology, with the lamellae normals aligned parallel to the machine direction (i.e. a structure consisting of parallel aligned 'shish-kebabs'). This deformation is presumably caused by localised melting and recrystallisation during the MD drawing process. The second orientation step in transverse direction (TD) causes the separation and inclination of the stacked lamellae and, finally, results in a fibrillar network morphology. Depending on the draw ratios applied in MD and TD, a preferential orientation of the fibrils can be present. [56, 57]

The fibrillar network of BOPP homopolymer films can be observed during AFM investigations and has been reported by a variety of research groups [58-63]. Nevertheless, the structure of BOPP copolymer (and also terpolymer) film surfaces appears different during AFM analysis, as shown by Moosheimer and Bichler [64]. It

is assumed that the interruption of the PP polymer chain by co/termonomers must prevent the formation of the fibrillar morphology and, consequently, results in a rather granular surface texture of the BOPP film.

For further information on the processing, structure and morphology of polypropylene, the reader is referred to references [50-52, 65].

4.1.2 BOPP film additives and film production

Depending on the final application of PP, additives have to be incorporated into the polymer prior to further processing into products, such as films, moulded products or fibres. The additive package for PP confers stabilisation to the polymer, as well as optimised processing characteristics and end-use properties. In the case of PP films, these additives can include: [50, 51, 66]

Stabilisers (antioxidants, light stabilisers) prevent or retard thermal-oxidative and photo-oxidative degradation of PP and consequently deterioration of its physical properties, as PP is an inherently unstable polymer. Therefore, PP must be stabilised against thermal oxidation (when it is in the melt state during processing and during service of the film) and photo-oxidation (especially for outdoor applications). Primary antioxidants disrupt the oxidation cycle (free radical chain reaction) degrading PP by acting as radical scavengers, whilst secondary antioxidants decompose hydroperoxides generated during the degradation process and stop the initiation of further oxidation cycles. Optimal protection against thermal oxidation is often obtained when combining primary and secondary antioxidants and thus taking advantage of synergistic effects.

Acid scavengers (neutralising agents, antacids) neutralise the acid residues originating from the polymerisation catalyst.

Nucleating agents promote nucleation of crystal structures in the melt, thus affecting the size and number of crystal structures known as spherulites.

Antistatic agents reduce the static charge built up due to the electrical insulating nature of PP. This helps to prevent the attraction and accumulation of debris on the film surface and also reduces static blocking (sticking together) of film.

Slip agents reduce the coefficient of friction between the film and manufacturing or processing equipment. After extrusion, slip agents intentionally migrate to the film surface and act as a lubricant.

Antiblock particles prevent the adjacent layers of film sticking to one another by protruding from the film surface and reducing the contact area by separating the individual film layers, i.e. they act as spacers. Thus, they improve handling of the film during processing. Antiblock particles consist of inorganic materials, typically silica.

There are two different processes for manufacturing biaxially oriented polypropylene film: the tubular process (‘double-bubble’) and the more common tenter process (also referred to as the stenter process) [50, 67]. In both cases, the manufacturing of

the BOPP film begins with melting and homogenising of the PP and incorporation of the additive package, if not yet included during production of the polymer granules. This is done by an extruder.

In the case of tentered BOPP (see *Figure 4-4* for illustration), the molten PP is then fed to a slit die that spreads it as a thick film onto a chill roll (cooling can also be achieved via a water quench bath). Subsequently, the film is reheated and stretched in the machine direction as the stretch rolls run faster than the rolls for reheating (MD draw ratio about 1:4 to 1:6 [50]). After cooling, the film is passed on to the next section for stretching in the transverse direction. Here, the film edges are grasped by clips that move apart in a V-shape, whilst the film passes through a temperature regulated hot air oven (TD draw ratio about 1:7 to 1:10 [50]).

Stretching is generally conducted at a temperature of 120 °C to 160 °C [51] (just below the melting point). In order to reduce shrinkage (i.e. prevent a memory effect), the BOPP film is heated to a slightly higher oven temperature (after TD stretching). Thus, the film is annealed and stabilised (heat setting). Afterwards, the film is cooled, the edges are trimmed off and the film is wound up. In general, pre-treatment (mainly corona, see Chapter 4.2.3) of the film is accomplished after heat setting. Instead of this *sequential two step orientation* process, a contactless *simultaneous orientation* process on a tenter system is possible as well (LISIM linear motor simultaneous stretching system, developed by Brückner Maschinenbau GmbH & Co. KG [68]).

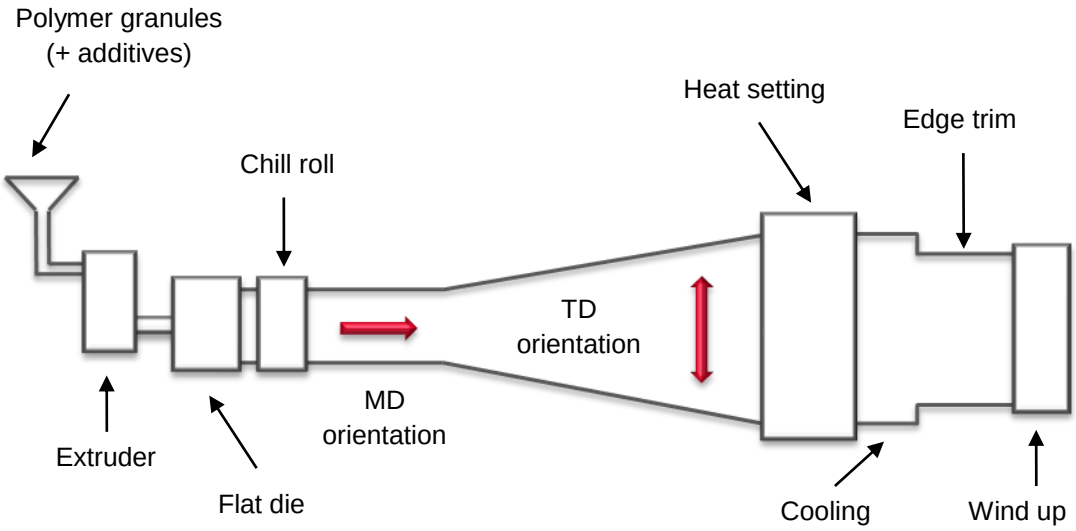

Figure 4-4: Schematic representation of BOPP film production by means of the tenter process (adapted from reference [51])

For the tubular process, a thick-walled cast-tube (=' first bubble') is extruded using a circular die and subsequently is cooled and flattened. After reheating (temperatures similar to tenter process), the tube is expanded to a bubble (= 'second bubble') by injection of air through the die and is at the same time stretched in the machine direction (rolls at the end of the bubble run faster than at the beginning of the bubble), thus resulting in a *simultaneous biaxial orientation* of the film (draw ratio in both directions approximately 1:8 [67]). The bubble is then cooled, collapsed/flattened, slit into two separate films, annealed and wound into a roll. Corona treatment may also be carried out in order to increase the surface polarity of the film. *Figure 4-5* illustrates the described tubular process.

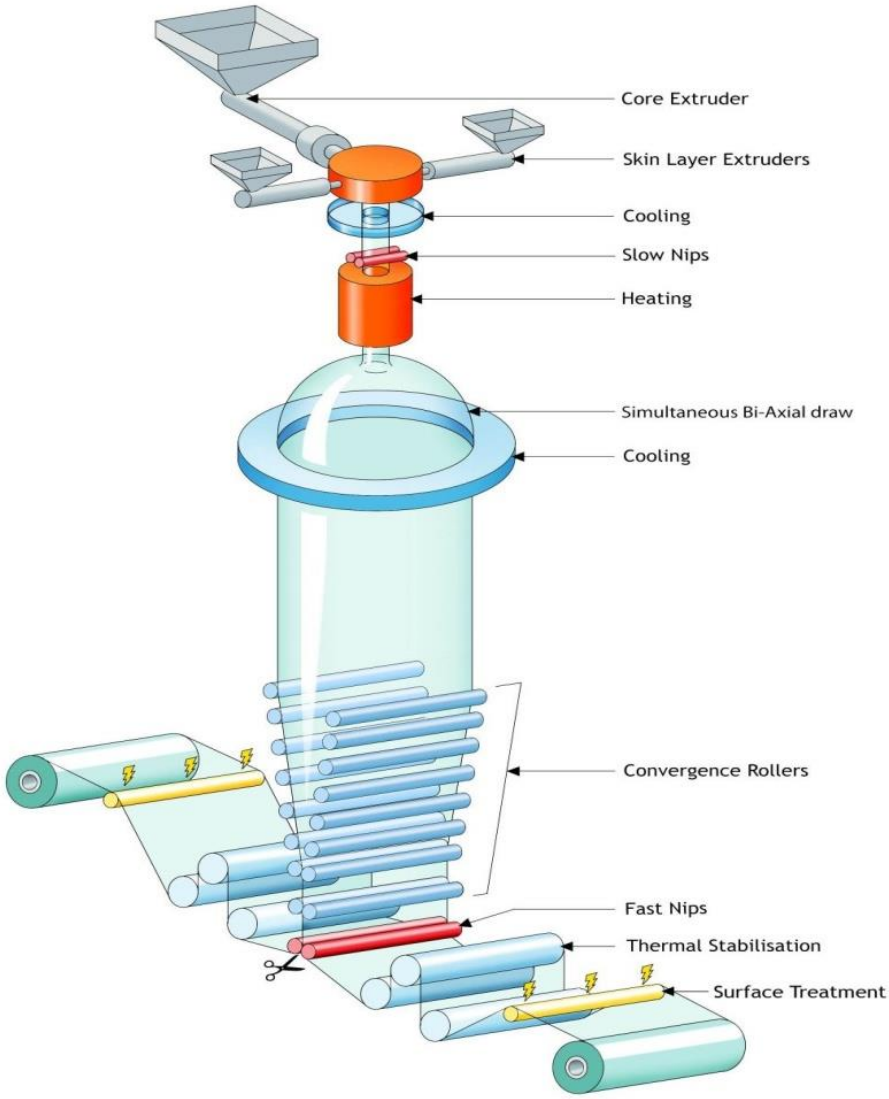

Figure 4-5: BOPP film production via tubular process [source: Innovia films]

The orientation of PP causes an alignment of the polymer chains, hence giving the BOPP film its special end-use properties. This entails a rise of crystallinity, which

improves stiffness and strength (depending on draw ratio). Increased crystallinity also results in good water vapour barrier, which is of great importance for food packaging applications. However, the oxygen barrier is still low, and therefore coating (e.g. PVdC or inorganic barrier layers) of the BOPP film is required. Additionally, the dielectric strength is enhanced by the orientation process and, consequently, BOPP film can be used as an insulating material, for example in capacitors. Further positive effects are the improvement of optical features (such as clarity) and a higher strength at low temperatures. A negative aspect is that with rising stiffness the tear strength decreases. [50, 51]

In general, BOPP films are coextruded, producing a multilayer structure (note the three extruders feeding a coextrusion die and subsequent film orientation in *Figure 4-5*). Standard packaging grade BOPP films for vacuum web coating usually consist of three layers with a PP homopolymer core and a skin layer on each side, as illustrated in *Figure 4-6*. These skin layers are 0.5 to 3 µm in thickness and are made from a PP co- or terpolymer (with ethylene and/or butylene) in order to modify the BOPP film surface and achieve heat-sealability. The outer layers also contain the previously mentioned antiblock particles or slip agents. However, the latter additives are not used for metallising grade films as they entail poor coating adhesion. For metallising grade films, it is, additionally, becoming more common to add antiblock particles only to one skin layer, i.e. the side that is not meant to be coated [69]. Recently, also five-layer and even seven-layer films have become more popular. A five-layer structure, for example, enables the coextrusion of PP with a non-miscible polymer such as EVOH or polyamide via the use of a tie-layer. [67, 70]

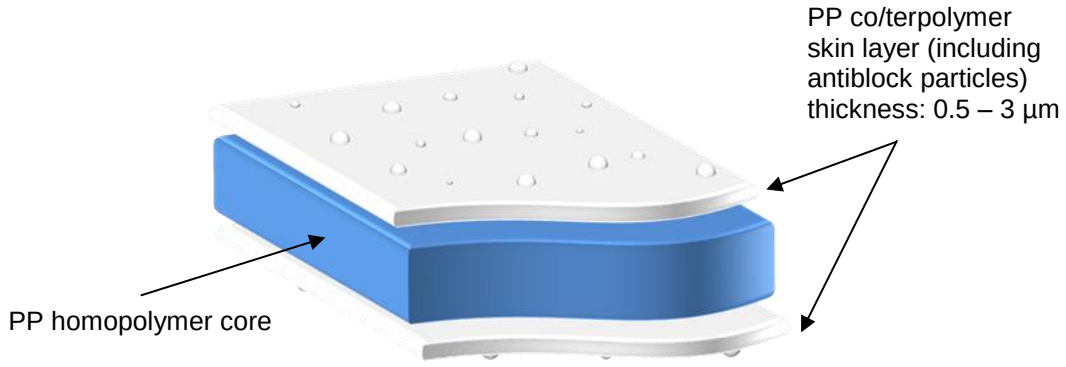

Figure 4-6: Common three-layer structure of standard packaging grade BOPP film

BOPP film is the most important material in the range of PP films, the others being cast (unoriented) PP (CPP) and monoaxially oriented PP (MOPP) film [67].

4.2 Plasma treatment

Due to the hydrocarbon nature of polyolefins, the surface of BOPP film is nonpolar and therefore has low surface energy, which causes the film to be hydrophobic, with poor wettability. This creates significant complications with any kind of further conversion, which involves adhesion of other materials to the film, such as laminating, printing or coating. Controlled surface oxidation of the film increases surface energy and thus leads to enhanced adhesion of adhesives, inks or inorganic coatings. Plasma pre-treatment is one of several methods that can induce surface oxidation of the film. [67]

4.2.1 Plasma description and characteristics

Plasma is the fourth state of matter and describes an ionised or partly ionised, gaseous and conductive environment. The name ‘plasma’ is due to Irvin Langmuir, who introduced this term as he believed it was analogous to biological plasma. A plasma contains a variety of different species, such as electrons, ions, neutral atoms/molecules, radicals, excited species and also photons (ultraviolet (UV) to visible radiation). As the amounts of positive and negative charges are identical, the plasma can be described as quasi-neutral. The various species within the plasma are created by different chemical processes, mainly due to inelastic collisions of electrons, gas atoms/molecules or ions. These reactions include ionisation, excitation, dissociation, charge transfer and recombination, but also photoionisation, photoexcitation and relaxation. A main characteristic of a plasma is that, depending on the type of gas used, the plasma glows a particular colour. This is caused by emission of electromagnetic radiation during relaxation of excited plasma species. [71, 72]

To initiate and sustain all these reactions and hence preserve a stable plasma state, energy needs to be continuously added. This can be achieved by means of thermal energy (e.g. heat source), different kinds of radiation (e.g. electromagnetic radiation like UV) or electrical energy (e.g. an electric field). The type of energy input has a substantial effect on the kind of plasma that is generated and its properties, such as the quantity (flux) of the different plasma species and their energies. [71, 73]

Plasmas can be established at different pressures. Therefore, one can distinguish between low-pressure plasmas, high-pressure plasmas and atmospheric-pressure plasmas (e.g. corona treatment may be regarded as type of atmospheric-pressure plasma). Typically, low-pressure plasmas are utilised as in-line film pre-treatments prior to vacuum web coating. [72]

Another important characteristic is the plasma temperature. In general, the plasma does not have a single temperature, but different temperatures for various plasma species (electron temperature, ion temperature and gas/neutrals temperature). High-pressure plasmas are so-called isothermal plasmas or equilibrium plasmas, as ions, electrons and neutral gas species have approximately the same temperature. In low-pressure plasmas electrons have a relatively high temperature, while ions and gas molecules are at low or ambient temperatures. Therefore, they are called non-isothermal plasmas, non-equilibrium plasmas or 'cold' plasmas. Since low-pressure plasmas ensure minimal thermal stress, they are ideally suited for treatment of sensitive materials like polymers. [71, 74]

The temperature is directly related to energy, and thus these two parameters can be regarded as equivalent (1 eV ≙ 11600 K). The energy of plasma species, such as UV photons or atomic species, needs to be high enough in order to break covalent bonds of the polymer. Further important features of plasmas are the densities of the different plasma species (for example charge carrier density) and the degree of ionisation. These plasma characteristics can vary from position to position within the plasma and are therefore not uniform. [71, 72]

4.2.2 Effects of plasma treatment on polymers

Plasma pre-treatment of polymer films is used to modify and improve surface properties of the material. During treatment, the different energetic particles and UV-photons present in the plasma strike and interact with the polymer surface. If their energy is sufficiently high, they can break covalent bonds in the carbon backbone and induce chemical reactions. The various effects that plasma can have on the polymer surface are: [74-76]

Cleaning: An important effect of plasma treatment is the cleaning of the polymer surface from loosely-bonded organic contamination in the form of low-molecular-weight material, such as oligomers or polymer additives (e.g. antioxidants, slip additives). However, contamination such as debris is unlikely be removed by plasma treatment (even with some degree of etching, see below), due to the different forces and mechanisms attaching them to the polymer surface [4].

Ablation/Etching: Unlike cleaning, a greater amount of material is removed from the surface by plasma etching. This ablated material generally originates from the polymer itself, like a weak boundary layer consisting of low-molecular-weight polymer chains or amorphous parts in semi crystalline polymers, which are etched at a higher rate than the crystalline regions. Etching can result in *smoothing* [77, 78] as well as *roughening* [79, 80] of the polymer surface.

Cross-linking (casing: cross-linking via activated species of inert gases): This effect is due to the use of noble gases for polymer plasma treatment. Noble gases are not able to create functional groups on the polymer surface, but can cause bond breaking within the polymer chains. Consequently, cross-linking and branching can occur. However, some researchers revealed that cross-linking may also take place on plasma treated polymers when reactive gases such as oxygen are used.

Chemical modification/activation: When pre-treating BOPP films, chemical modification is the desired effect of plasma treatment. Reactive gases like oxygen form plasma species that react with the polymer surface by creation of polar functional groups (in case of oxygen mainly hydroxyl, carbonyl and carboxyl groups) and thus increase the surface polarity. These functionalities can interact with the depositing vacuum coating, hence giving rise to better adhesion. As the polarity may decrease with time of storage (ageing), plasma pre-treatment is applied in-line prior to deposition. In industrial applications, BOPP is mostly treated by plasmas containing oxygen.

4.2.3 Further pre-treatment possibilities

Several types of surface pre-treatment exist for use on polymers. These treatments have similar effects on the surface as described in the previous chapter and generally serve the goal of improving adhesion to the polymer and boosting performance of the final product.

Corona pre-treatment: This important and widely used method of surface activation is considered a type of plasma treatment. However, it is performed at atmospheric pressure (referred to as 'ionised air'). Thus, it is usually applied at film production site (see Chapter 4.1.2). The main purpose of the treatment is to form polar functional groups at the film surface. Nevertheless, compared to other plasma treatments, corona treatment is less uniform, and the effects are known to decay with time/storage due to ageing processes. [67, 81]

Flame pre-treatment: This treatment can also be classified as a type of plasma treatment under atmospheric conditions. During flame treatment, the film surface is exposed to a combustion flame (generally methane, propane or butane) with an excess of oxygen (oxidising flame). The chemical effects taking place are similar to corona treatment. To prevent thermal stress, the film passes over a chilled roll during treatment. In comparison to corona treatment, flame treatment is used less frequently. [67, 82]

Chemical pre-treatment: Wet-chemical treatment of polymeric film surfaces also represents an important pre-treatment method. Similar to the previously mentioned techniques, the surface is oxidised and etched. This can be achieved, for instance, by means of strong acids (sulphuric acid, chromic acid). Chemical treatments are applied to a lesser extent than plasma treatments due to the associated environmental concerns. [74, 83]

Ozone pre-treatment: On using this procedure, the polymer surface is treated by exposure to ozone (with or without UV radiation). It is believed that oxidation takes place and functional groups are formed. Researchers observed that ozone treatment without UV radiations shows less efficiency. Nevertheless, this form of treatment is not commonly applied on an industrial scale. [59, 84]

Solvent pre-treatment: Solvent cleaning of polymers can remove contaminations and additives and, thus, adhesion may be improved. However, some polymers may be attacked and their properties degraded by contact with certain solvents. [85]

Mechanical pre-treatment: By grinding, blasting, brushing or similar processes contaminants are removed from the polymer surface, whilst surface roughness is increased. This can results in enhanced adhesion. [85]

In the industrial application of polymer film treatments, corona, flame or chemical treatments are commonly used. In contrast to low-pressure plasma pre-treatment, which is applied in-line prior to the vacuum deposition process, the former methods are usually carried out in-house by the film manufacturer. Performing a pre-treatment in-line, only moments before vacuum coating, reduces any changes of the treated polymer surface due to ageing.

With all types of film treatment, it is also of great importance to prevent over-treatment and thus degradation of the polymer and formation of a weak boundary layer consisting of low-molecular-weight oxidised material. This will, in turn, be detrimental to the adhesion properties of vacuum deposited coatings. [4, 77, 86]

In addition to in-line plasma treatment, modern aluminium metallisers may also offer the possibility of in-line post-treatment after coating deposition. This can improve the properties of the coated films (e.g. barrier) and also has an effect on the downstream processability (e.g. laminating, printing).

It is important to state here that most of the commercially available ‘corona’ treatment systems (e.g. the corona treaters at film manufacturer’s site) are somewhat incorrectly termed as ‘corona’ treaters, as they do not make use of ‘true’ coronas but rather atmospheric dielectric barrier discharges [63, 87, 88]. A ‘true’ corona uses an asymmetric electrode arrangement, e.g. a pointed and a planar electrode, with the streamers formed at the small, pointed electrode being extinguished before they reach the other electrode [87]. Hence, both electrodes can be metallic. The ‘corona’ treatment employed when treating polymer films uses a dielectric sleeve to cover one of the electrodes [81] and consequently creates a type of dielectric barrier discharge, although the electrode geometry can be somewhere between ‘true’ corona (asymmetric electrode arrangement) and dielectric barrier discharge (symmetric electrode arrangement).

The term corona, though, will be used in this thesis when describing the treated film surfaces, as this is the type of treatment stated in the individual datasheets supplied by the film manufacturers and, furthermore, the true treatment configuration is not known. Nevertheless, one needs to bear in mind the differences between ‘true’ corona and dielectric barrier discharge.

4.3 Vacuum coating

Thin film coatings (ranging from a few nm to several µm) are of great importance in many applications, such as decorative and wear-resistant coatings, solar cells or various devices for electronics/microelectronics (e.g. metallic or transparent electrical conductor films) and optics (e.g. reflective coatings) [72]. When applying inorganic coatings to polymer films for food packaging applications, the intention is to optimise the moisture, gas and aroma barrier performance.

4.3.1 Physical vapour deposition

Different processes have been developed for deposition of thin films. Among those techniques utilised in roll-to-roll vacuum web coating are *physical vapour deposition (PVD)* processes, as well as *chemical vapour deposition (CVD)* processes. During PVD, the coating material is evaporated from the solid phase into the gaseous phase by the introduction of energy (thermal evaporation, sputtering or arc evaporation). The evaporated coating flux is transported to the substrate (film) and finally condenses/deposits at its surface, thus forming a coating layer. Typically, PVD processes take place in a sub-atmospheric environment, either in high-vacuum to reduce gas phase collision of the coating atoms and the inclusion of impurities in the growing coating or in the presence of a reactive gas, e.g. for deposition of oxides or nitrides [89]. CVD processes use precursor gases and involve the decomposition or high temperature reduction of the precursor species in order to deposit the desired coating on the substrate surface. Also here, a reaction with a gas is possible for the formation of compounds such as oxides. If a plasma is applied to induce the decomposition of the precursor, the process is called plasma enhanced CVD (PECVD) or plasma assisted CVD (PACVD). [72, 90]

The three main variants of PVD techniques [91] will be described in the following sections:

Thermal evaporation deposition

For this kind of deposition, the coating material is vaporised via input of thermal energy. This can be achieved in different ways, the most common of which are the following two methods: [72, 89, 90, 92]

Resistance heating: In this case, the coating material is melted and evaporated by means of an electric current passing through (and thus heating) a wire (in contact with the coating material) or a boat/crucible (filled with the coating material). These sources are usually made from high melting point materials. In industrial roll-to-roll

systems, resistance heated boats (commonly made from intermetallic mixtures) are used, onto which the coating material is fed continuously in the form of a wire.

Electron beam evaporation: An electron beam is focussed onto the coating material (in a crucible) in order to melt and evaporate it. The electrons are accelerated by high voltages, and electric/magnetic fields are applied to focus and bend the beam onto the coating material. This method offers the advantage that even high melting point materials such as tungsten can be evaporated.

Figure 4-7 illustrates the resistance and electron beam evaporation techniques.

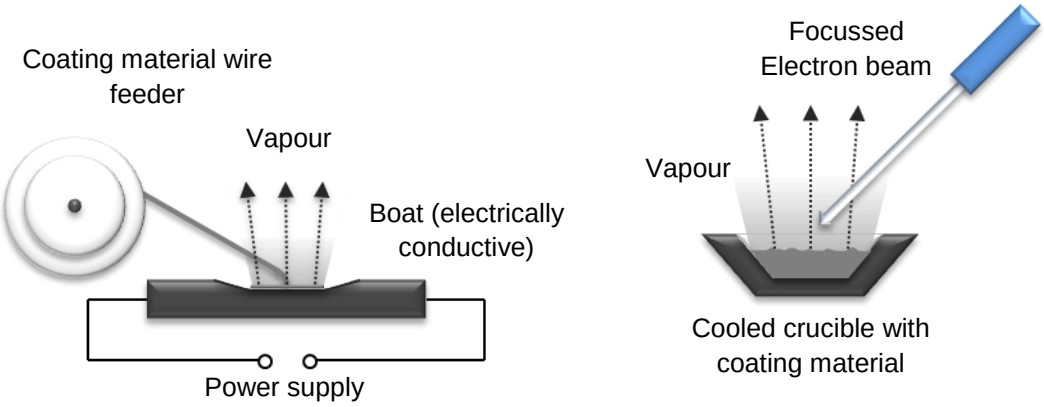

Figure 4-7: Evaporation of coating material via resistance heating (left) and electron beam heating (right)

Plasma assisted evaporation is also possible (resistance heating or electron beam evaporation), e.g. for the deposition of transparent aluminium oxide coatings [25, 27].

Further evaporation possibilities include *induction heating, radiant heating, arc-discharge* or *laser*. Induction heating, for example, has been used in Japan to produce transparent barrier layers based on silicon oxide [4].

Sputter deposition

In contrast to thermal evaporation deposition, the sputter process uses an inert gas to 'physically vaporise' the coating material. During sputter deposition processes, energetic gas ions originating from a plasma are accelerated towards the target (a solid plate of the source material, which acts as the cathode) by an electric field, bombard it and, if their energy is sufficient, knock atoms/atom clusters out of its surface through a momentum exchange mechanism. These atoms/atom clusters then diffuse to the substrate (located opposite the target), where they are deposited as a thin film. Additionally, secondary electrons are released from the target. These

electrons are of great importance for sustaining the plasma. In general, inert gases such as argon are used at a pressure of about 0.1 to 1 Pa to create the plasma. To reduce gas phase scattering of the sputtered particles, the distance between target and substrate needs to be relatively short (typically 60 to 100 mm). A *magnetron sputter source* uses a magnetic field, which is configured parallel to the target surface, in order to increase the yield of sputtered particles and secondary electrons. Hence, the electrons are trapped in immediate vicinity of the target surface, which increases the electron-atom collision rate. This, in turn, results in an enhanced ionisation in the plasma, which provides increased levels of target bombardment and thus increased sputtering and deposition rates. The magnetic confinement of the plasma also lowers the required operating voltage and enables operation at a lower sputtering pressure. [72, 91, 93]

The main principle and components of the magnetron sputtering process are schematically shown in *Figure 4-8*.

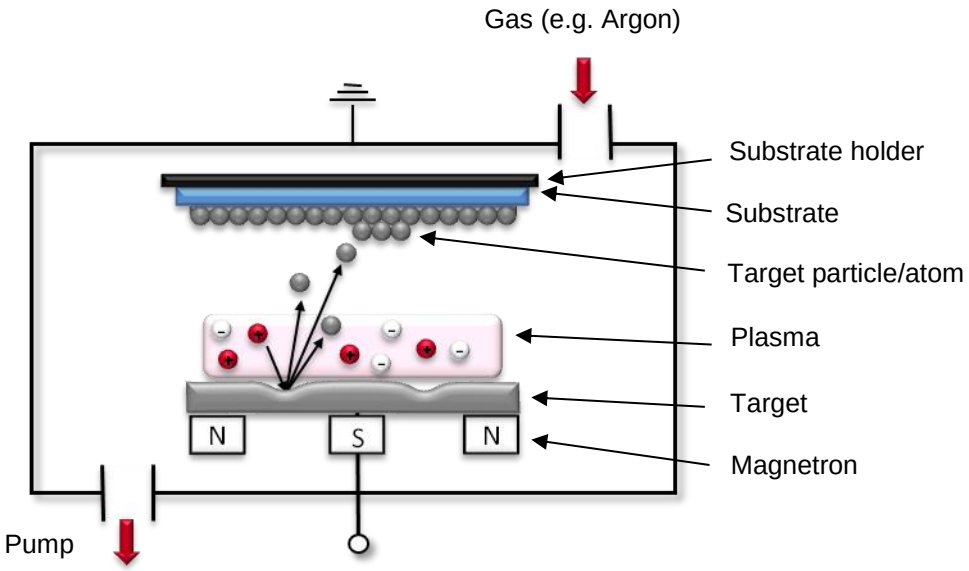

Figure 4-8: Basic principle of magnetron sputtering process

Ion plating deposition

During ion plating, the substrate and the condensing coating material are exposed to a persistent concurrent bombardment with highly energetic particles. These particles are ions (and recombined energetic neutrals) that derive from a reactive/inert gas or even from the depositing coating material itself. The ions can be generated by a plasma in the substrate region or remotely by an ion-beam ('ion-gun'). Thermal evaporation, sputtering and other processes are used to create the coating flux. This deposition process gives good adhesion of the coating to the substrate, and dense coatings can be achieved. [72, 91]

4.3.2 Vacuum web coating

Vacuum web coating takes place in so-called roll-to-roll systems (see *Figure 4-9*). These consist of special winding mechanisms that enable a semi-continuous coating process. The roll of film is placed into the coater, and a vacuum is generated. The film is then unwound from the original roll, pre-treated using an in-line plasma process (if required), coated whilst passing over the coating drum and then the film is rewound onto a second roll. The coating drum can be cooled during evaporation in order to prevent thermal stress within delicate films. The choice of the source for the coating material depends on factors including the material itself, the required web speed during coating and the aimed uniformity of the coating thickness. In the majority of cases, resistive evaporation, electron beam evaporation or sputter deposition are utilised. [67, 89]

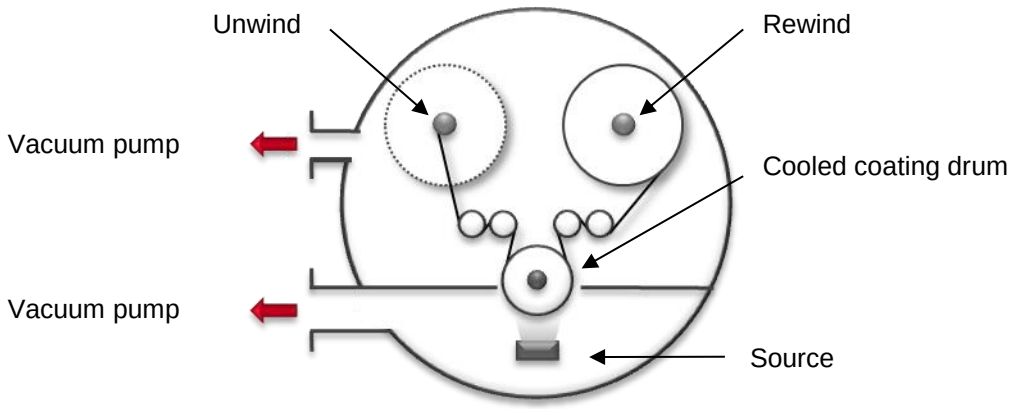

Figure 4-9: Mechanism of vacuum web coating (adapted from reference [67])

In industrial film metallising for packaging applications, speeds up to 1000 m/min and a coating width of 4.45 m [4] are possible. Film rolls with a length of more than 60000 m can be coated within one run. Primarily, wire-fed resistively heated evaporation boats are used as an evaporation source. These coaters are generally referred to as metallisers. Coating thickness is monitored in-line during coating via special sensors, e.g. an optical beam (measures optical density (OD) or light transmission) or an eddy current probe (measures electrical resistance). Feedback loop control allows the wire feed rate to be adjusted in order to maintain optimal and uniform coating thickness. [13, 92]

4.4 Conversion of vacuum coated films

A polymer film, vacuum coated with a thin inorganic barrier layer, will always require further conversion processes in order to obtain the final flexible packaging material. This is necessary to protect the thin barrier layer from damage and consequently loss of barrier properties and intended functionality during packaging application. The protection can be achieved by laminating the coated film against another polymer film and thus embedding the barrier layer between two polymer films or by applying another, polymer based, organic coating on top of the inorganic layer. In addition to the task of protecting the barrier layer, conversion processes are used to confer further functional properties to the vacuum coated film such as heat-sealability (e.g. lamination against a heat-sealable film or applying a heat-sealable topcoat). Moreover, printing is used to enhance the customer appeal of the packaging material as well as to provide the customer with necessary information. Finally, coating and lamination can also be applied in order to satisfy food contact requirements of the materials used.

Lamination describes a process whereby two or more webs are combined by bonding them to one another, generally under application of temperature and/or pressure, and can be achieved either by *adhesive lamination* or *extrusion lamination*. For the latter process, the webs are joined together using a molten thermoplastic polymer, frequently polyethylene, extruded between the materials. In the case of adhesive lamination, one can distinguish between dry and wet processes. The former ones require drying prior to combing the webs, which is the case for hot melt adhesives and certain solvent- or water-based adhesives. During wet processes, no drying is conducted prior to combining the webs. Solventless adhesives, which do not need any drying process at all, fall under this category as well as some solvent- or water-based adhesives. For the latter ones, though, drying is performed after joining the webs and, consequently, one or more of the materials is/are required to be permeable to the solvent/water. Furthermore, there are adhesives that can be cured via electron beam or UV irradiation. Similarly to the application of printing inks (see later), there is also a variety of ways to apply the adhesive onto the polymer web (e.g. gravure, smooth roll, flexo). [1, 67, 94]

Coating (topcoating) can be carried out instead of lamination in order to protect the inorganic barrier layer. A broad variety of coating chemistries, as well as (application) techniques (in atmosphere or under vacuum), is available. Mentioned here should be extrusion coating, similar to extrusion lamination, and coating of solutions, emulsions and dispersions, which are very similar to the application (and drying) of the adhesive during lamination, but in both cases without adding a second

web [95]. There are, furthermore, vacuum deposition processes for organic topcoats usually carried out in-line with the deposition of the inorganic barrier layer (i.e. without breaking the vacuum), such as acrylate flash evaporation deposition, which according to Yializis [96] has the capability to replace lamination processes. Nevertheless, a large-scale industrial realisation of this deposition technique has not taken place, due to the limitations and problems associated [97]. Another vacuum deposited topcoat, which has been employed on an industrial scale, is a melamine based coating trademarked as 'Freshure', which additionally also provides barrier properties [98]. It may sometimes also be necessary to use a primer (very thin coating) or pre-treatment (see Chapter 4.2) in order to boost the adhesion of the topcoat to the required level [1]. As well as topcoats, some of these layers can also be applied prior to deposition of inorganic barrier layers as undercoats.

Printing onto flexible packaging materials is mainly accomplished via two processes, gravure printing and flexographic printing, which distinguish themselves in the way the ink is applied onto the material. If printing directly onto the thin barrier layer is not possible in a satisfactory way, so-called primers (primer coatings) can be applied in order to enhance printability and ink adhesion/reception. [95]

One process, which is inevitably involved during any type of conversion, is the *winding* process. This, and also the other conversion processes, imply that the barrier coating may get into contact with parts of the winding and web handling mechanism, such as rollers, and it is consequently important to avoid stress induced damage and possible loss of barrier. Depending on the downstream process and the web width required therefore, *slitting* can be carried out along with winding the film. [67]

A typical packing structure with vacuum coated BOPP, for example, consists of metallised BOPP laminated against a reverse printed BOPP. This structure then needs to be folded and/or formed into packaging, e.g. via lidding machines or vertical form-, fill- and sealing machines.

4.5 Adhesion

A critical requirement for good performance of vacuum coated films is an acceptable level of adhesion of the coating to the base substrate. This is not only of importance for further processing/converting operations (e.g. to reduce delamination), but may also affect the final properties of the product, for example barrier performance.

4.5.1 Definition of adhesion and cohesion

Adhesion is a complex phenomenon affected by many parameters. The term *adhesion* can be defined in different ways, mainly depending on the field of application. According to the American Society for Testing and Materials (ASTM D907), *adhesion* is “the state in which two surfaces are held together by interphase forces” [99]. In addition to that, the ASTM distinguishes between *mechanical adhesion* – “adhesion between surfaces in which the adhesive holds the parts together by interlocking action” [99] – and *specific adhesion* – “adhesion between surfaces which are held together by intermolecular forces of a chemical or physical nature“ [99].

Cohesion is the phenomenon that occurs within a homogeneous material and keeps the molecules/atoms together by interatomic and intermolecular forces. These forces act between all neighbouring atoms/molecules. At the surface of a homogeneous material, however, the cohesive forces cannot be shared in all directions as neighbouring ‘partners’ are missing. Thus, atoms/molecules located at the surface try to overcome this issue via ‘looking for other partners’, which is the first step leading to the phenomenon of adhesion. [100, 101]

4.5.2 Adhesion theories

To explain the phenomenon of adhesion, a variety of models has been developed and established, the so-called *adhesion theories*. The number of theories given in the relevant literature may vary and, furthermore, exact boundaries between some of the different theories cannot always been drawn (see e.g. adsorption/chemisorption/thermodynamic theories of adhesion) [83, 100-103]. None of the models/theories, however, offers a universal solution to the occurrence of adhesion. So the theory which is applicable to a certain adhesion event depends on the individual situation. It may involve only one or a combination of several adhesion theories. Therefore, the appropriate theory/ies have to be selected on a case-by-case basis. [83]

The following models are presented in accordance with the ASTM definition stated above, divided into mechanical and specific adhesion cases.

Mechanical adhesion *(mechanical theory)*

The simplest and oldest attempt to explain adhesion is the mechanical theory. This model describes the interlocking of two different surfaces via a 'lock-and-key' effect due to surface irregularities and roughness. The adhesive (or in our case the evaporated coating) penetrates into the pores and cavities of the surface and, thus, the materials are joined together. This kind of interlocking can occur on the macro-scale as well as on the micro-scale [104]. The model of mechanical interlocking is, for example, used to explain adhesion for electroless plating of polymers. In this case, the polymeric material is initially treated to roughen its surface and afterwards plated with the metal. [101-103]

However, this model cannot explain the fact that strong adhesion can also be achieved on smooth surfaces. Therefore, the different theories of specific adhesion are applied. This fact may also lead to the question of whether mechanical adhesion can be seen as an independent mechanism of adhesion at all. Since pores and irregularities increase the contact area between surface and coating/adhesive (in comparison to smooth surfaces), the effectiveness of specific adhesion mechanisms is enhanced, and this might be the reason for high adhesive strength on rough surfaces. [83]

Specific adhesion

Specific adhesion includes all models that involve physical, chemical or thermodynamic interactions at the interface between the two surfaces [100].

Electrostatic theory

The theory of electrostatic interaction was originally developed by Derjaguin et al. [105]. As soon as two surfaces of different origin are brought into contact, the difference in the chemical potential of these materials (e.g. polymer and metal) results in a charge carrier diffusion of electrons and thereby in the formation of an electrical double layer at the interface. Thus, a system similar to a plate capacitor is created between the two materials. The electrical attraction within the double layer gives the adhesive strength and is accountable for the observed resistance to separation. Weaver [106] was the first to provide proof of electrostatic interactions taking place between polymers and vacuum evaporated metals. [101, 107]

Diffusion theory

This theory uses the phenomenon of fractional Brownian motion to explain the adhesion between two surfaces and has been introduced by Voyutskii. He suggested that when two materials (usually polymers) are placed into close contact with each other, inter-diffusion of molecules or polymer chains across the interface occurs. Hence, the two materials are interlocked by entanglements. Main requirements for this mechanism are mutual solubility, mobility of the molecule segments and a temperature above the glass transition temperature, as the fractional Brownian motion is temperature-dependent. This model is only applicable to a few situations, for instance the welding of plastics. However, the theory explains the adhesion of one polymer to itself (so-called '*autoadhesion/autohesion*'), which, for example, may cause blocking of certain polymer film rolls. Faupel et al. [108] observed the diffusion of metal atoms into polymers and state that this may account for enhanced adhesion of metals deposited onto polymers. Furthermore, also Bartha and co-workers [109] discuss a possible diffusion of aluminium into a polyimide surface at elevated deposition temperature. [83, 100, 103]

Theory of chemical interaction (also referred to as *adsorption theory* [102])

This theory is the most commonly applied concept for adhesive strength. It predicates that adhesion is due to a range of forces interacting between the molecules and atoms located at the surfaces of the two materials. Thereby, the following forces can be involved; primary bonds, such as covalent, ionic or metallic bonds, acid-base interactions and secondary bonds, e.g. hydrogen bonds and several types of Van der Waals forces. Which interactions, however, are of importance in a certain situation, depends on the chemical properties of the materials. Generally, Van der Waals forces are involved in nearly every case as they are universally present. A common requirement for all these types of interactions is a sufficiently close contact between the two surfaces as the forces only act over a small distance. *Table 4-1* shows the strength (bond energy) and acting range of the different forces. The theory of chemical interaction suggests that the same interatomic and intermolecular forces that account for cohesion within a homogeneous material also cause adhesive strength at the interface between two different materials. [83, 102]

One can also say that the theory of chemical interaction combines and generalises the *polarisation theory* of De Bruyne (principle: dipole character of molecules [100]) and the *chemical bonding/chemisorption theory* (adhesion via primary chemical bonds [103], sometimes hydrogen bonding is included in this theory as well). Definition and classification of bond types considered for this adhesion theory vary

in literature. Some authors may only take Van der Waals forces into account for the adsorption theory, whilst others include all types of bonds/interactions (as is the case in this thesis). To determine the adhesive forces present at the interface, thermodynamic measurement techniques can be applied.

Table 4-1: Primary and secondary bonds [110]

Bond type	Bond energy	Equilibrium length
	kJ/mol	nm
Primary, chemical		
Ionic	600 – 1000	0.2 – 0.4
Covalent	60 – 800	0.1 – 0.3
Metallic	100 – 350	0.2 – 0.6
Acid-base interactions		
Conventional Brønsted	< 1000	
Lewis	< 80	
Secondary, physical		
Hydrogen bonds	~ 50	0.3
Van der Waals		
Permanent dipole – dipole interactions (Keesom)	5 – 20	0.4
Dipole – induced dipole interaction (Debye) [111]	< 2	< 1
Dispersion forces (London)	1 – 40	< 1

Thermodynamic theory

The fundamental principle of this model is the process of wetting and spreading. According to the thermodynamic theory, adhesion is generated by adsorption (involving Van der Waals forces) of the coating material to the substrate material, if both materials are in immediate molecular contact. The adhesive strength depends on the surface energies of the materials. Many methods have been developed to measure surface energies for solids and liquids, like the Wilhelmy plate method (for solids), the pendant drop method or the spinning drop method (both for liquids). Nevertheless, the most commonly applied method (for solids) is the contact angle measurement via the sessile drop method, which will be described later in this thesis in more detail (refer to Chapter 5.6.3.1). [100, 101, 103]

The thermodynamic theory is closely linked to the chemical interaction/adsorption theory, which may be a reason why this theory is frequently incorporated into the

latter (see Allen [102]). Thus, the question arises of whether the thermodynamic theory can be seen as an independent model itself or whether it just represents a kind of measurement mechanism to characterise adhesive forces/adhesion.

In the application of vacuum coating, it has been shown that a higher surface energy due to polar functional groups created by plasma pre-treatment usually results in a better adhesion of the deposited layer [74]. However, although a high surface energy is generally assumed an essential requirement for strong adhesion, it is not always sufficient in itself. So even if a high surface energy has been measured, this may not necessarily result in strong adhesion of the coating to the substrate film, which has been proven for metallised BOPP by Bichler et al. [77].

Weak boundary layer theory

This theory does not describe an adhesion mechanism but circumstances that may lead to adhesion failure. According to Bikerman [112], an interlayer is formed between the two surfaces, i.e. the substrate and the coating material, so that no direct connection between them is possible. This interlayer presents the weakest point of the joint and usually is the place where failure of adhesion occurs. The layer can be due to many parameters, for instance impurities in the materials or of the environment, inclusion of air or reaction of the material with the environment (for example with air, oxidation). Such a layer may be removed by special pre-treatment methods. [103, 112]

Here, it is important to state that pre-treatment (e.g. with plasma) can also cause the formation of a weak boundary layer and hence reduce adhesion as a layer consisting of low-molecular-weight material can be generated by plasma over-treatment [77].

4.5.3 Measurement of adhesion

Testing adhesion of evaporated coatings to substrate films is of major importance in order to control the coating process and to achieve products of reproducible and constant quality.

On looking for an appropriate method of adhesion measurement, the question emerges whether adhesion can be really measured. Many techniques have been developed to assess adhesion, but, in order to understand what exactly is measured and how to interpret and use the results, two terms need to be defined. Hence, Packham [113], Lacombe [114] and Mittal [115-117] distinguish between *fundamental* or *basic adhesion* and *practical* or *experimental adhesion*:

Fundamental or *basic adhesion* is due to the forces acting between the atoms/molecules at the interface of the two materials and, thus, is tied to the theories of adhesion and the definition according to ASTM. Only on occasion might it be possible to calculate values of fundamental/basic adhesion from a theoretical model or determine them from experimental results, but in most cases fundamental/basic adhesion cannot be calculated or in any way directly measured.

Practical or *experimental adhesion* is the adhesion that is detected by a test method (usually destructive). In the case of thin film adhesion, it is the force or work needed to separate the two materials, i.e. the coating and the substrate. The so-called peel tests or pull-off tests are the most commonly applied tests to detect the bond strength between the deposited layer and the substrate film. One main requirement is that the break should occur at the interface (adhesive failure) and not within one of the materials (cohesive failure). Results obtained via different test methods depend strongly on the specific test conditions and are usually not directly comparable. Consequently, different techniques give different results. The measured value can be seen as the sum of fundamental adhesion and “the work spent in other processes, such as the inelastic deformation of the polymer” [115], since practical adhesion represents a function of fundamental adhesion and additional factors.

A variety of techniques to determine coating-to-substrate adhesion exists, which have been presented in literature [114, 115, 117-119]. Amongst others, peel tests (see above) [77, 120], the fragmentation test [121, 122] and nano-indentation/scratch tests [123-125] play an important role for investigating the adhesion properties of vacuum deposited thin films.

It is, furthermore, important to consider the main requirements for an ideal test. Such a test should be “non-destructive, easily adaptable to routine testing [...], relatively

simple to perform and interpret, amenable to standardization and automation, reproducible and, if possible, quantitative and directly related to coating reliability in specific applications" [118]. However, no test method fulfilling all these requirements exists to date. The most widely used tests in the vacuum web coating industry are the 'scotch tape test' (qualitative test) and the peel test (quantitative test) mentioned above.

4.6 Permeation and barrier properties

Generally speaking, permeation describes the phenomenon whereby a gaseous, vaporous or fluid substance (e.g. oxygen, water vapour but also aromas) passes through a solid material (e.g. film) from one side to another. This process is of great importance for food packaging, since the packaging material needs to provide a barrier in order to minimise permeation of substances out of the packaged produce as well as vice versa. The permeation of oxygen through the packaging material to the food, for example, may accelerate deterioration processes and, thus, decrease the quality of packaged goods.

4.6.1 Permeation through plain polymer films

Gases and vapours can be transported through the polymer (i.e. film) by two different processes: [1]

Pore effect: The gaseous and vaporous substances permeate through the polymer via small pores, pinholes or cracks.

Solution-diffusion effect: The gases and vapours dissolve in the polymeric material and diffuse through it due to a gradient in concentration.

In general, the solution-diffusion model is applied to describe the permeation process of gaseous species through polymer films, as pores are usually undesired and should not be present. The driving force for permeation is a gradient in concentration and partial pressure, respectively, of the permeating substance. Thus, permeation through the film takes place in order to compensate for this difference in concentration. During permeation processes, the following steps take place: [126]

- *Adsorption* (i.e. attachment) of the gas molecules to the polymer surface on the high-concentration side
- *Solution* in the polymeric material
- *Diffusion* through the polymer via fractional Brownian motion due to the concentration gradient
- *Desorption* of the gas molecules from the polymer surface on the low-concentration side, i.e. release of dissolved molecules

Figure 4-10 illustrates the different stages of permeation through a polymer film of the thickness *l.*

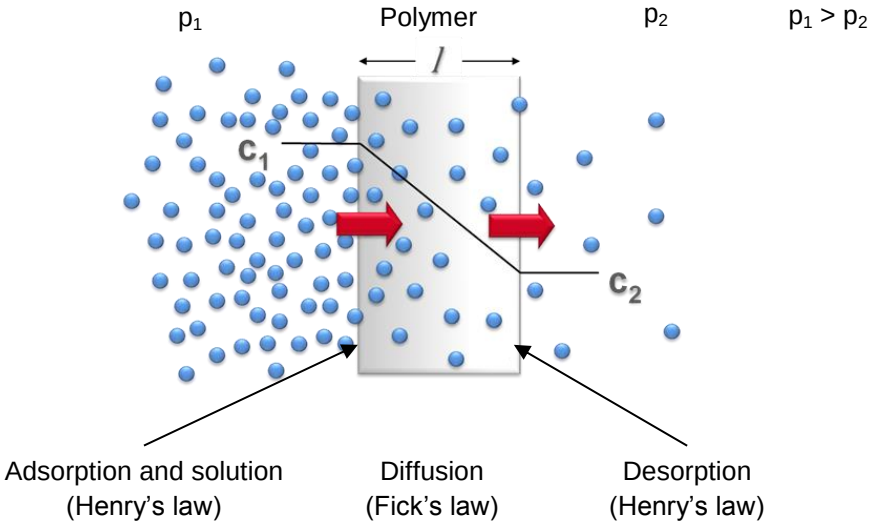

Figure 4-10: Model for the permeation of gases and vapours through polymers (adapted from reference [1])

The following parameters and equations are used to describe the phenomenon of permeation of vapours and gases (permeants): [1, 126]

Fick's first law characterises the diffusion of substances through the homogeneous polymeric film:

$$J = -D \cdot \frac{\partial c}{\partial x} \tag{4-1}$$

Where: J rate of diffusion $[\frac{mol}{m^2 \cdot s}]$

D diffusion coefficient $[\frac{m^2}{s}]$

$\frac{\partial c}{\partial x}$ concentration gradient $[\frac{mol}{m^3 \cdot m}]$

If a steady state (J = constant and no variation of concentration with time) is present, integration of (4-1) yields (illustration see *Figure 4-10*):

$$J = D \cdot \frac{c_1 - c_2}{l} \tag{4-2}$$

Where: l film thickness $[m]$

c surface concentration of permeant in polymer $[\frac{mol}{m^3}]$

In the event of gases, it is more common to use the partial pressure instead of the concentration. The solution of gas molecules in a solid polymer can be explained by means of Henry's law. It represents the relationship between the partial pressure and the corresponding concentration:

$$c = S \cdot p \tag{4-3}$$

Where: p partial pressure [Pa]

S solubility/sorption coefficient [$\frac{mol}{m^3 \cdot Pa}$]

The permeability coefficient (or just called permeability) arises from the following equation:

$$P = D \cdot S \tag{4-4}$$

Where: P permeability coefficient [$\frac{mol \cdot m}{m^2 \cdot s \cdot Pa}$]

The permeability coefficient P, solubility/sorption coefficient S and diffusion coefficient D represent temperature dependent variables and can be further defined using an Arrhenius-type relationship:

$$P = P_0 \cdot e^{E_P/R \cdot T} \qquad S = S_0 \cdot e^{E_S/R \cdot T} \qquad D = D_0 \cdot e^{E_D/R \cdot T} \tag{4-5}$$

Where: P_0, S_0, D_0 constants unique to the system

E_P, E_S, E_D apparent activation energies (specific for each material) [$\frac{J}{mol}$]

T absolute temperature [K]

R gas constant: $8.314\ \frac{J}{mol \cdot K}$

Combining (4-2) with Henry's law (4-3) and (4-4) leads to:

$$J = P \cdot \frac{p_1 - p_2}{l} = Q \cdot (p_1 - p_2) \tag{4-6}$$

The permeance (referred to as 'permeability' by Langowski [126]) $Q = \frac{P}{l}$ [$\frac{mol}{m^2 \cdot s \cdot Pa}$], frequently named transmission rate, is of practical relevance for film samples with a thickness l.

Here, it is important to mention about the inconsistent terminology and use present in literature with regards to the terms permeability, permeability coefficient and transmission rate, which cannot necessarily be used interchangeably. A publication

dedicated to this subject with respect to multilayer laminate structures is by Cooksey et al. [127].

Similarly to the temperature dependence stated above in Equation (4-5), the permeance Q of a polymer can generally be described by an Arrhenius-type equation: [128, 129]

$$Q = Q_0 \cdot e^{E_Q/R \cdot T} \tag{4-7}$$

Where: Q_0 constant/ unique to the system

E_Q apparent activation energy of permeations (specific for each material) $[\frac{J}{mol}]$

This approach is also used for vacuum coated polymer films and enables the investigation of the apparent activation energy of permeation und thus collection of information about permeation mechanisms for vacuum deposited barrier layers, such as SiO_x, aluminium or AlO_x [128, 130, 131].

For composites/laminates consisting of several layers of polymers with the permeance Q_i per layer i, an analogy to electrical conductances in series exists, this is the so-called ideal laminate theory [132, 133]. Therefore, the overall permeance Q_{total} can be determined the following way:

$$\frac{1}{Q_{total}} = \frac{1}{Q_1} + \frac{1}{Q_2} + \cdots \tag{4-8}$$

All calculations presented in this chapter are valid for the following basic assumptions: [1]

- A steady state, one-dimensional diffusion takes place
- A linear gradient in concentration is present
- D and S are independent of the concentration

Oxygen and water vapour (and also aromas) are the permeants of main interest with regards to food packaging. Differences between the permeation of water vapour and gases through polymers exist as water is a polar and reactive molecule and, hence, can interact with the polymer. The extent and type of interaction with water depend on the specific properties of the polymer, and vary strongly for different polymers. Important factors affecting the permeation of gases and vapours through polymers include, amongst others; size and shape of the permeating molecule, polarity

(chemistry) of the polymer and permeant, the degree of crystallinity, cross-linking and orientation in the polymer, the degree of swelling (plasticising) of the polymer in presence of condensable vapours and liquids, the polymer's glass transition temperature and also the system composition with regard to additives, composites, copolymers or polymer blends. Furthermore, the environment in terms of temperature, pressure and relative humidity and, thus, the test conditions for transmission rate analysis will affect the permeation of the substances of interest. [1, 134, 135]

4.6.2 Permeation through polymer films with inorganic coatings

Polymer films are vacuum coated with thin inorganic layers (e.g. AlO_x, aluminium, SiO_x) in order to improve their barrier properties and reduce permeation of water vapour and oxygen.

However, the solution-diffusion model and thus a calculation according to Equation (4-8), which can be used for most polymer multilayer systems, cannot be applied in the case of inorganic coatings due to the structure/nature of the coating, specifically the presence of defects. If the inorganic coatings had the same structure as their respective bulk materials, the expected oxygen and water vapour permeation rates would be by far lower than generally measured [131, 136]. The bulk material, as well as a bulk-like 'defect-free' thin coating, would effectively give virtually perfect barrier properties [137, 138].

The model commonly applied for permeation through inorganic layers on polymer films is the so-called pinhole or defect model shown in *Figure 4-11* (left image). The pinhole model is based on the work by Prins and Hermans [139], who introduced the model to describe the permeation through a metallised polymer film. Since then, further work and modelling, including numerical simulations, have been carried out by a number of research groups [140-150].

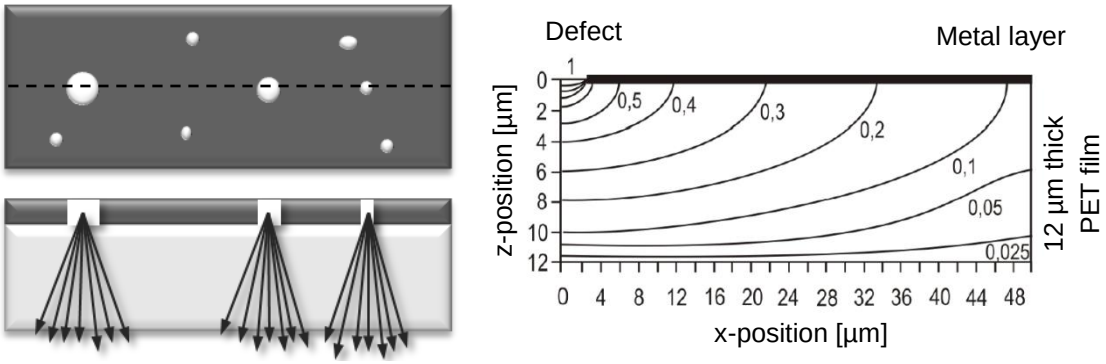

Figure 4-11: Left: Pinhole model (top view and cross-section) [151]; right: normalised concentration profile (created by simulation) around a defect in a metallised 12 µm thick polyethylene terephthalate film [152]

According to the pinhole model, the gases and vapours only permeate through statistically distributed defects ('pinholes'[b]) in the inorganic coating but not through the barrier layer itself, i.e. the rest of the coating apart from the defects is assumed

[b] In general, only larger, i.e. macro-scale (see later in this section), defects are referred to as pinholes. Furthermore, it is worth mentioning that a pinhole is defined here as a defect in the coating layer only, i.e. uncoated area, without any corresponding defect in the underlying polymeric substrate [140].

to be impermeable. After passing through the defects in the inorganic coating, the permeating substances diffuse out in all directions (lateral diffusion) within the polymer, and a three-dimensional concentration profile (see *Figure 4-11*, right image) is created. [151, 153]

Since defects can be classified according to their size, Langowski [126] distinguishes between two types (or size categories) of defects:

- macroscopic defects (a few nm to several µm) and
- microscopic defects or pores[c] (subnanometre range to a few nanometres; can be regarded as comparable/equivalent to the nano-defects in an analogous defect model established by Roberts et al. [131]).

Whilst macroscopic defects can be detected with a range of analytical techniques including optical (for opaque coatings only), scanning electron and atomic force microscopy, the presence of microscopic defects has only been proven indirectly. The permeating substances can pass mainly unhindered through the macroscopic defects; nevertheless, the flow through microscopic defects will be hindered by, e.g., surface diffusion or possibly capillary actions [4]. Langowski's defect classification is similar to a model suggested by Roberts at al. [131] for permeation of gases and water vapour through SiO_x coated polymer films. However, they proposed an additional third transport mechanism through the amorphous lattice of the oxide, which is, though, less important and almost negligible at room temperature. A further, similar categorisation of defects has been developed by Affinito and Hilliard [154].

Defects can be generated by contaminants (e.g. dust contamination being present during the coating process), antiblock particles or high surface roughness of the plain uncoated film. These contaminants/particles and surface irregularities prevent the formation of a homogeneous (defect-free) coating layer. If the coating material is not capable of compensating for these defects, a low coating quality with damaged or uncoated surface areas can result. Another source of defects (also referred to 'transmission gates' in the coating) is the handling of the film after coating. Scratches and coating pick-off can be generated by direct contact between the coating layer and parts of the winding mechanism or antiblock particles (located on the non-coated side of the film). Downstream processing, such as slitting or laminating, can also lead to damage of the inorganic barrier layer. Additionally, the coating process itself and the growth/nucleation mechanisms of the depositing coating layer can be the origin of defects. [126, 132, 133, 140]

[c] It should be noted here that the definition and size classification of pores will vary in literature, depending on the specific reference (see e.g. [4, 131]).

Whilst the permeation of oxygen can be explained quite well to be predominantly due to permeation through macroscopic defects in the coating (see detailed review for transparent oxide coatings by Chatham [155]), additional effects need to be considered in the case of water vapour permeation, and further investigations are still necessary. It is assumed that, in addition to macroscopic defects in the inorganic coating, water vapour may pass through microscopic defects, such as grain boundaries and nano-porous structures [131, 150, 156]. Thereby, capillary condensation [133], attractive/chemical interactions and reactions [128, 157, 158], including dissociation of water vapour [159, 160] or hydrogen bonding [129], may occur.

Numerical simulations (based on macroscopic defects analysed via optical, scanning electron and atomic force microscopy) carried out for metallised BOPP by Hanika et al. [156] show good agreement between the simulated results and the oxygen transmission rates (OTR) actually measured. However, in the case of water vapour transmission rate (WVTR), the measured values are higher than expected based on the numerical simulations, thus indicating additional/different permeation mechanisms for water vapour.

An important quality parameter, which quantifies the effect of a coating on the barrier performance of the polymer film, is the barrier improvement factor (BIF). This characteristic value is defined as the ratio of the permeance (transmission rate) of the plain polymer film Q_0 to the coated film Q [126]:

$$BIF = \frac{Q_0}{Q} \tag{4-9}$$

It is important to note, though, that the BIF value depends on the polymer film thickness (which affects the value of Q_0).

4.6.3 Barrier requirements for packaging applications

Barrier requirements for various applications, including sensitive foodstuffs, are shown in *Figure 4-12*. The barrier performance that can be achieved by a coated polymer film strongly depends on the respective coating technique. Whilst transparent oxide coatings produced via evaporation techniques [32, 34, 64] fulfil the 'moderate' barrier requirements for food packaging, PECVD [161, 162] and sputtered [163-165] coatings on polymer films can provide even better barrier performance. By the use of atomic layer deposition, water vapour transmission rate values in the range of 10^{-3} to 10^{-5} g/(m^2 d) and oxygen transmission rate values below 4 x 10^{-3} cm^3/(m^2 d) can be achieved [11, 166-168].

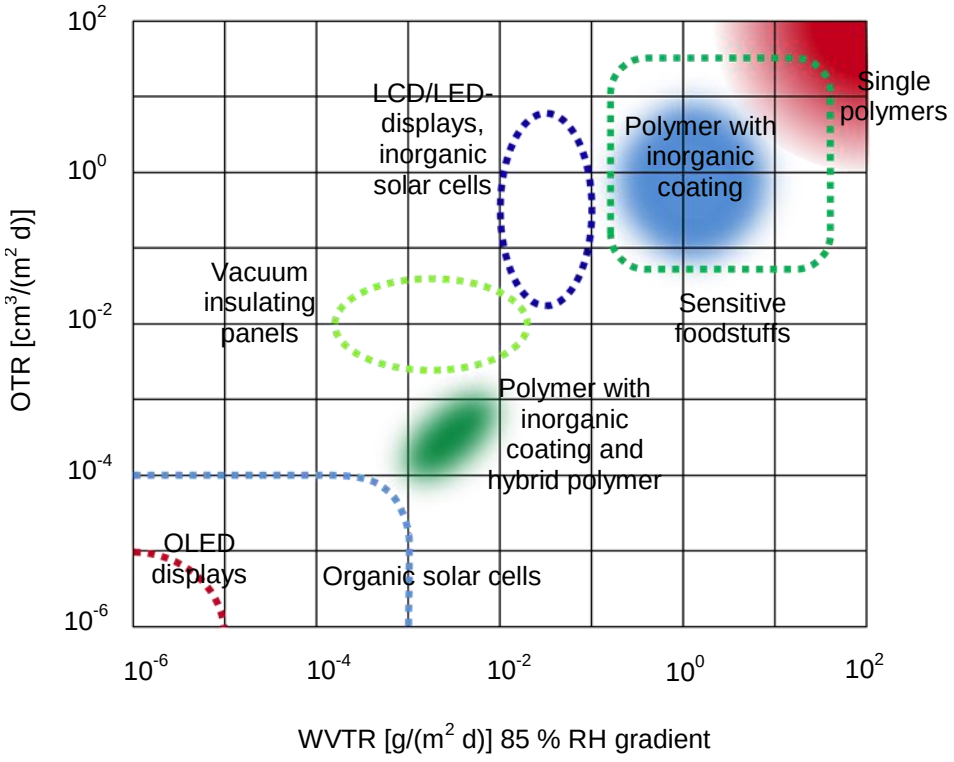

Figure 4-12: Barrier requirements for various applications (dotted lines) and barrier performance of flexible polymer systems (shaded areas); reference temperature 23 °C [133]

More detailed information on the oxygen and water vapour barrier requirements for a selection of sensitive foodstuffs, such as coffee, oil or meat, and pharmaceutical products is given in *Figure 4-13*.

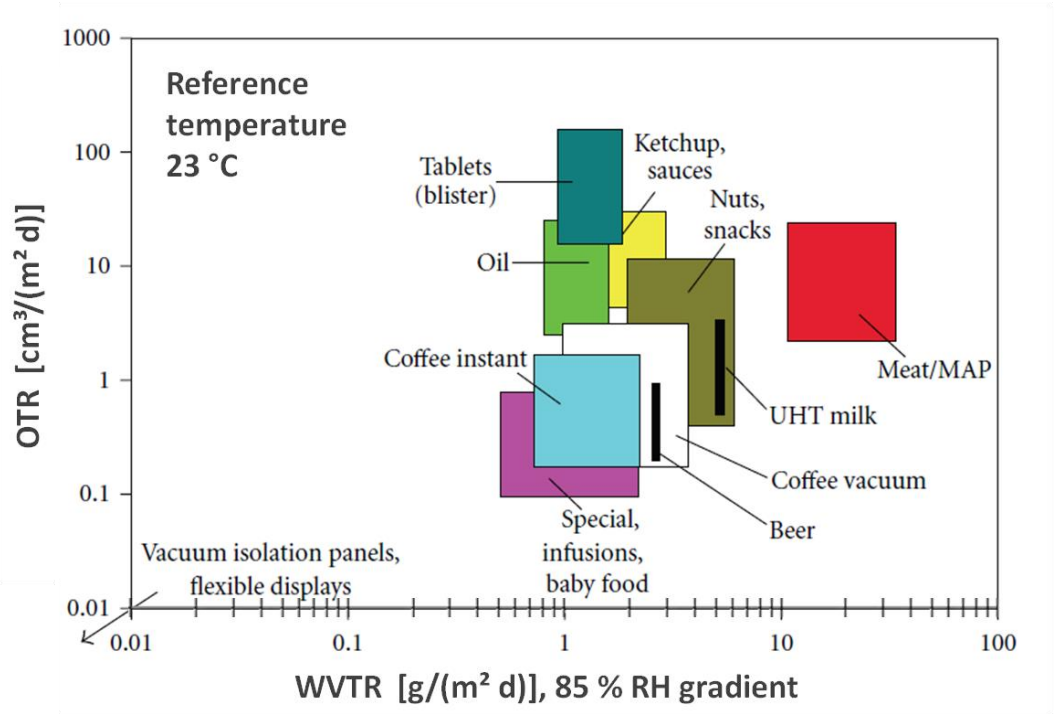

Figure 4-13: Barrier requirements for various sensitive foodstuffs and pharmaceutical products [169]

5 EXPERIMENTAL DETAILS

5.1 AlO_x coating process and roll-to-roll vacuum coater

The deposition of the transparent AlO_x barrier layers is achieved via reactive thermal evaporation of aluminium, using a 'boat-type' roll-to-roll metalliser. Therefore, aluminium wire is continuously fed onto resistively heated boats, where it evaporates and forms an aluminium vapour cloud. Oxygen is introduced into the aluminium vapour cloud, reacts with the coating flux (presumably on the substrate) and a transparent aluminium oxide film is deposited onto the web as it passes with a set speed over the coating drum. This basic principle of reactive thermal evaporation is further illustrated in *Figure 5-1*.

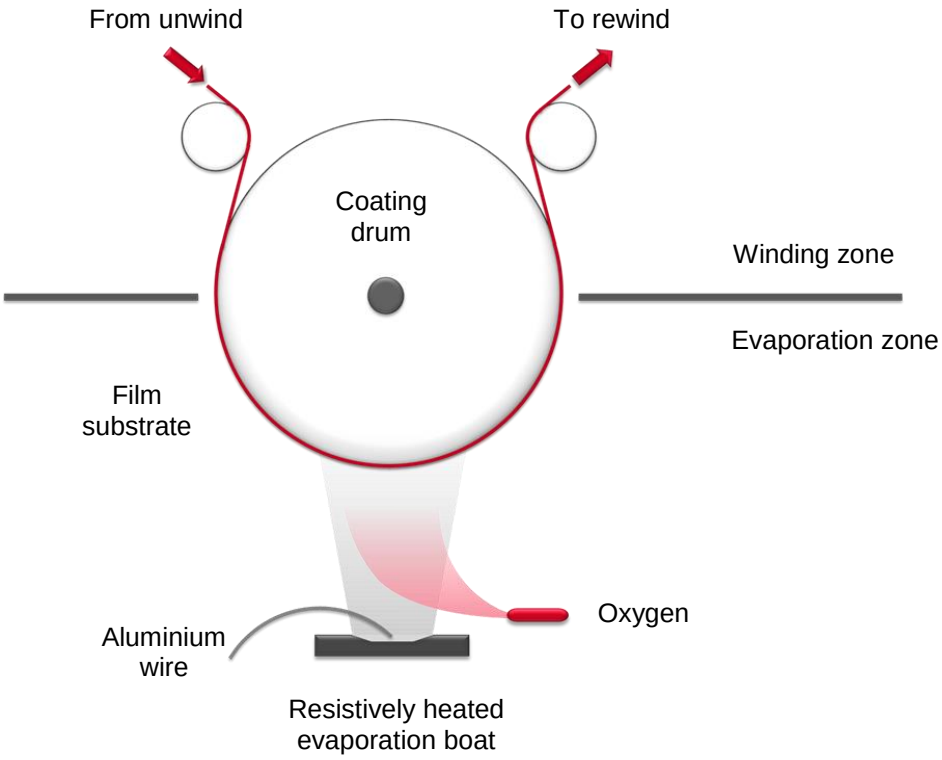

Figure 5-1: Schematic representation of reactive evaporation of aluminium for the production of transparent AlO_x barrier coatings via a roll-to-roll process

The coating trials were conducted on industrial roll-to-roll vacuum web coaters with AlO_x coating systems at Bobst Manchester Ltd., formerly General Vacuum Equipment (Manchester, United Kingdom). The roll coater models used for the trials were a K4000 and a K5000 metalliser. The K4000 machine provides an in-line source of resistively heated evaporation boats and allows coating of a maximum web width of 2450 mm, whilst the K5000 has a staggered arrangement of the evaporation boats and can handle web widths up to 2850 mm. Films were coated at a web speed of 420 m/min and, additionally, in-line plasma pre- and post-treatments with optimised gas recipes (with oxygen) were conducted. An image of a K5000

vacuum web coater is shown in *Figure 5-2*, whilst the main components (apart from the pumping system and electronics) of the vacuum web coater (in this case a K4000) are illustrated in the cross-section of *Figure 5-3* and further described in *Table 5-1*.

Figure 5-2: K5000 vacuum web coater at Bobst Manchester [source: Bobst]

For the deposition process, the vacuum coater is initially pumped down to a base pressure of 1 to 5 x 10^{-5} mbar (0.001 to 0.005 Pa) in the evaporation chamber. After heating up the boats, feeding aluminium wire onto the boats and accelerating the web to the required line speed, the shutter is opened to enable coating of the film. Oxygen is added and similar to the aluminium metallisation process, a control loop is used to monitor the optical properties (i.e. OD or light transmission) of the coated film via an optical transmission beam (operating at a wavelength of 626 nm) and control the deposition to a certain OD set point. Depending on the specific platform and process, the pressure in the evaporation zone during deposition is between 1 x 10^{-4} and 1 x 10^{-3} mbar (0.01 to 0.1 Pa), while the pressure in the plasma treater units is kept between 2 – 5 x 10^{-2} mbar (2 – 5 Pa). Aluminium wire with a minimum aluminium content of 99.8 % (1.6 mm diameter, produced by Manfisa, Irurtzun, Spain) and oxygen gas with a purity ≥ 99.5 % (supplied by BOC, UK) was used for the coating trials.

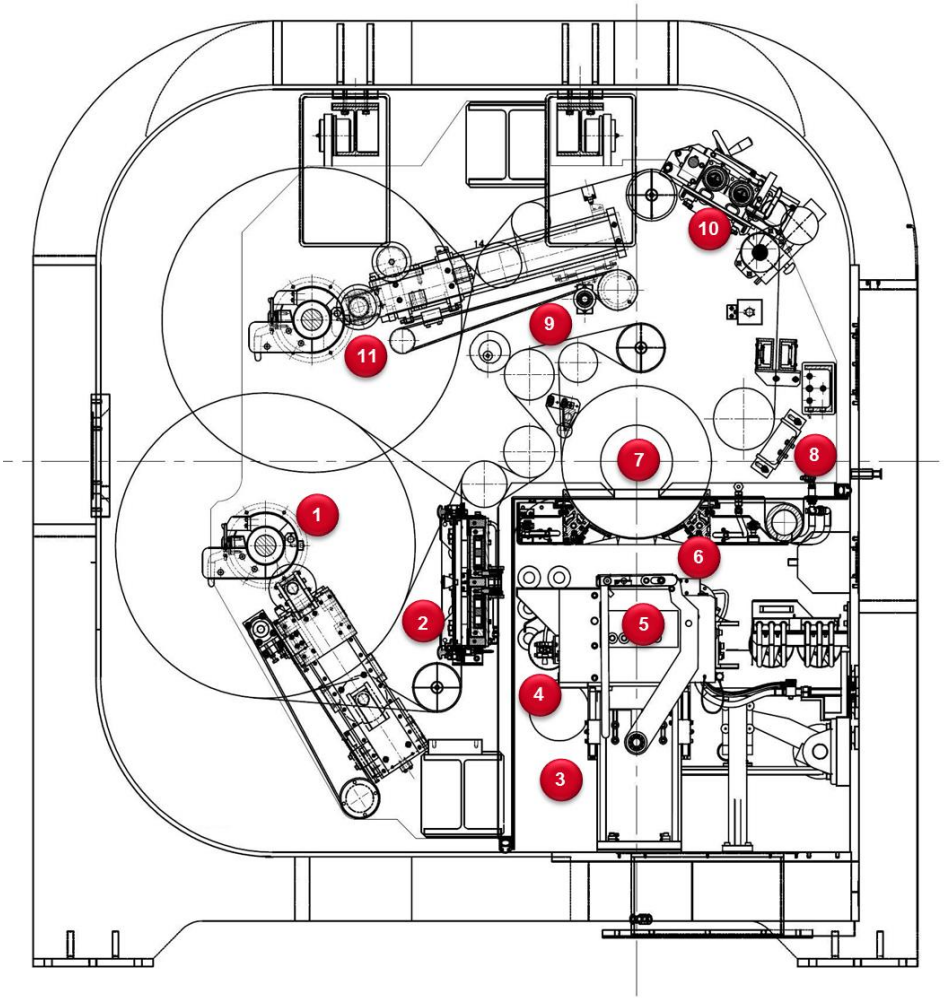

Figure 5-3: Cross-section of vacuum web coater at Bobst Manchester (K4000) [source: Bobst]

The plasma treater unit comprises a plasma source consisting of two magnetically enhanced water cooled electrodes, which work similarly to magnetron sputter targets. A 10 kW power supply is connected to the electrodes and an exciter circuit is used to produce a sinusoidal alternating voltage at frequencies between 20 and 100 kHz. In order to minimise the sputter effect, the pressure at the plasma treater units is kept high (here 2 – 5 x 10^{-2} mbar), thus decreasing the mean free path. Due to proprietary knowledge, the deposition process (e.g. exact machine parameters and set points) as well as the precise details of the plasma treatment cannot be described in further detail.

Table 5-1: Main components of vacuum web coater shown in Figure 5-3

	Component	Description/function
1	Unwind	For uncoated film
2	Plasma pre-treater	
3	Evaporation chamber	
4	Aluminium spool and wire feeder	Coating material
5	Source	Resistively heated evaporation boats
6	Shutter	Between source and coating drum
7	Coating drum	Cooled to ensure low thermal stress on the film
8	Optical beam	Monitors optical density/light transmission (a measure for coating thickness)
9	Winding mechanism	
10	Plasma post-treater	
11	Rewind	For winding up coated film

5.2 Flame and atmospheric plasma treatment

Atmospheric plasma and flame treatments were performed off-line by Enercon Industries Corp. (Menomonee Falls, Wisconsin, USA), using their flame treater with PowerFlame technology (see *Figure 5-4*) and atmospheric plasma treater with Plasma4 technology (see *Figure 5-5*). The aim of this investigation was to increase the oxygen content incorporated into the BOPP film surface and yield higher levels than normally obtained for corona treated BOPP film.

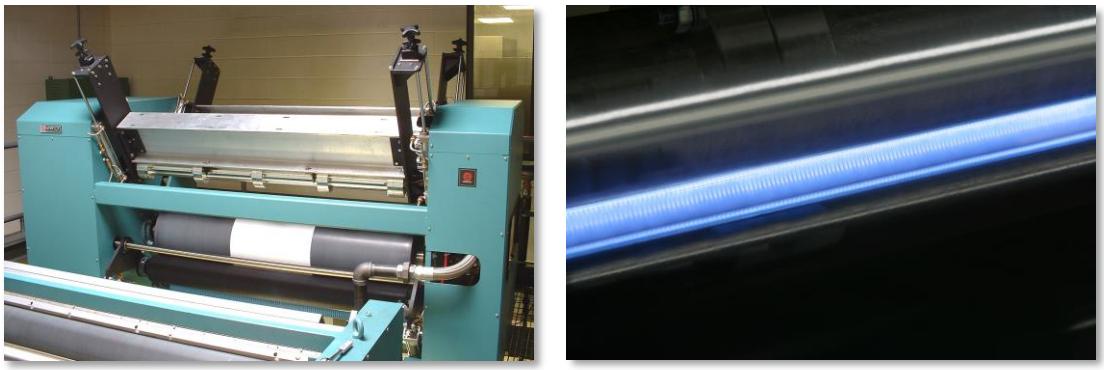

Figure 5-4: Enercon Industries flame treater (left) and flame 'plasma' (right) [source: Enercon Industries]

Three sets of pre-treatment trials were carried out using BOPP B (for more information on substrate material refer to Section 5.5), which had already been corona treated after extrusion at the film manufacturer's site. Firstly, three different flame treatment intensities, secondly, three different atmospheric plasma treatment levels and finally, a combination ('Plasma Synergy') of both (plasma on top of flame) were accomplished, thus resulting in nine different pre-treatment variations.

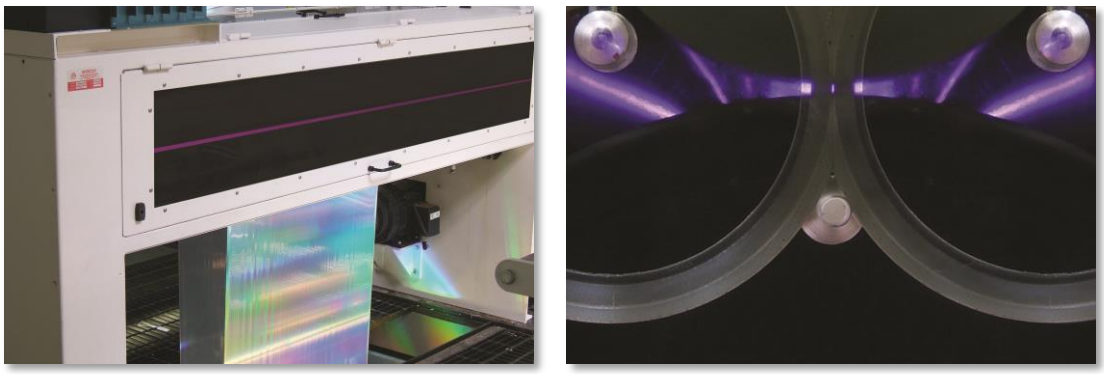

Figure 5-5: Enercon Industries atmospheric plasma treater (left) and plasma discharge (right) [source: Enercon Industries]

The flame treatment was carried out by the combustion of an air/natural gas mixture with an air/gas mixing ratio of 10:1. Whilst the treatment intensity was varied by changing the web speed, the air flow was 1200 l/min at a burner to film gap of 7 mm with the film being cooled from the reverse side via a chill roll. The atmospheric plasma treatment uses a dielectric barrier discharge ignited between two ceramic electrodes. For the atmospheric plasma treatment, an argon/oxygen (80/20) gas mixture was used and all trials were carried out at the same web speed via changing the power coupled into the plasma. The flame treater can process widths up to 1500 mm, whilst the atmospheric plasma treater is limited to a treatment width of 1200 mm. Due to proprietary knowledge, no more information could be shared by Enercon Industries. The main parameters of the nine treatment trials are summarised in *Table 5-2*.

A4 sheets of BOPP B, subjected to the flame, plasma and combined flame/plasma treatment, were mounted onto a PET carrier web and coated with AlO_x barrier layers at Bobst (see description of coating system in Section 5.1), using additional in-line plasma pre-treatment. Moreover, A4 reference samples of BOPP C and PET (refer to Chapter 5.5 for information on film substrates) were also coated in the same run in order to evaluate whether the coating of the A4 sheets is a representative technique for the AlO_x coating process of film rolls.

Table 5-2: Treatment parameters for flame and atmospheric plasma treatment of BOPP B

Treatment	Intensity level	Flame		Atmospheric plasma	
		Web speed	Energy density	Web speed	Energy density
		m/min	kJ/m²	m/min	kJ/m²
Flame (PowerFlame)	1	137	22.6	-	-
	2	122	25.8	-	-
	3	107	29.0	-	-
Atmospheric Plasma (Plasma4)	1	-	-	38	1.3
	2	-	-	38	2.6
	3	-	-	38	3.9
Flame + plasma (Plasma Synergy)	1	137	23	38	1.3
	2	122	26	38	2.6
	3	107	29	38	3.9

5.3 Acrylate deposition

Acrylate deposition was carried out utilising a coating system designed and licensed by Sigma Technologies International Inc. (Tucson, Arizona, USA). This system has been fitted to the research roll-to-roll coater (manufactured by Aerre/Arcotronics, Italy) of the University of Oxford, Department of Materials (Oxford, UK). This coater has a single chilled drum with 600 mm diameter and can handle webs of a width of 350 mm with speeds adjustable up to 300 m/min. In addition to the acrylate deposition, the coater has further coating and treatment capabilities with a planar dual magnetron sputtering source, an evaporation source with resistively heated boats and a radio frequency plasma treater, which have not been used in this project. Photos of the outside and inside of the Oxford roll coater are shown in *Figure 5-6* and *Figure 5-7*.

Figure 5-6: Oxford roll coater; left: vacuum chamber closed, acrylate evaporator visible; right: vacuum chamber open, showing winding mechanism and coating drum [source: Oxford Materials]

The acrylate deposition is achieved via flash evaporation of a monomer liquid in vacuum. These monomers condense as a liquid film on the substrate surface and are subsequently cured by UV light or electron beam radiation in order to obtain a cross-linked layer. In contrast to conventional vacuum deposition processes, such as sputtering or evaporation, where the growing coating in general shows a tendency to reproduce the substrate topography (and may even increases its roughness), the condensing monomer film covers and conceals the surface characteristics of the substrate, before it is cured and cross-linked to form a solid film in a second step. Thus, it is possible to achieve a smoothing/planarisation effect. [170]

For this polymer deposition process, the liquid monomer chosen for the acrylate coating is initially degassed and stirred, whilst atmospheric gases are removed from

the liquid with a vacuum pump. After this first step, the liquid is introduced into a very hot enclosure (evaporator) via a spray nozzle thus forming a mist of micro droplets that instantly vaporise (flash evaporation). From this evaporator, the monomer gas is transported through a narrow slit into the coating chamber and deposits as a liquid film on the moving substrate. Once the monomers have condensed as a liquid film, they are cross-linked to a polymer film via irradiation with UV light or an electron beam. [171]

The acrylate deposition system of the Oxford roll coater is equipped with an electron beam for curing, see *Figure 5-7*.

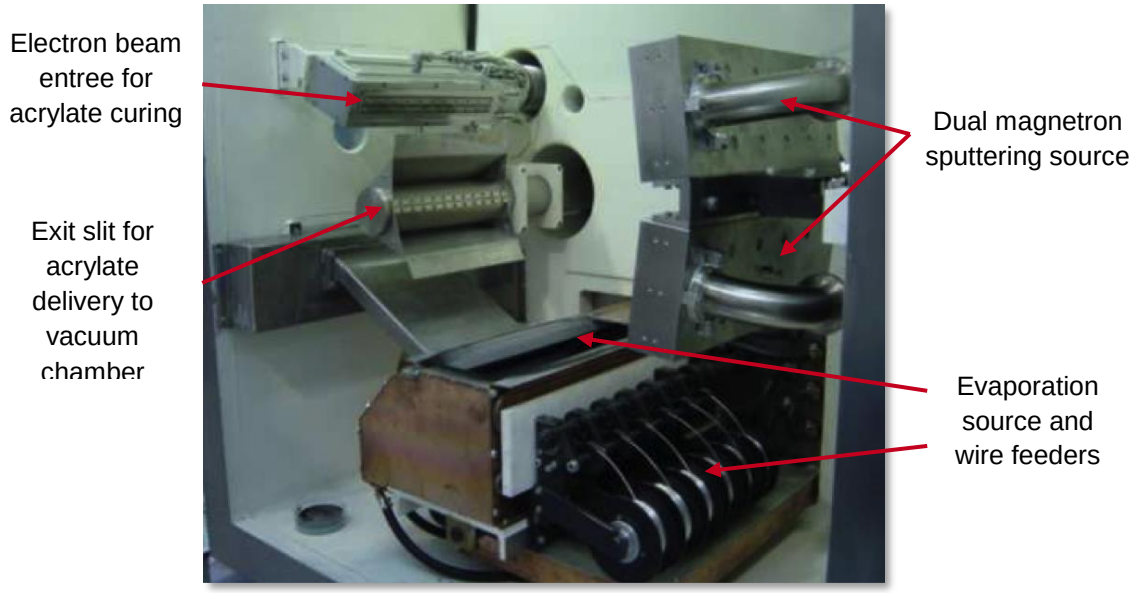

Figure 5-7: Inside view of Oxford roll coater showing acrylate deposition system, evaporation source and sputtering source [source: Oxford Materials]

Further possible deposition techniques for polymer layers from monomers include amongst others, spin coating [172], CVD processes [173], coating via an extrusion head [171, 174] or via a wire-bar [175], usually followed by a polymerisation/ cross-linking step.

In this investigation, acrylate coatings were used as polymer topcoats in order to protect the thin AlO_x barrier layer and polymer undercoats, applied to the plain polymer film prior to AlO_x deposition, to smoothen/planarise the polymer film surface. The plain BOPP films coated with an undercoat were later coated with an AlO_x barrier layer at Bobst (see description of coating system in Section 5.1), via mounting them with Kapton tape to a PET carrier web. AlO_x coated film samples for acrylate topcoats were taken from previous trials conducted at Bobst. Therefore, acrylate deposition took place as an off-line process, with the samples being exposed to environmental conditions before and after AlO_x coating. Tripropylene

glycol diacrylate (TPGDA, technical grade, produced by Sigma-Aldrich) was chosen as a monomer and acrylate coatings of two thicknesses (approximately 1 and 5 µm) were deposited onto AlO_x coated and plain film samples of BOPP A, B and C (for more information on substrate films see Section 5.5). The coating was conducted on A4 samples that were mounted with Kapton tape to the coating drum of the Oxford roll-to-roll coater. In addition to the A4 samples, silicon wafers were coated as control samples to measure the actual acrylate thickness.

Due to problems with the pump at the degassing chamber, the monomer liquid could not be degassed for the trials conducted. Prior to acrylate coating, the chamber was pumped to a base pressure of 3.5 to 4 x 10^{-2} Pa. Coating took place at a web speed of 50 m/min, which is equivalent to a drum rotation of approximately 26.5 revolutions per minute, with a drum temperature of 17 to 18 °C. Based on previous trials conducted by the team at Oxford with TPGDA, volumes of 1.1 and 4.6 ml of monomer liquid were chosen for the aimed acrylate thicknesses of 1 and 5 µm, respectively, and the monomer liquid was introduced into the evaporator (approx. 270 °C) at a rate of 0.5 ml/min using a syringe. Thus, acrylate deposition took place in multiple passes (samples mounted onto rotating drum), with an electron beam radiation for curing (400 mA, 6 kV).

5.4 Lamination process

Lamination trials of AlO_x coated BOPP were carried out on an industrial scale, using solvent-based and solventless adhesive lamination.

5.4.1 Solvent-based adhesive lamination

The solvent-based adhesive lamination was conducted on a Bobst Rotomec CL850 laminator at Bobst Italia Spa. (formerly Rotomec Spa., San Giorgio Monferrato, Italy). A photo of the laminator is shown in *Figure 5-8* and a schematic representation, which depicts the individual components of the laminator for a better understanding of the lamination process, is illustrated in *Figure 5-9*. For the solvent-based lamination, the adhesive (mixed with solvent) is applied onto the film coming from unwind 1. Subsequently, the adhesive is dried in order to remove the solvent, the film is combined with the second web from unwind 2 at the lamination nip and, finally, the laminate is rewound.

Figure 5-8: CL850 laminator at Bobst Italia

A flexo trolley coating system (schematically illustrated and described in *Figure 5-10*) was used to apply the adhesive onto the film. This technique is advantageous for delicate substrates, since there is a 'kiss' contact between rollers C and D, i.e. the adhesive is acting as a lubricant and there is no pressure placed onto the substrate. The adhesive used in this investigation was a solvent-based two-component polyurethane adhesive (Adcote 811A-EA+Catalyst F, produced by Rohm and Haas) with a high initial tack. According to the datasheet, this adhesive is suitable for the lamination of a wide range of materials, including transparent films,

SiO_x coated films and metallised films. Furthermore, the adhesive is suitable for sterilisable and boil-proof laminated structures. Ethyl acetate was used as the solvent.

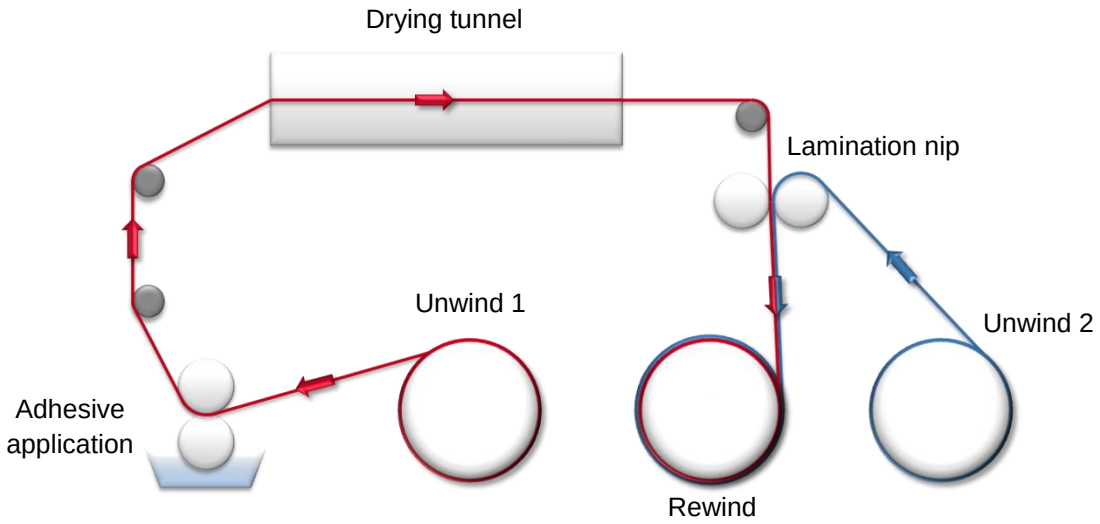

Figure 5-9: Schematic diagram of lamination process configuration

In this study, AlO_x coated BOPP C (for more information on substrate film see Section 5.5) was laminated against another 20 µm BOPP film. After setting up the laminator, the following two trial options were pursued. Firstly, the adhesive was coated onto the plain 20 µm BOPP film (corona treated side), in order to avoid any damage to the AlO_x coating during adhesive application and drying (trial 1).

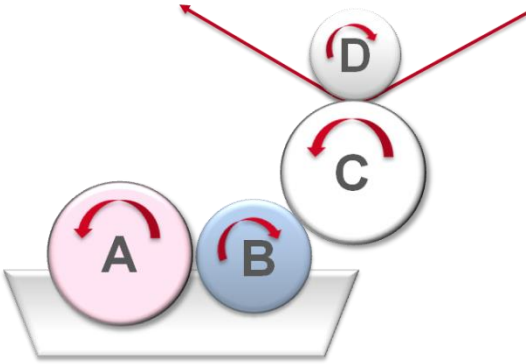

A Rubber roller, presses adhesive into engraving on roller B, immersed into adhesive

B Engraved roller with ceramic coating, control of adhesive application weight, immersed into adhesive

C Rubber roller, runs at faster speed than D (web speed) in order to transfer the adhesive uniformly onto the web

D Chromium plated back pressure roller

Figure 5-10: Flexo trolley system for solvent-based adhesives

For the second trial, the two unwind reels were swapped and the adhesive was applied onto the AlO_x coating, dried and then laminated against the uncoated BOPP. This is the standard procedure when metallised BOPP is laminated against reverse printed BOPP. In order to avoid changes of the repeat length of the printed film and

in order to keep the content of residual solvents low, the preference is to apply the adhesive onto the metallised BOPP. If the adhesive was applied onto the printed BOPP, more intense drying (which may affect the print repeat length) would be required, since the ink absorbs solvent and retains it. The solvent retention within the laminate needs to be kept low, in order to prevent any off-flavour during final packing application and spoilage of the packaged foodstuffs. More information on the parameters and settings used for the lamination trials can be found in *Table 5-3*.

Table 5-3: Conducted lamination trials (solvent-based adhesive lamination)

Trial	Application weight	Web speed	Drying tunnel temperatures			Lamination nip temperature
			Zone 1	Zone 2	Zone 3	
	g/m²	m/min	°C	°C	°C	°C
1: Adhesive onto BOPP	2.9	150	70	80	90	45
2: Adhesive onto AlO_x	3.1	150	70	80	90	45

5.4.2 Solventless adhesive lamination

In addition to solvent-based adhesive lamination, which has some drawbacks, such as the pollution and danger due to solvent use, the drying of the adhesive required prior to lamination in order to remove the solvent and the retention of solvent in the laminate to some degree, solventless adhesive lamination was also carried out. These trials were conducted with AlO_x coated BOPP B, which was laminated against uncoated BOPP B (for more information on substrate film see Section 5.5). The lamination of the AlO_x coated film was performed at one of the project partner's customers, who do not want to be named. Therefore, machine make and model cannot be disclosed in this thesis. Two adhesives were selected; a higher solids fast curing adhesive to minimise any problems with out-gassing due to the barrier properties of the film (Novacote SF-783-A + CA-379) and, in addition to that, a standard solventless adhesive (Novacote SF-3277/3 + CA-3278/7, both produced by Coim Novacote Flexpack). Both adhesives are solvent-free two-component polyurethane adhesives and are suitable for a comparable application range as the solvent-based adhesive described in Section 5.4.1. The lamination process configuration is similar to that shown in *Figure 5-9*, apart from the drying tunnel being at ambient temperature and a heated roller of 60 °C (high performance adhesive)/45 °C – 50 °C (standard adhesive) following the lamination nip in order to initiate the link between the catalyst and the resin. Furthermore, the adhesive is applied onto the polymer film via flat/smooth roller transfer application, which is schematically depicted in *Figure 5-11*. Here, several rollers are heated in order to decrease the viscosity of the solvent-free adhesive.

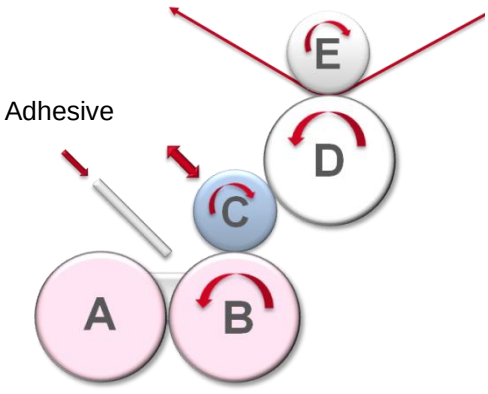

A,B Metering rollers, gap between A and B for rough metering of adhesive, chromium plated steel, roller A stationary, both heated

C Rubber transfer roller, sized to coated web width, movable to control adhesive thickness

D Coating roller, chromium plated steel, heated

E Rubber counter impression roller

Figure 5-11: Flat/smooth roller transfer application system for solventless adhesives

With adhesive 1 (high performance adhesive), two trials were performed, similarly to the trials conducted with the solvent-based adhesive. Initially, the adhesive was applied onto the uncoated BOPP film, which was then laminated against the AlO_x

coated BOPP. After that, the reels were swapped and the adhesive was applied onto the AlO_x layer itself. Regarding adhesive 2 (standard adhesive), only one trial was performed, whereby the adhesive was coated onto the plain BOPP film. More information on the lamination parameters is summarised in *Table 5-4*. The temperature of the coating roller D and the metering rollers A and B was slightly higher for adhesive 1, compared to adhesive 2. This is due to the higher solids content and consequently higher viscosity of adhesive 1.

Table 5-4: Conducted lamination trials (solventless adhesive lamination)

Adhesive	Trial	Application weight	Web speed	Temperature		
				Metering rollers	Coating roller	Lamination nip
		g/m²	m/min	°C	°C	°C
High performance	1: Adhesive onto BOPP	2.1	120	50	50	50
High performance	2: Adhesive onto AlO_x	2.1	120	50	50	50
Standard	Adhesive onto BOPP	2.5	130	40	45	45

After the lamination process, the laminated film rolls were stored in a hot room at 40 °C for one week in order to accelerate the curing process and to obtain the bond strength required.

5.5 Substrate films

Various standard packaging (metallising) grade BOPP films and a PET base film (all corona treated in-house by the film manufacturer), as well as a BOPP film coextruded with a special high surface energy polymer as a skin layer (produced by Brückner Maschinenbau GmbH & Co. KG, Siegsdorf, Germany), were coated with an AlO_x barrier layer. The coatings were applied to the corona treated side of each film and the high surface energy polymer skin layer, respectively. All standard packaging grade BOPP films used consist of a three-layer coextruded structure with a homopolymer core and either co- or terpolymer skin layers, containing antiblock additives, on each side (as described in Chapter 4.1.2). In contrast to the standard packaging grade BOPP films, the BOPP film with the special polymer skin layer consists of a five-layer coextruded structure, with no antiblock particles added to the high surface energy polymer skin layer. The PET film coated as a reference material is a monolayer film, with antiblock particles dispersed throughout the single layer. Furthermore, all films contain a variety of additives to stabilise the polymer film and guarantee optimised film handling and end-use properties. Exact film compositions are, however, commercially sensitive information not made available by the individual film producers. As no manufactures should be named here, the BOPP films have been coded as stated in *Table 5-5*. Furthermore, this table contains information on the film thickness and structure.

Table 5-5: BOPP and PET substrate films used for AlO_x coating

Film type	Thickness µm	Structure	Additional information
BOPP A	30	3 layers	Corona treated one side
BOPP B	15	3 layers	Corona treated one side
BOPP C	20	3 layers	Corona treated one side
BOPP D	20	3 layers	Corona treated one side
BOPP E	22	3 layers	Corona treated one side, heat shrinkable BOPP
BOPP F	18	5 layers	High surface energy polymer skin layer
PET	12	1 layer	Corona treated one side

In the further progression of the project, a biodegradable polylactic acid (PLA) film was also coated in order to produce an environmentally friendly transparent barrier film. This film was Nativia NBSS20 produced by Taghleef Industries, which is a three-layer coextruded BOPLA (biaxially oriented PLA) film for metallising, with one side corona treated.

5.6 Analysis

5.6.1 Barrier properties (permeation measurements)

5.6.1.1 Oxygen transmission rate

The oxygen transmission rate (OTR) was measured in compliance with ASTM F1927 [176]. The basic principle is to measure the quantity of oxygen passing through a film test sample (with a given area) in a certain period of time and under specific conditions (23 °C, 50 % RH). The resulting values are then indicated in terms of $cm^3/(m^2\ d)$.

Therefore, the sample is mounted between the two halves of a test cell, as shown in *Figure 5-12*. Whilst the upper half of the test cell is continuously flushed with oxygen humidified to 50 % RH), nitrogen (also humidified to 50 % RH) is routed through the lower half of the test cell, picks up the oxygen that permeates through the test sample from the upper to the lower half and carries it to the electrochemical detector. In order to ensure that no oxygen originates from contamination of the nitrogen carrier gas, the nitrogen is either routed through an oxygen trap prior to entering the test cell (Systech 8001) or a gas mixture consisting of nitrogen and 3 % hydrogen is used, which passes through a catalyst (before being admitted to the test cell). Therefore, any residues of oxygen that happen to be in the carrier gas react with the hydrogen by forming water (Mocon Oxtran).

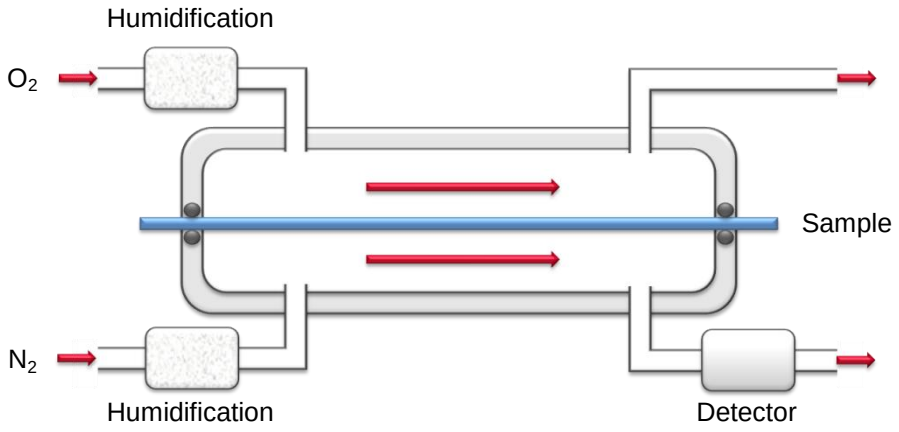

Figure 5-12: Schematic illustration of measurement principle for oxygen transmission rate

The electrochemical detector consists of two electrodes, a graphite-cathode and a cadmium-anode, amongst which a redox reaction takes place:

Graphite-cathode: $O_2 + 2\ H_2O + 4\ e^- \rightarrow 4\ OH^-$

Cadmium-anode: $2\ Cd + 4\ OH^- \rightarrow 2\ Cd(OH)_2 + 4\ e^-$

One molecule of oxygen generates four electrons and thus a corresponding electrical current. Hence, the measured current is directly proportional to the amount of oxygen passing through the sensor.

For OTR (as well as for WVTR, see Section 5.6.1.2) measurements, the tests are stopped when permeation equilibrium (i.e. a constant transmission rate) is reached.

A *Mocon Oxtran 2/20* and a *Systech Illinois 8001* oxygen permeation analyser were used to determine the OTR.

The Systech Illinois 8001 permeation analyser exhibits a measurement range of 0.008 to 432000 $cm^3/(m^2\ d)$ at a 50 cm^2 test area, whilst the Mocon Oxtran 2/20 has a test range of 0.005 to 200 $cm^3/(m^2\ d)$ (50 cm^2 test area) at a resolution of 0.001 $cm^3/(m^2\ d)$ and with a repeatability of ± 1 % or ± 0.005 $cm^3/(m^2\ d)$ (whichever is greater). No further system specifications are given for the Systech Illinois 8001 model by the manufacturer.

5.6.1.2 Water vapour transmission rate

Determination of water vapour transmission rate (WVTR) was performed according to ASTM F1249 [177] and ISO 15106-3 [178]. Similarly to the previously described method, the amount of water vapour passing through a film test sample (with a given area) in a certain period of time and at a given temperature (37.8 °C) and RH gradient is determined. The measurement results are expressed in terms of g/(m^2 d) and are calculated for a 90 % RH gradient (correction for deviation from 90 % test RH assuming a linear correlation between WVTR and RH).

The film sample is mounted as shown for OTR determination in *Figure 5-12*. However, for this test nitrogen is admitted to both halves of the test cell. The RH in the upper half of the test cell is adjusted to a certain value via humidification, whilst dry nitrogen is admitted to the lower half, i.e. the nitrogen passes through a desiccant, instead of the humidification shown in *Figure 5-12*, before entering the test cell. Any water vapour permeating through the tested sample from the upper to the lower half is picked up by the dry nitrogen and is routed to the detector. In the case of the *Mocon Permatran-W 3/33*, this is a pressure-modulated infrared detector (ASTM F1249), which measures the amount of infrared energy absorbed by the water in the carrier gas nitrogen and produces an electrical signal proportional to the concentration of water. This signal is then compared to the signal obtained for a reference film of known WVTR in order to calculate the WVTR of the test sample. The *Systech 7001* detector cell is a phosphorus pentoxide sensor (ISO 15106-3). It consists of a quartz tube with two platinum electrodes wound around it. These windings are coated with a thin layer of phosphorus pentoxide, which absorbs all water present in the carrier gas. The constant DC voltage applied between the two electrodes causes an electrolytic decomposition of water into oxygen and hydrogen and the electric current required for electrolysis is a direct measure of the amount of water present in the gas stream.

During all WVTR measurements of coated films (Al and AlO_x), the coating faces the 0 % RH side in order to avoid damage of the barrier layer due to exposure to high RH and extensive oxidation.

The Systech Illinois 7001 offers a test range of 0.002 to 18 g/(m² d) for a 50 cm² test area (no further details provided by manufacturer), whilst the Mocon Permatran-W 3/33 has a test range of 0.005 to 10 g/(m² d) (50 cm² test area, 10 sccm carrier gas flow) at a resolution of 0.0001 g/(m² d) and with a repeatability of ± 0.5 % (1 – 10 g/(m² d)), ± 1.0 % (0.1 – 1 g/(m² d)) and ± 2.0 % (0.005 – 0.1 g/(m² d)).

5.6.2 Surface topography and roughness

5.6.2.1 Differential interference contrast optical microscopy

Differential interference contrast (DIC) optical microscopy represents a special illumination technique for optical light microscopy, which enables the production of images that give a three-dimensional impression of the specimen surface. This technique makes use of differences in the optical path length across the sample surface. In the case of reflected light DIC, differences in path length are generated by the surface topography (raised/lowered areas) of the specimen. These optical path gradients are then transformed in to image contrast.

The basic principle is the use of an illumination source that is split into two perpendicular polarised light beams by a DIC prism (Wollaston or Nomarski prism). The two beams are focussed by the objective, displaced/sheared at the sample plane and, hence, are reflected by two points on the sample surface that are lying closely spaced to one another (displacement is slightly less than the resolution of the objective lens). Afterwards, the reflected light beams pass through the objective lens and are then recombined in the same DIC prism, which leads to their interference at the analyser. If the two light beams were reflected by points located at different surface heights (i.e. not the same flat surface region), they exhibit a difference in phase/path length. This phase difference induces the edges of an object to appear either brighter or darker in the image (compared to their surroundings), which leads to the generation of image contrast and a deceptive three-dimensional appearance.

More information on DIC light microscopy can be found in references [179, 180].

Differential interference contrast microscopy images in this thesis were obtained using a Zeiss Axio Imager.M2m optical microscope in reflected light DIC mode.

5.6.2.2 Scanning electron microscopy

Scanning electron microscopy (SEM) enables the imaging of surfaces beyond the resolution of light microscopy, based on the use of an electron beam to examine the sample surface. Consequently, magnifications up to 300000 x are possible [181].

During SEM analysis, a focussed electron beam spot is raster scanned across the sample surface and the interactions of the primary electrons with the atoms present in the specimen surface are examined. When the electrons enter the sample surface, they induce a variety of interactions, which result in the production and emission of secondary electrons, backscattered electrons, Auger electrons and X-ray photons. The emission of X-rays can be used to obtain compositional information via an energy dispersive X-ray detector or a wavelength dispersive X-ray detector. However, as the primary electrons can penetrate relatively deep into the sample and cause X-ray emission, the chemical composition obtained represents quite a large volume of the sample (typical analytical depth of several microns) and energy/wavelength dispersive X-ray analysis is not as surface sensitive as X-ray photoelectron spectroscopy (see Chapter 5.6.3.2). Secondary and backscattered electrons can be used to obtain surface images, since they reveal topographical information. When the surface topography is imaged, electrons emitted from the sample surface are collected by an appropriate detector, whilst the electron beam is scanned across the sample surface. Whereas secondary electrons are emitted from the first few nanometres of the sample surface due to inelastic scattering of the primary electrons, backscattered electrons are primary electrons scattered elastically by the nucleus of an atom. Due to this interaction, SEM topographical images based on backscattered electrons also contain compositional information (i.e. an element with a higher atomic number will appear brighter). Conventionally, electrons with an energy larger than 50 eV are regarded as backscattered electrons, whilst those with an energy of less than 50 eV are counted as secondary electrons. In general, secondary electrons are used to acquire surface topographical images. The contrast in an SEM topography image (via secondary electron detector) is generated by the number of secondary electrons produced by each point of the specimen surface. This amount depends on the orientation of the sample topography relative to the electron beam and detector, as well as the angle between sample surface and incident electron beam. With decreasing glancing angle, the yield in secondary electrons increases and, consequently, changes in the surface slope result in changes of the secondary electron intensity.

For more information on the working principle and instrumentation of SEM, the reader is referred to references [181, 182].

For the SEM investigation of the uncoated and AlO_x coated polymer films, a Zeiss Supra 40VP field emission gun scanning electron microscope was utilised and samples were examined in high vacuum without applying any conductive layer to avoid masking surface detail. In order to minimise sample charging, a low acceleration voltage of 0.4/0.5 kV was used.

5.6.2.3 Atomic force microscopy

Atomic force microscopy (AFM) uses a small sharp tip or colloid probe (depending on application) mounted to a cantilever spring (material usually silicon, length typically 100 to 200 µm [183], spring constant 0.01 to 50 N/m [184]) to scan the sample surface and, thus, give true topographical (height) information. The force interacting between the tip and the specimen causes a deflection of the cantilever according to Hooke's law. In general, this deflection is determined optically, i.e. a laser beam is focussed onto the end of the cantilever, and the reflected beam is detected by a photodiode array (segmented photodiode), see *Figure 5-13*. During raster scanning, the cantilever or the sample is moved by a piezoelectric translator, and, consequently, the surface area of interest is examined. [183, 185]

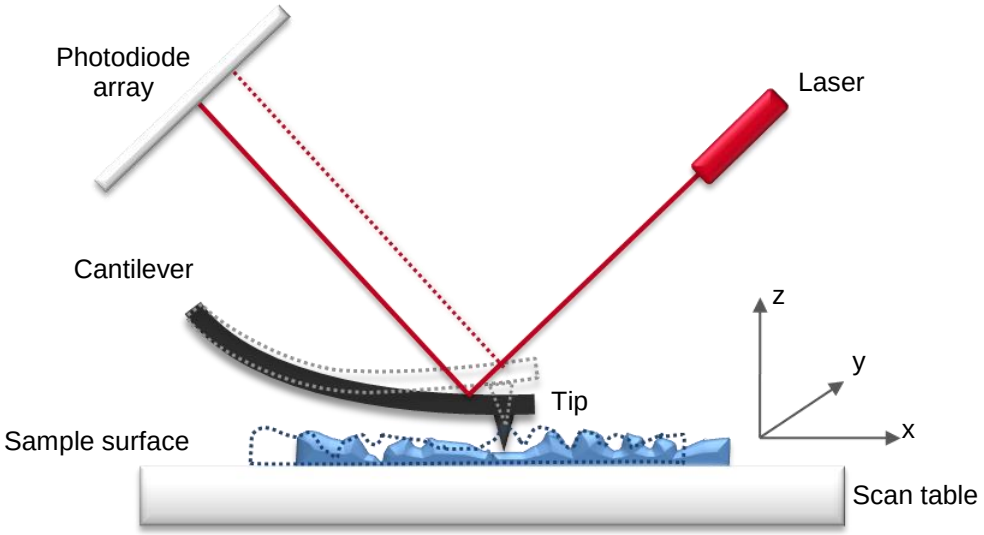

Figure 5-13: Basic operating principle of atomic force microscopy

For analysing the surface topography, AFM can be operated in different modes. In *contact mode* AFM, the sample and the tip are in permanent mechanical contact during scanning the surface. However, this mode is not suitable for all materials, as soft and delicate specimens may be damaged or deformed and, additionally, tip contamination is more likely. Therefore, during *dynamic mode* AFM, the cantilever oscillates (usually around its resonant frequency) and its tip can either be in contact with the sample at the turning point of oscillation (called *tapping mode* or *intermittent-contact mode*) or not (referred to as *non-contact mode*). Interaction in non-contact mode takes place via Van der Waals forces. [59, 186, 187]

The acquired AFM surface data is evaluated using the following specific parameters [188]:

- Roughness average (R_a) value, which is defined as the arithmetic mean of the height variation:

$$R_a = \frac{1}{N} \cdot \sum_{j=1}^{m} \sum_{i=1}^{n} \left| z(x_i, y_j) - \bar{z} \right| \tag{5-1}$$

- Root mean square (RMS or R_q) value, which describes the standard deviation of the height (z-value):

$$R_q = RMS = \sqrt{\frac{1}{N} \cdot \sum_{j=1}^{m} \sum_{i=1}^{n} \left(z(x_i, y_j) - \bar{z} \right)^2} \tag{5-2}$$

Where:

$$\bar{z} = \frac{1}{N} \cdot \sum_{j=1}^{m} \sum_{i=1}^{n} z(x_i, y_j) \tag{5-3}$$

(The mean height $\bar{z}$ represents the average z-value of the topography scan.)

$z(x_i, y_j)$	height (z-value) for the coordinates x_i and y_j of the scanned area
n	number of points per line (in the scan/area of interest)
m	number of lines (in the scan/area of interest), usually $n = m$
$N = n \cdot m$	number of points per scan (or area of interest)

The RMS value and R_a value are the most common parameters to describe surface roughness. Furthermore, the RMS value measured by AFM has been proven to be a valid and reliable parameter to characterise nano-scale roughness on polymer surfaces [189].

A WiTec alpha500 and a Veeco DI CP II atomic force microscope in pulsed force mode (a specific intermittent-contact mode) and tapping mode, respectively, were used to acquire roughness data and topography images. The results delivered for the same samples by the two different atomic force microscopes and imaging modes were in good agreement. All images were corrected by first order line-wise levelling. Root mean square and roughness average values were calculated from 5 x 5 µm^2 size scans. Therefore, several scans were performed on different sample areas that did not exhibit antiblock particles in order to obtain a mean value and the standard deviation.

For the pulsed force mode, silicon cantilever probes with a nominal cantilever spring constant of 2.8 N/m, a resonance frequency of about 75 kHz and a tip radius of

curvature of less than 10 nm were applied. The images were acquired using a scan rate of 0.5 lines per second. For the measurements carried out in tapping mode, the silicon cantilevers had a nominal spring constant of 40 N/m, a resonant frequency of 300 kHz and a tip radius of curvature < 12 nm. The scan rate was varied between 1 and 1.5 lines per second. All AFM images are composed of 512 lines with 512 points per line.

5.6.3 Analysis of surface chemistry and chemical composition

5.6.3.1 Surface energy determination via contact angle measurement

Contact angle analysis and surface energy determination can be regarded as techniques to assess the surface chemistry in an indirect way.

On applying the sessile drop method, a droplet of the probe liquid (with known liquid surface energy) is placed onto the surface of the material, thus forming a three phase system, i.e. solid, liquid and vapour. Contact angle determination is then achieved via establishing the tangent at the point where all three phases meet, as shown in *Figure 5-14*.

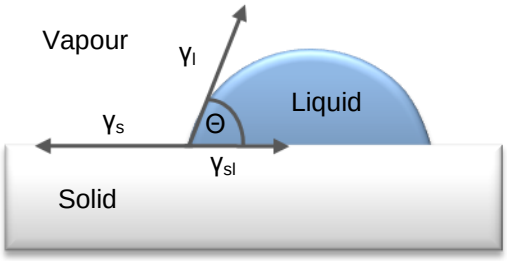

Figure 5-14: Liquid droplet on solid surface in equilibrium

The equation that describes the thermodynamic equilibrium of the three phases (solid, liquid, vapour) is the so-called Young-equation (influence of vapour phase neglected for the following calculations, thus resulting in a simplified Young-equation):

$$\gamma_l \cdot \cos\theta = \gamma_s - \gamma_{sl} \quad \text{(Young-equation)} \tag{5-4}$$

Where:
- γ_l surface energy of liquid phase [$^{mN}/_{m}$]
- γ_s surface energy of solid phase [$^{mN}/_{m}$]
- γ_{sl} interfacial energy between solid and liquid [$^{mN}/_{m}$]
- θ contact angle between solid and liquid droplet

This equation consists of two measurable/known quantities (Θ and γ_l) and two unknown quantities (γ_s and γ_{sl}). Consequently, to determine the solid surface energy, γ_s, an additional equation is needed.

Many concepts have been developed to solve the Young equation, including an empirical method by Zisman et al. [190] and further important approaches by Girifalco and Good [191], Fowkes [192], Owens and Wendt [193], Kaelble [194], Neumann et al. (equation of state) [195, 196], Wu [197, 198] and Van Oss et al. [199, 200]. The concept used in this thesis is the so-called Owens-Wendt-Rabel-

Kaelble method [193, 194, 201], which is one of the most common techniques applied to assess the surface energy of polymeric materials [202] (this reference also gives a good overview of the various concepts developed to determine the surface energy of solids).

The Owens-Wendt-Rabel-Kaelble method can be seen as an extension of Fowkes' approach, who postulated that the surface energy consists of two components, the dispersive surface energy component, γ^d, (representing Van der Waals dispersion forces) and the non-dispersive 'polar' surface energy component, γ^p (representing dipole-dipole interaction, hydrogen bonds etc.):

$$\gamma = \gamma^d + \gamma^p \tag{5-5}$$

According to the Owens-Wendt-Kaelble approach, the interfacial energy is given by the following equation, whereby the geometric mean is used to take the 'polar-polar' and 'dispersive-dispersive' interactions between solid and liquid phase into account:

$$\gamma_{sl} = \gamma_s + \gamma_l - 2\sqrt{\gamma_s^d \cdot \gamma_l^d} - 2\sqrt{\gamma_s^p \cdot \gamma_l^p} \tag{5-6}$$

Combining (5-6) with the Young-equation (5-4) results in:

$$\gamma_l \cdot (\cos\theta + 1) = 2\left(\sqrt{\gamma_s^d \cdot \gamma_l^d} + \sqrt{\gamma_s^p \cdot \gamma_l^p}\right) \tag{5-7}$$

Linear regression (according to Rabel [201]) to y = m · x + t yields:

$$\underbrace{\frac{\gamma_l \cdot (\cos\theta + 1)}{2 \cdot \sqrt{\gamma_l^d}}}_{y} = \underbrace{\sqrt{\gamma_s^p}}_{m} \cdot \underbrace{\frac{\sqrt{\gamma_l^p}}{\sqrt{\gamma_l^d}}}_{x} + \underbrace{\sqrt{\gamma_s^d}}_{t} \tag{5-8}$$

The only unknown quantities in Equation (5-8) are the polar and dispersive surface energy of the solid phase, here polymer or AlO_x layer, γ_s^p and γ_s^d. Different test liquids with known polar and dispersive surface energies are applied, and their contact angle on the specimen to be tested is measured. From these values x and y are determined by linear regression via slope, m, and y-intercept, t.

In this study, the contact angles of the three test liquids shown in *Table 5-6* were assessed. At least five drops of a few µl per fluid (on different surface areas) were

measured for an average value of the contact angle. For the calculation of the surface energies, the liquid surface energies as stated in reference [203] were used (see also *Table 5-6*). These values have been recommended by the manufacturer of the measurement equipment. It is important to mention here that the surface energy values reported for diiodomethane in literature vary. Whilst in this thesis diiodomethane is regarded as a completely nonpolar fluid (γ^p = 0 mN/m), other researchers state polar surface energy parts not equal to zero, e.g. γ^p = 1.3 mN/m [193], γ^p = 2.3 mN/m [194] or γ^p = 6.7 mN/m [198]. The effect of using a polar part different from 0 mN/m, as well as the surface energy results following the calculation method according to Wu [198] (harmonic mean instead of geometric mean), are presented in Appendix A1.

Table 5-6: Test liquids for contact angle measurement [203]

Test liquid	$\gamma = \gamma^d + \gamma^p$	γ^d	γ^p
	mN/m	mN/m	mN/m
Water	72.8	21.8	51
Diiodomethane	50.8	50.8	0
Ethylene glycol	47.7	30.9	16.8

Further details on the theoretical background of contact angle measurement and surface energy determination can be found in references [202, 204, 205].

Contact angles were measured with a Krüss MobileDrop system and DSAII software. When curve fitting and measurement of contact angles was not possible with the Krüss system, the acquired images were analysed using a drop shape analysis plugin for ImageJ [206].

Additionally, dyne inks/pens conformal to ASTM D2578 [207] were used to assess the surface energy of some polymer films. The dyne fluids consist of a dye and different mixing ratios of solvents in order to obtain different surface energies. When using the dyne pens (or cotton wool for dyne inks), a continuous line is drawn on the surface to be investigated and the fluid's wetting property is visually examined. To start with, a test ink of medium surface energy (e.g. 38 mN/m) is applied. If the liquid film stays as a full line and does not contract within 2 s, the surface energy of the tested material is identical to or higher than the surface energy of the test fluid. Consequently, the test is repeated with a higher surface energy liquid. If the line of the test ink changes and forms small droplets within less than 2 s, the surface energy of the specimen is lower than the surface energy of the test liquid used. In this case, the next applied test liquid has a lower surface energy. By performing the

described procedure, the range of the surface energy for the examined sample can be reduced step by step.

In general, it is important to know that different techniques, i.e. contact angle measurement or wettability method (dyne inks), as well as different calculation approaches, the angles used for calculation (static, advancing or receding angle) or the use of different liquids, will entail different results and, consequently, care must be taken when making comparisons [208]. This is also further discussed in the Appendix A1.

5.6.3.2 X-ray photoelectron spectroscopy

X-ray photoelectron spectroscopy (XPS), also known as electron spectroscopy for chemical analysis (ESCA), is a qualitative and quantitative surface analysis technique that allows the acquisition of the elemental composition (detection of all elements apart from hydrogen) of the specimen examined, as well as the atomic binding states of the elements present. Analysis is possible between a probing depth of 1 nm and up to approximately 10 nm and with a detection limit around 0.2 atomic% (at%; limit depending on the respective element) [209].

The XPS technology is based on the principle of photoemission. Therefore, the specimen to be analysed is irradiated with X-rays of a defined energy, h·v. If this energy is higher than the binding energy, E_b, of the core electrons (of the atoms present at the sample surface), these electrons are removed and emitted as so-called photoelectrons. The kinetic energy, E_k, of one photoelectron is given by Equation (5-9):

$$E_k = h \cdot \nu - E_b - \phi \tag{5-9}$$

Where:
- E_k kinetic energy of electron [eV]
- E_b binding energy of electron [eV]
- h Planck's constant: $4.13566733 \cdot 10^{-15}\ eVs$
- ν frequency of X-rays [Hz]
- ϕ spectrometer work function [eV]

The kinetic energies of the ejected photoelectrons are measured and used to calculate the binding energy, which is the only unknown quantity in Equation (5-9). Binding energies are specific for each chemical element and, consequently, they can be used to identify the elements present at the surface of the sample examined and quantify their atomic fractions by counting the respective photoelectrons. In addition to photoemission, a second effect inevitably takes place, as the created core hole needs to be filled by another electron of the outer shell. Due to conservation of energy, this process results in the emission of an X-ray photon (X-ray fluorescence) or of another electron (Auger emission).

XPS only allows the detection of photoelectrons that derive from a depth < 10 nm, since the mean free path within the sample is very low. Thus, this technique shows an extremely high surface sensitivity. A way of varying the analytical depth is given by changing the electron take-off angle (~0° to 90°, maximum depth of up to 10 nm at 90°). In order to prevent scattering of the photoelectrons by gas molecules (after

leaving the sample surface), XPS analysis is conducted in ultrahigh vacuum (10^{-6} to 10^{-8} Pa).

XPS analysis does not only allow the quantification of the atomic fractions of the elements present, but also gives information about their chemical state/environment. This second effect is due to the fact that a chemical bond to another element changes the core electron binding energy (thus the measured kinetic energy) as a function of the binding partner's electronegativity. This change results in a chemical shift (up to a few eV) of the binding energy and, consequently, one or more shoulders (or side peaks) can be formed in the XPS spectrum next to the main peak of the element investigated. A chemical shift can be seen as the shift of binding energy relative to the pure/unfunctionalised element and the different states can be assessed via peak fitting in high-resolution XPS spectra.

For more detail on XPS analysis, the reader is directed to references [210, 211].

XPS measurements were performed using a Thermo Scientific Theta Probe small spot XPS instrument, equipped with a monochromatic Al Kα X-ray source, at an electron take-off angle of 37° with respect to the sample surface (analytical depth of 5 to 6 nm). The sampled area is an elliptical spot with a transverse diameter of 800 µm. As the samples were of an insulating nature, argon was bled into the chamber during analysis in order to compensate for any charging effects occurring. Furthermore, all binding energies were referenced to the carbon 1s peak at 285 eV. The survey and high-resolution spectra were acquired using pass energies of 300 eV and 50 eV, respectively. Peak fitting and quantification of atomic fractions were accomplished via Thermo Advantage 4.8.3 software using a Gaussian (70 %) – Lorentzian (30 %) product function and sensitivity factors according to Scofield [212], respectively.

For the depth profiling and etching of AlO_x coated polymer films, an argon ion beam at a 3 kV acceleration voltage and 1 µA current was used and samples were etched for 60 s per iteration, followed by a 20 s break before the composition was determined. An area of approximately 3 x 3 mm² (larger than analysed area) was etched for this investigation.

The XPS analysis was carried out at the University of Surrey, Department of Mechanical Engineering Sciences (Guildford, United Kingdom). The author did not operate the XPS equipment, but did analyse the raw data acquired.

5.6.3.3 Static secondary ion mass spectrometry

Static secondary ion mass spectrometry (SSIMS or static SIMS) is a further technique for the analysis of the chemical composition of surfaces with a very high surface sensitivity at a probing depth of approximately 1 nm [213, 214].

During static SIMS, which is conducted in ultrahigh vacuum, the sample surface investigated is bombarded with energetic primary particles (usually positively charged ions), which interact with the sample and lead to the ejection of atoms and molecules from its surface. In static SIMS, the flux of primary particles is below a certain threshold value and, hence, the likelihood of the sample being sputtered is low, i.e. the sample surface remains mainly intact during the analysis. If the emitted secondary particles carry a positive or negative charge (i.e. they are secondary ions), they can be detected. Consequently, they are separated according to their mass to charge ratio (m/z) via a mass spectrometer. A time-of-flight (TOF) spectrometer accelerates all secondary ions to the same kinetic energy and, subsequently, separates them according to their mass in a field-free drift tube, based on the fact that the higher the mass, the longer the ion will take to pass through the tube and reach the detector. Using a TOF mass analyser offers the advantage that all secondary ions ejected from the sample surface can be detected in parallel (without scanning a mass range), since they reach the detector sequentially, dependent on their mass. [215, 216]

Positive and negative TOF-SSIMS analysis was performed using a Kore Technology Surface Seer instrument equipped with an argon ion source and a reflectron mass analyser. During analysis, the samples were exposed to bombardment by pulsed primary argon ions (5 kV, 4 nA, 128 µs cycle time). The investigated surface area was 400 x 400 µm², which is equivalent to the cross-section of the ion beam used. Two areas were analysed per sample and data was averaged over these two measurements. The ion dose suffered by the samples during the five minute acquisition time (for a positive or negative spectrum) is approximately 2.2×10^{12} ions/cm², which is below the static SIMS limit [217]. Charge compensation was carried out using a 40 eV electron flood gun.

SSIMS analysis was performed by research staff at Innovia Films Ltd. (Wigton, United Kingdom).

5.6.3.4 Fourier transform infrared spectroscopy

Infrared (IR) spectroscopy is based on the absorption of IR energy by specific chemical functionalities within a molecule and, therefore, can be used to identify and also quantify chemical compounds. The absorption of IR light results in the excitation of certain vibrational modes, which are characteristic of the chemical functionalities present. However, in order for a molecule (or chemical functionality) to be IR active, its electric dipole moment has to change during the vibrational motion. Several vibrational modes exist, which are either based on a change in chemical bond length (expansion/contraction of chemical bond, stretching vibrations) or bond angle (bending vibrations, e.g. rocking, deformation, wagging or twisting). If the frequency (i.e. wavelength) of the incoming IR radiation is equivalent to the characteristic frequency of a vibrational mode, then the radiation can be absorbed, which leads to an increase of the vibrational motion of this specific functionality. Depending on the experimental set up, liquid, solid or gaseous phases can be investigated using IR spectroscopy. The mid-IR range (4000 cm^{-1} to 400 cm^{-1}) is generally used to obtain IR spectra, since many chemical functionalities and molecules absorb strongly within this range.

During Fourier transform infrared (FTIR) spectroscopy, the spectral absorption data is concurrently collected for a wide wavenumber/wavelength range by the use of an interferometer and, in order to obtain a spectrum, the raw data collected (i.e. interferogram) is Fourier transformed. This offers the possibility to perform several scans for a sample within a short period of time (since the data is measured for all wavelengths simultaneously and no scanning through the investigated wavelength range is required) and, hence, noise can easily be reduced.

Attenuated total reflectance (ATR) spectroscopy is based on the principle of total internal reflectance. When a light beam travels from a medium of high refractive index (i.e. ATR crystal) to a medium of lower refractive index (i.e. sample) at an angle of incidence that is larger than a so-called critical angle (depends on the refractive indices of the two media), then total internal reflectance will occur. Nevertheless, an evanescent wave is generated at the point of total internal reflectance, which penetrates into the sample. The absorption of the sample alters the evanescent wave and, consequently, the totally reflected IR beam is attenuated, which is measured by the detector.

The depth of penetration during ATR spectroscopy is wavelength dependent and is defined as the depth at which the intensity of the evanescent wave has fallen to 1/e, i.e. 37 % of its original value. This is described by Equation (5-10):

$$d_p = \frac{\lambda}{2\,\pi\,n_1\left(sin^2\theta - \left({}^{n_2}/_{n_1}\right)^2\right)^{1/2}} \quad (5\text{-}10)$$

Where:
- d_p depth of penetration [μm]
- λ wavelength [μm]
- n_1 refractive index of ATR crystal
- n_2 refractive index of sample
- θ angle of incidence

Additional information on FTIR and ATR FTIR spectroscopy can be consulted in references [218-220].

FTIR spectra for the investigation of the BOPP skin layer composition were recorded on a Perkin Elmer Spectrum GX with a Specac Golden Gate ATR accessory (angle of incidence 45°) and Spectrum 5.3.1 software. For each spectrum, 16 scans at a resolution 4 cm^{-1} were performed and film samples were clamped using a torque of 3.5 kN m.

FTIR spectra of the peel test samples were acquired using a Thermo Scientific Nicolet 380 FTIR spectrometer with a Smart iTR ATR accessory (angle of incidence 45°) and Omnic 7.3 software. Here, 32 scans were carried out per spectrum at a resolution of 4 cm^{-1}. The clamping pressure/torque could not be accurately adjusted using the Smart iTR. Both ATR tools (Smart iTR and Specac Golden Gate) represent single reflection diamond ATR accessories.

Finally, the film extracts (Soxhlet extraction with n-hexane) were investigated using a Thermo Scientific Nicolet Nexus instrument with Omnic 7.2 software, after being re-dissolved in n-hexane and sandwiched between two NaCl disks.

5.6.4 Adhesion measurement via peel test

Measurement of coating adhesion was performed according to the EMA[d] (European Metallizers Association) test procedure for metal adhesion (seal test) [221]. Therefore, a 50 µm thick ethylene acrylic acid (EAA) film is sealed to the coated surface of the film (105 °C, 4 bar, 20 s) and, after conditioning, is peeled off with a tensile tester at a speed of 50 mm/min, according to the setup shown in *Figure 5-15*. The required force is measured by the load cell of the tensile tester and results are expressed in terms of N/(15 mm). In order to obtain an average peel force value and its standard deviation, at least 10 specimens are measured for each coating trial. This test is also further described and discussed in reference [120].

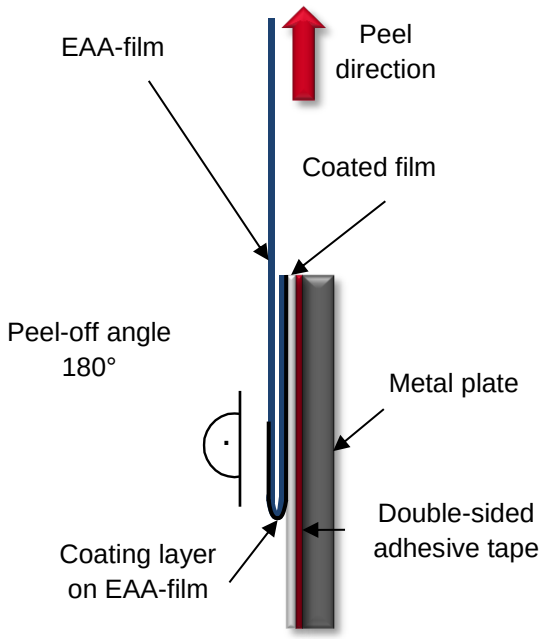

Figure 5-15: Cross-sectional view of sample during peel test

A RDM HSE-3 heat sealer and a Mecmesin VersaTest tensile tester with a 25 N load cell and Mecmesin DataPlot software was used in this investigation. The EAA film was 50 µm Integral E100, produced by DOW.

[d] The EMA has ceased its operations and members are now organising under the Association of International Metallizers, Coaters and Laminators (AIMCAL).

5.6.5 Transmission electron microscopy (coating thickness)

For transmission electron microscopy (TEM) analysis, samples of very low thickness (generally less than 200 nm) are investigated via the application of a focussed electron beam. The low sample thickness is required in order to ensure that the electrons can travel through the sample ('electron transparency'). TEM uses an array of magnetic lenses, arranged above and below the sample investigated, in order to transport the signal originating from the sample to the detector, which can be a fluorescent screen, a film plate or a camera. Whilst passing through the sample, the incident electrons interact with the atomic nuclei present and compositional (as well as structural and thickness) differences result in different efficiencies of electron scattering. This entails image contrast during bright-field TEM, since the scattered (or diffracted) beams are blocked out by the objective aperture and are not passed on to the detector (e.g. high atomic numbers will scatter to a larger extent and hence appear darker). The high resolution capabilities of TEM principally stem from the use of a highly focussed electron beam, as well as the extremely low wavelength of the incident electrons, which is a lot smaller than the wavelength of light or X-rays. Finally, one still has to bear in mind that despite the exceedingly low sample thickness a three-dimensional specimen is examined, but only a two dimensional image is obtained and, consequently, the depth resolution of TEM is limited. [222]

Samples of the AlO_x coated polymer films were embedded in an epoxy resin (TAAB low viscosity resin of medium hardness, polymerisation at 60 °C for 24 hours), cross-sectioned with an ultramicrotome (Reichert-Jung Ultracut ultramicrotome) to a sample thickness of approximately 70 to 80 nm and, finally, analysed using a FEI Tecnai 12 Biotwin transmission electron microscope at a 100 kV acceleration voltage with a Gatan Orius SC1000 camera.

5.6.6 Analytical equipment

Table 5-7 summarises the analytical methods and equipment used. Listed at the bottom are additional techniques and analytical tools that were applied in the course of this project, but are not described in further detail in Chapter 5.6.

Table 5-7: List of analytical equipment used

Measured/investigated characteristic	Technique/ apparatus	Manufacturer and model	Location
OTR	Permeation tester	Mocon Oxtran 2/20 Systech 8001	Bobst Manchester
WVTR	Permeation tester	Mocon Permatran-W 33/3 Systech 7001	Bobst Manchester
Surface topography	DIC light microscopy	Zeiss Axio Imager.M2m	Innovia Films
Surface topography	SEM	Zeiss Supra 40VP field emission gun scanning electron microscope	Manchester Metropolitan University
Surface topography and roughness	AFM	WITec alpha500 (pulsed force mode), Veeco di CP II (tapping mode)	Innovia Films and Fraunhofer Institute for Process Engineering and Packaging
Contact angles and surface energy	Contact angle measurement	Krüss MobileDrop	Manchester Metropolitan University
Surface energy	Wettability test with dyne inks and dyne pens	Corona Supplies Ltd. (dyne inks), Dyne Technology (dyne pens)	Innovia Films and Bobst Manchester
Film surface composition and coating stoichiometry	XPS	Thermo Scientific Theta Probe	University of Surrey
Film surface composition	Static SIMS	Kore Technology Surface Seer	Innovia Films
Skin layer composition, polymer identification and film extract composition	FTIR spectroscopy	Thermo Scientific Nicolet 380 with Smart iTR, Perkin Elmer Spectrum GX with Specac Golden Gate ATR, Thermo Scientific Nicolet Nexus	Manchester Metropolitan University and Innovia Films
AlO_x adhesion/peel force	Peel test	RDM HSE-3 heat sealer, Mecmesin VersaTest tensile tester	Bobst Manchester

Table 5-7: Continuation

AlO_x coating thickness	TEM	FEI Tecnai 12 Biotwin	University of Manchester
Film shrinkage	Thermal shrinkage tester	Lenzing Instruments TST1	Innovia Films
Tensile properties (for barrier on elongation)	Tensile tester	Hounsfield H10KS	Manchester Metropolitan University
Heat treatment (effect on barrier)	Oven	Carbolite	Manchester Metropolitan University
Optical density	Densitometer	MacBeth TD931	Bobst Manchester
Light transmission	Spectro-photometer	Hitachi U-4000	Manchester Metropolitan University
Surface topography	White light profilometry	MicroXAM (phase shift) surface mapping microscope	Manchester Metropolitan University
Acrylate thickness	Stylus profilometry	Dektak IID	Manchester Metropolitan University
Residual solvents	Gas chromatography	N.I.R.A Neptune 801	Bobst Italia
Gelbo-flex	Gelbo-flex tester	United States Testing Co. model 5000	Innovia Films
Molecular weight distribution	Gel permeation chromatography (GPC)	Viscotek HT-GPC Module 350A	Innovia Films
Extract identification	Liquid chromatography-mass spectrometry (LC-MS)	Agilent 6540 Q-TOF LC-MS	Manchester Metropolitan University

5.7 Experimental structure

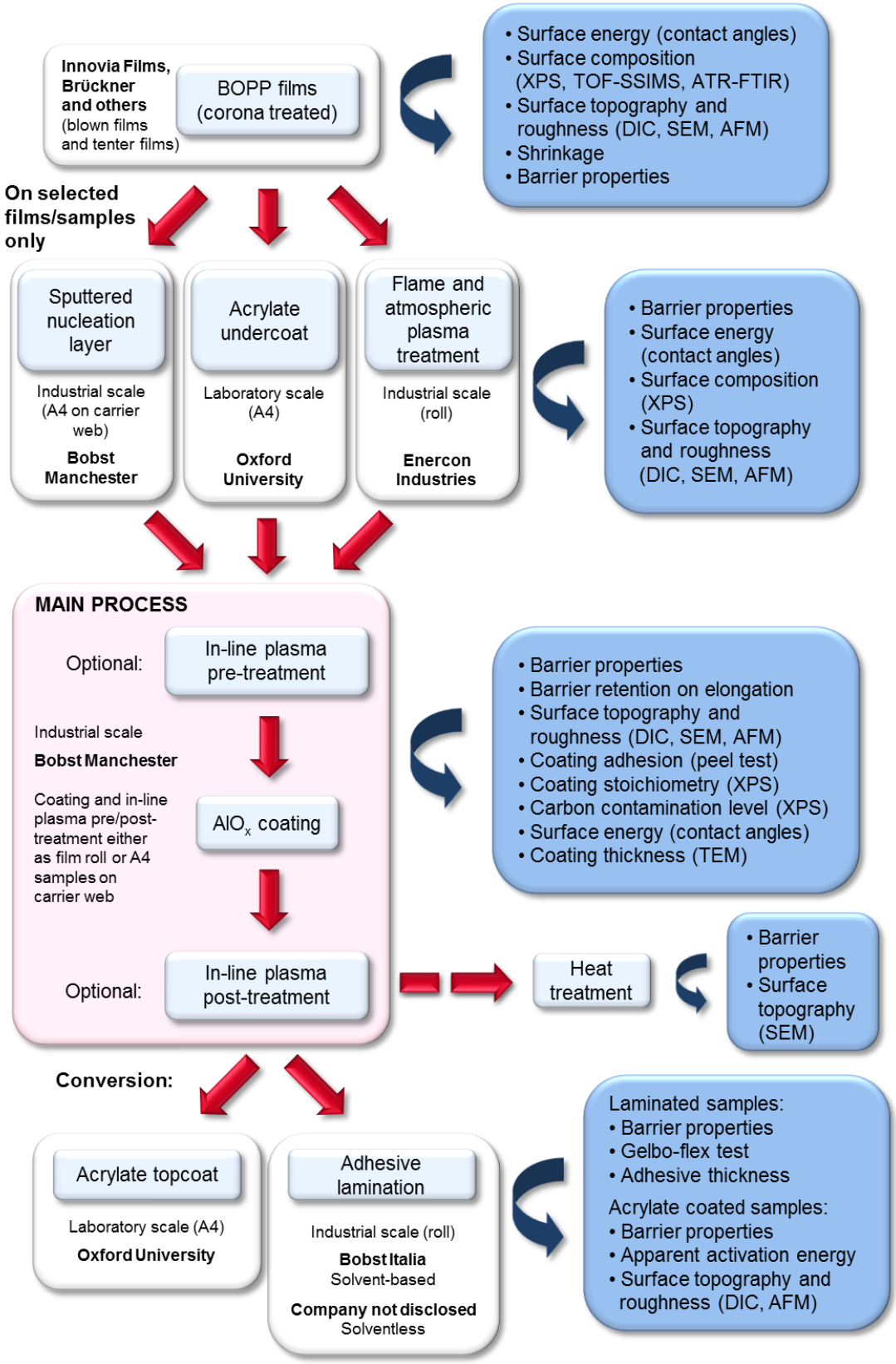

Figure 5-16: Experimental flow chart

Displayed in *Figure 5-16* is an experimental flow chart for the work carried out in the course of this project. The left-hand side describes the individual process steps (upstream and downstream of the AlO_x coating process) investigated, as well as the film materials used, whilst on the right-hand side (in blue boxes), the analysed material characteristics and analytical techniques applied are stated. As can be seen, the polymer films were analysed and investigated using a variety of techniques in order to accurately characterise each process step.

6 RESULTS AND DISCUSSION

6.1 Characterisation of uncoated polymer films

6.1.1 Oxygen and water vapour barrier performance

The barrier performances of the uncoated BOPP films and PET reference film, which were coated with reactively evaporated AlO_x barrier layers in the course of this project, are summarised in *Table 6-1* (including their film thickness). When uncoated films are measured for their barrier properties, they can give quite a broad range for OTR and WVTR, within which the results are scattered. Consequently, for each film type a range is given for the respective transmission rate. For the calculation of BIF (barrier improvement factor) values, which will be done later when the barrier results after AlO_x coating are presented (see *Table 6-10*), the mean value of this range will be used.

Table 6-1: Oxygen and water vapour barrier properties of plain (uncoated) polymer films

Film	Thickness	OTR	WVTR
	µm	cm³/(m² d)	g/(m² d)
BOPP A	30	1250 – 1450	4 – 5
BOPP B	15	2500 – 2900	7 – 8
BOPP C	20	2000 – 2100	6 – 7
BOPP D	20	1750 – 1850	4 – 5
BOPP E	22	1550 – 1650	3.5 – 4.5
BOPP F	18	400 – 500	4 – 5
PET	12	100 – 110	40 – 50

In general, all uncoated films (apart from BOPP F with the different polymer skin layer) exhibit barrier performances that fall within the typical range for the individual polymer film type and the respective film thickness [126, 135]. As mentioned in Chapter 4.1, the barrier properties of BOPP films are, amongst others, affected by the degree of orientation and crystallinity, i.e. a higher degree of orientation entails a higher degree of crystallinity and therefore improves the moisture barrier. These properties have, nevertheless, not been investigated in this study. Furthermore, the specific composition of the core and the skin layers, i.e. homopolymer and co/terpolymer, as well as the respective thicknesses of these layers, will affect the overall barrier performance of the coextruded film. This is, for example, obvious for BOPP F, which has been coextruded with a different (high surface energy) polymer as skin layer. As can be concluded from the transmission rate values stated in *Table*

6-1, the skin layer drastically improves the OTR of the BOPP film, but appears not to have such a significant effect on the water vapour barrier.

BOPP E, a film designated for heat shrink applications, reveals an improved oxygen barrier, as well as slightly enhanced water barrier, for its thickness, compared to BOPP A to C. This is due to the design of heat shrinkable films, which contain so-called hydrocarbon resins as additives (generally in the core layer), in order to tailor and improve their shrink properties [223-225]. One positive effect of these resins is the improvement of OTR and WVTR of the BOPP film (mechanism explained further at the end of this chapter). This also suggests that BOPP D, though this film was not labelled as a heat shrinkable BOPP, may have some hydrocarbon resin added, thus improving its plain film barrier performance. If this is the case and BOPP D might be a heat shrinkable film, then the investigation of the shrinkage of the polymer films (refer to Chapter 6.1.4) will reveal more information.

The general differences in plain film barrier performance seen between BOPP and PET are due to the different polymer properties, such as the glass transition temperature and polarity. BOPP at room temperature is above its glass transition temperature T_g (0 to 10 °C [55] for isotactic PP), which means that all amorphous parts are in a rubbery state and therefore more mobile. Furthermore, the 'free volume' is increased above T_g. Consequently, molecules such as gases can more easily permeate the polymer matrix. In contrast to that, PET at room temperature is below its T_g (69 to 115 °C [55]), hence all amorphous parts of the semi crystalline PET are in the glass state, the 'free volume' is reduced and the permeating molecules have a more tortuous path to negotiate through. For the WVTR of PET and BOPP, the polarity of the film also plays an important role. Due to the polar nature of PET, in contrast to the nonpolar BOPP, it can swell in the presence of moisture and this leads to an increased water vapour permeation rate. [1, 134, 226]

The barrier improvement seen by the use of hydrocarbon resins in BOPP films is presumably due to the amorphous hydrocarbon material having a higher glass transition temperature than PP and, therefore, being in the glass state at room temperature. Within the PP polymer, the hydrocarbon component accumulates in the amorphous regions of the polypropylene polymer and, hence, makes these less permeable.

6.1.2 Surface topography and roughness

The uncoated BOPP and PET film samples were investigated at a range of resolutions, using optical microscopy, scanning electron microscopy imaging and finally atomic force microscopy analysis.

6.1.2.1 Differential interference contrast optical microscopy

Starting with the lowest magnification level, the films were analysed using light microscopy with a DIC illumination mode at two different magnification scales. Representative low-magnification DIC images of the uncoated BOPP films (corona treated side) are shown in *Figure 6-1*.

Despite the low magnification level of light microscopy relative to SEM, this analysis already reveals significant differences between the various BOPP films, as well as the PET reference film (images for PET shown later in *Figure 6-3*). BOPP F, which has a different polymer skin layer, shows the smoothest surface, since no antiblock particles have been included in the formulation. However, surface imperfections are also present in this film and a slightly wavy surface structure is visible. Compared to BOPP F, the plain film surfaces of the other BOPP films appear rougher due to the presence of antiblock particles but also due to the background structure of these films. The standard packaging grade BOPP films have been produced with antiblock particles added to the skin layers, which in all cases are of roughly spherical shape (although it has become more common not to use any antiblock particles in the skin layer of films to be vacuum coated [69]). There are, however, distinct differences observable between the BOPP films in terms of antiblock particle size and distribution density. BOPP A, B and E barely show large antiblock particles in *Figure 6-1* and predominantly feature smaller (submicron size) antiblock particles, which will be more pronounced on the high-magnification DIC images presented later (*Figure 6-2*). In contrast to that, BOPP C and D reveal substantially larger antiblock particles with diameters of up to 10 µm. Here, it also appears that BOPP D exhibits slightly less of these large antiblock additives when compared to BOPP C. More information on the subject of antiblock particles and their size/amount, will be given by the results of the antiblock particle count, presented in Section 6.1.2.2.

BOPP A also exhibits features (lowered, round-shaped areas with a diameter of approximately 50 to several 100 µm, see *Figure 6-1* top left) that are an unwanted phenomenon that can emerge during the film production process. Their origin is, so far, not completely understood. However, it is assumed that these topographical features are closely related to the crystal structures of the polypropylene film, which are induced during cooling of the extruded cast-sheet/tube, modified during

reheating (both steps before the orientation process) and deformed during the sequential/simultaneous stretching procedure. Similar topographical features on the surface of BOPP films have also been reported and investigated by Tamura and co-workers [227, 228].

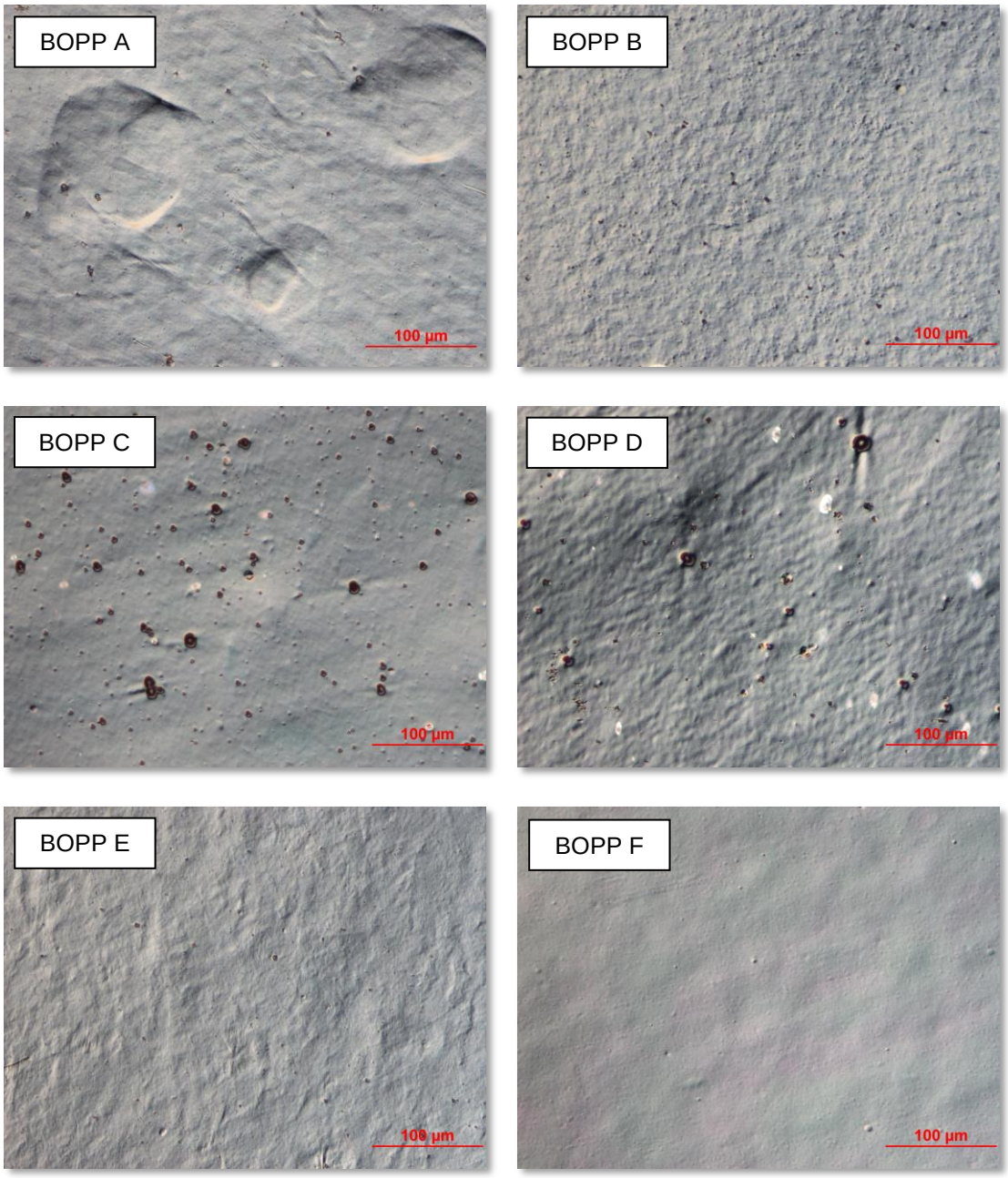

Figure 6-1: Low-magnification DIC images of uncoated BOPP films; top left: BOPP A; top right: BOPP B; middle left: BOPP C; middle right: BOPP D; bottom left: BOPP E; bottom right: BOPP F

The light diffraction/interference phenomena seen for BOPP D and to a lesser extent also for BOPP C in *Figure 6-1* may be caused by larger antiblock particles trapped

between the skin layer and the core, thus creating a cavity between the coextruded layers.

Leaving the antiblock particles and other features aside, each BOPP film has a specific underlying surface pattern. Here, BOPP A and C exhibit a very smooth and less textured background, which on this magnification level appears more similar to BOPP F, whilst BOPP B, D and E feature an intensely textured background pattern, however, with individual variations ('softer' bumpiness of BOPP D and E compared to the 'spiky' and edged texture of BOPP B).

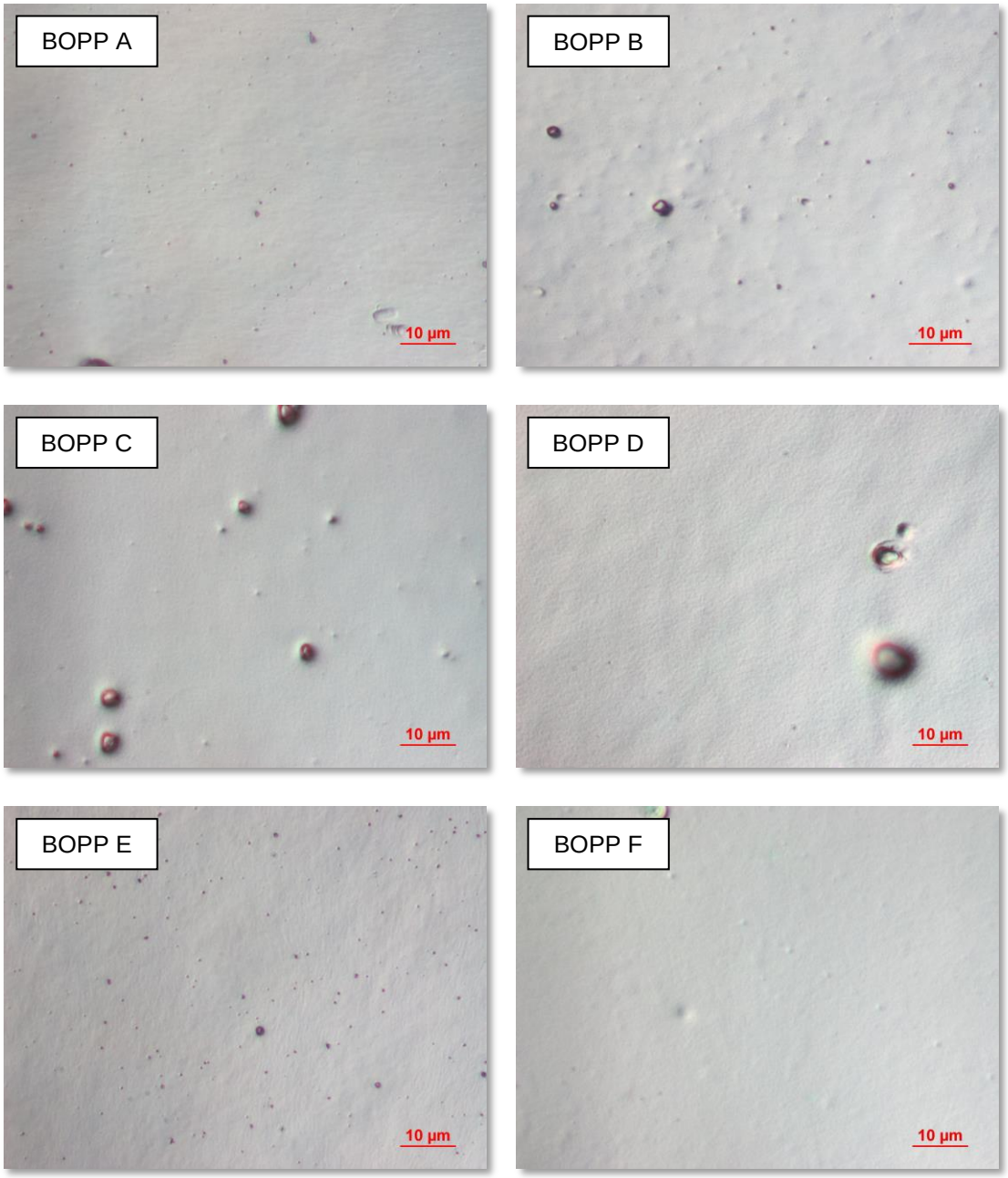

Figure 6-2: High-magnification DIC images of uncoated BOPP films; top left: BOPP A; top right: BOPP B; middle left: BOPP C; middle right: BOPP D; bottom left: BOPP E; bottom right: BOPP F

When increasing the magnification level of light microscopy (see *Figure 6-2*), additional surface characteristics for each film become observable. All films show a granular[e] surface background structure, which gives an 'orange-peel' appearance. Even BOPP F, which had a different polymer as skin layer, exhibits a similar texture. However, individual differences can, once again, be detected. BOPP A shows a texture that has a horizontal orientation and it is suspected that this is the machine direction of the film, based on the track marks (see bottom right of *Figure 6-2*, top left image) presumably left by a detached antiblock particle, which runs in the same direction. Also BOPP E exhibits an orientation, in this case however vertical. By contrast, no orientation of the grainy texture can be found for the other BOPP films. Overall, the grains appear the most pronounced for BOPP D, whilst BOPP B reveals additional mounds in its surface.

Also on this magnification level, differences in antiblock particle size and number density are noticeable. BOPP E features the largest number of submicron size antiblock particles, followed by BOPP A and then BOPP B, whilst BOPP C and D feature fewer but substantially larger antiblock particles (diameter > 1 µm). As already noticed on the lower magnification DIC images, BOPP D exhibits the least antiblock particles and no submicron particles are visible at all.

Additional features found on the BOPP films (see *Figure 6-2* top left, middle right and bottom right image) have either been created by antiblock particles, which detached from the BOPP surface, thus leaving indentations and track marks, or by antiblock particles of the rear side of the film, which upon contact in roll form created surface damage and indentations. Dislocated antiblock particles (indentations where they once resided) and other defects, such as scratches (from film handling and contact of the film with the equipment), can be found on all BOPP films. The latter can also be seen when investigating the PET film and similar abrasion defects on PET film have been shown in DIC images by Bishop [92].

On comparing the film surface of the BOPP films that contain antiblock particles with the standard grade PET film, a huge disparity becomes obvious. In the low-magnification DIC image (see *Figure 6-3*, left), the PET film exhibits a far greater surface roughness, created by a vast amount of antiblock particles than any of the investigated BOPP films. Furthermore, in the PET film, these antiblock particles are of various sizes and do not appear to be of spherical shape. Even in the high-

[e] The terms grainy/grains/granular are used here, and also for the SEM and AFM investigation, to describe the roughly spherical-shaped features of the surface texture of the polymer films (uncoated and coated). It is assumed that this granular structure (particularly pronounced in the AFM images) is caused by the crystalline structure of PP (i.e. spherulites and/or lamella).

magnification DIC image (see *Figure 6-3*, right), very small antiblock particles, comparable to those found on BOPP A, B and E, are visible. However, the antiblock particles on the BOPP films appear 'to lie on the surface', are not completely covered by the polymer and have a tendency to be easily removed. In contrast to the latter, the antiblock particles in the PET film seem to be further embedded in the polymer, such that the polymer fully enrobes the particle, even though they are still protruding from underneath the polymer. This is thought to be due to the production process of the PET film, whereby the (low-cost) film used comprises a typical single-layer structure, with the antiblock particles dispersed throughout this layer [67]. BOPP films generally are multilayer structures (typically three layers), with the antiblock particles just added to the polymer granules of the skin layers. The low-magnification DIC image of PET (*Figure 6-3*, left) looks very similar to SEM images (of comparable magnification) published by Numata et al. [229], DIC images by Jamieson and Windle [140] and DIC images by Bishop [92], although for the former two the PET substrate was coated with an inorganic barrier layer. As will be discussed later (see Section 6.2.2.1), a difference between coated and non-coated films cannot be established at this magnification level.

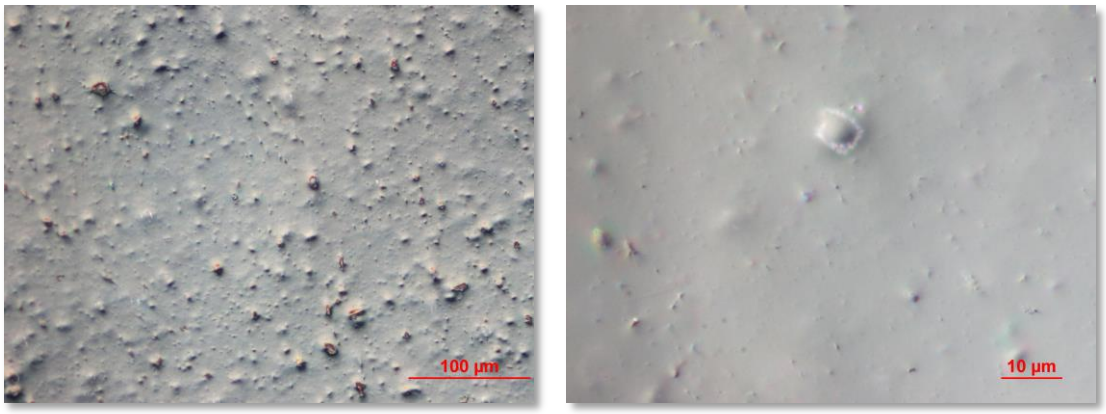

Figure 6-3: DIC images of uncoated PET at two different magnification levels

The examination of the plain film surface topography at various magnification levels is important, in order to investigate which plain film surface characteristics have the capability to negatively impact barrier properties of the AlO_x coated film. Scratches and scuff marks, or other similar abrasion type defects on the film surface, presumably due to contact of the film with the film processing equipment, have also been detected in light microscopy and large area AFM investigations of AlO_xN_y coated and uncoated PET film conducted by Erlat et al. [230]. Based on their results, they concluded that these features were over-coated by the 70 to 90 nm barrier layer and did not cause large uncoated areas but just local thickness variations. However, they consequently also emphasise that these plain film surface

characteristics are crucial and need to be considered in regards to barrier performance, especially for thinner coatings.

Furthermore, antiblock particles are thought to be critical for the barrier performance obtained after vacuum coating. Several research groups have shown antiblock particle related defects in inorganic barrier layers, such as coating fracture near the particle in the film surface [231, 232], as well as indentations in the coating created by antiblock particles of the rear film side, which again lead to cracks and coating fracture [126]. Mueller and co-workers [233] also found that when metallising a BOPP film surface without any antiblock particles, the number of defects/pinholes could be drastically reduced and the barrier performance was significantly better, compared to metallised standard BOPP. Analogous results were published by Rochat et al. [234] for SiO_x barrier layers deposited onto PET film containing antiblock additives in the surface layer, in contrast to a PET film free of these. It can consequently be assumed that the number of antiblock particles can have a major impact on the number of pinholes/defects in the coating, though not every particle in the film surface will necessarily create a defect. If antiblock particles dislocate from the film surface or leave imprints before coating, then these surface imperfections may be over-coated by the barrier layer. However, if this happens after coating, defects (uncoated areas) will inevitably be created.

6.1.2.2 Antiblock particle count

As stated in the previous chapter, antiblock particles can play an important role with respect to the number of defects in the barrier layer and hence the barrier performance achieved. Consequently, antiblock particle counts and classifications into sizes were carried out using light microscopy.

For this investigation, an appropriate magnification level had to be selected in order to ensure the data collected was representative for all films analysed, i.e. the specific background surface features did not affect the results and also the smaller antiblock particles (as present on BOPP A, B and E) were detected and evaluated. A 500 x magnification was chosen, which was equivalent to an investigated area of 22600 µm², and 15 random areas of this size were analysed per polymer film. The particle count was averaged over these areas.

For the analysis itself, the microscope images (in reflected light mode) are overexposed with light and a certain threshold value is set, which dictates that everything darker will be detected as an antiblock particle. The software then measures the area of each dark spot and calculates its equivalent diameter. Subsequently, the antiblock particles are categorised according to their size in intervals of 0.1 µm (i.e. 0 µm< x ≤ 0.1 µm, 0.1 µm < x ≤ 0.2 µm, …). Nevertheless, this technique also has some small drawbacks, which, in the interest of completeness, should be mentioned. In order to capture the majority of the antiblock particles present in the investigated area, the threshold value needs to be of the right order, which generally leads to a slight overestimation of the true size of the antiblock particle (see also top images in *Figure 6-4*, the red area on the right image is larger than the true dark area on the left image). Furthermore, two coalescent antiblock particles will be counted as one particle of a bigger size and other surface features and contaminations, which create dark areas in the image, will additionally be counted as antiblock particles. All antiblock particles are assumed to be of spherical shape, which in the case of BOPP is a good approximation, but does not reflect the situation for PET. Finally, some submicron antiblock particles, which cannot be resolved at the selected magnification level (see for example antiblock particles in SEM investigation, *Figure 6-6*), will not be taken into consideration.

Figure 6-4 illustrates the antiblock count procedure with the overexposed images of the film surface (left column) and the same images showing the areas detected as antiblock particles marked in red (right column). The images are shown for two extreme situations; a small amount of large antiblock particles (BOPP C) and a large amount of small antiblock particles (BOPP E and PET).

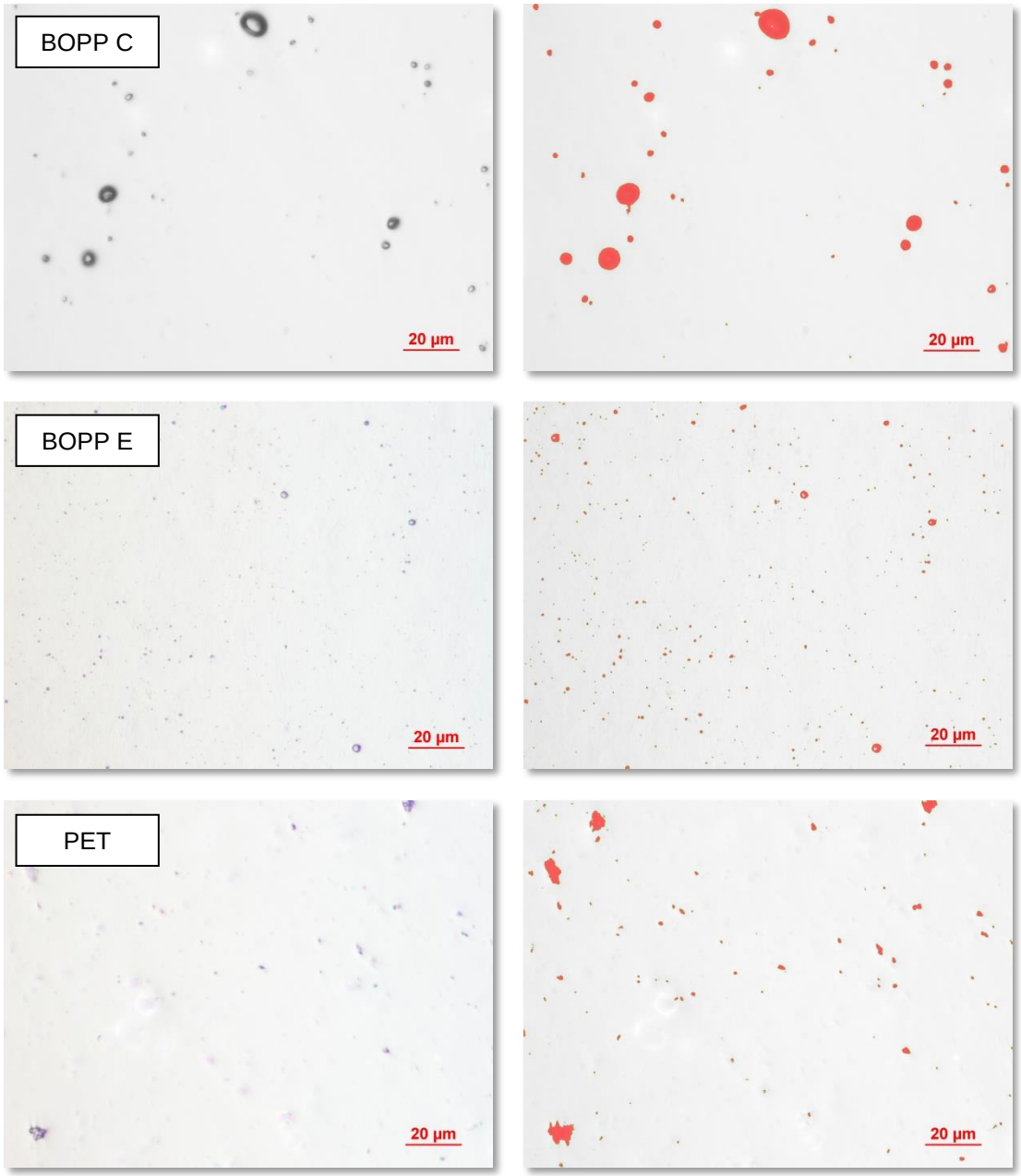

Figure 6-4: Light microscope images showing antiblock particle count on polymer films; top: BOPP C; middle: BOPP E; bottom: PET; marked in red are areas recognised as antiblock particles

For PET, it becomes noticeable that the antiblock particles are more angular and, furthermore, are embedded in the polymer, which makes it difficult to detect and estimate the 'true' size of each particle. As can be seen from *Figure 6-4*, bottom, some of the antiblock particles, which appear as light coloured 'bumps', are counted as antiblock particles of much smaller size.

The results of the antiblock particle count are summarised in *Figure 6-5* and, additionally, *Table 6-2* for the polymer films investigated (all films apart from BOPP F, which was not examined because of the absence of antiblock particles). In

summary, the antiblock particle count confirms the results of the DIC light microscopy investigation.

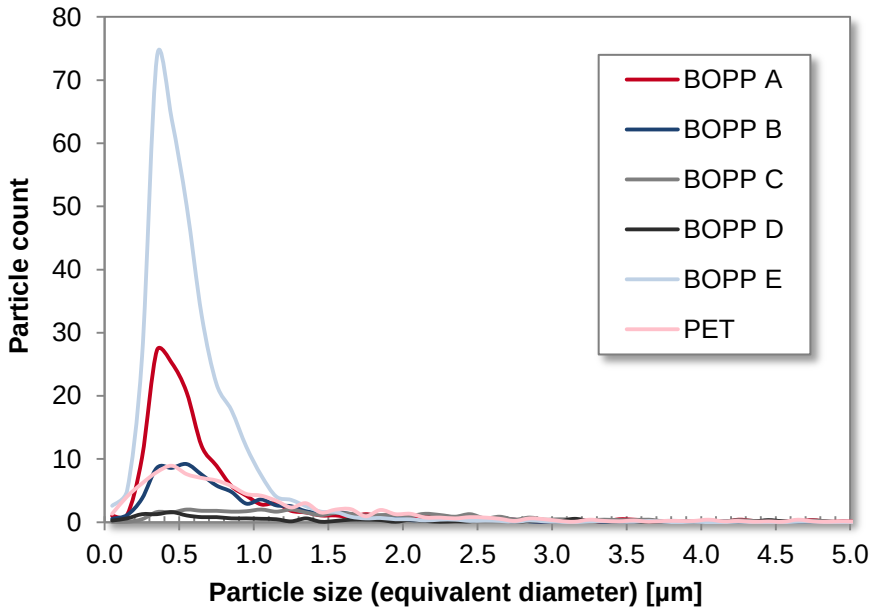

Figure 6-5: Antiblock particle size distributions (22600 µm² area) for BOPP films and PET reference film

From *Figure 6-5* and *Table 6-2* it can be seen that BOPP F has the largest amount of submicron antiblock particles, followed by BOPP A and then BOPP B and PET, which revealed very similar antiblock particle size distributions. Once again, it should be emphasised here that for PET, the antiblock particle sizes obtained in this investigation do not necessarily reflect the actual sizes.

Table 6-2: Cumulative and total amounts of antiblock particles for BOPP films and PET reference film

Film	Antiblock particle count per 22600 µm² area					per mm²
	≤ 1 µm	> 1 µm	> 5 µm*	> 10 µm*	Total	Total
BOPP A	116	25	1.7	0.2	141	6263
BOPP B	53	24	0.5	0	77	3383
BOPP C	13	31	3.1	0.5	44	1935
BOPP D	9	10	1.7	0.2	19	823
BOPP E	305	27	0.2	0	332	14720
PET	60	34	1.0	0	94	4153

*Decimal place shown to indicate differences

BOPP C and D exhibit far fewer submicron antiblock additives. Nevertheless, just considering antiblock particles above 1 µm does not expose significant differences, with only BOPP D showing a smaller number, compared to the rest of the films. Only when investigating the cumulative amounts of antiblock particles larger than 5 or 10 µm, can one detect that there is a very low number for BOPP B and E, whilst BOPP C contains the largest number of antiblock particles of this size, followed by BOPP A and D. With respect to the total number of antiblock particles, all films behave identically as seen for the submicron range.

For all films, the maximum of the particle size distribution is found for an antiblock diameter between 0.3 and 0.6 µm, apart from BOPP C, which exhibits a maximum at approximately 1 µm. The antiblock particle size distributions acquired here are similar in shape to distributions obtained by Fayet and co-workers [235] for different grades of PET films. Nevertheless, in their case, the peak antiblock diameter values range between 1 and 1.5 µm, which is considerably larger than found in this study for PET and also BOPP A to D. Fayet et al. also deposited SiO_x barrier layers onto three PET film grades and found that the OTR increased with rising number of antiblock particles per mm².

The average antiblock size between 0.3 and 0.6 µm found here is surprisingly close to the results of defect/pinhole counts published by Hanika et al. [156]. Based on their light microscope, SEM and AFM investigations of metallised BOPP, they state that the maximum number of defects is found for a defect area of approximately 0.5 µm², which corresponds to an equivalent diameter of 0.8 µm. Furthermore, their defect area distribution function exhibits a similar shape to the antiblock size distributions shown in *Figure 6-5*, with a steeper decline from the maximum towards the smaller particle sizes (defect areas), compared to the larger ones. Work on the defect size distributions in SiO_x coatings on PET carried out by Rochat et al. [234] also revealed similar shaped curves, with the maximum located for a defect diameter around 1 µm. They investigated SiO_x coated PET films with and without antiblock additives and obtained analogous shaped curves in both cases, but an increased defect density, as well as increased mean defect size when the additives were present. This could suggest that there is a direct correlation between antiblock particles, their size and the defects created in an inorganic barrier layer.

Calculating the total amount of antiblock particles per mm² (see *Table 6-2*, last column), the results obtained (apart from BOPP D) reveal larger numbers, especially BOPP E than a typical number of 10^3/mm² as stated by Langowski [126] and Henry et al. [232]. However, different film grades are likely to have different antiblock particle amounts per mm² [235].

6.1.2.3 Scanning electron microscopy

In order to investigate the plain film surfaces beyond the resolution offered by light microscopy, SEM analysis was carried out. No conductive coatings (as is usually done for samples of an insulating nature) were applied for this investigation to avoid masking important surface details. To minimise charging effects, low acceleration voltages of 0.4 to 0.5 kV were used.

The low-magnification SEM images (not shown here) are in agreement with the DIC light microscopy analysis (see Section 6.1.2.1) and confirm the differences in antiblock particle size and distribution seen on the different polymer films. On the high-magnification SEM images shown in *Figure 6-6*, the typical background structure of each individual film becomes observable. The granular texture of the BOPP films ('orange-peel'), which was already indicated in the high-magnification DIC images, is distinctively visible in the SEM images and specific differences can be detected. BOPP A and also BOPP E show an orientation, i.e. additional waviness, of the background structure, which in both cases runs approximately diagonal across the image, whilst the surface of BOPP B and also PET reveal a 'bumpy' and undulating background structure. As discussed in Section 6.1.2.1, it is assumed that the oriented texture of BOPP A and E is aligned in the machine direction and caused during film stretching. By contrast, BOPP C, D and F do not show such background structures, but appear very even and smooth. (One might say, though, that BOPP F exhibits some degree of unevenness.)

Furthermore, differences in the grain size (i.e. coarse or fine orange-peel) can be observed between the BOPP films. BOPP B appears to have the largest grains, followed by BOPP D and then BOPP C. Not taking the oriented texture of BOPP A and E into account, they both exhibit a finer-grained structure. BOPP F, which was very difficult to investigate during SEM analysis, due to missing surface features (such as antiblock particles) that can be used to focus the image, displays a structure with a similar grain size to BOPP C. The PET film does not exhibit a graininess or orange-peel that is comparable to BOPP in the SEM images.

With respect to judging the roughness of the films based on the SEM images, it is important to state that the 'roughness impression' of the surface will be affected by the contrast and brightness settings of the individual SEM image, which are not identical for all films. Consequently, AFM analysis (see Chapter 6.1.2.4) is used to investigate the film surface roughness. This analysis and the images associated will also illustrate the differences in grain size, as discussed above.

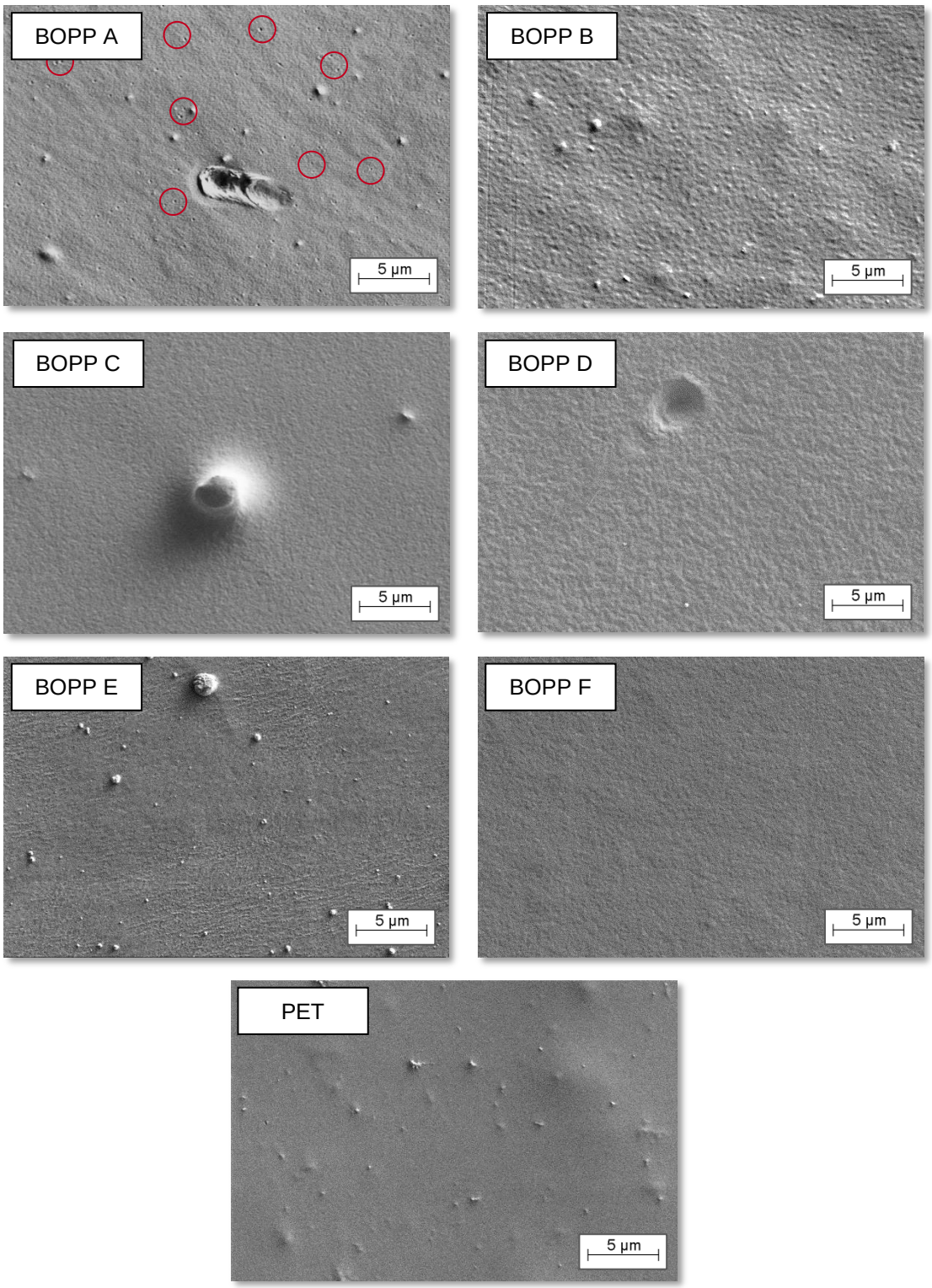

Figure 6-6: SEM images of uncoated polymer films; top left: BOPP A; top right: BOPP B; second row left: BOPP C; second row right: BOPP D; third row left: BOPP E; third row right: BOPP F; bottom: PET

The differences in antiblock particle size are also obvious on the SEM images shown in *Figure 6-6*. BOPP A, B and E as well as the PET film reveal a vast majority of submicron size antiblock particles, in contrast to BOPP C and D. For the PET film, one can detect that many of the small antiblock particles are completely

encapsulated by the polymer and, thus, rather appear as small bumps, which presumably have not been detected during the antiblock particle count (refer to Section 6.1.2.2)

The damage/imprint seen on BOPP A and BOPP D (*Figure 6-6*, top left and second row right) are created by antiblock particles, either dislocating from the film surface or leaving an imprint when located at the rear side of the film. As discussed in Chapter 6.1.2.1, detached antiblock particles are a common phenomenon for BOPP films, where the antiblock particles are added to the outer skin layers only and thus are less incorporated into the film, and antiblock particles frequently detach during film conversion and winding.

Finally, one key difference was seen in that BOPP A was covered in defects shaped like small craters or 'dimples' (*Figure 6-6*, top left, a few features marked with red circles) with diameters of 50 nm to several 100 nm (measured via AFM, see Section 6.1.2.4). These defects were originally assumed to be caused by micro-arcs appearing during corona treatment at the film production site. However, based on further SEM analysis of a variety of BOPP film samples, corona treatment could be excluded as a potential source of the defects and it was concluded that the heat setting/thermo fixation may cause the craters. This process step is conducted after the orientation process, in order to stabilise the film and prevent unintentional shrinkage, and it is suspected that during this re-heating process, volatile components within the film surface flash evaporate off and, consequently, leave crater-shaped defects. Similar defects could not be detected on any other film investigated here.

The presence of any kind of defect in the uncoated film surface will be of importance when the film is coated with the thin inorganic barrier layer, as certain defects may be reproduced in the coating whilst others will be over-coated and might even disappear.

6.1.2.4 Atomic force microscopy

In addition to the light microscope and SEM imaging, the uncoated films were examined using AFM analysis. Therefore, a scan size of 5 x 5 µm² was chosen and, additionally, the surface roughness was investigated. Representative AFM images of the BOPP films are shown in *Figure 6-7* and for the PET reference film in *Figure 6-8*. For all these images, the same z-scale bar (-15 nm to 15 nm) was adjusted in order to present directly comparable images.

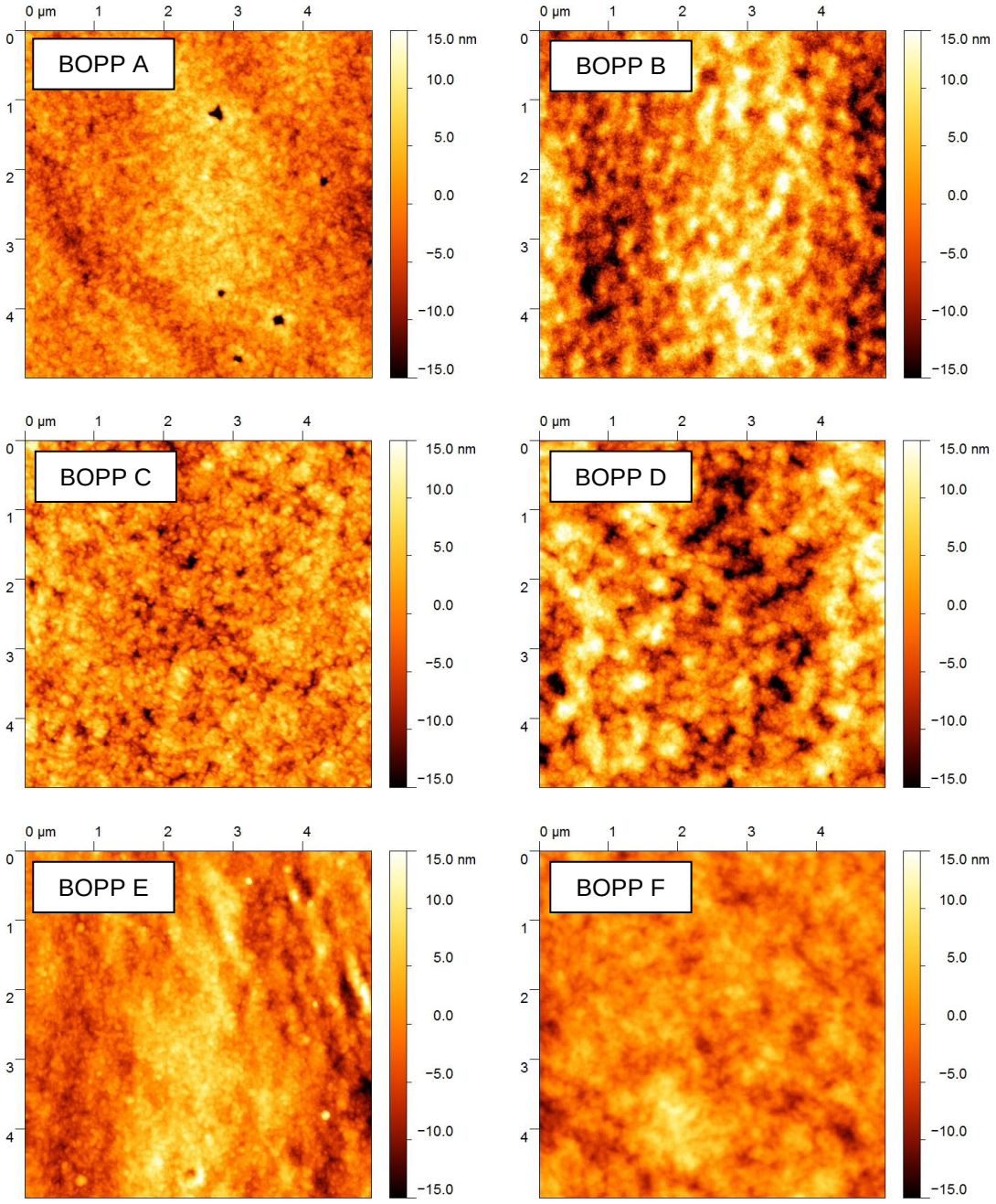

Figure 6-7: 5 x 5 µm² AFM scans of uncoated polymer films; top left: BOPP A; top right: BOPP B; middle left: BOPP C; middle right: BOPP D; bottom left: BOPP E; bottom right: BOPP F

AFM analysis of the plain films confirmed the results of the SEM investigations and revealed a granular surface structure (for the BOPP films), as well as the typical background textures. For example, BOPP A, B and E again show a waviness/bumpiness that overlays the granular structure, whilst BOPP C, D and F appear very even. For BOPP B and D, the granular texture gives the impression of being coarser, which was also detected during the SEM investigations. In the case of BOPP E, one can also observe some distinct light coloured 'spots' in the 5 x 5 µm² (see *Figure 6-7*, bottom left), which are small antiblock particles that could not be avoided during analysis. Furthermore, craters/dimples were detected by the AFM examinations of plain BOPP A (see *Figure 6-7*, top left). The AFM analysis also allowed the size of these defects to be measured, which range from 50 nm to several 100 nm in diameter and some tens of nm in depth (see Appendix A2). AFM did not reveal these crater/dimple-shaped defects on any of the other BOPP films, nor the PET film. Further investigations of the craters with respect to their shape and depth were carried out and can be found in Appendix A2.

The granular surface texture, which has already been discussed for the SEM images and, furthermore, was already visible to some extent in the high-resolution DIC images (especially for BOPP C and D), is presumably caused by the crystalline structure/morphology of the polypropylene (altered by the orientation/drawing process, see also short discussion in Chapter 4.1.1). Nevertheless, O'Hare et al. [236] state that they did not detect any evidence for a spherulitic structure in their studies of corona treated BOPP. In the latter publication, it is, however, also stated that the presence of a spherulitic structure depends on the film and its properties, such as degree of crystallinity, molecular weight, as well as the film processing conditions. One important property that appears to affect the surface structure is the skin layer composition in terms of co- or terpolymers (with ethylene and/or butylene). Also this has been previously addressed in Chapter 4.1.1.

O'Hare et al. [236] show a similar 5 x 5 µm² AFM image of corona treated BOPP, which exhibits a grainy surface texture and a waviness in the background. AFM scans of uncoated BOPP copolymer films (propylene-ethylene) presented by Moosheimer and Bichler [64] and Moosheimer et al. [237] also exhibit a comparable granular texture. Nevertheless, in earlier publications from the latter research group, the BOPP copolymer surfaces appeared different in the AFM images [77, 238, 239]. This is, though, not too surprising, based on the vast differences seen here for standard BOPP films.

In contrast to the BOPP films, the PET surface exhibits a very smooth and fine texture with no noticeable grains of comparable size to the BOPP films. The small

light coloured 'spots' and bumps in the lower half of the AFM image (refer to *Figure 6-8*) are assumed to be caused by small antiblock particles in the PET film surface. The PET film (as well as BOPP E, see *Figure 6-7*, bottom left) showed a very large number of these submicron antiblock particles (see SEM images, *Figure 6-6*) and it was, therefore, hard to measure a 5 x 5 µm² area that did not exhibit any. It should be further noted that the surface texture seen here for PET also appears a lot finer and less granular than seen in AFM images published by Moosheimer and Langowski [132] and Low and Xu [240].

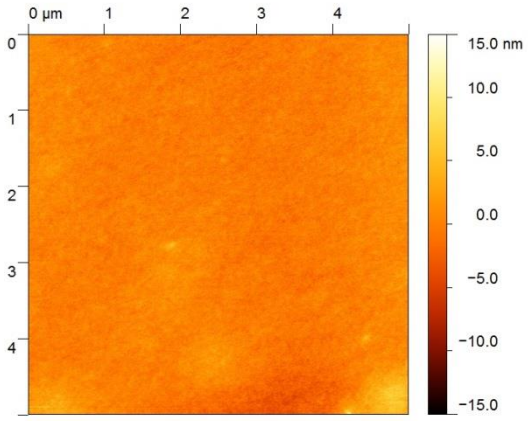

Figure 6-8: 5 x 5 µm² AFM scan of PET

The AFM analysis was additionally used to gain information about the roughness of the film surface in terms of RMS and R_a values. Therefore, several (at least 10) scans were performed per film sample and, to ensure statistical reliability and reproducibility of the roughness results, the scans were conducted randomly on different locations on the BOPP film. Additionally, scans for roughness evaluation were not acquired on areas where large antiblock particles were present. The AFM images presented in *Figure 6-7* and *Figure 6-8* already give a quite good idea about the roughness of the individual film surfaces, based on the coloration of the AFM images, which is confirmed by the roughness values summarised in *Table 6-3*.

The PET film revealed the smoothest surface roughness, with a mean RMS value of 1.7 nm and R_a value of 1.3 nm, which are in good agreement with values reported by Benmalek and Dunlop [241], Deng et al. [130] and also the roughness data obtained for some of the PET film surfaces investigated by Phillips [242]. This is followed by BOPP F, which had a high surface energy polymer as its skin layer. All standard BOPP films exhibit larger surface roughness values than the PET film (and BOPP F). The larger surface roughness of BOPP/PP, in comparison to PET, has also been stated by other researchers [130, 241] and the roughness values obtained here for the various standard BOPP films are comparable to these and further

results [78, 243] when comparable scan sizes are used to acquire the roughness data (4 x 4 µm² in references [241, 243] and 5 x 5 µm² in reference [78]).

Table 6-3: Surface roughness in terms of RMS and R_a values (mean value and standard deviation) of uncoated polymer films, determined from 5 x 5 µm² AFM scans

Film	Side	RMS	R_a
		nm	nm
BOPP A	Corona	4.1 ± 0.7	3.3 ± 0.5
BOPP B	Corona	6.1 ± 1.9	4.8 ± 1.6
BOPP C	Corona	4.1 ± 0.3	3.3 ± 0.2
BOPP D	Corona	6.2 ± 0.5	4.9 ± 0.4
BOPP E	Corona	4.4 ± 0.7	3.5 ± 0.5
BOPP F	High surface energy polymer	3.0 ± 0.3	2.3 ± 0.3
PET	Corona	1.7 ± 0.3	1.3 ± 0.2

The largest RMS and R_a values were measured for BOPP B and D. In the case of BOPP D, this is due to the intensely pronounced coarse-granular structure, whilst for BOPP B the larger roughness is caused by the contribution of waviness and bumps in the background texture. O'Hare and co-workers [236] present a 5 x 5 µm² AFM image of a BOPP film that shows a similar granular structure and also wavy background texture. However, their RMS value is calculated from a 1 x 1 µm² scan size and hence, at 2.4 nm, is lower than the values obtained here. BOPP roughness values lower than measured in this thesis have been reported by other researchers that used a lower scan size (in general 1 x 1 µm²) to determine the roughness parameters [78, 130, 244]. The 5 x 5 µm² scan size used in this thesis tends to result in larger mean roughness values and corresponding standard deviations (e.g. for BOPP A, B and E, refer to *Table 6-3*), since the additional texture overlaying the grainy surface structure causes an additional variation of the roughness. For BOPP B, this additional texture is highly pronounced (see SEM and AFM images in *Figure 6-6* and *Figure 6-7*, respectively) and entails an extraordinary large standard deviation. Also Mahlberg and co-workers [78] found that, with increasing the scan size, surface roughness increases due to the inhomogeneity of the PP film. The first order line-wise levelling (applied to all AFM scans) does not remove this texture and, therefore, it can distort the RMS and R_a values. However, as this texture is part of the film surface and not caused by the analytical technique or sample preparation (see also high-magnification DIC images in *Figure 6-2* and SEM images in *Figure 6-6*), it should be taken into account when obtaining roughness data. Higher-order line-wise levelling has been carried out in Section 6.4.1.3 and the effect on AFM

images and surface roughness (for BOPP A to C) is summarised in *Figure 6-63* and *Table 6-29*, respectively.

BOPP A and C feature identical RMS and roughness average values, despite the very different appearance of the surface itself, with defects/craters and waviness being present for BOPP A (*Figure 6-7*, images top and middle left). Therefore, just looking at the surface roughness parameters does not expose critical differences in the film surface topography.

The effect of plain film surface roughness and topography (and also coating roughness, see Section 6.2.2.3) on the barrier properties of inorganic barrier layers deposited thereon has been discussed to a large extent in literature, and not all results and conclusions are in agreement. Whilst Langowski [126] states that so far no clear relationship between the substrate topography and the barrier performance after coating could be established, Benmalek and Dunlop [241], who evaporated SiO_x and sputtered AlO_x barrier layers onto different polymer films, emphasise that on a rougher surface a thicker coating will be required in order to completely cover the surface topography. They mention substrate shadowing effects to be responsible for non-satisfactory barrier properties after coating. Also Low and Xu [240] underline the importance of a smooth polymer substrate surface as a critical requirement for the water vapour barrier performance of sputtered AlO_x layers. Bichler et al. [245] showed an improvement of the oxygen barrier properties of AlO_x coated BOPP film (electron beam evaporation) following oxygen plasma pre-treatment and attributed this to the smoothing of the polymer surface, induced by the plasma treatment, resulting in the homogeneous growth of the coating. Analogous conclusions were drawn by Bahre and co-workers [246], who found that excessive plasma treatment of a PET film surface resulted in roughening and hence barrier degradation of subsequently deposited CVD SiO_x barrier layers (i.e. no complete layer formed).

Furthermore, the smoother surface of acrylate layers, applied onto polymer films prior to depositing the inorganic barrier layer, has been argued to be the main reason for the barrier improvement obtained when used as undercoats. Therefore, these layers are frequently referred to as smoothing layers. The effect of acrylate undercoats will be discussed in Chapter 6.4.1.

With the evaporation process being a ‘line-of-sight’ deposition [72], larger surface irregularities, such as the previously described antiblock particles (especially when several microns in size), are quite likely to play an important role with regards to shadowing effects. It is however not known whether, at the scale investigated by AFM (5 x 5 µm²), the surface roughness, as defined by the grains, waviness and

small bumps, can cause shadowing effects. Furthermore, the evaporation source consisting of multiple aligned evaporation boats, as well as the moving substrate, may outweigh shadowing effects to some degree.

6.1.3 Surface chemistry

6.1.3.1 Surface energy via contact angle measurement

The plain polymer films were further characterised in terms of surface chemistry via contact angle measurement (the most surface sensitive of any conventional surface analysis methods [247]) for surface energy determination. This technique can be regarded as an indirect method to assess information about the chemical composition of the different substrate film surfaces. Since it has been shown in literature that polymer surface energy plays an important role for the nucleation and growth of evaporated coatings [130, 248], as well as for the adhesion and barrier properties of metallised BOPP [77, 249], this parameter is analysed in order to investigate its effect on the barrier properties of the films after AlO_x coating.

The results obtained for the various BOPP films and PET reference film are summarised in *Table 6-4*. Replicate measurements of at least five samples were carried out for each film type. In addition to the side that is coated with the AlO_x barrier layer (i.e. corona treated side or high surface energy polymer skin layer), the table also states the surface energies obtained for the reverse side of the polymer films.

As can be seen from the results presented in *Table 6-4*, the total surface energies of the corona treated side of BOPP A, B, C and E are within a range of 36 to 38 mN/m, which is a typical level to be expected for corona treated BOPP film [236, 250-252]. In contrast to that, the total and also polar surface energy of BOPP D is lower, with a mean value of 33.0 mN/m and a polar fraction of 4.5 mN/m. Nevertheless, also here similar values have been reported for corona treated BOPP film in literature [63]. The dispersive surface energies for all corona treated BOPP films are very similar, between 28 and 30 mN/m, which is the characteristic value for the total (and dispersive) surface energy of untreated BOPP (see later in this section). One reason for the unusually low surface energy of the corona treated side of BOPP D might be the age of the film, as the time of contact angle measurement and AlO_x coating was approximately three years after film production (whilst the age of the other films was less than one year). It is well known that corona treated polypropylene film undergoes an ageing process, also called hydrophobic recovery [60, 243, 250, 253]. Data published by Novák et al. [254], for example, shows that for corona treated BOPP the surface energy initially drops and then stabilises at a value of about 36 mN/m (investigated time range of approximately 350 days, same surface energy calculation method used as in this thesis). Kullberg [255] reports that the surface energy of corona treated BOPP declines from start values of 52 to 56 mN/m to

stable values around 38 to 40 mN/m (time range 174 days). These final values compare well with the data presented here for the standard commodity grade BOPP films (apart from BOPP D). Nevertheless, other researchers report different values, e.g. reference [60], and the ageing behaviour, as well as the initially obtained surface energy level, depends on many factors, such as corona treatment process variables (e.g. power, treater roll temperature) and film surface composition (homo-, co- or terpolymer) [63, 256].

Table 6-4: Total, dispersive and polar surface energies of BOPP films and PET reference film, as determined by contact angle measurement

Film	Side	Surface energy		
		Polar	Dispersive	Total
		mN/m	mN/m	mN/m
BOPP A	Corona	8.9 ± 0.6	29.1 ± 0.4	38.0 ± 0.4
	Reverse	0.1 ± 0.0	29.8 ± 0.5	29.9 ± 0.5
BOPP B	Corona	7.8 ± 0.6	28.6 ± 0.3	36.4 ± 0.4
	Reverse	0.1 ± 0.0	29.2 ± 0.3	29.3 ± 0.3
BOPP C	Corona	7.0 ± 1.0	29.4 ± 0.8	36.4 ± 0.6
	Reverse	0.0 ± 0.0	28.8 ± 0.2	28.8 ± 0.2
BOPP D	Corona	4.5 ± 0.8	28.5 ± 0.7	33.0 ± 0.3
	Reverse	0.1 ± 0.1	28.3 ± 0.5	28.4 ± 0.5
BOPP E	Corona	7.6 ± 1.0	29.4 ± 0.8	37.0 ± 0.2
	Reverse	0.5 ± 0.1	28.3 ± 0.4	28.8 ± 0.3
BOPP F	High surface energy polymer	6.2 ± 1.3	36.2 ± 1.4	42.4 ± 0.3
	Reverse	0.1 ± 0.0	29.0 ± 0.1	29.1 ± 0.1
PET	Corona	9.6 ± 0.9	38.6 ± 0.9	48.2 ± 1.3
	Reverse	8.6 ± 0.5	37.4 ± 0.4	46.0 ± 0.3

The thermodynamically driven ageing process causes the polymer surface to revert back to its initial relatively hydrophobic state. This can be explained by a variety of mechanisms including; reorientation of initially surface protruding functional groups, created by the treatment, back towards the bulk polymer; migration of mobile short polymer chains from the bulk to the polymer surface; internal migration of low-molecular-weight oxidised material; or diffusion of additives to the film surface. The extent of the latter diffusion related events depends strongly on ambient conditions [74, 253, 257]. Consequently, more pronounced differences in the polarity/chemistry of the corona treated film surfaces may also be present for the other standard BOPP

films (A, B, C, E), but are not detected due to the nature of the contact angle measurement, which only probes the outermost atomic layers. Furthermore, the films are AlO_x coated in vacuum and in this environment volatile components may desorb from and leave the film surface more readily due to the lower vapour pressure. The surface is a dynamic system and in vacuum, it is different to the surface in atmosphere. Thus, these components may interfere with the contact angle measurements conducted under atmospheric conditions, but have less impact for the depositing coating in vacuum. In order to further characterise the films and detect possible differences, the exact chemical composition of the plain BOPP films needs to be studied by XPS analysis (see Chapter 6.1.3.2).

The reverse sides of BOPP A to F reveal typical surface energies for untreated BOPP film [63, 236, 251]. A polar surface energy deviating from 0 mN/m (this value would be expected for the nonpolar hydrocarbon PP) can be explained by either backside treatment or contamination on the film surface (e.g. from the atmosphere or film additives) affecting the contact angle measurement. It is also worth mentioning that in the case of BOPP, treated and untreated surface, there is a good agreement between the total surface energy values obtained via different methods (Wolf and Sparavigna [251] used the calculation method according to Wu [198], whilst Strobel et al. [250] used the wettability method according to ASTM D2578 [207] and O'Hare et al. [236] applied the same approach as used in this thesis, but with a variation in the test liquids used).

The total surface energies of BOPP F (the film with the modified skin layer) and PET are higher, compared to the standard BOPP films, which is due to a higher dispersive surface energy component, as can be detected from *Table 6-4*. This difference is caused by the different chemical surface composition of these films and it is assumed that this surface chemistry is an important nucleation condition for the depositing AlO_x layer. The total surface energy of 42.4 mN/m measured for BOPP F in this study is lower than expected, since a value of 52 to 56 mN/m is stated in data published by the manufacturer [258]. However, the high surface energy polymer skin layer is in contact with the low surface energy reverse side of BOPP F (a polypropylene copolymer) when stored in roll form and material may be transferred from the reverse onto the special skin layer, thus reducing the surface energy measured (similar to the decay of AlO_x surface energy, see Section 6.2.4). The corona treated PET film shows a total surface energy that is lower than would usually be expected for treated PET, whilst the value measured for the untreated side is comparable to the reported value of 47 mN/m [259]. The lower surface energy of the corona treated PET film can be explained by an ageing process,

similar to BOPP [253]. There are, though, deviations in the contribution of the dispersive and polar part towards the total surface energy (when results obtained in this thesis are compared to results of reference [259]), which may be attributed to the different calculation technique applied (reference [259] uses Wu [198]). Nevertheless, another research group [260] reports different surface energy values for untreated and corona treated PET, despite using the same calculation approach applied in this thesis (but, apart from water, different test fluids).

The surface energies were additionally examined using dyne pens according to ASTM D2578. Whilst for BOPP A to F, these results were in line with the results obtained via contact angle measurement and the calculation approach used, there was a strong discrepancy for the surface of the corona treated PET film. However, different techniques (i.e. test fluids, calculation methods) can result in different surface energies [208]. The use of different measurement techniques may also be the reason for the deviating results obtained for BOPP F in this study, compared to the film manufacturer.

6.1.3.2 X-ray photoelectron spectroscopy

Whilst contact angle measurement only probes the outermost portions of the surface (sampling depth approximately 0.5 nm [261]), XPS analysis has a greater sampling depth (in this study 5 to 6 nm). Therefore, ageing processes of corona treated BOPP film (as discussed in Chapter 6.1.3.1), which presumably take place in the top few nanometres of the film surface, should not affect the outcome of XPS analysis, as found by Strobel et al. [250, 253]. Furthermore, the AlO_x coating process takes place in vacuum, as does the XPS analysis, and it is anticipated that the film surface will be different in vacuum than it is in atmosphere, where contact angle measurements take place. It can, therefore, be argued that the contact angle measurement does 'not see the same surface', as do the arriving atoms and molecules during deposition, and an analytical technique conducted in vacuum is a more representative technique. Nevertheless, XPS analyses more than just the outermost surface.

The film surface compositions (side to be coated) in at% of the BOPP films and PET reference film are summarised in *Table 6-5*. In order to evaluate the XPS data, the sensitivity factors according to Scofield [212] were applied. Most of the results shown in *Table 6-5* represent single measurements. Only for BOPP D and E, three repeat measurements each were carried out and standard deviations for the oxygen content were found to be 0.2 at% (BOPP E) and 1.0 at% (BOPP D), respectively.

Table 6-5: Polymer film compositions, as analysed via XPS

Film	Side	C	O	N	Al	O/C ratio
		at%	at%	at%	at%	
BOPP A	Corona	93.0	7.0	-	-	0.08
BOPP B	Corona	95.4	4.6	-	-	0.05
BOPP C	Corona	89.6	10.4	-	-	0.12
BOPP D	Corona	94.0	5.3	-	0.7	0.06
BOPP E	Corona	95.8	4.2	-	-	0.04
BOPP F	High surface energy polymer	80.3	10.3	9.4	-	0.13
PET	Corona	72.6	27.4	-	-	0.38

As can be observed from *Table 6-5*, the oxygen content of the standard commodity grade BOPP films varies over quite a large range, from 4.2 to 10.4 at%. If one looks back at the total and polar surface energies stated in *Table 6-4* (Chapter 6.1.3.1), no clear correlation can be drawn between both polar or total surface energy and the

oxygen content in the film surface. If one compares for example BOPP D with BOPP B and E, then all three reveal similar oxygen contents of approximately 4 to 5 at%. Nevertheless, the total and also polar surface energies of BOPP D are considerably lower than for BOPP B and E. BOPP C shows the highest oxygen content, 10.4 at%, which is significantly greater than the oxygen content for all other standard grade BOPP films, although its surface energy with 36.4 mN/m is only average, even lower than the surface energy of BOPP A and E. The oxygen contents (and O/C ratios) obtained here for the corona treated BOPP films A to E fall within the broad range of values reported in literature for corona treated BOPP [61, 63, 86, 236, 244, 250, 252, 262-264]. It can be seen from the references that the measured oxygen content depends on various factors, such as the applied corona energy/dose; the film composition (e.g. co-, ter- or homopolymer skin layer); the type and time of corona treatment (e.g. laboratory/industrial-scale, treatment after film orientation by producer); as well as the electron take-off angle used for XPS analysis (affects sampling depth). Consequently, it is difficult to make a direct comparison with specific values stated in literature.

The small amount of aluminium detected on BOPP D is attributed to film additives that can contain aluminium compounds, such as acid scavengers (e.g. hydrotalcites or zeolites) or antiblock particles (e.g. aluminosilicate) [50, 51, 66]. No other film additives were picked up by the XPS analysis.

BOPP F has a different surface composition, since this film has a different polymer coextruded as its skin layer in order to enhance the barrier properties after vacuum coating. This polymer additionally contains 9 to 10 at% nitrogen, whilst the oxygen content is comparable to BOPP C. Due to a confidentiality agreement with the film supplier, BOPP F was not further investigated and its composition will not be further discussed.

The PET film has a higher oxygen content, compared to the other films. The value of 27.4 at% agrees well with values reported by O'Hare et al. [260] for corona treated PET, but the O/C ratio appears slightly low when compared to results of Strobel et al. [253]. Nevertheless, as already stated for BOPP, the oxygen content, as detected by XPS, can be affected by many factors.

In contrast to PET and the skin layer of BOPP F, which both contain oxygen in their 'native' form, the oxygen content in the BOPP film surface is induced by the corona treatment, during which oxygen-containing functional groups are incorporated into the BOPP film surface. The process leading to the formation of new chemical groups is proposed as a three step mechanism, proceeding mainly via radical reactions [265]. During initiation, hydrogen is abstracted from the PP polymer chain

thus creating radicals. This first step is followed by the propagation process, whereby oxygen (e.g. from molecular oxygen, atomic oxygen, ozone or OH-species) bonds to the carbon atoms. The oxygen-containing radicals created this way can undergo further propagation reactions. Finally, the reaction is terminated (elimination of radicals), thus resulting in stable end-products. Even though corona treatment is applied in air, no nitrogen is incorporated into the film surface, as found by other researchers [266]. This is attributed to the higher stability of the triple bond in nitrogen, compared to the double bond in oxygen [267]. The incorporation of nitrogen by plasma pre-treatment is generally only achieved when oxygen is not present [63].

In order to investigate the oxygen-functional groups created by the corona treatment on the surface of BOPP A to E, high-resolution XPS spectra of the carbon 1s (C1s) peak (see *Figure 6-9* for BOPP C) and also oxygen 1s (O1s) peak were evaluated by peak deconvolution. The fitted peaks were assigned as reported in *Table 6-6*, using XPS reference data published by Beamson and Briggs [268]. To take the vibrational fine structure of polypropylene into consideration, two peaks were fitted for C-C/C-H bonds (though, also the fitting of four peaks is possible [236]). Curves for (up to) three different oxygen-containing functionalities were fitted to the carbon 1s peak, in a similar way to Langowski [63] (for corona treated BOPP) and other researchers [269-271] (for oxygen plasma treated PP). Nevertheless, some research groups have fitted up to six peaks [62, 236].

Table 6-6: C1s and O1s peak deconvolutions and their assignment for corona treated BOPP films

Element	Peak	Binding energy (centre)	Shift	Assignment
		eV	eV	
Carbon (C1s)	1	285	-	C-C, C-H (single bond to hydrogen or carbon)
	2	285.7	+ 0.7	C-C, C-H (single bond to hydrogen or carbon)
	3	286.5	+ 1.5	C-OH (hydroxyl group)
	4	287.8	+ 2.8	C=O (carbonyl group)
	5	289.2	+ 4.2	C-OOH (carboxyl group)
Oxygen (O1s)	1	532.5	-	C=O (double bond to carbon)
	2	533.5	-	C-O- (single bond to carbon)

There are some slight deviations of the binding energies for the two oxygen peaks (here: 532.5 and 533.5 eV, see *Table 6-6*) to the values tabulated in reference [268]. This variation is attributed to the fact that the reference data has been obtained for functional groups that are embedded in a polymer, whilst the data here is for oxygen-containing groups that are 'free' on the surface.

Figure 6-9 shows the peak deconvolution for the C1s peak of corona treated BOPP C. BOPP C revealed the highest oxygen content of all standard BOPP films and, therefore, the individually fitted peaks for the oxygen-containing functionalities are the most pronounced.

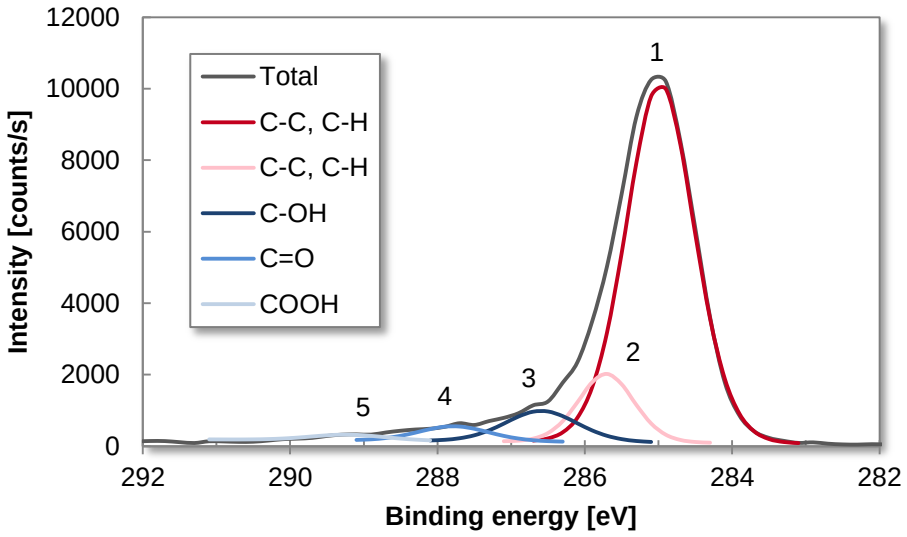

Figure 6-9: High-resolution XPS spectrum for C1s peak deconvolution of corona treated BOPP C

Using the peak fitting stated in *Table 6-6*, the amounts of the individual oxygen-functional groups for each film can be estimated and the results obtained are summarised in *Table 6-7*. The values given represent the relative amount within the C1s peak (i.e. concentration relative to total C1s peak area). The sum of the at% values of the three oxygen-functional groups is approximately equal to the oxygen content stated in *Table 6-5* (for each film type). Nevertheless, it will not be identical, since the peak fitting represents a source of uncertainty.

BOPP C shows the highest content of each individual oxygen-containing functional group (refer to *Table 6-7*), followed by BOPP A. This was to be expected, based on the results of the total oxygen contents stated in *Table 6-5* (BOPP C ≈ 10 at%, BOPP A ≈ 7 at%, BOPP B, D and E approximately 4 to 5 at%).

It is noticeable from the data presented in *Table 6-7* that, the lower the oxidised state of the species (e.g. hydroxyl groups), the larger the amount of this functionality

that is induced by the corona treatment. This has also been found by other researchers, for oxygen plasma, flame and corona treated polypropylene [63, 236, 244, 271, 272]. Whilst it was possible to fit the peaks for all three oxygen-functional groups to the C1s peaks of BOPP A to C, no peak for carboxyl groups could be fitted to the data of BOPP D and E, which is attributed to the low oxygen contents of these films. Although BOPP B revealed a similar low oxygen content, a small peak representing carboxyl functionalities could be fitted (0.5 at%). Nevertheless, it has been reported in literature that the number of peaks that can be fitted (and thus types of functional groups created) may vary, depending on the corona treatment level [63, 236]. Furthermore, Boyd and co-workers [62] found that higher oxidised oxygen-containing species are lost from the surface with ageing time at a higher rate than other oxidised species. Nevertheless, they also noted a decrease of oxygen content (O/C ratio) with ageing, which disagrees with findings by Strobel at al. [250], who stated that the results of the XPS analysis (at various electron take-off angles) were not affected by the ageing process. The at% values reported in *Table 6-7* for the various functional groups compare well with results published by Langowski [63] for corona treated BOPP (homo- and copolymer surfaces).

Table 6-7: Concentrations of oxygen-containing functional groups relative to total C1s peak area

Film	Hydroxyl C-OH	Carbonyl C=O	Carboxyl COOH
	at%	at%	at%
BOPP A	5.5	1.9	0.9
BOPP B	4.1	1.0	0.5
BOPP C	7.0	3.3	1.4
BOPP D	4.4	0.9	-
BOPP E	4.5	1.2	-

The importance of oxygen in BOPP film surfaces has been emphasised by Mount [69], who states that a large amount of hydroxyl groups in the film surface represents the optimum state for barrier metallisation, whilst a larger concentration of higher oxidised carboxyl species has a negative impact on the barrier properties of the metallised film. Furthermore, McClure et al. [249] show that the incorporated oxygen in the film surface of BOPP (generated by plasma treatment) plays an important role for the oxygen barrier properties, as well as coating-to-substrate adhesion, after metallisation. Additionally, several other research groups report on the effect and importance of oxygen generated by pre-treatment in the PP/BOPP

film surface for the adhesion of vacuum deposited aluminium layers [77, 269, 270]. Friedrich and co-workers [273], for example, discuss the significant impact of carboxyl groups, and also hydroxyl groups, on the adhesion of evaporated aluminium to PP. Even though the vast amount of literature cited here refers to aluminium metallisation of BOPP, it can be assumed that also for AlO_x coating the BOPP film surface chemistry, as generated by the (corona) treatment, is critical for the functional properties of the vacuum coated film.

6.1.3.3 Static secondary ion mass spectrometry

In addition to XPS analysis, TOF-SSIMS analysis of the corona treated BOPP films was carried out. This analytical technique provides a lower probing depth (compared to XPS) of approximately 1 nm or less [213, 214]. The main purpose for using an additional technique to analyse the BOPP film surface chemistry was to confirm the results obtained via XPS analysis. Based on the fact that during each of these surface analyses, only a very small fraction of the film surface (400 x 400 µm² for TOF-SSIMS) is examined, it is important to obtain reliable and representative data. Consequently, the two analyses were performed independently of each other on different samples. For the TOF-SSIMS analysis, two areas per BOPP film type were analysed. The incorporation of oxygen into the film surface is noticeable in the negative ion spectra from the intensity of the O^- and OH^- peak (m/z 16 and 17, respectively), as reported by other researchers [62, 271, 274-276]. The O^-/CH^- (m/z 16 : m/z 13) and $(O^- + OH^-)/CH^-$ (m/z 16 + 17 : m/z 13) intensity ratios can be used as parameters to describe the oxygen content and hence degree of oxidation of the polymer (if it only contains carbon, hydrogen and oxygen) and allow correlation of the SSIMS findings to XPS O/C ratios [277].

In order to characterise the samples with respect to the oxygen incorporated by the corona treatment, the intensity ratios stated above were used and results are presented in *Table 6-8*. In addition to examining the corona treated side of the BOPP films, the untreated reverse side of BOPP D and E were analysed as references.

Table 6-8: Peak intensity ratios from negative TOF-SSIMS spectra for corona treated and untreated sides of BOPP films

Film	side	O^-/CH^-	$(O^- + OH^-)/CH^-$
BOPP A	Corona	0.80 ± 0.14	1.47 ± 0.08
BOPP B	Corona	0.57 ± 0.03	0.99 ± 0.09
BOPP C	Corona	1.47 ± 0.05	2.54 ± 0.12
BOPP D	Corona	0.84 ± 0.03	1.55 ± 0.01
BOPP D	*Reverse*	0.00 ± 0.00	0.01 ± 0.00
BOPP E	Corona	0.53 ± 0.12	1.09 ± 0.11
BOPP E	*Reverse*	0.01 ± 0.00	0.01 ± 0.00

As can be seen from *Table 6-8*, the intensity ratios (O^-/CH^-, as well as $(O^- + OH^-)/CH^-$) are the highest for BOPP C, followed by BOPP A and D, which appear very similar. Finally, the lowest values were obtained for BOPP B and E, which also revealed a comparable level. For the O^-/CH^- ratio, it is noticeable that the standard deviation for BOPP A and E is slightly increased, compared to the other films, whilst for the $(O^- + OH^-)/CH^-$ ratio, all films apart from BOPP D exhibit larger standard deviations. Traces of oxygen were found in the surface of the untreated sides of BOPP D and E, which can be attributed to general oxidation of the film or backside treatment (during corona treatment). The TOF-SSIMS results appear to be very much in agreement with the XPS data stated in *Table 6-5*, which revealed the highest oxygen content for BOPP C, followed by BOPP A and then BOPP D.

Plotting the SSIMS intensity ratios versus the XPS O/C ratios, see *Figure 6-10*, yields a good correlation between the two sets of data, with coefficients of determination of $R^2 = 0.90$ for the $(O^- + OH^-)/CH^-$ ratio and $R^2 = 0.92$ for the O^-/CH^- ratio. Consequently, using the SSIMS O^-/CH^- intensity ratio results in a slightly better correlation between XPS and SSIMS data. A good correlation between the XPS O/C ratio and TOF-SSIMS $(O^- + OH^-)/CH^-$ ratio (with $R^2 = 0.85$) has also been established by Briggs and co-workers [276], for polyethylene treated by a variety of oxidising techniques, including corona and flame treatment.

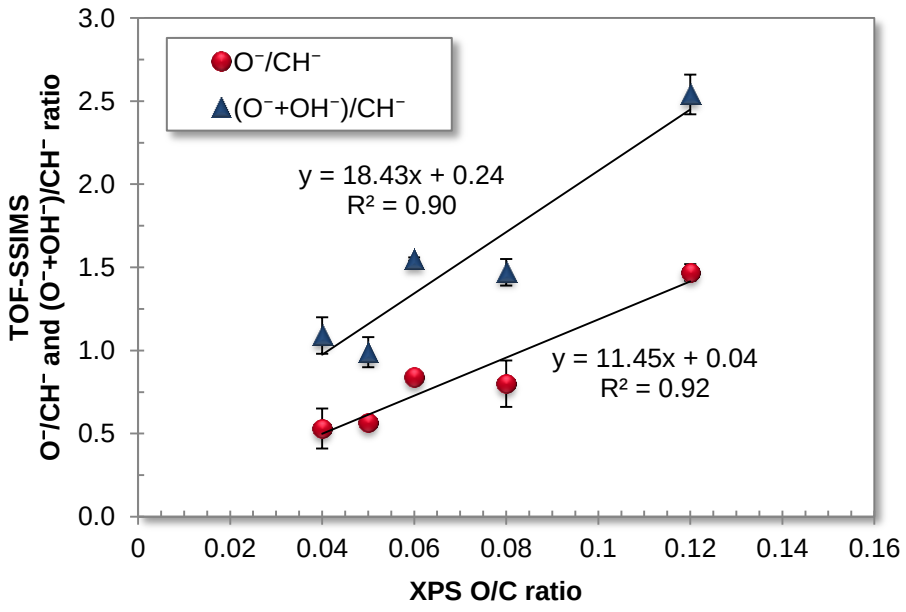

Figure 6-10: Correlation between TOF-SSIMS intensity ratios (O^-/CH^- and $(O^- + OH^-)/CH^-$) and XPS atomic O/C ratios for corona treated BOPP films

Nevertheless, as mentioned earlier, SSIMS and XPS have different sampling depths of approximately 1 nm and 5 to 6 nm (37° electron take-off angle), respectively,

which can have an effect on the results and correlation obtained. Results by Occhiello at al. [271] provide support that SSIMS analysis can be affected by the ageing process taking place on the treated polypropylene surface, whilst XPS results appeared uninfluenced. In the case of the BOPP films investigated here, the film samples were of different ages. Furthermore, also matrix effects play a role during the SSIMS analysis, e.g. the sputtering yield of O^- ions in SSIMS appears to depend on the type of oxygen functionality [277].

The TOF-SSIMS analysis also showed levels of antioxidant film additives, with mass fragments of m/z = 203, 219 and 259 in the positive ion spectra and m/z = 231 in the negative spectra, which are characteristic for the antioxidant Irganox 1010 [278, 279]. Furthermore, no elements of antiblock particles, such as silicon, were detected, which indicates that these filler particles are covered by a polymer layer that is at least as thick as the analytical depth of the SSIMS analysis.

6.1.3.4 Skin layer composition via infrared spectroscopy

In addition to characterising the surface chemistry of the BOPP films with respect to the composition of the top few nanometres (via XPS and SIMS), ATR-FTIR spectroscopy was used to investigate the skin layer composition of the standard BOPP films. As stated in Section 5.5, all standard commodity grade BOPP films used here comprise a three-layer structure, with a homopolymer core and either a co- or terpolymer skin layer on each side. The use of ATR-FTIR spectroscopy will allow the determination of whether ethylene and/or butylene are present in the skin layer. For this analysis, the methylene rocking bands in the region between 770 and 720 cm^{-1} are investigated. Whilst the presence of butylene is identified from a peak at around 770 cm^{-1}, caused by the ethyl side branch of the butylene repeat unit (methylene rocking mode of ethyl branches) [280, 281], the presence of ethylene, as an addition to the PP, is determined from the methylene rocking bands near 725 cm^{-1}. Orthorhombic crystal structures in polyethylene (PE) give rise to two characteristic peaks (at around 730 cm^{-1} and 720 cm^{-1}), whereas the amorphous phase exhibits a broader peak at around 723 cm^{-1} [282, 283]. For ethylene-propylene copolymers, the peak at approximately 733 cm^{-1} is assigned to the methylene rocking of a $(–CH_2–)_n$ sequence with n = 3 or 4 and the peak at around 722 cm^{-1} to a sequence with n = 5 or more [284]. Thus, their presence indicates a block-type copolymer.

ATR-FTIR spectra of the corona side (i.e. the side that is later coated with AlO_x) of the five standard BOPP films, showing the region between 800 and 700 cm^{-1}, are displayed in *Figure 6-11*. To facilitate visual assimilation of the data, the various spectra are stacked up the y-axis and the wavenumber regions of interest (770 cm^{-1}, 733 cm^{-1} and 722 cm^{-1}) are highlighted with vertical lines.

As can be seen, the absorption band at around 770 cm^{-1}, characteristic for the presence of butylene, is present for all five BOPP films; nevertheless, in all cases slightly shifted towards a lower value of the wavenumber (approximately 768/767 cm^{-1}). Furthermore, there are differences in peak intensity present. BOPP D reveals the strongest peak, followed by BOPP C and then BOPP B, whilst BOPP A and E exhibit weaker absorption bands. The intensity of the absorption band will be affected by the content of butylene in the skin layer, as well as thickness of the skin layer.

TEM imaging of cross-sections of BOPP films revealed skin layer thicknesses less than 1 µm (typically around 0.5 µm or less), while the penetration depth of the

evanescent wave in ATR-FTIR is approximately 2.6 µm[f] at 770 cm^{-1}. As the ethylene component (which will be discussed later) was not particularly strong, it is assumed that the higher intensity of the peak around 770 cm^{-1} is due to a higher content of butylene in the skin layer of the respective films and not due to a thicker skin layer.

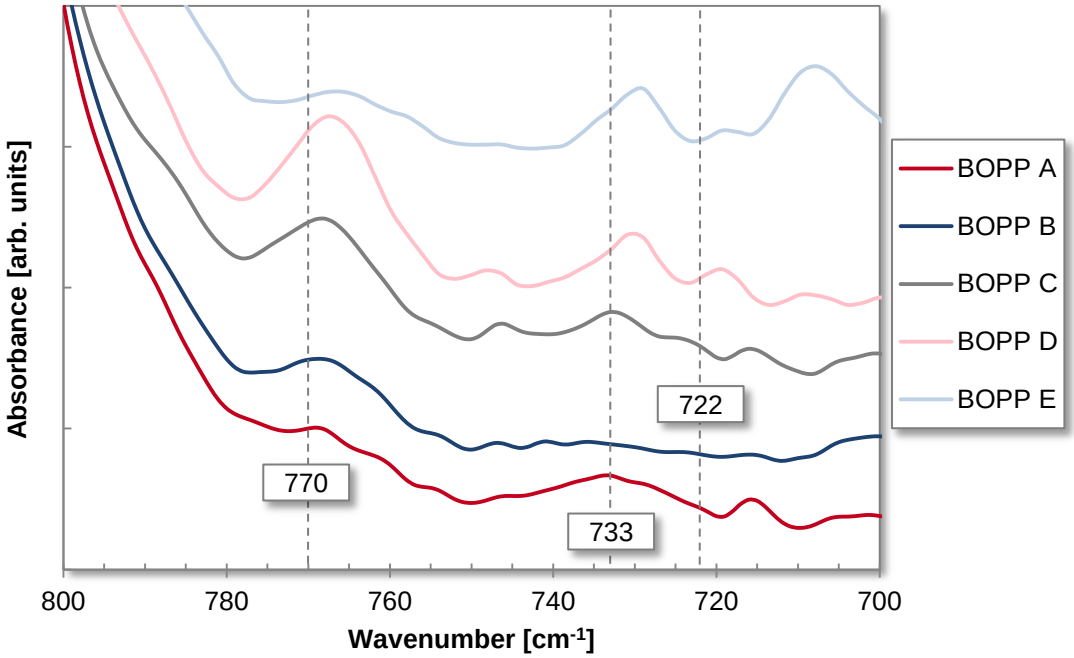

Figure 6-11: ATR-FTIR spectra of BOPP films (corona treated side) for the investigation of methylene rocking bands

When investigating the characteristic absorption bands for the presence of ethylene derived structural units, BOPP A displays only a peak at 733 cm^{-1}, hence indicating a rather random PE content. BOPP B shows no peaks around 733 cm^{-1} and 722 cm^{-1} and it is thus concluded that this film does not contain PE in its skin layer. BOPP C, D and E all show both characteristic PE absorption bands, although for BOPP D and E the two peaks are shifted to slightly lower wavenumbers (730 cm^{-1} and 720 cm^{-1}, respectively). The peak around 722/720 cm^{-1} is the most pronounced for BOPP D, then E and finally C. Therefore, the skin layers of these latter three BOPP films contain long sequences of ethylene derived structural units indicating a block copolymer structure. In summary, it was found that all films apart from BOPP B, which appears to have a polypropylene-butylene copolymer skin layer, exhibit a terpolymer skin layer with different levels of butylene.

[f] During ATR-FTIR, here with a diamond crystal, the IR radiation has a wavelength-dependent penetration depth, which at 770 cm^{-1} is approximately 2.6 µm for PP, see Equation (5-10) (using a refractive index of 1.5 for PP [285] and 2.4 for the diamond crystal [218]).

In the case of metallised BOPP, Campbell and Wolters [256] have shown that with a certain level of butylene in a corona treated propylene-butylene copolymer skin layer, the barrier properties of the metallised BOPP could be improved, compared to a propylene-ethylene copolymer skin layer. Hence, their research indicates that the skin layer composition can play a role for the barrier levels to be obtained after vacuum deposition of a barrier layer. They, however, attributed this to differences in surface smoothness, though no extensive AFM roughness evaluation and data is presented.

6.1.4 Shrink properties of BOPP films

The final analysis carried out for the uncoated standard grade BOPP films was the determination of the film shrink properties. It is assumed that the shrinkage properties of the film substrate may play a role for the barrier properties of the inorganic barrier layer deposited thereon. This is due to the compressive forces acting on the oxide layer when the film shrinks due to the thermal load applied during coating deposition (although the web will initially expand [92]). The overall effect may act to densify the coating and, hence, improve its structure, reducing porosity and increasing barrier performance.

For this test, film sample strips are heated from 50 °C to 140 °C at a rate of 10 °C/min, while their shrinkage is determined using a Lenzing Instruments TST1 thermal shrinkage tester. The sample strips were kept flat during the measurement using a pre-tension that corresponds to an applied tensile stress of approximately 0.2 MPa. The investigation was carried out for the machine direction (MD) and the transverse direction (TD) of the BOPP films and a PET reference film, and results are illustrated in *Figure 6-12*. Two samples for each film type and direction (MD/TD) were measured and identical graphs were obtained in all cases.

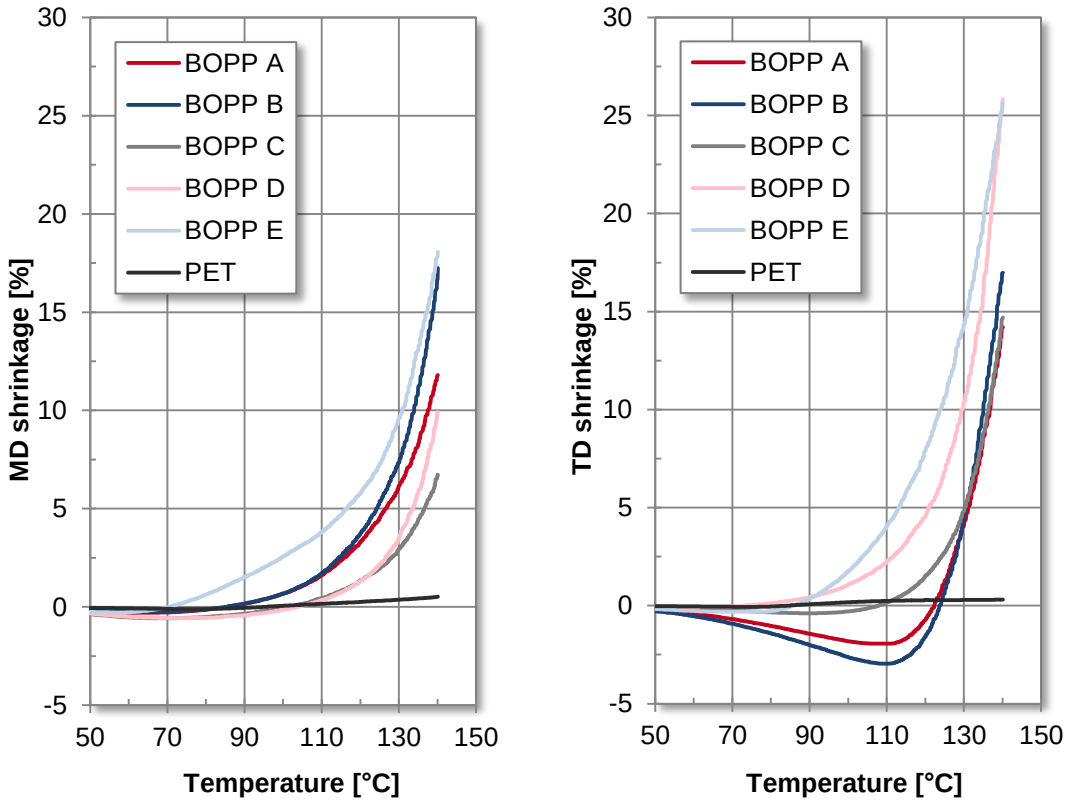

Figure 6-12: Shrinkage as a function of temperature for BOPP A to E and PET reference film; left: MD shrinkage; right: TD shrinkage

Figure 6-12 reveals that all films initially showed an expansion (in MD and TD), due to the heating process, before the onset of shrinkage. This expansion is only very marginal for the PET film (not noticeable in *Figure 6-12*) and intensely pronounced for BOPP A and B for the transverse direction. BOPP A and B show relatively balanced shrinkage properties, i.e. the maximum shrinkage value at 140 °C for MD and TD is nearly identical (BOPP A: 12 – 14 % and BOPP B: 17 %). However, for the other films, especially BOPP C and D, there is a larger difference between MD and TD maximum shrinkage (BOPP C: MD 7 % and TD 15 %, BOPP D: MD 10 % and TD 26 %, BOPP E: MD 18 % and TD 26 %). The vast differences seen for BOPP C and D, with the TD shrinkage being double the value (or more) of the MD shrinkage, indicates that these films were produced via sequential stretching, whereby a less balanced orientation is obtained (MD draw ratio around 1:5 and TD draw ratio between 1:8 and 1:10) [68]. Using simultaneous orientation, e.g. via the tubular (double-bubble) process or LISIM linear motor simultaneous stretching system, the process window for orientation is significantly larger and identical draw ratios can be achieved [68], therefore enabling a more balanced orientation and hence more balanced shrink properties, as found for BOPP A, B and also E. In contrast to the BOPP films, PET only shrinks marginally (MD 0.5 %, TD 0.3 % at 140 °C), since it is a more thermally stable polymer film at the temperature range investigated. Rochat and co-workers [286] determined the shrinkage of 12 µm PET using a similar test (25 to 150 °C, 10 °C/min heating rate, 1 MPa tensile stress, MD or TD not specified) and found a shrinkage of approximately 0.1 % at 150 °C. This is lower than found in this thesis. However, Rochat used a higher pre-tension (tensile stress) and, additionally, showed that the shrinkage depended on the applied tensile stress, with the shrinkage being increased for lower stresses. Their data also revealed that further shrinkage takes place on cooling the samples down, which led to an overall shrinkage of 0.7 % for the full cycle (25 → 150 → 25 °C). Also the BOPP films investigated here will additionally shrink when they cool down to room temperature. This has not been measured and, consequently, is not shown in *Figure 6-12*. Nevertheless, it is of importance as the data by Rochat et al. suggests that the overall shrinkage may be a lot larger than determined via *Figure 6-12*.

The MD and TD curves for BOPP E, a shrink BOPP, run above the shrinkage curves of all the other BOPP films (except from a section of the TD shrinkage versus temperature plot, whereby the graph for BOPP D reveals a higher shrinkage) and, furthermore, cross the temperature axis (transition from expansion to shrinkage) at lower values (MD 70 °C, TD 86 °C). Nevertheless, for the TD shrinkage BOPP D exhibits a lower point of intersection with 72 °C. Based on the high TD shrinkage (26 % at 140 °C) obtained for BOPP D, which is identical to the value of the shrink

BOPP (BOPP E), and the fact that the TD shrinkage versus temperature curve of BOPP D is located above the curves of BOPP A, B and C, it is assumed that BOPP D might be a heat shrinkable BOPP film. Such films are modified intentionally in order to increase shrinkage properties. This is, furthermore, supported by the fact that the plain film barrier performance of BOPP D (especially OTR) was improved, compared to the other standard (non-shrink) BOPP films, see Section 6.1.1 (which can be caused be the use of a hydrocarbon resin in the core, as done for shrink BOPP films).

In order to obtain the shrinkage behaviour for shrink BOPP films, these films are subjected to a gentler heat setting regime (some degree of heat setting is required, in order to keep the film dimensionally stable under normal storage conditions). Furthermore, hydrocarbon resins are added to the film (core layer), which also improves the barrier properties of the plain BOPP film (see Section 6.1.1).

The temperature of the (BOPP) film during deposition is difficult to estimate and, furthermore, will not be constant during deposition. On the one hand, the web will be cooled by the cooled deposition drum and, on the other hand, the web is exposed to the heat load of the deposition process. The former is affected by several factors, such as the drum temperature and the heat transfer between film and drum, which in turn depends on the contact between film and drum, film roughness (affected by antiblock particles), web speed, film material and others. The heat load during reactive AlO_x evaporation consists of the following components: the thermal radiation from the resistively heated boats, the latent heat of the condensing coating, and the heat of chemical reaction, i.e. exothermic reaction of AlO_x formation. [22, 29, 92]

Whilst Schiller and co-workers [29] state a maximum allowable substrate film temperature of 80 °C, during the deposition of 20 nm thick barrier layers onto PET, the temperature profiles published by Bishop [92] show a maximum temperature between 80 °C and 110 °C (no details of deposition thickness are given). Additionally, the data obtained by McCann et al. [287] gives a maximum of 112 °C, when depositing a 35 nm thick aluminium coating onto 12.5 µm PET. Consequently, this data may give a rough estimate of the (maximum) film temperature during deposition.

As can be seen from *Figure 6-12*, a temperature of 70 °C to 86 °C is needed in order to induce the shrinkage of BOPP D and E in TD, whilst the other films require higher temperatures of at least 110 °C, in order to move from film expansion to shrinkage. When investigating the MD, BOPP E starts shrinking from 70 °C, BOPP A and B from 85 °C and BOPP C and D from 100 °C onwards.

6.1.5 Summary of film properties

For a better comparison and ease of understanding of the differences between the various BOPP films investigated, the film properties examined and results obtained in Chapter 6.1 are summarised *Table 6-9*. Additionally, film thickness and film structure, as stated in the film datasheets obtained from the respective manufactures (see also *Table 5-5*), are listed.

Table 6-9: BOPP film properties (uncoated)

Film property	BOPP A	BOPP B	BOPP C	BOPP D	BOPP E	BOPP F
Thickness [µm]	30	15	20	20	22	18
Structure	3 layers	3 layers	3 layers	3 layers	3 layers	5 layers
OTR [cm³/(m² d)]	1250 – 1450	2500 – 2900	2000 – 2100	1750 – 1850	1550 – 1650	400 – 500
WVTR [g/(m² d)]	4 – 5	7 – 8	6 – 7	4 – 5	3.5 – 4.5	4 – 5
Antiblock particles [per mm²]	6263 (mostly 1 < µm)	3383 (mostly 1 < µm)	1935 (mostly 1 > µm)	823 (mostly 1 > µm)	14720 (mostly 1 < µm)	No antiblock particles
RMS roughness [nm]	4.1 ± 0.7	6.1 ± 1.9	4.1 ± 0.3	6.2 ± 0.5	4.4 ± 0.7	3.0 ± 0.3
Total surface energy [mN/m]	38.0 ± 0.4	36.4 ± 0.4	36.4 ± 0.6	33.0 ± 0.3	37.0 ± 0.2	42.4 ± 0.3
XPS oxygen content [at%]	7.0	4.6	10.4	5.3	4.2	10.3 (9.4 at% nitrogen)
Skin layer composition (FTIR)	Ter-polymer; propylene/ ethylene/ butylene	Co-polymer; propylene/ butylene	Ter-polymer; propylene/ ethylene/ butylene	Ter-polymer; propylene/ ethylene/ butylene	Ter-polymer; propylene/ ethylene/ butylene	Different polymer
Shrink properties and film orientation process	Balanced; simulta-neous orientation	Balanced; simulta-neous orientation	Un-balanced; sequential orientation	Un-balanced; sequential orientation suspected shrink BOPP	Rather balanced; simulta-neous orientation; shrink BOPP	Not measured

6.2 Characterisation of AlO_x coated polymer films

After the detailed characterisation and discussion of the uncoated BOPP films, the results with respect to the AlO_x coated films will now be presented, starting with the barrier levels that were obtained for the different AlO_x coated BOPP film types.

6.2.1 Oxygen and water vapour barrier performance

6.2.1.1 General barrier levels obtained with AlO_x coating

The barrier performance of the various AlO_x coated BOPP films and the PET reference film is summarised in *Table 6-10*. For each coating trial presented here and in the sections to follow, at least two OTR and two WVTR measurements were performed. Due to the length of time of a single barrier measurement, which can be up to 24 hours or longer, it is, unfortunately, not always possible to perform more than two replicate measurements (although most of the values stated in *Table 6-10* were averaged over at least four individually measured samples). The values in *Table 6-10* represent the average transmission rates and their standard deviations. In order to illustrate the barrier enhancement obtained by the thin AlO_x barrier layer, the plain (uncoated) film barrier properties, previously stated in *Table 6-1*, are additionally displayed. All average transmission rate values and BIF values (barrier improvement factor, an important quality indicator commonly used to characterise the effect of vacuum deposited barrier coatings) are displayed with three and two significant figures, respectively (apart from the plain film barrier performance). The BIFs were calculated using the mean value of the given transmission rate range for the uncoated polymer film and the average transmission rate after AlO_x coating.

Apart from the coating trials conducted for BOPP D, BOPP E and the PET reference film, three different trials were performed for each film type, in order to investigate the effect of in-line (low-pressure) plasma treatment on the AlO_x barrier levels obtained. For the first trial, no in-line plasma treatment was applied, for the second trial pre-treatment only was used and the final trial was carried out with pre- and additional post-treatment after AlO_x deposition. The plasma treatment was performed using power settings and gas recipes (with oxygen) previously optimised at Bobst Manchester, which due to proprietary knowledge cannot be further disclosed.

Table 6-10: Barrier properties (OTR and WVTR) of AlO_x coated BOPP and PET films, including results following in-line plasma pre- and post-treatment

Film	Plasma treatment	OTR		WVTR	
		cm³/(m² d)	BIF	g/(m² d)	BIF
BOPP A 30 µm	*(uncoated)*	*1250 – 1450*	-	*4 – 5*	-
	No plasma	271 ± 35	5.0	3.99 ± 0.06	1.1
	Pre	179 ± 42	7.5	3.43 ± 0.35	1.3
	Pre + post	257 ± 15	5.3	3.98 ± 0.30	1.1
BOPP B 15 µm	*(uncoated)*	*2500 – 2900*	-	*7 – 8*	-
	No plasma	228 ± 12	12	5.78 ± 0.01	1.3
	Pre	118 ± 22	23	5.47 ± 0.35	1.4
	Pre + post	82.6 ± 17.7	33	5.89 ± 0.18	1.3
BOPP C 20 µm	*(uncoated)*	*2000 – 2100*	-	*6 – 7*	-
	No plasma	47.0 ± 5.4	44	5.89 ± 0.23	1.1
	Pre	35.3 ± 3.1	58	6.08 ± 0.17	1.1
	Pre + post	26.7 ± 3.1	77	4.73 ± 0.07	1.4
BOPP D 20 µm	*(uncoated)*	*1750 – 1850*	-	*4 – 5*	-
	Pre	77.1 ± 9.7	23	2.41 ± 0.58	1.9
BOPP E 22 µm	*(uncoated)*	*1550 – 1650*	-	*3.5 – 4.5*	-
	Pre	48.9 ± 6.8	33	2.86 ± 0.61	1.4
BOPP F 18 µm	*(uncoated)*	*400 – 500*	-	*4 – 5*	-
	No plasma	0.89 ± 0.01	506	2.19 ± 0.06	2.1
	Pre	0.83 ± 0.30	542	0.56 ± 0.07	8.0
	Pre + post	0.60 ± 0.14	750	0.64 ± 0.18	7.0
PET	*(uncoated)*	*100 – 110*	-	*40 – 50*	-
	Pre + post	0.62 ± 0.13	169	0.68 ± 0.14	66

As can be seen from *Table 6-10*, the OTR and WVTR measured for AlO_x coated PET are both below 1 cm³/(m² d) and 1 g/(m² d), respectively, which is typical for AlO_x coated standard grade PET film. Transmission rate values around 1 cm³/(m² d) and 1 g/(m² d) are reliably and consistently achieved on standard packaging grade PET film, using the AlO_x coating system described in Section 5.1. Nevertheless, when coating standard packaging grade BOPP films with reactively evaporated AlO_x, the barrier performance can vary to a large extent and appears to be strongly affected by the individual base material itself. BOPP, in contrast to PET, is a nonpolar polymer with a completely different surface chemistry (as shown in

Sections 6.1.3.1 and 6.1.3.2), which can have a large impact on coating nucleation and growth of AlO_x barrier layers [130]. For AlO_x coated BOPP A, for example, the OTR was very inconsistent and the application of plasma treatment did not appear to bring any significant improvement. None of the trials performed resulted in a clear enhancement of the oxygen barrier down to levels below 100 cm³/(m² d), which would be comparable to aluminium metallised BOPP (an OTR < 100 cm³/(m² d) is generally guaranteed in a datasheet for metallised standard BOPP film). For comparison purposes, BOPP A, B and C have also been coated with aluminium (optical density of 2.0 to 2.1) and the barrier properties obtained are stated in *Table 6-11*. Whilst metallised BOPP B and C reveal typical oxygen barrier levels, metallised BOPP A exhibits a larger average OTR value of 130 cm³/(m² d), which is not so much better than the oxygen barrier of AlO_x coated BOPP A when the AlO_x layer was deposited with in-line plasma pre-treatment only. The reason for the poor barrier performance of AlO_x and aluminium coated BOPP A will be explained later in this chapter.

Table 6-11: Barrier properties (OTR and WVTR) of metallised BOPP films with an OD of 2.0 to 2.1

Film	Plasma treatment	OTR		WVTR	
		cm³/(m² d)	BIF	g/(m² d)	BIF
BOPP A	Pre	130 ± 15	10	0.87 ± 0.02	5.2
BOPP B	Pre	24.7 ± 3.6	110	0.34 ± 0.03	22
BOPP C	Pre	19.4 ± 2.2	106	0.16 ± 0.01	41

In contrast to AlO_x coated BOPP A, AlO_x coated BOPP B revealed better barrier properties owing to the application of plasma pre- and post-treatment, whilst without any plasma treatment the oxygen barrier was similar to AlO_x coated BOPP A. Even though an average OTR of less than 100 cm³/(m² d) was achieved when conducting in-line plasma pre-and post-treatment, there was still quite a large scatter of the data, as noticeable from the relatively large standard deviation. This may be caused by the thin 15 µm BOPP film being less supportive and, hence, the ceramic and brittle AlO_x barrier layer being more prone to damage when handled, compared to a thicker substrate film. Nevertheless, for metallised BOPP B (see *Table 6-11*), a far better OTR was obtained when using plasma pre-treatment only.

BOPP C delivered acceptable (e.g. < 100 cm³/(m² d)) oxygen barrier performance even without any in-line plasma treatment. With the application of pre- and post-treatment, a mean OTR of 26.7 cm³/(m² d) was achieved for this film. This result is

nearly as good as the average oxygen barrier of 19.4 $cm^3/(m^2\ d)$ achieved for metallised BOPP C (refer to *Table 6-11*).

For BOPP D and E, only one trial each with plasma pre-treatment was conducted and, consequently, no conclusions can be drawn about the effect of in-line plasma treatment on barrier. It is, however, noticeable from *Table 6-10* that both films reveal acceptable oxygen barrier levels after AlO_x coating, but with the OTR of AlO_x coated BOPP E being considerably better than measured for AlO_x coated BOPP D. The oxygen barriers of these two AlO_x coated films also exhibit standard deviations that are lower than obtained for BOPP B.

In the case of BOPP F, which is coextruded with a special high surface energy polymer skin layer in order to enhance barrier performance after coating, remarkable barrier improvement for OTR (and WVTR) could be obtained by applying the AlO_x layer (refer to *Table 6-10*). Even without any in-line treatment, the OTR improved significantly to less than 1 $cm^3/(m^2\ d)$, due to the different surface chemistry of the skin layer. According to barrier data presented by Wolf and co-workers [258], the coating of this film with SiO_x or aluminium resulted in even lower OTR (and WVTR) values, although no remarks on in-line treatment were made.

The OTR values for both BOPP B and C clearly revealed an improvement in the barrier levels obtained when in-line plasma pre- and post-treatments were applied. Pre-treatment improves barrier by chemical modification of the plain film surface, which enhances coating nucleation/growth conditions and, hence, affects the final coating structure in terms of coating density/porosity [151]. During this chemical modification, functional groups are incorporated into the film surface [63, 74] (similar as discussed for the corona treatment, see Chapter 6.1.3.2), which can act as nucleation sites for the depositing coating [151]. Furthermore, plasma treatment is generally accompanied by a cleaning effect, during which low-molecular-weight species loosely bonded to the film surface (e.g. oligomers) can be removed [74] and, hence, they do no longer interfere with the depositing coating. Bichler and co-workers [245] showed an improvement of the oxygen barrier properties of AlO_x coated BOPP homopolymer film (electron beam evaporation) following oxygen plasma pre-treatment. Their oxygen transmission rate was reduced from a value of 230 $cm^3/(m^2\ d)$ (no treatment) to values of 100 $cm^3/(m^2\ d)$ or less for oxygen plasma treated BOPP. They attributed this, though, to the smoothing of the polymer surface induced by the plasma treatment, resulting in the homogeneous growth of the coating. However, as will be shown in Section 6.2.2.3, no significant difference in surface roughness between the plain and AlO_x coated films was found (apart from BOPP E) and, hence, a smoothing effect of the plasma pre-treatment is excluded.

The bombardment of the coating during post-treatment can result in a densification of the outermost atomic layers of the coating, which may protect the AlO_x layer and reduce oxygen permeation. Overall, though, these barrier results suggest that barrier performance of AlO_x coated BOPP is very much base film dependent.

When investigating the WVTR of the AlO_x coated BOPP films, it is clear that, with the exception of BOPP F following pre-treatment, no significant moisture barrier improvement was obtained in the trials conducted, i.e., the BIF values are negligible. Although it should be mentioned that the WVTR was slightly better for AlO_x coated BOPP D and E, which is less noticeable from the BIF values based on the fact that the plain films already had a marginally better WVTR, compared to the other BOPP films. Nevertheless, an acceptable water barrier level would be less than 1 g/(m² d), i.e. similar to AlO_x coated PET or metallised BOPP (see *Table 6-10* and *Table 6-11*). That good oxygen barrier has been achieved whilst still lacking water barrier improvement indicates that oxygen and moisture permeation through inorganic barrier layers are dominated by different mechanisms, as discussed in more detail in Chapter 4.6.2. However, plain BOPP film already has an inherently good water barrier, compared to plain PET (refer to *Table 6-10*). For BOPP F, the data presented in *Table 6-10* also shows the importance of in-line plasma pre-treatment for obtaining a water barrier performance of less than 1 g/(m² d) for the AlO_x coated film. Once again, the improvement of WVTR with plasma pre-treatment is attributed to the chemical modification and cleaning induced by the plasma treatment. It is assumed that any low-molecular-weight material on top of the high surface energy polymer skin layer (presumably transferred from the reverse side of the film, similar as discussed in Section 6.2.4 for the AlO_x coating) is removed by the plasma and, thus, cannot compromise the depositing coating. This presumably results, along with the functional groups created on the treated film surface, in a better nucleation of the coating and therefore a denser structure, which exhibits fewer defects with a size of a few nanometres down to the subnanometre range (referred to as microscopic defects [126] or nano-defects [131]) that would predominantly affect water vapour permeation.

There is a vast amount of literature published on the barrier performance of AlO_x coated polymer films produced via PVD techniques, such electron beam evaporation [130, 245, 288-290] or sputtering [157, 164, 165, 232, 240, 290-293]. The focus here lies, however, on comparing the barrier results obtained in this study to AlO_x coated films produced by analogous techniques, i.e. via reactive evaporation on a ‘boat-type’ roll-to-roll metalliser, as done in the following paragraphs.

The oxygen and water vapour barrier performance obtained here for AlO_x coated PET is better than the barrier levels published by Barker and co-workers [16] and Kelly [3] for oxygen-rich and metal-rich AlO_x layers on 12 µm PET, produced via a comparable deposition process (reactive evaporation of aluminium from boats with the application of a proprietary plasma technique). For AlO_x coated BOPP, Kelly [2] states an OTR of approximately 31 cm³/(m² d) and WVTR of 3.1 g/(m² d); however, no details of the uncoated film (such as thickness, barrier properties or treatment) are revealed. Nevertheless, Kelly's data also indicates that the WVTR was not significantly improved by the AlO_x barrier layer, as was found to be the case here. The OTR of 31 cm³/(m² d) compares well with the values obtained for AlO_x coated BOPP C (pre-treatment only and pre- and post-treatment). Furthermore, AlO_x coated BOPP C revealed slightly lower WVTR when the film was aged (see Section 6.2.1.2). A comparable WVTR was also achieved for AlO_x coated BOPP D and E.

The average OTR of 0.62 cm³/(m² d) and WVTR of 0.68 g/(m² d) achieved here for AlO_x coated PET are, furthermore, similar to data presented by Trassl and co-workers [40] for the reactive AlO_x deposition onto PET, using a 'boat-type' metalliser with or without plasma assistance during deposition. Although Trassl states slightly enhanced WVTR values (0.3 to 0.5 g/(m² d)) when applying plasma assistance. In the case of AlO_x coated BOPP, the plasma assistance results in an OTR of 25 to 40 cm³/(m² d), which is similar to the OTR obtained in this study for AlO_x coated BOPP C. Nevertheless, the plasma assisted AlO_x deposition creates a significant improvement of the WVTR level to values between 0.15 to 0.4 g/(m²d), due to the densification of the depositing coating. Without plasma assistance, the WVTR is not improved, whilst the OTR ranges between 300 and 1500 cm³/(m² d) (measured at 0 % RH) [39], which is a lot higher than obtained here for all standard BOPP films, apart from BOPP A.

Misiano and co-workers [42] state an OTR of 6.4 cm³/(m² d) and WVTR of 4.9 g/(m² d) for their reactively deposited AlO_x barrier layer (20 to 30 nm thick) on 12 µm PET using a two-step process (repeated four times), whereby an initially partially oxidised AlO_x layer is produced, which is subsequently further oxidised using a reactive plasma. Hence, the barrier performance obtained here in this project for AlO_x coated PET is superior, compared to the levels measured in the latter publication.

Finally, the barrier results obtained by Kobayashi and co-workers [294] for reactively evaporated AlO_x layers on PET should be stated, although, in their case, induction heating of a crucible was used. Their 35 nm thin AlO_x coating on a 25 µm PET substrate showed an optical transparency comparable to that of the substrate and

revealed an OTR of 2.7 $cm^3/(m^2\ d)$, which is lot higher than obtained in this thesis. No data on moisture barrier performance is given in the publication.

In the following section, possible reasons for the observed differences in barrier properties of the various AlO_x coated BOPP films will be discussed.

BOPP A

Plain BOPP A exhibited crater/dimple-shaped defects (see Sections 6.1.2.3 and 6.1.2.4 for SEM and AFM investigations, respectively), which also appeared to be reproduced as defects in the AlO_x and aluminium coating, as will be discussed in more detail in Sections 6.2.2.2 and 6.2.2.3. These defects are assumed to act as permeation pathways for oxygen molecules, hence impairing the OTR after AlO_x coating and metallisation. Rossi and Nulman [144] showed in a theoretical study that "many small holes in a barrier layer are much more effective in compromising the system barrier properties than a few large holes with the same total area" and analogous results were obtained via numerical simulations of the permeation through defects in inorganic barriers layers on polymers conducted by Hanika et al. [156]. This is due to the better spreading of the permeating molecules within the polymer substrate when a larger number of defects is present. Czeremuszkin and co-workers [146] showed (for 13 µm PET) that, when pinholes with a diameter of 200 nm, an average defect distance of 3.2 µm and a number density of $1.11 \times 10^7\ cm^{-2}$ are present (surface coverage by the coating larger than 99 %), no barrier improvement at all can be obtained by the coating. Consequently, the vast amount of permeation defects (50 to several 100 nm in diameter, see Section 6.2.2.3) found on coated BOPP A is very likely to be the reason for the poor barrier performance of this film. Moreover, as the defects appear randomly distributed over the film surface, the measured OTRs of coated BOPP A scatter heavily (large standard deviations) and, additionally, the presence of defects also conceals any effect (i.e. barrier improvement) of the in-line plasma pre- and post-treatment on the barrier performance. The slightly better oxygen barrier performance of metallised BOPP A, in comparison to AlO_x coated BOPP A, may be explained by differences in the coating thickness. The AlO_x layer is approximately 10 nm thin (refer to Chapter 6.2.5), whilst a metallised polymer film of 2.0 OD equates to a coating thickness of roughly 35 nm (including oxide layers at the free surface and interface) [295]. It will, furthermore, be shown in Section 6.2.1.4 that with increasing the AlO_x coating thickness, oxygen barrier improves, which is attributed to the permeation defects in the coating becoming narrowed and partially closed up. That the water barrier of metallised BOPP A (see *Table 6-11*) is a lot better than for the AlO_x coated opponent is most probably due to differences in the permeation mechanisms of

water vapour and oxygen, as proposed by the results reported in Section 6.2.1.3, which indicated that the presence of 'metallic' aluminium enhances moisture barrier of the coated film (independent of defects being present in the coating).

BOPP B

This film will be discussed later, as observations made for the other BOPP film are required, in order to explain BOPP B's barrier properties after AlO_x coating.

BOPP C

BOPP C (and also all remaining BOPP films) neither exhibited crater-shaped defects on the uncoated film, nor permeation defects in the AlO_x coated film (see Sections 6.1.2.3, 6.1.2.4, 6.2.2.2 and 6.2.2.3). However, a significant difference was seen after XPS analysis of the plain films, which revealed that BOPP C had 10.4 at% oxygen in its film surface, twice as much as measured for BOPP B, D and E (see Chapter 6.1.3.2). The higher oxygen content, i.e. higher amount of oxygen-containing functional groups, is assumed to result in a better nucleation and growth of the coating (more nucleation sites) and hence denser structure of the AlO_x layer, therefore improving its (oxygen) barrier properties [151]. This would also explain that even without applying any in-line plasma pre-treatment, the oxygen barrier performance already revealed an acceptable level of 47.0 ± 5.4 cm³/(m² d). Moreover, it also suggests that interfering low-molecular-weight substances on the film surface, which probably affected the contact angle measurement and surface energy determination of the plain film (Chapter 6.1.3.1), must have at least (partially) desorbed in vacuum, thus 'freeing' the nucleation sites (oxygen-containing functional groups) and enabling the AlO_x layer to deposit without major interference. For BOPP A, a larger oxygen content (compared to BOPP B, D and E) of 7.0 at% was also discovered. However, the effect of this on the structure/density of the coating and hence oxygen barrier is cancelled by the presence of defects in the AlO_x layer.

BOPP D and E

BOPP D and E showed a lower oxygen content of around 4 and 5 at% (as did BOPP B, refer to Chapter 6.1.3.2). Consequently, the effect on nucleation, growth and density of the AlO_x layer is a lot lower than for BOPP C (10.4 at% oxygen). No craters or permeation defects were present in the uncoated and coated films, respectively (see Sections 6.1.2.3, 6.1.2.4, 6.2.2.2 and 6.2.2.3). However, BOPP E was a heat shrinkable BOPP film and also BOPP D revealed increased shrink properties (see Section 6.1.4). Hence, it is assumed that these films shrink to a larger extent during coating deposition, due to being exposed to the heat load from the deposition process. This film shrinkage induces a compression of the coating,

therefore densifying the AlO_x layer and improving OTR and also slightly WVTR. The shrinkage data presented in *Figure 6-12* (Chapter 6.1.4) reveals a higher degree of shrinkage for BOPP E (in MD and TD), compared to BOPP D, which would explain the better oxygen barrier of AlO_x coated BOPP E. A patent by Dai Nippon Printing [296] also suggests a heat/annealing treatment (after deposition), in order to improve the barrier properties of polymer films coated with vapour deposited inorganic oxides by shrinking the substrate film and hence increasing the density of the coating.

BOPP B

BOPP B did not show a higher oxygen content, or reveal increased shrink properties (refer to Sections 6.1.3.2 and 6.1.4) and, consequently, the effect of these two parameters can be excluded. Furthermore, this film did not exhibit craters and defects in the uncoated film and AlO_x layer, respectively (see Sections 6.1.2.3, 6.1.2.4, 6.2.2.2 and 6.2.2.3). Therefore, the barrier improvement obtained depends strongly on the in-line plasma pre-treatments and its effects on AlO_x nucleation. For BOPP B, a vast improvement in oxygen barrier is seen when applying in-line treatment, with the average OTR value dropping from around 230 $cm^3/(m^2\ d)$ to 120 $cm^3/(m^2\ d)$ (see *Table 6-10*). This effect is much greater than obtained for BOPP C, which inherently had more than twice as much oxygen, where the mean OTR dropped from 47.0 $cm^3/(m^2\ d)$ to 35.3 $cm^3/(m^2\ d)$ due to in-line pre-treatment. Consequently, the plasma pre-treatment could not induce changes to the film surface of BOPP C that were as significant as the ones induced for BOPP B. Furthermore, on additional trials carried out for BOPP B, whereby the plasma pre-treatment power was increased, the OTR could be further decreased.

BOPP F and PET

BOPP F, similar to PET, represents a different polymer film surface (different chemistry, see Sections 6.1.3.1 and 6.1.3.2), which will affect the nucleation and film growth conditions for the depositing film and, thus, result in a denser (less porous) coating microstructure. Deng and co-workers [130] investigated AlO_x coated PET and BOPP, whereby the AlO_x layer was produced via electron beam evaporation in a roll-to-roll process. They found that on BOPP, the AlO_x layer exhibited a microstructure with larger particles than on PET, presumably caused by a lower number of nucleation sites, and hence argued that the greater boundaries between larger particles resulted in more pathways for oxygen permeation and therefore higher OTR for the AlO_x layer on BOPP.

For PET, the effect of film shrinkage may be neglected as a way to densify the AlO_x layer, since this thermally more stable film can be expected to shrink a lot less than BOPP during AlO_x deposition (see shrink properties, Section 6.1.4). This, again, confirms the importance of the film surface chemistry for the microstructure/density of the AlO_x layer.

BOPP F was, additionally, produced without any antiblock particles in the special skin layer, which will also have an impact on the barrier properties, since antiblock particles can result in defects in the coating (discussed in more detail in Chapter 6.1.2.1).

For BOPP F, the improvement of OTR (compared to AlO_x coating on standard BOPP) is, additionally, due to the fact that the high surface energy skin layer has a lower permeability to oxygen than BOPP, as can be seen from the plain film oxygen barrier performance, see Section 6.1.1, *Table 6-1*. As described by Jamieson and Windle [140] and also Beu and Mercea [143], applying a thin and less permeable coating (e.g. polymer) to the polymer film prior to metallisation (or in this case AlO_x coating) can improve barrier performance, in the case of a defect driven permeation through the inorganic coating due to a change of the concentration gradient in the polymer in the vicinity of the defects. This has also been suggested by Hanika et al. [149] and Langowski [126] and is further discussed for acrylate undercoats in Chapter 6.4.1.1. However, this cannot explain the barrier improvement seen for water vapour when AlO_x coating BOPP F, since the polymer skin does not appear to offer a significant water barrier improvement, compared to standard BOPP (see *Table 6-1*). Therefore, it must be the nucleation and growth of the AlO_x on a different polymer skin chemistry that has a major impact on moisture barrier.

In summary, it appears to be the AlO_x coating microstructure that determines the barrier properties; the denser (i.e. less porous) the coating, the better the OTR and also WVTR. Two ways found here to 'densify' the AlO_x layer are the nucleation/growth of the AlO_x itself, i.e. the number of nucleation sites as determined by the surface chemistry (native or treated) of the film, and the shrinkage of the substrate film, which leads to a compression of the AlO_x layer. A further way to densify the coating would be the use of plasma assistance during deposition [38-40]. Moreover, densification processes can be carried out off-line after coating deposition, such as heat-treatment of the coated film in order to induce shrinkage of the polymer [296] (see also Chapter 6.2.1.6). Additionally, the ageing process of AlO_x coated films (discussed later in Chapter 6.2.1.2) represents a densification process, as the coating is assumed to take up oxygen and/or moisture from the ambient and, furthermore, creep effects of the film may take place.

Finally, the effect of antiblock particles on the barrier performance should also be mentioned here. Despite BOPP E revealing a vast amount of submicron antiblock particles (see Section 6.1.2.2), the oxygen barrier performance was good. As stated before, it has been shown by theoretical and numerical studies [144, 156] that a large number of small defects is more effective in reducing the barrier properties of a coated polymer film, compared to a few larger defects with the same overall area. If one would assume that the majority of the antiblock particles of BOPP E would induce defects in the AlO_x layer, then one would expect a far higher OTR, more similar to AlO_x coated BOPP A, which revealed a vast number of defects. Consequently, it is argued that the antiblock particles did not necessarily create defects in the AlO_x layer and that antiblock particle-induced defects may be of more importance when lower OTRs of AlO_x coated BOPP are desired (e.g. less than 10 $cm^3/(m^2\ d)$. The DIC light microscopy, antiblock count and SEM investigations of plain PET (see Section 6.1.2) also showed a large amount of antiblock particles on PET (similar distribution to BOPP B, see *Figure 6-5*), but the OTR and WVTR of the AlO_x coated PET were less than 1 $cm^3/(m^2\ d)$ and 1 $g/(m^2\ d)$, which also here suggests that the effect of antiblock particle-induced defects is low. Nevertheless, as discussed in detail in Chapter 6.1.2, there are differences between PET and BOPP regarding the incorporation and embedding of the antiblock particles into the polymer film.

6.2.1.2 Ageing and transmission rate trends during barrier measurements

In addition to the final barrier values, obtained by the barrier measurement when a permeation equilibrium is reached, it is also of interest to investigate the behaviour of the AlO_x coated BOPP film samples during barrier measurements and the dependency of this behaviour on the age of the measured AlO_x coated film sample.

In the case of WVTR measurements, no significant barrier improvement has been achieved with standard packaging grade BOPP film (when samples were not aged, as will be shown in this chapter). It is, however, interesting to note that during the water vapour barrier measurement, a permeation equilibrium is never reached, but the measured transmission rate constantly drops, although the slope decreases with proceeding time. This behaviour is shown in *Figure 6-13* for AlO_x coated BOPP A and in *Figure 6-14* for AlO_x coated BOPP C. During these measurements, the AlO_x layer is facing towards the 0 % RH side of the test cell. It is common practice when testing aluminium coated films to face the coating to towards the 0 % RH side, since it is well-known that the aluminium is attacked and corroded when facing the high RH side of the test cell.

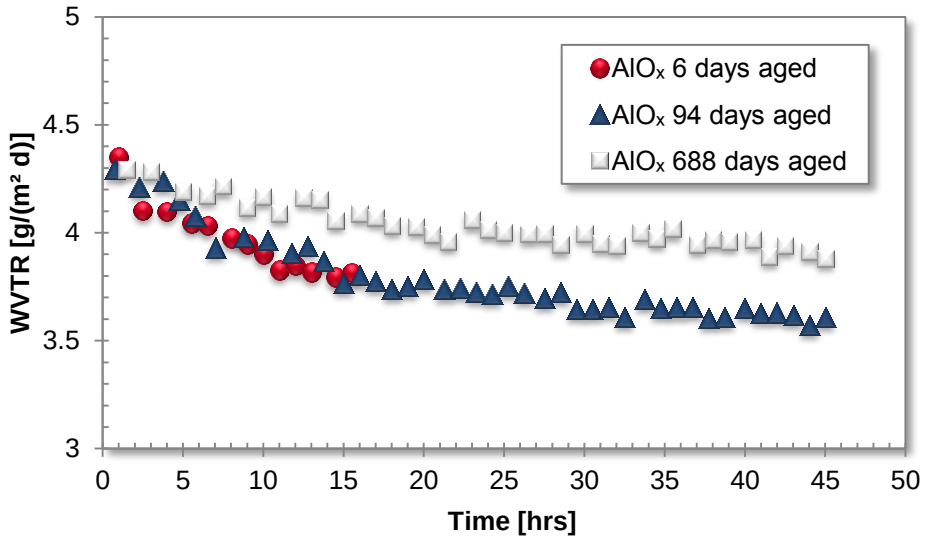

Figure 6-13: Change of WVTR during barrier measurement of AlO_x coated BOPP A for samples of different ages

As can be seen for AlO_x coated BOPP A from *Figure 6-13*[g], the WVTR trend begins from a value that is approximately equivalent to that of the plain film WVTR (see *Table 6-1*, WVTR (BOPP A) = 4 – 5 g/(m² d)) and then decreases continuously over

[g] The test length of barrier measurements (as shown in *Figure 6-13*, *Figure 6-14*, *Figure 6-15* and *Figure 6-16*) may vary, depending on permeation equilibrium. Furthermore, tests are run either during day/night time or over the weekend and may be stopped early, if the sample reveals a non-satisfactory barrier performance.

an extended period of 45 hours. Towards the end, the curves seem to flatten slightly. This behaviour is depicted for three samples of the same trial, which were measured 6, 94 and 688 days, respectively, after AlO_x deposition. Whilst the 6 and 94 days aged samples behave identically during WVTR measurement, the 688 days aged sample initially starts off from the same value, but then decreases at a lower rate. Here, it needs to be mentioned that the initial measurements were carried out using a RH gradient of 100 % to 0 %[h] and values were calculated for the typically stated RH of 90 %. The last measurement (688 days) was performed at a lower RH, after the permeation test system was changed, in order to be able to adjust the required RH. Consequently, the lower slope of the 688 days aged sample does not necessarily need to be due to the age of the sample, but may well be caused by the exposure to a lower RH gradient during the measurement. On a larger scale, though, the differences in slope and final WVTR value are only small between the three samples. Overall, it can be concluded from *Figure 6-13* that in the case of AlO_x coated BOPP A, ageing did not result in an improvement of WVTR.

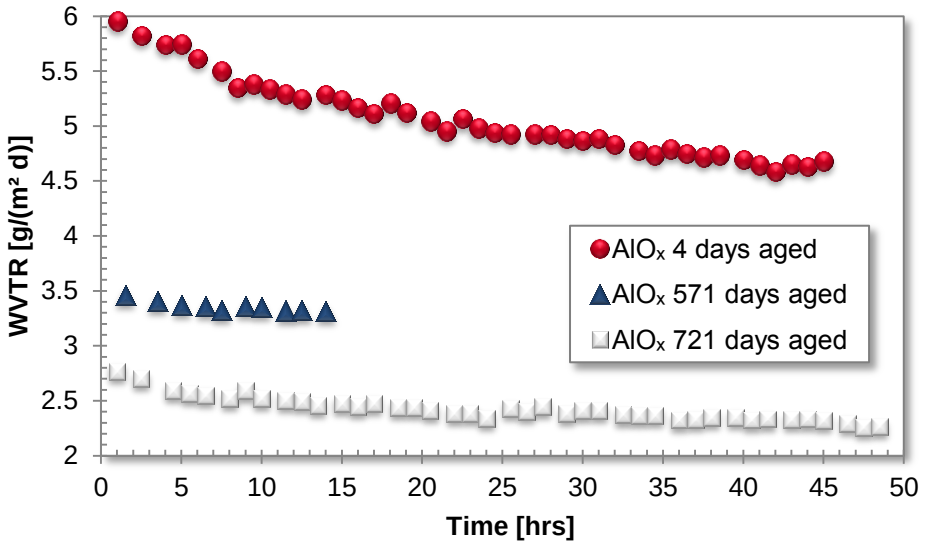

Figure 6-14: Change of WVTR during barrier measurement of AlO_x coated BOPP C for samples of different ages

AlO_x coated BOPP C showed the same trend, with WVTR values constantly decreasing during barrier measurement, as can be observed in *Figure 6-14*. The 4 days aged sample starts the measurement with a value, which is more or less identical to the uncoated film (see *Table 6-1*, WVTR (BOPP C) = 6 – 7 g/(m² d)).

[h] This is a normal and common way of measuring film samples on a Mocon Permatran-W 3/33, because the RH can be easily adjusted to 100 % using moist sponges. The WVTR for the stated RH of 90 % is calculated by the software, assuming a linear correlation between RH and WVTR. The system can also be changed to accurately adjust the test RH between 35 % and 90 % (as done later), which, however, requires more maintenance.

Nevertheless, when 571 and 721 days old samples of the same trial were measured, a clear difference in barrier performance was detected. Whilst for the 4 days old sample a final WVTR value of 4.68 g/(m² d) was recorded, the 571 days old sample showed a final value of 3.31 g/(m² d) (note the shorter measurement length of 14 hours) and the 721 days old sample a value of 2.26 g/(m² d); approximately half the value of the initial measurement. Moreover, the starting point of the latter two curves is already a lot lower (for the 721 days aged sample approximately half the start WVTR as measured for the 4 days old sample). Consequently, for AlO_x coated BOPP C, the sample age clearly improves WVTR. Similar to BOPP A, the slope during the two later measurements is a lot lower, which can, as stated before, either be due to the changed RH test conditions or the sample age.

In general, all AlO_x coated BOPP (including BOPP F) and PET film samples showed similar, constantly decreasing trends during WVTR measurement. In the case of BOPP F and PET, where a water barrier improvement was obtained (only two days ageing were required for both OTR and WVTR), the value at the start of the measurement was lower.

It is, therefore, assumed that the exposure to high humidity during barrier testing (although the AlO_x layer is not facing the high RH) has an effect on the AlO_x coating that improves its barrier performance. Since specific (hydrophilic) interactions between aluminium oxide and water molecules are well-known and documented [297], one process that may explain this behaviour is water uptake and the resultant swelling of the coating due to the high RH, which prevents further water molecules from passing completely unhindered through the coating. A barrier improvement of AlO_x coated films due to humidification and conditioning has also been observed by Kelly [2], who originally required this treatment in order to achieve acceptable barrier levels. A Japanese patent [298] also suggests a moist-heat treatment to enhance water vapour and oxygen barrier when films are already laminated. Vogt et al. [299] deposited polymer films onto a sputtered AlO_x layer on silicon wafers and exposed these samples to saturated water vapour at ambient temperature (22 ± 3 °C). They found that water did not induce a swelling of the AlO_x layer, but was accumulated at the AlO_x/polymer interface, which shows a strong attraction towards water and acts in a manner similar to a desiccant. Consequently, this absorption of water has a great effect on the permeation of water through the polymer/AlO_x composite and may be the reason for its water barrier properties. As mentioned before, the polymer film was deposited onto a sputtered AlO_x layer and it may well be that no moisture accumulation occurs if the AlO_x layer is deposited onto the polymer. Nevertheless, the measured WVTRs show that when exposed to high RH (during WVTR

measurement), the barrier of AlO_x coated films does improve over time. In the case of standard grade BOPP films, this improvement is, unfortunately, not down to the desired WVTR values of less than 1 g/(m² d), unless perhaps exposure would be for several weeks. But in industrial practice it is not possible to measure samples for such an extended period of time. The differences seen in ageing of AlO_x coated BOPP A and C with respect to the water barrier performance, will be further discussed at the end of this chapter.

Similar to the change of WVTR during barrier measurement, the behaviour during OTR measurement and the effect of sample age on the measurement was investigated. The curves of OTR versus test time for AlO_x coated BOPP A and C are shown in *Figure 6-15* and *Figure 6-16*, respectively.

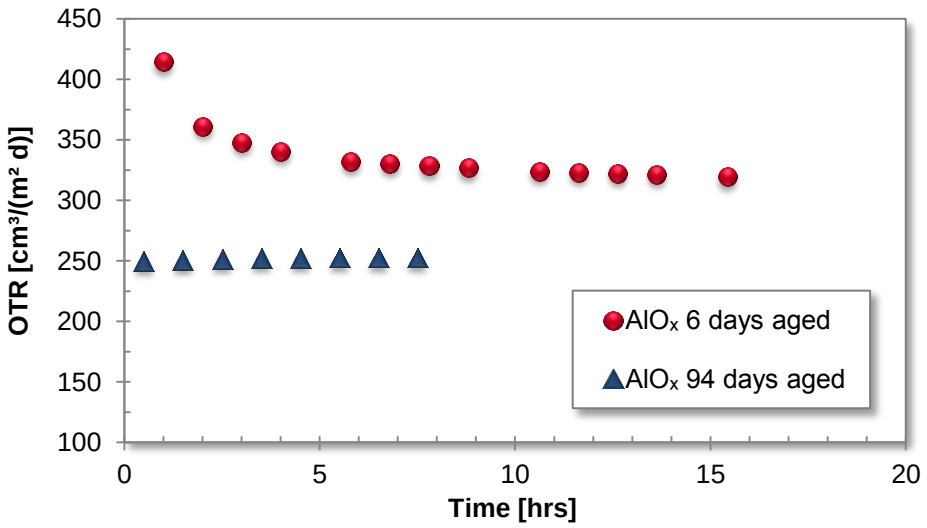

Figure 6-15: Change of OTR during barrier measurement of AlO_x coated BOPP A for samples of different ages

As can be observed from *Figure 6-15* and *Figure 6-16*, there is a clear dependence of the OTR behaviour during barrier measurement on the sample age. In the case of AlO_x coated BOPP A, the OTR of the 6 days aged sample still revealed a tendency to drop when the test was stopped after 15 hours. It can be seen from the slope at the end of this measurement that even extending the measurement over another 24 hours would not have yielded the final OTR value, which was obtained when a sample of the same trial was tested after 94 days, whereby a constant OTR value is measured from the beginning of the barrier test. It should be mentioned here, though, that the behaviour seen for the 94 days aged sample may have already been obtained with a sample of lower age. For BOPP C, a 4 days old sample required a measurement time of at least 45 hours to reach an equilibrium OTR of approximately 30 cm³/(m² d). A sample of the same trial aged for 11 days gives the

latter OTR value from the start of the measurement experiment. Consequently, also for the behaviour during OTR measurement, AlO_x coated BOPP A and C exhibit some differences, in that it is assumed that for BOPP C the ageing and barrier improvement happened a lot faster. This indicates that the presumed ageing process greatly depends on the base film and its effect on the coating structure.

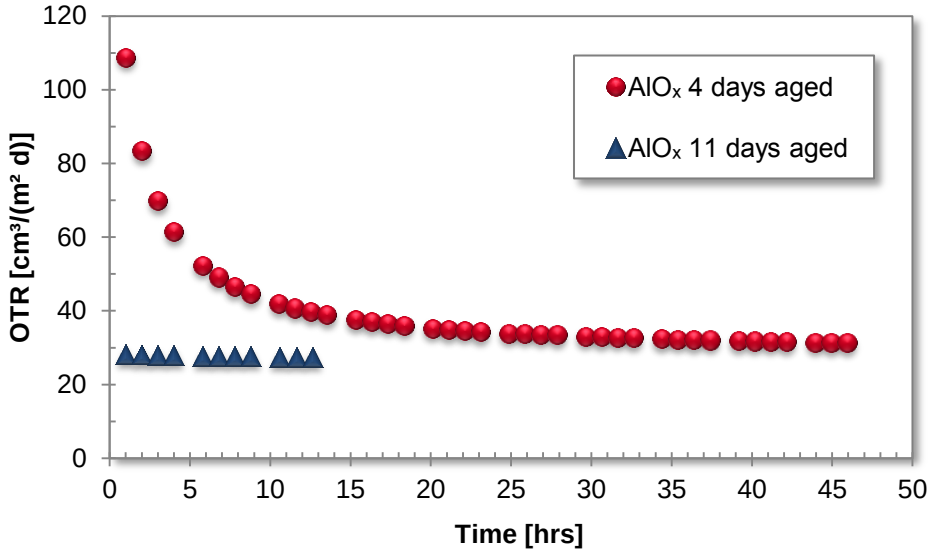

Figure 6-16: Change of OTR during barrier measurement of AlO_x coated BOPP C for samples of different ages

As will be shown later, during the time after coating, an ageing process takes place, which is indicated by a decrease of the OD, an aspect further explored in Chapter 6.2.7.1. The ageing process is believed to be due to oxygen and also moisture uptake of the coating (resulting in oxidation), as soon as the coated film is exposed to ambient conditions (after venting the vacuum web coater). The proposed incorporation of additional atoms and molecules into the AlO_x coating (i.e. oxygen, water) may cause the coating to swell and densify, similar to the discussion at the beginning of this section with respect to the WVTR measurement. Thus, pathways for permeating molecules become hindered and effectively blocked.

During barrier measurement (OTR and WVTR), the ageing process (if not yet completed) will presumably be accelerated by the RH and the pure oxygen (in the case of OTR measurement) on one side of the measurement cell, hence accounting for the observed behaviour during barrier measurement.

That an ageing or swelling process plays an important role for the barrier of AlO_x coated films has also been suggested by Kelly [2, 3]. As mentioned previously, he originally subjected the AlO_x coating to a humidification and conditioning procedure, in order to obtain adequate barrier performance. Additionally, he found that the loss

of oxygen barrier, due to stretching or other damage of the AlO_x coated film, could be recovered by exposure to high levels of RH. Consequently, it was assumed that exposure to high humidity led to swelling and hydration of the coating, thus narrowing the cracks (i.e. permeation pathways) in the AlO_x layer. Again, this is an important indication of a possible swelling process governing oxygen barrier properties.

The differences seen in ageing of AlO_x coated BOPP A and C with respect to the water and oxygen barrier performance can be explained by differences in the defect coverage of these two films. As will be shown later (see Chapters 6.2.2.2 and 6.2.2.3), the crater-shaped defects of plain BOPP A (refer to Sections 6.1.2.3 and 6.1.2.4) were reproduced as permeation defects in the AlO_x layer, whilst similar defects could not be found for AlO_x coated BOPP C (or the remaining BOPP films). These defects act as pathways for the unhindered permeation of oxygen and water vapour and, consequently, their presence overshadows the positive effects caused to the film structure by the ageing/swelling process (increase in coating density due to the uptake of water and/oxygen). This results in the fact that the OTR of AlO_x coated BOPP A needs a longer ageing time, compared to BOPP C, and that in the case of WVTR, no effect of ageing is seen as all the water vapour can permeate unhindered through the defects.

For AlO_x coated BOPP C, it was also observed that a stable, low oxygen barrier (approximately 30 $cm^3/(m^2\ d)$) was reached much faster than the improvement in WVTR. This is assumed to be due to the different permeation mechanisms of oxygen and water molecules (see Section 4.6.2 for more detail). Whilst the oxygen permeation is dominated by macroscopic defects (a few nm to several µm), water vapour may permeate through even smaller defects and voids (microscopic defects). Consequently, when the AlO_x coating is improved in its microstructure (i.e. densified) during ageing, the macroscopic defects are becoming blocked a lot quicker, whilst the time (and oxygen/water molecules) required to further enhance the AlO_x structure and gradually close up microscopic defects is a lot longer. How quickly this process happens, therefore, also depends on the initial (as deposited) density/structure of the AlO_x layer; the better/denser the initial coating, the quicker will be the ageing process in terms of obtaining good barrier levels (e.g. PET is quicker than BOPP C, which in turn is quicker than BOPP A). An improvement of WVTR with time was also seen for AlO_x coated BOPP D and F, but not B. This is attributed to the initially better coating microstructure of BOPP D and F (see also better oxygen barrier performance, compared to BOPP B, *Table 6-10*), caused by the increased shrink properties of these films. The water barrier improvement with

ageing time can here, furthermore, be enhanced by creep of the shrink BOPPs (compressive force), in addition to the swelling of the AlO_x layer. In the case of BOPP B, it appears that the AlO_x microstructure is a lot more porous and, consequently, no changes could be seen during the investigated time period.

6.2.1.3 Effect of stoichiometry of coating on barrier performance

As mentioned previously, no significant water barrier improvement has been obtained for AlO_x coated BOPP film (without extensive ageing), with the exception of BOPP F that had a different polymer as its skin layer. Nevertheless, when the BOPP films were metallised, the WVTR in all cases, even for BOPP A, was considerably enhanced to values of less than 1 g/(m² d), as can be noticed from *Table 6-11*. There are two main differences between the metallised and the AlO_x coated BOPP films; firstly, the coating chemistry (oxide versus metal) and, secondly, the coating thickness. The stoichiometry of the standard AlO_x coating was characterised using XPS, and it was found that the x-values range from 1.53 to 1.65, with no elemental (metallic) aluminium, i.e. the coating consists predominantly of stoichiometric Al_2O_3 (see Chapter 6.2.3). Furthermore, the thickness of the AlO_x barrier layer was determined to be approximately 10 nm (refer to Chapter 6.2.5), whilst the thickness of the aluminium coating of 2.0 to 2.1 OD (including surface and interface oxides) is roughly 35 nm [295]. Consequently, in this and the following chapter, the effect of AlO_x coating stoichiometry and AlO_x coating thickness, respectively, on barrier properties of the coated film will be investigated. For the first trials, the thickness of the coating was left approximately constant, whilst the amount of oxygen introduced during deposition was reduced, in order to deposit coatings with a higher aluminium content (darker coatings). This investigation was carried out for AlO_x coated BOPP A and B (using plasma pre-treatment only) and the oxygen and water vapour barrier levels obtained as a function of the AlO_x stoichiometry (x-value) are shown in *Figure 6-17* and *Figure 6-18* for BOPP A and BOPP B, respectively. Each data point represents an average value and standard deviations are illustrated as error bars. In addition to the AlO_x stoichiometry x-value, the content of elemental (metallic) aluminium is shown on a secondary horizontal axis. The values in at% reflect the concentration relative to the total aluminium 2p peak area. Heuristically determined trend lines are displayed in both graphs for the change of oxygen and water vapour barrier properties.

The samples of AlO_x coated BOPP B with varying aluminium content were characterised in terms of stoichiometry (and elemental aluminium content), in order to establish a correlation between aged OD and x-value (see Chapter 6.2.3.), which was then used to estimate the x-values and elemental aluminium contents for BOPP A, where only one sample was measured via XPS. Good agreement was obtained between the measured sample and the calculated x-value using the previously established correlation.

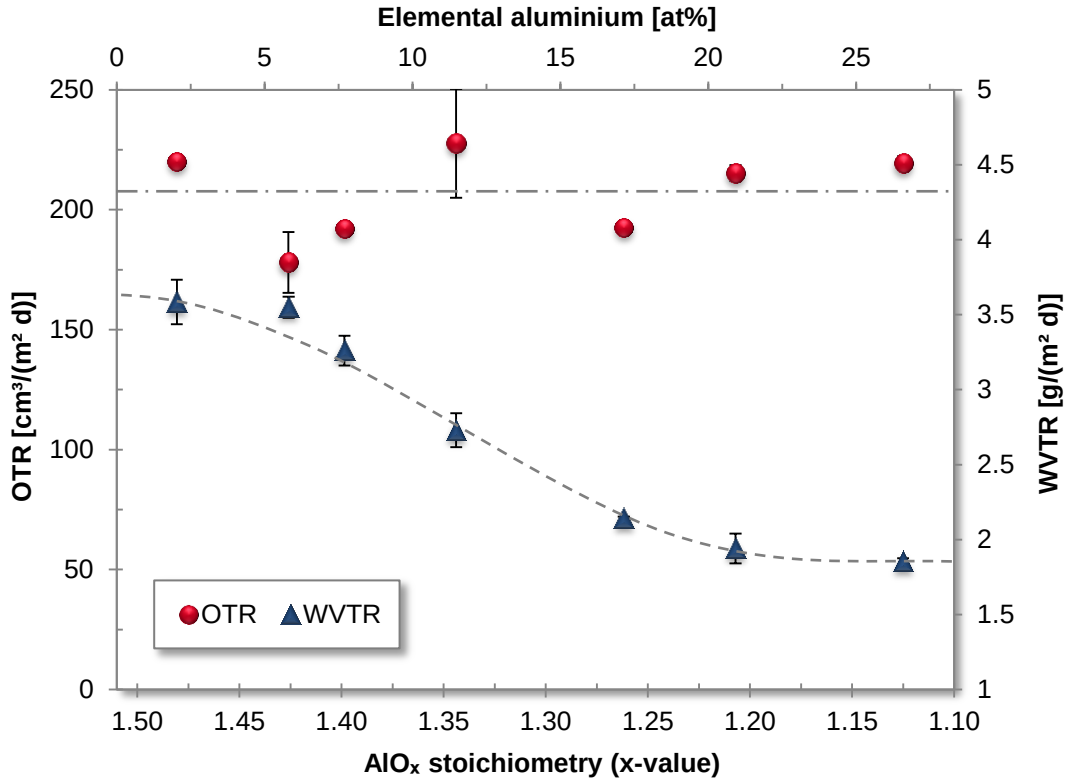

Figure 6-17: Change of AlO_x barrier performance with stoichiometry for AlO_x coated BOPP A

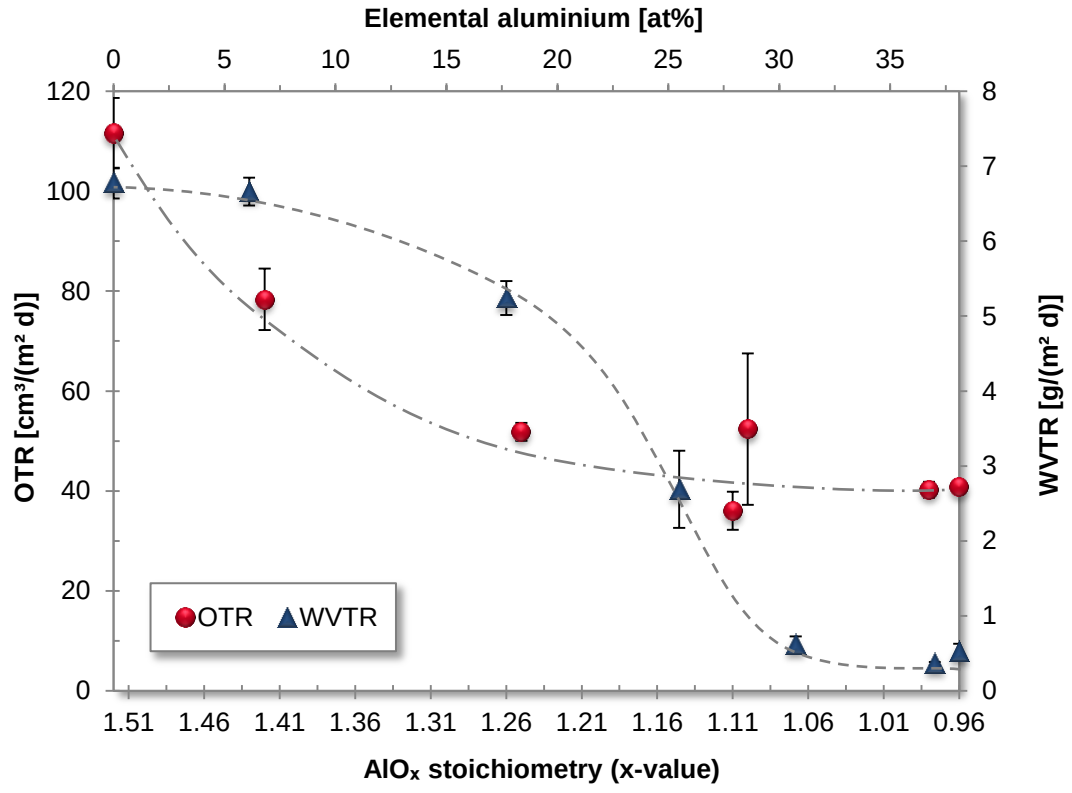

Figure 6-18: Change of AlO_x barrier performance with stoichiometry for AlO_x coated BOPP B

For both BOPP films the water vapour barrier could be improved by decreasing the amount of oxygen (and increasing the amount of aluminium) in the coating, i.e. lowering the x-value (see *Figure 6-17* and *Figure 6-18*). For BOPP A, a gradual drop of WVTR can be observed, which appears to level off at x-values of less than 1.2, with a final WVTR value of just below 2 g/(m² d). In contrast to that, the WVTR for BOPP B only decreases gradually in the beginning and then drops drastically between an x-value of 1.2 and 1.1 to WVTR values of approximately 0.5 g/(m² d). The starting point in both cases (BOPP A and B) is a WVTR value similar to, or marginally lower than, the plain film WVTR (see *Table 6-1*). In the case of BOPP B, it was consequently possible to obtain the required water barrier levels of less than 1 g/(m² d). Nevertheless, this is at the expense of losing transparency, since with increasing aluminium (metal) content, the coatings have a higher absorption and are grey. For BOPP A, however, the WVTR improvement was not down to the desired level. Furthermore, the onset of WVTR enhancement by increasing the aluminium content is seen for different x-values (for the two BOPP films) and, as described above, is more abrupt in the case of BOPP B.

The average OTR values for BOPP A did not improve with decreasing the x-value, but were unaffected, with values in the range of 150 to 250 cm³/(m² d). For BOPP B, by contrast, OTR was also enhanced with decreasing the x-value. Whilst the OTR of the 'standard'[i] AlO_x coated BOPP B was roughly 110 cm³/(m² d), this value dropped to approximately 40 cm³/(m² d) for x-values of less than 1.1. Reasons for the differences seen in OTR and WVTR change with stoichiometry for the two BOPP films investigated will be further discussed at the end of this chapter.

The results presented here afford an interesting insight into the permeation mechanisms, especially of water vapour. It seems that the aluminium metal content in the AlO_x layer plays an important role in preventing moisture from permeating unhindered through the coating. The decreasing WVTR with increasing metallic aluminium content suggests that a chemical reaction or interaction between metallic aluminium and water molecules may take place. Aluminium is known to be a very reactive metal and when exposed to ambient conditions, it immediately forms an oxide layer on its surface that is readily hydrated by the moisture present [300, 301]. Consequently, any (unreacted) metallic aluminium in the coating may have the tendency to react and interact with water, in a manner similar to corrosion processes. The metallic/elemental aluminium in the AlO_x layer could act analogous to a corrosion protection layer, with the unreacted metallic aluminium acting

[i] A 'standard' AlO_x coating from hereon is defined as an AlO_x barrier layer that has been deposited under standard conditions/settings, without purposely changing the stoichiometry. All coatings discussed so far (with varying in-line treatment) are 'standard' AlO_x layers.

sacrificially as a scavenger for moisture (since it has a strong affinity to water). It is, furthermore, interesting to note that the change of AlO_x stoichiometry did not show any resolvable effect on the nature of defects present on AlO_x coated BOPP A, which will be discussed later in the SEM and AFM analysis of the coated films (refer to Chapters 6.2.2.2 and 6.2.2.3). Nevertheless, SEM images of AlO_x (x = 1.1) coated and metallised BOPP A will be shown here for a better illustration and explanation (refer to *Figure 6-19*).

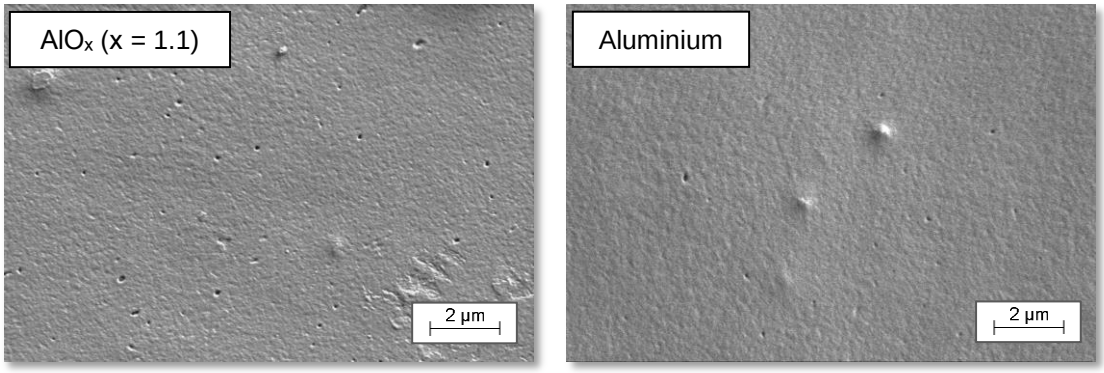

Figure 6-19: SEM images of AlO_x (x = 1.1) coated (left) and metallised BOPP A (right)

As can be detected from *Figure 6-19*, both films clearly reveal defects in the coating, which are assumed to act as pathways for permeating molecules. Despite the presence of the defects, the WVTR of the AlO_x coatings on BOPP A was improved with increasing the content of metallic/elemental aluminium, which gives some interesting information about water vapour barrier mechanisms for aluminium/AlO_x barrier layers. The interpretation is as follows: despite the presence of readily penetrable defects in the coating, the strong reactivity of water with metallic aluminium may cause permeating water molecules to react preferentially with the metallic (unreacted) aluminium in the coating. Nevertheless, for AlO_x coated BOPP B, a lower WVTR is reached than for AlO_x coated BOPP A when the x-value was decreased (refer to *Figure 6-17* and *Figure 6-18*), indicating that some water may still flow unhindered through the previously described defects. Furthermore, the presence of defects in the AlO_x coating on BOPP A, but not B, may also explain the different behaviour (shape of curves) when increasing the metallic aluminium content, with the WVTR change for BOPP A being gradual and located at a higher x-value, whilst for BOPP B the change is initially gradual and then very rapid. In the case of the aluminium layer on BOPP A, the WVTR is better, compared to the AlO_x coating with x = 1.1 (0.87 ± 0.02 g/(m² d) versus 1.86 ± 0.02 g/(m² d), see *Table 6-11* and *Figure 6-17*). This might be either caused by the thicker coating (35 nm [295] versus 10 nm, see Chapter 6.2.5) and the defects being narrowed down in size/diametre with increasing thickness (see Chapter 6.2.1.4) or the difference in the

content of metallic aluminium. It is, however, surprising and not yet explainable that a metal layer of comparable thickness to the AlO_x layer does not offer good barrier, neither water nor oxygen.

There is, furthermore, some practical evidence for the proposed chemical reaction/interaction dominating over the permeation through defects, given by Langowski et al. [302]. They state that for laminated structures containing metallised polymer films (used for vacuum insulating panels), the OTR is very susceptible to defects caused by bending and defects in the sealing area, whilst the latter two factors appear not to be detrimental to water vapour barrier properties.

Based on the improvement of OTR for AlO_x coated BOPP B with increasing metallic aluminium content, a change (improvement) in coating microstructure is assumed to accompany the change in stoichiometry. A change, i.e. reduction, in the number of defects/pinholes (antiblock generated, coating pick-off and/or further post deposition damages to the coating) is anticipated to play less of a role for the OTR enhancement, as the same film was used and all trials were run as one set without stopping the web or breaking the vacuum. That no effect is seen for AlO_x coated BOPP A must be caused by the defects not hindering the flow of oxygen (and the oxygen molecules not reacting with the metallic aluminium in the same manner as do the water molecules).

Nevertheless, it still needs to be considered that further densification of the AlO_x layer, possibly caused by the change in stoichiometry and/or a slight decrease in pressure during deposition (due to the lower amount of oxygen required for coatings with a lower x-values), could also lead to an improvement in water vapour barrier properties BOPP B. Nevertheless, for BOPP A the defects are still present and would allow the unhindered permeation of water vapour, unless the created ‘denser’ structure can hold the water molecules back in a different way, i.e. not via chemical interaction but possibly due to absorption (like a desiccant) or capillary reactions.

The general trends seen here for WVTR and OTR with change of AlO_x stoichiometry are in agreement with results published by other researchers for reactively evaporated AlO_x barrier layers. Barker et al. [16] analysed the barrier of oxygen- and metal-rich AlO_x coatings on PET and found that OTR was very similar for both, while WVTR was slightly improved for the metal-rich sample. Also Kelly [3] (see additionally European patent EP 0437946 [15]) reports on the oxygen and water vapour barrier of AlO_x coated PET improving with increasing aluminium content (i.e. increasing OD of the coating), with the water barrier enhancement being slightly greater. He, furthermore, states that an excess of oxygen decreases the density of the AlO_x layer, hence resulting in drastic barrier deterioration. Schiller and co-

workers [12, 27, 28, 34, 36] presented in various publications the relationship between OTR/WVTR and AlO_x stoichiometry/transparency (and later also oxygen flow during deposition), which exhibits an increasing trend for rising x-values (i.e. increasing oxygen flow). Additionally, Kobayashi et al. [294] found that when using excessive oxygen supply, the OTR of AlO_x coated PET increases, whilst coatings with lower optical transparency had improved oxygen barrier. They argue that this is caused by a suboptimal coating structure exhibiting defects due to the excess of oxygen inhibiting surface diffusion during film growth.

In summary, it needs to be mentioned that despite the barrier improvements observed (especially water barrier) when changing stoichiometry, these coatings are absorbing and grey in colour and, consequently, could not be rated as transparent barrier layers.

6.2.1.4 Effect of coating thickness on barrier performance

As stated in the previous chapter, the two main differences between AlO_x coated and aluminium coated BOPP are the coating chemistry/stoichiometry and the coating thickness. In this chapter, the effect of coating thickness on the barrier properties of the AlO_x coated BOPP film will be investigated. Therefore, BOPP A was coated with various thicknesses of AlO_x (using in-line pre-treatment only), whilst keeping the coating stoichiometry approximately constant. The coating thickness was determined using TEM (as described in Section 6.2.5) for a selection of the samples produced and a correlation between the on machine parameter of aluminium wire feed rate and resulting AlO_x thickness was established, which was then used to obtain an approximation of the thicknesses of the remaining samples (refer to Appendix A3). The results of this investigation are depicted in *Figure 6-20*, with barrier properties as a function of AlO_x coating thickness. Due to the OTR data scattering, especially for the lower coating thicknesses, no average values were calculated, but each data point represents an individual measurement. Additionally, heuristically determined trend lines are displayed.

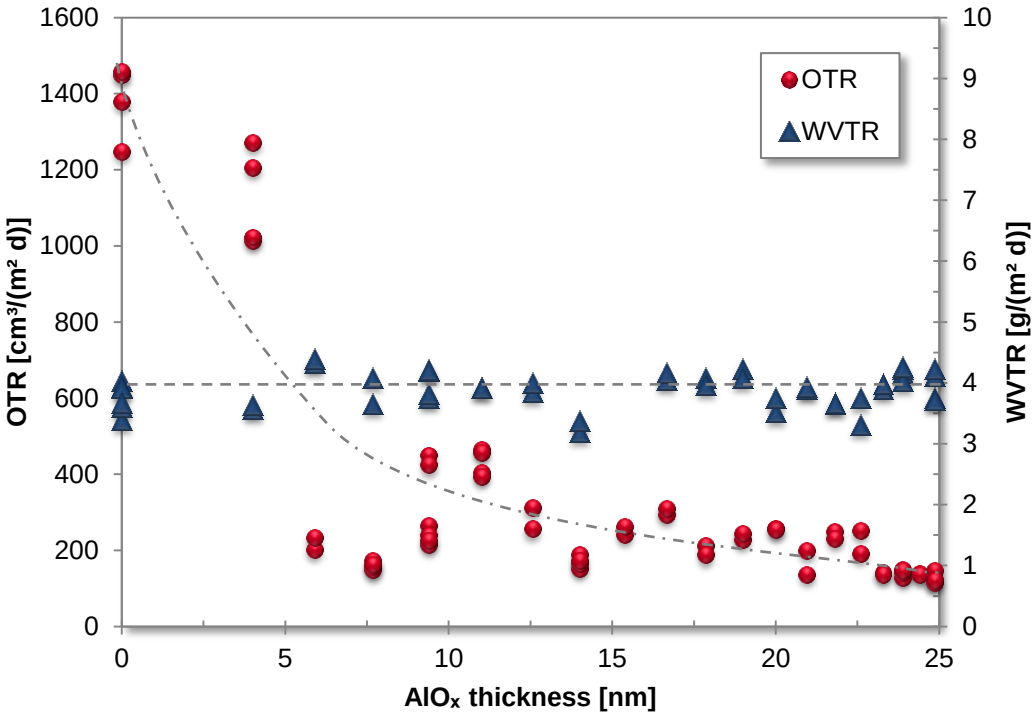

Figure 6-20: Change of AlO_x barrier performance with coating thickness for AlO_x coated BOPP A

As can be seen from *Figure 6-20*, there is a clear improvement of OTR with increasing AlO_x coating thickness. At a thickness of approximately 4 nm, the OTR is only marginally better than uncoated BOPP A, whilst from approximately 6 nm

onwards the OTR is enhanced. There is, however, still a large range of data scattering, predominantly between 5 nm and 15 nm coating thickness, which diminishes with increasing the AlO_x thickness further. With a thickness of roughly 25 nm, OTR values of 120 to 150 $cm^3/(m^2\ d)$ could be obtained. This is, nevertheless, still not down to the required level of less than 100 $cm^3/(m^2\ d)$ and, furthermore, the thickness in this case is more than twice the thickness (i.e. more material consumption) of a standard AlO_x layer (approximately 10 nm, refer to Chapter 6.2.5), which has given reliable barrier properties on other films (see Chapter 6.2.1.1, *Table 6-10*). Kelly [2] also states that the advantage of a thinner AlO_x layer lies in its better flexibility and crack resistance, compared to a thicker AlO_x, due to the ceramic and brittle nature of the coating.

In contrast to OTR, WVTR remains unchanged with increasing coating thickness and values fluctuate around 4 $g/(m^2\ d)$, i.e. similar to the plain film barrier performance. Changes in WVTR measurement length may also contribute to the variations seen in *Figure 6-20*, based on the observations described in Section 6.2.1.2.

The improvement detected for OTR is associated with the defects in the AlO_x coating on BOPP A (refer to Sections 6.2.2.2 and 6.2.2.3 and also *Figure 6-21*) getting partially closed up and narrowed with increasing coating thickness. Hence, the flow of oxygen molecules becomes further hindered. WVTR is unaffected by these changes to the defect size, based on the different permeation mechanisms for oxygen and water vapour, with water vapour being able to pass through smaller (‘microscopic’) defects (see also Chapter 4.6.2).

A decrease in transmission rate with increasing coating thickness has been reported by various researchers for different coatings, substrates and deposition techniques. In general, a graph showing the change of barrier properties with coating thickness can be divided into three zones. The initial drop (zone 1), seen when increasing coating thickness, is caused by the transition from nucleation and partial substrate coverage towards complete coverage, which is achieved at the so-called critical coating thickness. Based on the pinhole model, Decker and Henry [151] state that a coverage of at least 95 % is required in order to see an improvement by the application of a barrier layer, although Czeremuszkin et al. [146] showed that even at coverages as high as 99 % no barrier improvement at all may be obtained (depending on the size and number density of defects/pinholes). After the initial drop of transmission rate, the barrier properties remain approximately constant or drop further at a lower rate (zone 2, somewhere here lies the optimum coating thickness) until internal stress, poor adhesion and/or thermal load of the process affect the

coating structure (e.g. cause micro cracks) and, hence, decrease the barrier performance (zone 3). [155, 290, 303]

Consequently, the graph for OTR in *Figure 6-20* suggests that for the lowest AlO_x thickness deposited (approximately 4 nm), the substrate surface is not completely covered, since the OTR obtained is very similar to the plain film OTR. SEM analysis of this trial (see *Figure 6-21*, left) did not explicitly reveal uncoated film areas. Nevertheless, as will be discussed in the Chapters 6.2.2.2 and 6.2.2.3, the AlO_x layer was found to reproduce the underlying polymer substrate topography and no excessive SEM investigation was carried out for the 4 nm thick AlO_x coating on BOPP A. The previously mentioned defects can be clearly seen for the approximately 4 nm and 25 nm thin AlO_x layers on BOPP A (refer to *Figure 6-21*). The larger defects seen in the SEM images are created by dislocated antiblock particles (left image) or imprints of antiblock particles residing on the reverse side of the film, presumably before AlO_x coating (see also discussion of plain film topography, Section 6.1.2).

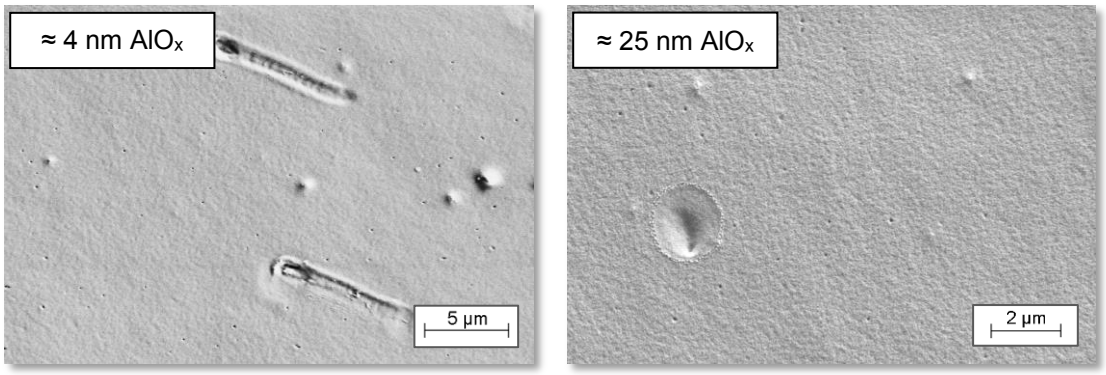

Figure 6-21: SEM images of approximately 4 nm thin AlO_x (left) and 25 nm thin AlO_x coatings on BOPP A (right)

The critical coating thickness in the case of AlO_x coated BOPP A appears to be between 5 to 10 nm, although the optimum for OTR is found for thicker AlO_x layers. Moreover, the thickness range investigated here does not cover zone 3, as no rise in OTR is seen for the thicker AlO_x layers.

Generally, it can be found that the critical coating thickness strongly depends on the type of coating (material, chemistry), the deposition technique, the permeating substance and also the type of substrate [290]. Henry and co-workers [160, 290] showed that 5 nm are sufficient to obtain oxygen barrier properties with electron beam evaporated AlO_x layers on PET, whilst for good water barrier a thickness of 10 nm was required. By contrast, Ludwig and Josephson [304] found stable oxygen barrier properties for AlO_x (electron beam) evaporated onto PET from 20 nm

onwards. For electron beam evaporation of AlO_x onto BOPP, Philips et al. [288] also reveal an effective AlO_x thickness of 10 nm for WVTR, with water vapour barrier properties tending to deteriorate after 30 nm, whilst Moosheimer and Bichler [64] state an optimum AlO_x thickness of 40 nm for oxygen barrier on BOPP.

Schiller and co-workers [10] report that a 20 nm thin layer is sufficient in improving WVTR of reactively electron beam evaporated AlO_x on PET (with and without plasma activation), whereas the optimum was located for approximately 50 nm and above 60 to 80 nm WVTR was found to increase. For OTR, the optimum AlO_x thickness (with plasma activation) was seen for approximately 60 nm. In the case of reactively evaporated AlO_x layers onto PET using resistively heated boats, Kelly [3] discovered an optimum thickness (for AlO_x barrier and robustness) between 20 and 25 nm, but explains that below 15 nm the coating appears discontinuous.

For sputtered AlO_x barrier layers on PET, Schiller and co-workers [32, 34] and also Langowski et al. [302] showed a critical thickness of 10 to 20 nm, with oxygen and moisture barrier properties not deteriorating up to 200 nm AlO_x thickness. Henry et al. [291] measured an optimum of 30 nm, whilst Miyamoto and co-workers [175] found an optimum of 10 nm (for OTR and WVTR).

As can be seen, the critical AlO_x coating thickness found here for BOPP A falls at the lower end of the broad range reported in literature for AlO_x barrier layers deposited by a variety of PVD techniques.

6.2.1.5 Barrier retention on elongation

An important property of flexible barrier materials for further conversion (e.g. printing, slitting and laminating) is their resistance to damage under repetitive strain, i.e. the retention of barrier properties on being subjected to straining action. A test method to investigate this property is the so-called flex durability or Gelbo-flex test (ASTM test method F392 [305]), during which films are repeatedly twisted and compressed. This test is aimed at determining the capability of the film structure to endure downstream processing/converting and also the ability of the final laminated packaging structure to survive repetitive strain (during transports/storage/retail), whilst still providing the necessary barrier properties. However, the Gelbo-flex test may represent a very aggressive and destructive test method and can lead to a high variation of the results obtained, if the coated but non-laminated film is tested [303]. It seems therefore not applicable to use the Gelbo-flex test for determining the effect of further film processing on the barrier properties of the AlO_x coated film prior to lamination (for Gelbo-flex of laminated and non-laminated AlO_x coated BOPP, refer to Chapter 6.5.1.5).

In order to avoid the issues related to the Gelbo-flex test, the AlO_x coated films were stretched to a pre-defined strain/elongation (between 0.5 and 5 %, stretching in the machine direction) by a tensile testing unit (Hounsfield H10KS with QMat 5.52 software) and, subsequently, the barrier properties were determined (test for stretch durability/resistance as suggested by Felts [303], however samples are measured in the relaxed state). This test should simulate the behaviour of the AlO_x coated film during film handling (e.g. web tension during winding of the film) and give evidence about the effects of downstream processing on the barrier properties of the AlO_x coated and non-laminated film.

Plots of OTR and WVTR versus applied (then released) strain/elongation are shown in *Figure 6-22* for AlO_x coated PET, in *Figure 6-23* for AlO_x coated BOPP C, in *Figure 6-24* for AlO_x coated BOPP E and in *Figure 6-25* for AlO_x coated BOPP F. Data points represent average values, whilst error bars indicate the standard deviations.

For AlO_x coated PET (see *Figure 6-22*), these investigations clearly show that WVTR starts to deteriorate at lower levels of elongation than OTR. Furthermore, the shape of the two curves is completely different. Whilst WVTR starts increasing between 1 and 1.5 % elongation with a decreasing slope, OTR starts to deteriorate slowly between 3 and 4 % elongation and then increases rapidly, i.e. WVTR has a decreasing rate of change with elongation, whereas OTR has an increasing rate.

Kelly [2] found that for AlO_x coated PET (reactive evaporation from boats, AlO_x thickness 20 to 25 nm, see [3, 16]), the oxygen barrier can withstand higher elongations than the moisture barrier, which in his analysis was lost above 1.3 to 1.5 % elongation. In a later publication, Kelly [3] furthermore shows graphs which indicate that at up to 3 % elongation OTR only increases slowly (for a transparent AlO_x layer), but more rapidly beyond this value. Additionally, he reports that for slightly grey, i.e. metal-rich coatings, the resistance to barrier loss (oxygen as well as water barrier) is improved, which eases the conversion of these films. A further study by Barker and co-workers [17], also involving Kelly, investigated these coatings (metal- and oxygen rich AlO_x on PET) for their stretching induced gas barrier loss towards oxygen, helium and argon using mass spectrometric techniques. Finally, the increase in OTR, which begins between 3 to 4 % elongation (refer to *Figure 6-22*), also agrees well with results presented more recently by Skinner [18].

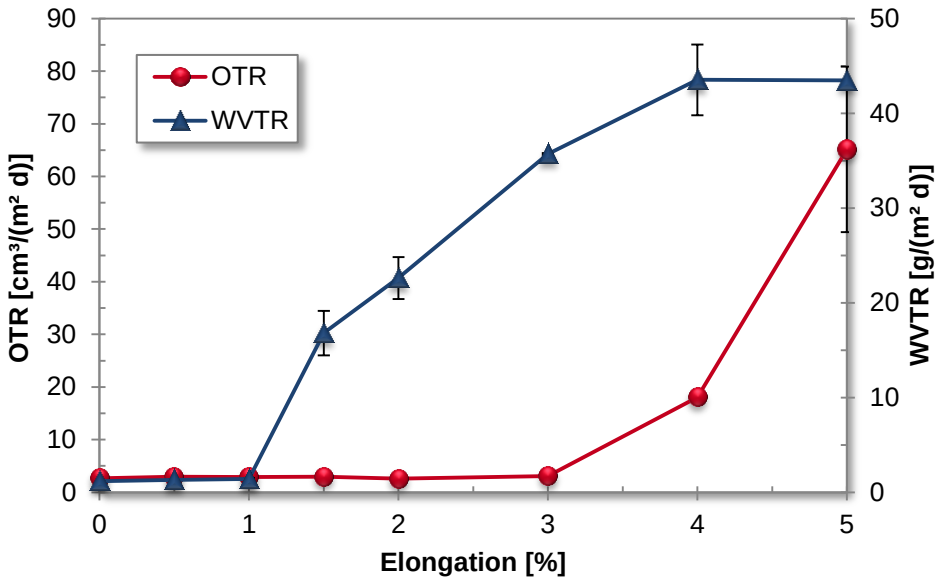

Figure 6-22: Change of barrier properties upon elongation of AlO_x coated PET

The WVTR behaviour shown in *Figure 6-22* is additionally in good agreement with results yielded by Schiller et al. [32, 36] (also presented later by Ludwig [37, 39] and Trassl [40]). Their reactively evaporated AlO_x coatings (30 nm and 10 nm thick on 12 µm PET, boat evaporation, no plasma assistance) started to deteriorate between 1.0 and 1.5 % elongation, with the thinner coating enduring more elongation. However, they do not show how WVTR behaves with further elongation. The paper by Schiller et al. also suggests that plasma activation during reactive AlO_x deposition can improve the retention of moisture barrier on stretch, as no substantial moisture

barrier loss occurred up to 1.75 % (30 nm AlO_x) and 2.00 % elongation (10 nm AlO_x). This improved flexibility is of advantage for conversion of the coated film [34].

Further data on the barrier behaviour upon stretching is published by Felts [303] for 60 nm thick AlO_x layers on 13 µm PET (reactive evaporation, no information whether boat or electron beam). He found the onset of oxygen barrier failure to occur between 2 to 3 % elongation, with the OTR rising from less than 10 cm³/(m² d) to more than 20 cm³/(m² d) for an elongation above 4 %. Komada and co-workers [306] discuss the barrier retention on stretch behaviour of evaporated AlO_x on 12 µm PET (no further information on deposition process or coating thickness provided) and indicate that beyond 3 % the OTR rises rapidly. Also these two publications compare well with the behaviour found here for AlO_x coated PET.

Data for reactively evaporated AlO_x on 12 µm PET (25 nm thick, presumably electron beam evaporation) by the Toyobo Research Institute in Japan [307-309] shows that the OTR rises marginally up to 2 % elongation, but reaches approximately 20 cm³/(m² d) for 3 % and then rises severely. In graphs published by Langowski [310] for AlO_x coated PET (industrial, reactive evaporation onto 12 µm PET, no further information provided), the gas barrier has already deteriorated for an elongation of 2 %; however, the stretch resistance is improved by lamination. Hence, the latter two publications show behaviour that is inferior compared to the results found in this thesis. Further results for the barrier retention on stretch behaviour of AlO_x coated PET are reported by Smith at al. [311] and Lohwasser [312].

A vast amount of literature with regards to the change of barrier upon elongation is, also published for SiO_x coatings on PET [146, 147, 303, 306, 311, 313, 314].

In contrast to PET, AlO_x coated BOPP C and also E already start losing their oxygen barrier at lower elongations. In the case of BOPP C (refer to *Figure 6-23*), this is between 1.5 and 2.0 % elongation when the OTR rises from values around 30 cm³/(m² d) to more than 100 cm³/(m² d), although there is already a marginal rise from approximately 22 to 25 cm³/(m² d) to a value of 30 cm³/(m² d) for 1.5 % elongation. This is slightly different for BOPP E (see *Figure 6-24*). Here, OTR gradually increases from an initial mean value of 50 cm³/(m² d) at 0 % elongation to 86 cm³/(m² d) for 2 % elongation. At 3 % elongation, the average OTR has gone beyond 150 cm³/(m² d) and for even higher elongations appears more similar to the oxygen barrier of uncoated BOPP E (refer to *Table 6-1*). For completeness, *Figure 6-23* and *Figure 6-24* also show the WVTR values for the AlO_x coated BOPP films. Nonetheless, as the film did not provide significant moisture barrier improvement

(investigations carried out before long-term ageing), the WVTR was not affected by the elongation and values remain largely unaffected (only fluctuations visible).

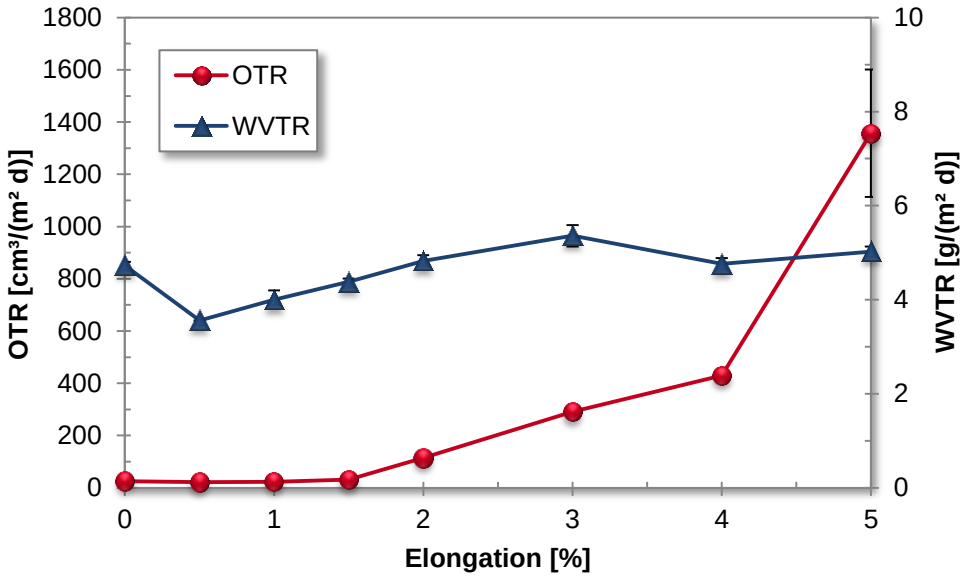

Figure 6-23: Change of barrier properties upon elongation of AlO_x coated BOPP C

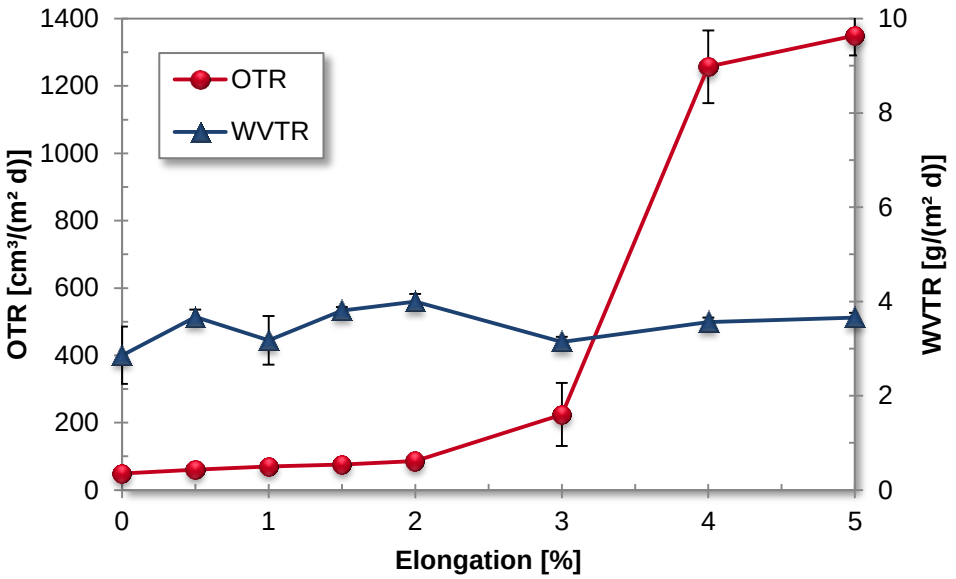

Figure 6-24: Change of barrier properties upon elongation of AlO_x coated BOPP E

Interestingly, there are few published studies on the barrier retention on elongation behaviour for AlO_x coated BOPP, compared to PET. Langowski [310] shows the change of gas transmission rate properties, observed for different gases with stretching the film and reveals an initial gradual and then rapid increase starting from 1 % elongation onwards. Based on other publications by this research group (e.g. [77, 245]), it is assumed that the AlO_x barrier layers were deposited onto BOPP via electron beam evaporation of Al_2O_3. In a later publication from the same

research group by Bichler and co-workers [315], they show the oxygen barrier retention for a laminated AlO_x coated BOPP, which is improved, compared to the results for a non-laminated film shown in the previous publication.

In the case of BOPP F (see *Figure 6-25*), which represents a special BOPP film with a different polymer skin layer, the OTR deteriorates between 2 and 3 %, though it is already slightly increased at 2 % elongation (from below 1 cm³/(m² d) to a mean value of 1.3 cm³/(m² d)). The WVTR rises rapidly between 1.5 and 2 % elongation, from values below 1 g/(m² d) to values similar to that of the uncoated film (see *Table 6-1*).

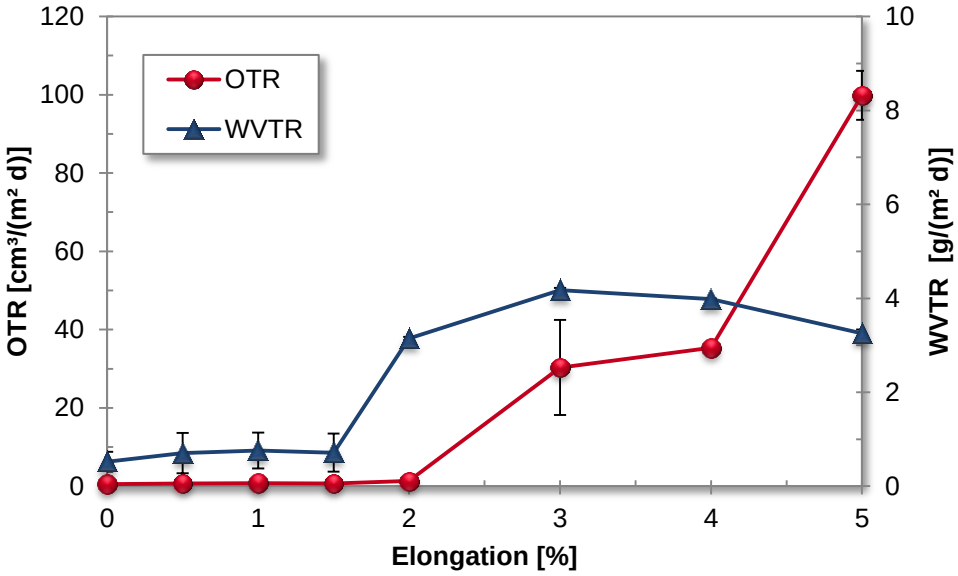

Figure 6-25: Change of barrier properties upon elongation of AlO_x coated BOPP F

In summary, for all films investigated, the trend in the OTR curve is quite similar, with a slow increase in the beginning followed by a rapid rise of the measured barrier values for higher elongations. In contrast to that, WVTR of AlO_x coated films (i.e. PET and BOPP F) reveals less stretch resistance and, consequently, increases more rapidly at a lower level of elongation. It is, furthermore, noticeable from the results presented here, as well as from the literature cited, that the individual behaviour strongly depends on the substrate and presumably also the deposition technique and coating thickness. Here, it should also be mentioned that all samples investigated in this thesis were measured for their barrier properties in a relaxed state and not, as originally done by Felts [303], in a stretched state (i.e. under the applied tension required for elongation), which may affect the measured transmission rate values. Nevertheless, the publications cited here generally do not state under which conditions the barrier tests were carried out.

Another central observation is the behaviour of OTR during barrier measurement of the stretched film samples (predominately BOPP C and E) for elongations just before a significant increase of OTR (e.g. for BOPP E around 1.5 to 2 %). Here, it is noticeable that the OTR constantly drops during barrier measurement and, finally, gradually levels off, sometimes after test times of more than 50 hours. This behaviour is not observed for the non-stretched samples, which were aged at the time of the investigation (for more information on the behaviour of aged and non-aged samples during OTR measurement, refer to Chapter 6.2.1.2). It is consequently assumed that the oxygen barrier at low elongation can be improved during barrier measurement, due to the exposure to 50 % RH. As discussed in more detail in Section 6.2.1.2, a swelling process is proposed take place, which may lead to the cracks generated being partially closed up. However, during stretching to very high levels of elongation, the cracks remain open to such an extent that even swelling of the AlO_x cannot prevent the unhindered flow/permeation of oxygen through these cracks. The partial recovery of the oxygen barrier properties of stretched/damaged AlO_x coated films (laminated and non-laminated) by exposure to high RH was also reported by Kelly [3], who attributed the improvement to a swelling/hydration of the AlO_x and hence narrowing of the cracks. He also states that water barrier could not be recovered significantly.

It is, furthermore, also important to look at the tensile properties and elastic/plastic deformation of the polymer substrate used. Therefore, force versus elongation (in machine direction) curves were determined for the four polymer films used and are shown in *Figure 6-26*. The force applied was normalised to a 1000 mm film width.

As can be seen, PET is the most rigid substrate and exhibits a transition from elastic (linear correlation between force and elongation according to Hooke's Law) to plastic deformation between 1.0 and 1.5 % elongation, which is when WVTR of AlO_x coated PET starts to deteriorate (see *Figure 6-22*). For the BOPP films, the transition can be found at a lower elongation of approximately 0.5 %. In the case of BOPP F, this is lower than the onset of water barrier deterioration (between 1.5 and 2 %, see *Figure 6-25*). However, this film is coextruded with a different polymer skin layer and this skin layer may have different tensile properties, compared to the main body (polypropylene) of the film. Due to the low thickness of the skin layer, the overall tensile properties determined and shown in *Figure 6-26* are likely to be dominated by the polypropylene part of the film structure. Within an elongation range of 0 % to 1 % (i.e. approximately up to their elastic limits), BOPP E, BOPP F and PET behave nearly identically. In contrast to BOPP E and F, BOPP C requires significantly lower forces in order to obtain the same elongations.

As the samples are measured for their barrier properties after stretching, i.e. in a relaxed state, the elastic limit of the films is likely to be of importance. This point can be located beyond the linear range of the force versus elongation curve and is characterised by the fact that after the force is released, no permanent elongation remains [316]. This suggests that the higher the elastic limit and the more of the deformation can be recovered, the less the barrier (of the coated film, predominantly oxygen barrier) will be affected when the film is relaxed. As PET withstands a higher strain before plastic deformation sets in, the onset of barrier deterioration (see oxygen barrier) will be at a higher elongation level, compared to the AlO_x coated standard BOPP films, which exhibit the transition from elastic to plastic deformation at a lower elongation. This means that due to the polymer 'springing back' into its original shape, cracks and defects, created in the AlO_x layer by the stretching procedure, may be closed up again (if the coating has not detached from the substrate, i.e. buckled). It is consequently assumed that there is a correlation between elastic limit and the onset of barrier deterioration, which however will also be dependent on the permeation mechanism of the substances of interest (e.g. macro-defect dominated permeation for oxygen; additional permeation mechanisms through microscopic defects assumed for moisture, see Chapter 4.6.2).

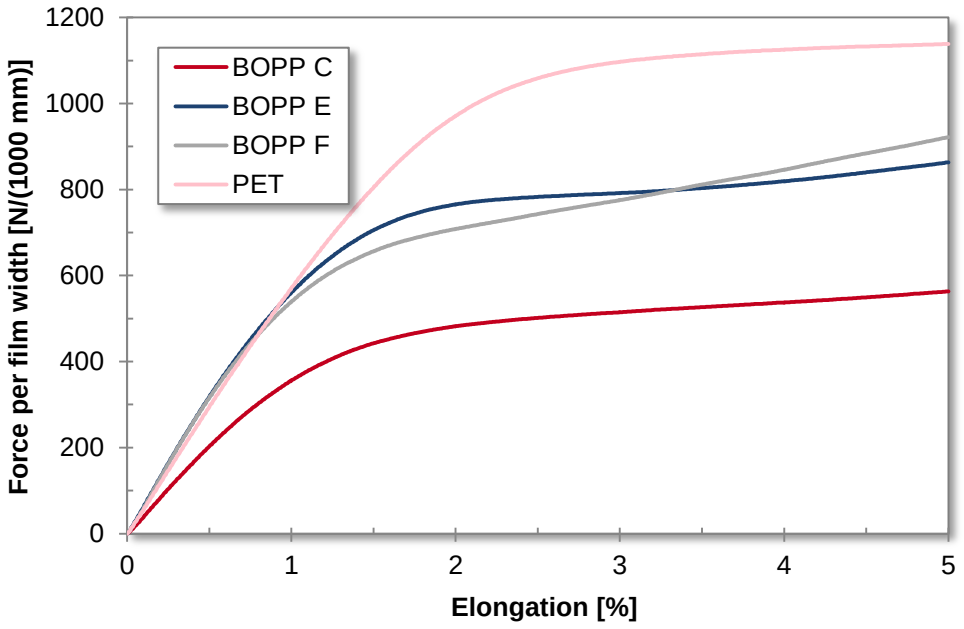

Figure 6-26: Force versus elongation curves for polymer substrates investigated

Finally, samples of AlO_x coated BOPP E were investigated after stretching in machine direction using SEM analysis. SEM images for 0, 3, 4 and 5 % elongation are shown in *Figure 6-27*. Up to an elongation of 3 %, no cracks were visible in the SEM images, whilst for 4 and 5 % elongation cracks propagating perpendicular to

the loading direction, as well as buckling of the coating (transverse to the cracks), can be detected. Nevertheless, the perpendicular cracks are difficult to make out. The buckles present areas, where the coating presumably has cracked and delaminated from the substrate, similar as observed during the fragmentation test [317, 318]. Also Kelly [3] obtained similar results for AlO_x coated PET. He states that transverse cracks were visible for elongations between 3 to 5 % and additional longitudinal cracks appeared for higher elongations. Consequently, he argues that for elongations below the visible onset of cracking, additional changes, which cannot be imaged using SEM analysis, may take place (such as delamination of the oxide layer from the substrate) and affect the barrier performance of the AlO_x coated and stretched film. For AlO_x coated BOPP E (*Figure 6-27*), there is a further drastic increase in OTR, from an average value of 225 $cm^3/(m^2\ d)$ at 3 % elongation to 1257 $cm^3/(m^2\ d)$ at 4 % elongation. However, for elongations of 2 % and lower, the mean OTR is less than 100 $cm^3/(m^2\ d)$ (also see *Figure 6-24*). Consequently, the sudden rise of OTR is in agreement with cracks and coating buckling appearing between 3 and 4 % elongation.

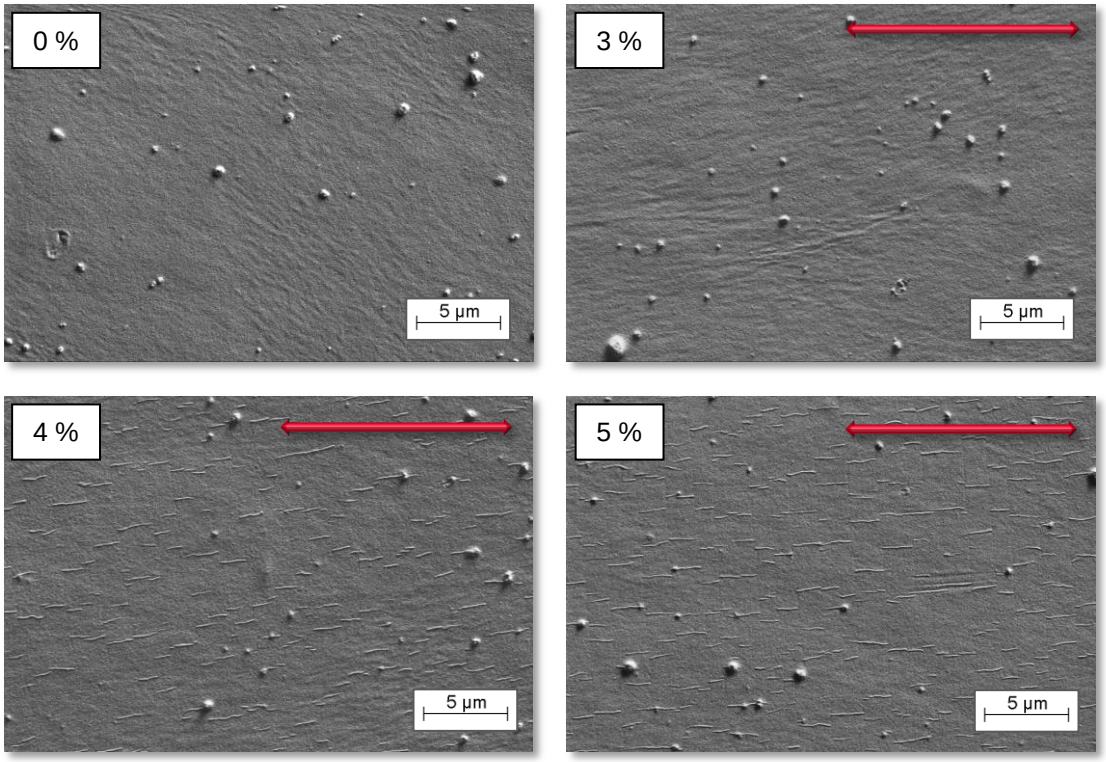

Figure 6-27: SEM images of AlO_x coated BOPP E after stretching/elongation in machine direction (horizontal as indicated by arrows); images taken in relaxed state; top left: 0 %; top right: 3 %; bottom left: 4 %; bottom right: 5 %

Also Czeremuszkin [146] observed no cracks for SiO_x (70 nm) coated PET for elongations up to 3 % (which is in agreement with the investigations presented

here), but only detected an increased number density of defects. For elongations of 4 % and onwards, cracks running transverse to the stretching direction emerged in increasing numbers. He, furthermore, found that the stretching procedure initiates cracks at existing defects and stress concentration sites, such as antiblock particles. Leterrier and co-workers [319] also state that the very first cracks are formed at existing coating defects sites.

When investigating the stretched samples via SEM, a relation between barrier retention upon stretching and the fragmentation test, which is used to characterise the adhesion of coatings, can be established. During the fragmentation test, the coated film is stretched uniaxially, whilst the damage to the coating (i.e. crack formation) is investigated as a function of the applied strain/elongation. Important parameters determined include, amongst others, the crack onset strain (i.e. elongation when cracks are visible) and saturation crack density. Here, it has also been found that antiblock additives reduce the crack onset of strain, i.e. cracks appear for lower elongations, as well as cohesive strength of the coating [234, 235]. Leterrier and co-workers [320, 321] have additionally shown that the crack onset strain depends on the coating thickness and decreases for thicker coatings. Furthermore, in their investigations for 20 nm thick SiO_x coatings on PET and PE, the crack onset strain appeared independent of the substrate [320]. Since in this study the AlO_x layer is only 10 nm thin (refer to Chapter 6.2.5), this low coating thickness may be the reason that no cracks are visible for lower strains/elongations.

6.2.1.6 Heat treatment of AlO_x coated films for barrier improvement

On the basis of the following:

- A patent [296] describing the positive effects of a so-called annealing treatment on the barrier properties of vapour deposited inorganic oxide barrier layers (such as SiO_x or AlO_x) on polymer films;
- The good barrier results obtained when AlO_x coating a shrink BOPP film (see Chapter 6.2.1.1).

A heat treatment was carried out for selected samples of AlO_x coated BOPP films (BOPP B, BOPP D and BOPP E). The temperature range explored in the patent mentioned previously was 30 to 150 °C. For the investigation conducted for this thesis, temperatures of 55 °C and 75 °C were selected, since these already resulted in considerable barrier improvement (depending on the annealing time) for the SiO_x and AlO_x coated polymer films investigated in reference [296] Furthermore, it was hoped to avoid possible heat damage (although the patent does not mention any damage at higher temperatures). For this study, the samples selected (see above) were incubated in a Carbolite oven (in air) for periods of one and two weeks, respectively, and subsequently the barrier properties were determined. Results are summarised in *Table 6-12* (BOPP B), *Table 6-13* (BOPP D) and *Table 6-14* (BOPP E).

Table 6-12: Barrier properties (OTR and WVTR) of AlO_x coated BOPP B following different heat treatments

Temperature	Time	OTR		WVTR	
°C	days	cm³/(m² d)	BIF	g/(m² d)	BIF
-	*0*	*80.2 ± 3.9*	-	*6.16 ± 0.07*	-
55	7	61.0 ± 3.6	1.3	5.75 ± 0.16	1.1
	14	68.4 ± 2.3	1.2	5.84 ± 0.44	1.1
75	7	281 ± 52	-	5.90 ± 0.01	1.0
	14	308 ± 85	-	5.79 ± 0.18	1.1

As can be seen, a broad range of results was obtained, with no clear consistency of the heat treatments for the different films investigated. Heat treatment at 55 °C, at both incubation periods, slightly enhanced the OTR of BOPP B (see *Table 6-12*), whilst WVTR was unaffected. In contrast to the latter, treatment at 75 °C appears to have damaged the AlO_x coated BOPP B, as a drastic deterioration in OTR was

observed, whilst WVTR was unaffected, as was the case previously. That no barrier deterioration is seen in the latter case (i.e. 75 °C) for WVTR is due to the fact that WVTR was only marginally enhanced from the plain film WVTR by the application of the AlO_x barrier layer.

Table 6-13: Barrier properties (OTR and WVTR) of AlO_x coated BOPP D following different heat treatments

Temperature	Time	OTR		WVTR	
°C	days	cm³/(m² d)	BIF	g/(m² d)	BIF
-	*0*	*77.1 ± 9.7*	-	*1.47 ± 0.09*	-
55	7	79.7 ± 14.9	1.0	0.76 ± 0.09	1.9
	14	71.4 ± 16.8	1.1	0.89 ± 0.01	1.7
75	7	76.4 ± 9.2	1.0	0.89 ± 0.06	1.7
	14	75.6 ± 9.5	1.0	0.61 ± 0.17	2.4

For BOPP D (see *Table 6-13*), the outcome is different to BOPP B. In this case, OTR is neither improved or impaired by the two heat treatments (although there are some fluctuations), whilst WVTR is enhanced for all treatment conditions. It has to be noted, though, that the WVTR prior to any heat treatment was already improved (due to ageing), compared to the values measured originally for this film (a value 2.41 ± 0.58 g/(m² d) was previously obtained, see *Table 6-10*).

Table 6-14: Barrier properties (OTR and WVTR) of AlO_x coated BOPP E following different heat treatments

Temperature	Time	OTR		WVTR	
°C	days	cm³/(m² d)	BIF	g/(m² d)	BIF
-	*0*	*48.9 ± 6.8*	-	*1.98 ± 0.74*	-
55	7	46.8 ± 0.1	1.0	1.80 ± 0.15	1.1
	14	53.0 ± 0.3	-	1.71 ± 0.04	1.2
75	7	81.6 ± 4.0	-	1.88 ± 0.31	1.1
	14	96.4 ± 6.3	-	2.39 ± 0.11	-

Finally, the heat treatment results for BOPP E (see *Table 6-14*) are more similar to BOPP B, although this film is a shrink BOPP and it was expected to show more similarities to BOPP D, which also exhibited enhanced shrink properties (refer to Section 6.1.4). The heat treatment at 55 °C left the OTR effectively unchanged

(based on the standard deviation obtained for the non-heat-treated film, the changes seen for the mean OTR are not rated as significant), whilst after the treatment at 75 °C, the OTR is increased. This deterioration in barrier is enhanced for the longer treatment/incubation time at 75 °C. Also for BOPP E, the WVTR at the time of this investigation had already improved due to the ageing process from its original value of 2.86 ± 0.61 g/(m² d) (refer to *Table 6-10*) to 1.98 ± 0.74 g/(m² d). The 55 °C treatment did not induce any significant improvement in WVTR, although the standard deviations are reduced. After incubation at 75 °C, WVTR was unaffected by the one-week-long treatment, but deteriorated after two weeks.

According to reference [296], the barrier improvement obtained by the heat/annealing treatment is caused by the shrinkage of the polymer substrate film or its surface, which induces a densification of the coating, as well as the closing of pores in the coating, and hence an improvement of oxygen and water vapour barrier properties. In this patent, a variety of AlO_x and SiO_x coatings (ranging from 15 to 30 nm in thickness) were deposited onto 12 µm PET and 15 µm nylon substrates, using coating techniques such as PECVD, induction heating and reactive electron beam evaporation. For the heat treatment, a wide temperature and time range (30 to 150 °C, 1 to 120 hours) was investigated and an improvement of WVTR and OTR was found in all cases, which generally increased for higher temperatures and longer treatment times. No barrier deterioration due to the heat treatment and possible heat damage are reported. However, in the investigation presented here, only some of the treatments resulted in a (rather small) barrier improvement and, furthermore, this was strongly dependent on the BOPP substrate. A possible reason for these findings and also the observed barrier deterioration upon heat treatment may be the different polymer substrate used in this project. PET and nylon, with a melting point/range of 265 °C and 175 to 352 °C (depending on type of nylon; for the most common nylon grades: 220 to 301 °C) [55], respectively, are more heat resistant films, compared to BOPP (melting point of crystalline PP: 186 °C [55]). The lower heat resistance of BOPP could be a possible reason for the observed barrier degradation, presumably induced by heat damage to the substrate film. Furthermore, the shrinkage results presented in Chapter 6.1.4 show that all BOPP films shrink a lot more than the PET reference film (in MD as well as TD) and BOPP B additionally exhibits a pronounced expansion in TD for temperatures lower than 120 °C (see Chapter 6.1.4, *Figure 6-12*). Consequently, the expansion of BOPP B (and hence tensile damage induced to the AlO_x layer) may be the origin of the oxygen barrier deterioration for the heat treatment at 75 °C observed for AlO_x coated BOPP B. On the other hand, the higher shrinkage of the BOPP films, in contrast to the PET film, may also be a reason for barrier deterioration, as it could

possibly result in compressive forces too high for the AlO_x layer. Additionally, the RH during heat treatment may play a role. Although the patent [296] states that the RH does not need to be controlled, a higher humidity may be beneficial for barrier enhancement induced by the heat treatment (see argumentation on ageing, Chapter 6.2.1.2).

Henry and co-workers [322] report on heat induced damage of SiO_x coated 12 µm PET films (electron beam evaporation) after a heat treatment of 14 hours at 60 °C. This treatment resulted in a deterioration of gas barrier properties, which was attributed to thermally induced cracks/fractures in the SiO_x layer (determined via SEM and AFM analysis). Rochat et al. [286], who conducted annealing treatments of 12 µm PET coated with a 7 nm PECVD SiO_x barrier layer, state that the as-deposited and annealed samples exhibited equal oxygen barrier properties, i.e. no barrier deterioration was observed. Their annealing treatment consisted of a heating cycle from 25 °C to 150 °C and back at a heating rate of 10 °C/min and with a 10 minute holding step at 150 °C. For sputtered SiO_x barrier layers on PET, Iwamori and co-workers [323] found an improvement of OTR with annealing the samples at 120 °C for two hours in vacuum. Nevertheless, in this case the SiO_x oxygen content was decreased during annealing treatment and this change of stoichiometry may also entail the improved OTR.

In summary, one can notice that annealing/heat treatments of polymer films coated with inorganic barrier layers have been conducted by various research groups and a broad variety of results was reported. Whilst some state that the barrier properties could be enhanced, others found that the treatment induced no changes or even deteriorated the barrier performance.

Due to the drastic barrier deterioration observed for AlO_x coated BOPP B when heat treatment was carried out at 75 °C, the sample incubated for 14 days at this temperature was further examined using SEM analysis and representative images at two different magnification levels are depicted in *Figure 6-28*.

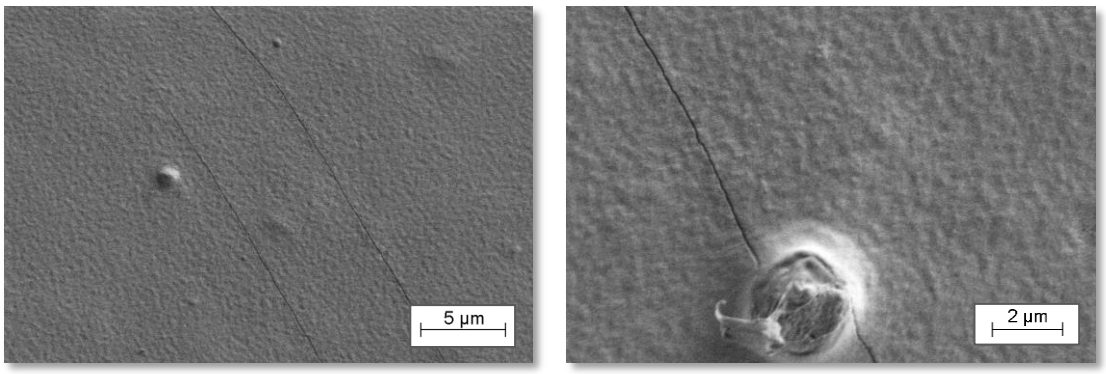

Figure 6-28: SEM images of AlO_x coated BOPP B after heat treatment at 75 °C for 14 days (two different magnification levels)

After the treatment, the AlO_x coated film exhibits distinct cracks in its coating (refer to *Figure 6-28*), which have previously not been found when AlO_x coated BOPP B was examined (no heat treatment, see Chapter 6.2.2.2, *Figure 6-29*). It is consequently argued that the heat treatment induced the formation of cracks in the AlO_x layer, probably due to a suspected expansion of BOPP B during heat treatment (see previous discussion in this chapter). No further samples, i.e. of AlO_x coated and heat treated BOPP D or E, were investigated.

6.2.2 Surface topography and roughness

After the characterisation of the barrier levels obtained with reactively evaporated AlO_x layers on BOPP, the coated films were investigated for their surface topography and roughness (analogous to the uncoated polymer films), starting from the relatively low magnification of optical microscopy, via scanning electron microscopy to atomic force microscopy.

6.2.2.1 Differential interference contrast optical microscopy

The samples of AlO_x coated BOPP and PET were initially analysed using DIC optical microscopy. However, at the magnification level provided by this technique, no differences could be detected between the coated and uncoated polymer films. This was to be expected, based on the AlO_x coating thickness, which is in the nanometre range (see Chapter 6.2.5), and, therefore, cannot alter the surface at this magnification level. Furthermore, also Jamieson and Windle [140], who analysed aluminium coated PET, report that the metal layer does not affect the surface structure, as seen at the magnification level of DIC optical microscopy. Consequently, for representative DIC light microscopy images and the corresponding discussion of surface characteristics, the reader is referred to Section 6.1.2.1.

6.2.2.2 Scanning electron microscopy

Similar to the investigation of the uncoated films, SEM analysis was carried out for the AlO_x coated polymer films and representative images are shown in *Figure 6-29*. Once again, no conductive coatings (e.g. gold coatings) were applied in order to avoid masking the surface details and altering the surface structure. Nevertheless, higher magnification SEM images, e.g. as depicted in *Figure 6-29*, could be obtained for the AlO_x coated films, in contrast to the uncoated films (see *Figure 6-6*), which is attributed to the ceramic AlO_x layer being less affected by the electron beam than the soft polymer.

In general, the AlO_x coatings revealed the same surface characteristics and also textures as found for the uncoated films. For example, the wavy and bumpy background structures were once again detected for AlO_x coated BOPP A, B and E (not visible in the specific scan shown in *Figure 6-29* for BOPP A). Also the differences in the granular texture (coarse/fine) are noticeable in the SEM images. Furthermore, the observations regarding the individual antiblock particle sizes and distribution densities are analogous to the uncoated films. It is, consequently, argued that the thin AlO_x coating reproduces the underlying plain film surface

topography and does not alter the fine-scale surface structure. This aspect will be further explored, and discussed in relation to relevant literature, in Section 6.2.2.3, together with the AFM analysis of the coated polymer films.

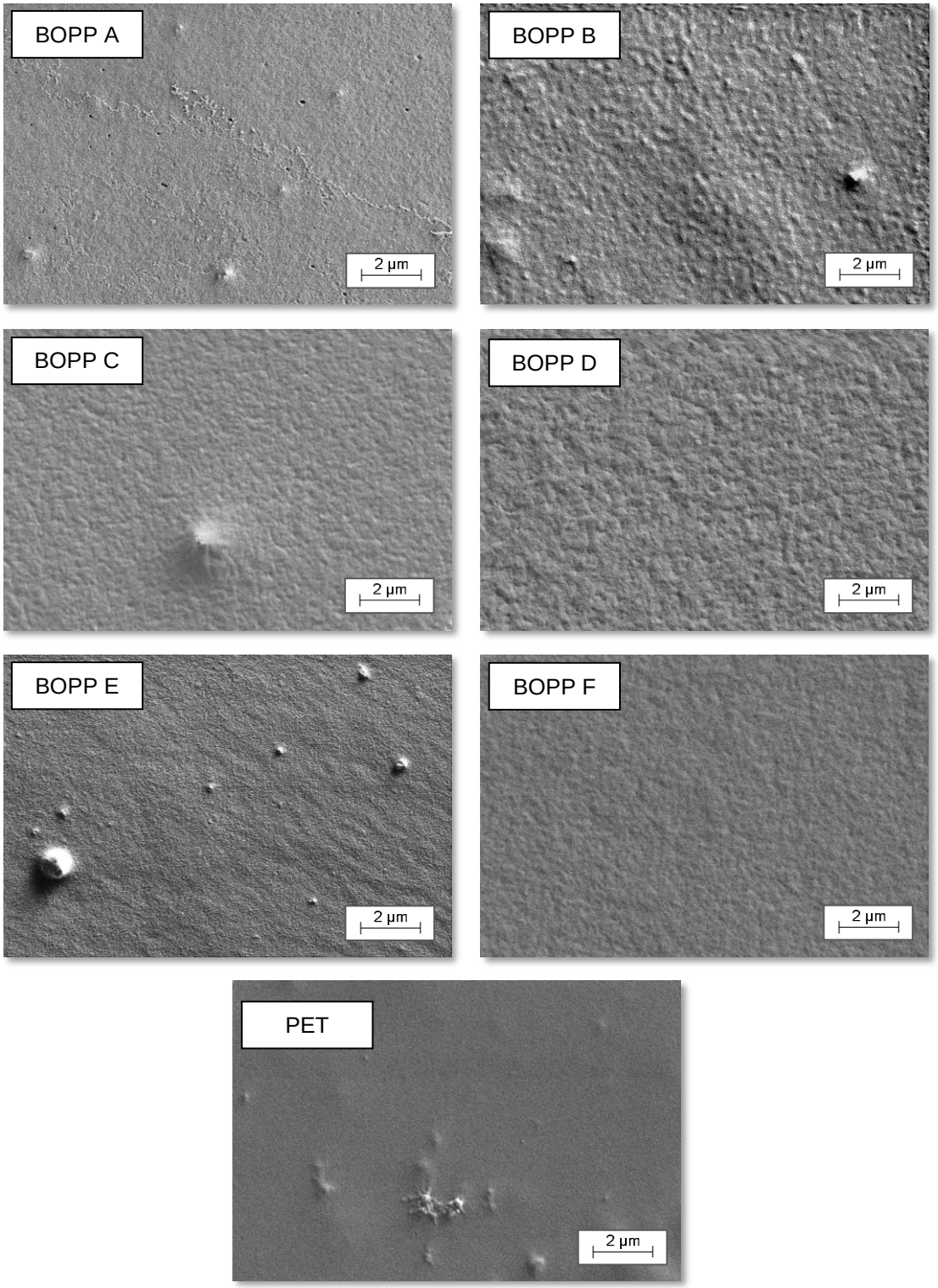

Figure 6-29: SEM images of AlO_x coated polymer films; top left: BOPP A; top right: BOPP B; second row left: BOPP C; second row right: BOPP D; third row left: BOPP E; third row right: BOPP F; bottom: PET

Schiller and co-workers [29] show SEM images (topography and cross fracture) of very thick (approximately 3 µm) AlO_x layers, deposited onto PET via reactive electron beam evaporation with and without plasma activation. For the latter sample, the topography is crazed, appears 'cauliflower-like' and a columnar structure is visible at the fractured surface, whilst the former sample (with plasma activation) is smoother and significantly denser. Nevertheless, their results cannot really be compared to the surface topographies illustrated here in *Figure 6-29*, due to the vast differences in coating thickness, which will inevitably have an effect on the coating surface structures.

In the SEM investigation of the AlO_x coated films, an important and critical observation was once again made for BOPP A. Plain BOPP A already revealed crater-shaped defects in the SEM and AFM investigations (see Sections 6.1.2.3 and 6.1.2.4, respectively) and, when investigating the AlO_x coated film, it appeared that these defects were reproduced in the AlO_x coating. From the impression given by the SEM images, the defects visible on the AlO_x coated film are actually likely to be holes in the coating, with dimensions in the same range as the craters found on plain BOPP A (see Chapter 6.1.2.4 and Appendix A2 for more information on the plain film surface defects). It is important to discuss here the likelihood of the defects seen in the SEM analysis of AlO_x coated BOPP A (*Figure 6-29*, top left, and higher resolution image, see *Figure 6-30*) being true holes in the coating. The SEM investigation shows the defects as very dark/black and distinct spots, which means that almost no secondary electrons are produced by these features and, therefore, suggests that these features are deep holes. Judging from the AFM analysis of the plain film surface and the cross-sections through the crater-shaped defects (refer to Appendix A2), it is likely that the 'bottom' of the craters will be coated with the AlO_x barrier layer. Nevertheless, the shallow side angles of the craters, as seen in the AFM cross-sections, are presumably an AFM imaging artefact and it is, therefore, concluded that these sides are a lot steeper and not necessarily coated with the barrier layer (at least to the full thickness). Hence, holes are created. Furthermore, the barrier data obtained for AlO_x coated and metallised BOPP A (see Chapter 6.2.1.1) reinforces the idea of true holes (i.e. permeation pathways) in the coating, as neither of them showed acceptable oxygen barrier performance. Even when the AlO_x thickness was increased, OTR could not be improved to less than 100 $cm^3/(m^2\ d)$ (see Section 6.2.1.4). The other films, by contrast, exhibited better oxygen barrier performance for the metallised and 'standard' AlO_x coated (standard stoichiometry and thickness, see Sections 6.2.3 and 6.2.5) films. Consequently, it is concluded that the presence of holes/defects in the barrier layer is the only possible explanation for the barrier performance of coated (AlO_x and aluminium) BOPP A,

since oxygen permeation, which is a macro-defect driven process (see Section 4.6.2), will be drastically affected and increased by these defects. As already discussed in Section 6.2.1.1, Rossi and Nulman [144], who investigated the effect of defects in a barrier layer on the overall permeation through the coated polymer, came to the principal conclusion that “many small holes in a barrier layer are much more effective in compromising the system barrier properties than a few large holes with the same total area”. This finding would be in line with the vast amount of defects found on AlO_x coated BOPP A and the low oxygen barrier properties achieved. Furthermore, Czeremuszkin and co-workers [146] indicated that a 13 µm thick PET film coated with a barrier layer can lose all its barrier properties, even though a surface coverage of more than 99 % is present. They calculated this for the presence of pinholes with a diameter of 200 nm, an average defect distance of 3.2 µm and a number density of 1.11×10^7 cm^{-2}, assuming the coating is impermeable, apart from the defects. The defects on AlO_x coated BOPP A and their dimensions, i.e. depth and diameter, were further analysed using AFM analysis. Similar to the crater-shaped defects in uncoated BOPP A, the defects are roughly 50 to several 100 nm in diameter and some tens of nanometres in depth. It can also be seen from *Figure 6-29* that the distance between the defects generally is a few µm. Consequently, it appears plausible that the OTR of AlO_x coated BOPP A is remarkably high.

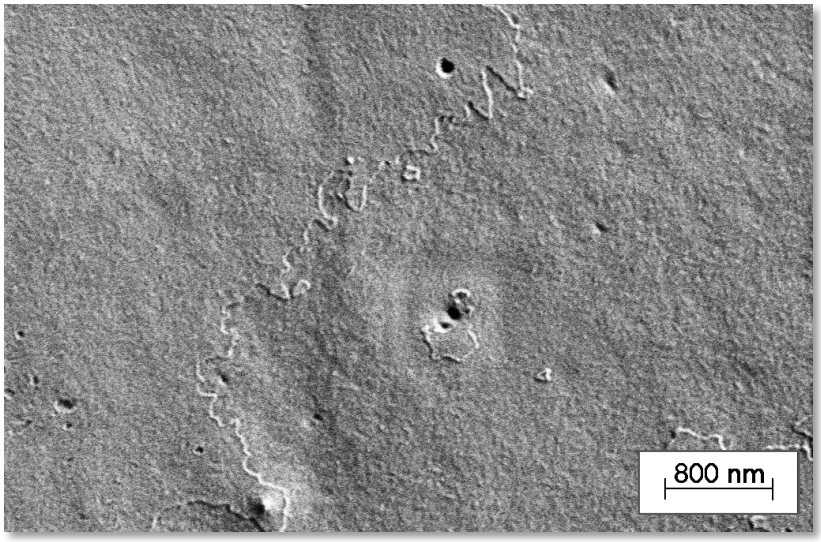

Figure 6-30: High-resolution SEM image of defects (and thickness variations) on AlO_x coated BOPP A (centre ‘square’ is damage due to focussing)

In addition to the defects, AlO_x (and also aluminium) coated BOPP A showed surface structures that appeared to be variations in coating thickness. This is clearly visible for the AlO_x coated film in *Figure 6-29* (image top left) and *Figure 6-30*. These

thickness irregularities, as well as the defects, could not be found on any other AlO_x coated film. Additionally, uncoated BOPP A did not show any surface texture or pattern similar to the thickness irregularities discovered for the AlO_x coated film. The growth/thickness variations give the impression of a liquid contamination on the plain film surface, which is not visible in the SEM images of the uncoated film, but has caused the AlO_x to grow in a different manner (e.g. less dense). Even though BOPP A is classified as a 'high purity film without additive migration', it will still contain the necessary stabilisers (antioxidants) and an acid scavenger. Antioxidants such as Irganox 1010 and Irgafos 168 are of lipophilic nature and can migrate to the film surface [324]. However, these antioxidants are essential and, therefore, will be present in all BOPP films. Acid scavengers can be based on metallic stearates, zeolite structures and other metallic salts [50]. Stearates are also used as slip and release agents in polymers and, therefore, intentionally migrate to the film surface [66, 325, 326]. In general, these low-molar-mass additives (slip/release additives) are undesirable in vacuum web coating processes since, due to their hydrophobic nature, they affect the wetting and adhesion of the depositing coating (metallisation) [92]. In order to find out whether migratory additives, such as stearates, have caused the growth patterns found on AlO_x coated BOPP A, the formulations for each layer (three-layer structure) of the supplied BOPP films are required. However, exact film formulations are extremely sensitive business proprietary information. In the case of BOPP C, XPS analysis of the coated film revealed the presence of calcium, which was attributed to the additive calcium stearate being used in the BOPP film formulation (see Chapter 6.2.4). However, as this film did not exhibit the thickness variations when AlO_x coated, it is concluded that the observed phenomenon cannot be caused by the use of calcium stearate as a film additive (acid scavenger). It is, therefore, not known what induced the growth/thickness irregularities found for AlO_x coated BOPP A.

The SEM analysis of the coated films was additionally used to investigate the effect of antiblock particles on the creation of visible defects in the barrier layer. To begin with, it should be repeated that PET, as well as BOPP E, showed a large number of antiblock particles of submicron size, although according to the antiblock count (see Chapter 6.1.2.2) BOPP E revealed substantially more antiblock particles than PET. It must, however, partially be acknowledged that on PET not all antiblock particles were necessarily captured by the antiblock counting technique. Due to the rough surface appearance and the high concentration of antiblock particles, one would have expected a lot of defects to be generated in the coating and hence impaired barrier performance of the AlO_x coated films. Nevertheless, despite the vast amount of antiblock particles present on these films, the barrier properties after AlO_x coating

were good, with the PET film revealing an average OTR and WVTR of less than 1 $cm^3/(m^2\ d)$ and 1 $g/(m^2\ d)$, respectively and BOPP E showing a mean OTR of less than 50 $cm^3/(m^2\ d)$ (for the measured OTR and WVTR values refer to *Table 6-10*, Chapter 6.2.1.1). If one would assume that the antiblock particles created uncoated areas, i.e. defects, the OTR would be expected to be a lot higher, based on Rossi and Nulman's [144] study discussed previously with regards to the permeation defects on AlO_x coated BOPP A. It is, consequently, assumed that antiblock particles do not necessarily create defects in the barrier layer, but can be over-coated and that good barrier performance can be obtained on films containing large numbers of antiblock particles. A possible explanation could be that most of the antiblock particles are initially over-coated by the barrier layer (if no shadowing effects take place) and defects are mainly created after deposition when the film is wound into a roll. Then, the barrier layer on top of the antiblock particles, which act as spacers between adjacent surfaces in the rolls of film [327], is in contact with the reverse side of the BOPP film (and possibly antiblock particles located on this side) and can be abraded at the point of contact. If both large antiblock particles of several microns and small, submicron antiblock particles are present, it can be expected that the points of contact will be predominantly on the larger antiblock particles. Consequently, coating damage and abrasion will preferentially occur at these particles, whilst the smaller ones will not create defects.

Some of these presumably abrasion-type defects generated by the presence of antiblock particles are shown in *Figure 6-31* for AlO_x coated and metallised BOPP C.

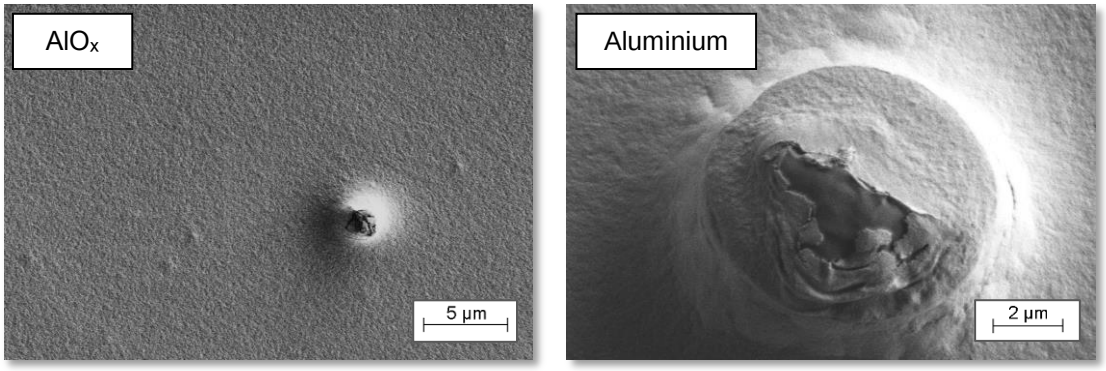

Figure 6-31: Antiblock particle generated defects in AlO_x coated BOPP C (left) and metallised BOPP C (right)

Several researchers have indicated that antiblock particles have an effect on the barrier levels obtained with inorganic barrier layers, such as aluminium and SiO_x. Mueller and co-workers [233] show barrier results for a metallised (2.1 to 2.5 OD) antiblock-free BOPP film and reveal an OTR of 1 $cm^3/(m^2\ d)$. This value is typically

only obtained when metallising PET and is by a factor of approximately 20 better than the best OTR results obtained here for metallised BOPP (see *Table 6-11*, Chapter 6.2.1.1). The good barrier performance of this film was attributed to the absence of antiblock particles and hence the smoother surface and largely reduced number of pinholes/defects. Rochat et al. [234] deposited 10 nm thick SiO_x coatings onto PET, with and without antiblock additives, and found a higher OTR when additives were present. Finally, also Fayet and co-workers [235] found that the OTR of 40 nm thick SiO_x coatings on PET could be improved with a reduced number of antiblock particles on the substrate film surface. This confirms that antiblock particles are of importance with respect to the oxygen barrier performance after coating. Especially the publication regarding metallised BOPP by Mueller et al. suggests that, when extremely low OTR values are to be obtained, antiblock particles in the BOPP substrate play a major role. For PET, it should again be mentioned that the antiblock particles appear more incorporated into the polymer film and, consequently, rather create mounds (see *Figure 6-29*), in contrast to BOPP, where the antiblock particles seem to 'lie' on the surface and detach from the surface easily. These mounds are assumed to be more easily coated without creating defects.

6.2.2.3 Atomic force microscopy

In order to confirm the SEM results and obtain additional information about the surface roughness of the coatings, AFM analysis was carried out. Representative AFM scans (5 x 5 µm²) for all films are shown in *Figure 6-32* and *Figure 6-33*. For comparison purposes, the AFM scan images of the uncoated BOPP films are also displayed.

As can be seen from *Figure 6-32* and *Figure 6-33*, in all cases the uncoated and AlO_x coated polymer look very similar and exhibit the same structure and surface characteristics. For the BOPP films, this is the previously discussed (see Chapters 6.1.2.3 and 6.1.2.4 for uncoated films and Chapter 6.2.2.2 for AlO_x coated films) granular texture with pronounced individual differences for the various films types and, additionally, the typical background structure. For example, the waviness and bumpiness can be observed in the AFM images for AlO_x coated, as well as uncoated, BOPP A, B and E. Consequently, the AFM analysis of the surface structure is in very good agreement with the SEM results and indicates that the thin AlO_x layer retains the underlying plain film surface topography and characteristics and, hence, is conformal to the substrate. For BOPP A, the AlO_x layer also reproduces the crater-shaped defects, which can be seen from *Figure 6-32*, top right image. Furthermore, the thickness variations, discussed in detail in the previous chapter, were also found during AFM analysis and will be further investigated later in this chapter, along with the dimensions of the defects in the AlO_x layer on BOPP A. The surface of PET, uncoated and AlO_x coated, appears smoother, compared to the 'standard' BOPP films. However, it can be noticed that small antiblock particles could hardly be avoided during AFM image acquisition on the PET film (which was also the case for BOPP E). The AFM images obtained for AlO_x coated PET appear similar in their structure to AFM images published by Henry and co-workers [157, 160] for sputtered and electron beam evaporated AlO_x layers on PET, but only if sections of comparable area are considered.

Some of the scans of AlO_x coated BOPP may seem to reveal slightly finer detail, compared to the plain film. This may be due to the fact that the soft polymer is more easily affected by the scanning motion than the hard AlO_x, or, as suggested by Affinito and co-workers [328, 329], due to the addition of grain boundaries and growth imperfections by the coating. However, with AFM analysis and interpretation of images one, in general, needs to be cautious (especially for small scan sizes), since the quality/state of the tip (i.e. tip radius) has a great impact on the quality of the scans, as well as the fine surface details imaged. Furthermore, additional or different 'textures' can be caused by tip contamination or an unsuitable (i.e. too

large) tip radius [330]. As discussed by Westra et al. [331], AFM images affected and convoluted by tip artefacts are not necessarily identified as they still reveal a granular texture, which is typical for a thin coating of columnar growth. For this thesis, however, a vast amount of different films (coated and non-coated) was investigated using different tips, as well as different AFM equipment, and reproducible images were obtained, which also agree with the SEM investigations. This leads us to the conclusion that, at the scan size shown, the AFM images represent the true surface of the investigated samples.

That a thin barrier layer can exhibit the same structure as the underlying substrate has also been found by Moosheimer [332, 333] for electron beam evaporated aluminium layers (60 nm) on BOPP homopolymer film (AFM analysis of 5 x 5 µm² areas). In a later publication [237], this was also confirmed for aluminium layers deposited onto a BOPP film with a copolymer skin layer, although the SiO_x coating did not reproduce the BOPP copolymer structure (here: 10 x 10 µm² areas investigated). No coating thicknesses were stated in the later publication, but based on previous work (e.g. [245, 332]) by this research group, an aluminium thickness of 60 nm and SiO_x thickness of 100 nm is assumed.

For 40 nm thin AlO_x layers electron beam evaporated onto BOPP homo- and copolymer films, the AFM analysis of 5 x 5 µm² areas by Moosheimer [332, 333] reveals that the coating does not replicate the typical homo- or copolymer surface texture, but is a lot smoother (RMS and R_a less than half the value of the uncoated film). This observation is in complete contrast to the findings of this thesis (see also roughness data in *Table 6-15*, which will be discussed later). However, Affinito and co-workers [329] found in their AFM investigations (10 x 10 µm²) that electron beam evaporated and sputtered AlO_x layers (both 20 nm thick) on PET exhibit a surface topography nearly identical to the one of the underlying PET substrate. They, furthermore, state that additional SEM investigations [328] indicated that the coating does not only replicate the substrate surface topography, but also adds grain boundaries and growth imperfections. Deng et al. [130] investigated electron beam evaporated AlO_x layers of 1 nm and 10 nm thickness on PET and BOPP, using 1 x 1 µm² AFM scans. In the case of PET, they found that the 1 nm and also 10 nm AlO_x layer revealed a different surface topography to the uncoated PET, which consisted of fine particles, although the roughness of all three samples was identical within experimental error. For BOPP, by contrast, it was difficult to identify differences between the coated and non-coated film as the AFM images appeared very similar; however, the 10 nm thin AlO_x layer exhibited a significantly larger roughness, compared to the BOPP substrate and the 1 nm thin coating.

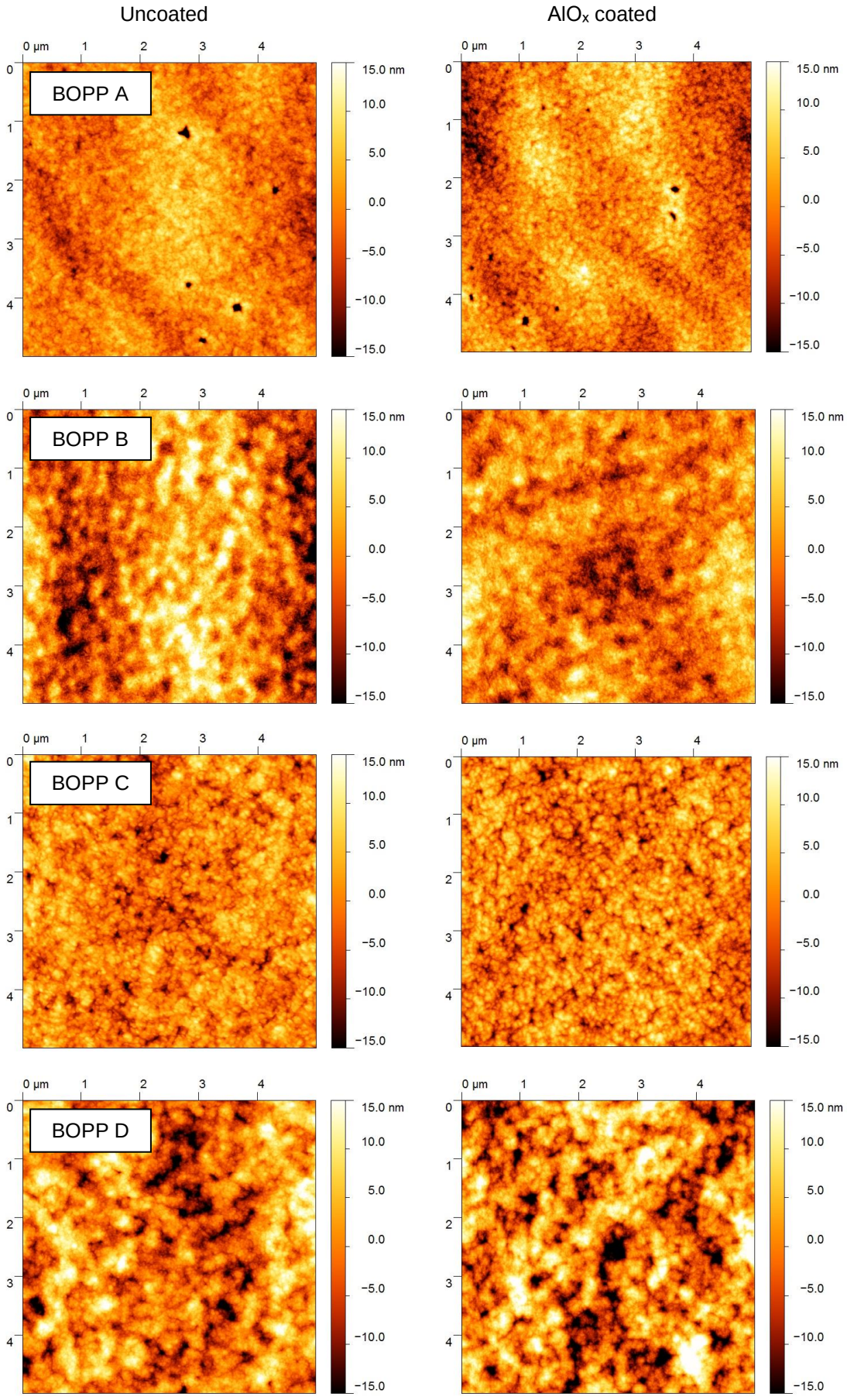

Figure 6-32: 5 x 5 µm² AFM scans of uncoated (left column) and AlO_x coated (right column) polymer films; from top to bottom: BOPP A, BOPP B, BOPP C and BOPP D

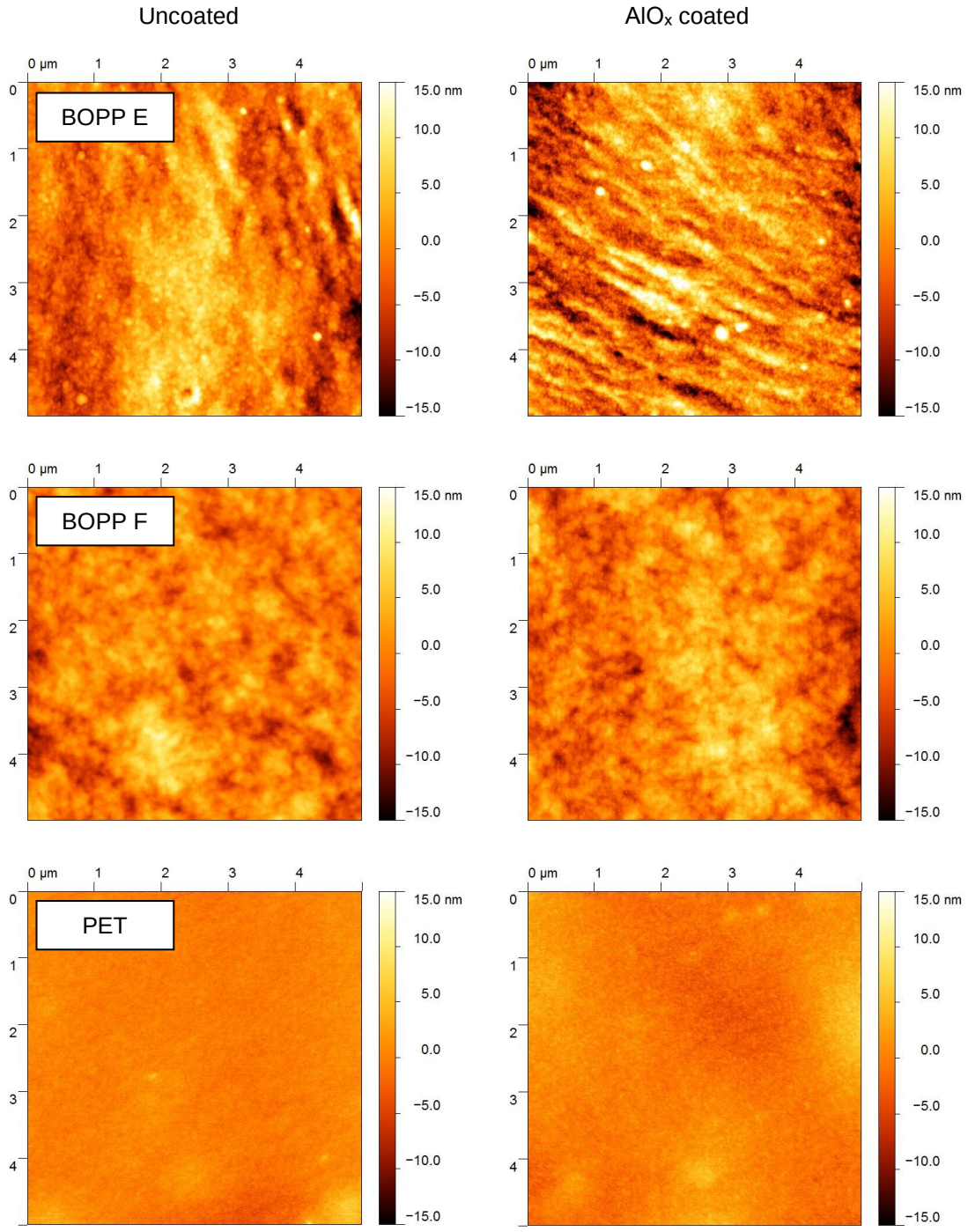

Figure 6-33: 5 x 5 µm² AFM scans of uncoated (left column) and AlO_x coated (right column) polymer films; from top to bottom: BOPP E, BOPP F and PET

As can be seen from the referenced literature, the findings (i.e. conformal coatings or not) of the various researchers differ and appear to depend on the substrate material, the type of coating, the coating thickness and presumably also the AFM scan size selected for the investigation. The use of a smaller AFM scan size, whilst still obtaining good resolution images, may also lead to differences being detected between the coated and non-coated substrate in the case of the samples produced

and analysed in the course of this work. This investigation was, nevertheless, not carried out.

Figure 6-34 depicts a 10 x 10 µm² scan acquired on AlO_x coated BOPP A. This AFM image clearly reveals that the previously described coating/growth irregularities are true variations is coating thickness, as can be detected from the change in colouration along the line running nearly vertically through *Figure 6-34* (see red arrow). Due to the surface texture, however, the thickness change is only visible at the step edge (a change of approximately 10 nm is measurable in some AFM cross-sections) and, otherwise, is concealed by the surface morphology. A thickness change of 10 nm is quite remarkable, considering that the thickness, as determined via TEM, is approximately 10 nm (see Chapter 6.2.5). It is, nevertheless, still assumed that the AlO_x coating is present at both sides of the 'step-edge' and that the thickness irregularities are not caused by large uncoated areas (although at the 'step edge' itself, uncoated areas may exist). The defects were found to have similar dimensions to the craters in the uncoated film (refer to Chapter 6.1.2.4) with diameters between 50 nm and several 100 nm and some tens of nanometres in depth.

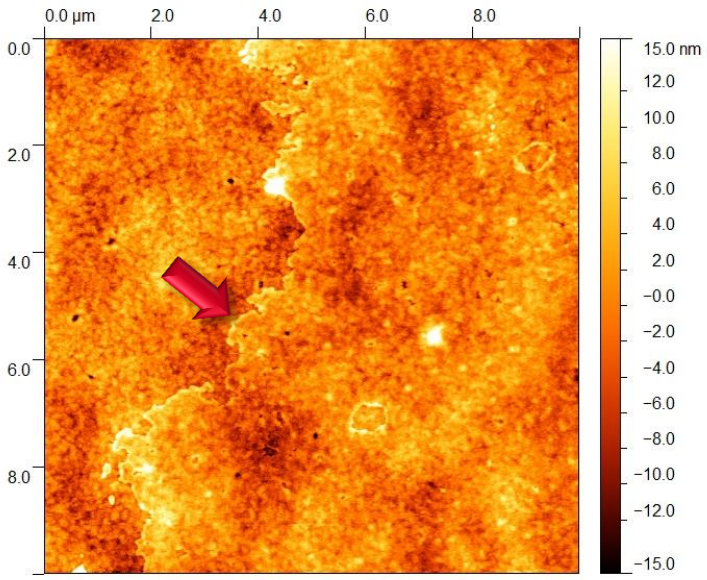

Figure 6-34: 10 x 10 µm² AFM scan of AlO_x coated BOPP A showing defects and thickness irregularities

The AFM analysis was additionally used to assess the surface roughness of the coatings. Therefore, several scans per film type (in general at least five) were acquired on different areas to obtain the mean values for RMS and roughness average. If possible, antiblock particles were avoided in the scanned areas. The results of this analysis are summarised in *Table 6-15*.

Table 6-15: Surface roughness in terms of RMS and R_a values (mean value and standard deviation) of uncoated and AlO_x coated polymer films, determined from 5 x 5 µm² AFM scans

Film	Description	RMS	R_a
		nm	nm
BOPP A	Uncoated	4.1 ± 0.7	3.3 ± 0.5
	No plasma	4.7 ± 0.8	3.7 ± 0.6
	Pre	4.1 ± 0.6	3.3 ± 0.5
	Pre + post	4.1 ± 0.6	3.2 ± 0.5
BOPP B	Uncoated	6.1 ± 1.9	4.8 ± 1.6
	No plasma	6.3 ± 1.2	5.0 ± 0.9
	Pre	5.8 ± 0.9	4.6 ± 0.7
	Pre + post	6.0 ± 0.7	4.8 ± 0.6
BOPP C	Uncoated	4.1 ± 0.3	3.3 ± 0.2
	Pre	4.6 ± 0.2	3.6 ± 0.2
	Pre + post	4.3 ± 0.3	3.4 ± 0.2
BOPP D	Uncoated	6.2 ± 0.5	4.9 ± 0.4
	Pre	7.7 ± 0.8	6.1 ± 0.7
BOPP E	Uncoated	4.4 ± 0.7	3.5 ± 0.5
	Pre	4.7 ± 0.4	3.7 ± 0.3
BOPP F	Uncoated	3.0 ± 0.3	2.3 ± 0.3
	No plasma	3.3 ± 0.1	2.6 ± 0.1
	Pre	3.2 ± 0.3	2.5 ± 0.3
	Pre + post	3.0 ± 0.3	2.4 ±0.3
PET	Uncoated	1.7 ± 0.3	1.3 ± 0.2
	Pre + post	1.8 ± 0.3	1.4 ± 0.3

On all the film samples, with the exception of BOPP D, the AlO_x coating has very similar or sensibly identical roughness parameters (within experimental error) to the uncoated substrate (*Table 6-15*). BOPP D was the only sample on which the AlO_x layer was considerably rougher than the uncoated substrate, although in the AFM images the structure of the uncoated and coated film appeared very similar. In the case of BOPP D, this may be due to the film's shrink properties (see Chapter 6.1.4), which are argued to play a major role for the barrier properties after AlO_x coating (refer to Chapter 6.2.1.1). It is assumed that the shrinkage of BOPP D during and also after deposition (when the film cools down) results in a change of the coated film surface, hence inducing the increased roughness. Also BOPP E was a shrink

BOPP and exhibited good oxygen barrier properties after AlO_x coating (see Chapter 6.2.1.1). Nevertheless, the surface roughness of the AlO_x coated film is not significantly larger than the roughness of the uncoated substrate, which may be caused by the wavy background texture concealing the shrinkage effect on the measured roughness data.

Finally, it should be stated that the roughness of the coated BOPP films appeared to be dynamic and exhibited a change with time, presumably due to the ageing process of the coating (swelling of AlO_x and creep of substrate, refer to Section 6.2.1.2). The topographical appearance in the AFM images, though, remained merely unaffected by the age. When the roughness of AlO_x coated BOPP C was re-assessed more than one and a half years later, the RMS of the pre-treated sample was substantially increased from 4.6 ± 0.2 nm to 5.7 ± 0.6 nm and the RMS of the pre- and post-treated sample from 4.3 ± 0.3 nm to 5.0 ± 0.3 nm.

Deng et al. [130], who used electron beam evaporation to deposit 1 nm and 10 nm AlO_x layers onto PET and BOPP, found the roughness of the substrate and the coatings was the same only in the case of PET. For polypropylene, the 10 nm AlO_x layer showed increased roughness, relative to the plain film (the thickness of the coatings investigated in this thesis is identical, see Section 6.2.5; however, Deng et al. [130] used a smaller scanned area (1 x 1 μm^2)). Therefore, they hypothesised an island growth mechanism for the AlO_x layer on polypropylene and a layer-by-layer growth mechanism on PET, after the initial stage of nucleation. The work presented here, however, suggests that there is no difference for BOPP, compared to PET, as for each BOPP film type (apart from BOPP D), the plain and AlO_x coated film showed similar/identical surface roughness. Moreover, also Henry et al. [232] discovered that sputtered AlO_x layers (5 to 17 nm thick) on PET exhibit similar roughness to the uncoated PET substrate. In later publications, Henry and co-workers [160, 290] investigated a range of AlO_x, AlO_xN_y and SiO_x coatings on PET, which were produced via sputtering, electron beam evaporation and plasma assisted electron beam evaporation, with thicknesses ranging between 10 nm and 57 nm. In all cases, the roughness of the coating was similar to that of the PET substrate. Low and Xu [240] produced 8 nm and 80 nm thin AlO_x barrier layers on various polymer substrates via sputter deposition. They state that the thin 8 nm coating followed the surface topography of the substrate, but with increased roughness, whilst the fully grown 80 nm coating revealed a comparable roughness to the substrate.

The surface roughness of a barrier coating has been discussed by many researchers as playing a critical role in the barrier performance of the coating.

Phillips and co-workers [242, 288] used AFM analysis to investigate electron beam evaporated AlO_x and SiO_x layers (of comparable/identical thickness) on PET and BOPP. For both substrates, they found that the AlO_x layers were considerably smoother than the SiO_x layers and, furthermore, exhibited better moisture barrier properties. Hence, they assumed that a correlation between water vapour barrier and surface roughness of the coating exists. Also Garcia-Ayuso et al. [334], who deposited AlO_x, SiO_x and mixed (SiO_xAl_y) coatings onto commercial 12 µm PET film by a variety of techniques, including chemical vapour deposition and electron beam evaporation, found that coatings exhibiting a smaller roughness than the PET substrate had better water barrier properties than coatings with larger mean RMS values. This relationship could, however, only be established when a small AFM scan size of 0.5 x 0.5 µm² was applied. The same correlation between moisture barrier and coating RMS (over 1 x 1 µm² areas) was found by Miyamoto and co-workers [175] for transparent barrier layers deposited onto PET film with acrylate undercoats. In the case of oxygen barrier performance and a possible correlation with coating roughness, Erlat et al. [129] discovered that smoother PECVD SiO_x coatings on PET had lower OTRs (also here roughness was obtained from 1 x 1 µm² scan areas).

Nevertheless, Henry et al. [157] indicated that they could not find a clear relationship between water barrier and roughness of sputtered Al and AlO_x coatings on PET. Also in later publications by Henry et al. [160, 290], where a variety of AlO_x and SiO_x coatings deposited onto PET via a range of techniques was analysed, no correlation between barrier performance and coating roughness could be recognised. Nevertheless, it was stated that, despite the comparable coating roughness, the coatings exhibited a different grain size (determined from 1 x 1 µm² AFM scans), which was smaller for the sputtered coatings, in comparison to the electron beam evaporated coatings. It was, consequently, argued that a smaller grain size (corresponding to a low density of small pores) reflects a denser coating structure, which in turn entails better water barrier performance. This correlation between grain size or packing density and water barrier properties has also been found for sputtered AlO_xN_y coatings on PET [159, 335] and similar results were, additionally, published by Garcia-Ayuso and co-workers [336]. Hanika et al. [156] discovered, though, the exact opposite for aluminium coatings evaporated onto BOPP. In their case, a sample with low water barrier properties revealed smaller grains than a sample with better barrier performance, as identified from 1 x 1 µm² scans. Hence, they concluded that a smaller grain size results in more grain boundaries and thus more permeation pathways for water vapour.

Based on the referenced literature, the AFM investigation of surface areas of 1 x 1 µm² or less may give some vital information on possible differences in the surface structure induced by the coating, as well as water barrier performance of the AlO_x coated film. With respect to the latter, it can be seen that BOPP F and PET (coated and uncoated) exhibited a lower surface roughness than all the standard BOPP film (coated and uncoated) and, additionally, they also showed good moisture barrier levels after AlO_x coating (refer to *Table 6-10*, Chapter 6.2.1.1). Hence, this agrees with some of the referenced literature stating that a smoother coating will exhibit better WVTR. Nevertheless, it is not assumed that this is the reason for the differences seen in water barrier performance between the different AlO_x coated films, but that the nano-structure of the coating (as affected by the polymer surface chemistry and coating nucleation/growth) plays a more important role. This nano-structure appears not to affect the roughness of the AlO_x coating, as measured by AFM, i.e. it is beyond the resolution of this analytical technique at the chosen scan size of 5 x 5 µm². Overall, it is argued that the surface roughness of the polymer films (coated and uncoated) is not the governing factor for the barrier performance after coating and, hence, that no correlation between coating roughness and moisture/oxygen barrier is present.

6.2.3 Coating stoichiometry

The stoichiometry of the AlO_x barrier layers was determined using XPS analysis. In order to prevent a distortion of the stoichiometry results, etching was carried out to remove absorbed water present on the AlO_x coating, any carbon contamination and surface hydroxides. Therefore, an area of approximately 3 x 3 mm² (larger than the investigated area, which is an elliptical spot with a transverse diameter of 800 µm) was etched using a 3 kV (1 µA) argon ion beam. Three to four levels of etching (60 seconds each) were performed for each sample. It was found that after the first etch most of the carbon contamination had already disappeared, and in the case of 'standard' AlO_x coatings the stoichiometry (x-value) did not change with increasing etch levels. Additionally, on some samples, a complete depth profile was performed (see *Figure 6-35*). In order to evaluate the raw XPS data obtained, the sensitivity factors according to Scofield [212] were used, as these were recommended by the equipment manufacturer based on Al_2O_3 reference sample tests. Preferential sputtering of oxygen during the argon etching of the AlO_x layer, which would affect the stoichiometry measured by XPS, was shown not to take place in the case of Al_2O_3 and, furthermore, no lower aluminium oxides are formed (i.e. no reduction of Al_2O_3 during argon ion bombardment) [337, 338].

Figure 6-35 shows an XPS depth profile obtained for AlO_x coated BOPP C. The trial selected was performed using in-line plasma pre- and post-treatment.

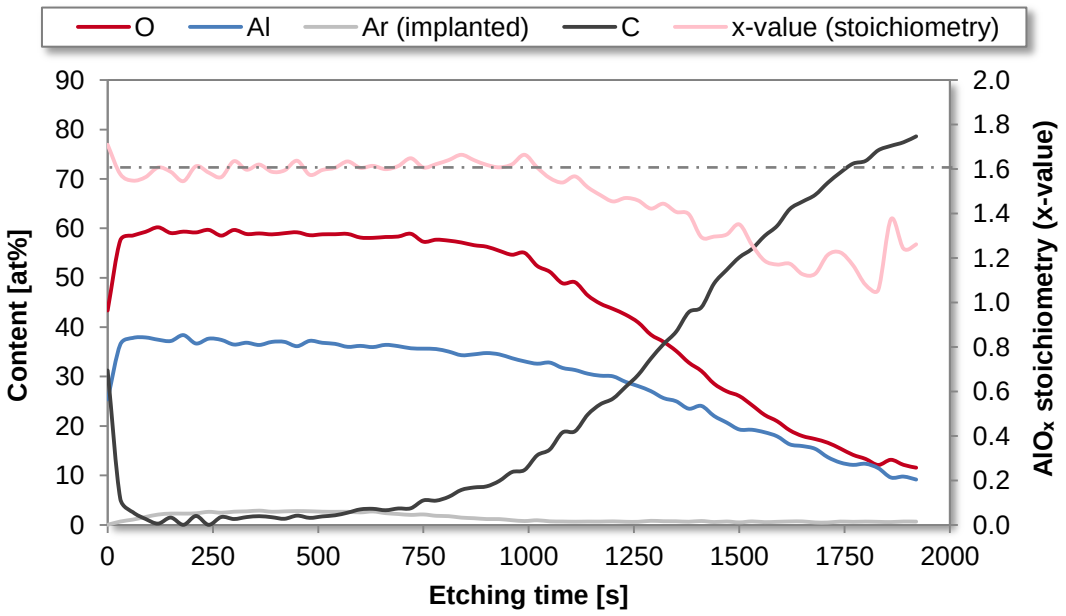

Figure 6-35: XPS depth profile of AlO_x coated BOPP C following plasma pre- and post-treatment

The etching time was not converted into AlO_x thickness, since the etch rate for the AlO_x coatings is not known and may also change during depth profiling (e.g. near the interface). Instead, TEM analysis was used for AlO_x thickness determination; refer to Chapter 6.2.5.

There are several important observations that can be made from *Figure 6-35*. Firstly, there is a large amount of carbon based contamination (approximately 30 at%) on top of the AlO_x coating (see also investigations of AlO_x surface energy, Chapter 6.2.4). This amount significantly reduces with etching of the surface. That there is still a carbon signal after removing the surface contamination can be caused by surface roughness and shadowing effects. Secondly, during etching, argon is implanted into the AlO_x layer (approximately 2.5 at%). This is due to the coating being a ceramic, and consequently, hard material. As soon as the AlO_x-polymer interface is reached, the argon signal drops, since the argon ions can travel a lot deeper into the soft polymer and, hence, are not detected by the XPS analysis. After an etching time of around 1000 s, the Argon signal is roughly 0 at%, which indicates that the polymer substrate is now predominantly etched. Furthermore, it was found that x-values were slightly reduced from $x = 1.7$ at the surface (in general, the x-value is between 1.7 and 2.0 for the non-etched sample), down to around 1.6, after the initial etching period; the dashed/dotted line in *Figure 6-35* effectively illustrates this effect. After more extended etching times (greater than approximately 1000 s), the x-values begin to drop and cease to become valid, due to removal of the coating (i.e. the polymer is etched excessively). Overall, there is no change of stoichiometry with coating thickness (i.e. no gradient), apart from the increased x-value on the coating surface due to the presence of aluminium hydroxide and absorbed water. This agrees with the XPS sputter depth profile of an oxygen-rich AlO_x layer deposited onto PET that has been published by Barker and co-workers [16]. They also show the initial carbon based contamination, which diminishes to a very low level after the etching starts. Furthermore, also here the oxygen and aluminium amounts remain approximately constant throughout the coating thickness, hence indicating the absence of a stoichiometry gradient in the coating. Nevertheless, if one would calculate the x-values based on the XPS peak areas given in their depth profile, this would result in x-values of less than one (as the aluminium line runs above the line for oxygen). This is surprising, based on the fact that no elemental aluminium was present for this sample and, hence, it is assumed it would be Al_2O_3 (as also stated in one of their earlier publications [2]). It can only be assumed that the peak areas shown have not yet been corrected using the relative sensitivity factors for the individual elements. The results found here are, moreover, different from a German patent [339] describing the deposition of reactively evaporated AlO_x

barrier layers. In this patent, the AlO_x coatings have a stoichiometry gradient, which exhibits a very thin but sub-stoichiometric layer with a maximum of metallic aluminium near the substrate interface. In the investigations carried out in this thesis, neither a stoichiometry gradient nor metallic/elemental aluminium were detected.

Further selected samples of AlO_x coated BOPP and the PET reference film (all samples aged by the time of XPS measurement) were investigated for their stoichiometry using three to four levels of etching. In the case of BOPP C, the x-value is taken from the depth profile shown in *Figure 6-35*. The results are summarised in *Table 6-16*. Also stated are the ODs at the time of the XPS measurement. Each x-value represents the average value over the etch levels performed and, additionally, standard deviations are given. In order to show the variation in x-values, two decimal places are displayed, although, given the accuracy of the analysis and variations seen within one sample, only one decimal place is reasonable to characterise the stoichiometry.

Table 6-16: AlO_x stoichiometry of coated polymer films, as analysed via X-ray photo electron spectroscopy

Film	Plasma treatment	Stoichiometry x-value	OD
BOPP B	Pre	1.53 ± 0.03	0.03/0.04
	Pre + post	1.61 ± 0.02	0.03
BOPP C	Pre + post	1.57 ± 0.03	0.04
BOPP E	Pre	1.64 ± 0.03	0.04
BOPP F	Pre	1.64 ± 0.02	0.03/0.04
	Pre + post	1.60 ± 0.04	0.04/0.05
PET	Pre + post	1.65 ± 0.03	0.04

As can be detected from *Table 6-16*, the x-values range from approximately 1.53 to 1.65 and no differences in stoichiometry are seen by the application of an additional plasma post-treatment. Furthermore, no elemental (i.e. metallic) aluminium was found, but all aluminium was in an oxidised state. This indicates that the AlO_x layer consists principally of stoichiometric Al_2O_3, although for some samples the x-value is marginally higher than the stoichiometric value of 1.5. Slightly increased x-values have also been reported by Kim et al. [340] for PECVD deposited AlO_x layers, which could be reduced by annealing-treatments. For (non-reactive) magnetron sputtered AlO_x layers, Segda and co-workers [341] and Cueff et al. [342, 343] obtained

stoichiometric or oxygen-rich films (x-values ranging from 1.46 to 1.93), depending on the individual deposition conditions, such as plasma pressure. In the case of reactively electron beam evaporated AlO_x layers, Zywitzki and co-workers [344, 345] report nearly stoichiometric AlO_x coatings with x-values ranging from 1.43 to 1.67 (with and without plasma activation), whilst Schiller et al. [33] obtained values between 1.50 and 1.55 for plasma activated deposition. Finally, Misiano and co-workers [42] report x-values of 1.8 and 1.9 for approximately 20 and 30 nm thick reactively deposited AlO_x barrier layers. These results indicate that a slight excess of oxygen in the AlO_x (Al_2O_3) can be normal and generally is affected by the specific deposition conditions, as well as the deposition process.

Kelly [2] and Barker et al. [16] state that their analysis of reactively evaporated AlO_x barrier layers on PET (20 to 25 nm, boat evaporation) revealed that these substantially consisted of Al_2O_3, if the coatings were clear (i.e. oxygen-rich), and an Al_2O_3 matrix with finely dispersed aluminium metal crystallites, if they were grey (i.e. metal-rich). Also the coated films analysed in this thesis were transparent (OD 0.03 to 0.04, see *Table 6-16*, plain film OD for BOPP: 0.03, PET: 0.04). The XPS analysis of absorbing ('greyish') coatings will be discussed at the end of this chapter.

It is worth mentioning here that the use of sensitivity factors according to Wagner [346, 347] resulted in calculated x-values of 2.4 to 2.6, which is a lot higher than the value of 1.5 for Al_2O_3. Consequently, this would be more representative for a coating consisting of aluminium oxyhydroxide AlO(OH) and aluminium hydroxide $Al(OH)_3$. Nevertheless, the instrument supplier confirmed that this was the case when analysing an Al_2O_3 reference sample, as they obtained an x-value of 1.48 using Scofield and 2.48 when using Wagner. Consequently, Scofield sensitivity factors were used for all XPS data presented in this thesis. X-values between 2.2 and 2.6 have, for example, been reported by Maiti and co-workers [348] for electron beam evaporated AlO_x layers. They state that sensitivity factors supplied with the instrument were used, but do not give further information.

In addition to the analysis of 'standard' AlO_x coatings, AlO_x coatings whereby the stoichiometry was purposely changed in order to yield a higher aluminium content were analysed using XPS. These coatings were deposited onto BOPP A, as well as BOPP B, using in-line plasma pre-treatment only (see also corresponding barrier results in Section 6.2.1.3). For this investigation, the coating thickness was left approximately constant whilst the amount of oxygen introduced was changed. This resulted in 'greyish', absorbing coatings. In the case of BOPP B, all these coatings were also analysed for their stoichiometry and elemental/metallic aluminium content using XPS. As for the 'standard' AlO_x coatings, the samples were subjected to three

levels of etching at 60 seconds each, in order to remove surface hydroxides and carbon based contamination. Nevertheless, this time it was found that with increasing the etching time, the x-value did not remain constant but dropped further for all 'greyish' samples, indicating a stoichiometry gradient through the coating thickness. Consequently, the x-value obtained for the 'deepest' etch (180 seconds) was used to characterise the coatings. The fact that for metal-rich AlO_x coatings the stoichiometry is not constant across the coating thickness has also been shown in depth profiles by Barker et al. [16], who found that the oxygen content initially dropped quickly and then rose slowly back to the same level, when the etching depth moved closer towards the coating-polymer interface.

Whilst for the 'standard' AlO_x coatings (see *Table 6-16*), no metallic aluminium was detected, the investigation of 'darker/greyish' AlO_x coatings did reveal the presence of metallic/elemental aluminium. This can be detected from high-resolution XPS spectra of the aluminium 2p (Al2p) peak. The peak for oxidised aluminium is around a binding energy of 74 to 75 eV, whilst the peak for elemental aluminium emerges at around 72 to 73 eV [349]. The progression of the Al2p peak with changing AlO_x stoichiometry (for coatings on BOPP B) is depicted in *Figure 6-36*. In order to highlight the differences in stoichiometry between the samples, two decimal places are given for the x-values.

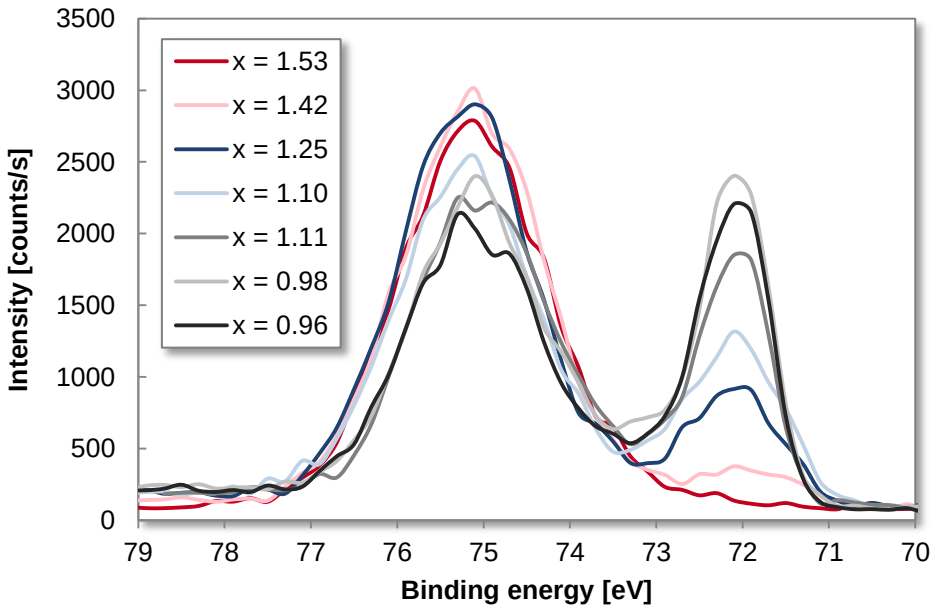

Figure 6-36: High-resolution XPS spectra of Al2p peak for AlO_x coatings on BOPP B of various stoichiometries (after 180 seconds argon ion etching)

As can be seen from *Figure 6-36*, the peak for oxidised aluminium is located at 75 eV, whilst the peak attributed to elemental aluminium appears at 72 eV. Slight

variations from the binding energies given in literature can be caused by the fact that all peaks have been referenced to the C1s peak at 285 eV, in order to compensate the occurrence of charging effects. Furthermore, *Figure 6-36* shows that as the x-value decreases, the height of the 72 eV peak (for aluminium metal) increases in intensity, whilst the 75 eV peak (for oxidised aluminium) reduces in intensity. Overall, this indicates that with a reduction in x-value, the amount of metallic aluminium in the AlO_x coating increases. The sample with x = 1.53, i.e. 'standard' AlO_x (dark red line in *Figure 6-36*), did not contain any elemental aluminium, hence no peak at 72 eV is noticeable. This is, once again, in agreement with XPS results by Barker and co-workers [16], who found no metallic aluminium in their oxygen-rich AlO_x coating, but for the metal-rich AlO_x coating the XPS spectrum clearly revealed a peak for elemental aluminium, in their case at 72.3 eV. Hoffmann and co-workers [289] state that an insufficient amount of oxygen, i.e. increased amount of aluminium, during reactive electron beam evaporation of aluminium leads to absorbing coatings, which consist of a mixture of Al_2O_3 and aluminium. Also Yoon et al. [350], who used plasma activated reactive electron beam evaporation, state that sub-stoichiometric, i.e. aluminium-rich, dark films were deposited at lower oxygen pressure, whilst at higher oxygen pressure the coatings were clear and approached the x-value of stoichiometric films.

With the XPS results obtained for BOPP B, a correlation was established between the aged OD of these coatings (measured after six months, i.e. the values had stabilised, as also stated in reference [15]) and the x-value, as well as a correlation between the x-value and the content of elemental aluminium. These correlations (*Figure 6-37* and *Figure 6-38*) are very good with coefficients of determination of $R^2 = 0.94$ and $R^2 = 0.99$, respectively, being obtained. The amount of elemental/metallic aluminium is given in at%, which reflects the concentration relative to the total Al2p peak area.

Also shown in *Figure 6-37* and *Figure 6-38* are the results for one measurement performed on a sample of 'dark' AlO_x on BOPP A (blue triangle, this sample has not been used to establish the linear correlation). It is evident that this measurement on BOPP A is in very good agreement with the correlation obtained for BOPP B. The relationships established here were used to determine the x-value, as well as the elemental aluminium content, of AlO_x coatings on BOPP A with varying stoichiometry, which were not assessed using XPS analysis. The results were then applied to create the graphs for the investigation of barrier properties as a function of AlO_x stoichiometry on BOPP A (see Chapter 6.2.1.3, *Figure 6-17*).

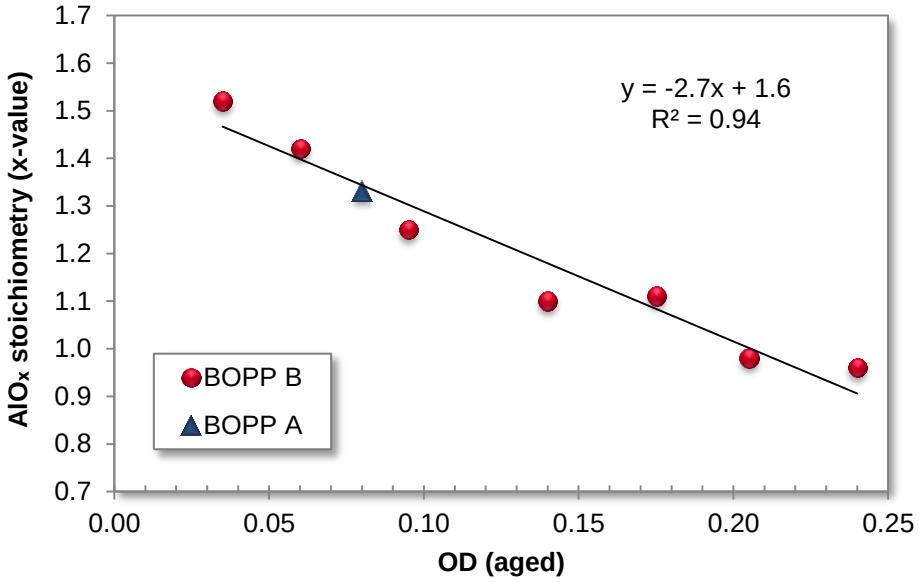

Figure 6-37: Correlation between aged OD of AlO_x coatings on BOPP films and stoichiometry (x-value), as determined via XPS

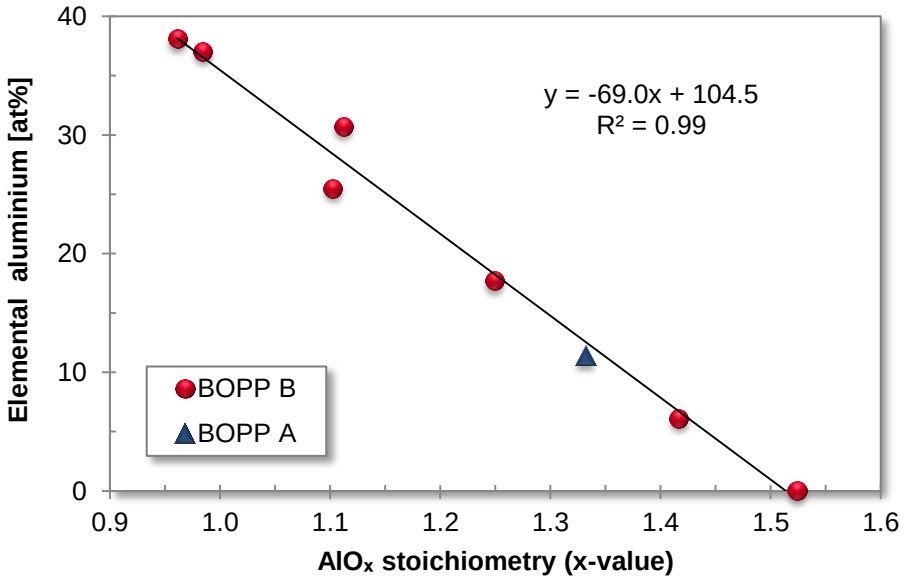

Figure 6-38: Correlation between AlO_x stoichiometry (x-value) and content of elemental aluminium, as determined via XPS

6.2.4 Coating surface energy and contact angles

Coating surface energy is an important factor to be considered for conversion of vacuum coated films, such as printing or laminating on top of the barrier layer. These process steps require a high surface energy, as this usually results in better wetting of inks or the adhesive used for lamination. Good wetting, in general, is the first step towards good adhesion. For lamination, for example, a surface energy of more than 38 mN/m is required [34].

The AlO_x coated BOPP films were analysed at regular time intervals using contact angle measurement to investigate any change of surface energy that may take place. During the extended time period of 700 days, which was investigated, samples swatches were stored under ambient conditions (approx. 20 ± 3 °C) without precise control of environmental parameters, since this is seen as a more realistic approximation to the storage conditions of industrial film rolls. Surface energy results for AlO_x coated BOPP A, B, C and F are plotted as a function of time in *Figure 6-39*. Additionally, the graph shows the surface energy measured for an AlO_x coated PET reference film. Whilst the experiment for BOPP A, C and F was run in parallel (as all samples were AlO_x coated at around the same time), the measurements of AlO_x coated BOPP B and PET were started later, due to these films being produced at a different time. Each data point in *Figure 6-39* is made up of an average of five replicate surface energy determinations; the error bar represents the standard deviation.

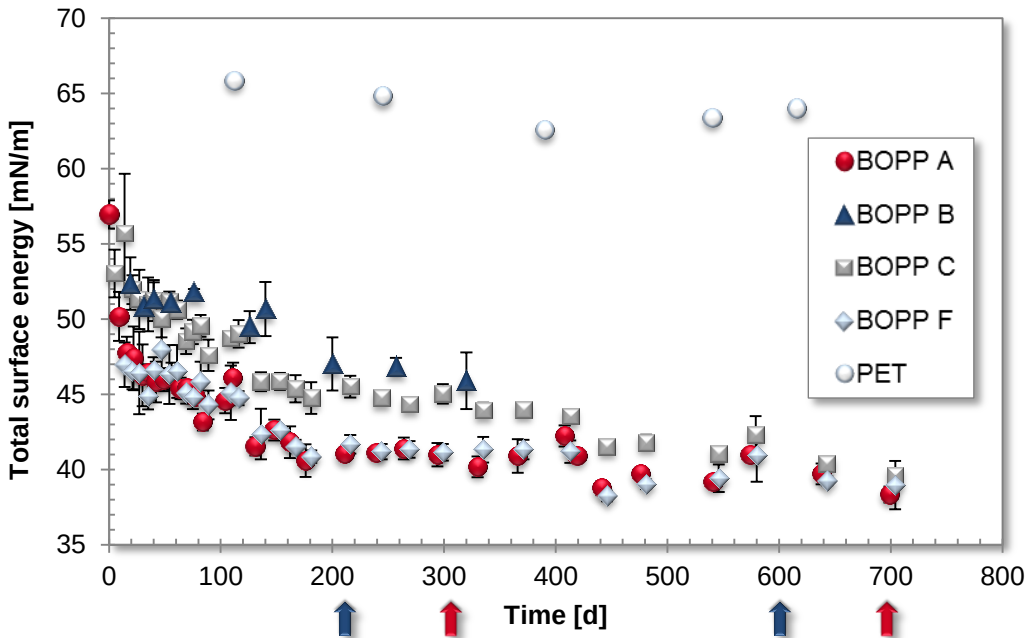

Figure 6-39: Change of total surface energy of AlO_x coated BOPP films with storage time (in days after coating process); arrows mark time of XPS measurements

For AlO_x coated BOPP A, which was initially analysed only hours after coating (the other samples were not), a rapid decrease of the total surface energy from an average starting value of 57.0 ± 0.9 mN/m to a value of approximately 46 mN/m is visible within the first 50 days after coating. This is followed by a further decay at a lower rate until around 175 days of age. From this time onwards, there is a still measurable, but very slow, decline with a final value of 38.3 mN/m after 699 days. AlO_x coated BOPP F behaves nearly identically to BOPP A, and also BOPP C shows similar behaviour, although the average AlO_x surface energy is somewhat higher than for the other films (curve shifted upwards by approximately 4 to 5 mN/m, see *Figure 6-39*). However, over extended time periods, AlO_x coated BOPP C appears to approach surface energy values similar to AlO_x coated BOPP A and F. BOPP B was coated later in the project and, consequently, could not be analysed for the same length of time. The values obtained for AlO_x coated BOPP B up to the point investigated are, nevertheless, similar to AlO_x coated BOPP C. Indeed, they appear even a bit higher. For comparison, *Figure 6-39* also contains the surface energies obtained for AlO_x coated PET. These values are considerably higher (63 to 66 mN/m) and also only reveal a marginal decrease with time. A one day aged AlO_x coated PET sample (comment: not the same sample as investigated in *Figure 6-39*) shows a total surface energy of about 66.9 mN/m, approximately 10 mN/m higher than the 'fresh' AlO_x coating on BOPP A. The values obtained here for AlO_x coated PET are slightly higher than results published by Schiller et al. [34], who used a plasma assisted roll-to-roll coating process to deposit AlO_x coatings onto PET and report values between 54 and 62 mN/m for an investigated period of 23 days (measurement technique not stated in this publication). The reason for the differences seen between the various BOPP films, as well as PET film, will be explained later in this chapter.

On splitting the total surface energy into its polar and dispersive parts, it can be seen from *Figure 6-40* (provided as an example for AlO_x coated BOPP A; note, the other films behave identically) that the drop in total surface energy over time is predominantly due to a drop in the polar fraction. Whilst the dispersive surface energy remains approximately constant (perhaps a small initial decline), with average values around 29 to 31 mN/m, the polar surface energy drops drastically from approximately 25 to 13 mN/m within the first 150 days and then very slowly decays further to a value of approximately 10 mN/m after 699 days. It is obvious from *Figure 6-40* that the total and polar surface energy reveal the same declining trend with storage time.

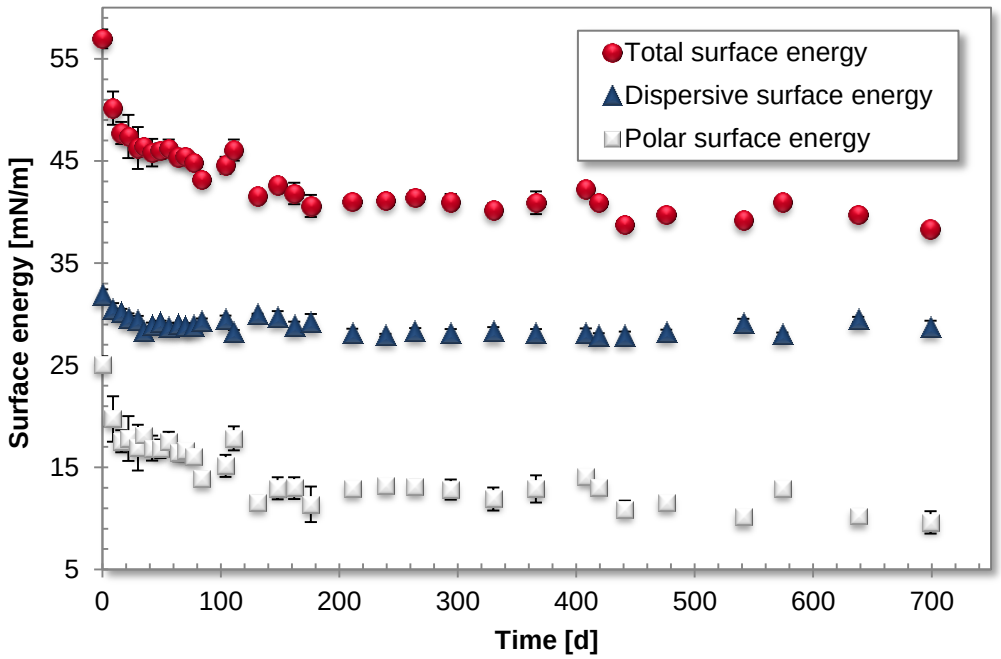

Figure 6-40: Change of surface energy of AlO_x coated BOPP A with storage time

The decay of coating surface energy of vacuum coated films, especially BOPP, with time is a well-known phenomenon within the metallising and converting industries [72, 351-353]. This effect is considered to be due to the transfer of mobile low-molecular-weight polymeric material (oligomers) and migratory additives from the reverse side of the coated film onto the coating, and also migration from the bulk polymer through the coating onto its surface (via defects in the coating) during storage. The freshly deposited layer of either aluminium oxide or aluminium would exhibit a very high surface energy (several 100 mN/m for clean metal and metal oxides [72, 354]) and, therefore, is extremely reactive. Consequently, the surface can readily (and rapidly) attract mobile materials and contaminants, in order to lower its surface energy. This occurs as soon as the film is wound into a roll after the coating process, and the fresh coating surface is in direct contact with the uncoated back surface of the polymer film. Consequently, it is inevitable in a roll-to-roll coating process. [4, 355] The process is driven by thermodynamics, similar to the ageing of corona treated film (refer to Section 6.1.3.1), with the aim to minimise the surface energy, i.e. match the low surface energy of the reverse side of the BOPP film and, thus, obtain an energetically favourable and stable state.

This sequence of events explains the reduction of surface energy and the already very low surface energy measured on the day of the coating process (mean value of 57.0 mN/m for AlO_x coated BOPP A). According to the literature, a clean metal oxide surface should have a surface energy of several 100 mN/m (see previous paragraph). The reduction in surface energy of the oxide coating on the film is,

therefore, clearly due to immediate contact (after deposition) with the reverse side of the BOPP film. In the case of all BOPP films, including BOPP F with the high surface energy polymer skin layer, this reverse side of the film is either a co- or terpolymer of polypropylene, and the average surface energy of this side was less than 30 mN/m in all cases (refer to Section 6.1.3.1). As for this study, the samples were stored in swatches, whereby the AlO_x coating was always touching the reverse side of the BOPP film. Taking the previously described SEM images of AlO_x coated BOPP A, B and C into account (see Section 6.2.2.2), it may well be that mobile polymeric material migrates through the defects present in the AlO_x coating on BOPP A, thus resulting in the lower surface energy for AlO_x on BOPP A, compared to BOPP B and C. Nevertheless, AlO_x on BOPP A and F gave nearly identical surface energy levels and BOPP F showed the best oxygen and water barrier performance, with no defects in the coating (and also no antiblock particles in the plain film surface that may cause defects). Consequently, only very limited permeation through the coating will occur on BOPP F. Furthermore, a different polymer is below the AlO_x coating. An additional observation, supporting the idea of transfer of polymeric material from the reverse side of the BOPP film, is the dispersive surface energy of the AlO_x coating, which is 29 to 31 mN/m. The latter is virtually identical to the surface energy of the reverse side of the BOPP films (polar part of reverse side is about 0 to 0.5 mN/m, i.e. negligible in this case). The amount of mobile polymeric material and additives in/on the BOPP film will vary, depending on each film supplier, the specific film manufacturing (extrusion) conditions and polymer grade used. The latter two both govern the polymer weight distribution of the BOPP film. The more mobile material that is present, the quicker and more pronounced the decay of the AlO_x surface energy will be.

In order to further investigate the materials/components in the polymer films that could possibly be transferred or migrate onto the AlO_x coating, BOPP A, B and C were subjected to a Soxhlet extraction with a nonpolar solvent (n-hexane), and the extracts obtained were further analysed for their composition and molecular weight distribution, using FTIR spectroscopy and gel permeation chromatography (GPC). The results of this examination are presented in Appendix A4.

Differences between PET and BOPP in terms of the surface energy decay characteristics of the AlO_x coated side can be explained by the difference in glass transition temperature (T_g) of the two polymers. BOPP at ambient temperature will be above its T_g (in the range of 0 to 10 °C [55] for isotactic PP) and, consequently, all amorphous parts will be in a rubbery state. In this state, polymer chains and fragments are more flexible and mobile. By contrast, PET has a higher T_g (69 to

115 °C [55]). Thus, in PET the oligomers and polymer chains in the amorphous regions are less mobile; it is, therefore, argued that less migration will occur. In addition to that, fewer film additives are required during PET film production.

To further investigate the type and amount of contamination present on the AlO_x coated films, XPS analysis was used (without etching the coating surface). AlO_x coated BOPP C and PET were analysed at two different times (with a one year time gap) after the coating process (see arrows in *Figure 6-39*, blue: PET after 195 and 560 days, red: BOPP C after 285 and 650 days). The average carbon amounts measured on the samples at these two times are summarised in *Table 6-17*.

Table 6-17: Carbon contamination of AlO_x coated BOPP C and PET, as determined via XPS analysis

Film structure	Carbon contamination	
	1st measurement	2nd measurement (after 1 year)
	at%	at%
AlO_x coated BOPP C	11.9*	24.8 ± 9.1
AlO_x coated PET	10.0*	15.2 ± 2.6

*only single measurement taken

As can be seen from the data obtained, the AlO_x layer on BOPP shows a larger amount of carbon than the AlO_x layer on PET, which is in agreement with the AlO_x surface energy being higher for the PET substrate. Furthermore, an increase in carbon contamination from the first to the second measurement is observable, larger for BOPP than for PET, which reflects the drop of AlO_x surface energy with time. The difference in carbon contamination level between AlO_x coated BOPP and PET for the first measurement is, however, only marginal, despite the difference in surface energy (AlO_x coated PET ≈ 65 mN/m, AlO_x coated BOPP C ≈ 45 mN/m), which suggest that there is also a difference in the type of contamination present. This appears quite plausible, based on the assumption that the contamination in one case comes from PET, which inherently has a higher surface energy than BOPP (see Section 6.1.3.1), and in the other case from BOPP. The carbon based contamination levels found for the AlO_x coated films are equivalent to contamination layers of thicknesses between 0.2 nm (10 at% carbon) and 0.8 nm (30 at% carbon) [356]. XPS depth profiles carried out by Barker and co-workers [16] for 20 to 25 nm thick AlO_x barrier layers on PET also show the typical carbon contamination on the surface. The authors attributed the hydrocarbon levels found to either contamination

during sample transfer from the deposition chamber to the XPS equipment or migration of low-molecular-weight polymeric material.

Closer examination of the high-resolution C1s spectra obtained from the AlO_x coated film surfaces in all cases revealed two peaks (see *Figure 6-41*), one at 285 eV, which can be assigned to C-C and C-H bonds, and a smaller side peak at 289 to 290 eV, assigned predominantly to carboxyl/acid functionalities but also ester functionalities [268].

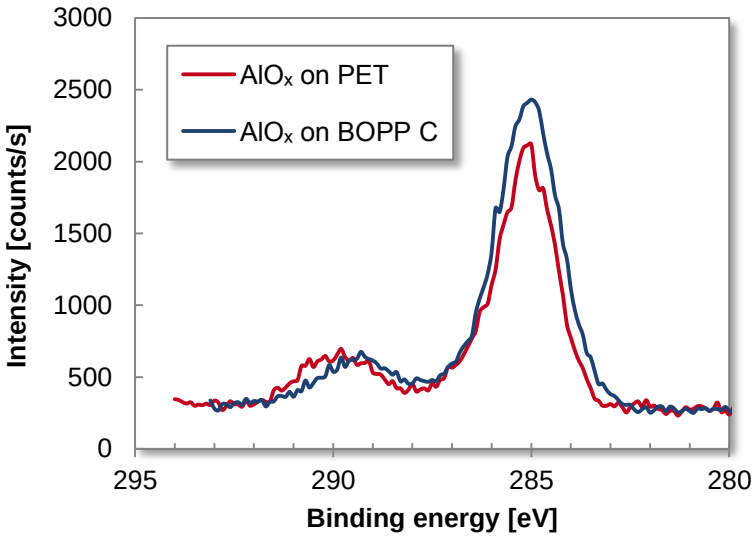

Figure 6-41: High-resolution XPS spectra of C1s peak for AlO_x coated BOPP C and PET film (2^{nd} measurement after 1 year)

Apart from the missing peak for hydroxyl groups, *Figure 6-41* reveals a typical signature spectrum of carbon contamination, which is seen when analysing metal and metal oxide surfaces that have been exposed to atmosphere via XPS [354]. Based on the high surface energy of the pristine metal oxide surface, this is to be expected, since bipolar molecules will be attracted to the surface and align with their polar part (i.e. ester or carboxyl functionality) towards the oxide and with their nonpolar/hydrocarbon tail facing away [354]. On top of this layer, nonpolar molecules will be absorbed. In our case, the bipolar molecules may originate from film additives, such as antioxidants, e.g. Irganox1010 (contains ester functionalities), which is a common additive used in BOPP films, or acid scavengers, e.g. metallic stearates (acid functionality) or metallic salts based on other acids [50]. XPS also showed traces of calcium on AlO_x coated BOPP C, which could be a residue from calcium stearate (used as an acid scavenger film additive) and would, therefore, confirm the transfer of material from the reverse side of the film (or migration from underneath the coating).

XPS does, however, not reveal the origin of the carbon based contamination on the AlO_x surface, i.e. cannot tell whether the material comes from the film (reverse side or underneath coating) or the atmosphere (even though samples of the swatches have only been openly exposed to atmosphere during contact angle measurements and shortly during XPS sample preparation). Consequently, further examinations were carried out.

Firstly, a swatch of AlO_x coated BOPP A was prepared whereby the individual film sheets were separated by paper from one another. The surface energy of this sample was investigated periodically with time. Additionally, a 'normal' swatch was kept of the same coating trial (i.e. AlO_x touching BOPP reverse side, but not paper) and investigated for surface energy in parallel. The results of this investigation are depicted in *Figure 6-42*. As mentioned previously, five surface energy measurements were carried out for each data point in order to obtain mean values and a standard deviation. Additionally, trend lines were fitted to the data, a second order polynomial for the 'paper' sample and a power trend line for the 'swatch' sample. As can be observed from *Figure 6-42*, the AlO_x surface energy of the 'swatch' sample reveals a rapid drop within the first 50 days of investigation (similar as seen in *Figure 6-39*), whilst the paper separated sample decreases at a slower rate. After approximately 450 days, both samples exhibit very similar surface energies.

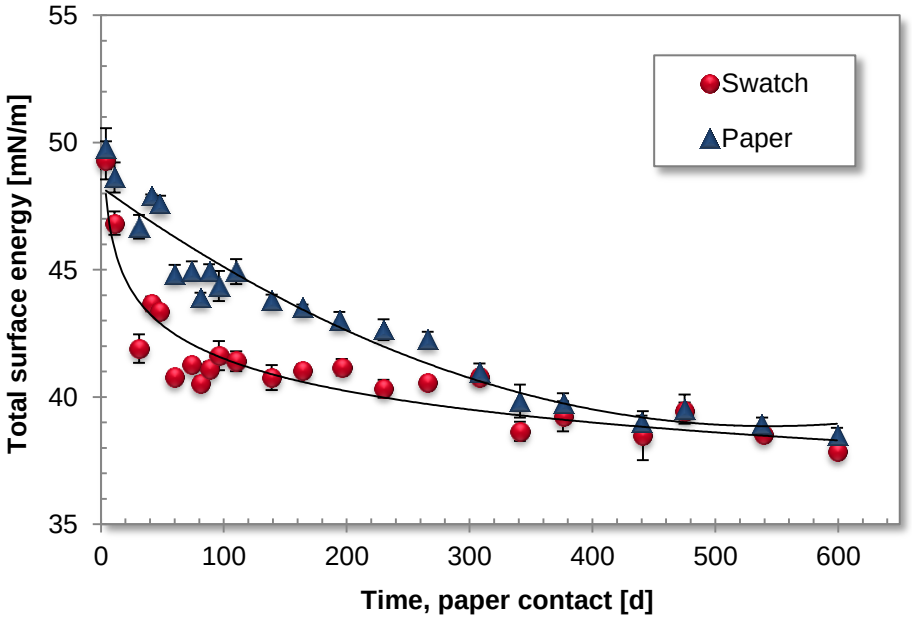

Figure 6-42: Change of total surface energy of AlO_x coated BOPP A (swatch and paper separated sheets) as a function of time (since separation)

Here, it is assumed that the mobile polymeric material, readily available on the reverse side of the BOPP film, is quickly transferred onto the AlO_x layer, therefore the strong decline of surface energy for the swatch sample. In contrast to that, this material is not present for the 'paper' sample and the surface energy decreases at a slower rate, due to the time needed for the migration of material from the polymer underneath through defects in the coating. Obviously, this migration is also taking place for the 'swatch' sample, in addition to the transfer of material from the reverse side. Moreover, in the case of AlO_x coated BOPP A, there was a large number of defects present in the coating, as detected by the SEM and AFM investigation, refer to Chapter 6.2.2. This would indicate that the decrease of surface energy for the paper separated sample is still quite strong, due to the vast amount of these defects. Since standard printer paper was used to separate the film sheets, it can, however, not be excluded that material was also transferred onto the AlO_x layer from the paper. Nevertheless, the difference in the shape of decline for the two data sets in *Figure 6-42* indicates that there is a transfer from the reverse side, in addition to the migration through defects. It can also be assumed that the AlO_x layer is only attracting low surface energy material, in order to minimise its surface energy. During this investigation, the non-coated side of the BOPP film (in the 'swatch' and 'paper' samples) was also investigated, in order to exclude a transfer of material from the paper. No difference in surface energy between the two samples, as well as no change with time, could be detected.

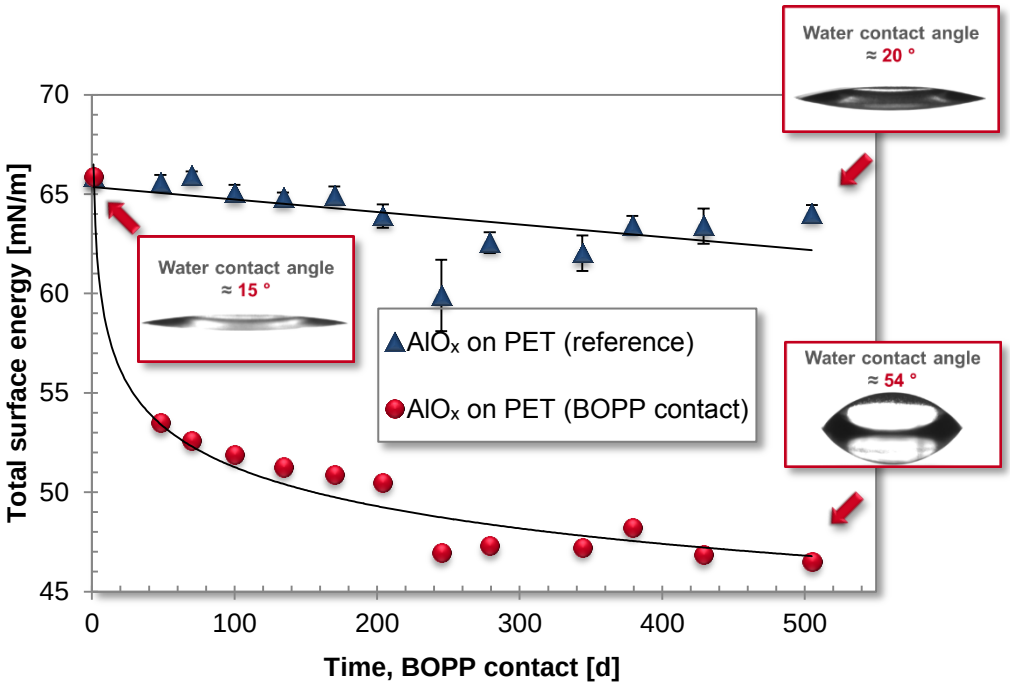

Figure 6-43: Change of total surface energy of AlO_x coated PET (swatch and BOPP separated sheets) as a function of time (since separation)

In order to see if the drop of surface energy is related to transfer of low-molar-mass polymeric material from the reverse side of the BOPP film, a second experiment was conducted. Sheets of AlO_x coated PET were interleaved with sheets of plain BOPP A, such that every AlO_x layer was in contact with the non-corona treated side of BOPP A. Once again, this sample and a reference swatch sample (i.e. AlO_x coated PET in contact with PET reverse side) were investigated for changes in surface energy with time. Results of this examination are presented in *Figure 6-43*, together with the water contact angle and drop images at the start point and terminal points of the investigation. Each point represents an average of five surface energy determinations and trend lines have been fitted to the data sets (linear trend line for reference sample, power trend line for BOPP contact sample).

Figure 6-43 reveals a distinct and rapid drop of the AlO_x surface energy when in contact with the BOPP film. Once again, this initial strong decrease within the first 50 days of contact is in agreement with the trend shown in *Figure 6-39* and *Figure 6-42*. After this initially very strong drop, the surface energy decays at a slower rate, similar to the AlO_x coated PET reference sample (swatch), which only exhibits a very slow decreasing trend. The drastic change in surface energy is accompanied by a large increase in water contact angle, as depicted by the drop images in *Figure 6-43*. This investigation finally confirms that it is the initial contact of the AlO_x coating with the reverse side of the BOPP film (low surface energy) that causes the significant drop of coating surface energy.

For completeness of the original analysis, i.e. the change of AlO_x surface energy with time (see *Figure 6-39*), the contact angle data, which is the basis for the calculation of surface energy, will be shown as well. The change of contact angles for the three fluids used (water, diiodomethane, ethylene glycol) is illustrated in *Figure 6-44*. Each data point represents an average of at least five contact angle measurements (on different drops) and error bars indicate standard deviations.

A rise of all contact angles with storage time can be detected from the graphs. This increase is the strongest for the polar test fluids, water and ethylene glycol, indicating that polar interactions decrease, which is in accordance with the drop of surface energy being predominantly due to a drop of the polar fraction (see *Figure 6-40*). Whilst the water contact angle still appears to exhibit a rising trend, the ethylene glycol contact angle seems to have levelled off and stabilised at a value just above 50° for all three BOPP film types.

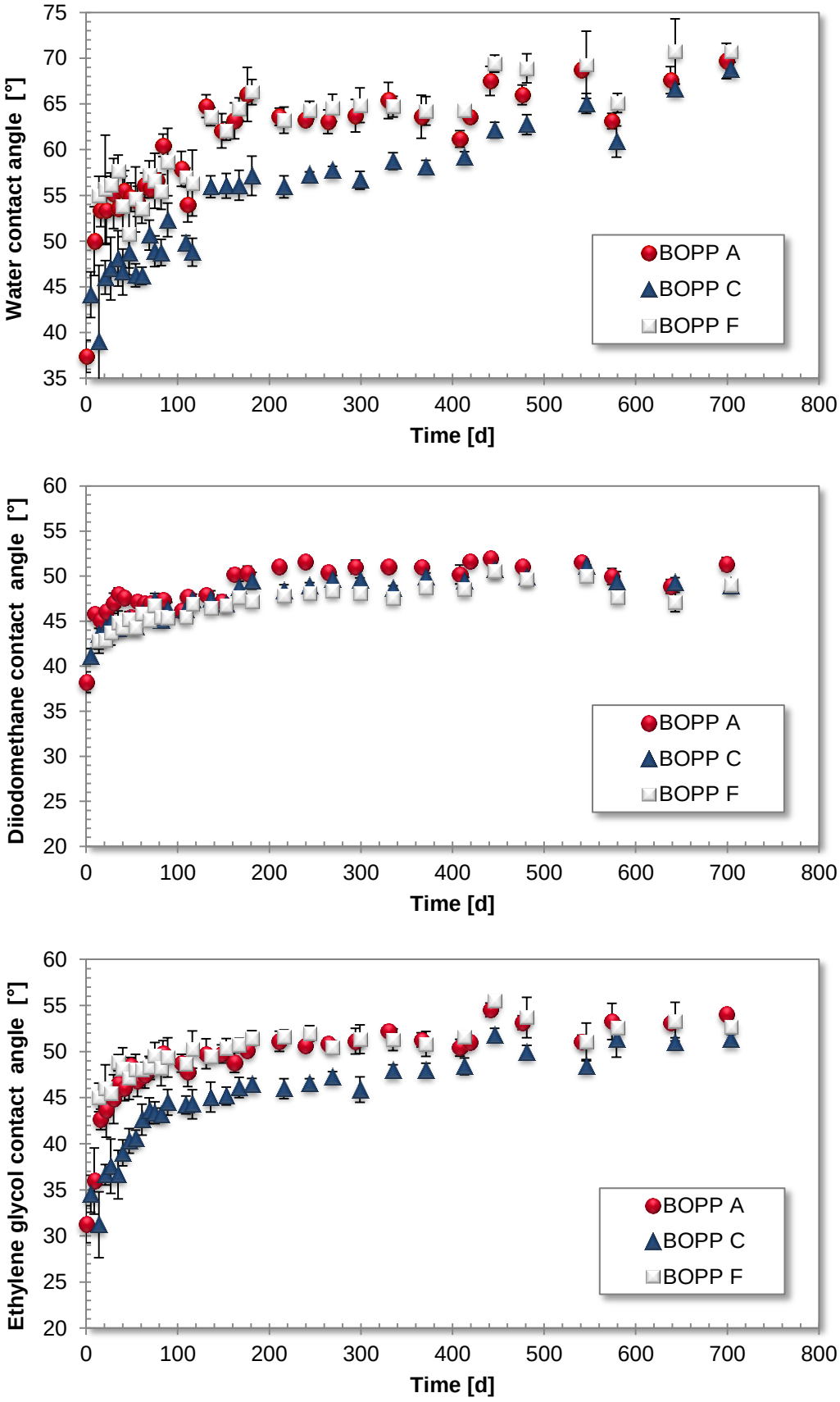

Figure 6-44: Change of water (top), diiodomethane (middle) and ethylene glycol (bottom) contact angle with time for AlO_x coated BOPP A, C and F

AlO_x coated BOPP A and F show very similar values for the water and ethylene glycol contact angle, whereas for BOPP C these angles are initially lower but merge in with the values of the other films with increasing storage time. Also this is in agreement with the surface energy data presented in *Figure 6-39*. It can, furthermore, be seen that the water contact angle shows the largest standard deviations (see error bars in *Figure 6-44*), closely followed by ethylene glycol, whilst the variation of diiodomethane contact angle for one data point is the lowest. This is thought to be due to the fact that the transferred material on the outermost surface is predominantly nonpolar, and polar fluids are very sensitive to slight variations in the distribution of this material. The contact angle with diiodomethane also displays an increase with time; nevertheless, this increase is small, relative to that with water and ethylene glycol, and the contact angle quickly reaches a limiting value with all three films. It is assumed that the differences observed between the three film types for the diiodomethane contact angle are not significant. The small initial rise seen in *Figure 6-44*, middle graph, explains the marginal drop of the dispersive surface energy depicted in *Figure 6-40*. This indicates that dispersive interactions (between the AlO_x surface and the test fluid) are reduced, which may be caused by a change in the composition of the polymeric material on top of the AlO_x layer.

With the decay of surface energy (and increase of contact angles) being due to a migration/transfer process, storage temperature and its fluctuations will play an important role in enhancing or decelerating the observed phenomenon. As variations in surface energy (and water/ethylene glycol contact angle) appear to be coincident (e.g. fluctuations between 100 and 120 days or 400 and 450 days for BOPP A, C and F, see *Figure 6-39* and *Figure 6-44*), it is assumed that these events are caused by variations in storage temperature over the investigation period, or variations in ambient conditions during testing. Additionally, other parameters, such as surface roughness, affect contact angle measurement and, thus, surface energy values obtained [357-359]. In general, it is assumed that a R_a of less than 0.5 µm has a negligible effect on the contact angle and hence surface energy [359]. In this work, surface roughness has been measured via AFM on 5 x 5 µm² areas where no antiblock particles were present and, under these condition, the RMS and R_a values were less than 10 nm for the polymer films (coated and uncoated). However, the surface area covered by the liquid droplet will inevitably include antiblock particles, which can protrude up to several µm from the surface, as observed in the SEM images, large area AFM scans and white light profilometry investigations (images not shown in this thesis). It is, therefore, possible that these surface protrusions may have affected the contact angle measurements.

6.2.5 Coating thickness

In order to determine the thickness of the reactively evaporated AlO_x layers, film samples were embedded in an epoxy resin, cross-sectioned with an ultramicrotome and subsequently examined using TEM. A selection of AlO_x coated films was investigated, including samples that showed good/bad barrier performance and samples subjected to the different plasma treatments. Specific measurements taken are summarised in *Table 6-18* and an example of a TEM cross-section, used to determine the coating thickness, is shown in *Figure 6-45* (bottom image). For each measurement, several TEM images were acquired and, moreover, also within each image two to three thickness measurements were performed. As can be seen from the thickness values stated in *Table 6-18*, the average thickness in all cases is between 9.4 and 10.2 nm, independent of the barrier performance and also independent of the application of a plasma treatment. This thickness is approximately only one fourth of the thickness of an aluminium barrier layer on a standard metallised film with an optical density of 2.5 [295], which is used in food packaging applications

Table 6-18: AlO_x coating thickness, as determined via transmission electron microscopy

Film	Plasma treatment	Thickness
		nm
BOPP A	Pre + post	10.1 ± 0.5
BOPP B	No	9.8 ± 0.4
	Pre + post	9.6 ± 0.7
BOPP C	No	9.9 ± 0.6
	Pre	10.2 ± 0.5
	Pre + post	10.1 ± 0.6
BOPP D	Pre	9.5 ± 0.5
BOPP E	Pre	9.8 ± 0.5
PET	Pre + post	9.4 ± 0.6

Figure 6-45 shows representative TEM cross-section images for AlO_x coated BOPP C at two different magnification levels. Similar high-resolution TEM cross-sectional images for AlO_x coatings (on PET) have been published by Kobayashi et al. [294], Barker et al. [16] and Phillips et al. [288]. For standard commodity grade BOPP films, TEM generally revealed the typical three-layer structure, with a core layer surrounded by a skin layer on each side. One of these skin layers, i.e. the skin

layer that is coated, is visible in *Figure 6-45* (top image) and *Figure 6-46* and reveals a thickness of less than 0.5 µm. It is, furthermore, noticeable from the lower magnification TEM image that the AlO_x layer is fractured and appears inconsistent. This damage is a result of the sample preparation process, i.e. the compression during microtoming, and the different elastic properties of the BOPP polymer, the embedding medium and the ceramic AlO_x layer. Similar damage has also been reported by other researchers investigating TEM cross-sections of thin oxide layers on polymer substrates [360].

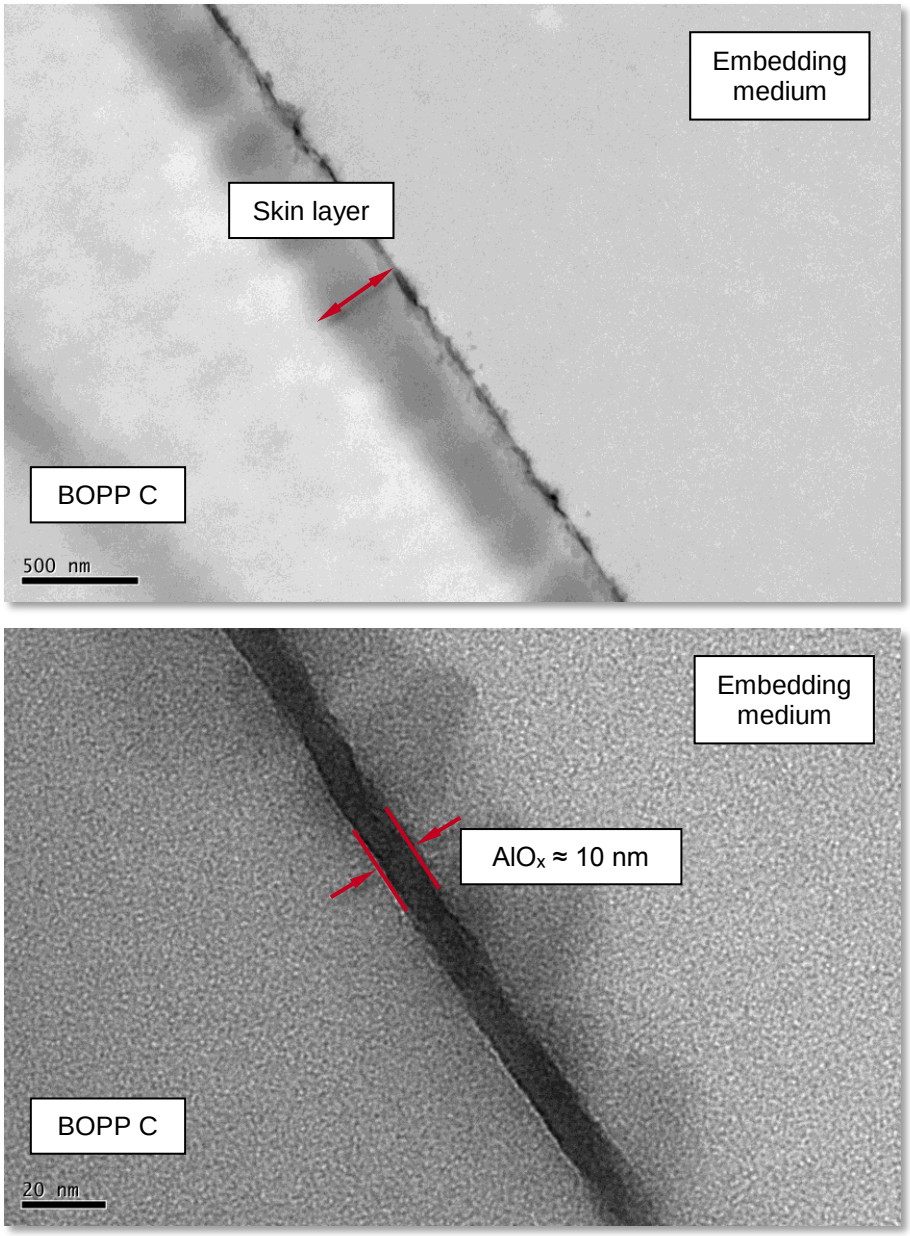

Figure 6-45: Transmission electron microscope cross-sections of AlO_x coated BOPP C at different magnification levels

The coating thickness found in this study is similar to aluminium oxide barrier layers deposited by other researchers [37, 40, 288], using evaporation processes, who

found that effective barrier properties can be obtained at such a coating thickness. However, it disagrees with Kelly [3], who stated that below 15 nm coating thickness, the reactively evaporated AlO_x layer is discontinuous and barrier properties are impaired[j].

In addition to enabling the investigation of AlO_x coating thickness, TEM also revealed other interesting observations. For example, antiblock particles were found in the TEM cross-sections, as illustrated in *Figure 6-46*. From this image, it can be seen that, if an antiblock particle of less than a micron in size is fully enclosed by the BOPP skin layer, the antiblock particle will not necessarily create a defect in the coating, but can be over-coated by the AlO_x layer.

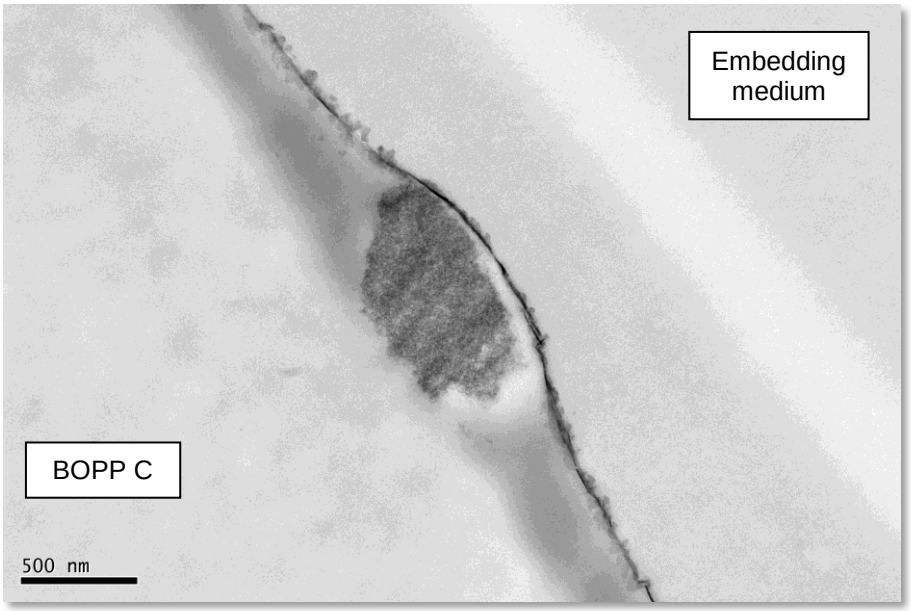

Figure 6-46: Transmission electron microscope cross-section of AlO_x coated BOPP C with antiblock particle in skin layer

Attempts were also made to investigate the structure of the AlO_x coating, using the TEM cross-section images. Here, it appeared that the coating was 'darker' near the polymer interface and also at the free surface (near the embedding medium), as can be seen in *Figure 6-45* (bottom image). Nevertheless, this could not specifically be detected for certain samples/films or treatments only. Consequently, no structural differences were visible between the AlO_x coatings on the various BOPP films and PET reference film at the resolution level provided by TEM analysis. It is, therefore, concluded that the structure and potential differences of the approximately 10 nm thin AlO_x coatings cannot be resolved using TEM analysis of cross-sections. There

[j] More information on AlO_x coating thicknesses, used by other researchers for barrier applications, can be found in Chapter 6.2.1.4. These coatings were produced by a variety of techniques including electron beam evaporation (reactive/non-reactive) and sputtering.

are, though, techniques available for the analysis of the microstructure and also crystallinity of thin (barrier) layers on polymer films. Therefore, the polymer substrate is dissolved/etched away using ortho-chlorophenol or trifluoroacetic acid (for PET) and toluene (for BOPP) and the remaining coating (on a copper grid) is subsequently analysed using TEM (combined with electron diffraction). This technique was reported successful for SiO_x, AlO_x and aluminium coatings on PET [16, 129, 140, 157, 291, 361-363] and aluminium coatings on BOPP [332, 333]. In the latter work, it was also found that in the case of AlO_x layers on BOPP (electron beam evaporated), the coating decomposed in the toluene along with the polymer and, hence, no TEM analysis was possible. Based on this (and also due to time constraints), similar analysis was not carried out for this project. Barker and co-workers [16] found (using the technique described above) that oxygen-rich AlO_x coatings (i.e. no metallic aluminium measured via XPS, see Chapter 6.2.3) of 25 nm thickness on PET are solely amorphous, whilst metal-rich coatings (i.e. metallic aluminium present as seen via XPS) of 20 nm thickness consist of an amorphous oxide matrix with dispersed aluminium crystallites. Furthermore, Zywitzki et al. [344, 345] also detected that up to a substrate temperature of 700 °C, AlO_x layers deposited via reactive electron beam evaporation are amorphous. In the latter case, thick (several µm) oxide layers were deposited onto stainless steel and analysed using X-ray diffraction. Thinner coatings in the range of 10 to 60 nm were, however, not investigated by this research group [364]. They, additionally, state that by the use of plasma assistance, this threshold temperature could be reduced to 600 °C, at which the first signs of a crystalline γ-phase emerged [345]. Similar results for crystalline/amorphous coatings with regards to the deposition temperature have also been reported by Bunshah and Schramm [365] and Yoon et al. [350] for plasma activated electron beam evaporation. Moosheimer [332, 333], however, concluded from AFM scans that in his case of AlO_x layers deposited onto BOPP via (non-reactive) electron beam evaporation, a polycrystalline coating was obtained. This was, though, not further investigated using X-ray or electron diffraction (see above).

Although the deposition temperature is quite difficult to estimate (see short discussion in Chapter 6.1.4), it is known that the temperature is a lot lower than required for crystalline AlO_x, based on the references above. Furthermore, the literature cited refers in all cases to reactive electron beam evaporation and it is expected that during boat evaporation the species in the gas phase will have lower energies, compared to electron beam evaporation. Therefore, an even higher temperature may be required to yield a crystalline phase. It is, consequently, assumed that the barrier layers deposited here are of an amorphous nature.

6.2.6 Coating adhesion (peel test)

As vacuum coated films are further converted by laminating another polymer on top of the coating or by applying a topcoat to protect the barrier layer (see Chapters 6.4.2 and 6.5), good coating-to-substrate adhesion is an important criterion in order to prevent delamination during the final packaging application of the composite material. The adhesion strength of the reactively evaporated AlO_x coating to the BOPP films was assessed using a peel test designed for the determination of the adhesion of aluminium coatings on polymer films. A main requirement for the validity of this test is the achievement of full coating, i.e. metal, removal. Earlier investigations of AlO_x adhesion to BOPP films have shown that this peel test can be applied in the case of AlO_x coated polymer films, as full coating removal was possible and visible to the naked eye, despite the transparency of the coating. This is shown for peel test samples (after peeling) of AlO_x coated BOPP D in *Figure 6-47*. For better visual clarity, a white coloured double-sided adhesive tape is used for the peel tests.

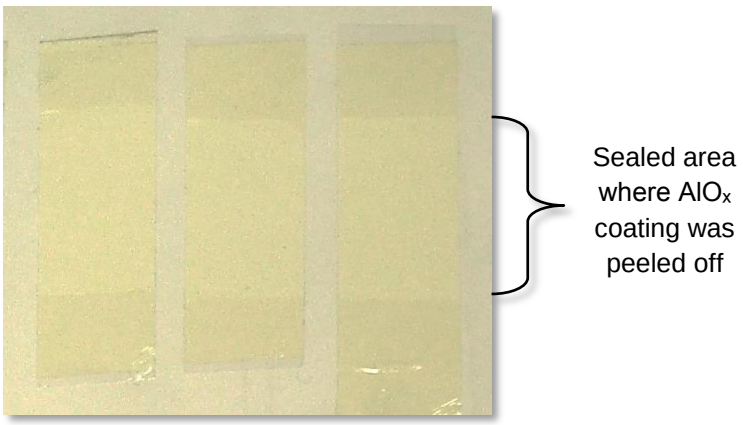

Figure 6-47: AlO_x coated BOPP D (0.03 OD when AlO_x coated) after peel test, coating removed visibly in centre area of each strip

In general, the AlO_x coated BOPP films (when aged) have a light transmission of 91 to 93 % (converted from 0.04 – 0.03 OD), with the light transmission of the uncoated BOPP film being similar or marginally higher (refer to Chapter 6.2.7). The peel strength values obtained and corresponding standard deviations are summarised in *Table 6-19* for the AlO_x coated BOPP films investigated and also for the PET reference film. Additionally, BOPP A, B and C were metallised (2.0 to 2.1 OD) and the measured adhesion of the aluminium layer is also displayed. Full 'visual' coating removal was obtained for all coatings (AlO_x and aluminium) on BOPP. In all cases, apart from BOPP F, very high peel strength values were obtained for the AlO_x coated films. With the exception of BOPP C, these values (for

the AlO_x coated BOPP films) exceed the adhesion values obtained for aluminium metallised standard packaging grade BOPP film, which are generally (a lot) less than 1.75 N/(15 mm) [64, 77, 245]. Also Kelly [2] mentions that the adhesion of the oxide to a polymer substrate is considerably higher than that of the metal itself, though no actual adhesion values are quoted.

Table 6-19: Measured peel forces for AlO_x coated films and metallised references following no plasma and in-line plasma pre- and post-treatments

Film	Plasma treatment	Peel force N/(15 mm)
BOPP A	No plasma	3.16 ± 0.11
	Pre	3.15 ± 0.12
	Pre + post	3.13 ± 0.08
	**Metallised (pre)*	*0.82 ± 0.04*
BOPP B	No plasma	3.46 ± 0.08
	Pre	3.51 ± 0.10
	Pre + post	3.50 ± 0.16
	**Metallised (pre)*	*0.78 ± 0.03*
BOPP C	No plasma	5.05 ± 0.17
	Pre	5.07 ± 0.12
	Pre + post	5.04 ± 0.14
	**Metallised (pre)*	*4.89 ± 0.06*
BOPP D	Pre	4.65 ± 0.09
BOPP E	Pre	3.61 ± 0.15
BOPP F	No plasma	0.60 ± 0.02
	Pre	0.58 ± 0.01
	Pre + post	0.54 ± 0.02
PET	Pre + post	> 6.00

*no AlO_x, but aluminium coating

It is, additionally, obvious from *Table 6-19* that the adhesion strength values obtained for BOPP film type A, B, C and also F appear unaffected by the plasma pre-treatment. Since plasma pre-treatment is generally applied in order to enhance adhesion of vacuum deposited barrier layers, an increase in the measured peel force would be expected (if over-treatment is avoided), as for example found for metallised BOPP [77, 249, 270]. This is attributed to the incorporation of functional

groups into the BOPP film surface, which act as nucleation sites and interaction points between coating and substrate, therefore enhancing adhesion properties. In the case of the AlO_x layers deposited here, average peel force values around 3.1 to 3.2 N/(15 mm) are obtained for BOPP A, 3.5 N/(15 mm) for BOPP B, 5.0 N/(15 mm) for BOPP C and 0.5 to 0.6 N/(15 mm) for BOPP F, which are independent of the application of in-line pre-treatment. The reason for the low peel force values achieved for BOPP F is related to the base film being coextruded with a different polymer as the skin layer and will be discussed later in this chapter. It is, furthermore, important to note that high peel force values were not only achieved independent of the plasma pre- treatment applied, but also independent of the barrier performance (see barrier properties of AlO_x coated BOPP A, Chapter 6.2.1.1, *Table 6-10*), thus indicating that insufficient barrier properties are not related to poor adhesion.

The high peel strength values (obtained for the standard BOPP films), together with the apparent independence from the plasma pre-treatment, suggest that in addition to the AlO_x coating some polymeric material, such as the skin layer of the BOPP films, is removed during the peel test. Furthermore, when performing the peel tests on BOPP C, material was also peeled off from outside the sealed area. Consequently, the peeled-off EAA films were further analysed using single bounce diamond ATR-FTIR spectroscopy, to detect the possible presence of polypropylene and investigate the locus of the adhesion failure [120]. The evanescent wave in ATR-FTIR spectroscopy has a wavelength dependent penetration depth, which is in the region of up to a few µm for PP (refer to Equation (5-10); refractive indices taken from references [218, 285]). Consequently, small residues of polymeric material on the peeled-off EAA film will not be detected. However, if a layer with a thickness of several 100 nm of polymer is peeled off, e.g. the BOPP skin layer, this will be visible in the ATR-FTIR spectra. For all of the AlO_x coated BOPP films, ATR-FTIR confirmed that polymeric material, presumably the BOPP skin layer (and in the case of BOPP F, the high surface energy polymer skin layer), was present on the peeled-off EAA film. *Figure 6-48* shows the ATR-FTIR spectra obtained for the EAA film (top), the corona side of BOPP A (middle) and the peeled-off EAA film (bottom). The bottom spectrum (peeled-off EAA) shows peaks that are unique to the BOPP film and unique to the EAA film, thereby indicating presence of both polymers in the sample. For PP, the peaks in question are around 2950 cm^{-1} and 1370 cm^{-1} (asymmetric C-H stretching of $-CH_3$ group and symmetric C-H bending of $-CH_3$ group, respectively [366]) and for the EAA film, the peaks in question occur at around 1700 cm^{-1} and as a double peak around 720/730 cm^{-1} (C=O stretching of carboxyl group and CH_2 rocking of polyethylene, respectively [282, 367]).

Consequently, this investigation shows that cohesive failure occurred during the peel tests, i.e. the locus of failure is not at the interface between coating and substrate, but within the substrate itself. As the failure in a multilayer structure generally initiates at the weakest point of the system [117], it can be assumed that the adhesion of the AlO_x coating to the BOPP film exceeds the measured values, which most likely represent the adhesion between the skin layer and the core layer of the BOPP film.

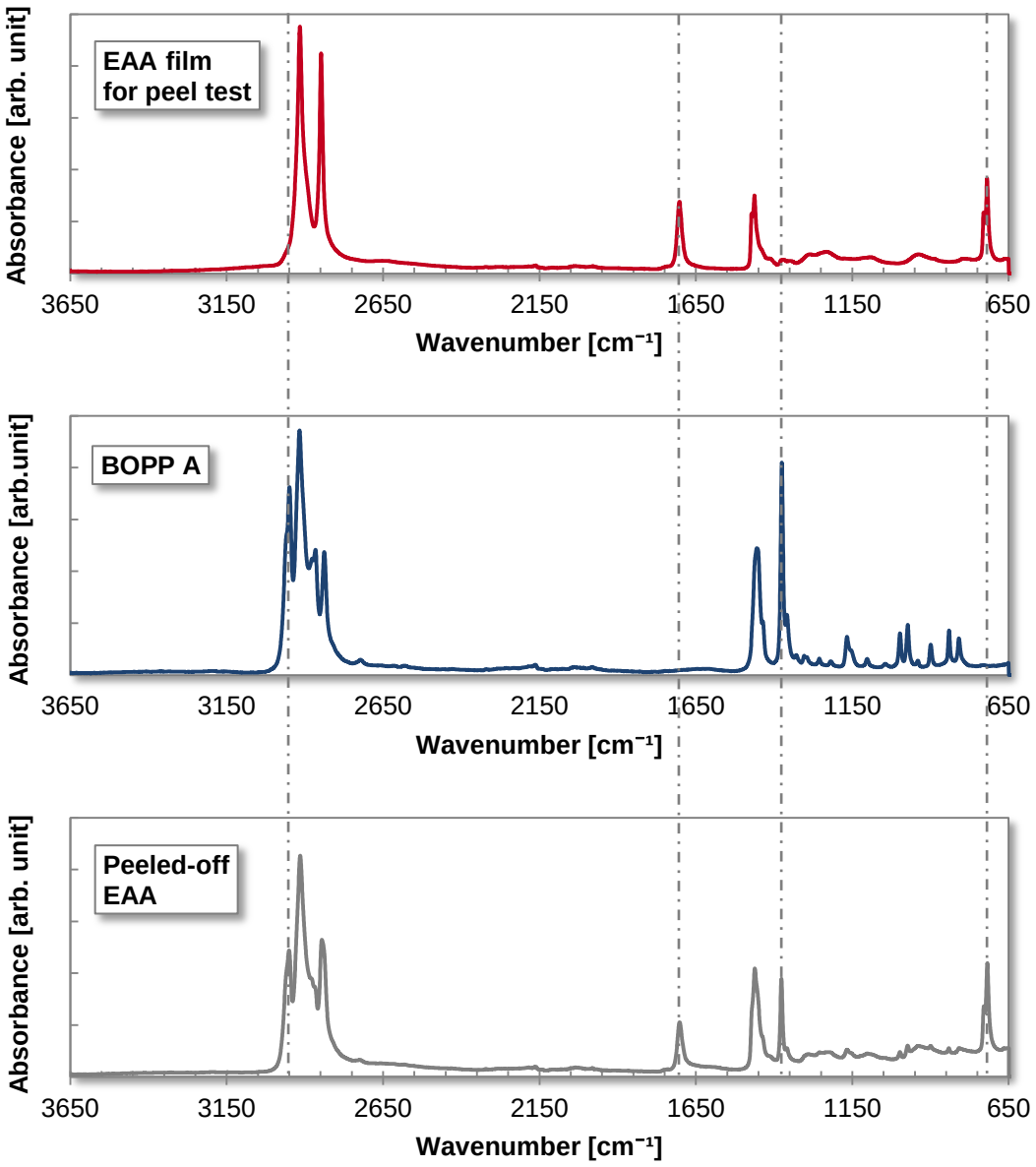

Figure 6-48: ATR-FTIR spectra of the EAA film used for peel tests (top), BOPP film A (middle) and the peeled-off EAA film (bottom)

In the case of metallised BOPP C, the ATR-FTIR also showed BOPP skin layer removal, similar to the AlO_x coated films. This was to be expected, based on the peel force value (see *Table 6-19*), which is nearly identical to the values obtained for

AlO_x coated BOPP C. Nevertheless, BOPP C was the only metallised film to reveal such a high peel force value and also ATR-FTIR confirmed no skin layer removal for metallised BOPP A and B (see low peel force values for these films in *Table 6-19*).

The 'abnormal' behaviour of metallised BOPP C is attributed to the fact that this BOPP film revealed a larger amount of oxygen, and hence oxygen-containing functional groups, in its surface (refer to Chapter 6.1.3.2). It is, consequently, argued that the increased presence of functional groups resulted in the better aluminium adhesion on BOPP C. Additionally, Friedrich et al. [273] reported that for PP functionalised with various oxygen-containing groups (via treatment and primer layers) prior to aluminium evaporation, cohesive failure within the PP substrate was obtained during peel tests, depending on the type of functionalisation.

For AlO_x coated PET, it was, nonetheless, not possible to peel off the AlO_x layer. Here, the EAA film stretched until it tore at values around 6 to 7 N/(15 mm), without removing any AlO_x or parts of the PET film. This is attributed to the PET substrate used being a single-layer and not a coextruded film. Due to the high intrinsic strength of this single-layer material, no cohesive failure within the PET film could occur. Indeed, in the case of PET, the EAA peel test is known to be reaching its limits [120]. Furthermore, a value of approximately 7.5 N/(15 mm) has been reported by other researchers [368, 369] to be the upper limit when using the EAA peel test (EAA thickness assumed to be 50 µm), whilst beyond this value the EAA film breaks due to its low cohesive strength. Nevertheless, Cueff and co-workers [370] also used an EAA peel test (different sealing conditions and peel speed) to determine the adhesion of 75 nm thick sputtered AlO_x layers on 12 µm PET and state values of up to 20 N/(15 mm). This is surprisingly high, as in our case the EAA film could not withstand a force of more than 7 N/(15 mm) before tearing. However, the thickness of the EAA film used was not stated (this would affect the strength of the EAA film), the sealing and peeling conditions were different (125 °C, 300 s, peel rate 100 mm/min) and, furthermore, it is not known whether the PET substrate was a single-layer material or multilayer coextruded film. Increasing the peel rate and also the use of a thicker EAA film have been shown to lead to a rise of the peel force value measured [371, 372]. Miyamae and Nozoye [373] report on cohesive failure of the substrate for peel tests carried out on AlO_x coated PET (15 nm coating thickness, reactive electron beam evaporation), as detected via XPS analysis. Nevertheless, they only state that an auxiliary sheet is used to peel the AlO_x layer off (180° peel test, 300 mm/min), but do not further specify the material type or how it is bond to the AlO_x coating.

With respect to the EAA peel test carried out for standard BOPP films coated with AlO_x barrier layers, Moosheimer and Bichler [64, 333] report on the adhesion of 40 nm thin AlO_x layers electron beam evaporated onto BOPP films with a homopolymer and copolymer (propylene-ethylene) skin layer. They investigated the effect of oxygen plasma and corona pre-treatment. In the case of the copolymer skin layer, average peel force values around 2.4 N/(15 mm) were obtained for the corona treated film, as well as the non-treated and oxygen plasma treated film. For the homopolymer BOPP, the value was approximately 1.4 N/(15 mm), but also largely independent of the oxygen plasma pre-treatment. Only the corona treated homopolymer BOPP revealed a lower peel force value. In this publication, the independence of AlO_x adhesion from the pre-treatment was attributed to the oxygen being readily available from the coating material and, consequently, the small amount of oxygen incorporated into the BOPP by the pre-treatment being not effective in improving adhesion. Nevertheless, they did not investigate whether the polymer skin layer was peeled off along with the AlO_x coating, although the high peel force values obtained for the copolymer skin layer would suggest that this may have been the case (similar as found in this study for different co/terpolymer skin layers). That the peel force values are still lower than achieved here can be due to differences in the EAA film used (e.g. the film thickness; Moosheimer [371] used a 25 µm thick EAA film; apart from this, the test was identical to the one used in this thesis) and, of course, differences in the BOPP film substrate. The measured peel force is, additionally, also affected by the deformation of the EAA film [120], which in the case of the AlO_x coated BOPP films investigated here was elastic, as well as plastic.

In order to rule out the possibility of the EAA film melting through the thin AlO_x layer onto the BOPP surface, thus leading to the high peel forces, peel force values for an EEA film sealed to the plain BOPP film surface (corona treated side/high surface energy skin polymer side) were determined under the same conditions. The results of this investigation are summarised in *Table 6-20*.

For all standard BOPP films, apart from BOPP D, the values obtained are between 0.1 to 0.9 N/(15 mm), clearly below the measured peel force values for the AlO_x coated BOPP films, and ATR-FTIR analysis did not show polypropylene on the peeled-off EAA. The only exceptions to this outcome are BOPP D and also BOPP F. For these two films, the skin layer is removed during peel tests for the plain and the AlO_x coated BOPP, as confirmed by ATR-FTIR. From *Table 6-19* and *Table 6-20*, it can also be seen that the measured peel force values for BOPP D and F in both cases (EAA sealed to AlO_x coated and uncoated BOPP) are identical. In the case of

BOPP D, this may be due to a lower sealing temperature of the skin layer, presumably induced by the relatively high butylene content (refer to Section 6.1.3.4). Also BOPP C revealed a higher butylene content, and this may also be the reason for the relatively high peel force of 0.82 ± 0.18 N/(15 mm), which is greater than obtained for the other standard BOPP films. In general, it can be assumed that the peel force measured for the plain film may not only be affected by the sealing temperature of the skin layer (and hence skin layer composition), but also the age of the film and consequently contamination of the film surface with low-molecular-weight material or film additives.

Table 6-20: Measured peel force values for EAA film sealed to plain BOPP films

Film	Side	Peel force
		N/(15 mm)
BOPP A	Corona	0.15 ± 0.01
BOPP B	Corona	0.09 ± 0.00
BOPP C	Corona	0.82 ± 0.18
BOPP D	Corona	4.61 ± 0.13
BOPP E	Corona	0.51 ± 0.06
BOPP F	High surface energy polymer	0.58 ± 0.02

For BOPP F, the peel force value for the AlO_x coated film (0.5 to 0.6 N/(15 mm)) is quite low, compared to the other AlO_x coated BOPP films. This is due to the fact that coextruding and orienting the different polymer skin layer with the polypropylene film is quite difficult, owing to the different polymer characteristics (e.g. melting point, mechanical properties). Consequently, an adhesive layer is required to tie the high surface energy polymer skin layer to the BOPP core film [70]. In the case of BOPP F, this results in a lower adhesion between the skin layer and the core, compared to the adhesion between a standard co/terpolymer skin layer and the homopolymer core. Hence, the skin layer readily peels off when the EAA film is sealed to uncoated BOPP F.

In addition to the 'standard' AlO_x coating on BOPP, peel tests were also carried out for a thicker AlO_x layer (on BOPP A), for a BOPP film containing migratory additives and for different AlO_x stoichiometries (BOPP B). In the case of an approximately 25 nm thick AlO_x layer on BOPP A, peel force values similar to the standard 10 nm thin AlO_x coating were obtained, and ATR-FTIR also revealed that parts of the BOPP film were removed during the peel test. This value is higher than obtained for metallised BOPP A (2.0 – 2.1 OD, see *Table 6-19*), which has a coating thickness of

approximately 35 nm [295]. For BOPP films containing migratory (slip) additives, such as erucamide (note: these films were not intended for vacuum web coating according to their specification), average peel forces ranged between 0.5 and 2 N/(15 mm), and ATR-FTIR did not show PP material on the peeled-off EAA. This is not surprising, since slip additives are known to reduce the adhesion in the case of metallised films [92].

For the investigation of the effect of coating stoichiometry on AlO_x adhesion, four samples of AlO_x coated BOPP B were chosen, ranging from a 'standard' stoichiometry with $x \approx 1.5$ to the sample with the highest aluminium content with $x \approx 1.0$ (more information on the stoichiometry of the AlO_x coatings can be found in Chapter 6.2.3). The peel force results are presented in a column chart in *Figure 6-49*. The length of the red columns is equivalent to the average peel force measured, whilst the grey outline represents the standard deviation.

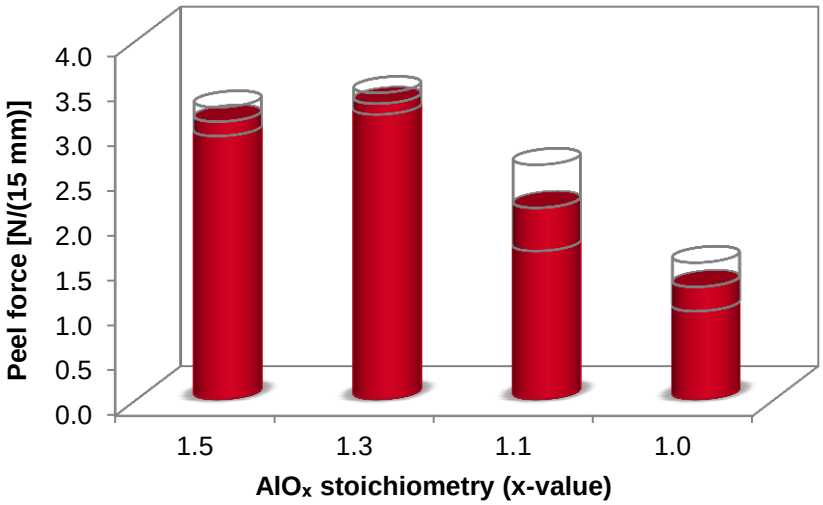

Figure 6-49: Peel force values obtained for AlO_x coated BOPP B as a function of AlO_x stoichiometry

As can be seen from *Figure 6-49*, there is a clear declining trend of the measured peel force with decreasing the x-value, i.e. increasing the (metallic) aluminium content in the AlO_x coating. For an x-value of 1.5 and 1.3, the peel force values are identical within experimental error. When the x-value is further reduced to 1.1 and 1.0, the average peel force value measured drops and standard deviations are increased. ATR-FTIR revealed full BOPP skin layer removal across the sealed area for an x-value of 1.5, whilst for x = 1.3 some samples showed small patches where the skin layer was not peeled off. For x = 1.1 and 1.0, the amount of patches without BOPP skin layer removal increased drastically and spread across the whole sealed area. These patches are, additionally, visible to the naked eye, since at the border

between polymer substrate removal and no removal a narrow strip of the dark AlO_x coating remains, as can be seen from *Figure 6-50*. The investigation of peel force values as a function of AlO_x stoichiometry exposes an interesting observation, in that the coating adhesion appears to drop when the amount of metallic aluminium in the coating is increased.

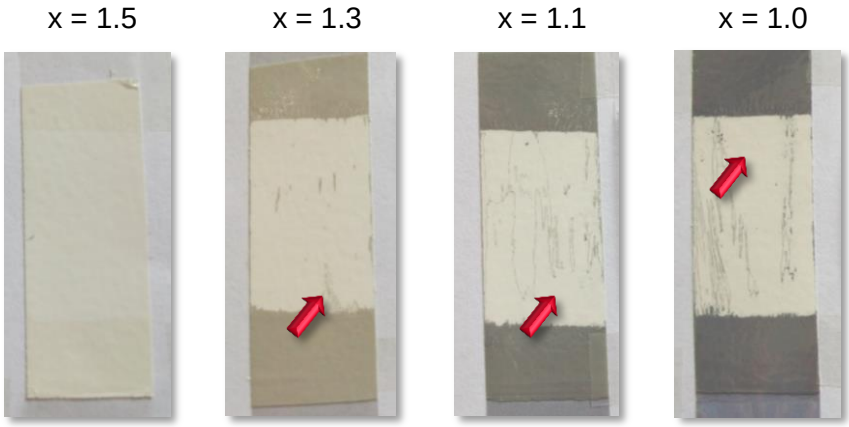

Figure 6-50: AlO_x coated BOPP B of various stoichiometries after peel test; marked with red arrows are areas without polymer substrate removal

In summary, it is quite surprising that the adhesion depends on AlO_x stoichiometry and, furthermore, generally appears a lot lower for metallised BOPP. It has been shown by McClure and Copeland [295] and McClure et al. [249] that, when metallising PET as well as BOPP, there is always an aluminium oxide layer of approximately 3 nm at the interface between the BOPP/PET film and the aluminium coating (and also at the free surface of the aluminium coating). Based on that, one would expect to get the same good adhesion (and skin layer peel-off), as obtained for AlO_x layers, in the case of metallised BOPP. However, if the weakest point in this 'multilayer system' (BOPP/AlO_x/Al/AlO_x) is between the AlO_x and the aluminium layer, the failure during peel test would occur at this plane. This means that the metal layer would be peeled off and the transparent interfacial AlO_x layer (of approximately 3 nm thickness) would be left behind on the film substrate. Therefore, it would be interesting to use further analytical techniques, such as XPS analysis and TEM cross-sections, on the peel test samples of metallised BOPP (with full visual coating removal), in order to investigate the locus of adhesion failure. Nakamura and Nakamae [269] have done a XPS study on samples of metallised PP following a peel test, but could, however, not detect any aluminium (only carbon and oxygen) on the substrate surface in the case of full aluminium coating removal (as judged visually).

6.2.7 Optical properties

6.2.7.1 Optical density

A critical property and substantial requirement of the AlO_x coated polymer films is their transparency. As mentioned previously in Chapter 6.2.1.2, an important process, so-called 'ageing', takes place as soon as the film is exposed to an ambient environment, i.e. the coated film roll is exposed to atmospheric gases (after the vacuum in the coater is released). This process is supposed to be due to oxidation of unreacted (metallic) aluminium in the as-deposited AlO_x coating, which is caused by the uptake of oxygen and humidity from the atmosphere, and leads to a decrease in OD (increase in light transmission) over time until a stable condition is reached. In the case of metallised polymer films, it is well-known that an oxidation phenomenon takes place (due to the reactivity of aluminium), which leads to a decline of the measured OD with time until a stable surface oxide is formed (approximately 3 nm in thickness), which protects the remaining metal layer from further oxidation [295, 374, 375].

For the AlO_x coated films, it is also suspected that this oxygen/moisture uptake (probably resulting in swelling/densification) of the coating plays an important role in conferring the barrier properties to the AlO_x coating (discussed in detail in Section 6.2.1.2). For the following investigation, the OD profile for AlO_x coated BOPP A was measured with a densitometer (orthochromatic response) immediately after the coating process and subsequently during the following few days. A measurement was taken every 1 cm of the film width and results are illustrated in *Figure 6-51*.

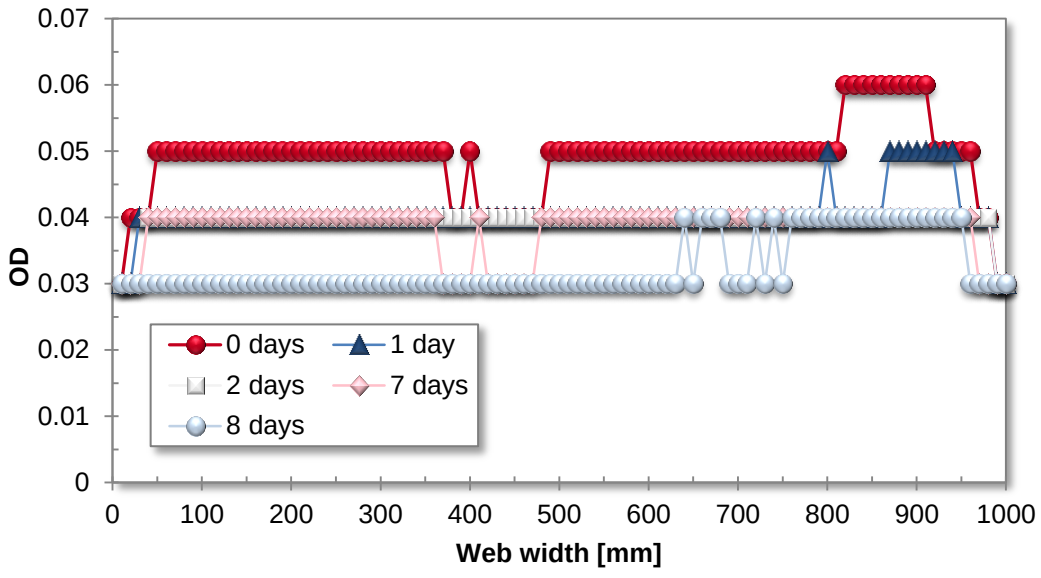

Figure 6-51: Variation of OD profiles for AlO_x coated BOPP A with time

Immediately after coating, the OD level was around 0.05 to 0.06. After only one day, the OD level decreased down to 0.04 and after 8 days most of the points measure 0.03 OD, which is equivalent to the plain film OD. Consequently, the target OD level for transparent packaging applications, which is between 0.03 and 0.04 OD, has been reached. Furthermore, differences between 0.03 and 0.04 OD on an individual film sheet are not visible to the naked eye. The behaviour shown in *Figure 6-51* is typical for AlO_x coated polymer films, independent of the substrate, although there can be some individual variations.

Kelly [2] gives an OD range of 0.5 to 0.8 for laminates of AlO_x coated PET, which is slightly 'darker' than the coatings obtained here. Although these ODs refer to a laminate, it is assumed that the OD of the non-laminated film is identical, since it was found in this project that the lamination (i.e. addition of an additional adhesive and polymer layer) did not alter the OD of the AlO_x coated film. Here, it should also be mentioned that the light source used (i.e. wavelength range) to determine the optical density will affect the values measured (similar to the light transmission that can be determined for different wavelengths in the visible spectrum, see Chapter 6.2.7.2). In this thesis, an orthochromatic response densitometer was used. Nevertheless, it is unknown which type of equipment was used by the reference cited.

As can be seen from *Figure 6-51*, when AlO_x barrier coatings are produced via reactive evaporation, they are not deposited as completely transparent but as marginally absorbing layers and, as a result, slightly grey coatings are initially obtained. It has been mentioned by several researchers and patents that an initial sub-stoichiometric and absorbing coating is deposited, which is further oxidised in a secondary post deposition oxidation step, e.g. via exposure to atmosphere, further downstream processing inside the vacuum chamber or also by the use of plasma techniques [15, 42, 376-378]. Furthermore, Schiller and co-workers [27] state that when coatings are deposited with an excess of oxygen (i.e. the coating is deposited fully transparent), the layer properties are poor due to the porous structure and insufficient barrier properties are obtained.

6.2.7.2 Light transmission

In addition to the OD, measured with an orthochromatic transmission densitometer, the light transmission was measured over the wavelength range of 400 to 750 nm (visible light) using a spectrophotometer. For this investigation, various AlO_x coated and non-coated BOPP films, as well as the PET reference film (coated and non-coated), were investigated. The measurements were conducted after the OD had stabilised (see Section 6.2.7.1). In *Figure 6-52*, the spectra of AlO_x coated and plain BOPP A and PET are depicted. Additionally, the spectrum of BOPP C is displayed, in order to show that the uncoated BOPP films exhibit very similar visible light transmission. The average light transmission values over the wavelength range of 400 to 750 nm are summarised in *Table 6-21*. From the graphs and the average values, it can be detected that there is virtually no difference between the individual coated and non-coated films, hence indicating that the AlO_x layer is transparent and non- or only marginal absorbing, with most of the absorption (reduction from 100 % light transmission) being caused by the underlying polymer.

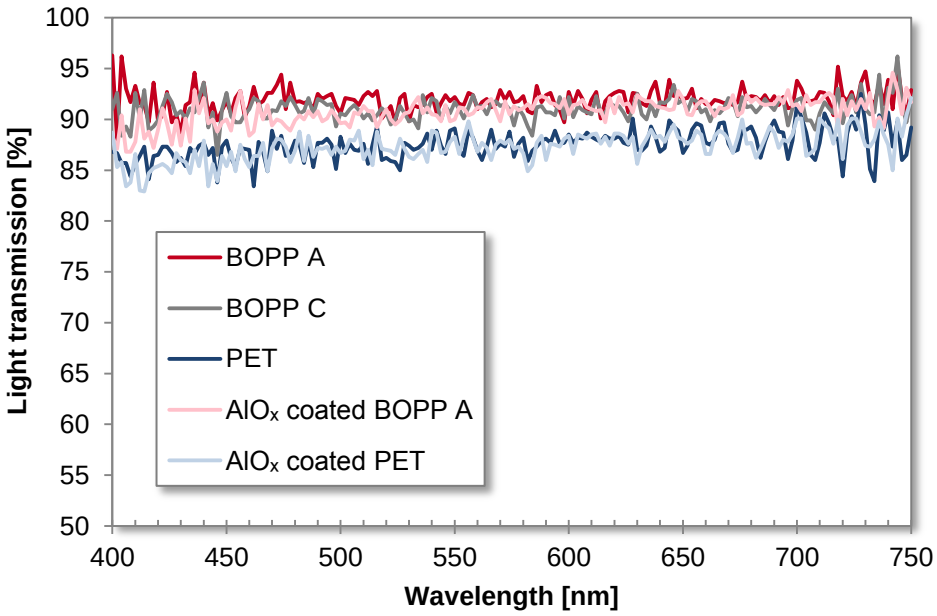

Figure 6-52: Light transmission spectra for AlO_x coated and non-coated polymer films

Nevertheless, the light transmission for PET (plain and AlO_x coated) is lower than for BOPP, which is due to the inherently lower light transmission of the PET substrate, in contrast to BOPP. Light transmission for all samples investigated is quite uniform over the analysed wavelength range. However, noise is always present and is increased towards the wavelength of UV and IR radiation (a function of the visible light source used). Furthermore, if one converts the OD generally measured on a densitometer for uncoated 12 µm PET film (0.04) and uncoated 20 to 30 µm thick

BOPP film (0.03) to the corresponding light transmission, values of 91.2 % and 93.3 %, respectively, are obtained. These values are higher than the values measured using a spectrophotometer (refer to *Table 6-21*), which may be attributed to the densitometer using an orthochromatic response (i.e. not sensitive to red light).

Table 6-21: Light transmission of uncoated and AlO_x coated films, averaged over the investigated wavelength range of 400 to 750 nm

Film	Coating	Light transmission
		%
BOPP A	(uncoated)	91.9 ± 1.2
	AlO_x	90.8 ± 1.3
BOPP C	(uncoated)	91.0 ± 1.2
PET	(uncoated)	87.5 ± 1.5
	AlO_x	87.3 ± 1.5

The results found here are in broad agreement with data published by Schiller et al. [27], who showed that AlO_x layers of 20 nm thickness are fully transparent for an x-value of approximately 1.4 onwards. The AlO_x layers deposited in this project are even thinner (roughly 10 nm, see Chapter 6.2.5) and also exhibit a stoichiometry in this range (refer to Chapter 6.2.3). Kobayashi and co-workers [294] state an optical transparency of 80 % for a 25 µm thick uncoated PET substrate, which was approximately maintained after AlO_x deposition via reactive evaporation of aluminium when the oxygen flow was controlled appropriately. Nevertheless, in their case, the optical transparency was measured at a wavelength of 350 nm. Misiano et al. [42] measured a light transmission of 81.2 % at 550 nm for their reactively evaporated AlO_x layer on 12 µm PET, which indicates a small reduction from the light transmission of the uncoated substrate (85 %). After industrial lamination with PE, the light transmission was further reduced to 80.6 %. Fahlteich and co-workers [293] show a nearly constant light transmission just above 90 % in the visible wavelength range for their uncoated 100 µm PET substrate, which was decreased, though, by the application of a sputtered AlO_x barrier layer (to approximately 85 to 88 %). Also Louch et al. [379] measured a light transmission of approximately 90 % in the range of 400 to 750 nm for their PET substrate (no thickness stated), whilst Ludwig and Josephson [304] display a transmission spectrum for 12 µm uncoated PET that is comparable to the respective spectrum shown in *Figure 6-52*. In the latter publication, SiO_x barrier coatings were deposited, which slightly reduced the visible light transmission. The differences seen in the visible light transmission of the

uncoated PET substrates may be caused by different film grades (e.g. stabilised PET has a higher light transmission than non-stabilised PET at 550 nm wavelength [164]). For AlO_x coated PET, BOPP and PLA, Schiller and co-workers [12, 36] state an optical transmission of more than 98 %, although the wavelength used for this measurement, as well as the optical properties of the substrates, are not specified.

6.3 Flame and atmospheric plasma treatment of BOPP film

Based on the good barrier results obtained for AlO_x coated BOPP C, which were attributed to the higher oxygen content in the plain film surface, additional pre-treatment trials were carried out off-line, with the aim of increasing the oxygen content in the BOPP film surface. The film chosen for this investigation was BOPP B, which was initially corona treated after extrusion by the film manufacturer.

Flame treatment was selected as the first treatment for this study, since it has been found to be capable of incorporating large amounts of oxygen into the film surface without creating water-soluble low-molecular-weight oxidised material, i.e. there is less chance of over-treating the film surface and inducing excessive chain scissoring, as is the case for high corona treatment levels [61, 266]. Consequently, with flame treatment, high surface energy levels can be maintained over a longer period of time due to little/no ageing [255, 266]. Additionally, atmospheric plasma (dielectric barrier discharge) treatment, which has found widespread interest in recent years, and a combination of flame and atmospheric plasma treatment was performed. It has to be noted, though, that atmospheric plasma treatment can also suffer from the drawback of low-molecular-weight material formation [62, 88].

6.3.1 Surface topography

The surface topography of the treated films was initially examined using DIC light microscopy, in order to detect whether the flame and/or plasma treatment induced any visible changes to the surface topography at this level of magnification. In the following, the investigation only focusses on three of the treated samples, which are the ones that were subjected to the highest treatment levels of each treatment type (refer to *Table 5-2*, Chapter 5.2). To distinguish the three film samples, they will be referred to as flame, plasma and flame/plasma treated samples, without stating the respective treatment intensities.

Figure 6-53 shows high-resolution DIC images of corona treated BOPP B, i.e. the film surface before any additional off-line treatment, flame treated BOPP B, plasma treated BOPP B and flame/plasma treated BOPP B. It is noticeable from the images shown that the magnification level of light microscopy does not reveal any changes induced by the treatments. All four samples exhibit the same surface texture, i.e. bumpiness and granular structure. This is, nevertheless, not too surprising, as the treatments applied are known to only cause changes on the levels resolvable by SEM and AFM.

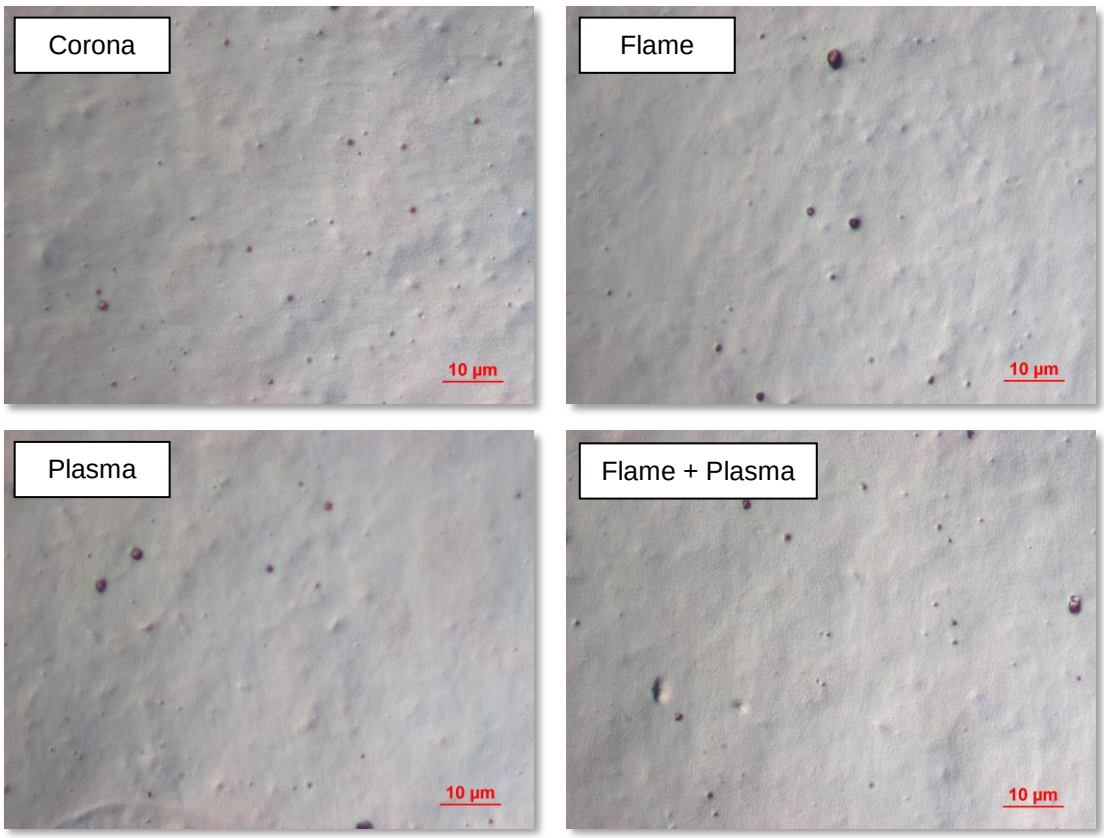

Figure 6-53: DIC light microscopy images of BOPP B (before AlO_x coating); top left: corona treated; top right: flame treated; bottom left: plasma treated; bottom right: flame/plasma treated

Consequently, SEM analysis was carried out for the three treatment variations, and representative images are depicted in *Figure 6-54*. Because the BOPP film samples are of an insulating nature and were not coated with a conductive layer to ease SEM analysis, well-focussed images at this magnification level were difficult to acquire. Judging from the SEM micrographs presented in *Figure 6-54*, the plasma and the combined flame/plasma treatment appear to have altered the surface topography of corona treated BOPP B, whilst the SEM image of the flame treated sample looks very similar to the one of the corona treated sample, but slightly less focussed. The changes in surface topography caused by the former two treatments are presumably due to etching and oxidising of the film surface. Nevertheless, the coarse-granular texture is still visible for all films. The most pronounced change can be seen for the sample treated by atmospheric plasma only. In this case, distinct globular mounds or nodules were created upon treatment, which are generally associated with low-molecular-weight oxidised material (further discussed later in this section, together with the results of AFM analysis). Also the BOPP film exposed to a combination of flame and atmospheric plasma treatment appears to show some of these globular features. Nevertheless, the number of these features is a lot lower and the film appears more similar to the corona or flame treated sample.

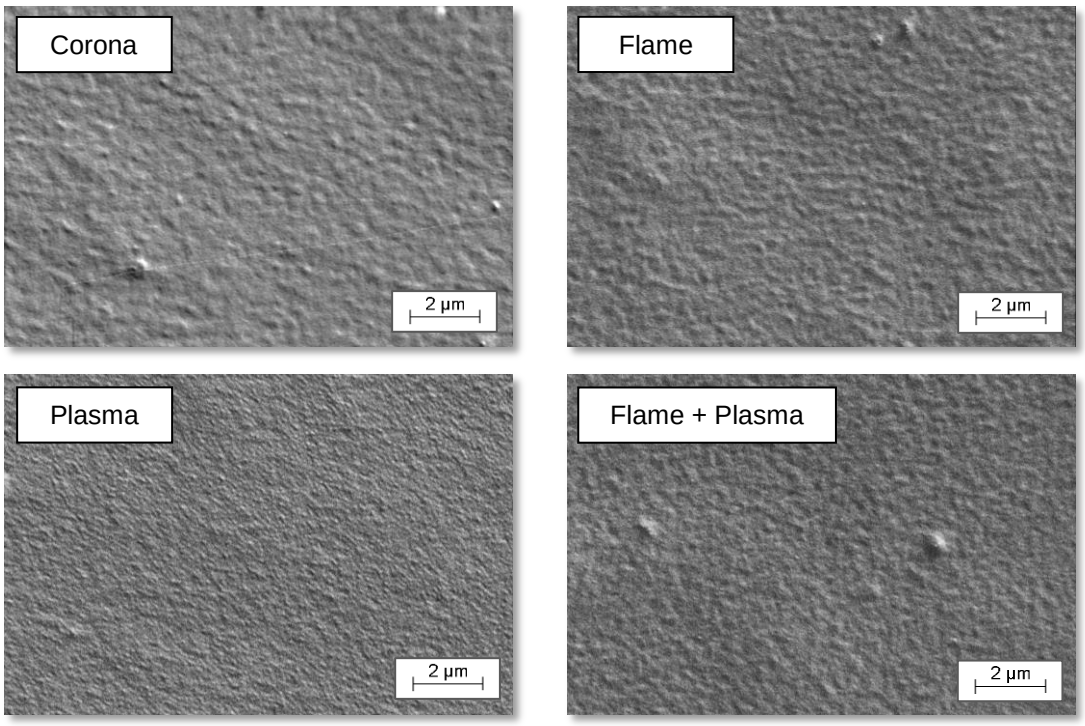

Figure 6-54: SEM images of BOPP B (before AlO_x coating); top left: corona treated; top right: flame treated; bottom left: plasma treated; bottom right: flame/plasma treated

AFM analysis was conducted using a scan size of 5 x 5 µm² as previously (refer to Chapters 6.1.2.4 and 6.2.2.3) and representative AFM images of this investigation are displayed in *Figure 6-55*, whilst the roughness data (mean values obtained from at least nine individual scans) is summarised in *Table 6-22*.

From the images presented in *Figure 6-55*, it can be concluded that the flame treatment did not induce changes to the film surface topography of corona treated BOPP B, since both scans (corona and flame treated BOPP B) show the same granular and bumpy texture without alteration. The atmospheric plasma treatment, however, shows a strongly modified surface topography. The bumpy background texture can still be recognised, but it is now covered in globular, droplet-like mounds or nodules. A similar treatment induced effect can be observed for the combined flame and atmospheric plasma treated sample, nevertheless, with the globular mounds being somewhat smaller in size. These additional globular features, which appeared after the off-line treatment, were also distinctively noticeable in the SEM image of plasma treated BOPP B and, to a lesser degree, in the one of flame/plasma treated BOPP B (see *Figure 6-54*). The globular features seen for these two treatment variations are believed to be caused by agglomerated low-molecular-weight oxidised material and have been observed by various researchers for corona treated [60, 61, 236, 252, 262, 266, 380] and also plasma treated (atmospheric- and low-pressure) [62, 78, 381-383] polypropylene using AFM and

SEM techniques. Here, it is important to state again that many corona treatments are somewhat incorrectly referred to as ‘corona’ treatment, since they do not make use of a true corona discharge, based on their electrode configuration (see also Chapter 4.2.3). It is, hence, difficult to draw a line between the results obtained by other researchers for ‘corona’ treated PP and atmospheric-pressure (air) plasma treated PP.

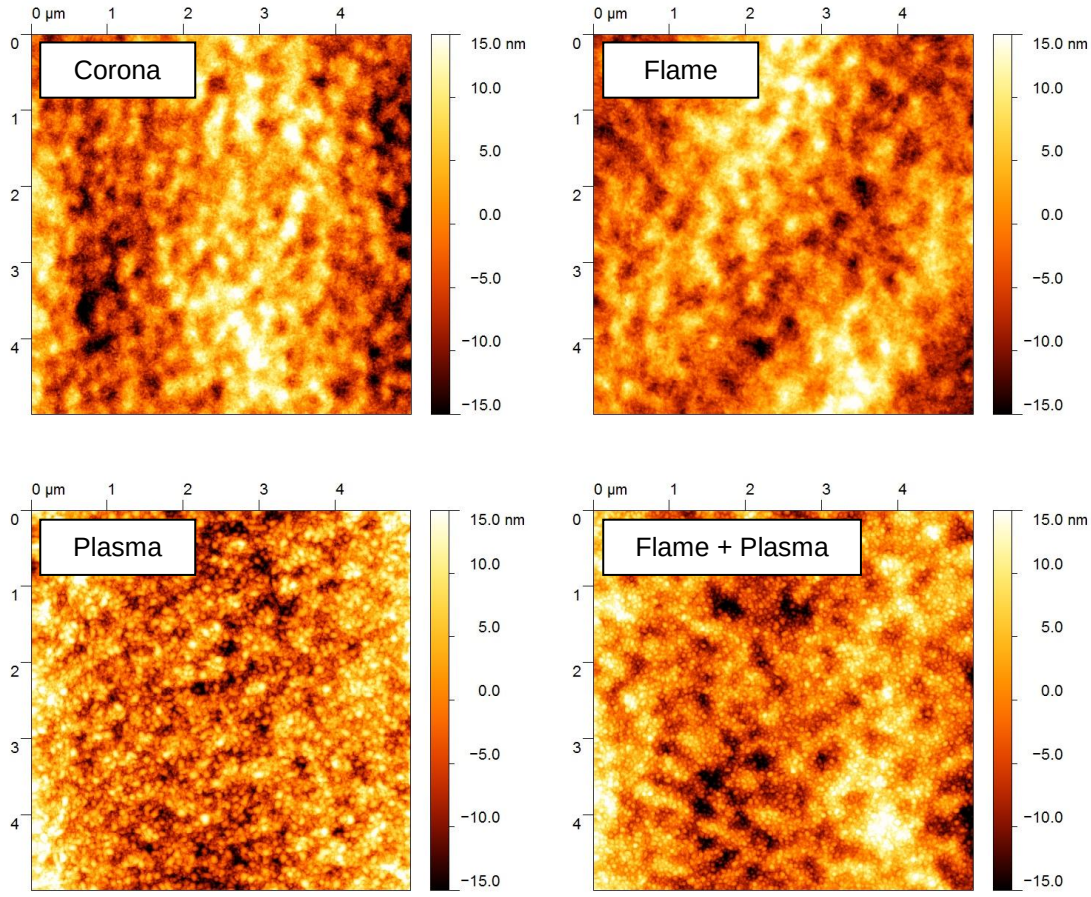

Figure 6-55: 5 x 5 µm² AFM images of BOPP B (before AlO_x coating); top left: corona treated; top right: flame treated; bottom left: plasma treated; bottom right: flame/plasma treated

Although not all nine treatment variations were investigated for their surface topography, it is assumed that samples subjected to the same treatment (with lower intensity) will exhibit similar features, but presumably less pronounced, since it has been shown by other researchers that the size of the globular mounds increases with rising treatment level [61, 62, 262].

According to Jones et al. [61] and O’Hare et al [236], the low-molecular-weight materials created upon corona treatment are water-soluble and can already be formed at low corona treatment levels. Nevertheless, distinctive globular mounds were not discovered during AFM analysis of the standard corona treated BOPP films

(BOPP A to E, see Chapter 6.1.2.4). This may be due to the lower treatment intensities used in industrial practise (compared to laboratory results) and consequently very small globular features, which are not distinctively visible in a 5 x 5 µm² AFM image.

In this investigation, flame treatment was not found to create globular mounds, associated with low-molecular-weight oxidised material, which is in line with investigations of flame treated BOPP carried out by Strobel et al. [266]. Nevertheless, these researchers describe that flame treatment also changes the BOPP film surface and induces the formation of small nodules, which is supposed to be due to the oxidation process taking place. No differences between corona treated BOPP B and the same film subjected to additional flame treatment could be observed here, using 5 x 5 µm² AFM scans. As Strobel and co-workers used a scan size of 1 x 1 µm², it may well be that possible changes induced by the flame treatment cannot be resolved using a scan size of 5 x 5 µm². In an earlier paper [384] by the same research group, it is also stated that flame treatment does not cause a change of the BOPP surface roughness at a resolution of less than 50 nm (using SEM analysis).

Based on the above, the globular mounds found for the flame and subsequently plasma treated sample were created by the atmospheric plasma treatment only. However, the preceding flame treatment resulted in the globular features being reduced in size, although both plasma treated samples (with and without flame treatment) were subjected to the same treatment intensity. Consequently, the changes of the BOPP film surface induced by the flame treatment must have protected the surface from the formation of a greater extent of low-molecular-weight oxidised material upon additional atmospheric plasma treatment.

From the roughness data presented in *Table 6-22*, it can be seen that, despite the changes in surface topography induced by the plasma treatment, the surface roughness did not change considerably, although the mean roughness values show an increasing trend. Due to the large standard deviations, this can, however, not be regarded as significant. Also Strobel and co-workers [384] state that they did not detect any roughening of the BOPP film surface owing to flame treatment. Nevertheless, atmospheric plasma (dielectric barrier discharge) treatments have been reported in the literature to cause roughening of polypropylene [382, 383, 385, 386]. The references cited here all used air as a gas for the dielectric barrier discharge, whilst a mixture of argon (80 %) and oxygen (20 %) was used in this study. However, Leroux and co-workers [382] found that up to a certain treatment level, no change in roughness could be observed. They, furthermore, state that the

effects on surface roughness will not only depend on the treatment level, but also the gas chemistries applied and changes in roughness will be higher when using nitrogen or oxygen, compared to argon.

Table 6-22: Surface roughness in terms of RMS and R_a values (mean value and standard deviation) of treated BOPP B

Film	Treatment	RMS	R_a
		nm	nm
BOPP B	Corona	6.1 ± 1.9	4.8 ± 1.6
	+ Flame	6.2 ± 1.6	4.9 ± 1.3
	+ Plasma	6.4 ± 0.9	5.1 ± 0.7
	+ Flame + Plasma	6.6 ± 1.3	5.2 ± 1.1

6.3.2 Surface chemistry

6.3.2.1 Surface energy (contact angle measurement and dyne inks)

The treated BOPP film surfaces were also analysed for their surface energy, using contact angle measurement and dyne inks according to the ASTM D2578 [207] (wettability test). The roll of corona treated BOPP B used in this investigation revealed an initial surface energy of 37.4 ± 0.1 mN/m, as determined via contact angle measurement (36 mN/m via dyne inks), before being subjected to flame and atmospheric plasma treatment. The surface energy was subsequently measured immediately after treatment was carried out (using dyne inks) and approximately two months after the treatment (via dyne inks and contact angle measurement). The results of these analyses are summarised in *Table 6-23*. In contrast to the analysis of surface topography, which was only carried out for the three highest treatment intensities (see Chapter 6.3.1), all nine treatment variations were analysed for their surface energy.

Table 6-23: Surface energies and water contact angles of BOPP C following flame and atmospheric plasma treatments

Treatment	Intensity level	Surface energy			Water contact angle**
		Dyne inks*	Dyne inks**	Contact angle measurement**	
		mN/m	mN/m	mN/m	°
Corona	-	36	-	37.4 ± 0.1	70.8 ± 0.4
+ Flame	1	40	42	34.4 ± 1.8	78.8 ± 4.0
	2	44	44	33.6 ± 0.2	81.0 ± 1.0
	3	46	44	34.1 ± 0.2	80.5 ± 1.1
+ Plasma	1	40	38	38.0 ± 0.6	69.9 ± 1.6
	2	42	38	38.2 ± 0.4	70.2 ± 0.8
	3	46	40	39.1 ± 0.8	68.6 ± 2.2
+ Flame + Plasma	1	46	44	35.7 ± 1.3	77.7 ± 3.9
	2	48	44	37.6 ± 0.9	73.2 ± 2.3
	3	50	46	36.8 ± 0.4	74.7 ± 1.9

*measured after treatment (does not apply to corona sample)
**measured after approximately two month (does not apply to corona sample)

On studying the initial surface energies obtained using dyne inks right after treatment was carried out, one can see that the levels achieved are quite high. Within the first two months after treatment, no significant drop of surface energy can

be seen for flame treated BOPP B (comparing the results obtained with dyne inks), which is in agreement with reports by Kullberg [255] and Strobel et al. [266], who observed no loss or only a marginal loss of wettability in the case of flame treated BOPP. After two months, the values of flame treated BOPP B are also a lot higher than the range of 36 to 38 mN/m, typically found for corona treated BOPP (see Chapter 6.1.3.1, Table *6-4*). Nonetheless, the treatments involving atmospheric plasma show a decline, which is more pronounced for the two higher treatment intensity levels (still only comparing the results obtained by the use of dyne inks). This may be explained in the light of the AFM results presented in Chapter 6.3.1, since this analysis revealed globular mounds, which are assumed to consist of low-molecular-weight oxidised material, for samples subjected to atmospheric plasma treatment. Strobel et al. [266] observed a more significant decrease of wettability for corona treated BOPP that showed the same globular surface features, whilst for flame treated BOPP, no globular mounds and no significant drop in wettability were detected. It is, hence, argued that the presence of low-molecular-weight oxidised material may play a role in the observed drop of surface energy, maybe due to its mobility that may ease reorientation effects.

Leroux et al. [382], who investigated atmospheric air plasma treated PP, also found that the surface energy had slightly dropped within one month of treatment (more pronounced for higher treatment intensities). The water contact angle of approximately 70° found here for atmospheric plasma treated BOPP also compares well with their results and values obtained by Cui and Brown [386], both using the sessile drop method. Wang and He [385], though, report a lot lower (static) water contact angles, but also by far higher oxygen contents than measured here via XPS (see Chapter 6.3.2.2).

However, what is surprising is the huge discrepancy seen between the surface energy obtained via contact angle measurement and dyne inks for the two month aged samples, when flame treatment was involved. For the atmospheric plasma treated sample only, the two measurement techniques yield nearly identical results, whilst for the samples involving flame treatment, a difference of approximately 6 to 10 mN/m is evident between the results of the two techniques. It is anticipated that the unusually high water contact angles for samples subjected to flame treatment (see *Table 6-23*, last column), which are even higher than the water contact angle of corona treated BOPP B prior to flame treatment, are causing the low surface energies determined via contact angle measurement. In general, one has to be careful when low-molecular-weight oxidised materials are present, since these are soluble in water and other polar solvents (i.e. some of the test liquids used to

determine surface energy) and, hence, can affect and alter the contact angle measurements and surface energy determination [250, 266, 387]. Nevertheless, in the case of flame treatment only, no low-molecular-weight oxidised material was visibly present in the AFM analysis (see Section 6.3.1) and, consequently, could not affect the measurements. Furthermore, when low-molecular-weight oxidised material was extensively detected in the case of the plasma treated (but not flame treated) sample, the two different measurements are relatively consistent with each other, as they are also for the corona treated film. Although it is known that different techniques of surface energy determination generally give different values, and results of different techniques should therefore not be compared [208], this appears (for the measurements stated here) only to be the case when flame treatment was involved.

Strobel and co-workers [387] found that flame treatment (in comparison to corona treatment) commonly results in more wettable films and, additionally, appears to have the shallowest depth, with the incorporated oxygen being more concentrated within the outermost 2 to 3 nm. This research group generally measures the advancing and receding contact angles in preference to static water contact angles. They [384], as well as Morra and co-workers [261], specify that the advancing water contact angle is more affected by the unmodified components of the film surface, whilst the receding water contact angle is more sensitive to the oxygen-containing functional groups resulting from the treatment. Their results [266, 387] also show that the receding water contact angle for flame treated BOPP is a lot lower than for corona treated BOPP, even though the oxygen contents are comparable. Furthermore, whilst the receding contact angle is extremely low, the advancing contact angle is still very high (for flame treated BOPP) and can be even greater than obtained for corona treated BOPP with the same oxygen content.

The measurement of surface energy using the ASTM wettability method is, furthermore, closely linked with the receding contact angle, since the test liquid is applied onto the treated surface and its retraction (i.e. receding) behaviour is examined and judged visually [384]. In contrast to that, it is assumed that the static contact angles are more affected by the advancing contact angles. In this thesis, static contact angles were determined in order to calculate the surface energy. From *Table 6-23* it can be seen that the (static) water contact angle of the flame treated (and flame/plasma treated) BOPP B is remarkably higher than for atmospheric plasma or corona treated BOPP B. Furthermore, for the lowest treatment intensities, larger standard deviations were obtained.

If it is assumed that the atmospheric plasma treated BOPP B in this study is very similar to the corona treated BOPP investigated by Strobel et al., then differences seen here for flame treated BOPP B and atmospheric plasma treated BOPP B using the two surface energy measurement techniques agree closely with their results obtained from advancing and receding contact angles (see previous remarks on the terms ‘corona’ and ‘dielectric barrier discharge’ treatment in Chapters 4.2.3 and 6.3.1). In other words, the wettability test according to ASTM D2578 gave higher surface energy values for flame treated BOPP, due to its correlation with the receding contact angles (receding water contact angles on flame treated BOPP are very low, i.e. good wetting). However, the surface energy calculated from static contact angle measurements is lower, due to it being more affected by the advancing contact angle (advancing water contact angles on flame treated BOPP are relatively high). The plasma treated BOPP, not involving any flame treatment, is supposed to be similar to a corona treated BOPP, which shows less contact angle hysteresis (i.e. differences between advancing and receding contact angles) than flame treated BOPP.

6.3.2.2 X-ray photoelectron spectroscopy

XPS analysis was performed for the three highest treatment intensities of each treatment type, in order to determine the amounts of oxygen incorporated into the film surfaces by the respective treatments. Results are summarised in *Table 6-24*. Additionally, the composition of corona treated BOPP B prior to any additional off-line treatment is stated. It is assumed that the samples of lower treatment intensities, which have not been analysed for their surface composition, would reveal lower or similar levels of oxygen incorporation.

Table 6-24: Composition of BOPP B following various surface treatments, as analysed via XPS

Treatment	C	O	Si	O/C ratio
	at%	at%	at%	
Corona	95.4	4.6	-	0.05
+ Flame	93.5	6.5	-	0.07
+ Plasma	91.4	8.0	0.6	0.09
+ Flame + Plasma	90.2	9.6	0.2	0.11

From *Table 6-24* it can be understood that all off-line treatments induced an increase of the original oxygen content caused by the corona treatment. The highest oxygen content is obtained by the combination of flame and atmospheric plasma treatment, followed by the samples subjected to atmospheric plasma treatment only, whilst the flame treatment on its own increased the oxygen content by roughly 2 at%. Consequently, the aim of increasing the oxygen content of BOPP B was obtained. Nevertheless, only the combination treatment of flame and atmospheric plasma led to an oxygen content similar as found for corona treated BOPP C (10.4 at%, see Chapter 6.1.3.2, *Table 6-5*). No nitrogen was incorporated by any of the treatments and, in addition to carbon and oxygen, the samples subjected to atmospheric plasma treatment show traces of silicon. This is attributed to the BOPP film surface being etched by the plasma treatment. The material removal caused by the etching results in antiblock particles, which commonly consist of silica and previously were enrobed by more than 6 nm of polymer, now falling within the analytical depth (here 5 to 6 nm) of the XPS analysis. Garbassi et al. [272] found silicon after flame treatment of BOPP and also mention the possible appearance of filler particles as the origin.

Although the vast amount of literature only reports on either corona, flame or atmospheric plasma treated polypropylene, but not the combination of several treatments, the properties of the samples produced in this study will still be compared to data obtained by other research groups for flame or plasma treated samples. The total amount of oxygen found in the flame (and beforehand corona) treated sample is lower than values reported for flame treated PP by Garbassi et al. [272] and Awaja et al. [388]. The latter even found traces of nitrogen in the surface of flame treated PP. However, Sheng and co-workers [389] yielded very similar oxygen contents when treating polypropylene homo- and copolymers via a mild flame, whilst for an intense flame, higher oxygen concentrations were measured (analysis conducted at a comparable XPS electron take-off angle). Furthermore, the O/C ratio reported here for the flame treated sample falls within the range of values measured by Strobel et al. [266], who investigated different flame treatment levels using XPS analysis at a similar electron take-off angle.

For atmospheric plasma treated PP, the amounts of incorporated oxygen and O/C ratios reported by various authors are generally a lot higher than measured in this study [62, 382, 385, 386]. Air was employed as a gas for treatment in the referenced literature, which means that a comparable amount of oxygen was present during treatment; although for the trials conducted here, a mixture of argon (80 %) and oxygen (20 %) was used.

As already stated in Chapter 6.1.3.2 for the XPS analysis of corona BOPP treated films, the results for the oxygen content depend on many parameters and one needs to bear in mind that on a laboratory/research scale, the treatment intensities (and hence incorporated oxygen) may be a lot higher than in industrial practise. Furthermore, in this thesis, films were corona treated prior to being subjected to flame and/or atmospheric plasma treatment and it is not known how this may have affected the outcome.

The XPS data was further processed via C1s peak deconvolution, in order to determine the oxygen-functional groups created upon treatment. This procedure has already been explained in detail in Section 6.1.3.2 and results for the three treatments investigated here, including the results for the corona treated BOPP prior to any off-line treatment, are summarised in *Table 6-25*. For all treatments, the lower oxidised species, e.g. hydroxyl groups, are found in larger amounts than the higher oxidised oxygen-functional groups. This is in agreement with the results obtained for the different corona treated BOPP films in Chapter 6.1.3.2 and also the published literature on flame [272, 388] and atmospheric plasma treated PP [62, 382, 386]. Nevertheless, these researchers, in general, found larger amounts of the individual

components, which is due to the larger total amounts of oxygen incorporated by the treatments. From *Table 6-25* one can further conclude that the flame and plasma treatment appeared not to change the amount of hydroxyl groups, but rather introduced higher oxidised carbonyl and carboxyl groups. The combination of flame and atmospheric plasma treatment increased all three oxygen-containing functionalities to the highest levels obtained in this study. Nonetheless, the peak fitting data presented in *Table 6-25* should not be overinterpreted, since this evaluation technique adds uncertainty and is susceptible to small variations in the fitted peaks.

Table 6-25: Concentrations of oxygen-containing functional groups relative to total C1s peak area for BOPP B following various surface treatments

Treatment	Hydroxyl C-OH	Carbonyl C=O	Carboxyl COOH
	at%	at%	at%
Corona	4.1	1.0	0.5
+ Flame	3.9	2.2	0.8
+ Plasma	4.1	2.9	1.9
+ Flame + Plasma	5.4	3.5	2.6

6.3.3 Barrier properties after AlO_x coating

A4 samples of BOPP B, which were subjected to the various flame and atmospheric plasma treatments stated in *Table 5-2*, were mounted on a PET carrier web and, subsequently, coated with an AlO_x barrier layer using in-line plasma pre-treatment. Additionally, A4 samples of BOPP C and the PET reference film were coated in the same run, in order to investigate whether the AlO_x coating of A4 samples is representative of AlO_x coating rolls of films. The barrier results obtained for these A4 samples are summarised in *Table 6-26*. Also shown in the table are the oxygen and water vapour barrier properties of uncoated BOPP B and AlO_x coated BOPP B that was corona treated only. The latter result is from a trial that has not been conducted via coating of A4 samples, but via coating a roll of film

Table 6-26: Barrier properties (OTR and WVTR) of AlO_x coated BOPP B, following various treatments (corona, flame, atmospheric plasma), and A4 reference samples (BOPP C and PET)

Off-line treatment	Intensity level	OTR		WVTR	
		cm³/(m² d)	BIF	g/(m² d)	BIF
Uncoated	-	*2500 – 2900*	-	*7 – 8*	-
Corona	-	*119 ± 17*	*23*	*5.29 ± 0.22*	*1.4*
+ Flame	1	122 ± 20	22	1.84 ± 0.10	4.1
	2	116 ± 22	23	1.45 ± 0.33	5.2
	3	153 ± 18	18	1.21 ± 0.01	6.2
+ Plasma	1	154 ± 45	18	3.43 ± 0.27	2.2
	2	149 ± 26	18	2.84 ± 0.88	2.6
	3	175 ± 26	15	1.81 ± 0.19	4.1
+ Flame + Plasma	1	164 ± 7	16	1.89 ± 0.68	4.0
	2	147 ± 19	18	1.32 ± 0.40	5.7
	3	167 ± 8	16	1.97 ± 0.08	3.8
BOPP C	-	*150 ± 5*	*14*	*1.52 ± 0.04*	*4.3*
PET	-	*2.39 ± 0.74*	*44*	*1.59 ± 0.79*	*28*

From *Table 6-26*, it is evident that the oxygen barrier performance of AlO_x coated BOPP B, which was subjected to flame and/or atmospheric plasma treatment, was not improved to the required levels of less than 100 cm³/(m² d), i.e. similar to that obtained for AlO_x coated BOPP C (see Chapter 6.2.1.1, *Table 6-10*). In fact, the oxygen barrier performance is even worse (for most of the samples) than obtained

previously for BOPP B when it was not exposed to additional off-line treatments. Nevertheless, if one looks at the OTR measured for BOPP C and PET, which were also coated as A4 samples, then these films reveal a considerably lower oxygen barrier, in comparison to the previous trials, whereby film rolls were coated with AlO_x (see Chapter 6.2.1.1, *Table 6-10*). It, consequently, seems plausible that the AlO_x coating of A4 samples may not be representative of AlO_x coated film rolls, with respect to oxygen barrier performance. It is, nevertheless, still assumed that this technique can reveal important tendencies. On examining the water vapour barrier properties of the flame and/or atmospheric plasma treated samples after AlO_x coating, one can observe a clear improvement, compared to the sample of BOPP B that has not been subjected to additional off-line treatment. Furthermore, with increasing the treatment intensity, the flame treated and also plasma treated samples show a clear enhancement of moisture barrier. This improvement is associated with the AlO_x layer, as the uncoated and off-line treated samples (flame and/or plasma) had water barrier properties that were typical of uncoated BOPP B. It is also significant that BOPP C, AlO_x coated as an A4 sample, exhibits a far better WVTR than obtained previously, even after extensive ageing (see Section 6.2.1.2). However, the water barrier performance of the A4 sample of AlO_x coated PET is inferior, relative to a value of less than 1 g/(m² d) for coating a PET film roll (refer to Chapter 6.2.1.1, *Table 6-10*). Nevertheless, it can be seen from the high standard deviation for WVTR that there were also A4 samples of AlO_x coated PET that had a WVTR of less than 1 g/(m² d).

The observation regarding the good WVTR of AlO_x coated BOPP C led to further investigations for possible causes. In contrast to the previous AlO_x coating trials conducted for BOPP B and C (see barrier results in Chapter 6.2.1.1, *Table 6-10*), the trials stated in *Table 6-26* were performed using a different metalliser model. A K4000 metalliser was used previously, whilst a K5000 was used for the trials summarised in *Table 6-26*. It was found that the pressure during AlO_x deposition was around 1.0×10^{-4} mbar (0.01 Pa), which is one order of magnitude lower than for the previous trials conducted on a K4000 metalliser model. It is, consequently, assumed that this lower pressure has a major impact on the coating structure and hence barrier performance, in that the higher mean free path at lower pressure results in fewer collisions of aluminium atoms with oxygen molecules and thus less energy-loss of the evaporated aluminium. This may lead to a denser and less porous AlO_x coating. Nevertheless, when BOPP B was corona treated only (and coated as a roll of film, rather than an A4 sheet, see second row in *Table 6-26*), the oxygen and water vapour barrier is identical to the equivalent trial conducted under higher pressure, i.e. on a K4000, (see Chapter 6.2.1.1, *Table 6-10*, BOPP B, pre-

treatment only). It can, therefore, be concluded that the water barrier improvement was due to a combination of lower pressure and higher oxygen content in the BOPP film surface.

It is notable that other researchers also mention the possible effect of pressure on barrier properties. Hoffmann and co-workers [289] state that an increase in oxygen flow during reactive evaporation of aluminium induces a rise of pressure, if the oxygen is not gettered by the aluminium, and, consequently, can impair coating density and barrier performance. Furthermore, Schiller et al. [22, 27] mention that a higher oxygen partial pressure results in coatings of reduced density and hence lower barrier properties. It is, however, important to state here that an increase in oxygen flow/pressure will additionally result in a different coating stoichiometry, if more oxygen is incorporated into the coating, which can also affect the barrier performance. Consequently, the various deposition parameters are very much interrelated.

All samples subjected to flame treatment show good water barrier properties, with mean WVTRs of less than 2 g/(m² d). The best water barrier was obtained for the flame treated film with the highest treatment intensity, although the oxygen content was 'only' 6.5 at%, compared to 10.4 at% for BOPP C (see Chapter 6.3.2.2, *Table 6-24* and Chapter 6.1.3.2, *Table 6-5*). This may be explained by the fact that flame treatment has been found to have a shallower modification depth than corona treatment, which leads to the oxygen-containing groups being more concentrated near the outer surface of the flame treated film [387]. Hence, for corona treated BOPP C, some of the oxygen detected may be more deeply incorporated within the first 5 to 6 nm of the film surface, whilst for flame treated BOPP B (all treatment intensities), most of the oxygen is nearer to the outer surface and, thus, is 'more readily available' for the depositing coating.

For the atmospheric plasma treated BOPP (no flame treatment involved), a clear improvement of WVTR with rising treatment intensity can be seen. Although not all samples were measured for their oxygen content via XPS, it is assumed that this barrier enhancement reflects the increasing oxygen content in the film surface induced by the atmospheric plasma treatment.

Based on the variability introduced by coating A4 samples, further interpretation of the variations in WVTR for the different treatments, with respect to the effect of the different functional groups incorporated (e.g. effect of carboxyl groups on barrier properties as suggested by Mount [69]), will not be carried out.

Finally, it is important to state that AlO_x coating of A4 samples gives information on important trends, but is suspected to be not absolutely representative of coating film rolls with AlO_x. It is assumed that the greater extent of film handling, involved when mounting the samples before coating and retrieving them after coating, increases the risk of damage to the ceramic and brittle AlO_x layer. This damage may, consequently, affect and deteriorate the barrier performance. Nevertheless, that reasonable water vapour barrier was achieved, whilst oxygen barrier properties were deteriorated (see results for BOPP films coated as A4 samples in *Table 6-26*), indicates different permeation mechanisms for oxygen and moisture through the ceramic AlO_x layer, which appear to be not yet completely understood. If defects are present (presumably due to the extensive film handling), then oxygen barrier will be impaired, as it is known that oxygen permeation is dominated by a macro-defect driven permeation mechanism (refer to Chapter 4.6.2). However, one would also expect the water barrier to be low, since it appears to be a logical assumption that if the defects are large enough to facilitate the unhindered permeation of oxygen (larger molecule), also water vapour (smaller molecule) would pass through unhindered. In Chapter 6.2.1.3, it was found that 'dark' AlO_x on BOPP A had improved water vapour barrier, despite the presence of defects in the coating. This was attributed to the metal aluminium content in the coating scavenging the moisture. In the case of the A4 samples coated with AlO_x, the transparency suggests that no elemental aluminium is present and, hence, there must be an additional or different factor with respect to water vapour permeation that has not yet been considered.

6.4 Acrylate coatings

For the deposition of acrylate coatings as top- and undercoats, initial investigations were carried out on the plain BOPP films used in this study (BOPP A, B and C) to examine their surface topography and asperities. In the case of BOPP (and other polymer) films, these asperities are predominantly caused by protruding antiblock particles, a film additive added to the skin layer polymer of the BOPP film in order to facilitate film handling. Further surface irregularities may be induced by dislocating antiblock particles leaving imprints in the film surface, imprints created by debris or antiblock particles located on the reverse side of the film and scratches/marks due to contact of the film with rollers during production/winding. For this early examination, white light profilometry was chosen. This analytical technique allows obtaining real topographical (height) information without requiring sample contact and, thus, represents an ideal technique for analysing polymer films on the required scale. AFM, by contrast, is generally used for investigations of smaller sample areas and, furthermore, is more complex to handle, especially when there are large height variations across the scan width and tip-sample contact may temporarily be lost. On the investigated scale, no difference between plain and AlO_x coated film is seen due to the low coating thickness of only 10 nm. Consequently, only plain film samples were analysed for the protrusion extent of antiblock particles.

The results revealed that large antiblock particles (diameter approximately 10 µm) protrude up to nearly 5 µm from the BOPP film surface, for all three film types. There was, though, a larger amount of antiblock particles of this size found on BOPP C (see also Sections 6.1.2.1 and 6.1.2.2). This suggests that in order to planarise the film surface and conceal all surface irregularities, an acrylate thickness of approximately 5 µm would be required. However, aiming for a low-cost industrial product and based on the acrylate thicknesses applied by other researches (frequently around 1 µm or less [96, 136, 159, 170, 175, 299, 329, 390]), the general thickness of the acrylate coating to be deposited as under- and topcoat was chosen to be 1 µm. In addition to the 1 µm thick acrylate coatings, thicker coatings of approximately 5 µm were deposited for comparison.

Thickness measurements of the acrylate coating step edges created on silicon wafers (coated as reference samples) with a Dektak IID stylus profilometer showed thicknesses of 0.75 ± 0.09 µm and 5.04 ± 0.35 µm for the thin and thick acrylate layers, respectively.

6.4.1 Acrylate undercoats

6.4.1.1 Barrier properties

The barrier performance obtained with acrylate undercoats with an average thickness 0.75 µm and 5.04 µm is summarised in *Table 6-27*. Additionally, the acrylate coated films were measured for their barrier properties prior to AlO_x deposition. These results, together with the barrier performance of the plain polymer films (no acrylate and no AlO_x coating) and the AlO_x coated films without any undercoat, are shown in *Table 6-27*. All AlO_x coating trials were conducted with in-line plasma pre-treatment only. Whilst the acrylate coated samples (A4) were AlO_x coated after mounting them onto a carrier web, the samples without acrylate coatings were taken from trials conducted on film rolls.

Table 6-27: Barrier properties (OTR and WVTR) of AlO_x coated BOPP films with acrylate undercoats of 0.75 µm and 5.04 µm thickness

Film	Description	OTR	WVTR
		cm³/(m² d)	g/(m² d)
BOPP A 30 µm	Plain (uncoated)	1250 – 1450	4 – 5
	Plain + AlO_x	202 ± 24	3.43 ± 0.35
	Plain + 0.75 µm acrylate	1350 ± 24	4.34 ± 0.05
	Plain + 5.04 µm acrylate	895 ± 23	4.20 ± 0.21
	0.75 µm acrylate + AlO_x	18.9 ± 2.9	1.33 ± 0.11
	5.04 µm acrylate + AlO_x	23.2 ± 7.8	1.92 ± 0.11
BOPP B 15 µm	Plain (uncoated)	2500 – 2900	7 – 8
	Plain + AlO_x	118 ± 22	5.47 ± 0.35
	Plain + 0.75 µm acrylate	2100 ± 88	7.54 ± 0.43
	Plain + 5.04 µm acrylate	1270 ± 8	7.50 ± 0.06
	0.75 µm acrylate + AlO_x	15.8 ± 2.7	2.15 ± 0.21
	5.04 µm acrylate + AlO_x	28.5 ± 0.6	2.34 ± 0.10
BOPP C 20 µm	Plain (uncoated)	2000 – 2100	6 – 7
	Plain + AlO_x	35.3 ± 3.1	6.08 ± 0.17
	Plain + 0.75 µm acrylate	1680 ± 129	6.59 ± 0.08
	Plain + 5.04 µm acrylate	1160 ± 66	6.15 ± 0.20
	0.75 µm acrylate + AlO_x	15.8 ± 1.9	1.93 ± 0.21
	5.04 µm acrylate + AlO_x	13.8 ± 3.1	2.69 ± 0.08

When comparing the barrier performance of the plain film with the acrylate coated film (no AlO_x), one can see that the acrylate layer improves the oxygen barrier, but has no impact on the water barrier. This is due to the barrier properties of the acrylate, which has a better oxygen barrier but a poorer water barrier, when compared to BOPP [149]. Nevertheless, the improvement of OTR by application of an acrylate layer is only small, in contrast to the improvement that can be obtained with inorganic barrier layers. It has also been noted by other researches that the acrylate layer on its own does, in general, not induce a big improvement of barrier properties, compared to the barrier performance of the uncoated film [159, 175, 290, 329, 390, 391]. Especially on thick substrates, no improvement at all could be seen when applying a thin acrylate coating. It is worthwhile mentioning here that on a 100 µm thick PET, an acrylate layer of 1 µm may not show any barrier improvement, whilst on a 12 µm PET substrate it may do, as for "very large values of the substrate thickness, the permeability of the substrate alone will reach the value of the permeability of the coated substrate" [126][k]. This is also the reason that the oxygen barrier improvement with the acrylate layers deposited here onto BOPP (without AlO_x) is more pronounced for the thinner BOPP film substrates of 15 and 20 µm thickness (see *Table 6-27*, especially thin acrylate). When the acrylate thickness is increased from 0.75 µm to 5.04 µm, the improvement of oxygen barrier is even more distinct and also noticeable for BOPP A.

On comparing the oxygen and water vapour barrier performance after AlO_x coating the acrylate pre-coated BOPP films with the AlO_x coated plain BOPP films, it is noticeable that in all cases the OTR, as well as the WVTR, is improved. As discussed in Section 6.2.1.1, AlO_x coated BOPP C showed the best oxygen barrier performance of all standard packaging grade BOPP films, whilst AlO_x coated BOPP A showed inferior oxygen barrier properties, compared to all coated BOPP films. After applying acrylate undercoats, all BOPP films reveal very similar barrier properties against oxygen, as well as water vapour. Especially for the 0.75 µm thick acrylate undercoats, the OTR values after AlO_x application are nearly identical for all three BOPP film types. For the 5.04 µm acrylate undercoat, slight variations in OTR can be found for AlO_x coated BOPP A and, to a larger extent, for AlO_x coated BOPP B. These variations are attributed to the larger extent of film handling, when the AlO_x coating is applied to A4 samples on a carrier web, and thus a higher chance of inflicting damage to the thin AlO_x barrier layer (see also discussion in Chapter 6.3.3). WVTR for all AlO_x coated BOPP films with acrylate undercoats is in the range of 1.5 to 2.5 g/(m² d). In this case, BOPP A shows slightly better WVTR,

[k] The author of this reference refers to the transmission rate or permeance as 'permeability'; see more information in Chapter 4.6.1.

compared to BOPP B and C. This may be due to BOPP A being a thicker, more rigid substrate and, therefore, being less prone to film handling induced damage of the AlO_x layer. Nevertheless, once again the variations in WVTR are mainly put down to the increased film handling when coating A4 samples. Overall, the barrier results suggest that the surfaces of all three films must be very similar after acrylate deposition, as resembling barrier levels are obtained. It is also noticeable that increasing the acrylate thickness from 0.75 µm to 5.04 µm does not result in any additional improvement in terms of water or oxygen barrier performance after AlO_x coating. A 0.75 µm thin acrylate layer is, therefore, sufficient to change the surface properties of the BOPP films in order to enhance barrier properties after AlO_x coating. Finally, it should be repeated here that the barrier results for the AlO_x coating of A4 samples presented in Chapter 6.3.3 indicated that AlO_x coating of film rolls may give better barrier properties than obtained for A4 sheets.

The benefits of using (organic) acrylate undercoats prior to deposition of inorganic barrier layers has been reported by various research groups, for AlO_x layers on PP [392], on PET [136, 170, 175, 329] and other material combinations [149, 159, 172, 390, 391]. The barrier improvement obtained by applying an acrylate undercoat has been accredited to a variety of properties that the acrylate layer confers to the polymer films. Acrylate layers (as undercoats) are frequently referred to as planarisation layers, since they have the capability to eliminate surface roughness and conceal surface defects/irregularities (such as antiblock particles) present on the polymer film surface [96, 136, 159, 170, 175, 390]. Therefore, they smooth/flatten the substrate surface and decouple its defects from the subsequently deposited inorganic barrier layer. Such defects, for instance, can be sharp high protrusions in the film surface, which endure most of the load once the coated film is wound into roll form and, therefore, may serve as initiation points of cracks in the inorganic barrier layer [329]. The planarisation effect of acrylate layers is due to the unique deposition technique, as described in Section 5.3. In this study, this means that defects in the uncoated film surface, such as the previously shown dimples/craters on BOPP A (see Sections 6.1.2.3 and 6.1.2.4), can no longer be reproduced in the thin barrier layer. Furthermore, if antiblock particles are over-coated by the acrylate, i.e. do not protrude through this layer, they can no longer generate defects in the thin AlO_x barrier layer subsequently deposited.

Yializis [392] and Shaw and Langlois [390] also mention that the superior thermal properties of an acrylate layer, compared to the polypropylene film, make the surface a better substrate for the deposition of inorganic barrier layers such as AlO_x.

Hanika et al. [149] and Langowski [126] emphasise the importance of the permeability of the applied polymer layer, i.e. the polymer adjacent to the inorganic barrier layer. Acrylates, in contrast to BOPP, have lower oxygen permeability and, consequently, they argue that this results in lower OTRs when applying an inorganic coating (in their case aluminium) to the acrylate coated BOPP, compared to the non-acrylate coated BOPP. Based on the higher permeability of the acrylate to water vapour, the WVTR is increased when using an acrylate layer prior to aluminium coating. Furthermore, they state that if the thickness of the undercoat is above the so-called critical thickness (dictated by defect density and size, typically less than 2.5 µm [393]), then the overall barrier performance is defined by the combination of inorganic barrier layer and undercoat. In our case, however, OTR and WVTR were improved by the application of an acrylate undercoat. Nevertheless, the improvement in WVTR is not down to the desired levels of less than 1 g/(m² d). That applying a less permeable coating/lacquer to the polymer film prior to metallisation (or in this case AlO_x coating) can improve barrier performance, in the case of macro-defect driven permeation, has previously been proposed by Jamieson and Windle [140] and Beu and Mercea [143]. This is due to a change of the concentration gradient of the permeating substance in the polymer layer next to the defect. Graff and co-workers [136] also emphasise the role of the permeability of the polymer material used in organic/inorganic multilayered structures.

Finally, an acrylate deposited onto a polypropylene substrate represents a complete change of surface chemistry (and also polarity), which may offer more nucleation sites (higher nucleation rates) to the depositing inorganic coating, thus resulting in a denser coating structure, as suggested by Yializis [392] and Miyamoto et al. [175].

In summary, the acrylate provides the depositing inorganic barrier layer a completely different substrate surface in terms of roughness/topography (on the scale of light microscopy, as well as atomic force microscopy, see Chapters 6.4.1.2 and 6.4.1.3), chemistry and also thermal and structural properties, upon which to nucleate and grow. Here, it is assumed that it is especially the different chemical functionality of the acrylate, in contrast to the BOPP, that allows the AlO_x to nucleate and grow in a different, presumably denser, structure. This results in the lower OTR values and, more important, the lower WVTR values. The reasons leading to this assumption will be pointed out now. Firstly, the thicker acrylate layers did not induce an additional (oxygen) barrier enhancement, which would be expected if the barrier improvement would be due to the better oxygen barrier properties of the acrylate. Furthermore, acrylates do not have better water barrier properties, compared to BOPP, and, hence, the water barrier improvement yielded by the acrylate undercoat cannot be

explained by the water barrier properties of the acrylate layer. Furthermore, all three films reveal very similar oxygen and moisture barrier properties after AlO_x coating (for both acrylate thicknesses), despite still exhibiting very different surface topographies on a lower magnification level (see next chapter). This may exclude the smoothing as a main reason for the barrier improvement.

6.4.1.2 Surface topography (DIC light microscopy analysis)

The following sections discuss the changes in surface topography and roughness, which were induced by the application of the acrylate layer. Therefore, the plain and AlO_x coated BOPP films were investigated by DIC light microscopy and, additionally, atomic force microscopy to obtain information on the nano-scale surface roughness.

Samples were initially examined using light microscopy. The effect of the acrylate layer on the surface of the plain BOPP films is depicted in *Figure 6-56*, *Figure 6-57* and *Figure 6-58* for BOPP A, B and C.

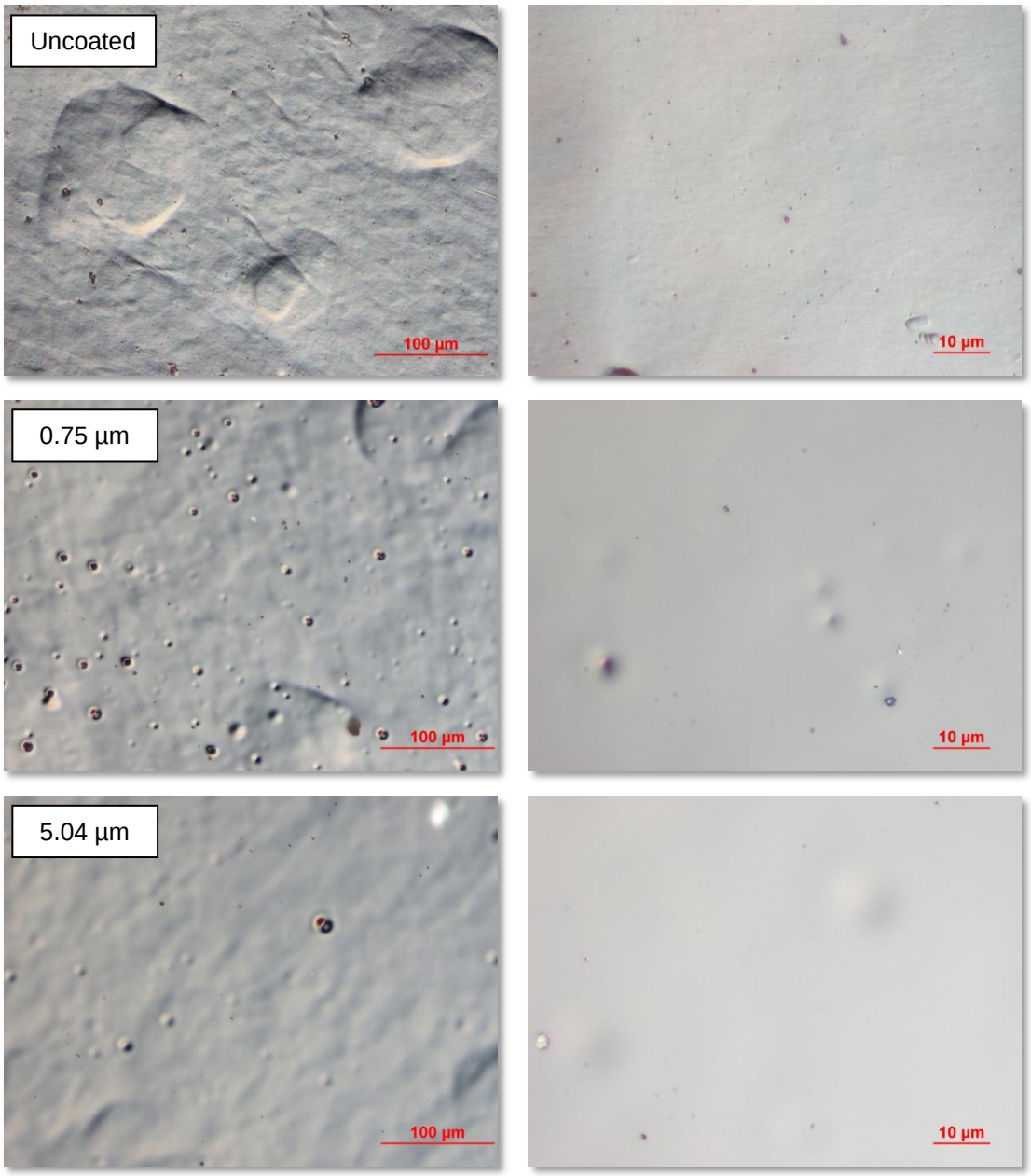

Figure 6-56: DIC light microscopy images of plain and acrylate coated BOPP A at two different magnifications; top: uncoated film; middle: 0.75 µm acrylate; bottom: 5.04 µm acrylate

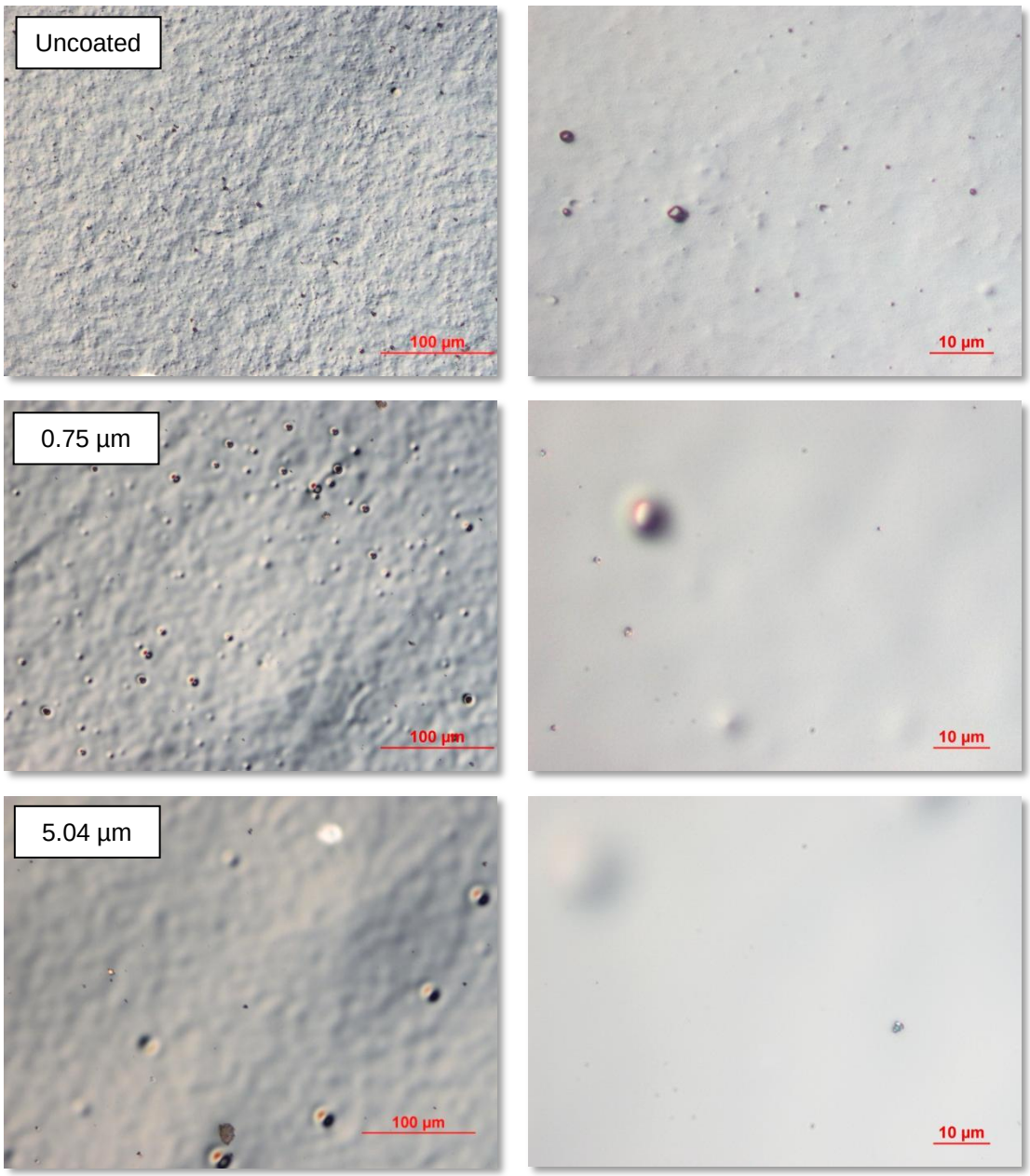

Figure 6-57: DIC light microscopy images of plain and acrylate coated BOPP B at two different magnifications; top: uncoated film; middle: 0.75 µm acrylate; bottom: 5.04 µm acrylate

When looking at the lower magnification DIC images, one can see that for all BOPP films, the finer surface details disappear with the application of the acrylate layer, independent of the acrylate thickness. For BOPP A, the previously described lowered, round-shaped surface features (see Section 6.1.2.1) are still visible; however, the edges of these large recessed areas appear smoother and their 'volume' appears partially filled after acrylate coating, especially for the thicker 5.04 µm acrylate layer. Due to the size and distribution of these features, they are more obvious on lower magnification DIC images, shown later in *Figure 6-59*.

Plain BOPP B had a very rough and intensely structured surface prior to acrylate deposition. This surface texture already disappears after applying the 0.75 µm thick acrylate and is even more disguised with the 5.04 µm acrylate layer.

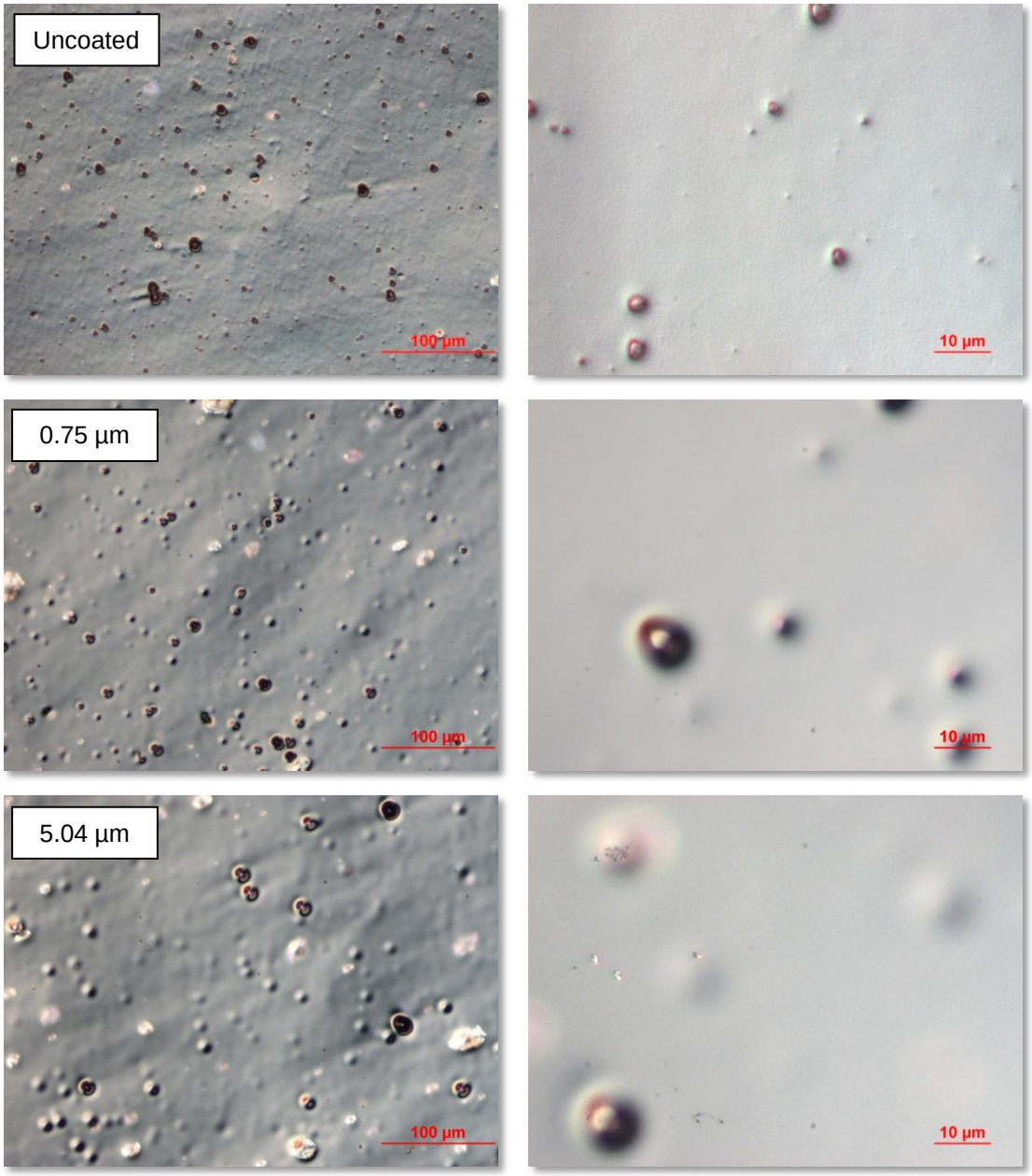

Figure 6-58: DIC light microscopy images of plain and acrylate coated BOPP C at two different magnifications; top: uncoated film; middle: 0.75 µm acrylate; bottom: 5.04 µm acrylate

Also for BOPP C, the fine detail surface structure (as seen in DIC) of the plain film is concealed by the acrylate layer. In summary, at the lower magnification level shown in *Figure 6-56* to *Figure 6-58*, differences in surface topography are still noticeable between BOPP A, B and C after acrylate coating (at both thicknesses), which have been induced by the underlying plain film surface characteristics (e.g. lowered,

round-shaped surface features on BOPP A, roughness/bumps on BOPP B, large antiblock particles on BOPP C).

On comparing the 0.75 µm thick deposits with the plain film surfaces (still at the lower magnification level), it appears that the thin acrylate layer induces additional circular-shaped surface features. This is particularly pronounced for BOPP A and B and less obvious for BOPP C. The former two BOPP films already showed a smaller number of antiblock particles with a diameter of more than 5 µm (see Section 6.1.2.2), compared to BOPP C, which featured substantially larger antiblock particles. Consequently, for BOPP A and B, the surface features seen after applying the 0.75 µm thick acrylate layer cannot solely be caused by large antiblock particles that could not be over-coated and eliminated by the acrylate layer, but must be generated by the acrylate itself (or its deposition process). This becomes also obvious if one compares the number of large antiblock particles on plain BOPP A and B with the number of surface features appearing after acrylate coating with a thickness of 0.75 µm in *Figure 6-56* and *Figure 6-57*.

In contrast to that, plain BOPP C (see *Figure 6-58*, top) reveals a vast amount of large antiblock particles (dark spots in *Figure 6-58*, top) and this amount appears very similar to the number of circular features found after acrylate coating with a thickness of 0.75 µm, as well as 5.04 µm. Thus, investigating BOPP C only would suggest that the acrylate enhances the appearance of large antiblock particles, but not that the acrylate promotes the appearance of additional surface features.

When investigating the 5.04 µm thick acrylate layers, the number of the previously mentioned circular features is largely reduced, compared to the 0.75 µm thick acrylate layer, and is more resembling the number of large antiblock particles found on the respective plain BOPP films A to C. Therefore, for the 5.04 µm thick acrylate layer, these features are quite likely generated by large antiblock particles in the BOPP film surface. It also appears that the features have an increased diameter, compared to the respective antiblock particles on the plain film. This may be due to the acrylate forming a skin over the protruding antiblock particle, thus reducing the slope around the particle, but increasing the overall diameter of it (in top view). Consequently, the acrylate layer may enhance and amplify the size of over-coated antiblock particles.

The origin of the circular-shaped features on the 0.75 µm thick acrylate will be further investigated at the end of this section, via analysis of the acrylate layers deposited onto the silicon wafers.

On comparing the higher magnification DIC images of the BOPP films pre- and post-acrylate deposition, one can observe that the typical background structure of each BOPP film and small submicron size antiblock particles are completely eliminated, already by the 0.75 µm thick acrylate layer. This is particularly pronounced for BOPP A and also BOPP B, which exhibited more submicron size antiblock particles, compared to BOPP C. The 5.04 µm thick acrylate coat additionally masks larger antiblock particles. All three BOPP film types look very similar, virtually identical, after acrylate coating and show the same 'featureless' surface background. Consequently, one can no longer distinguish between the different BOPP film types at this magnification level.

At a lower magnification level, there are, however, still distinctive differences (after acrylate coating) between the three BOPP film types, in terms of protrusions caused by antiblock particles and other surface characteristics, such as the surface background structure observable on this scale (refer to *Figure 6-59* for lower magnification images of the acrylate coated BOPP films). Despite the topographical differences, the barrier performance of all three BOPP film types was very similar after AlO_x coating and was not significantly affected by the acrylate thickness (see *Table 6-27*). It can, therefore, be concluded that the barrier performance is mainly due to the newly generated chemical functionality of the surface, which in turn enhances the growth of the AlO_x coating and hence its structural and barrier properties. It is evident from this study that the surface topography has less impact on the barrier properties.

DIC investigations of AlO_x coated polymer films have shown that at the highest magnification level provided by the DIC light microscopy analysis, one cannot distinguish between plain and AlO_x coated surfaces, thus indicating that the resolution offered cannot resolve the thin AlO_x layer. Therefore, DIC images of the acrylate undercoats with deposited AlO_x barrier layer are not shown in this investigation.

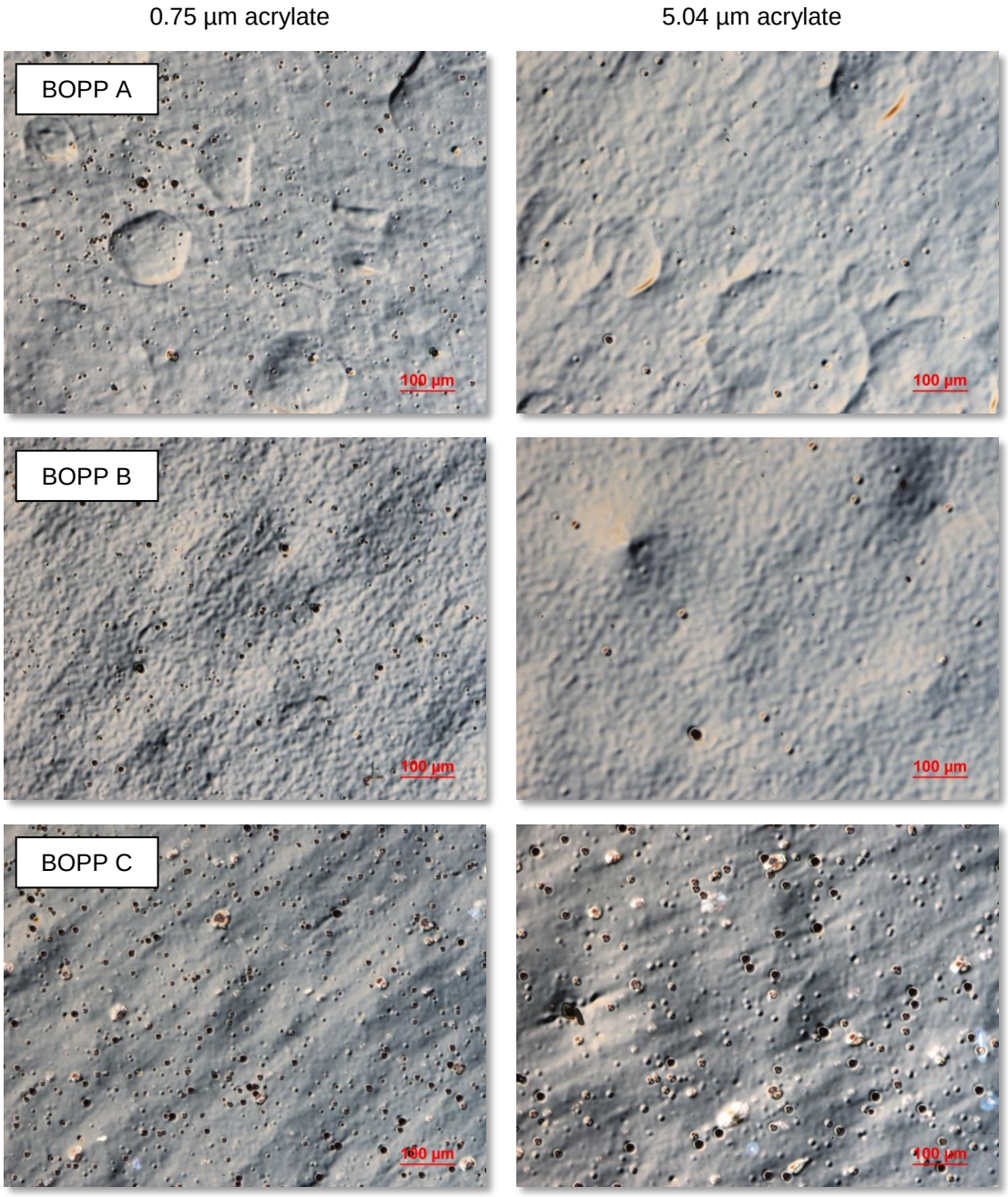

Figure 6-59: DIC light microscopy images of acrylate coated BOPP films at lower magnification; left: 0.75 µm acrylate; right: 5.04 µm acrylate; top: BOPP A; middle: BOPP B; bottom: BOPP C

Based on the observation of 'additional' circular-shaped features, assumed to be due to the 0.75 µm thick acrylate layers, the silicon wafers (coated as reference sample with each run) were also investigated by DIC light microscopy. The pristine wafers have a featureless surface, without any structures similar in size and shape to the antiblock particles found on the BOPP films. Consequently, the wafer surfaces should still be featureless after acrylate coating, if the features found for acrylate coated BOPP (distinctively pronounced for the 0.75 µm thick acrylate) are caused by antiblock particles only. DIC images of the uncoated, 0.75 µm thick coated and

5.04 µm thick coated silicon wafer are shown in *Figure 6-60* (same magnification as DIC images in first column of *Figure 6-56*, *Figure 6-57* and *Figure 6-58*).

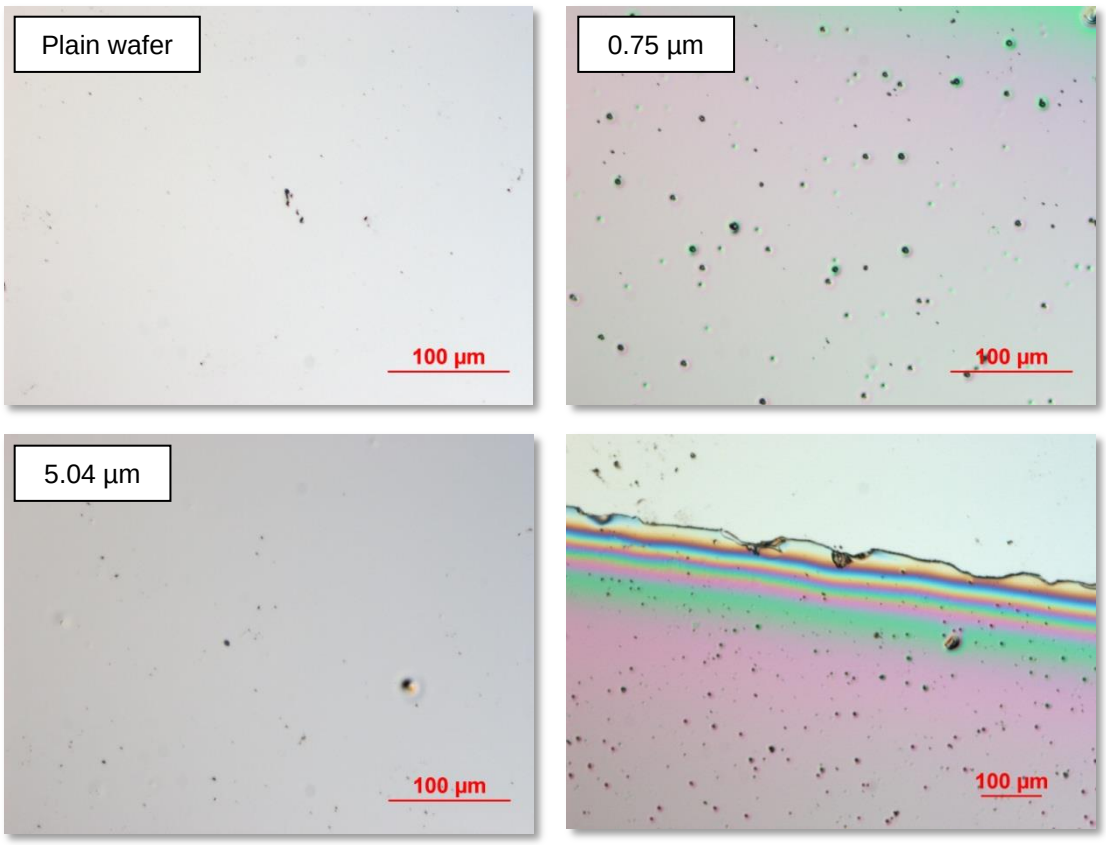

Figure 6-60: DIC light microscopy images of plain and acrylate coated silicon wafers; top left: plain wafer; top right: 0.75 µm thick acrylate; bottom left: 5.04 µm thick acrylate; bottom right: step edge on wafer with 0.75 µm thick acrylate on bottom (lower magnification)

From the DIC images in *Figure 6-60*, it becomes obvious that there are additional features emerging after acrylate coating with a 0.75 µm thick layer. The uncoated silicon wafer has a very smooth and structureless surface appearance and just exhibits a few dark spots that can be attributed to contaminants, such as dust or debris. In contrast to that, characteristic circular-shaped features appear after coating with an acrylate layer of 0.75 µm thickness. These are similar in number and size to the circular structures found on the BOPP films after acrylate coating. As suggested by the investigation of BOPP A and B (both coated with a 0.75 µm thick layer of acrylate), these must be caused by or during acrylate deposition.

Figure 6-60 additionally indicates that there are also some features evident for the thicker acrylate layer. Further investigation of the silicon wafer with the thin acrylate coating using white light profilometry revealed that the round features found have the shape of small pits surrounded by a ring-shaped elevation. In contrast to this, the features on the acrylate coated BOPP films appear inverted, with a mound

surrounded by a circular trench. One possible explanation for this may be a dewetting phenomenon, occurring between acrylate deposition and curing process. This dewetting phenomenon may result in different appearances, depending on the individual substrate properties (silicon wafer versus BOPP film), and can be caused by contaminations on the surface or even antiblock particles. Hence, the presence and/or inclusion of contamination (dust/debris on the BOPP film and silicon wafer surface, presumably held by static forces) during acrylate deposition may result in the formation of the observed features in the acrylate layer. Dewetting would also elucidate that the previously described features diminish with increasing thickness. For thinner acrylate layers, the structures are more distinctive and, subsequently, start to disappear with increasing acrylate thickness, i.e. the contaminations become over-coated. Furthermore, it is assumed that the exposure to ambient conditions, associated with off-line acrylate coating of A4 samples, represents a source of contamination. The latter can, of course, be reduced or eliminated entirely, if the acrylate layer is applied in-line via a roll-to-roll process along with the inorganic barrier layer and without breaking the vacuum, as done by other researchers [96, 136, 170, 390]. Henry and co-workers [394], who used the same monomer TPGDA to deposit acrylate layers onto polyethylene naphthalate, state that large protrusions may occasionally occur on the acrylate coating. They suggest that these features may be due to acrylate droplets curing as ‘flakes’ and, subsequently, falling onto the substrate. On the other hand, Affinito et al. [170] report that the use of an electron beam for curing can result in a charge built up of the polymer film and subsequent electrostatic discharge (when in contact with the grounded rollers) may lead to the formation of pits in the surface.

There are, though, a lot more of these features observable for BOPP C (for both acrylate thicknesses), compared to BOPP A and B, thus suggesting that large antiblock particles (which were found to a greater extent on BOPP C) also create some of these characteristic features. This would be in good agreement with findings of Yializis’ [392] SEM investigations. He reports that whilst smaller defects were covered by an approximately 1.5 µm thick acrylate layer, larger defects, such as protruding antiblock particles, were still replicated in the acrylate layer.

6.4.1.3 Surface roughness (AFM analysis)

In addition to light microscopy, samples were characterised using atomic force microscopy. No extensive SEM investigations were carried out, as it was concluded that this would not offer any additional vital information to the results obtained from the combination of DIC optical microscopy and AFM analysis.

For the AFM analysis, areas of 5 x 5 µm² were analysed and at least eight scans were performed per sample on different surface areas to obtain average values and standard deviations for RMS and roughness average. Care was taken not to perform any scans in the direct vicinity of large protruding surface features. Representative AFM scans of the uncoated BOPP films and the acrylate layer (in this case 0.75 µm acrylate coating on BOPP A) are illustrated in *Figure 6-61*.

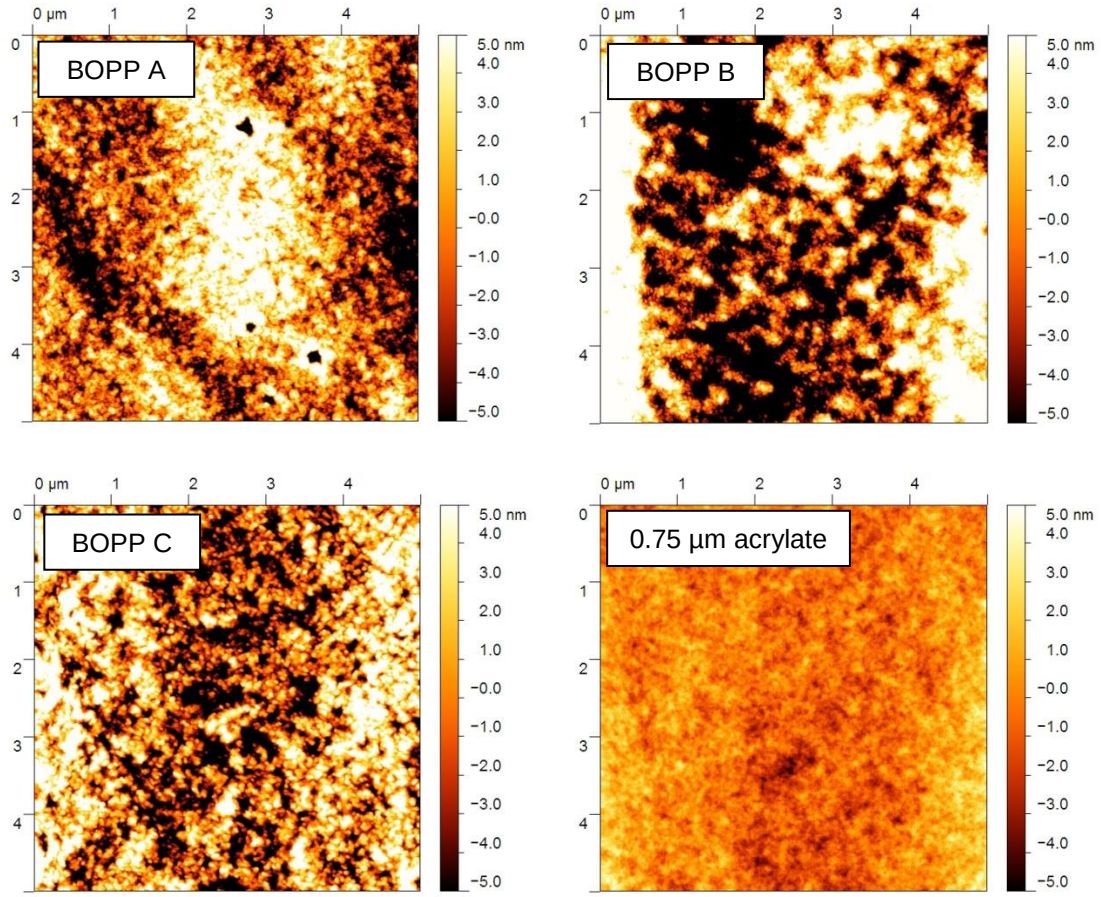

Figure 6-61: 5 x 5 µm² AFM scans pre- and post-acrylate deposition; top left: plain BOPP A; top right: plain BOPP B; bottom left: plain BOPP C; bottom right: 0.75 µm acrylate on BOPP A

In all cases, i.e. thick and thin acrylate layers on all three BOPP films, the scans revealed the same smooth surface texture. This could be expected, since all samples were coated with the same material. The acrylate layer exhibits a fine

surface texture, consisting of very fine granular-like features (see *Figure 6-61*, bottom right). The only difference observable between the various samples investigated was the additional background structure that the granular texture was superimposed on. This is an additional waviness that affects the measured surface roughness values to a large extent, as will be shown later. In order to obtain directly comparable AFM images, all images in *Figure 6-61* have the same scale bar for the z-value. Thus, it is clearly noticeable from the colouration of the images that the acrylate layer is a lot smoother, compared to the surface of the uncoated BOPP films.

The AFM images, additionally, show that the acrylate layer covers over and eliminates the characteristic surface texture of the plain BOPP films. In the case of BOPP A, no craters/dimples are visible and also the background structure (here showing a diagonal orientation) is concealed. Similar effects can be observed for BOPP B, where the undulating structure is masked by the acrylate layer. This suggests that also on the scale of the AFM investigation, the acrylate layer has a planarisation effect, covering and eliminating all characteristic substrate surface features. Overall, the structure on the AFM images of the acrylate coatings in this study looks similar to the structure of AFM images obtained by Henry et al. [391] (for 0.2 µm thick acrylate layers deposited onto polyethylene naphthalate).

Representative AFM images of an uncoated and an AlO_x coated acrylate layer are shown in *Figure 6-62* (here for a 5.04 µm thick acrylate layer on BOPP A). After AlO_x coating, the surface structure appeared to be slightly altered, with the granular features increased in size. Thus, the images give the impression that the fine-granular structure is more pronounced and coarse. Still, however, the AlO_x coated and non-coated acrylate layers look very similar.

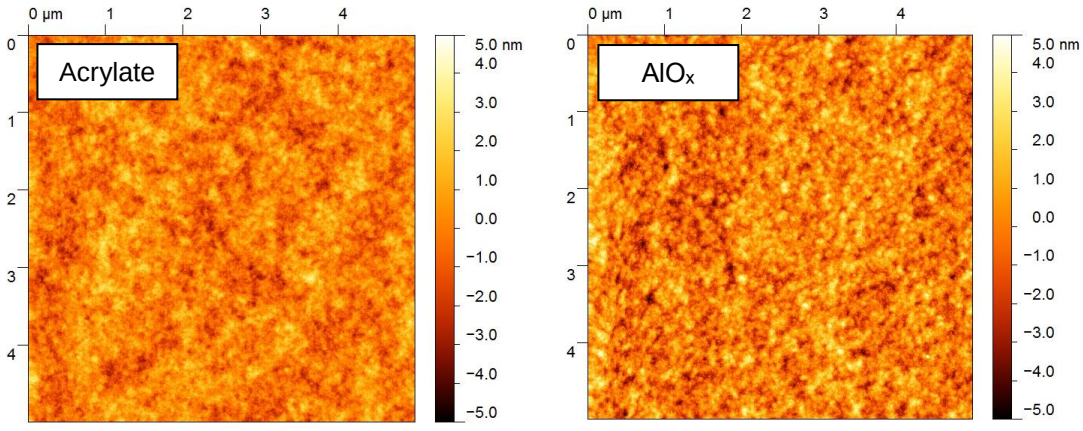

Figure 6-62: 5 x 5 µm² AFM scans pre- and post-AlO_x deposition; left: 5.04 µm acrylate on BOPP A; right: BOPP A with 5.04 µm acrylate undercoat and AlO_x layer

The noticeable change of surface structure with AlO_x coating differs from the results found previously, when AlO_x coatings were applied without any undercoat. Without any acrylate undercoat, the AlO_x coatings replicated the underlying substrate surface structure. The slightly enhanced grain-like features after AlO_x coating of the acrylate may be due to the nucleation and growth of the inorganic barrier coating starting from preferred nucleation sites, which increase in size. Consequently, this can result in the formation of larger grains and addition of grain boundaries, as suggested by Affinito et al. [329]. Nevertheless, one needs to remember that the quality and resolution of AFM images strongly depends on the AFM tip radius; if the tip radius increases (due to tip contamination or wear), the fine-scale topography can no longer be imaged [330, 331]. There may have been variations in AFM tip radius, either as supplied by the manufacturer, or induced by the use of the tip, e.g. faster wear of the tip due to the AlO_x being a hard material (compared to the soft polymer). This wear/deterioration of the tip may have not been noticed when the surface texture has not such fine detail that a slight increase in tip radius would lead to these details no longer being imaged. In the case of acrylate coated films, the hypothesis of tip deterioration (change in tip radius) is supported by observations made during AFM analysis. A tip that gave repeatable fine-scale AFM images for the acrylate layers of various samples was used on several AlO_x coated samples and, subsequently, again on an acrylate layer, where the fine-scale topography could then no longer be imaged. Furthermore, several new and unused tips could not resolve the fine detail that other AFM tips revealed for acrylate layers. These tips were, consequently, not applied in this investigation.

The AFM investigation was further used to obtain information about the surface roughness before and after acrylate and AlO_x deposition (in terms of RMS and roughness average values) and results are summarised in *Table 6-28*.

As can be seen, in all cases, the roughness parameters are substantially lower for the acrylate coating (with and without AlO_x), compared to the plain BOPP films, with average RMS values ranging from 1.1 to 1.8 nm (apart from two anomalies, see later). This confirms the smoothing effect of acrylate layers on the investigated scale, which could already be observed when comparing the respective AFM images. There are, however, two outliers in surface roughness. These were obtained for the 0.75 µm thick acrylate layer on BOPP B and the 0.75 µm thick AlO_x coated acrylate layer on BOPP C, marked in red in *Table 6-28*. These comparatively large RMS and roughness average values are caused by an additional ‘waviness’ being present in the 5 x 5 µm² scans, which heavily impacts and increases the calculated roughness parameters. This additional surface topography, which

overlays the fine-granular structure of the acrylate, can only be explained by distortions being present in the thin 0.75 µm thick acrylate, presumably induced by underlying antiblock particles or contamination inclusions (although it was attempted not to perform AFM scans in the direct vicinity of large surface features, such as the circular-shaped characteristics described earlier). It may, furthermore, only be due to the individual sample used for AFM analysis, which only represents a small area of the overall coated film surface.

Table 6-28: Surface roughness of plain, acrylate (undercoat) and AlO_x coated BOPP films (calculated from 5 x 5 µm² AFM scans)

Film	Description	Root mean square	Roughness average
		nm	nm
BOPP A	Plain film	4.1 ± 0.7	3.3 ± 0.5
	+ 0.75 µm acrylate	1.3 ± 0.2	1.0 ± 0.2
	+ 0.75 µm acrylate + AlO_x	1.8 ± 0.7	1.5 ± 0.6
	+ 5.04 µm acrylate	1.4 ± 0.2	1.1 ± 0.1
	+ 5.04 µm acrylate + AlO_x	1.5 ± 0.3	1.2 ± 0.2
BOPP B	Plain film	6.1 ± 1.9	4.8 ± 1.6
	+ 0.75 µm acrylate	3.3 ± 0.7	2.6 ± 0.6
	+ 0.75 µm acrylate + AlO_x	1.7 ± 0.3	1.4 ± 0.2
	+ 5.04 µm acrylate	1.4 ± 0.3	1.1 ± 0.2
	+ 5.04 µm acrylate + AlO_x	1.6 ± 0.2	1.3 ± 0.2
BOPP C	Plain film	4.1 ± 0.3	3.3 ± 0.2
	+ 0.75 µm acrylate	1.1 ± 0.1	0.9 ± 0.1
	+ 0.75 µm acrylate + AlO_x	2.8 ± 0.5	2.2 ± 0.4
	+ 5.04 µm acrylate	1.3 ± 0.2	1.0 ± 0.2
	+ 5.04 µm acrylate + AlO_x	1.7 ± 0.4	1.4 ± 0.3

This explanation is additionally supported by the fact that outliers only appeared for the thinner 0.75 µm acrylate (see also later topcoats, Section 6.4.2.2), which revealed a substantially larger amount of the circular surface features, compared to the 5.04 µm thick acrylate layer. It has to be noted that a small degree of waviness (i.e. additional background structure) was also present for all other acrylate layers, which can be seen from the variation of mean RMS values between 1.1 and 1.8 nm and the respective standard deviations. This was, however, not to the same extent as found for the two samples described above. Not taking these two outliers into account, all surfaces reveal very similar roughness values before and after AlO_x

coating. Thus, despite the marginal changes in granular structure, one cannot necessarily conclude that the AlO_x layer increased the surface roughness significantly (though the mean values for RMS and roughness average are slightly higher after AlO_x coating). Apart from the two outliers, RMS figures obtained for the acrylate layers (AlO_x coated and uncoated) are very much in agreement with findings by Affinito and co-workers [329], who state that RMS surface roughness of acrylate layers with and without inorganic coatings typically is of the order of 0.8 to 1.5 nm. However, in their investigations this was only valid for UV radiation cured acrylate coatings, whilst for electron beam cured acrylates (as they are in this study) a higher surface roughness was claimed (although no values are reported in their publication).

A way of removing the effect of additional surface topography (such as the waviness, which is also a main component of the topography of the plain BOPP films, see *Figure 6-61*) is to level the AFM images with a polynomial of higher order, such as 7^{th} order line-wise levelling (which was the highest degree offered by the AFM software). All AFM images were generally levelled by a 1^{st} order linear to remove lines caused by the scanning motion and the effect of sample tilt. If the 7^{th} order levelling is sufficient to remove all waviness in the scan, this will give the surface roughness caused by the grain-like structure only. It has to be noted, though, that the waviness is part of the surface texture of the films (also seen in SEM images) and not an artefact induced by the AFM scanning process. Therefore, for describing the 'true' surface roughness (on 5 x 5 µm²), a 7^{th} order line-wise levelling is not valid. Using 7^{th} order line-wise levelling, however, helps to remove unwanted interference of roughness parameters by the overlying surface texture. Surface roughness results obtained after 7^{th} order line-wise levelling are summarised in *Table 6-29*, whilst the effect it has on the appearance of AFM scans is shown in *Figure 6-63*. Due to the low RMS and roughness average values after 7^{th} order line-wise levelling, two decimal places are shown for the respective parameters.

From *Table 6-29* it is evident that the two outliers were eliminated by the levelling procedure when using a polynomial of higher order. Furthermore, also the roughness values of the plain BOPP films are decreased, as the levelling reduced the effect of the additional overlying surface texture, which largely affected BOPP A and B, on the calculated roughness values. This is also evident when comparing the AFM images of 1^{st} and 7^{th} order line-wise levelling in *Figure 6-63*.

Table 6-29: Surface roughness of plain, acrylate (undercoat) and AlO_x coated BOPP films after 7th order line-wise levelling (calculated from 5 x 5 µm² AFM scans)

Film	Description	Root mean square	Roughness average
		nm	nm
BOPP A	Plain film	2.53 ± 0.13	1.99 ± 0.11
	+ 0.75 µm acrylate	0.86 ± 0.01	0.69 ± 0.01
	+ 0.75 µm acrylate + AlO_x	1.09 ± 0.03	0.87 ± 0.02
	+ 5.04 µm acrylate	0.88 ± 0.01	0.70 ± 0.01
	+ 5.04 µm acrylate + AlO_x	1.18 ± 0.05	0.94 ± 0.04
BOPP B	Plain film	3.55 ± 0.20	2.81 ± 0.15
	+ 0.75 µm acrylate	0.89 ± 0.02	0.71 ± 0.01
	+ 0.75 µm acrylate + AlO_x	1.04 ± 0.04	0.82 ± 0.03
	+ 5.04 µm acrylate	1.02 ± 0.04	0.81 ± 0.03
	+ 5.04 µm acrylate + AlO_x	1.35 ± 0.17	1.08 ± 0.13
BOPP C	Plain film	3.45 ± 0.13	2.72 ± 0.10
	+ 0.75 µm acrylate	0.90 ± 0.01	0.71 ± 0.01
	+ 0.75 µm acrylate + AlO_x	1.18 ± 0.09	0.93 ± 0.06
	+ 5.04 µm acrylate	0.84 ± 0.01	0.67 ± 0.01
	+ 5.04 µm acrylate + AlO_x	1.24 ± 0.11	1.00 ± 0.08

A comparison of the roughness values for the acrylate undercoat pre-and post-AlO_x deposition also indicates that the AlO_x layer slightly increased the surface roughness in all cases. This is now in agreement with the previous findings based on AFM images, which showed a more pronounced and coarse granular structure for the AlO_x coated acrylate undercoats. It is, once again, emphasised here that the coarser structure observed for the AlO_x coated acrylate layer has not been confirmed to be solely due to the AlO_x layer itself, but may well be an imaging artefact of AFM analysis.

When comparing the images of the plain film surfaces and also their roughness parameters (after 1st and 7th order levelling), it becomes clear that BOPP A and B are strongly affected by the superimposed waviness (large decline in RMS), whilst for BOPP C, the change in roughness and appearance is only small. Furthermore, the scan of BOPP A shows that not all waviness could be removed by the 7th order levelling.

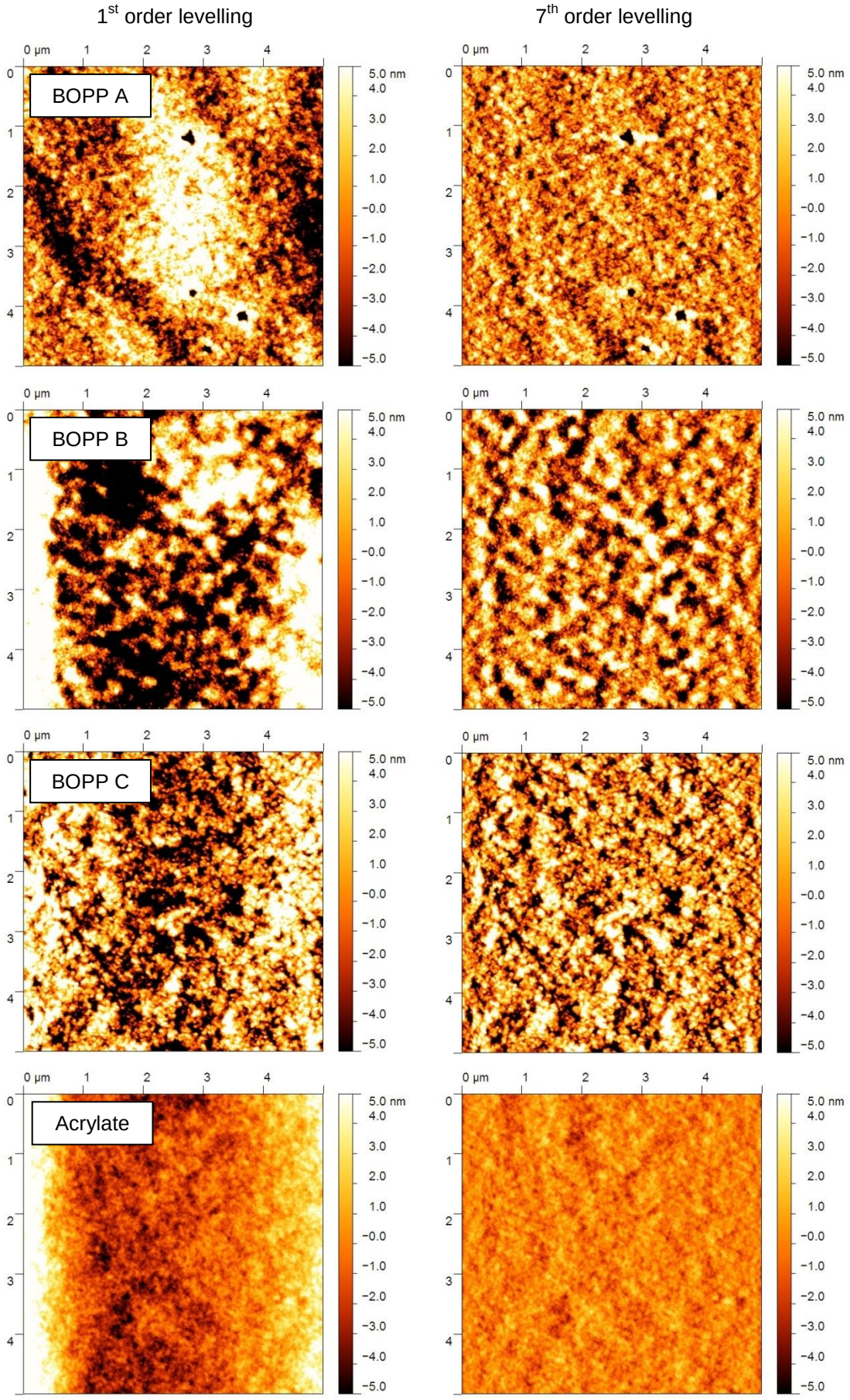

Figure 6-63: 5 x 5 µm² AFM scans; left 1st order levelled and right 7th order levelled; from top to bottom: BOPP A, BOPP B, BOPP C and BOPP B with 0.75 µm thick acrylate

6.4.2 Acrylate topcoats

6.4.2.1 Barrier properties

Along with depositing acrylate undercoats onto the three plain BOPP films, AlO_x coated versions of the same BOPP films were provided with an acrylate topcoat during the same runs (0.75 µm and 5.04 µm thick acrylate layers). The samples chosen for this investigation have previously been AlO_x coated with the additional application of in-line plasma pre- and post-treatment (coated as rolls of film). The barrier levels measured before and after acrylate topcoat deposition are outlined in *Table 6-30*. Also listed in this table are the respective BIF values induced by the acrylate topcoat and the plain film barrier performance.

Table 6-30: Barrier properties (OTR and WVTR) of AlO_x coated BOPP films with acrylate topcoats of 0.75 µm and 5.04 µm thickness

Film	Description	OTR		WVTR	
		cm³/(m² d)	BIF	g/(m² d)	BIF
BOPP A 30 µm	Plain (uncoated)	1250 – 1450	-	4 – 5	-
	Plain + AlO_x	257 ± 15	-	3.98 ± 0.30	-
	AlO_x + 0.75 µm acrylate	49.0 ± 4.7	5.2	2.70 ± 0.09	1.5
	AlO_x + 5.04 µm acrylate	38.1 ± 0.1	6.7	2.32 ± 0.03	1.7
BOPP B 15 µm	Plain (uncoated)	2500 – 2900	-	7 – 8	-
	Plain + AlO_x	82.6 ±17.7	-	5.89 ± 0.18	-
	AlO_x + 0.75 µm acrylate	28.9 ± 8.5	2.9	5.17 ± 0.20	1.1
	AlO_x + 5.04 µm acrylate	16.2 ± 1.1	5.1	4.45 ± 0.10	1.3
BOPP C 20 µm	Plain (uncoated)	2000 - 2100	-	6 – 7	-
	Plain + AlO_x	26.7 ± 3.1	-	4.73 ± 0.07 2.32 ± 0.05*	-
	AlO_x + 0.75 µm acrylate	13.7 ± 0.5	1.9	0.46 ± 0.07	10.3
	AlO_x + 5.04 µm acrylate	8.12 ± 0.06	3.3	0.36 ± 0.03	13.2

*aged (measurement taken later, see Section 6.2.1.2)

The measurements summarised in *Table 6-30* expose an obvious oxygen barrier improvement owing to the deposition of an acrylate topcoat. The improvement is larger than could be expected based on the ideal laminate theory (Equation (4-8)) and is the most pronounced for AlO_x coated BOPP A and the least for AlO_x coated BOPP C, as can be concluded from comparing the individual BIFs. This means that

on films that already had better oxygen barrier properties after AlO_x coating, the barrier enhancement derived from an acrylate topcoat is not as great. It is, furthermore, noticeable that for all samples, an increase of acrylate layer thickness further lowered the respective OTR values and their standard deviations. This is in contrast to the acrylate undercoats, where an increase of acrylate thickness did not result in further barrier improvement after AlO_x coating. When comparing the WVTRs before and after acrylate topcoat deposition, only a minute improving effect is evident for BOPP A and B, which is marginally increased for the thicker topcoat. For BOPP C, by contrast, the application of acrylate topcoats resulted in WVTR values of less than 1 g/(m² d) for both topcoat thicknesses. I should, however, be mentioned here that AlO_x coated BOPP C, in contrast to AlO_x coated BOPP A and B, showed an improvement of water barrier with time (see Chapter 6.2.1.2), although this improvement was not 'spectacular' (WVTR halved within approximately two years after coating). This film has been the best performing BOPP film with AlO_x coating, which was attributed to the higher oxygen content in the BOPP film surface (see Chapter 6.1.3.2).

The barrier enhancement when using acrylate (and other polymer based) topcoats has been reported by several research groups [96, 175, 290, 391, 392, 395]. In general, the improvement of barrier properties was attributed to the protection of the inorganic barrier layer from intense stress (which can create coating fracture) and damage/scratching during winding (in vacuum and during subsequent conversion), due to the polymer coats abrasion resistance and mechanical robustness [175, 329, 390, 392, 396]. This is especially of importance when the acrylate coating is applied in-line (in vacuum), without any contact of the thin inorganic barrier layer with the equipment (rollers etc.) prior to deposition of the topcoat. It is this initial contact of the barrier layer with the equipment and also the reverse side of the film during rewind that can already result in the formation of defects in the coating (and thus induce deterioration of barrier properties). Applying an in-line topcoat eliminates this source of defects. In this study, however, the topcoats were applied off-line on A4 samples that were previously AlO_x coated in a roll-to-roll process and, consequently, were exposed to contact with the equipment and reverse side of the film and further handling (e.g. cutting of samples, mounting for acrylate deposition etc.). Therefore, damage to the originally pristine inorganic barrier layer may have been inflicted before deposition of the acrylate. It is, thus, assumed that the improvement in barrier performance must be associated with other effects occurring during acrylate deposition. Here, it is important to mention Affinito's and Hilliard's [154] idea of the infiltration of the polymer topcoat (i.e. acrylate) into the defects of the inorganic coating, such as pinholes, damage/cracks or even grain boundaries. This 'pore

filling' process results in a reduction of the permeability/diffusion coefficient (for the respective permeant) within the defects from that of air to that of the polymer/acrylate, which is a lot lower [4]. Consequently, the overall permeation through the topcoated film can be significantly reduced. This approach has also been taken up by other researchers, for example for the plugging of defects by nano-particles as described by Ramadas and co-workers [397], the filling of defects with an adhesive during lamination as stated by Miesbauer et al. [133] or the healing of defects/flaws in SiO_x barrier coatings by deposition and cross-linking of organosilane layers [314, 398]. Even before Affinito and Hilliard, Amberg-Schwab et al. [395] suggested the compensation of macroscopic defects induced by the application of a hybrid polymer topcoat and schematically show the 'pore filling' effect. Furthermore, analytical evidence has been found that confirmed the filling of pores (nano-defects) when using a monomer deposition process for polymer layers [173].

Here, it is assumed that the 'pore filling' is the predominant reason for the improved barrier performance, especially oxygen barrier, after application of the acrylate topcoat. AlO_x coated BOPP A exhibited a large amount of defects in its coating (refer to Sections 6.2.2.2 and 6.2.2.3), which was assumed to be the reason for the high OTR values (prior to topcoat deposition). With the application of the topcoat, the filling of these defects largely impacts and reduces the OTR and, therefore, results in the higher BIFs, compared to the other BOPP films.

It is still surprising, though, that only on AlO_x coated BOPP C, the topcoat also significantly improved WVTR, whilst for BOPP A and B the improvement is negligible. It is thought here that due to the lack of larger defects (as present in the AlO_x layer on BOPP A and presumably also BOPP B) the smaller defects (maybe even microscopic defects/nano-defects, see Section 4.6.2) in the AlO_x coating of BOPP C are filled with the acrylate and, consequently, the water vapour permeation is reduced. When larger (macroscopic) defects are present in the inorganic barrier, then these are believed to get preferably filled.

In addition to that, the barrier properties of the acrylate itself, which is now adjacent to the inorganic barrier layer, play an important role in reducing the permeation rates, as discussed in the previous section about acrylate undercoats (refer to Chapter 6.4.1.1). The acrylate, with its better oxygen barrier compared to BOPP, changes the concentration gradient for oxygen in direct vicinity to the defects/pinholes in the AlO_x layer and, therefore, reduces the overall oxygen permeation. This effect becomes more pronounced with increasing the thickness of the acrylate layer. Furthermore, a thicker acrylate layer will also cover larger

antiblock particles protruding further from the coated BOPP film surface. These antiblock particles are known to generate defects in thin inorganic barrier layers [231, 232]. Langowski also states that “when an inorganic layer lies between two polymer layers having very different permeation coefficients, the combination of the polymer material with the lower permeability and the inorganic layer dictate the overall permeability” [126].

For BOPP C, it is also worth mentioning that the topcoat is more effective in enhancing barrier performance (OTR and WVTR) than an acrylate undercoat. Similar findings have also been published by other researchers [96, 175].

On combining several organic (e.g. acrylate) and inorganic layers to multilayer structures (not done in this study), the barrier improvement is assigned to an increase in lag time (time until equilibrium permeation is reached), due to the generated tortuous paths that the permeating substance has to negotiate. Once the lag time has passed and a steady-state (equilibrium) permeation is reached, the amount of permeating molecules and hence transmission rate will be a lot higher than originally obtained/measured. This means that in organic/inorganic multilayer structures, the permeation is decelerated, but not completely eliminated. [136]

However, the various barrier improvements achieved strongly depend on the acrylate chemistry used, as well as on the type of inorganic barrier layer and its properties (see the different results for under- and topcoats on PET with aluminium oxide and indium cerium oxide barrier layers, as obtained by Miyamoto et al [175]).

6.4.2.2 Surface topography and roughness

In addition to the acrylate undercoats on BOPP A to C, the acrylate topcoats on the AlO_x coated BOPP films were also examined in terms of surface topography and roughness, using DIC light microscopy and 5 x 5 µm² AFM scans.

As the thin AlO_x layer did not change the surface topography of the BOPP films (and could neither be detected in DIC light microscopy), it is not surprising that the DIC images of the acrylate topcoats look identical to the DIC images shown for the respective acrylate undercoats in Chapter 6.4.1.2. Consequently, analogous observations can be made with respect to the smoothing effect of the two acrylate thicknesses on the different BOPP films for various magnification levels, as well as the circular-shaped features appearing for the 0.75 µm thick acrylate layer. Based on the similarities and the extensive discussion in Chapter 6.4.1.2, no light microscope images of the acrylate topcoats will be shown and discussed in this section.

The same applies to the AFM investigation of the acrylate topcoats. Also here, a minimum of eight scans per sample was carried out to obtain statistically reliable roughness results. Once again, all acrylate layers showed a very smooth surface appearance and exhibited the same fine-granular surface structure as already seen when investigating the acrylate undercoats on the plain BOPP films (see *Figure 6-61*, bottom right). This was to be expected, based on the fact that all acrylate layers of a respective thickness (5.04 µm or 0.75 µm) were deposited in the same experiment. Furthermore, also in the case of the topcoats, the fine-grainy texture was overlaid by an additional surface waviness, which affected the measured surface roughness values and their standard deviations (see *Table 6-31*, analogous to the discussion in Chapter 6.4.1.3). Due to the appearance of the acrylate topcoats being identical to the undercoats, no AFM images are shown in this chapter and the reader is referred to *Figure 6-61*, bottom right, for an AFM image of the acrylate surface and Chapter 6.2.2.3, for a discussion of the AFM investigation of the AlO_x coated BOPP films. The roughness results obtained from the AFM analysis of the acrylate topcoats are presented in *Table 6-31*. For comparison, the roughness parameters of the individual AlO_x coated BOPP films prior to acrylate deposition are displayed.

For all BOPP films and both acrylate layer thicknesses, the acrylate coatings reveal a significant smoothing effect as can be deduced from the reduced RMS and roughness average values after acrylate deposition. This is, once again, in agreement with the findings for undercoats (see Section 6.4.1.3). Apart from one

anomaly (0.75 µm acrylate on AlO_x coated BOPP B), mean RMS values are of the order of 1.2 to 1.8 nm, i.e. comparable to the acrylate undercoats. The outlier in surface roughness (2.3 ± 1.0 nm) was, again, found for the thinner acrylate layer on BOPP B. As discussed in detail previously, this high roughness is due to an additional surface waviness superimposing the fine-granular texture.

Table 6-31: Surface roughness of AlO_x coated BOPP films and acrylate topcoats (calculated from 5 x 5 µm² AFM scans)

Film	Description	Root mean square	Roughness average
		nm	nm
BOPP A	AlO_x	4.1 ± 0.6	3.3 ± 0.5
	AlO_x + 0.75 µm acrylate	1.3 ± 0.3	1.0 ± 0.3
	AlO_x + 5.04 µm acrylate	1.2 ± 0.1	0.9 ± 0.1
BOPP B	AlO_x	6.0 ± 0.7	4.8 ± 0.6
	AlO_x + 0.75 µm acrylate	2.3 ± 1.0	1.9 ± 0.8
	AlO_x + 5.04 µm acrylate	1.5 ± 0.5	1.2 ± 0.5
BOPP C	AlO_x	4.3 ± 0.3	3.4 ± 0.2
	AlO_x + 0.75 µm acrylate	1.8 ± 0.3	1.4 ± 0.2
	AlO_x + 5.04 µm acrylate	1.5 ± 0.2	1.1 ± 0.2

Table 6-32 summarises the roughness results obtained for the acrylate topcoats after 7th order line-wise levelling, which largely removed the effect of the wavy background structure and led to a reduction of the mean RMS and roughness average values, compared to *Table 6-31*. Also this is in agreement with the finding for acrylate undercoats. All acrylate layers exhibit similar roughness values after 7th order line-wise levelling and one cannot conclude that the thicker acrylate layers are smoother than the thinner ones or vice versa.

Table 6-32: Surface roughness of AlO_x coated BOPP films and acrylate topcoats after 7th order line-wise levelling (calculated from 5 x 5 µm² AFM scans)

Film	Description	Root mean square	Roughness average
		nm	nm
BOPP A	AlO_x	2.66 ± 0.23	2.09 ± 0.17
	AlO_x + 0.75 µm acrylate	0.91 ± 0.01	0.73 ± 0.01
	AlO_x + 5.04 µm acrylate	0.96 ± 0.03	0.76 ± 0.02
BOPP B	AlO_x	3.24 ± 0.17	2.56 ± 0.14
	AlO_x + 0.75 µm acrylate	0.95 ± 0.02	0.76 ± 0.02
	AlO_x + 5.04 µm acrylate	0.94 ± 0.01	0.75 ± 0.00
BOPP C	AlO_x	3.72 ± 0.06	2.95 ± 0.04
	AlO_x + 0.75 µm acrylate	0.96 ± 0.01	0.77 ± 0.01
	AlO_x + 5.04 µm acrylate	0.93 ± 0.01	0.74 ± 0.01

6.4.2.3 Apparent activation energy of permeation

The apparent activation energies of oxygen and moisture permeation through the plain BOPP films, AlO_x coated BOPP films and topcoated films (with 0.75 µm acrylate) were determined, in order to obtain more information about the permeation mechanisms for water vapour and oxygen and how the latter are affected by the application of the acrylate topcoat. This investigation is especially interesting in the case of AlO_x coated BOPP C, where a WVTR of less than 1 g/(m² d) was obtained with an acrylate topcoat. The activation energy approach has been used by several research groups [128-130, 164, 399, 400] for polymer films coated with inorganic barrier layers. It can give evidence of a macro-defect driven permeation, possible chemical interactions and also hindered permeation through nano-defects, due to the sensitivity of the apparent activation energy to changes in transport mechanisms.

For this investigation, the temperature dependence of OTR and WVTR was determined via barrier measurements conducted at four different temperatures: 20 °C, 30 °C, 40 °C and the respective standard measurement temperature of 23 °C for OTR and 37.8 °C for WVTR. The RH conditions for a standard measurement were also used: 50 % RH for OTR and a 90 % RH gradient for WVTR. Since there can be a change in activation energy of gas permeation through the polymer when the transition between glassy and rubbery state takes place [401], temperatures in this investigation were selected so that they are all above the glass transition temperature of the BOPP film (T_g in the range of 0 to 10 °C [55] for isotactic PP). Samples were generally measured for approximately 24 hours to ensure that permeation equilibrium was reached. The results were subsequently transformed into an Arrhenius plot based on Equation (4-7), in order to obtain the apparent activation energies from the slope of the regression line. Due to the time consuming measurement procedure, only two samples were investigated for each film and coating, i.e. two plain film specimens, two AlO_x coated films and two topcoated films for each BOPP film type. Furthermore, only the 0.75 µm acrylate topcoats were investigated.

The average apparent activation energies obtained in this investigation are summarised in *Table 6-33*, whilst the respective Arrhenius plots for each BOPP film are shown in *Figure 6-64*, *Figure 6-65* and *Figure 6-66*. The two replicate measurements for one type of sample are marked with the same coloured symbol (but different shades) in the graphs (red circle: uncoated BOPP, blue triangle: AlO_x coated BOPP and grey square: topcoat on AlO_x coated BOPP).

Table 6-33: Apparent activation energies E_Q for oxygen and water vapour permeation through plain, AlO_x coated and topcoated BOPP films

Film	Description	E_Q (OTR)	E_Q (WVTR)
		kJ/mol	kJ/mol
BOPP A	Plain	41.4 ± 0.8	53.5 ± 1.3
	AlO_x	44.5 ± 1.0	50.3 ± 0.8
	AlO_x + 0.75 µm acrylate	37.9 ± 1.4	46.2 ± 0.1
BOPP B	Plain	43.1 ± 1.0	52.0 ± 0.1
	AlO_x	39.2 ± 1.0	49.2 ± 0.5
	AlO_x + 0.75 µm acrylate	40.7 ± 3.8	43.6 ± 0.2
BOPP C	Plain	41.5 ± 0.3	57.3 ± 0.2
	AlO_x	39.4 ± 0.3	51.8 ± 0.4
	AlO_x + 0.75 µm acrylate	39.2 ± 0.7	58.6 ± 1.1

It is obvious from the graphs that the linear trend line gave a very good fit in all cases, with coefficients of determination consistently being larger than 0.99. This means that activated rate processes are accountable for the oxygen and water vapour permeation of the samples investigated.

The activation energies for oxygen permeation obtained for all three plain BOPP films are of the order of 40 to 44 kJ/mol, which is in agreement with the range given in literature [130, 402-404]. There is, however, still a small variation visible for the individual film types, which is attributed to different film compositions (additives, coextruded films with homopolymer core and either co- or terpolymer skin layers of varying thicknesses), as well the degree of film orientation, which appears to have an effect on the activation energy based on comparisons between CPP and BOPP [403, 405].

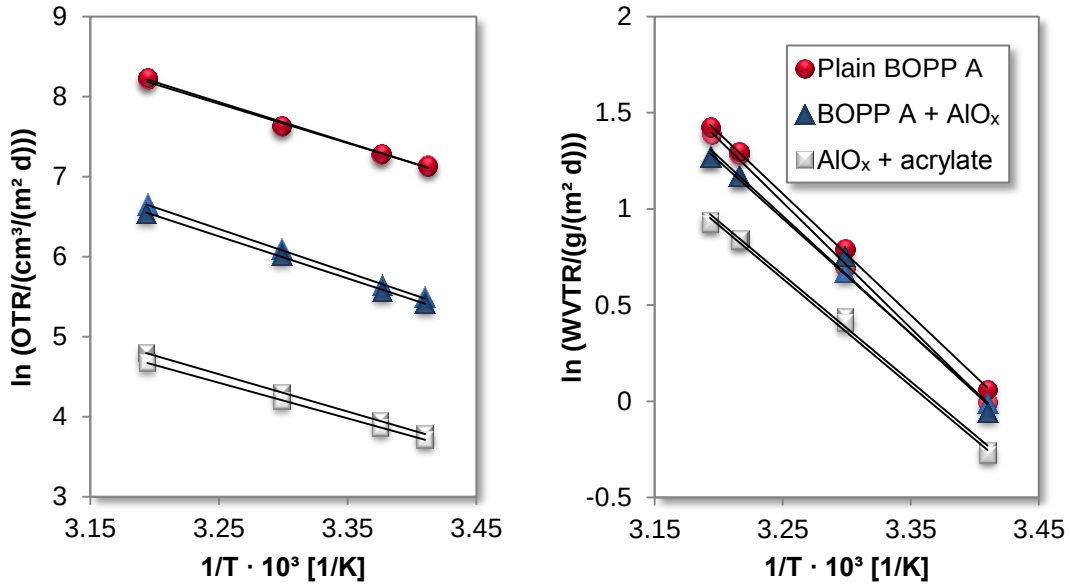

Figure 6-64: Arrhenius plots for determination of apparent activation energies of oxygen (left) and water vapour permeation (right) for BOPP A

After coating with AlO_x, the activation energy for BOPP A reveals a small increase, whilst for BOPP B and C a slight drop is visible. Nevertheless, only two samples each were measured in this investigation and, furthermore, other researchers report quite high standard deviations for the activation energy of oxygen permeation (around 3 to 5 kJ/mol, see Tropsha and Harvey [128]). Also, as stated above, slight variations in the film composition and degree of orientation may have an effect on the activation energy. It is, moreover, noticeable from *Figure 6-64* to *Figure 6-66* that the linear regression lines run very much in parallel for the oxygen plots. Consequently, it is assumed that the changes seen are not significant and that the activation energies are identical within experimental error, despite the improvement in oxygen barrier (to different degrees) by the application of the inorganic coating (see Chapter 6.2.1.1). This indicates that after coating with AlO_x, the permeation through the BOPP polymer film is the only temperature dependent and therefore rate-limiting process. The AlO_x layer primarily acts as a hurdle containing macroscopic defects, which the permeating oxygen molecules have to negotiate in order to enter/leave the polymer. Hence, the permeation of oxygen through the AlO_x coated BOPP films is via macroscopic defects, which do not physically hinder the flow of the permeating molecules. Analogous findings have been reported by other researchers for AlO_x coated PP and PET [130, 160, 165] and further material combinations (predominantly SiO_x on PET) [128, 129, 164, 399, 404, 405].

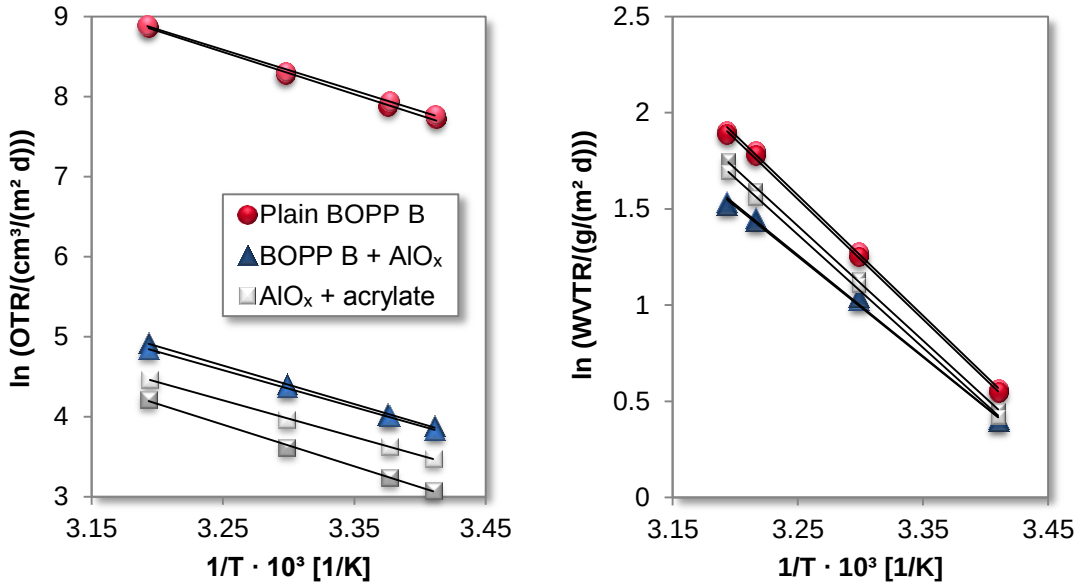

Figure 6-65: Arrhenius plots for determination of apparent activation energies of oxygen (left) and water vapour permeation (right) for BOPP B

The activation energy values for oxygen transport do, moreover, not change significantly after the deposition of the acrylate topcoat, although this resulted in a further enhancement of oxygen barrier properties (see *Table 6-30*). Only for BOPP A, a more distinct drop is noticeable, but the activation energy value obtained is still within the typical range for BOPP films. Once again, this suggests that the oxygen permeation through the AlO_x coated and acrylate topcoated films is still a macro-defect driven process, with the permeation through the BOPP substrate being the rate-limiting step. This is in agreement with results obtained by Henry and co-workers [406] for the application of an acrylate topcoat to AlO_x coated PET, but disagrees with findings of Miyamoto et al. [175]. The latter authors noted an increase of the activation energy for oxygen permeation by coating a PET substrate with AlO_x, as well as by the additional application of an acrylate topcoat (thickness < 1 µm). These inconsistencies of results may be explained by the effect of different vacuum deposition techniques (and conditions) and also the effect of the specific acrylate chemistry on the AlO_x layer properties in each individual case.

In this study, it is assumed that the improvement of OTR by the acrylate layer is due to the filling of macroscopic defects in the AlO_x coating ('pore filling') and due to the better oxygen barrier properties of the acrylate, in contrast to BOPP (see Chapter 6.4.2.1). It would be interesting to see what the activation energy (for oxygen permeation) of the acrylate layer on its own is, since this value may differ from the value for plain BOPP. Thus, if the permeation is dominated by the permeation through the acrylate (and not BOPP) as the rate-limiting step, the apparent activation energy of the AlO_x coated film with acrylate topcoat would be expected to

change towards the activation energy value for the acrylate. This may well be noticeable for the thicker 5.04 µm topcoat, which has not been investigated in this study.

The interpretation of the activation energy data for water vapour transport is, however, less straight forward, due to the larger spread and rather inconsistent behaviour of the data. The plain BOPP films reveal activation energies for moisture permeation, which range from 52.0 to 57.3 kJ/mol. These values differ from values reported in literature, though also here a broad range can be found (for example Deng et al. [130] report 64.6 ± 2.0 kJ/mol, while Tropsha and Harvey [128] state 38.9 ± 2.1 kJ/mol and Hanika [404] 27.7 kJ/mol).

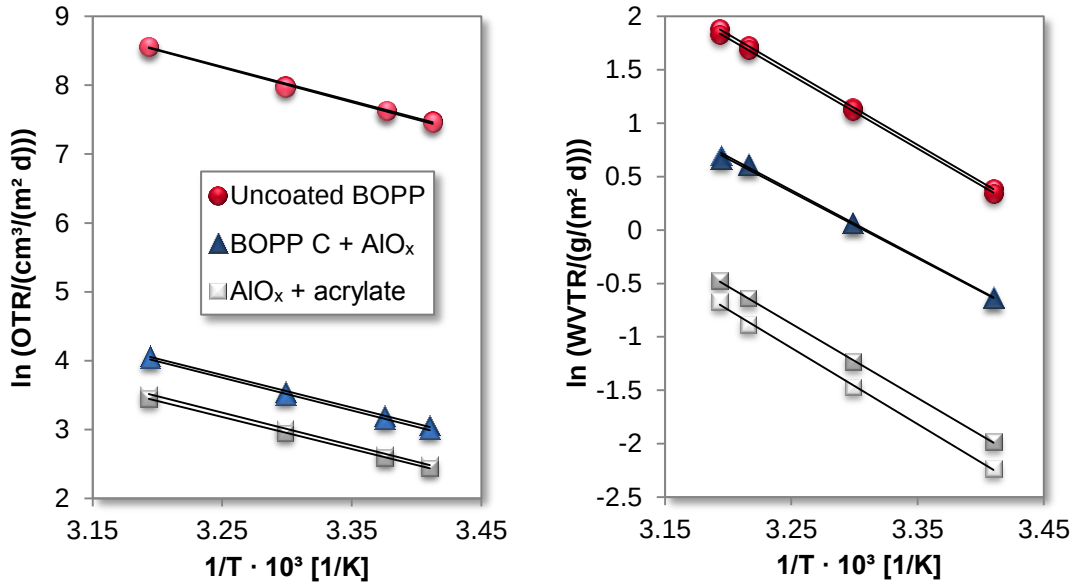

Figure 6-66: Arrhenius plots for determination of apparent activation energies of oxygen (left) and water vapour permeation (right) for BOPP C

For all three BOPP films, the activation energy is slightly decreased by the application of the AlO_x layer, which is accompanied by a negligible improvement of WVTR (refer to *Table 6-30*). A decrease of the activation energy for moisture permeation by the application of an inorganic barrier layer has been reported by Henry et al. [160] for a 10 nm AlO_x layer on PET produced via plasma enhanced PVD. They investigated a variety of AlO_x coatings (manufactured by different deposition techniques), as well as other inorganic barrier layers, and found a very broad range of 22 to 64 kJ/mol for the activation energy of water vapour permeation through the inorganic barrier layers on PET (uncoated PET 41.5 kJ/mol). This was subsequently assigned to the permeation mechanism being strongly influenced by the coating chemistry. No further comments were made as to why the coating could lead to an increase, as well as a decrease, of the activation energy, compared to the

uncoated substrate, whilst improving WVTR largely in all cases. In this study, however, the drop in moisture activation energy (induced by AlO_x coating) was rather small and, presumably, is not significant. Consequently, it is assumed that there may be some degree of chemical interaction, but the bulk of the water molecules still permeates unhindered through the AlO_x layer (see also the small enhancement of WVTR induced by AlO_x application, *Table 6-30*). This means that similar to the oxygen permeation through the AlO_x coated BOPP films, also the water vapour permeation is dominated by the transport through the polymer substrate as rate-limiting process.

In the case of BOPP A and B, the acrylate topcoat resulted in a further decrease of the calculated activation energy, whilst for BOPP C, an increase from 51.8 kJ/mol (BOPP C + AlO_x) to 58.6 kJ/mol (BOPP C + AlO_x + acrylate) was detected. An increase in activation energy can either be explained by a chemical interaction between the permeant and the coating or permeation through defects that physically hinder the flux of the permeating molecule, i.e. nano-defects/pores [129]. Nevertheless, it is assumed that by the application of the acrylate topcoat the AlO_x layer itself is not changed in its intrinsic structure or chemistry (apart from the proposed 'pore filling') and, hence, it appears unlikely that the acrylate induces a chemical interaction between permeating water molecules and the AlO_x layer. Furthermore, if this would be the case, a similar effect should have taken place for BOPP A and C (i.e. improvement of WVTR and increase of activation energy by the acrylate topcoat). Here, it is important to mention that AlO_x coated BOPP C was the only film that exhibited an improvement of water barrier with time. When the acrylate topcoats were deposited, more than one year after the AlO_x coated samples were produced, the WVTR had dropped to a value of around 2.32 g/(m² d) (approximately half the original value, see *Table 6-30*). After acrylate topcoat deposition, the WVTR was less than 1 g/(m² d), a significant improvement not obtained for any other BOPP film. It is, consequently, assumed that the 'pore filling' of smaller defects (e.g. smaller than the defects in the AlO_x layers on BOPP A), maybe even nano-defects, results in this water barrier improvement for the acrylate topcoat on AlO_x coated BOPP C and presumably also the rise in activation energy as the permeation becomes increasingly hindered. Henry et al. [406] and Miyamoto et al. [175] also report an increase of the activation energy for water vapour by the application of topcoats to AlO_x coated PET. In the former publication, the increase in activation energy is assigned to the topcoat leading to a reduction in the volume fraction of permeation channels for water molecules and hence an enhancement of the interaction between water vapour and oxide layer.

Regarding the interpretation of activation energy data for water vapour, it should be mentioned that there are also a few cases published where despite the unchanged activation energy (no change in activation energy is generally attributed to a macro-defect driven mechanism, as explained earlier for the oxygen permeation) additional investigations suggested a chemical interaction rather than a defect dominated permeation [128, 157]. Consequently, whilst the literature is very consistent in the reported data and associated evaluation for oxygen permeation, there is a broad spectrum of results and data interpretation available for the activation energy of water vapour, determined for polymer films coated with thin inorganic barrier layers.

Based on the data obtained here from the activation energy measurements (water vapour but also oxygen permeation) for the various AlO_x/acrylate coated and uncoated BOPP films, it is concluded that this evaluation approach is not an appropriate technique to asses information about the permeation mechanisms for water vapour and oxygen through inorganic AlO_x barrier layers on polymer films. The changes seen here (for the different film types and coating variations) are not significant enough to allow a truly reasonable and unambiguous interpretation with respect to barrier/permeation mechanisms and, hence, cast doubt on the activation energy approach.

6.4.2.4 Calculation of transmission rate for topcoated films

It is also possible to calculate an approximation for the expected transmission rate of the acrylate topcoated film, based on the permeability properties of the BOPP film and the acrylate, as well as the barrier improvement obtained through the application of the inorganic layer (see references [126, 153, 302]). Therefore, one has to imagine that the topcoated structure (BOPP/AlO_x/acrylate) is split along the middle of the inorganic barrier layer. The BOPP substrate, as well as the acrylate layer, is now covered by exactly the same AlO_x barrier layer, the latter being characterised by its size, shape and density of defects. These characteristic properties of the inorganic barrier layer can be described by its barrier improvement factor, which is now applicable for both polymers (BOPP and acrylate) adjacent to the inorganic layer. The overall transmission rate of this two-layer structure (i.e. layer 1 = AlO_x coated BOPP; layer 2 = AlO_x 'coated' acrylate) can be described by the following approximation, derived from the ideal laminate theory (Equation (4-8)) and the assumptions made above [126]:

$$Q_{total} \approx \left(\frac{BIF_{100}}{Q_{100,BOPP}} + \frac{BIF_{100}}{Q_{100,acrylate}}\right)^{-1} \quad (6\text{-}1)$$

Whereby BIF_{100} is the barrier improvement factor that would be obtained on a 100 µm thick BOPP substrate and can be approximated the following way (similar to Equation (4-9) but replacing Q_0 with Q_{100}; Q is the transmission rate of the AlO_x coated BOPP):

$$BIF_{100} \approx \frac{Q_{100,BOPP}}{Q} \quad (6\text{-}2)$$

As mentioned before, the BIF_{100} is now valid for the BOPP film, as well as the acrylate layer. Q_{100} is the transmission rate of the plain BOPP (or 'plain' acrylate) normalised for a 100 µm thick film/layer. The approach described in Equations (6-1) and (6-2) is, however, only valid, if the thickness of the polymers (acrylate and BOPP) is above a so-called critical thickness. Above this thickness, which for typical 'real' barrier layers is less than 2.5 µm [393], the transmission rate of the coated substrate is independent of the substrate thickness. Consequently, this calculation approach will only be used in the following for topcoats of a thickness of 5.04 µm.

The OTR values for the uncoated BOPP films (Q_{BOPP}) and the AlO_x coated BOPP films (Q) were measured and, hence, the corresponding $Q_{100,\ BOPP}$ and BIF_{100} values can be calculated. The results are stated in *Table 6-34*, along with the measured

OTR values required for the calculation. For the uncoated BOPP films, the centre values of the OTR ranges stated in *Table 6-1* are used.

Table 6-34: Oxygen barrier properties of plain (Q_{BOPP}) and AlO_x coated (Q) films, calculated normalised transmission rate of BOPP films (Q_{100}) and BIF_{100} values

Film (thickness)	Q_{BOPP}	Q	$Q_{100,BOPP}$	BIF_{100}
	cm³/(m² d)	cm³/(m² d)	cm³/(m² d)	
BOPP A (30 µm)	1350	257 ± 15	405	1.6
BOPP B (15 µm)	2700	82.6 ± 17.7	405	4.9
BOPP C (20 µm)	2050	26.7 ± 3.1	410	15

As can be seen, the Q_{100} values are very similar for BOPP A, B and C, which is to be expected as all three films are made from the same material.

The only unknown parameter in Equation (6-1) is now the normalised transmission rate of the acrylate, $Q_{100,\ acrylate}$. This transmission rate can be calculated using the OTR values measured for the 5.04 µm thick acrylate undercoats on the BOPP films (see *Table 6-27*). For this simple system consisting of two polymer layers (BOPP/acrylate), the ideal laminate theory (see Equation (4-8)) can be applied and $Q_{acrylate}$ can be calculated according to the following equation:

$$Q_{acrylate} = \left(\frac{1}{Q_{BOPP+acrylate}} - \frac{1}{Q_{BOPP}}\right)^{-1} \quad (6\text{-}3)$$

When this is done for all three BOPP films for an acrylate thickness of 5.04 µm and the respective normalised transmission rates are calculated, an average $Q_{100,\ acrylate}$ value of 132 cm³/(m² d) results. This value is, as expected, lower than the Q_{100} values for the BOPP films, which is of importance for the barrier improvement obtained by the acrylate topcoat, since the combination of the inorganic barrier layer and the polymer with the lower permeability determine the final barrier properties of the multilayer structure [126].

Now, Q_{total} can be assessed using Equation (6-1) and the results obtained are summarised in *Table 6-38*, together with the measured values for the 5.04 µm acrylate topcoat on the AlO_x coated BOPP films.

Table 6-35: Calculated (Q_{total}) and measured ($Q_{measured}$) oxygen transmission rates of AlO_x coated BOPP films with 5.04 µm acrylate topcoat

Film structure	Q_{total}	$Q_{measured}$
	cm³/(m² d)	cm³/(m² d)
BOPP A/AlO_x/Acrylate	63.8	38.1 ± 0.1
BOPP B/AlO_x/Acrylate	18.9	16.2 ± 1.1
BOPP C/AlO_x/Acrylate	6.63	8.12 ± 0.06

As can be seen, apart from BOPP A, the calculated and measured OTR for the acrylate topcoated AlO_x coated BOPP are in relatively good agreement. Only for BOPP A, the actually measured transmission rate is significantly lower than the calculated value. Here, it has to be noted that this calculation approach does not yet take a 'pore filling' effect by the acrylate into account, as discussed in Section 6.4.2.1. If this effect is considered, an additional term is added inside the brackets of Equation (6-1), which depends on the thickness of the inorganic barrier layer, the permeability of the acrylate, as well as characteristic defect properties, such as the defect density and effective mean area of one defect [133]. Nevertheless, in our case, these parameters are not known and, consequently, a calculation of Q_{total} with simultaneous consideration of 'pore filling' is not possible. It is obvious, though, that this additional term results in a further reduction of the overall transmission rate Q_{total} of the AlO_x/topcoated structure. It is assumed that this is one of the main reasons for the deviation between calculated and measured OTR for AlO_x/topcoated BOPP A. The SEM/AFM investigation of AlO_x coated BOPP A (see Chapters 6.2.2.2 and 6.2.2.3) revealed a substantial amount of defects in the AlO_x layer (with a diameter of 50 to several 100 nm), in contrast to the other AlO_x coated BOPP films. These defects presumably get filled by the acrylate and, thus, the OTR for BOPP A is lower. Despite the good agreement of the measured and calculated data for BOPP B and C (without considering 'pore filling'), this calculation cannot exclude that 'pore filling' also takes place for these films. It is, however, clear that for these films, a far smaller amount of defects is present (as seen in the AFM and SEM investigation), compared to AlO_x coated BOPPA.

In the case of WVTR, a calculation of the expected transmission rate analogous to OTR is not possible due to two reasons. Firstly, the calculated BIF_{100} value is less than one (for BOPP A and B), thus rendering the calculation approach invalid [126]. Furthermore, the water vapour transmission rate of the acrylate is unknown and cannot be calculated, as the application of the acrylate onto the plain BOPP films did not result in any water barrier improvement (i.e. Equation (6-3) is not applicable).

6.5 Lamination of AlO_x coated films

AlO_x coated BOPP films were converted using industrial-scale lamination processes. Solvent-based and solventless adhesive laminations were carried out. The aim of this study was to assess how AlO_x coated BOPP films perform after lamination and, thus, how their barrier properties can withstand downstream processing. This is an important objective in order to make AlO_x coated polymer film a fully commercially viable product within the packaging industry.

6.5.1 Solvent-based adhesive lamination of AlO_x coated BOPP

6.5.1.1 Barrier properties

The solvent-based adhesive lamination was performed using AlO_x coated BOPP C (in-line plasma pre-treatment only). As described in Section 5.4.1, two lamination trials were conducted. For the first trial, the adhesive was applied onto the uncoated BOPP film (as done by other researchers for SiO_x barrier layers [407]), whilst for the second trial, the adhesive was coated onto the AlO_x layer itself (which is standard for metallised film lamination). The barrier levels before and after adhesive lamination, along with the plain film barrier performance, are stated in *Table 6-36*.

Table 6-36: Barrier performance before and after lamination of AlO_x coated BOPP C

Description	OTR		WVTR	
	$cm^3/(m^2\ d)$	BIF (lamination)	$g/(m^2\ d)$	BIF (lamination)
Plain BOPP C	2000 – 2100	-	6 – 7	-
BOPP C + AlO_x (before lamination)	48.6 ± 8.2	-	4.76 ± 0.35	-
Lamination trial 1: adhesive onto uncoated BOPP	11.9 ± 0.6	4.1	2.63 ± 0.17	1.8
Lamination trial 2: adhesive onto AlO_x	183 ± 7	-	2.81 ± 0.08	1.7

The results shown in *Table 6-36* clearly demonstrate that conversion, such as lamination, of AlO_x coated BOPP is possible without damaging the barrier properties achieved via the reactively evaporated AlO_x coating. Furthermore, the oxygen barrier could even be improved by a factor of about four, compared to the AlO_x coated film prior to lamination. This improvement is greater than expected on the basis of the ideal laminate theory (see Equation (4-8), by adding a 20 µm BOPP film and an adhesive layer), which is in good agreement with results published by other researchers for the lamination of AlO_x coated PET [3, 294], SiO_x/AlO_x coated PET

[307], SiO_x coated BOPP [64, 237, 408], as well as metallised PET and BOPP [64, 149, 233, 237, 408]. The barrier improvement can be attributed to reasons similar to those for acrylate topcoats, as discussed in more detail in Section 6.4.2.1. Firstly, the barrier properties, i.e. permeability, of the polyurethane adhesive, which is now adjacent to the thin inorganic barrier layer and its defects, play an important role. Polyurethane adhesives, in general, have good oxygen barrier properties (better than BOPP) [126, 302], which has been stated by other researchers to be a possible reason for the barrier enhancement obtained during lamination [149, 233]. This is especially of importance if the adhesive thickness is above a so-called critical thickness, which depends on the size and density of defects, and in reality is typically less than 2.5 µm [393]. Then, the barrier properties of the adhesive dominate over those of the material laminated on top. Furthermore, the filling of defects (see Affinito and Hilliard [154]) in the inorganic barrier layer with the adhesive material can significantly improve the barrier properties of the laminated structure, as discussed by Miesbauer et al. [133]. Overall, a laminated film, where the AlO_x layer is over-coated by an adhesive, is a comparable structure to an acrylate topcoat applied onto an AlO_x coated film and, consequently, identical arguments for the barrier improvement can be made in both cases.

The oxygen barrier was, nevertheless, only enhanced by lamination when the adhesive was coated onto the plain BOPP. In the case of the adhesive being applied onto the AlO_x coating itself, the AlO_x coating clearly must have been damaged and, thus, the OTR increased, in our case by a factor of 3.8 (i.e. from a mean value of 48.62 to 183.05 $cm^3/(m^2\ d)$). This damage may happen during the application of the adhesive, during the subsequent drying process or during any contact of the rollers with the barrier coating. All these steps of the lamination process place additional strain on the coating and may result in scratches/cracks of the brittle AlO_x, which can act as permeation pathways for oxygen. However, the adhesive application itself via the flexo trolley is ‘cautious’ and good for delicate substrates, based on the ‘kiss’ contact between roller and film. The drying process is very short (drying tunnel approximately 7 m long, distance between application head and drying tunnel approximately 2 m, web speed 150 m/min) and, additionally, it can be assumed that stretching of the BOPP film due to web tensions is less than 1 %. Therefore, the barrier should not be affected (see barrier retention on elongation investigations, Section 6.2.1.5). Possible damage of the thin inorganic barrier layer and hence induced increase of OTR has been reported for metallised PET during extrusion lamination [149, 393] and is also mentioned by other researchers [151]. A further reason for the deterioration of oxygen barrier may be a possible interaction or chemical reaction between the adhesive or solvent (ethyl acetate) used and the thin

AlO_x layer. This will be further investigated in Section 6.5.1.3. The chemical attack of an aluminium metal layer in a laminated film structure is possible, despite its native protective oxide (which is not immune to chemical attack), and leads to the chemical conversion of aluminium to its transparent oxide or hydroxide, as stated by Mount [409]. This is generally induced in an acid or alkaline environment, due to the pH value of the adhesive. Nevertheless, Mount does not make any comments about a deterioration of barrier properties with the observed chemical attack of the aluminium barrier layer.

In the case of water vapour transmission rate, the barrier only improved by a factor of 1.7 to 1.8 (for both lamination trials). This, basically, just reflects the barrier improvement by adding an additional 20 µm BOPP film on top (e.g. for a twice as thick BOPP film, 40 µm instead of 20 µm, the value for the transmission rate is approximately halved). Based on the fact that the AlO_x layer did not significantly generate any barrier to moisture (compared to the plain BOPP film), this was to be expected.

6.5.1.2 Solvent retention and optical appearance

One important requirement for laminates produced using solvent-based adhesives is that the content of residual solvents is kept below a certain threshold value (typically less than 20 mg/m² for food packaging) in the final packaging material in order to avoid odour and/or off-flavour, which would spoil the taste of the packaged foodstuffs. Therefore, the residual solvents content is an important parameter that needs to be measured with regards to the 'real' product application. For the trials conducted, the amount of residual solvents was measured using a N.I.R.A Neptune 801 analyser, where the individual solvent components are separated and measured using a gas chromatography column and flame ionisation detector. Results are shown in *Table 6-37*. Two samples were measured for each lamination trial. The residual solvents predominantly consist of ethyl acetate, as to be expected, and some other solvents, such as methyl ethyl ketone, coming from the adhesive resin.

Table 6-37: Residual solvents content after lamination of AlO_x coated BOPP C

Description	Application weight	Total residual Solvents content
	g/m²	mg/m²
Lamination trial 1: adhesive onto uncoated BOPP	2.9	8.8/10.7
Lamination trial 2: adhesive onto AlO_x	3.1	4.1/4.2

As can be seen from *Table 6-37*, the residual solvents content is by far lower when the adhesive is applied onto the AlO_x layer (despite the higher application weight, which usually results in a higher residual solvents content). This suggests that the BOPP film absorbs a certain amount of solvents, whilst the AlO_x seems to prevent this absorption by acting as a barrier ('repels' the adhesive), thus resulting in the lower amount of total residual solvents. The amount of residual solvents depends on many factors, such as the web speed, capacity of the dryer, type of adhesive (e.g. high performance adhesive usually retain more solvents) and also the material the adhesive is applied onto (e.g. on printed film the ink can absorb solvents).

Inspecting the 'freshly' laminated samples initially showed an acceptable level of transparency. However, about 30 minutes after lamination, the laminates appeared to become 'foggy' and developed a 'spotted' appearance (for both trials, see *Figure 6-67*). The 'spots' look like small bubbles that are trapped between the laminated films. When the uncoated BOPP was laminated against itself with the same

adhesive, a clear laminate was obtained. This suggests that the AlO_x layer and a possible interaction (e.g. AlO_x repels adhesive) with the adhesive used are involved in the change of optical appearance. Nevertheless, the oxygen barrier was improved for trial 1 (see *Table 6-36*), despite the suspected interaction that induced the 'foggy' appearance.

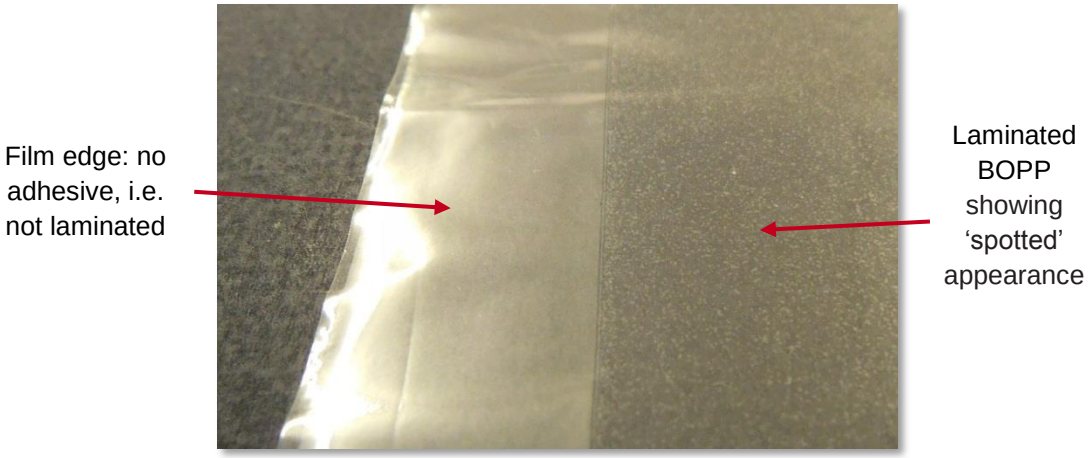

Figure 6-67: Photo of AlO_x coated and laminated BOPP C (trial 1)

Consequently, one further lamination trial was performed, whereby the adhesive was applied onto the plain BOPP. However, the application weight was increased to 3.8 g/m² and the lamination nip force/pressure and temperature were raised from 12 kg/cm to 20 kg/cm and 45 °C to 70 °C, respectively. The amount of residual solvents was measured (20.3 mg/m²), but the priority was to improve the optical appearance of the laminate and not to keep the residual solvents content below a certain level. Whilst an oxygen barrier performance similar to lamination trial 1 was obtained, the laminate of this trial also revealed a foggy appearance; however, to a lesser extent than the previous trials. In order to optimise the optical appearance and also residual solvents content and, thus, make the laminated AlO_x coated BOPP a commercially viable product for food packaging applications, further steps need to be taken by changing and optimising parameters, such as the adhesive and lamination conditions used.

6.5.1.3 Test of adhesive/solvent compatibility with AlO_x

Based on the oxygen barrier properties being impaired by the lamination process (when the adhesive was applied onto the AlO_x layer), further examinations were carried out in order to investigate a possible reaction/interaction between the AlO_x layer and either the adhesive or the solvent. Initially, a chemical attack of the AlO_x by the adhesive/solvent was assumed to be the main reason for the increased OTR. Therefore, the following tests were performed on samples taken of AlO_x coated BOPP C prior to lamination:

- (1) Ethyl acetate applied onto AlO_x layer and dried under ambient conditions
- (2) Ethyl acetate applied onto AlO_x layer and dried with heating gun
- (3) Ethyl acetate/adhesive mixture applied onto AlO_x layer and dried under ambient conditions
- (4) Ethyl acetate/adhesive mixture applied onto AlO_x layer and dried with heating gun
- (5) AlO_x layer exposed to heating gun

For these tests, the ethyl acetate and ethyl acetate/adhesive mixture were applied using a silicone brush, whilst a heating gun (sample distance 30 to 40 cm ≈ 75 to 85 °C, a few seconds exposure time) was used to imitate the drying in the lamination process. A standard performance two-component polyurethane adhesive was used in this investigation. The oxygen barrier performance, measured after the respective 'treatment' described above, is summarised in *Table 6-38*.

Table 6-38: Oxygen barrier performance of AlO_x coated BOPP C before and after tests for adhesive/solvent compatibility

Description	OTR
	cm³/(m² d)
BOPP C + AlO_x before lamination	48.6 ± 8.2
(1) AlO_x + ethyl acetate	52.6 ± 3.3
(2) AlO_x + ethyl acetate + heat	53.2 ± 6.4
(3) AlO_x + ethyl acetate/adhesive	24.7 ± 4.0
(4) AlO_x + ethyl acetate/adhesive + heat	25.3 ± 6.9
(5) AlO_x + heat	48.2 ± 4.7

No water barrier was investigated, since this characteristic could not be significantly enhanced by the AlO_x coating prior to lamination. As can be seen from the values stated in *Table 6-38*, neither the solvent ethyl acetate, nor the adhesive, the heat or

a combination resulted in an increase of the measured OTR values, thus indicating that no chemical attack took place. The OTR values are identical within experimental error, apart from tests (3) and (4), whereby through the application of the adhesive the OTR was even decreased. Reasons for this barrier improvement have been discussed previously in Section 6.5.1.1. In summary, this result suggests that the damage of the thin AlO_x barrier layer during lamination was mechanical and not chemical. Consequently, the adhesive application or any other contact of the AlO_x coating with parts of the lamination equipment (roller etc.) must be the cause of the barrier deterioration. A next test step would be to run the AlO_x coated film through the laminator with all nips closed but without any adhesive (e.g. dry) and, hence, not produce a laminate. This trial will enable to test for mechanical damage induced by the film handling in the laminator.

6.5.1.4 Calculation of transmission rate for laminate

Analogous to the calculations carried out for acrylate topcoats in Section 6.4.2.4, it is also possible to calculate an approximation for the expected transmission rate of the final laminate (BOPP C/AlO_x/adhesive/BOPP). The only difference is that for the laminate, there is an additional polymer layer present; the BOPP film (hereinafter named BOPP X) laminated against the AlO_x coated BOPP film. The overall transmission rate of this three-layer structure (i.e. layer 1 = AlO_x coated BOPP, layer 2 = AlO_x 'coated' adhesive, layer 3 = BOPP X) can now be calculated according the following equation, a modified version of Equation (6-1) in order to account for the effect of BOPP X:

$$Q_{total} \approx \left(\frac{BIF_{100}}{Q_{100,BOPP\ C}} + \frac{BIF_{100}}{Q_{100,adhesive}} + \frac{1}{Q_{BOPP\ X}} \right)^{-1} \quad (6\text{-}4)$$

As stated previously, the BIF_{100} (refer to Equation (6-2)) is now valid for BOPPC, as well as the adhesive. The thickness of the adhesive was assessed using light microscopy cross-sections (see *Figure 6-68*) of the laminate and via measuring the overall thickness of the laminate with a thickness gauge (assuming each individual BOPP film is 20 µm, as stated in the respective datasheets). For all lamination trials, an average adhesive thickness between 2.5 and 3 µm was measured, which is above the typical critical thickness of 2.5 µm, as is the film thickness of 20 µm for BOPP C.

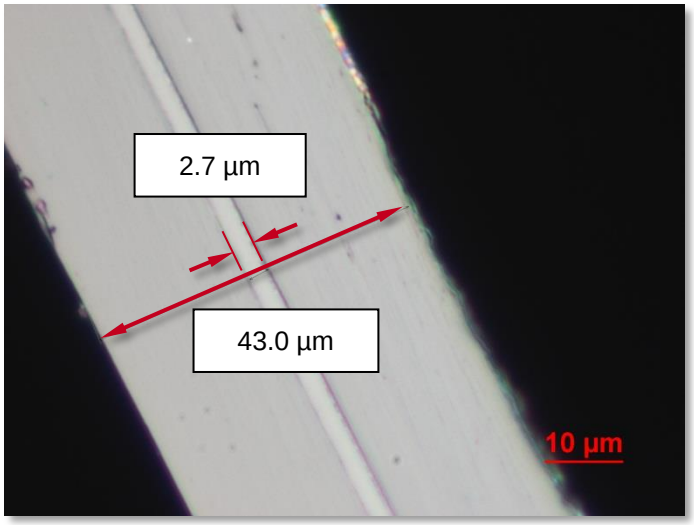

Figure 6-68: Light microscopy cross-section of laminated and AlO_x coated BOPP (trial 1) showing adhesive thickness

The OTR values for the uncoated BOPP films ($Q_{BOPP\ C}$ $Q_{BOPP\ X}$) and the AlO_x coated BOPP film (Q) have been measured (values stated below) and, consequently, $Q_{100,BOPP\ C}$ and BIF_{100} can be calculated:

$$Q_{BOPP\ C} = 2050\ cm^3/(m^2\ d)$$

$$Q_{BOPP\ X} = 1950\ cm^3/(m^2\ d)$$

$$Q = 48.6 \pm 8.2\ cm^3/(m^2\ d)$$

$$Q_{100,BOPP\ C} = 2050 \cdot \frac{20}{100}\ cm^3/(m^2\ d) = 410\ cm^3/(m^2\ d)$$

$$BIF_{100} \approx \frac{410}{48.6} = 8.4$$

The normalised transmission rate of the adhesive $Q_{100,\ adhesive}$ (see Equation (6-4)) can be calculated in a similar way as for $Q_{100,\ acrylate}$ for the acrylate topcoats (Section 6.4.2.4). In order to set up the laminator prior to laminating AlO_x coated BOPP C, BOPP X was laminated against itself. Samples of this lamination (i.e. without AlO_x) were investigated in terms of adhesive thickness (2.7 ± 0.7 µm) as well as OTR ($Q_{laminate}$ = 657 ± 6 cm³/(m² d)). The ideal laminate theory (Equation (4-8)) can be used for this three-layer system (BOPP X/adhesive/BOPP X), in order to calculate the OTR of the adhesive ($Q_{adhesive}$), as shown in Equation (6-5):

$$Q_{adhesive} = \left(\frac{1}{Q_{laminate}} - \frac{2}{Q_{BOPP\ X}}\right)^{-1} = 2010\ cm^3/(m^2\ d) \qquad (6\text{-}5)$$

With this result, a $Q_{100,\ adhesive}$ value of 54.3 cm³/(m² d) is obtained, which is a lot lower than the normalised transmission rate $Q_{100,\ BOPP\ C}$ of the BOPP film.

Now, Q_{total} can be assessed according to Equation (6-4), which yields a value of 5.67 cm³/(m² d) for an approximation of the OTR of the laminated AlO_x coated BOPP. Once again, a possible ‘pore filling’ mechanism is not considered using these equations.

The calculated value of 5.67 cm³/(m² d) is, however, still lower than the actually measured mean OTR of 11.9 cm³/(m² d) (refer to *Table 6-36*). Reasons for this deviation are, first of all, that the calculation only represents an approximation. Furthermore, a possible (marginal) damage of the AlO_x barrier layer may occur during conversion and there is, additionally, the uncertainty created by the calculation of the adhesive barrier properties. Due to variations in the lamination process, the adhesive permeability properties are subjected to larger fluctuations [393], which greatly affect the calculated Q_{total}.

6.5.1.5 Flex durability of AlO_x coated BOPP

An important test method to assess the functionality and barrier retention of a laminated film is the test method for flex durability (Gelbo-flex) according to ASTM F392 [305]. As mentioned in Chapter 6.2.1.5, this test is very destructive, if non-laminated (i.e. unprotected) AlO_x coated samples are used. During this test method, the film structure is subjected to a flexing action, which results in the sample being twisted and compressed/crushed as shown in *Figure 6-69*. This test serves the purpose of simulating the strain that the packaging material may be exposed to during further downstream processes after lamination (i.e. folding and forming into packaging) and whilst handled in the typical transport, storage and retail environment of the packaged foodstuffs. Using this test, defects can be created in the laminated film and subsequent barrier measurement (after a certain number of flexing cycles) will show whether the laminated structure can withstand this type of repetitive strain. In this investigation, a Gelbo-flex tester model 5000 manufactured by United States Testing Co., Inc. was used.

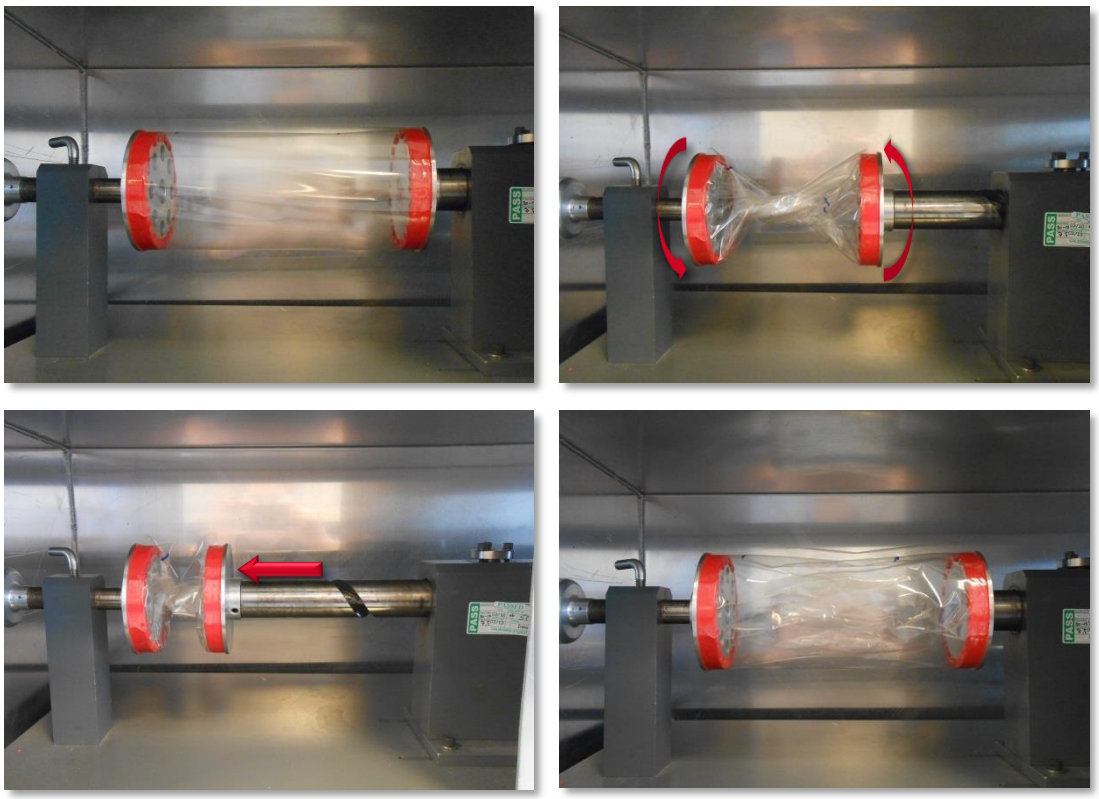

Figure 6-69: Different stages of the Gelbo-flex test during one cycle; top left: sample before test; top right: twisting motion; bottom left: crushing motion; bottom right: sample after one cycle

Based on published data about flex durability testing of laminated polymer structures with inorganic barrier layers (aluminium and SiO_x) [355, 395, 410-414], the barrier

investigation was carried out with a corresponding number of 1, 5, 10, 20, 50, 100, 250 and 500 cycles, using samples of laminated AlO_x coated BOPP C (lamination trial 1, refer to *Table 6-36*). The effect of the Gelbo-flex wearing test on the barrier performance (OTR and WVTR) of the laminated structure is illustrated in *Figure 6-70*. A logarithmic trend line was fitted to the OTR data, which resulted in a coefficient of determination of $R^2 = 0.94$, whilst a linear trend line was used for the WVTR data. For comparison, samples of AlO_x coated and non-laminated BOPP C were subjected to the same flex test. Results for the non-laminated film are depicted in *Figure 6-71*.

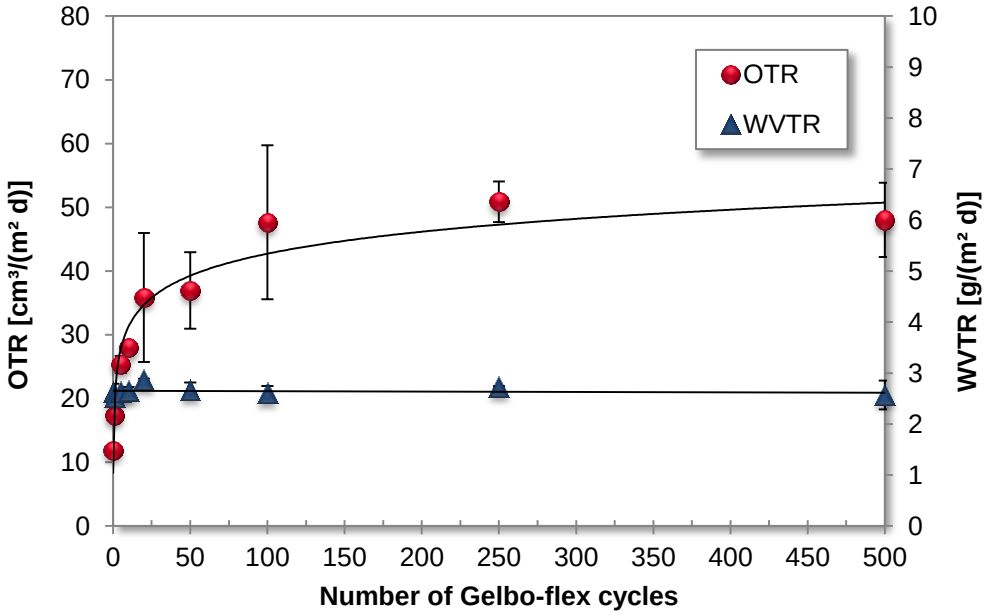

Figure 6-70: Relationship between OTR and WVTR of laminated AlO_x coated BOPP C and number of Gelbo-flex cycles

WVTR remains unchanged as the number of Gelbo-flex cycles increases (*Figure 6-70*). This observation was not unexpected, due to the fact that the AlO_x coating prior to lamination did not result in a significant improvement of the water barrier properties (see *Table 6-36*). Furthermore, the unaffected WVTR also reveals that no damage, such as holes, was created in the BOPP films themselves by the repeated twisting and crushing motion. In contrast to that, the OTR shows an initially strong increase within the first 20 cycles, with the transmission rate rising from 11.9 $cm^3/(m^2\ d)$ to 17.4 $cm^3/(m^2\ d)$ after one cycle only. After the initial strong rise, the rate of increase gradually declines and the OTR appears to level off for higher numbers of Gelbo-flex cycles. This shape of the curve, with the first few cycles inducing most of the damage to the oxygen barrier properties, is similar to results obtained by Doyon and co-workers [412] for a laminated structure with metallised PET. Furthermore, other researchers report deterioration of oxygen (and/or water)

barrier already after 20 or less cycles for laminates containing SiO_x coated PET [312, 407, 411] and metallised BOPP [410, 413]. Nevertheless, most of these studies do not investigate the effect of the Gelbo-flex test on barrier performance beyond 50 cycles. There is, though, also data published that shows that in laminates with metallised BOPP or metallised PE, the OTR and/or WVTR is only marginally affected by 100 cycles or more [355, 415]. However, the individual effect of the Gelbo-flex test on the barrier properties of laminates depends on many factors, including: the type/chemistry of inorganic barrier layer [416] and its thickness; the deposition process (CVD, PVD [306]); the substrate as well as the lamination process (extrusion, adhesive); the type of adhesive used (solventless, solvent-based, water-based [415]) and the additional polymer material(s) applied during lamination.

The loss of oxygen barrier with increasing cycle number, as seen in *Figure 6-70*, is due to the damage of the inorganic AlO_x layer, caused by the flexing and compressing action. Based on its ceramic nature, the thin AlO_x layer is brittle and will crack during the applied external stress and, therefore, create permeation pathways for oxygen molecules. In contrast to that, aluminium is ductile and, hence, may be less prone to defect formation during Gelbo-flex testing. In our case, we exclude damage to the polymer film itself, as the WVTR of the laminated film was unaffected by the Gelbo-flex test and number of cycles.

Visual inspection of the flexed samples (laminated) showed clear signs of material wear and creases, with the laminate also appearing to be partially disintegrated in the creases (especially after 100 or more cycles).

When investigating the non-laminated sample (see *Figure 6-71*), it becomes obvious that the Gelbo-flex test is a very destructive technique, resulting in fast and extensive barrier deterioration for the unprotected AlO_x coating. Already after one cycle, the OTR has increased to an average value of 140 $cm^3/(m^2\ d)$ and continues to rise rapidly up to 20 cycles (average OTR 975 $cm^3/(m^2\ d)$), whilst for 100 and more cycles, the mean OTR value stabilises around 1300 to 1400 $cm^3/(m^2\ d)$. This final value is, though, still lower than the OTR of the uncoated film (refer to Chapter 6.1.1, *Table 6-1*). From *Figure 6-71*, it can, furthermore, be detected that water barrier also deteriorates with flexing the samples. After one flexing cycle, the mean WVTR is still similar to the unflexed film (WVTR around 2.5 $g/(m^2\ d)$). This low WVTR value is due to the ageing of the film (see Section 6.2.1.2), which had already taken place at the time of the Gelbo-flex investigation. In contrast to the non-laminated AlO_x coated film, the laminated film did not further improve in water barrier, presumably due to the lamination preventing and terminating the ageing

process. Furthermore, the lamination was carried out before extensive ageing of the AlO_x coated BOPP film could take place. Nevertheless, for five or more cycles, the WVTR increases to average values around 4.5 g/(m² d), which is also still slightly lower than the plain film WVTR (see Chapter 6.1.1, *Table 6-1*). A slightly higher WVTR value was obtained for 100 Gelbo-flex cycles.

The drastic barrier deterioration seen for the non-laminated AlO_x coated BOPP, in contrast to the laminated opponent, is to be expected and it has been reported by various researchers that the barrier loss (after Gelbo-flex or stretching, see Section 6.2.1.5) is far less pronounced for laminated (or topcoated) films, compared to non-laminated unprotected structures with inorganic barrier layers [3, 303, 310, 314, 417, 418].

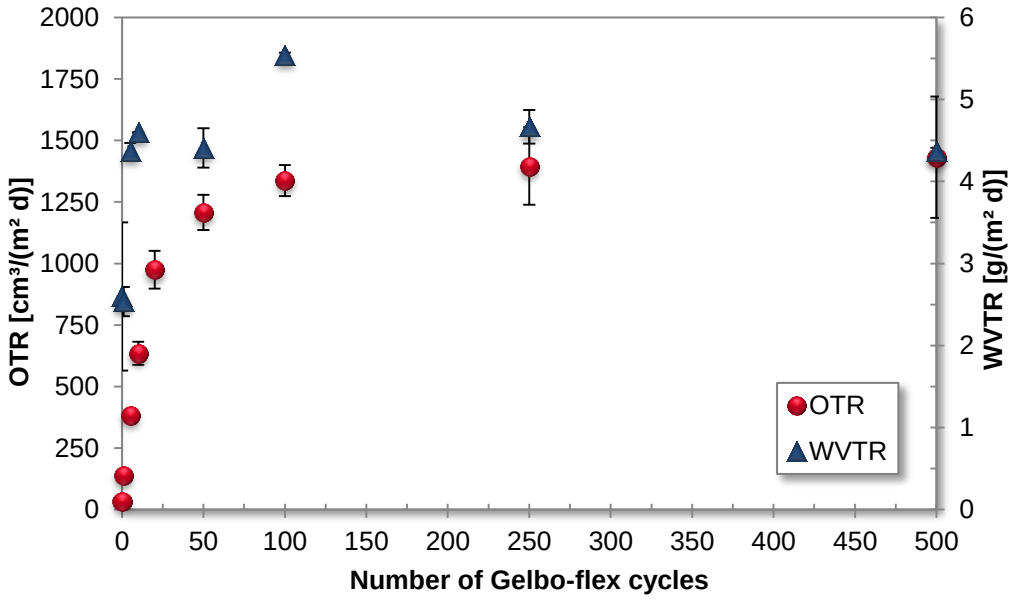

Figure 6-71: Relationship between OTR and WVTR of non-laminated AlO_x coated BOPP C and number of Gelbo-flex cycles

6.5.2 Solventless adhesive lamination of AlO_x coated BOPP

In addition to the solvent-based adhesive lamination, solventless adhesive lamination was also carried out. In this case, the lamination was performed using AlO_x coated BOPP B (in-line plasma pre-treatment only), which was laminated against uncoated BOPP B. Two adhesives were used, a high performance and a standard performance solventless adhesive. As described in further detail in Section 5.4.2, two trials were conducted with the high performance adhesive, analogous to the solvent-based adhesive lamination (Chapter 6.5.1), by applying the adhesive onto the plain BOPP (BOPP B) in trial 1 and onto the AlO_x coated BOPP in trial 2. For the standard solventless adhesive, only one trial was conducted, whereby the adhesive was applied onto the plain BOPP. The barrier performance pre- and post-lamination and, as a reference, the plain film barrier performance of BOPP B are listed in *Table 6-39*.

Table 6-39: Barrier performance before and after lamination of AlO_x coated BOPP B

Description	OTR		WVTR	
	$cm^3/(m^2\ d)$	**BIF (lamination)**	**$g/(m^2\ d)$**	**BIF (lamination)**
Uncoated BOPP B	2500 – 2900	-	7 – 8	-
BOPP B + AlO_x (before lamination)	119 ± 17	-	5.29 ± 0.22	-
Adhesive 1: adhesive onto uncoated BOPP B	71.5 ± 7.4	1.7	4.02 ± 0.44	1.3
Adhesive 1: adhesive onto AlO_x	89.6 ± 19.7	1.3	4.05 ± 0.19	1.3
Adhesive 2: adhesive onto uncoated BOPP B	83.2 ± 17.6	1.4	3.71 ± 0.15	1.4

As can be detected from *Table 6-39*, the AlO_x coated BOPP film (non-laminated) revealed an almost identical OTR and WVTR level to the trial stated in *Table 6-10* (Chapter 6.2.1.1), which was conducted using the same coating and pre-treatment parameters. Hence, this shows that repeatable barrier results can be obtained when BOPP B is AlO_x coated. However, as can be seen from the standard deviation for OTR, the data ranges between approximately 100 and 140 $cm^3/(m^2\ d)$. The average oxygen barrier post-lamination is slightly enhanced for all trials/adhesives, as is the water barrier. The improvement, however, is not as good as obtained for AlO_x coated and laminated BOPP C (see *Table 6-36*, Chapter 6.5.1.1). Moreover, after lamination of AlO_x coated BOPP B, the OTR still exhibits quite large standard deviations, which is not too surprising, based on the high OTR standard deviation

prior to lamination. This was not the case for the lamination of AlO_x coated BOPP C, whereby the OTR standard deviations pre- and post-lamination were a lot smaller. Possible reasons for the oxygen barrier improvement upon lamination, such as the effect of the adhesive barrier properties, have been discussed in detail in Chapter 6.5.1.1. For the water barrier, it can be seen from *Table 6-39* that the AlO_x coating on its own slightly reduced the WVTR of the uncoated film, as did the lamination process. Overall, the WVTR of the laminate is about half the value of the uncoated film, which indicates that the AlO_x layer does not result in any water barrier improvement for the laminated structure. This has also been found for the lamination of AlO_x coated BOPP C (see *Table 6-36*, Chapter 6.5.1.1).

In summary, the barrier obtained after lamination of BOPP B is still not satisfactory, which is assumed to be due to the insufficient barrier level of AlO_x coated BOPP B prior to lamination. The main finding of this lamination trial is, however, that the adhesive can be applied onto the AlO_x layer during lamination without inducing damage to the barrier layer that would affect and deteriorate the oxygen barrier properties. Although it appears that slightly better oxygen barrier was yielded when the adhesives were coated onto plain BOPP B (see *Table 6-39*), this is attributed to variations in OTR of AlO_x coated BOPP B (along the web length) before lamination (see OTR standard deviation) and not necessarily the application of the adhesive during the lamination process.

Consequently, the results obtained for AlO_x coated BOPP C, when the adhesive was applied onto the AlO_x coating (refer to *Table 6-36*, Chapter 6.5.1.1), could be regarded as an anomaly, which possibly was caused by a roller contamination/damage on the ‘wet path’ of the laminator. Therefore, this investigation (solvent-based adhesive lamination, adhesive applied onto AlO_x coating) should be repeated with attention paid to the rollers touching the AlO_x surface as a possible origin of mechanical damage to the AlO_x layer.

6.6 AlO_x coating of polylactic acid film for biodegradable barrier films

In recent years, the use of bioplastics in food packaging applications has been grabbing the headlines, owing to a rising awareness of environmental sustainability and recyclability. Consequently, there is an increased interest in replacing traditional synthetic and non-biodegradable polymers, such as PP, PET or PE, which are derived from petrochemical resources, with bioplastics based on renewable resources, such as corn or wheat and other biomass materials. Biodegradable polymers are defined as polymers that can be decomposed into natural materials (water, carbon dioxide, methane, biomass and/or inorganic compounds), generally via microbial degradation. Polylactic acid (PLA), a biodegradable thermoplastic polyester, has been extensively researched and is nowadays regarded as a good candidate to replace traditional synthetic polymers since it reveals the highest commercial potential. Hence, the use of PLA, also in conjunction with vacuum web coating, may provide a more environmentally-friendly solution for future food packaging materials. [1, 419]

6.6.1 Surface topography and chemistry of PLA film

The PLA film used in this study was a three-layer coextruded and biaxially oriented PLA film, which was corona treated in-house by the film manufacturer. No extensive SEM and AFM analyses were carried out. However, DIC light microscopy was performed to gain an impression of the film surface topography/structure and presence of antiblock particles, in order to compare the PLA film to the BOPP films and PET reference film investigated comprehensively in this thesis.

Representative high- and low-magnification DIC images of the corona treated side of the PLA film are shown in *Figure 6-72*. It is, once again, noted that after AlO_x coating, DIC light microscopy revealed identical surfaces, since the thin AlO_x coating and possible changes induced cannot be resolved by the use of light microscopy. Furthermore, based on the previous SEM and AFM investigations of uncoated and AlO_x coated BOPP and PET films (refer to Chapters 6.1.2.3, 6.1.2.4, 6.2.2.2 and 6.2.2.3), the coating is also assumed to be conformal for PLA film.

From *Figure 6-72*, one can observe that the PLA film exhibits a vast amount of antiblock particles of various sizes. Whilst on the lower magnification image, the PLA films appears quite different from the BOPP films and PET reference film investigated (refer to Chapter 6.1.2.1, *Figure 6-1* and *Figure 6-3*), the higher magnification DIC image reveals similarities to BOPP B (see *Figure 6-2*) and the PET film (see *Figure 6-3*), due to the bumps in the surface structure, which are presumably caused by the incorporated antiblock particles.

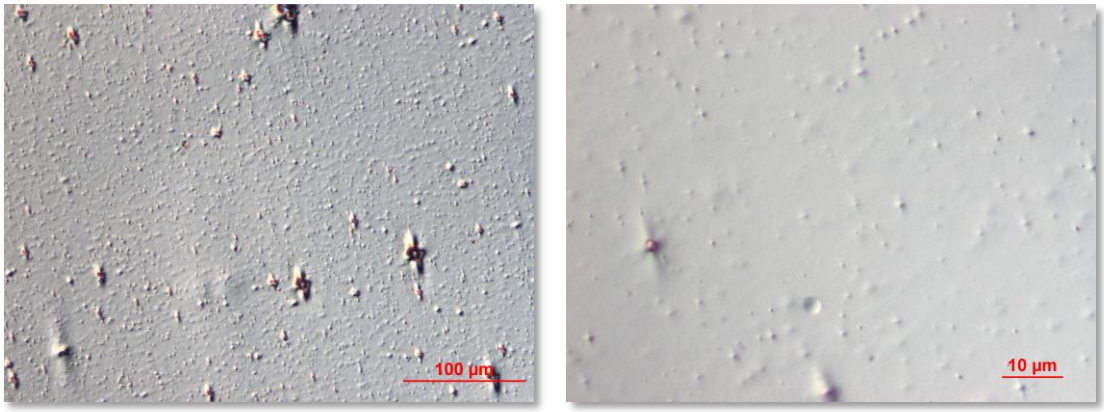

Figure 6-72: Low- (left) and high-magnification (right) DIC images of uncoated PLA

The surface energies of the corona treated side and the non-treated side of the PLA film were assessed using contact angle measurement. Five samples were evaluated for each mean value and each standard deviation and results are stated in *Table 6-40*. From the results presented, it can be seen that the corona treated side exhibits a marginally higher surface energy, compared to the untreated side, which is due to an increase of the polar component. The surface energies were, additionally, cross-checked using dyne pens and the results yielded 40 mN/m for the untreated and 44 mN/m for the treated surface, which is in broad agreement with the contact angle data summarised in *Table 6-40*.

Table 6-40: Total, dispersive and polar surface energies of PLA film, as determined by contact angle measurement

Film	Side	Surface energy		
		Polar	Dispersive	Total
		mN/m	mN/m	mN/m
PLA	Corona	11.4 ± 0.3	31.2 ± 0.3	42.6 ± 0.2
	Reverse	9.1 ± 0.2	31.7 ± 0.2	40.8 ± 0.1

Also in literature, comparable values for the surface energy of untreated PLA are reported by Jacobson et al. [420] (38 mN/m, via dyne inks), Auras et al. [421] (42 mN/m, via dyne inks) and Jamshidian and co-workers [422] (34.6 to 37.8 mN/m, via contact angle measurement, same calculation approach as used in this thesis, but additional fourth liquid; glycerol). The latter publication, which investigates the effects of different antioxidant film additives, also states dispersive surface energy components between 28.6 and 32.7 mN/m, which are in line with the data presented in this thesis. In another publication [423] by the same research group, a broader range of total, as well as dispersive and polar, surface energies was obtained, which

is presumably caused by the different film additives investigated in their work. Hirvikorpi and co-workers [424] studied the effect of corona treatment on PLA coated paperboard, which was subsequently coated with an AlO_x barrier layer via atomic layer deposition. For both non-treated and corona treated PLA, they report higher total surface energies (47.8 and 53.1 mN/m, respectively) than obtained in this thesis. However, the surface energy of the corona treated PLA dropped to 50.2 mN/m within seven days after treatment (same surface energy calculation method used as in this thesis, but only water and diiodomethane applied as test liquids).

XPS analysis of the corona treated side of the film was additionally carried out and the composition is summarised in *Table 6-41* (for more information on the XPS measurement see also Chapter 6.1.3.2). It is noticeable that the PLA film has a far higher oxygen content than any of the treated BOPP films, the BOPP film with the different polymer skin layer (BOPP F) or the PET reference film (see Chapter 6.1.3.2, *Table 6-5*, and Chapter 6.3.2.2, *Table 6-24*).

Table 6-41: PLA film composition, as analysed via XPS

Film	Side	C	O	O/C ratio
		at%	at%	
PLA	Corona	64.1	35.9	0.56

De Geyter et al. [425] investigated the effect of atmospheric dielectric barrier discharge treatment on PLA film and found that the O/C ratio increased from 0.47 to 0.61 by the use of an air plasma. The O/C value of 0.61 corresponds to a total amount of 37.8 at% oxygen and is in good agreement with the oxygen content and O/C ratio found here for corona treated PLA. Jamshidian and co-workers [422, 423] measured similar oxygen contents between 34.3 and 37.7 at% (apart from one exception). This was, however, for non-treated PLA films with various antioxidant additives.

6.6.2 Barrier properties of AlO_x coated PLA film

The PLA film was coated with an AlO_x barrier layer via A4 samples mounted on a PET carrier web (in-line plasma pre-treatment only). In order to investigate the effect of the corona treatment on AlO_x barrier performance, both sides of the film were coated and samples were analysed for their barrier properties. It has to be noted, though, that the non-treated reverse side of the PLA film was not examined for its surface topography and that possible differences in the surface topography/structure may also affect the barrier performance of the AlO_x layer.

The oxygen and water vapour barrier properties of the AlO_x coated PLA film and the plain film barrier performance are summarised in *Table 6-42*.

Table 6-42: Barrier properties (OTR and WVTR) of AlO_x coated PLA film

Film	Side	OTR		WVTR	
		cm³/(m² d)	BIF	g/(m² d)	BIF
PLA 20 µm	*(uncoated)*	*850 – 950*	-	*440**	-
	Corona	11.4 ± 1.4	79	5.14 ± 1.00	86
	Reverse	53.2 ± 4.7	17	10.18 ± 0.34	43

*WVTR value taken from film data sheet, as beyond equipment measurement range

On comparing the OTR and WVTR values obtained for the corona treated and non-treated side of the PLA film (see *Table 6-42*), a significant difference in AlO_x barrier performance can be detected. The oxygen barrier using the corona treated PLA film side is approximately five times better, compared to the OTR obtained for the reverse side of the PLA film, whilst the water barrier is better by a factor of approximately two. It should, however, be emphasised that in addition to the corona treatment (and hence surface chemistry and surface energy, see *Table 6-40*), there may be further differences between the two film sides, such as the skin layer composition (based on the type/grade of PLA used), antiblock particle amount, size and distribution density, as well as general surface topography.

The barrier results obtained here for the corona treated PLA (and in part also for the non-treated PLA) are comparable to or even better than the barrier performance of AlO_x coated PLA obtained by Schiller and co-workers [12, 36, 426] (see also Ludwig and co-workers [37-39] and Trassl and co-workers [40]) using plasma activated reactive evaporation of aluminium via resistively heated boats. Hirvikorpi et al. [427-429] deposited AlO_x barrier layers of 25 to 100 nm thickness via ALD onto PLA film and measured OTRs ranging from 30 to 60 cm³/(m² d). The WVTR, however, was

measured at 23 °C and 75 % RH, which generally should result in lower WVTRs than these measured at 37.8 °C and 90 % RH, and they state a value of 3.3 g/(m² d) for a 50 nm thin AlO_x layer. This research group also reports on AlO_x ALD layers deposited onto PLA coated board, which in some cases resulted in better OTRs and WVTRs [424, 429], and, furthermore, compared the findings to AlO_x barrier layers deposited via magnetron sputtering and electron beam evaporation, which in general yielded poorer barrier properties [428, 430]. In summary, it can be seen that the barrier properties obtained here are even comparable to the ones obtained via ALD deposition of AlO_x barrier layers onto PLA film, although ALD deposition techniques are generally believed to yield superior barrier performance.

Finally, one also needs to bear in mind that the samples were coated as A4 sheets mounted on a carrier web and not as a film roll. The previous investigation and comparison between the two coating techniques (see Section 6.3.3) using BOPP C and the PET reference film has shown that the barrier performance was impaired when coating A4 sheets, compared to the film roll. Consequently, the AlO_x coating of a PLA film roll may give even better results than obtained here with the A4 sheets.

7 SUMMARY AND CONCLUSIONS

This work investigates and discusses the deposition of transparent AlO_x barrier coatings onto polymer films for food packaging applications, with the main focus laid on BOPP as a substrate. The coatings were produced on an industrial-scale 'boat-type' roll-to-roll metalliser, via the reactive evaporation of aluminium in an oxygen atmosphere. If this coating process is controlled appropriately, then these coatings are transparent after a short ageing period and can give good barrier properties. The coated films, as well as the uncoated substrates, were characterised in terms of barrier performance, surface topography, substrate surface and coating composition and surface energy, coating adhesion, coating thickness and optical properties, using a range of analytical techniques. Furthermore, the effects of in-line plasma pre- and-post treatments, off-line pre-treatments, such as flame and atmospheric-pressure plasma treatment, acrylate under- and topcoats and, finally, adhesive lamination processes were investigated with respect to the barrier performance of the AlO_x coated and AlO_x coated and converted film.

The barrier properties (oxygen and water vapour transmission rate) of the AlO_x coated polymer films are discussed to be strongly dependent on the coating structure, i.e. the coating's density or porosity; the denser and less porous the AlO_x coating, the better will be the resulting barrier performance. This coating structure is supposed to be initially governed by the coating nucleation (i.e. number/density of nucleation sites) and the subsequent growth of the barrier layer, which for the standard deposition process has a thickness of approximately 10 nm. The coating nucleation in itself depends on the surface chemistry. Here, the surface chemistries of films such as PET, BOPP coextruded with a high surface energy skin layer and presumably also PLA appear more favourable for the growth of a dense AlO_x coating, compared to a standard commodity grade BOPP film. Consequently, good barrier properties with an AlO_x coating on a standard grade BOPP film are more difficult to achieve. Based on the analysis of the film surface chemistry of corona treated BOPP films, it was concluded that a higher oxygen content in the BOPP film surface will entail a better coating structure and hence improved barrier performance. Also flame and atmospheric-pressure plasma treatments are possible ways to change the BOPP film surface chemistry (by increasing the oxygen content in the outermost film surface to a higher level than can be obtained by corona treatment) and are assumed to positively impact the barrier performance. Unfortunately, the trials carried out using these treatments were not entirely conclusive, due to the suspected barrier deterioration brought by the coating of A4 samples rather than full rolls. Another way to modify the AlO_x coating structure and increase its density is the use of a BOPP film substrate with increased shrink properties (i.e. BOPP shrink film). The shrinkage of the BOPP substrate (which

presumably takes place when the web cools down after deposition) will result in the AlO_x layer being subjected to a compressive force, which will entail a densification of the coating. Similar effects can also be achieved by the use of a post-deposition off-line annealing/heat treatment, whereby the substrate material will also shrink. However, for the heat treatment trials conducted here, the resulting barrier enhancement appeared to be strongly dependent on the respective BOPP film and, furthermore, in some cases even heat induced damage and barrier deterioration were observed. In addition to increasing the AlO_x density via shrinkage of the polymer substrate, a possible swelling of the AlO_x layer can also increase its density. This process is presumed to take place off-line after AlO_x deposition, when the coated film is exposed to ambient conditions. The uptake/absorption and entrapping of oxygen and/or water molecules in the coating structure will result in a density increase of the AlO_x layer and, thus, improve its barrier properties. These assumptions have been made based on the fact that the AlO_x coated BOPP films, as well as the PET film, required an ageing period of a certain length of time before acceptable barrier properties were obtained. This ageing time is, however, a lot longer for BOPP, in contrast to PET. A final important factor to be considered for the AlO_x coating structure is the chamber pressure during coating deposition. During trials carried out later using a K5000 metalliser, it was observed that the coating pressure was one order of magnitude lower, compared to previous runs conducted on a K4000 model. Consequently, it was assumed that the lower deposition pressure, in combination with a higher oxygen content in the BOPP film surface, entailed a higher coating density and thus a drop of the WVTR of AlO_x coated BOPP film to values around 1.5 g/(m² d) or even less. With regards to the structure of the AlO_x coating, it should also be mentioned that the presence of defects (here: crater-shaped defects) in the uncoated BOPP film surface can be detrimental for the barrier performance obtained after AlO_x coating, since these defects can be reproduced in the AlO_x layer. These defects then act as pathways of unhindered permeation for any diffusing molecule and, hence, they cancel out any effect that the substrate surface chemistry may have induced on coating structure and barrier performance.

With respect to the permeation mechanisms for oxygen and water vapour, the investigations conducted confirm the widely discussed macro-defect driven permeation mechanism of oxygen through inorganic barrier layers, whilst for water vapour indications of a possible chemical interaction were found. This was based on the barrier performance of AlO_x coated BOPP films that, unlike standard AlO_x coated polymer films, contained elemental/metallic aluminium in addition to the oxidised aluminium and showed a drop of WVTR even down to levels of less than 1 g/(m² d).

Furthermore, a water barrier improvement was still observed even when the previously mentioned defects in the AlO_x layer were present, hence indicating that the suspected chemical interaction between elemental aluminium in the AlO_x layer dominates over a possible unhindered permeation through defects in the coating.

A different polymer skin layer, coextruded with the BOPP film, showed remarkable barrier improvement, with a barrier performance comparable to AlO_x coated PET, assigned to the change in surface chemistry and hence better coating nucleation and growth. If the equipment for the manufacturing of such a multilayer film is available (i.e. multilayer coextrusion of different polymers), a cost-effective production route is possible due the low skin layer thickness of less than 1 µm [258]. Nevertheless, this does not solve the problem of obtaining good barrier properties with AlO_x coatings on standard commodity grade BOPP film.

Regarding a definition or recommendation of the best initial surface to deposit an AlO_x barrier layer onto, the high surface energy polymer skin layer of BOPP F represents an ideal surface that appears to be very receptive for the AlO_x coating and, hence, results in a superior barrier performance. Nevertheless, as stated before, this layer is made from a different polymeric material. For a standard BOPP film with a polypropylene co- or terpolymer skin layer, it is suggested using a pre-treatment method prior to AlO_x deposition that induces a higher oxygen content in the film surface than generally accomplished by a standard corona treatment. Achieving this may also be affected by the type of co- or terpolymer material used as the skin layer. Additionally, it would be valuable to avoid the use of antiblock particles in the skin layer that will be vacuum coated, but only add these film additives on the reverse side in order to ensure good film handling. This would exclude any major interference or effect of these surface features on the barrier performance (although the antiblock particles on the reverse side may be capable of generating imprints and hence post-deposition defects in the barrier layer due to the roll-to-roll process). Furthermore, it appears beneficial to use a BOPP film with tailored shrink properties; however, this is not a property of the film surface, but accomplished via additions to the film core and film processing.

The investigation of the surface topography at different magnification levels revealed that for all film substrates the 10 nm AlO_x barrier layer replicated the underlying plain film surface topography, including defects, such as the crater-shaped defects mentioned earlier and discussed in detail in Appendix A2.

The coating composition in the case of ‘standard’ AlO_x layers was determined to be predominantly Al_2O_3, with no metallic/elemental aluminium present and no through

thickness variations in stoichiometry, although slightly increased oxygen contents were measured, compared to fully stoichiometric Al_2O_3.

The AlO_x surface energy of coated BOPP films revealed an initially quite high level, which diminished rapidly with time, due to a transfer of polymeric material and film additives from the reverse side of the BOPP film, as well as a migration through defects in the AlO_x layer. In the case of AlO_x coated PET, the surface energy could be maintained at a significantly higher level and exhibited a by far slower drop over time. These differences seen for BOPP and PET were attributed to different polymer properties, such as the glass transition temperature.

Regarding the adhesion of the AlO_x coating (as determined via a peel test), the main finding was that, in the case of BOPP, this adhesion was higher than the intrinsic strength of the BOPP film itself, hence resulting in cohesive failure within the substrate. In the case of PET, no peeling was possible as the adhesion was beyond the ultimate tensile strength of the EAA film used.

The use of an acrylate undercoat prior to AlO_x deposition resulted in an enhanced oxygen and also water vapour barrier performance of the AlO_x coated film, and furthermore, the barrier results appeared independent of the acrylate thickness, as well as the BOPP film substrate. The improvement obtained was predominantly attributed the new surface chemistry generated by the acrylate layer.

When conversion processes, such as adhesive lamination and the application of an acrylate topcoat, were investigated, it was found that in both cases, the barrier performance can be significantly enhanced, which was assigned to the barrier properties of the adhesive/acrylate itself, as well as a possible infiltration of the adhesive/acrylate into the defects of the AlO_x barrier layer (‘pore filling’).

Finally, barrier results obtained for AlO_x coated PLA films, though conducted using A4 samples on a carrier web, are very promising for an environmentally friendly transparent barrier solution.

8 FUTURE WORK

With respect to future work, the convertibility of AlO_x coated polymer films needs to be investigated in more detail. Initial lamination work has already been carried out; nevertheless, in the case of the solvent-based adhesive lamination, barrier deterioration was observed when the adhesive was applied onto the AlO_x layer. Consequently, additional research and repeat trials are required in order to find the cause of this damage to the barrier layer. Furthermore, different adhesives (solvent-based and solventless) and their effects on the barrier performance could be investigated and, along with this, optimum lamination conditions can be established. In addition to laminating, conversion processes also include printing. Here, gravure as well as flexographic printing should be studied in combination with the AlO_x barrier layer. In order to assess the suitability of the AlO_x coating for the printing process, the dependence of the barrier performance on the applied gravure pressure could be examined, as done by the Toyobo Research Institute in Japan [308, 309]. It may, furthermore, also be necessary to develop a protective topcoat for the AlO_x layer, which is applied priory to printing and may, additionally, eliminate the need for lamination. In the course of the work carried out for this thesis, topcoats have already been investigated. These were, however, acrylate topcoats deposited in vacuum. Although these coatings were applied off-line, in an industrial system running under production conditions the AlO_x and acrylate deposition would be conducted in the same chamber without breaking the vacuum. This could, nevertheless, possibly result in the required off-line ageing process not taking place and, thus, impair the barrier performance of the AlO_x coated film. Hence, an alternative to the acrylate topcoat is required, which preferably should take place in atmosphere using standard industrial coating lines at high speed (see also Chapter 4.4).

Furthermore, the effect of seeding/nucleation layers on the barrier performance of AlO_x coated BOPP could be investigated. Here, the initial work of sputtering 2.0 to 2.5 nm thick titanium seeding layers onto a variety of BOPP films has already been conducted. Due to their low thickness and the off-line oxidation, these seeding layers are nearly transparent and presumably largely consist of titanium oxides. The samples now need to be coated with an AlO_x layer and the barrier performance before and after AlO_x deposition should be determined, in order to assess whether seeding layers will help to obtain water barrier improvement with AlO_x coatings on BOPP to the required level of less than 1 g/(m² d). A positive effect of seeding layers on barrier performance has been suggested by other research groups [288, 431-433].

The increased content of oxygen in the film surface (found for one of the standard commodity grade BOPP films) and its supposed positive effects on the AlO_x barrier performance could also be verified by additional trials using off-line treatments, i.e. flame and/or atmospheric plasma. Also here, some initial work was carried out and delivered promising results. However, due to these trials being performed via coating A4 samples (and not a roll of film), barrier deterioration (for oxygen barrier) was suspected to take place and, hence, complicated the interpretation of the results. Consequently, it is suggested to repeat the off-line pre-treatment trials via treating and AlO_x coating a roll of film to confirm the suggested positive effects on AlO_x barrier performance. Regarding the low-molecular-weight oxidised material, discovered for atmospheric plasma treated BOPP via AFM analysis, it would also be interesting to investigate its impact on AlO_x adhesion.

The suggested chemical interaction during water vapour permeation through AlO_x coatings that contained elemental aluminium, i.e. 'dark' AlO_x coatings, can be further examined via activation energy measurements. Thereby, the two different AlO_x coated BOPP films (i.e. with and without defects in the AlO_x layer), as well as their metallised versions, could be assessed. If the activation energy approach is a suitable and correct technique to study permeation mechanisms, it is expected that a chemical interaction between permeating water molecules and elemental/metallic aluminium would induce a rise of the apparent activation energy, compared to an AlO_x coated sample with no elemental aluminium in the coating.

Finally, the structure of the AlO_x coating can be further analysed using AFM imaging at a lower scan size of 1 x 1 μm^2, as done by other researchers (see discussion in Chapter 6.2.2.3). This may reveal possible differences in surface topography and roughness between the uncoated and AlO_x coated polymer films and, therefore, give information about the intrinsic structure of the coating and its dependence on the polymer substrate, e.g. PET or BOPP. The coating structure could, moreover, be investigated using TEM analysis and electron diffraction techniques, after removing/dissolving the polymer substrates using appropriate chemicals (refer to end of Section 6.2.5).

9 REFERENCES

[1] G. L. Robertson, *Food packaging: Principles and practise*, 2nd ed., 2006, CRC press, Taylor and Francis Group, Boca Raton, FL.

[2] R. S. A. Kelly, *Development of clear barrier films in Europe,* 36th Annual Technical Conference Proceedings, Society of Vacuum Coaters, 1993, p. 312-316.

[3] R. S. A. Kelly, *Development of aluminium oxide clear barrier films,* 37th Annual Technical Conference Proceedings, Society of Vacuum Coaters, 1994, p. 144-148.

[4] C. A. Bishop, *Roll-to-roll vacuum deposition of barrier coatings* 2010, Scrivener Publishing and John Wiley & Sons, Hoboken, NJ - Salem, MA.

[5] J. Lange, Y. Wyser, *Recent innovations in barrier technologies for plastic packaging - A review,* Packaging Technology and Science, 2003, **16** (4), p. 149-158.

[6] D. Dodrill, *Barrier structure material options made crystal clear,* Medical Design Technology, Jan 2009, p. 22-25.

[7] *The future of transparent barrier films to 2011*, 2006, Pira International Ltd.

[8] R. Catalá, R. Gavara, *Review: Alternative high barrier polymers for food packaging,* Food Science and Technology International, 1996, **2** (5), p. 281-291.

[9] A. Yasuhara, T. Katami, T. Shibamoto, *Formation of dioxins from combustion of polyvinylidene chloride in a well-controlled incinerator,* Chemosphere, 2006, **62** (11), p. 1899-1906.

[10] S. Schiller, M. Neumann, H. Morgner, N. Schiller, *Plasma-activated high-rate deposition of oxides on plastic films,* 37th Annual Technical Conference Proceedings, Society of Vacuum Coaters, 1994, p. 203-210.

[11] M. D. Groner, S. M. George, R. S. McLean, P. F. Carcia, *Gas diffusion barriers on polymers using Al_2O_3 atomic layer deposition,* Applied Physics Letters, 2006, **88** (5), p. 051907.

[12] S. Günther, S. Straach, N. Schiller, A. L. Quiceno, A. G. Contreras, R. Ludwig, G. Hoffmann, *Innovative transparent barrier for packaging,* 52nd Annual Technical Conference Proceedings, Society of Vacuum Coaters, 2009, p. 727-729.

[13] R. Ludwig, R. Kulka, E. Josephson, *Vacuum web coating - State of the art and potential for electronics,* Proceedings of the IEEE, 2005, **93** (8), p. 1483-1490.

[14] R. S. A. Kelly, K. M. Revell, *Process for preparing barrier packaging materials*, 1992, Bowater Packaging Ltd., UK patent GB2246794 A

[15] R. S. A. Kelly, K. M. Revell, *Web barrier packaging material* 1997, Rexam Packaging Limited, European patent EP0437946 B1

[16] C. P. Barker, K. H. Kochem, K. M. Revell, R. S. A. Kelly, J. P. S. Badyal, *The interfacial chemistry of metallized, oxide coated, and nanocomposite coated polymer films,* Thin Solid Films, 1995, **257** (1), p. 77-82.

[17] C. P. Barker, K. H. Kochem, K. M. Revell, R. S. A. Kelly, J. P. S. Badyal, *Atomic force microscopy and permeability study of stretching-induced gas barrier loss of AlO_x layers,* Thin Solid Films, 1995, **259** (1), p. 46-52.

[18] A. Skinner, *Clear barrier films - Process, performance and opportunities,* AIMCAL Fall Technical Conference, 2006.

[19] *http://www.aimcal.org/member-news/articles/id/1295/celplast-becomes-the-exclusive-distributor-of-camvac-limiteds-camclearreg.aspx* [access: 26.10.2011].

[20] *Application profile Mylar® polyester film - Clear barrier heat sealable polyester film for raw meat*, DuPont Teijin Films: *europe.dupontteijinfilms.com/Download.aspx?pdfid=132* [access: 26.10.2011].

[21] *Application profile Mylar® polyester film - Clear barrier heat Sealable polyester film for cooked meats*, DuPont Teijin Films: *europe.dupontteijinfilms.com/Download.aspx?pdfid=131* [access: 26.10.2011].

[22] S. Schiller, M. Neumann, H. Morgner, N. Schiller, *How to produce Al_2O_3 coatings on plastic films,* Proceedings of 7th International Conference on Vacuum Web Coating, 1993, p. 194-219.

[23] S. Schiller, M. Neumann, G. Zeißig, H. Morgner, *High-rate EB evaporation of oxides for web coating,* Proceedings of 6th International Conference on Vacuum Web Coating, 1992, p. 46-69.

[24] S. Schiller, M. Neumann, H. Morgner, N. Schiller, *Progress in high-rate electron beam evaporation of oxides for web coating,* 36th Annual Technical Conference Proceedings, Society of Vacuum Coaters, 1993, p. 278-289.

[25] S. Schiller, G. Hoetzsch, M. Neumann, H. Morgner, O. Zywitzki, *Plasma-activated high rate evaporation using a low voltage electron beam system,* Surface and Coatings Technology, 1994, **68-69**, p. 788-793.

[26] J. Reschke, K. Goedicke, S. Schiller, *The magnetron-activated deposition process,* Surface and Coatings Technology, 1995, **76-77**, p. 763-769.

[27] N. Schiller, J. Reschke, K. Goedicke, M. Neumann, *Application of the magnetron activated deposition process (MAD-process) to coat polymer films with alumina in web coaters,* Surface and Coatings Technology, 1996, **86-87** (Part 2), p. 776-782.

[28] N. Schiller, J. Reschke, K. Goedicke, M. Neumann, *Deposition of alumina layers on plastic films using conventional boat evaporators,* 39th Annual Technical Conference Proceedings, Society of Vacuum Coaters, 1996, p. 404-412.

[29] S. Schiller, M. Neumann, H. Morgner, N. Schiller, *Reactive aluminum oxide coating of plastic films - Possibilities and limitations for high deposition rates,* 38th Annual Technical Conference Proceedings, Society of Vacuum Coaters, 1995, p. 18-26.

[30] S. Schiller, M. Neumann, F. Milde, *Web coating by reactive plasma activated evaporation and sputtering process,* 39th Annual Technical Conference Proceedings, Society of Vacuum Coaters, 1996, p. 371-377.

[31] S. Schiller, V. Kirchhoff, F. Milde, M. Fahland, N. Schiller, *Pulsed plasma activated deposition of plastic films,* 40th Annual Technical Conference Proceedings, Society of Vacuum Coaters, 1997, p. 327-332.

[32] N. Schiller, H. Morgner, M. Fahland, S. Straach, M. Räbisch, C. Charton, *Transparent oxide coatings on plastic webs for emerging applications,* 42nd Annual Technical Conference Proceedings, Society of Vacuum Coaters, 1999, p. 392-396.

[33] S. Schiller, V. Kirchhoff, N. Schiller, H. Morgner, *PVD coating of plastic webs and sheets with high rates on large areas,* Surface and Coatings Technology, 2000, **125** (1-3), p. 354-360.

[34] N. Schiller, S. Straach, M. Fahland, C. Charton, *Barrier coatings on plastic web,* 44th Annual Technical Conference Proceedings, Society of Vacuum Coaters, 2001, p. 184-188.

[35] *TopMet CLEAR datasheet*: Applied Materials.

[36] N. Schiller, S. Straach, S. Günther, A. L. Quiceno, A. G. Contreras, R. Ludwig, G. Hoffmann, *Innovative clear barrier technology for the packaging industry,* AIMCAL Fall Technical Conference, 2008.

[37] R. Ludwig, H. G. Lotz, G. Hoffmann, *Production proven vacuum web coating system with high process flexibility for robust and environmentally-friendly transparent barriers,* AIMCAL Fall Technical Conference, 2010.

[38] R. Ludwig, H. G. Lotz, G. Hoffmann, *Production proven vacuum web coating system for robust and environmentally-friendly transparent barriers,* 53rd Annual Technical Conference Proceedings, Society of Vacuum Coaters, 2010, p. 565-569.

[39] R. Ludwig, H. G. Lotz, G. Hoffmann, *Vacuum web coater for production of aluminium oxide based clear barrier on BOPP films,* BOPP Film Conference, 2011.

[40] R. Trassl, *Transparent barrier coatings for environmental-friendly packaging applications,* AIMCAL Fall Technical Conference, 2012.

[41] C. Misiano, E. Simonetti, F. Staffetti, F. Romanini, *New perspectives in Al_2O_3 based transparent oxide barrier coatings,* Proceedings of 7th International Conference on Vacuum Web Coating, 1993, p. 220-226.

[42] C. Misiano, F. Staffetti, E. Simonetti, P. Cerolini, *Inexpensive transparent barrier coatings on plastic substrates,* 39th Annual Technical Conference Proceedings, Society of Vacuum Coaters, 1996, p. 413-417.

[43] C. Misiano, E. Simonetti, *Apparatus for continuous reactive metal deposition in vacuum with web looping over upper and lower rollers*, 1995, Ce.Te.V. Centro Tecnologie Del Vuoto, US patent US5462602 A

[44] C. Misiano, E. Simonetti, F. Staffetti, *Method of and apparatus for making plastic film with barrier layers*, 1998, Ce.Te.V. Centro Technologie Del Vuoto, US patent US5704980 A

[45] http://www.foodproductiondaily.com/Packaging/Cost-effective-clear-aluminium-oxide-film-to-get-North-American-launch, [access: 26.10.2011].

[46] C. F. Struller, P. J. Kelly, N. J. Copeland, C. M. Liauw, *Characterization studies of aluminum oxide barrier coatings on polymeric substrates,* Journal of Vacuum Science & Technology A, 2012, **30** (4), p. 041502.

[47] C. F. Struller, P. J. Kelly, N. J. Copeland, C. M. Liauw, *Aluminum oxide barrier layers on polymer web,* AIMCAL Fall Technical Conference, 2012.

[48] C. Struller, N. Copeland, P. J. Kelly, *Aluminium oxide barrier layers on BOPP film,* BOPP Film Conference, 2013.

[49] C. F. Struller, P. J. Kelly, N. J. Copeland, *Aluminum oxide barrier coatings on polymer films for food packaging applications,* Surface and Coatings Technology, 2013, **in press**.

[50] *Polypropylene handbook*, E. P. Moore Jr., ed., 1996, Carl Hanser Verlag, Munich - Vienna - New York.

[51] C. Maier, T. Calafut, *Polypropylene - The definitive user's guide and databook* 1998, William Andrew Publishing/Plastics Design Library, Norwich, NY.

[52] H. Domininghaus, *Die Kunststoffe und ihre Eigenschaften*, 6th ed., P. Eyerer, P. Elsner and T. Hirth, eds., 2005, Springer Verlag, Berlin - Heidelberg - New York.

[53] *Handbook of polymer synthesis*, 2nd ed., H. R. Kricheldorf, O. Nuyken and G. Swift, eds., 2005, Marcel Dekker, New York, NY.

[54] J. A. Brydson, *Plastics materials*, 7th ed., 1999, Butterworth-Heinemann, Oxford.

[55] *Polymer data handbook*, 2nd ed., J. E. Mark, ed., 2009, Oxford University Press, New York, NY.

[56] T. Lüpke, S. Dunger, J. Sänze, H. J. Radusch, *Sequential biaxial drawing of polypropylene films,* Polymer, 2004, **45** (20), p. 6861-6872.

[57] Z. Bartczak, E. Martuscelli, *Orientation and properties of sequentially drawn films of an isotactic polypropylene/ hydrogenated oligocyclopentadiene blend,* Polymer, 1997, **38** (16), p. 4139-4149.

[58] H. Y. Nie, M. J. Walzak, N. S. McIntyre, *Draw-ratio-dependent morphology of biaxially oriented polypropylene films as determined by atomic force microscopy,* Polymer, 2000, **41** (6), p. 2213-2218.

[59] H.-Y. Nie, M. J. Walzak, N. S. McIntyre, *Atomic force microscopy study of biaxially oriented polypropylene films,* Journal of Materials Engineering and Performance, 2004, **13** (4), p. 451-460.

[60] S. Guimond, M. R. Wertheimer, *Surface degradation and hydrophobic recovery of polyolefins treated by air corona and nitrogen atmospheric pressure glow discharge,* Journal of Applied Polymer Science, 2004, **94** (3), p. 1291-1303.

[61] V. Jones, Strobel, M. J. Prokosch, *Development of poly(propylene) surface topography during corona treatment,* Plasma Processes and Polymers, 2005, **2** (7), p. 547-553.

[62] R. D. Boyd, A. M. Kenwright, J. P. S. Badyal, D. Briggs, *Atmospheric nonequilibrium plasma treatment of biaxially oriented polypropylene,* Macromolecules, 1997, **30** (18), p. 5429-5436.

[63] H.-C. Langowski, *Surface modification of polymer films for improved adhesion of deposited metal layers,* Journal of Adhesion Science and Technology, 2011, **25** (1-3), p. 223-243.

[64] U. Moosheimer, C. Bichler, *Plasma pretreatment of polymer films as a key issue for high barrier food packagings,* Surface and Coatings Technology, 1999, **116-119** (0), p. 812-819.

[65] A. N. Wilkinson, A. J. Ryan, *Polymer processing and structure development*, 1999, Kluwer Academic Publishers, Dordrecht.

[66] G. Wypych, *Handbook of antiblocking, release, and slip additives*, 2nd ed., 2011, ChemTec Publishing, Toronto.

[67] J. Nentwig, *Kunststoff-Folien: Herstellung - Eigenschaften - Anwendung*, 2006, Carl Hanser Verlag, München - Wien.

[68] J. Breil, *Oriented film technology*, in *Multilayer flexible packaging: Technology and applications for the food, personal care and over-the-counter pharmaceutical industries* J. R. Wagner Jr. , ed., 2010, Elsevier, Kidlington, p. 119-136.

[69] E. M. Mount, *Substrate/surface treatment/vacuum process interaction in high-barrier, metallized film manufacture,* Converting Quarterly, 2013, **Quarter 1**, p. 40-44.

[70] J. Breil, *Multilayer oriented films*, in *Multilayer flexible packaging: Technology and applications for the food, personal care and over-the-counter pharmaceutical industries* 2010, Elsevier, Kidlington, p. 231-237.

[71] G. Janzen, *Plasmatechnik*, 1992, Hüthig Buch Verlag, Heidelberg.

[72] D. M. Mattox, *Handbook of physical vapor deposition (PVD) processing*, 1998, Noyes Publications, Park Ridge, NJ.

[73] G. Franz, *Niederdruckplasmen und Mikrostrukturtechnik*, 2004, Springer-Verlag, Berlin - Heidelberg.

[74] E. M. Liston, L. Martinu, M. R. Wertheimer, *Plasma surface modification of polymers for improved adhesion: A critical review,* Journal of Adhesion Science and Technology, 1993, **7** (10), p. 1091-1127.

[75] E. Finson, S. Kaplan, L. Wood, *Plasma treatment of webs and films,* 38th Annual Technical Conference Proceedings, Society of Vacuum Coaters, 1995, p. 52-57.

[76] A. Brunold, F. Kleinert, R. Schnabel, S. Marinow, *Modifizierung von Polymeren im Niederdruckplasma - Verbesserung der Haftfestigkeit von Lackierungen, Gasphasenprozesse, Teil 1,* Metalloberfläche, 1997, **51** (1), p. 37-42.

[77] C. Bichler, H.-C. Langowski, U. Moosheimer, B. Seifert, *Adhesion mechanism of aluminum, aluminum oxide, and silicon oxide on biaxially oriented polypropylene (BOPP), poly(ethyleneterephthalate) (PET), and*

poly(vinyl chloride) (PVC), Journal of Adhesion Science and Technology, 1997, **11** (2), p. 233-246.

[78] R. Mahlberg, H. E. M. Niemi, F. S. Denes, R. M. Rowell, *Application of AFM on the adhesion studies of oxygen-plasma-treated polypropylene and lignocellulosics,* Langmuir, 1999, **15** (8), p. 2985-2992.

[79] K. Harth, H. Hibst, *Surface modification of polypropylene in oxygen and nitrogen plasmas,* Surface and Coating Technology, 1993, **59** (1-3), p. 350-355.

[80] K. Navaneetha Pandiyaraj, V. Selvarajan, R. R. Deshmukh, C. Gao, *Adhesive properties of polypropylene (PP) and polyethylene terephthalate (PET) film surfaces treated by DC glow discharge plasma,* Vacuum, 2008, **83** (2), p. 332-339.

[81] D. Briggs, *Corona discharge treatment*, in *Handbook of adhesion*, D. E. Packham, ed., 2005, John Wiley & Sons, Chichester, p. 89-90.

[82] D. Briggs, *Flame treatment*, in *Handbook of adhesion*, D. E. Packham, ed., 2005, John Wiley & Sons, Chichester, p. 195-196.

[83] F. Garbassi, M. Morra, E. Occhiello, *Adhesion*, in *Polymer surfaces - From physics to technology*, 1998, John Wiley & Sons, Chichester p. 350-398.

[84] H. Y. Nie, M. J. Walzak, B. Berno, N. S. McIntyre, *Atomic force microscopy study of polypropylene surfaces treated by UV and ozone exposure: Modification of morphology and adhesion force,* Applied Surface Science, 1999, **144-145**, p. 627-632.

[85] D. M. Brewis, *Pre-treatment of polymers*, in *Handbook of adhesion*, D. E. Packham, ed., 2005, John Wiley & Sons, Chichester, p. 381-383.

[86] M. Strobel, C. S. Lyons, *The role of low-molecular-weight oxidized materials in the adhesion properties of corona-treated polypropylene film,* Journal of Adhesion Science and Technology, 2003, **17** (1), p. 15-23.

[87] R. Seeböck, H. Esrom, M. Charbonnier, M. Romand, *Modification of polyimide in barrier discharge air-plasmas: Chemical and morphological effects,* Plasmas and Polymers, 2000, **5** (2), p. 103-118.

[88] D. Dixon, B. J. Meenan, *Atmospheric dielectric barrier discharge treatments of polyethylene, polypropylene, polystyrene and poly(ethylene terephthalate) for enhanced adhesion,* Journal of Adhesion Science and Technology, 2012, **26** (20-21), p. 2325-2337.

[89] *Verfahrenstechnik der Kunststoffmetallisierung - Physikalische Verfahren*, in *Kunststoff-Metallisierung*, 1991, Eugen G. Leuze Verlag, Saulgau, p. 65-85.

[90] R. F. Bunshah, *Vapor deposition technologies*, in *Handbook of hard coatings: Deposition technologies, properties and applications*, G. E. McGuire, S. M. Rossnagel and R. F. Bunshah, eds., 2001, Noyes Publications, William Andrew Publishing, LLC, Norwich, NY, p. 4-76.

[91] M. Nicolaus, M. Schäpers, *Fundamentals of thin-film technology*, in *Modern surface technology*, F.-W. Bach, A. Laarmann and T. Wenz, eds., 2006, Wiley-VCH Verlag, Weinheim, p. 31-50.

[92] C. A. Bishop, *Vacuum deposition onto webs, films, and foils*, 2007, William Andrew Publishing, Norwich, NY.

[93] P. J. Kelly, R. D. Arnell, *Magnetron sputtering: A review of recent developments and applications,* Vacuum, 2000, **56** (3), p. 159-172.

[94] R. Wolf, *A technology decision – Adhesive lamination or extrusion coating/lamination? ,* TAPPI PLACE Conference, 2010.

[95] T. E. Rolando, *Flexible packaging: Adhesives, coatings and processes*, Rapra Review Reports, 2000, Rapra Technology Limited, Shawbury.

[96] A. Yializis, M. G. Mikhael, R. E. Ellwanger, *Ultra high barrier films,* 43rd Annual Technical Conference Proceedings, Society of Vacuum Coaters, 2000, p. 404-407.

[97] J. D. Affinito, *Polymer film deposition by a new vacuum process,* 45th Annual Technical Conference Proceedings, Society of Vacuum Coaters, 2002, p. 429-443.

[98] S. Jahromi, *Freshure coatings: Environmentally friendly transparent high barrier coating,* AIMCAL Fall Technical Conference, 2011.

[99] *ASTM dictionary of engineering science and technology*, 10th ed., 2005, ASTM International, West Conshohocken, PA.

[100] C. Bischof, *ND-Plasmatechnik im Umfeld der Haftungsproblematik bei Metall-Polymer-Verbunden,* Materialwissenschaft und Werkstofftechnik, 1993, **24** (2), p. 33-41.

[101] *Grundlagen der Kunststoff-Metallhaftung*, in *Kunststoff-Metallisierung*, 1991, Eugen G. Leuze Verlag, Saulgau, p. 19-42.

[102] K. W. Allen, *A review of contemporary views of theories of adhesion,* Journal of Adhesion, 1987, **21** (3-4), p. 261-277.

[103] E. M. Petrie, *Theories of adhesion*, in *Handbook of adhesives and sealants*, 2007, McGraw-Hill, New York - Chicago - San Francisco, p. 39-58.

[104] K. W. Allen, *Mechanical theory of adhesion*, in *Handbook of adhesion*, D. E. Packham, ed., 2005, John Wiley & Sons, Chichester, p. 275-277.

[105] B. V. Derjaguin, V. P. Smilga, *Electronic theory of adhesion,* Journal of Applied Physics, 1967, **38** (12), p. 4609-4616.

[106] C. Weaver, *Adhesion of thin films,* Journal of Vacuum Science and Technology, 1975, **12** (1), p. 18-25.

[107] C. Bischof, W. Possart, *Adhäsion - Theoretische und experimentelle Grundlagen*, 1983, Akademie-Verlag, Berlin.

[108] F. Faupel, R. Willecke, A. Thran, *Diffusion of metals in polymers,* Materials Science and Engineering: R: Reports, 1998, **22** (1), p. 1-55.

[109] J. W. Bartha, P. O. Hahn, F. LeGoues, P. S. Ho, *Photoemission spectroscopy study of aluminum - polyimide interface,* Journal of Vacuum Science & Technology A, 1985, **3** (3), p. 1390-1393.

[110] K. W. Allen, *Adsorption theory of adhesion*, in *Handbook of adhesion*, D. E. Packham, ed., 2005, John Wiley & Sons, Chichester, p. 38-40.

[111] A. Pagliuca, A. R. Hutchinson, *Durability of resealed building joints*, in *Durability of building sealants: Proceedings of the international RILEM symposium* J. C. Beech and A. T. Wolf, eds., 1996, E & FN Spon, an imprint of Chapman & Hall, London, p. 105-122.

[112] J. J. Bikerman, *Causes of poor adhesion: Weak boundary layer,* Journal of Industrial and Engineering Chemistry, 1967, **59** (9), p. 40–44.

[113] D. E. Packham, *Adhesion*, in *Handbook of adhesion*, D. E. Packham, ed., 2005, John Wiley & Sons, Chichester, p. 14-16.

[114] R. Lacombe, *Adhesion measurement methods - Theory and practice* 2006, CRC Press, Boca Raton, FL.

[115] K. L. Mittal, *Adhesion measurement of thin films,* Electrocomponent Science and Technology, 1976, **3**, p. 21-42.

[116] K. L. Mittal, *Adhesion measurement: Recent progress, unsolved problems, and prospects*, in *Adhesion measurement of thin films, thick films, and bulk coatings*, K. L. Mittal, ed., 1978, American Society for Testing and Materials (ASTM), Philadelphia, PA, p. 5-17.

[117] K. L. Mittal, *Adhesion measurements of films and coatings: A commentary*, in *Adhesion measurements of films and coatings*, K. L. Mittal, ed., 1995, VSP, Utrecht, p. 1-13.

[118] D. S. Rickerby, *A review of the methods for the measurement of coating-substrate adhesion,* Surface and Coating Technology, 1988, **36** (1-2), p. 541-557.

[119] P. A. Steinmann, H. E. Hintermann, *A review of the mechanical tests for assessment of thin-film adhesion,* Journal of Vacuum Science & Technology A: Vacuum, Surfaces, and Films, 1989, **7** (3), p. 2267-2272.

[120] M. Jesdinszki, C. Struller, N. Rodler, D. Blondin, V. Cassio, E. Kucukpinar, H.-C. Langowski, *Evaluation of adhesion strength between thin aluminum layer and poly(ethylene terephthalate) substrate by peel tests — A practical approach for the packaging industry,* Journal of Adhesion Science and Technology, 2012, **26** (20-21), p. 2357-2380.

[121] L. Marras, O. Sbaizero, *The fragmentation test applied to adhesion measurements and microstructural characterization in plasma pre-treated metallized plastic webs,* Packaging Technology and Science, 2009, **22** (5), p. 293-302.

[122] G. Rochat, P. Fayet, *Characterization of mechanical properties of ultra-thin oxide coatings on polymers by uniaxial fragmentation tests,* Journal of Adhesion Science and Technology, 2012, **26** (20-21), p. 2381-2392.

[123] T. O. Kaariainen, P. J. Kelly, D. C. Cameron, B. Beake, H. Li., P. M. Barker, C. F. Struller, *Nanoscratch testing of atomic layer deposition and magnetron sputtered TiO_2 and Al_2O_3 coatings on polymeric substrates,* Journal of Vacuum Science & Technology A: Vacuum, Surfaces, and Films, 2012, **30** (1), p. 01A132.

[124] A. Khanna, D. G. Bhat, A. Harris, B. D. Beake, *Structure-property correlations in aluminum oxide thin films grown by reactive AC magnetron sputtering,* Surface and Coatings Technology, 2006, **201** (3–4), p. 1109-1116.

[125] S. J. Bull, E. G. Berasetegui, *An overview of the potential of quantitative coating adhesion measurement by scratch testing,* Tribology International, 2006, **39** (2), p. 99-114.

[126] H.-C. Langowski, *Permeation of gases and condensable substances through monolayer and multilayer structures*, in *Plastic packaging - Interactions with food and pharmaceuticals*, O. G. Piringer and A. L. Baner, eds., 2008, WILEY-VCH Verlag, Weinheim, p. 297-347.

[127] K. Cooksey, K. S. Marsh, L. H. Doar, *Predicting permeability & transmission rate for multilayer materials,* Food Technology, 1999, **53** (9), p. 60-63.

[128] Y. G. Tropsha, N. G. Harvey, *Activated rate theory treatment of oxygen and water transport through silicon oxide/poly(ethylene terephthalate) composite barrier structures,* The Journal of Physical Chemistry B, 1997, **101** (13), p. 2259-2266.

[129] A. G. Erlat, R. J. Spontak, R. P. Clarke, T. C. Robinson, P. D. Haaland, Y. Tropsha, N. G. Harvey, E. A. Vogler, *SiO_x gas barrier coatings on polymer substrates: Morphology and gas transport considerations,* The Journal of Physical Chemistry B, 1999, **103** (29), p. 6047-6055.

[130] C. S. Deng, H. E. Assender, F. Dinelli, O. V. Kolosov, G. A. D. Briggs, T. Miyamoto, Y. Tsukahara, *Nucleation and growth of gas barrier aluminium oxide on surfaces of poly(ethylene terephthalate) and polypropylene: Effects of the polymer surface properties,* Journal of Polymer Science Part B: Polymer Physics, 2000, **38** (23), p. 3151-3162.

[131] A. P. Roberts, B. M. Henry, A. P. Sutton, C. R. M. Grovenor, G. A. D. Briggs, T. Miyamoto, M. Kano, Y. Tsukahara, M. Yanaka, *Gas permeation in silicon-oxide/polymer (SiO_x/PET) barrier films: Role of the oxide lattice, nano-defects and macro-defects,* Journal of Membrane Science, 2002, **208** (1–2), p. 75-88.

[132] U. Moosheimer, H.-C. Langowski, *Permeation of oxygen and moisture through vacuum web coated films,* 42nd Annual Technical Conference Proceedings, Society of Vacuum Coaters, 1999, p. 408-414.

[133] O. Miesbauer, M. Schmidt, H.-C. Langowski, *Stofftransport durch Schichtsysteme aus Polymeren und dünnen anorganischen Schichten (Mass transport through layer systems consisting of polymers and thin inorganic coatings),* Vakuum in Forschung und Praxis, 2008, **20** (6), p. 32-40.

[134] C. E. Rogers, *Permeation of gases and vapours in polymers*, in *Polymer permeability*, J. Comyn, ed., 1985, Chapman & Hall, London, p. 11-73.

[135] L. K. Massey, *Permeability properties of plastics and elastomers - A guide to packaging and barrier materials* 2nd ed., 2003, William Andrew Publishing/Plastics Design Library, Norwich, NY.

[136] G. L. Graff, R. E. Williford, P. E. Burrows, *Mechanisms of vapor permeation through multilayer barrier films: Lag time versus equilibrium permeation,* Journal of Applied Physics, 2004, **96** (4), p. 1840-1849.

[137] W. G. Perkins, D. R. Begeal, *Diffusion and permeation of He, Ne, Ar, Kr, and D_2 through silicon oxide thin films,* The Journal of Chemical Physics, 1971, **54** (4), p. 1683-1694.

[138] R. M. Barrer, *Diffusion in and through solids*, 1941, Cambridge University Press, London.

[139] W. Prins, J. J. Hermans, *Theory of permeation through metal coated polymer films,* The Journal of Physical Chemistry, 1959, **63** (5), p. 716-720.

[140] E. H. H. Jamieson, A. H. Windle, *Structure and oxygen-barrier properties of metallized polymer film,* Journal of Materials Science, 1983, **18** (1), p. 64-80.

[141] P. Mercea, L. Muresan, V. Mecea, *Permeation of gases through metallized polymer membranes,* Journal of Membrane Science, 1985, **24** (3), p. 297-307.

[142] P. Mercea, L. Muresan, V. Mecea, D. Silipas, I. Ursu, *Permeation of gases through poly (ethylene terephthalate) membranes metallized with palladium,* Journal of Membrane Science, 1988, **35** (3), p. 291-300.

[143] T. A. Beu, P. V. Mercea, *Gas transport through metallized polymer membranes,* Materials Chemistry and Physics, 1990, **26** (3-4), p. 309-322.

[144] G. Rossi, M. Nulman, *Effect of local flaws in polymeric permeation reducing barriers,* Journal of Applied Physics, 1993, **74** (9), p. 5471-5475.

[145] G. Czeremuszkin, M. Latreche, A. S. da Silva Sobrinho, M. R. Wertheimer, *Simple model of oxygen permeation through defects in transparent coatings,* 42th Annual Technical Conference Proceedings, Society of Vacuum Coaters, 1999, p. 176-180.

[146] G. Czeremuszkin, M. Latreche, M. R. Wertheimer, *Permeation through defects in transparent barrier coated plastic films,* 43th Annual Technical Conference Proceedings, Society of Vacuum Coaters, 2000, p. 408-413.

[147] M. Yanaka, B. M. Henry, A. P. Roberts, C. R. M. Grovenor, G. A. D. Briggs, A. P. Sutton, T. Miyamoto, Y. Tsukahara, N. Takeda, R. J. Chater, *How cracks in SiO_x-coated polyester films affect gas permeation,* Thin Solid Films, 2001, **397** (1-2), p. 176-185.

[148] K. Mueller, H. Weisser, *Numerical simulation of permeation through vacuum-coated laminate films,* Packaging Technology and Science, 2002, **15** (1), p. 29-36.

[149] M. Hanika, H.-C. Langowski, U. Moosheimer, *Layer defects and the synergetic effect between inorganic and organic barrier layers,* 45th Annual Technical Conference Proceedings, Society of Vacuum Coaters, 2002, p. 519-524.

[150] M. Hanika, H.-C. Langowski, W. Peukert, *Simulation and verification of defect-dominated permeation mechanisms in multiple structures of inorganic and polymeric barrier layers,* 46th Annual Technical Conference Proceedings, Society of Vacuum Coaters, 2003, p. 592-599.

[151] W. Decker, B. Henry, *Basic principles of thin film barrier coatings,* 45th Annual Technical Conference Proceedings, Society of Vacuum Coaters, 2002, p. 492-502.

[152] M. Hanika, W. Peukert, H. C. Langowski, *Permeation durch vakuumbedampfte Kunststofffolien,* Chemie Ingenieur Technik, 2002, **74** (7), p. 984-989.

[153] H.-C. Langowski, *Stofftransport durch polymere und anorganische Schichten (Transport of Substances Through Polymeric and Inorganic Layers),* Vakuum in Forschung und Praxis, 2005, **17** (1), p. 6-13.

[154] J. D. Affinito, D. Hilliard, *A new class of ultra-barrier materials,* 47th Annual Technical Conference Proceedings, Society of Vacuum Coaters, 2004, p. 563-593.

[155] H. Chatham, *Oxygen diffusion barrier properties of transparent oxide coatings on polymeric substrates,* Surface and Coatings Technology, 1996, **78** (1-3), p. 1-9.

[156] M. Hanika, H. C. Langowski, U. Moosheimer, W. Peukert, *Inorganic layers on polymeric films – Influence of defects and morphology on barrier properties,* Chemical Engineering & Technology, 2003, **26** (5), p. 605-614.

[157] B. M. Henry, F. Dinelli, K. Y. Zhao, C. R. M. Grovenor, O. V. Kolosov, G. A. D. Briggs, A. P. Roberts, R. S. Kumar, R. P. Howson, *A microstructural study of transparent metal oxide gas barrier films,* Thin Solid Films, 1999, **355-356**, p. 500-505.

[158] P. F. Carcia, R. S. McLean, M. H. Reilly, *Permeation measurements and modeling of highly defective Al_2O_3 thin films grown by atomic layer deposition on polymers,* Applied Physics Letters, 2010, **97** (22), p. 221901.

[159] A. G. Erlat, B. M. Henry, C. R. M. Grovenor, A. G. D. Briggs, R. J. Chater, Y. Tsukahara, *Mechanism of water vapor transport through PET/AlO_xN_y gas barrier films,* The Journal of Physical Chemistry B, 2004, **108** (3), p. 883-890.

[160] B. M. Henry, A. G. Erlat, C. R. M. Grovenor, C. S. Deng, A. G. D. Briggs, T. Miyamoto, N. Noguchi, T. Niijima, Y. Tsukahara, *The permeation of water vapor through gas barrier films,* 44th Annual Technical Conference Proceedings, Society of Vacuum Coaters, 2001, p. 469-475.

[161] A. S. da Silva Sobrinho, M. Latrèche, G. Czeremuszkin, J. E. Klemberg-Sapieha, M. R. Wertheimer, *Transparent barrier coatings on polyethylene terephthalate by single- and dual-frequency plasma-enhanced chemical vapor deposition,* Journal of Vacuum Science & Technology A, 1998, **16** (6), p. 3190-3198.

[162] H. Tamagaki, T. Okimoto, T. Segawa, *Transparent high barrier coating on polymer web by PE-CVD roll coater,* 53rd Annual Technical Conference Proceedings, Society of Vacuum Coaters, 2010, p. 553-557.

[163] J. Fahlteich, W. Schönberger, M. Fahland, N. Schiller, *Characterization of reactively sputtered permeation barrier materials on polymer substrates,* Surface and Coatings Technology, 2011, **205, Supplement 2** (0), p. S141-S144.

[164] J. Fahlteich, M. Fahland, W. Schönberger, N. Schiller, *Permeation barrier properties of thin oxide films on flexible polymer substrates,* Thin Solid Films, 2009, **517** (10), p. 3075-3080.

[165] B. M. Henry, A. G. Erlat, A. McGuigan, C. R. M. Grovenor, G. A. D. Briggs, Y. Tsukahara, T. Miyamoto, N. Noguchi, T. Niijima, *Characterization of transparent aluminium oxide and indium tin oxide layers on polymer substrates,* Thin Solid Films, 2001, **382** (1-2), p. 194-201.

[166] P. F. Carcia, R. S. McLean, M. H. Reilly, M. D. Groner, S. M. George, *Ca test of Al_2O_3 gas diffusion barriers grown by atomic layer deposition on polymers,* Applied Physics Letters, 2006, **89** (3), p. 031915.

[167] E. R. Dickey, W. A. Barrow, *High rate roll-to-roll deposition of ALD thin films on flexible substrates,* 52nd Annual Technical Conference Proceedings, Society of Vacuum Coaters, 2009, p. 720-726.

[168] H. G. Kim, S. S. Kim, *Aluminum oxide barrier coating on polyethersulfone substrate by atomic layer deposition for barrier property enhancement,* Thin Solid Films, 2011, **520** (1), p. 481-485.

[169] M. Schmid, K. Dallmann, E. Bugnicourt, D. Cordoni, F. Wild, A. Lazzeri, K. Noller, *Properties of whey-protein-coated films and laminates as novel recyclable food packaging materials with excellent barrier properties,* International Journal of Polymer Science, 2012, **Volume 2012** (Article ID 562381).

[170] J. D. Affinito, M. E. Gross, C. A. Coronado, G. L. Graff, I. N. Greenwell, P. M. Martin, *A new method for fabricating transparent barrier layers,* Thin Solid Films, 1996, **290–291**, p. 63-67.

[171] M. E. Gross, P. M. Martin, *Chapter 11: Vacuum polymer deposition*, in *Handbook of deposition technologies for films and coatings: Science, applications and technology*, P. M. Martin, ed., 2010, Elsevier, Kidlington, p. 532-553.

[172] Y. G. Tropsha, N. G. Harvey, *Combinatorial barrier effect of the multilayer SiO_x coatings on polymer substrates,* 40th Annual Technical Conference Proceedings, Society of Vacuum Coaters, 1997, p. 64-69.

[173] G. Aresta, J. Palmans, M. C. M. van de Sanden, M. Creatore, *Evidence of the filling of nano-porosity in SiO_2-like layers by an initiated-CVD monomer,* Microporous and Mesoporous Materials, 2012, **151**, p. 434-439.

[174] P. M. Martin, J. D. Affinito, M. E. Gross, C. A. Coronado, W. D. Bennett, D. C. Stewart, *Multilayer coatings on flexible substrates,* 38th Annual Technical Conference Proceedings, Society of Vacuum Coaters, 1995, p. 163-167.

[175] T. Miyamoto, K. Mizuno, N. Noguchi, T. Niijima, *Gas barrier performances of organic-inorganic multilayered films,* 44th Annual Technical Conference Proceedings, Society of Vacuum Coaters, 2001, p. 166-171.

[176] *ASTM F1927 - 07 Standard test method for determination of oxygen gas transmission rate, permeability and permeance at controlled relative humidity through barrier materials using a coulometric detector*, 2007, ASTM International.

[177] *ASTM F1249 - 06 Standard test method for water vapor transmission rate through plastic film and sheeting using a modulated infrared sensor*, 2006, ASTM International.

[178] *ISO 15106-3 - Plastics - Film and sheeting - Determination of water vapour transmission rate - Part 3: Electrolytic detection sensor method*, 2003, International Organization for Standardization.

[179] D. B. Murphy, *Differential interference contrast (DIC) microscopy and modulation contrast microscopy*, in *Fundamentals of light microscopy and electronic imaging*, 2001, John Wiley & Sons, New York, NY, p. 153-175.

[180] M. Mansuripur, *Nomarski's differential interference contrast microscope* in *Classical optics and its applications*, 2009, Cambridge University Press, Cambridge p. 566-575.

[181] J. B. Bindell, *Scanning electron microscopy*, in *Encyclopedia of materials characterization*, C. R. Brundle, C. A. Evans Jr. and S. Wilson, eds., 1992, Butterworth-Heinemann, Stoneham, MA, p. 70-84.

[182] J. J. Bozzola, L. D. Russell, *The scanning electron microscope*, in *Electron microscopy: Principles and techniques for biologists*, 1999, Jones and Bartlett, Sudbury, MA, p. 203-239.

[183] H.-J. Butt, B. Cappella, M. Kappl, *Force measurements with the atomic force microscope: Technique, interpretation and applications,* Surface Science Reports, 2005, **59** (1-6), p. 1-152.

[184] D. S. N. Magonov, D. M.-H. Whangbo, *Scanning probe microscopes*, in *Surface analysis with STM and AFM*, 1996, VCH Verlagsgesellschaft mbH, Weinheim - New York - Basel - Cambridge - Tokyo, p. 21-46.

[185] R. Howland, L. Benatar, *A practical guide to scanning probe microscopy*, 2000, ThermoMicroscopes.

[186] R. García, R. Pérez, *Dynamic atomic force microscopy methods,* Surface Science Reports, 2002, **47** (6), p. 197-301.

[187] *Scanning force microscopy*, in *Characterization and analysis of polymers*, A. Seidel, ed., 2008, Wiley, Hoboken, N.J., p. 460-506.

[188] R. Volk, *Rauheitsmessung - Theorie und Praxis*, 2005, Beuth Verlag, Berlin - Wien - Zürich.

[189] F. Walther, W. M. Heckl, R. W. Stark, *Evaluation of nanoscale roughness measurements on a plasma treated SU-8 polymer surface by atomic force microscopy,* Applied Surface Science, 2008, **254** (22), p. 7290-7295.

[190] H. W. Fox, W. A. Zisman, *The spreading of liquids on low energy surfaces. I. Polytetrafluoroethylene,* Journal of Colloid Science, 1950, **5** (6), p. 514-531

[191] L. A. Girifalco, R. J. Good, *A theory for the estimation of surface and interfacial energies. I. Derivation and application to interfacial tension,* The Journal of Physical Chemistry, 1957, **61** (7), p. 904-909.

[192] F. M. Fowkes, *Attractive forces at interfaces,* Industrial & Engineering Chemistry, 1964, **56** (12), p. 40-52.

[193] D. K. Owens, R. C. Wendt, *Estimation of the surface free energy of polymers,* Journal of Applied Polymer Science, 1969, **13** (8), p. 1741-1747.

[194] D. H. Kaelble, *Dispersion-polar surface tension properties of organic solids,* The Journal of Adhesion, 1970, **2** (2), p. 66-81.

[195] A. W. Neumann, R. J. Good, C. J. Hope, M. Sejpal, *An equation-of-state approach to determine surface tensions of low-energy solids from contact angles,* Journal of Colloid and Interface Science, 1974, **49** (2), p. 291-304.

[196] D. Li, A. W. Neumann, *A reformulation of the equation of state for interfacial tensions,* Journal of Colloid and Interface Science, 1990, **137** (1), p. 304-307.

[197] S. Wu, *Surface tension and polarity of solid polymers*, in *Polymer interface and adhesion*, 1982, Marcel Dekker, New York, NY, p. 169-214.

[198] S. Wu, *Calculation of interfacial tension in polymer systems,* Journal of Polymer Science Part C: Polymer Symposia, 1971, **34** (1), p. 19-30.

[199] C. J. Van Oss, R. J. Good, M. K. Chaudhury, *The role of van der Waals forces and hydrogen bonds in "hydrophobic interactions" between biopolymers and low energy surfaces,* Journal of Colloid and Interface Science, 1986, **111** (2), p. 378-390.

[200] C. J. Van Oss, M. K. Chaudhury, R. J. Good, *Interfacial Lifshitz-van der Waals and polar interactions in macroscopic systems,* Chemical Reviews, 1988, **88** (6), p. 927-941.

[201] W. Rabel, *Einige Aspekte der Benetzungstheorie und ihre Anwendung auf die Untersuchung und Veränderung der Oberflächeneigenschaften von Polymeren,* Farbe und Lack, 1971, **77** (10), p. 997-1005.

[202] M. Zenkiewicz, *Methods for the calculation of surface free energy of solids,* Journal of Achievements in Materials and Manufacturing Engineering, 2007, **24** (1), p. 137-145.

[203] G. Ström, M. Fredriksson, P. Stenius, *Contact angles, work of adhesion, and interfacial tensions at a dissolving hydrocarbon surface,* Journal of Colloid and Interface Science, 1987, **119** (2), p. 352-361.

[204] D. Y. Kwok, A. W. Neumann, *Contact angle measurement and contact angle interpretation,* Advances in Colloid and Interface Science, 1999, **81** (3), p. 167-249.

[205] *Benutzerhandbuch - Drop shape analysis DSA1 v. 1.90 für Kontaktwinkelmess-System DSA100*, 2006, Krüss GmbH, Hamburg.

[206] A. F. Stalder, G. Kulik, D. Sage, L. Barbieri, P. Hoffmann, *A snake-based approach to accurate determination of both contact points and contact angles,* Colloids and Surfaces A: Physicochemical and Engineering Aspects, 2006, **286** (1–3), p. 92-103.

[207] *ASTM D2578 - 09 Standard test method for wetting tension of polyethylene and polypropylene films*, 2009, ASTM International.

[208] M. Zenkiewicz, *Wettability and surface free energy of corona-treated biaxially-oriented polypropylene film,* Journal of Adhesion Science and Technology, 2001, **15** (14), p. 1769-1785.

[209] D. Briggs, *X-ray photoelectron spectroscopy (XPS)*, in *Handbook of adhesion*, D. E. Packham, ed., 2005, John Wiley & Sons, Chichester, p. 621, 622.

[210] J. F. Watts, J. Wolstenholme, *An introduction to surface analysis by XPS and AES*, 2003, John Wiley & Sons, Chichester.

[211] M. H. Kibel, *X-Ray photoelectron spectroscopy*, in *Surface analysis methods in materials science*, D. J. O'Connor, B. A. Sexton and R. S. C. Smart, eds., 2003, Springer-Verlag, Berlin - Heidelberg, p. 175-201.

[212] J. H. Scofield, *Hartree-Slater subshell photoionization cross-sections at 1254 and 1487 eV,* Journal of Electron Spectroscopy and Related Phenomena, 1976, **8** (2), p. 129-137.

[213] M. J. Hearn, D. Briggs, S. C. Yoon, B. D. Ratner, *SIMS and XPS studies of polyurethane surfaces 2. Polyurethanes with fluorinated chain extenders,* Surface and Interface Analysis, 1987, **10** (8), p. 384-391.

[214] S. Hofmann, *Practical surface analysis: State of the art and recent developments in AES, XPS, ISS and SIMS,* Surface and Interface Analysis, 1986, **9** (1), p. 3-20.

[215] B. Katz, *Static secondary ion mass spectrometry*, in *Encyclopedia of materials characterization*, C. R. Brundle, C. A. Evans Jr. and S. Wilson, eds., 1992, Butterworth-Heinemann, Stoneham, MA, p. 549-558.

[216] J. C. Vickerman, D. Briggs, *TOF-SIMS: Materials analysis by mass spectrometry*, 2nd ed., 2013, IM Publications LLP and SurfaceSpectra Limited, Chichester - Manchester.

[217] D. Briggs, M. J. Hearn, *Interaction of ion beams with polymers, with particular reference to SIMS,* Vacuum, 1986, **36** (11–12), p. 1005-1010.

[218] Z. Monsef Khoshhesab, *Chapter 11 Reflectance IR spectroscopy*, in *Infrared spectroscopy - Materials science, engineering and technology*, T. Theophanides, ed., 2012, InTech, p. 233-244.

[219] B. H. Stuart, *Infrared spectroscopy: Fundamentals and applications*, 2004, John Wiley & Sons, Chichester.

[220] B. C. Smith, *Fundamentals of Fourier transform infrared spectroscopy*, 2nd ed., 2011, Taylor & Francis, Boca Raton, FL.

[221] *Test procedure metal adhesion - Seal test*, 1999, European Metallizers Association (EMA) - Technical Committee Films.

[222] K. E. Sickafus, *Transmission electron microscopy*, in *Encyclopedia of materials characterization*, C. R. Brundle, C. A. Evans Jr. and S. Wilson, eds., 1992, Butterworth-Heinemann, Stoneham, MA, p. 99-115.

[223] M. Jeschke, *Films, compositions and processes*, 2005, UCB, US Patent US6969556 B2

[224] R. A. Migliorini, D. A. Liestman, *Multi-layer oriented polypropylene films with modified core*, 2003, ExxonMobil Chemical Company, US Patent Application US20030211298 A1

[225] U. Murschall, H. Peiffer, G. Schlögl, *Biaxially oriented shrinkable polyolefin laminate, sealable both sides with barrier properties*, 1996, Hoechst Aktiengesellschaft, European Patent EP0489373 B1

[226] A. K. van de Vegt, *From polymers to plastics*, 2006, VSSD, Delft.

[227] S. Tamura, K. Ohta, T. Kanai, *Study of crater structure formation on the surface of biaxially oriented polypropylene film,* Journal of Applied Polymer Science, 2012, **124** (4), p. 2725-2735.

[228] S. Tamura, K. Takino, T. Yamada, T. Kanai, *Crater formation mechanism on the surface of a biaxially oriented polypropylene film,* Journal of Applied Polymer Science, 2012, **126** (S2), p. E501-E512.

[229] Y. Numata, T. Oya, M. Kuwahara, K. Ito, *Water vapor permeation studies of metal oxide/polymer coated plastic films,* 48th Annual Technical Conference Proceedings, Society of Vacuum Coaters, 2005, p. 660-662.

[230] A. G. Erlat, B. M. Henry, J. J. Ingram, D. B. Mountain, A. McGuigan, R. P. Howson, C. R. M. Grovenor, G. A. D. Briggs, Y. Tsukahara, *Characterisation of aluminium oxynitride gas barrier films,* Thin Solid Films, 2001, **388** (1–2), p. 78-86.

[231] A. S. da Silva Sobrinho, G. Czeremuszkin, M. Latrèche, G. Dennler, M. R. Wertheimer, *A study of defects in ultra-thin transparent coatings on polymers,* Surface and Coatings Technology, 1999, **116-119**, p. 1204-1210.

[232] B. M. Henry, A. G. Erlat, C. R. M. Grovenor, A. G. D. Briggs, Y. Tsukahara, T. Miyamoto, N. Noguchi, T. Niijima, *Microstructural and gas barrier properties of transparent aluminium oxide and indium tin oxide films,* 43rd Annual Technical Conference Proceedings, Society of Vacuum Coaters, 2000, p. 373-378.

[233] K. Mueller, C. Schoenweitz, H.-C. Langowski, *Thin laminate films for barrier packaging application – Influence of down gauging and substrate surface properties on the permeation properties,* Packaging Technology and Science, 2012, **25** (3), p. 137-148.

[234] G. Rochat, Y. Leterrier, P. Fayet, J. A. E. Månson, *Influence of substrate additives on the mechanical properties of ultrathin oxide coatings on poly(ethylene terephthalate),* Surface and Coatings Technology, 2005, **200** (7), p. 2236-2242.

[235] P. Fayet, B. Jaccoud, R. Davis, D. Klein, *Effect of anti-blocking particles on oxygen transmission rate of SiO_x barrier coatings deposited by PECVD on PET films,* 48th Annual Technical Conference Proceedings, Society of Vacuum Coaters, 2005, p. 237-240.

[236] L.-A. O'Hare, S. Leadley, B. Parbhoo, *Surface physicochemistry of corona-discharge-treated polypropylene film,* Surface and Interface Analysis, 2002, **33** (4), p. 335-342.

[237] U. Moosheimer, H.-C. Langowski, A. Melzer, *Permeation of oxygen, water vapor and aroma substances through vacuum web coated film,* 43rd Annual Technical Conference Proceedings, Society of Vacuum Coaters, 2000, p. 385-390.

[238] C. Bichler, T. Kerbstadt, H. C. Langowski, U. Moosheimer, *The substrate–barrier film interface in thin barrier film coating,* Surface and Coatings Technology, 1997, **97** (1–3), p. 299-307.

[239] C. Bichler, M. Bischoff, H.-C. Langowski, U. Moosheimer, *The substrate-process interface in thin barrier film coating,* 39th Annual Technical Conference Proceedings, Society of Vacuum Coaters, 1996, p. 378-383.

[240] H. Low, Y. Xu, *Moisture barrier of Al_xO_y coating on poly(ethylene terephthalate), poly(ethylene naphthalate) and poly(carbonate) substrates,* Applied Surface Science, 2005, **250** (1-4), p. 135-145.

[241] M. Benmalek, H. M. Dunlop, *Inorganic coatings on polymers,* Surface and Coatings Technology, 1995, **76-77** (Part 2), p. 821-826.

[242] R. W. Phillips, *Atomic force microscopy for thin film analysis,* Surface and Coatings Technology, 1994, **68–69** (0), p. 770-775.

[243] S. Süzer, A. Argun, O. Vatansever, O. Aral, *XPS and water contact angle measurements on aged and corona-treated PP,* Journal of Applied Polymer Science, 1999, **74** (7), p. 1846-1850.

[244] M. Vähä-Nissi, E. Kauppi, K. Sahagian, L.-S. Johansson, M. S. Peresin, J. Sievänen, A. Harlin, *Growth of thin Al_2O_3 films on biaxially oriented polymer films by atomic layer deposition,* Thin Solid Films, 2012, **522** (0), p. 50-57.

[245] C. Bichler, T. Kerbstadt, H. C. Langowski, U. Moosheimer, *Plasma-modified interfaces between polypropylene films and vacuum roll-to-roll coated thin barrier layers,* Surface and Coatings Technology, 1999, **112** (1–3), p. 373-378.

[246] H. Bahre, K. Bahroun, H. Behm, S. Steves, P. Awakowicz, M. Böke, C. Hopmann, J. Winter, *Surface pre-treatment for barrier coatings on polyethylene terephthalate,* Journal of Physics D: Applied Physics, 2013, **46** (8), p. 084012.

[247] M. Strobel, C. S. Lyons, *An essay on contact angle measurements,* Plasma Processes and Polymers, 2011, **8** (1), p. 8-13.

[248] R. L. W. Smithson, D. J. McClure, D. Fennell Evans, *Effects of polymer substrate surface energy on nucleation and growth of evaporated gold films,* Thin Solid Films, 1997, **307** (1–2), p. 110-112.

[249] D. J. McClure, C. Struller, H.-C. Langowski, *Evaporated aluminum on polypropylene: Oxide layer thicknesses as a function of oxygen plasma treatment level,* AIMCAL Fall Technical Conference, 2011.

[250] J. M. Strobel, M. Strobel, C. S. Lyons, C. Dunatov, S. J. Perron, *Aging of air-corona-treated polypropylene film,* Journal of Adhesion Science and Technology, 1991, **5** (2), p. 119-130.

[251] R. Wolf, A. C. Sparavigna, *Role of plasma surface treatments on wetting and adhesion,* Engineering, 2010, **2** (6), p. 397-402.

[252] S. Guimond, I. Radu, G. Czeremuszkin, D. J. Carlsson, M. R. Wertheimer, *Biaxially oriented polypropylene (BOPP) surface modification by nitrogen atmospheric pressure glow discharge (APGD) and by air corona,* Plasmas and Polymers, 2002, **7** (1), p. 71-88.

[253] M. Strobel, C. S. Lyons, J. M. Strobel, R. S. Kapaun, *Analysis of air-corona-treated polypropylene and poly(ethylene terephthalate) films by contact-angle measurements and X-ray photoelectron spectroscopy,* Journal of Adhesion Science and Technology, 1992, **6** (4), p. 429-443.

[254] I. Novák, A. Popelka, I. Chodák, J. Sedliačik, *Chapter 9 - Study of adhesion and surface properties of modified polypropylene*, in *Polypropylene*, F. Dogan, ed., 2012, InTech, p. 125-160.

[255] M. L. Kullberg, *Recent Developments in metallized biaxially oriented polypropylene film,* 40th Annual Technical Conference Proceedings, Society of Vacuum Coaters, 1997, p. 400-404.

[256] R. N. Campbell, D. Wolters, *Improved barrier properties with metallized films from corona process improvements and from copolymer characteristics,* Journal of Plastic Film and Sheeting, 2000, **16** (2), p. 108-123.

[257] F. Garbassi, M. Morra, E. Occhiello, *Wettability*, in *Polymer surfaces - From physics to technology*, 1998, John Wiley & Sons, Chichester, p. 317-349.

[258] M. Wolf, J. Breil, R. Lund, *Development of new BOPP barrier films by coextrusion and simultaneous biaxial orientation,* TAPPI PLACE Conference, 2008.

[259] R. M. Podhajny, *Corona treatment of polymeric films,* Journal of Plastic Film and Sheeting, 1988, **4** (3), p. 177-188.

[260] L.-A. O'Hare, J. A. Smith, S. R. Leadley, B. Parbhoo, A. J. Goodwin, J. F. Watts, *Surface physico-chemistry of corona-discharge-treated poly(ethylene terephthalate) film,* Surface and Interface Analysis, 2002, **33** (7), p. 617-625.

[261] M. Morra, E. Occhiello, F. Garbassi, *Knowledge about polymer surfaces from contact angle measurements,* Advances in Colloid and Interface Science, 1990, **32** (1), p. 79-116.

[262] M. Strobel, C. Dunatov, J. M. Strobel, C. S. Lyons, S. J. Perron, C. Morgen, *Low-molecular-weight materials on corona-treated polypropylene,* Journal of Adhesion Science and Technology, 1989, **3** (1), p. 321-335.

[263] M. Zenkiewicz, *Investigation on the oxidation of surface layers of polyolefins treated with corona discharge,* Journal of Adhesion Science and Technology, 2001, **15** (1), p. 63-70.

[264] E. M. Yorkgitis, K. C. Melancon, A. M. Hine, S. M. Giaquinto, *Glaciphobic polymeric materials,* Journal of Adhesion Science and Technology, 2012, **26** (4-5), p. 681-699.

[265] R. Dorai, M. J. Kushner, *A model for plasma modification of polypropylene using atmospheric pressure discharges,* Journal of Physics D: Applied Physics, 2003, **36** (6), p. 666-685.

[266] M. Strobel, V. Jones, C. Lyons, M. Ulsh, M. Kushner, R. Dorai, M. Branch, *A comparison of corona-treated and flame-treated polypropylene films,* Plasmas and Polymers, 2003, **8** (1), p. 61-95.

[267] L. Pauling, *The nature of the chemical bond and the structure of molecules and crystals: An introduction to modern structural chemistry*, 1960, Cornell University Press, Ithaca, NY.

[268] G. Beamson, D. J. Briggs, *High resolution XPS of organic polymers: The Scienta ESCA300 database*, 1992, John Wiley & Sons Ltd., Chichester.

[269] Y. Nakamura, K. Nakamae, *Adhesion between plasma-treated polypropylene films and thin aluminum films,* The Journal of Adhesion, 1996, **59** (1), p. 75 - 86.

[270] J. Friedrich, I. Loeschcke, J. Gähde, *Zur Adhäsion von Aluminium auf Polypropylen,* Acta Polymerica, 1986, **37** (11-12), p. 687-695.

[271] E. Occhiello, M. Morra, G. Morini, F. Garbassi, P. Humphrey, *Oxygen-plasma-treated polypropylene interfaces with air, water, and epoxy resins: Part I. Air and water,* Journal of Applied Polymer Science, 1991, **42** (2), p. 551-559.

[272] F. Garbassi, E. Occhiello, F. Polato, *Surface effect of flame treatments on polypropylene,* Journal of Materials Science, 1987, **22** (1), p. 207-212.

[273] J. F. Friedrich, R. Mix, G. Kühn, *Adhesion of metals to plasma-induced functional groups at polymer surfaces,* Surface and Coatings Technology, 2005, **200** (1–4), p. 565-568.

[274] D. Leonard, P. Bertrand, A. Scheuer, R. Prat, J. Hommet, J. Le Moigne, J. P. Deville, *Time-of-flight SIMS and in-situ XPS study of O2 and O2-N2 post-discharge microwave plasma-modified high-density polyethylene and hexatriacontane surfaces,* Journal of Adhesion Science and Technology, 1996, **10** (11), p. 1165-1197.

[275] D. M. Brewis, D. Briggs, R. H. Dahm, I. Fletcher, *A ToF-SIMS study of electrochemical pretreatments for polymers†,* Surface and Interface Analysis, 2000, **29** (9), p. 572-581.

[276] D. Briggs, D. M. Brewis, R. H. Dahm, I. W. Fletcher, *Analysis of the surface chemistry of oxidized polyethylene: Comparison of XPS and ToF-SIMS,* Surface and Interface Analysis, 2003, **35** (2), p. 156-167.

[277] A. Chilkoti, B. D. Ratner, D. Briggs, *Analysis of polymer surfaces by SIMS: Part 15. Oxygen-functionalized aliphatic homopolymers,* Surface and Interface Analysis, 1992, **18** (8), p. 604-618.

[278] A. S. Duwez, C. Poleunis, P. Bertrand, B. Nysten, *Chemical recognition of antioxidants and UV-light stabilizers at the surface of polypropylene: Atomic force microscopy with chemically modified tips,* Langmuir, 2001, **17** (20), p. 6351-6357.

[279] N. Médard, C. Poleunis, X. V. Eynde, P. Bertrand, *Characterization of additives at polymer surfaces by ToF-SIMS,* Surface and Interface Analysis, 2002, **34** (1), p. 565-569.

[280] F. M. Rugg, J. J. Smith, L. H. Wartman, *Infrared spectrophotometric studies on polyethylene. I. Structure,* Journal of Polymer Science, 1953, **11** (1), p. 1-20.

[281] J. P. Blitz, D. C. McFaddin, *The characterization of short chain branching in polyethylene using fourier transform infrared spectroscopy,* Journal of Applied Polymer Science, 1994, **51** (1), p. 13-20.

[282] H. Hagemann, R. G. Snyder, A. J. Peacock, L. Mandelkern, *Quantitative infrared methods for the measurement of crystallinity and its temperature dependence: Polyethylene,* Macromolecules, 1989, **22** (9), p. 3600-3606.

[283] S. Krimm, C. Y. Liang, G. B. B. M. Sutherland, *Infrared spectra of high polymers. II. Polyethylene,* The Journal of Chemical Physics, 1956, **25** (3), p. 549-562.

[284] G. Bucci, T. Simonazzi, *Contribution to the study of ethylene-propylene copolymers by infrared spectroscopy. Distribution of the monomeric units,* Journal of Polymer Science Part C: Polymer Symposia, 1964, **7** (1), p. 203-212.

[285] G. W. Schael, *Determination of polyolefin film properties from refractive index measurements. II. Birefringence,* Journal of Applied Polymer Science, 1968, **12** (4), p. 903-914.

[286] G. Rochat, Y. Leterrier, P. Fayet, J. A. E. Månson, *Stress controlled gas-barrier oxide coatings on semi-crystalline polymers,* Thin Solid Films, 2005, **484** (1–2), p. 94-99.

[287] M. J. McCann, S. J. Abbott, D. P. Jones, C. A. Bishop, *Heat load variations on web substrates as seen by deposition modelling,* AIMCAL Fall Technical Conference, 2012.

[288] R. W. Phillips, T. Markantes, C. LeGallee, *Evaporated dielectric colorless films on PET an OPP exhibiting high barriers toward moisture and oxygen,* 36th Annual Technical Conference Proceedings, Society of Vacuum Coaters, 1993, p. 293-301.

[289] G. Hoffmann, R. Ludwig, J. Meinel, G. Steiniger, *Transparent barrier coatings by reactive evaporation,* 37th Annual Technical Conference Proceedings, Society of Vacuum Coaters, 1994, p. 155-160.

[290] B. M. Henry, H. E. Assender, A. G. Erlat, C. R. M. Grovenor, G. A. D. Briggs, T. Miyamoto, Y. Tsukahara, *Gas barrier properties of transparent metal oxide coatings on PET film,* 47th Annual Technical Conference Proceedings, Society of Vacuum Coaters, 2004, p. 609-614.

[291] B. M. Henry, F. Dinelli, K. Y. Zhao, A. G. Erlat, C. R. M. Grovenor, A. G. D. Briggs, R. S. Kumar, R. P. Howson, *Characterization of oxide gas barrier films,* 42nd Annual Technical Conference Proceedings, Society of Vacuum Coaters, 1999, p. 403-407.

[292] C. Charton, N. Schiller, M. Fahland, A. Holländer, A. Wedel, K. Noller, *Development of high barrier films on flexible polymer substrates,* Thin Solid Films, 2006, **502** (1–2), p. 99-103.

[293] J. Fahlteich, M. Fahland, N. Schiller, *Permeation barrier properties of oxide layers on polymer film deposited by pulsed magnetron sputtering,* 50th Annual Technical Conference Proceedings, Society of Vacuum Coaters, 2007, p. 723-727.

[294] T. Kobayashi, Y. Itoh, Y. Nakano, E. Hirai, R. Hashimoto, S. Kamikawa, *Reactive vacuum vapor deposition of aluminum oxide thin films by an air-to-air metallizer,* Journal of Vacuum Science & Technology A: Vacuum, Surfaces, and Films, 2006, **24** (4), p. 939-945.

[295] D. J. McClure, N. Copeland, *Evaporated aluminum on polyester: Optical, electrical, and barrier properties as a function of thickness and time (part II),* AIMCAL Fall Technical Conference, 2010.

[296] K. Ohkawa, A. Tsuzuki, K. Yoshikata, *Manufacturing method of barrier-forming film*, 2007, Dai Nippon Printing Co., Ltd., US patent US7192625 B2

[297] H. Naono, M. Hakuman, *Analysis of adsorption isotherms of water vapor for nonporous and porous adsorbents,* Journal of Colloid and Interface Science, 1991, **145** (2), p. 405-412.

[298] I. Nobuhiko, S. Mamoru, A. Naoyuki, M. Takashi, *Manufacture of transparent barrier film*, 1991, Toppan Printin Co. Ltd., Japanese patent JP03108531 A

[299] B. D. Vogt, H. Lee, V. M. Prabhu, D. M. DeLongchamp, E. K. Lin, W. Wu, S. K. Satija, *X-ray and neutron reflectivity measurements of moisture transport through model multilayered barrier films for flexible displays,* Journal of Applied Physics, 2005, **97** (11), p. 114509.

[300] J. C. Bolger, A. S. Michaels, *Molecular structure and electrostatic interactions at polymer-solid interfaces*, in *Interface conversion for polymer coatings*, P. Weiss and G. D. Cheever, eds., 1968, Elsevier, New York - London - Amsterdam, p. 3-60.

[301] M. R. Alexander, G. E. Thompson, G. Beamson, *Characterization of the oxide/hydroxide surface of aluminium using x-ray photoelectron spectroscopy: A procedure for curve fitting the O 1s core level,* Surface and Interface Analysis, 2000, **29** (7), p. 468-477.

[302] H.-C. Langowski, A. Melzer, D. Schubert, *Ultra high barrier layers for technical applications,* 45th Annual Technical Conference Proceedings, Society of Vacuum Coaters, 2002, p. 471-475.

[303] J. T. Felts, *Transparent barrier coatings update: Flexible substrates* Journal of Plastic Film and Sheeting, 1993, **9** (2), p. 139-158.

[304] R. Ludwig, L. Josephson, *Clear barriers and high volume productivity,* TAPPI PLACE Conference, 2006.

[305] *ASTM F392 / F392M - 11 Standard test method for flex durability of flexible barrier materials*, 2011, ASTM International.

[306] M. Komada, T. Oboshi, K. Ichimura, *Novel transparent gas barrier film prepared by PECVD method,* 43rd Annual Technical Conference Proceedings, Society of Vacuum Coaters, 2000, p. 352-356.

[307] S. Yokoyama, K. Iseki, T. Ohya, S. Komeda, Y. Yamada, H. Ishihara, *A new ceramic-coated barrier film by dual element electron beam evaporation,* 42nd Annual Technical Conference Proceedings, Society of Vacuum Coaters, 1999, p. 420-424.

[308] Y. Yamada, K. Iseki, T. Okuyama, T. Ohya, Y. Morihara, *The properties of a new transparent and colorless barrier film,* 38th Annual Technical Conference Proceedings, Society of Vacuum Coaters, 1995, p. 28-31.

[309] T. Ohya, S. Suzuki, M. Yoshimoto, K. Iseki, S. Yokoyama, H. Ishihara, *A ceramic (SiO_2-Al_2O_3 mixture) coated barrier film by electron beam*

evaporation, 43rd Annual Technical Conference Proceedings, Society of Vacuum Coaters, 2000, p. 368-372.

[310] H.-C. Langowski, *Transparent barrier coatings for flexible packagings: Industrial and research activities in Germany,* 39th Annual Technical Conference Proceedings, Society of Vacuum Coaters, 1996, p. 398-401.

[311] A. W. Smith, N. Copeland, D. Gerrard, D. Nicholas, *PECVD of SiO_x barrier films,* 45th Annual Technical Conference Proceedings, Society of Vacuum Coaters, 2002, p. 525-529.

[312] W. Lohwasser, *Large scale electron beam web coating not only for packaging,* 43rd Annual Technical Conference Proceedings, Society of Vacuum Coaters, 2000, p. 362-367.

[313] G. Czeremuszkin, M. Latrèche, M. R. Wertheimer, A. S. da Silva Sobrinho, *Ultrathin silicon-compound barrier coatings for polymeric packaging materials: An industrial perspective,* Plasmas and Polymers, 2001, **6** (1-2), p. 107-120.

[314] Y. Leterrier, B. Singh, J. Bouchet, J. A. E. Månson, G. Rochat, P. Fayet, *Supertough UV-curable silane/silica gas barrier coatings on polymers,* Surface and Coatings Technology, 2009, **203** (22), p. 3398-3404.

[315] C. Bichler, K. Mayer, H.-C. Langowski, U. Moosheimer, *Influence of polymer film surfaces on adhesion and permeation properties of vacuum web coated high barrier films and laminates: Results of a cooperative research project,* 41st Annual Technical Conference Proceedings, Society of Vacuum Coaters, 1998, p. 349-354.

[316] *Tensile testing*, 2nd ed., 2004, ASM International, Materials Park, OH.

[317] Y. Leterrier, *Durability of nanosized oxygen-barrier coatings on polymers,* Progress in Materials Science, 2003, **48** (1), p. 1-55.

[318] J. Andersons, S. Tarasovs, Y. Leterrier, *Evaluation of thin film adhesion to a compliant substrate by the analysis of progressive buckling in the fragmentation test,* Thin Solid Films, 2009, **517** (6), p. 2007-2011.

[319] Y. Leterrier, L. Médico, F. Demarco, J. A. E. Månson, U. Betz, M. F. Escolà, M. Kharrazi Olsson, F. Atamny, *Mechanical integrity of transparent conductive oxide films for flexible polymer-based displays,* Thin Solid Films, 2004, **460** (1–2), p. 156-166.

[320] Y. Leterrier, J.-A. E. Månson, G. Rochat, P. Fayet, *Durability of thin PECVD SiO_x coatings on polymer films,* 41st Annual Technical Conference Proceedings, Society of Vacuum Coaters, 1998, p. 429-433.

[321] Y. Leterrier, J. Andersons, Y. Pitton, J. A. E. Månson, *Adhesion of silicon oxide layers on poly(ethylene terephthalate). II: Effect of coating thickness on adhesive and cohesive strengths,* Journal of Polymer Science Part B: Polymer Physics, 1997, **35** (9), p. 1463-1472.

[322] B. M. Henry, H. Nörenberg, F. Dinelli, C. R. M. Grovenor, G. A. D. Briggs, Y. Tsukahara, T. Miyamoto, *The effect of thermal cycling damage on the permeability and structure of transparent gas barrier films,* Chemical Engineering & Technology, 1999, **22** (12), p. 1010-1011.

[323] S. Iwamori, Y. Gotoh, K. Moorthi, *Silicon oxide gas barrier films deposited by reactive sputtering,* Surface and Coatings Technology, 2003, **166** (1), p. 24-30.

[324] B. Marcato, S. Guerra, M. Vianello, S. Scalia, *Migration of antioxidant additives from various polyolefinic plastics into oleaginous vehicles,* International Journal of Pharmaceutics, 2003, **257** (1-2), p. 217-225.

[325] C. Serré, M. Vayer, R. Erre, C. Ollive, *Morphology of the outermost layer of a compression molded composite based on unsaturated polyester resin,* Journal of Materials Science, 1999, **34** (17), p. 4203-4208.

[326] M.-F. Vallat, J. Schultz, C. Mauzac, M. Jacquin, *Characterization of the surface of bulk-molded compounds,* Polymers for Advanced Technologies, 1999, **10** (4), p. 237-243.

[327] T. Kromminga, G. Van Esche, *Anti-blocking additives*, in *Plastic additives handbook*, H. Zweifel, R. D. Maier and M. Schiller, eds., 2008, Carl Hanser Verlag, Munich, p. 613-628.

[328] J. D. Affinito, M. E. Gross, C. A. Coronado, G. L. Graff, I. N. Greenwell, P. M. Martin, *Polymer-oxide transparent barrier layers,* 39th Annual Technical Conference Proceedings, Society of Vacuum Coaters, 1996, p. 392-397.

[329] J. D. Affinito, S. Eufinger, M. E. Gross, G. L. Graff, P. M. Martin, *PML/oxide/PML barrier layer performance differences arising from use of UV or electron beam polymerization of the PML layers,* Thin Solid Films, 1997, **308–309**, p. 19-25.

[330] H. Y. Nie, N. S. McIntyre, *A simple and effective method of evaluating atomic force microscopy tip performance,* Langmuir, 2001, **17** (2), p. 432-436.

[331] K. L. Westra, A. W. Mitchell, D. J. Thomson, *Tip artifacts in atomic force microscope imaging of thin film surfaces,* Journal of Applied Physics, 1993, **74** (5), p. 3608-3610.

[332] U. Moosheimer, *Plasmavorbehandlung und Beschichtung von Kunststoffolien. Teil 1: Beschichtung von unbehandelten Kunststoffolien,* Materialwissenschaft und Werkstofftechnik, 1998, **29** (6), p. 312-324.

[333] U. Moosheimer, *Plasmavorbehandlung und Beschichtung von Kunststofffolien*, 1997, PhD Thesis, Universität Regensburg, Germany.

[334] G. Garcia-Ayuso, L. Vázquez, J. M. Martínez-Duart, *Atomic force microscopy (AFM) morphological surface characterization of transparent gas barrier coatings on plastic films,* Surface and Coatings Technology, 1996, **80** (1–2), p. 203-206.

[335] A. G. Erlat, B. M. Henry, C. R. M. Grovenor, A. G. D. Briggs, Y. Tsukahara, *Factors affecting water vapor permeation through PET/AlO_xN_y films,* 45th Annual Technical Conference Proceedings, Society of Vacuum Coaters, 2002, p. 503-508.

[336] G. Garcia-Ayuso, R. Salvarezza, J. M. Martínez-Duart, O. Sánchez, L. Vázquez, *Relationship between the microstructure and the water permeability of transparent gas barrier coatings,* Surface and Coatings Technology, 1998, **100–101**, p. 459-462.

[337] T. Kubart, T. Nyberg, S. Berg, *Modelling of low energy ion sputtering from oxide surfaces,* Journal of Physics D: Applied Physics, 2010, **43** (20), p. 205204.

[338] M. P. Seah, *A review of the analysis of surfaces and thin films by AES and XPS,* Vacuum, 1984, **34** (3–4), p. 463-478.

[339] M. Räbisch, S. Straach, M. Neumann, N. Schiller, *Coating a strip-shaped substrate with a transparent barrier layer of aluminum oxide through reactive evaporation of aluminum*, 2000, Fraunhofer-Gesellschaft Zur Foerderung Der Angewandten Forschung e.V., German Patent DE19845268 C1

[340] Y.-C. Kim, H.-H. Park, J. S. Chun, W.-J. Lee, *Compositional and structural analysis of aluminum oxide films prepared by plasma-enhanced chemical vapor deposition,* Thin Solid Films, 1994, **237** (1–2), p. 57-65.

[341] B. G. Segda, M. Jacquet, J. P. Besse, *Elaboration, characterization and dielectric properties study of amorphous alumina thin films deposited by r.f. magnetron sputtering,* Vacuum, 2001, **62** (1), p. 27-38.

[342] R. Cueff, G. Baud, M. Benmalek, J. P. Besse, J. R. Butruille, M. Jacquet, *Alumina coatings on polyethylene terephthalate: Characterisation and X-ray photoelectron spectroscopy study,* Surface and Coatings Technology, 1996, **80** (1-2), p. 96-99.

[343] R. Cueff, G. Baud, J. P. Besse, M. Jacquet, *Study of thin alumina coatings sputtered on polyethylene terephthalate films,* Thin Solid Films, 1995, **266** (2), p. 198-204.

[344] O. Zywitzki, G. Hoetzsch, *Effect of plasma activation on the phase transformations of aluminum oxide,* Surface and Coatings Technology, 1995, **76–77, Part 2** (0), p. 754-762.

[345] O. Zywitzki, K. Goedicke, H. Morgner, *Structure and properties of Al_2O_3 layers deposited by plasma activated electron beam evaporation,* Surface and Coatings Technology, 2002, **151–152** (0), p. 14-20.

[346] C. D. Wagner, *Sensitivity factors for XPS analysis of surface atoms,* Journal of Electron Spectroscopy and Related Phenomena, 1983, **32** (2), p. 99-102.

[347] C. D. Wagner, L. E. Davis, M. V. Zeller, J. A. Taylor, R. H. Raymond, L. H. Gale, *Empirical atomic sensitivity factors for quantitative analysis by electron spectroscopy for chemical analysis,* Surface and Interface Analysis, 1981, **3** (5), p. 211-225.

[348] N. Maiti, A. Biswas, R. B. Tokas, D. Bhattacharyya, S. N. Jha, U. P. Deshpande, U. D. Barve, M. S. Bhatia, A. K. Das, *Effects of oxygen flow rate on microstructure and optical properties of aluminum oxide films deposited by electron beam evaporation technique,* Vacuum, 2010, **85** (2), p. 214-220.

[349] J. F. Moulder, W. F. Stickle, P. E. Sobol, K. D. Bomben, *Handbook of X-ray photoelectron spectroscopy*, J. Chastain and R. C. King Jr., eds., 1995, Physical Electronics Inc., Eden Prairie, MN.

[350] J. S. Yoon, G. F. Potwin, H. J. Doerr, C. V. Deshpanday, R. F. Bunshah, *Fabrication of aluminum oxide films with high deposition rates using the activated reactive evaporation technique,* Surface and Coatings Technology, 1990, **43–44, Part 1** (0), p. 213-222.

[351] C. A. Bishop, *Question re. decline in metal coating surface energy*, 2010: http://www.convertingquarterly.com/blogs/vacuum-web-coating/id/1588/question-re-decline-in-metal-coating-surface-energy.aspx [access: 09.08.2011].

[352] E. M. Mount, *Aluminium layer contamination in wound rolls of metallized films*, 2010: http://www.convertingquarterly.com/blogs/substrate-secrets/id/2190/aluminum-layer-contamination-in-wound-rolls-of-metallized-films.aspx [access: 09.08.2011].

[353] E. M. Mount, *PET film coatings for maintaining the surface energy of the films*, 2011: http://www.convertingquarterly.com/blogs/substrate-secrets/id/2661/pet-film-coatings-for-maintaining-the-surface-energy-of-the-films.aspx [access: 09.08.2011].

[354] J. E. Castle, *The composition of metal surfaces after atmospheric exposure: An historical perspective,* The Journal of Adhesion, 2008, **84** (4), p. 368-388.

[355] J. V. Marra, *Metallized OPP film, surface characteristics and physical properties,* Journal of Plastic Film and Sheeting, 1988, **4** (1), p. 27-34.

[356] G. C. Smith, *Evaluation of a simple correction for the hydrocarbon contamination layer in quantitative surface analysis by XPS,* Journal of Electron Spectroscopy and Related Phenomena, 2005, **148** (1), p. 21-28.

[357] S. Palzer, C. Hiebl, K. Sommer, H. Lechner, *Einfluss der Rauhigkeit einer Feststoffoberfläche auf den Kontaktwinkel,* Chemie Ingenieur Technik, 2001, **73** (8), p. 1032-1038.

[358] D. Quéré, *Wetting and roughness,* Annual Review of Materials Research, 2008, **38**, p. 71-99.

[359] A. Rudawska, E. Jacniacka, *Analysis for determining surface free energy uncertainty by the Owen-Wendt method,* International Journal of Adhesion and Adhesives, 2009, **29** (4), p. 451-457.

[360] G.-S. Park, *Cross-sectional TEM studies of transparent thin multilayers on polymeric substrates utilizing ultramicrotomy,* Surface and Coatings Technology, 1999, **115** (1), p. 52-56.

[361] D. J. Brown, *Aluminized polyester films: Influence of substrate on metal texture,* Thin Solid Films, 1987, **149** (1), p. 105-111.

[362] Y. De Puydt, P. Bertrand, P. Lutgen, *Study of the Al/PET interface in relation with adhesion,* Surface and Interface Analysis, 1988, **12** (9), p. 486-490.

[363] J. Weiss, C. Leppin, W. Mader, U. Salzberger, *Aluminium metallization of polyester and polypropylene films: Properties and transmission electron microscopy microstructure investigations,* Thin Solid Films, 1989, **174, Part 1** (0), p. 155-158.

[364] G. Hoetzsch, O. Zywitzki, H. Sahm, *Structures, properties and applications for PVD Al_2O_3 layers - A comparison of deposition technologies,* 40th Annual Technical Conference Proceedings, Society of Vacuum Coaters, 1997, p. 77-85.

[365] R. F. Bunshah, R. J. Schramm, *Alumina deposition by activated reactive evaporation,* Thin Solid Films, 1977, **40** (0), p. 211-216.

[366] M. C. Tobin, *The infrared spectra of polymers. III. The infrared and Raman spectra of isotactic polypropylene,* The Journal of Physical Chemistry, 1960, **64** (2), p. 216-219.

[367] N. Kang, Y. Z. Xu, J. G. Wu, W. Feng, S. F. Weng, D. F. Xu, *The correlation between crystalline behavior of polyethylene segments and hydrogen bonds among carboxyl groups in ethylene-acrylic acid copolymers,* Physical Chemistry Chemical Physics, 2000, **2** (16), p. 3627-3630.

[368] A. Hagemeyer, H. Hibst, J. Heitz, D. Bauerle, *Improvements of the peel test for adhesion evaluation of thin metallic films on polymeric substrates,* Journal of Adhesion Science and Technology, 1994, **8** (1), p. 29-40.

[369] J. F. Silvain, J. J. Ehrhardt, *An overview on metal/PET adhesion,* Thin Solid Films, 1993, **236** (1–2), p. 230-235.

[370] R. Cueff, G. Baud, M. Benmalek, J. P. Besse, J. R. Butruille, H. M. Dunlop, M. Jacquet, *Characterization and adhesion study of thin alumina coatings sputtered on PET,* Thin Solid Films, 1995, **270** (1-2), p. 230-236.

[371] K. Mayer, U. Moosheimer, *Haftungsmessung dünner Schichten auf Kunststoffen. Beschreibung des Standardverfahrens vom Fraunhofer-Institut für Verfahrenstechnik und Verpackung, IVV,* Coating, 1997, **30** (12), p. 446-450.

[372] U. Moosheimer, A. Melzer, H.-C. Langowski, *European thematic network "Vacuum coating of polymer films for packaging and technical applications",* 44th Annual Technical Conference Proceedings, Society of Vacuum Coaters, 2001, p. 458-463.

[373] T. Miyamae, H. Nozoye, *Poly(ethylene terephthalate) surface and alumina/poly(ethylene terephthalate) interface studied using sum-frequency generation spectroscopy,* Surface Science, 2005, **587** (1–2), p. 142-149.

[374] N. Copeland, R. Astbury, *Evaporated aluminum on polyester: Optical, electrical, and barrier properties as a function of thickness and time (Part I),* AIMCAL Fall Technical Conference, 2010.

[375] D. J. McClure, D. Sowatske, J. Repaal, *Rate of growth of oxide layers on metal films vacuum deposited onto plastic film substrates,* AIMCAL Fall Technical Conference, 2012.

[376] G. Hoffmann, R. Ludwig, G. Steiniger, *Method for coating a sheet with a transparent metal oxide laye*, 1998, Balzers und Leybold Deutschland Holding Aktiengesellschaft, European patent EP0695815 B1

[377] T. Krug, K. Rübsam, A. Meier, G. Steiniger, M. Kano, N. Sasaki, T. Miyamoto, M. Sekiguchi, *Method for treating an oxide layer*, 1997, Balzers und Leybold Deutschland Holding Aktiengesellschaft, Toppan Printing Co., Ltd, European patent EP0555518 B1

[378] C. Misiano, E. Simonetti, *Apparatus for continuous reactive metal deposition in vacuum and its application*, 1998, Ce.Te.V. Centro Tecnologie Del Vuoto, European patent EP0629715 B1

[379] S. Louch, S. Edge, M. Hodgson, K. Luxmore, *Transparent conducting oxides on polymer webs,* 52nd Annual Technical Conference Proceedings, Society of Vacuum Coaters, 2009, p. 746-750.

[380] R. M. Overney, R. Lüthi, H. Haefke, J. Frommer, E. Meyer, H. J. Güntherodt, S. Hild, J. Fuhrmann, *An atomic force microscopy study of corona-treated polypropylene films,* Applied Surface Science, 1993, **64** (3), p. 197-203.

[381] R. Mahlberg, H. E. M. Niemi, F. Denes, R. M. Rowell, *Effect of oxygen and hexamethyldisiloxane plasma on morphology, wettability and adhesion properties of polypropylene and lignocellulosics,* International Journal of Adhesion and Adhesives, 1998, **18** (4), p. 283-297.

[382] F. Leroux, C. Campagne, A. Perwuelz, L. Gengembre, *Polypropylene film chemical and physical modifications by dielectric barrier discharge plasma treatment at atmospheric pressure,* Journal of Colloid and Interface Science, 2008, **328** (2), p. 412-420.

[383] O. D. Greenwood, R. D. Boyd, J. Hopkins, J. P. S. Badyal, *Atmospheric silent discharge versus low-pressure plasma treatment of polyethylene, polypropylene, polyisobutylene, and polystyrene,* Journal of Adhesion Science and Technology, 1995, **9** (3), p. 311-326.

[384] M. Strobel, M. C. Branch, M. Ulsh, R. S. Kapaun, S. Kirk, C. S. Lyons, *Flame surface modification of polypropylene film,* Journal of Adhesion Science and Technology, 1996, **10** (6), p. 515-539.

[385] C. Wang, X. He, *Polypropylene surface modification model in atmospheric pressure dielectric barrier discharge,* Surface and Coatings Technology, 2006, **201** (6), p. 3377-3384.

[386] N.-Y. Cui, N. M. D. Brown, *Modification of the surface properties of a polypropylene (PP) film using an air dielectric barrier discharge plasma,* Applied Surface Science, 2002, **189** (1–2), p. 31-38.

[387] M. Strobel, M. J. Walzak, J. M. Hill, A. Lin, E. Karbashewski, C. S. Lyons, *A comparison of gas-phase methods of modifying polymer surfaces,* Journal of Adhesion Science and Technology, 1995, **9** (3), p. 365-383.

[388] F. Awaja, M. Gilbert, G. Kelly, B. Fox, R. Brynolf, P. J. Pigram, *Surface properties of polypropylene following a novel industrial surface-treatment process,* Surface and Interface Analysis, 2008, **40** (11), p. 1454-1462.

[389] E. Sheng, I. Sutherland, D. M. Brewis, R. J. Heath, *An X-ray photoelectron spectroscopy study of flame treatment of polypropylene,* Applied Surface Science, 1994, **78** (3), p. 249-254.

[390] D. G. Shaw, M. G. Langlois, *Use of vapor deposited acrylate coatings to improve the barrier properties of metallized films,* 37th Annual Technical Conference Proceedings, Society of Vacuum Coaters, 1994, p. 240-244.

[391] B. M. Henry, D. Howells, J. A. Topping, H. E. Assender, C. R. M. Grovenor, L. Marras, *Microstructural and barrier properties of multilayerd films,* 49th Annual Technical Conference Proceedings, Society of Vacuum Coaters, 2006, p. 654-657.

[392] A. Yializis, *High oxygen barrier polypropylene films using transparent acrylate-Al_2O_3 and opaque Al-acrylate coatings* 38th Annual Technical Conference Proceedings, Society of Vacuum Coaters, 1995, p. 95-102.

[393] H.-C. Langowski, *Flexible Materialien mit ultrahohen Barriereeigenschaften (Flexible ultra high barrier materials),* Vakuum in Forschung und Praxis, 2002, **14** (5), p. 297-302.

[394] B. M. Henry, J. A. Topping, A. Searle, H. E. Assender, C. R. M. Grovenor, M. Creatore, M. C. M. van de Sanden, *Barrier properties of transparent multilayer films,* 50th Annual Technical Conference Proceedings, Society of Vacuum Coaters, 2007, p. 700-703.

[395] S. Amberg-Schwab, M. Hoffmann, H. Bader, M. Gessler, *Inorganic-organic polymers with barrier properties for water vapor, oxygen and flavors,* Journal of Sol-Gel Science and Technology, 1998, **13** (1-3), p. 141-146.

[396] J. S. Lewis, M. S. Weaver, *Thin-film permeation-barrier technology for flexible organic light-emitting devices,* IEEE Journal of Selected Topics in Quantum Electronics, 2004, **10** (1), p. 45-57.

[397] S. Ramadas, S. Z. Ma, M. Auch, S. J. Chua, *Nanoparticulate barrier films and gas permeation measurement techniques for thin film solar and display applications,* AIMCAL Fall Technical Conference, 2008.

[398] P. Fayet, G. Rochat, Y. Leterrier, B. Singh, J. Bouchet, J. A. E. Månson, *Polysiloxane super-toughening of silica gas barrier coatings on polymer substrates,* AIMCAL Fall Technical Conference, 2009.

[399] A. S. da Silva Sobrinho, G. Czeremuszkin, M. Latrèche, M. R. Wertheimer, *Defect-permeation correlation for ultrathin transparent barrier coatings on polymers,* Journal of Vacuum Science & Technology A: Vacuum, Surfaces, and Films, 2000, **18** (1), p. 149-157.

[400] M. Deilmann, M. Grabowski, S. Theiß, N. Bibinov, P. Awakowicz, *Permeation mechanisms of pulsed microwave plasma deposited silicon oxide films for food packaging applications,* Journal of Physics D: Applied Physics, 2008, **41** (13), p. 135207.

[401] H. Yasuda, T. Hirotsu, *The effect of glass transition on gas permeabilities,* Journal of Applied Polymer Science, 1977, **21** (1), p. 105-112.

[402] S.-I. Hong, J. M. Krochta, *Oxygen barrier performance of whey-protein-coated plastic films as affected by temperature, relative humidity, base film and protein type,* Journal of Food Engineering, 2006, **77** (3), p. 739-745.

[403] M. Kurek, D. Klepac, M. Ščetar, K. Galić, S. Valić, Y. Liu, W. Yang, *Gas barrier and morphology characteristics of linear low-density polyethylene and two different polypropylene films,* Polymer Bulletin, 2011, **67** (7), p. 1293-1309.

[404] M. Hanika, *Zur Permeation durch aluminiumbedampfte Polypropylen- und Polyethylenterephtalatfolien*, 2004, PhD Thesis, Technische Universität München, Germany.

[405] L. Körner, A. Sonnenfeld, P. R. von Rohr, *Silicon oxide diffusion barrier coatings on polypropylene,* Thin Solid Films, 2010, **518** (17), p. 4840-4846.

[406] B. M. Henry, A. G. Erlat, C. R. M. Grovenor, A. G. D. Briggs, T. Miyamoto, Y. Tsukahara, *Gas permeation studies of metal oxide/polymer composite films,* 45th Annual Technical Conference Proceedings, Society of Vacuum Coaters, 2002, p. 514-518.

[407] T. Matsui, T. Hachisuka, C. Okawara, S. Yoshida, *High gas barrier performance of SiO_x coating multilayer laminate film,* 50th Annual Technical Conference Proceedings, Society of Vacuum Coaters, 2007, p. 719-722.

[408] H.-C. Langowski, U. Moosheimer, *Vacuum web coating of polymers: An update on European collaborative R&D activities,* 42nd Annual Technical Conference Proceedings, Society of Vacuum Coaters, 1999, p. 387-391.

[409] E. M. Mount, *How can metal in metallized films and laminations disappear?,* Converting Quarterly, 2013, **Quarter 1**, p. 15.

[410] E. Finson, J. Felts, *Transparent SiO_2 barrier coatings: Conversion and production status,* 37th Annual Technical Conference Proceedings, Society of Vacuum Coaters, 1994, p. 139-143.

[411] W. Lohwasser, O. Frei, H. Severus, A. Wisard, *Electron-beam oxide coating on plastic films for packaging, development, production and application,* 38th Annual Technical Conference Proceedings, Society of Vacuum Coaters, 1995, p. 40-46.

[412] G. Doyon, A. Clément, S. Ribéreau, G. Morin, *Canadian bag-in-box wine under distribution channel abuse: Material fatigue, flexing simulation and total closure/spout leakage investigation,* Packaging Technology and Science, 2005, **18** (2), p. 97-106.

[413] B. Minnich, *Barrier performance in pouch packaging - Metallized polypropylene vs. aluminum foil barrier,* TAPPI PLACE Conference, 2005.

[414] S. Mrkić, K. Galić, M. Ivanković, *Effect of temperature and mechanical stress on barrier properties of polymeric films used for food packaging,* Journal of Plastic Film and Sheeting, 2007, **23** (3), p. 239-256.

[415] N. Abedin, L. Jopko, *How good is your barrier packaging in the real world?,* TAPPI PLACE Flexible packaging symposium: New technologies, 2013.

[416] D. Chiba, K. Mikami, H. Sakamoto, H. Tsuchiya, *Heat sterilizable gas barrier film deposited on polyamide by plasma-enhanced CVD,* 49th Annual Technical Conference Proceedings, Society of Vacuum Coaters, 2006, p. 613-616.

[417] G. I. Deak, S. C. Jackson, *Mylar polyester films with inorganic glass coatings,* 36th Annual Technical Conference Proceedings, Society of Vacuum Coaters, 1993, p. 318-323.

[418] D. Illsley, *Gas barrier coatings,* Nanotechnology and Food Contact Materials Workshop - 8th June 2010.

[419] N. Peelman, P. Ragaert, B. De Meulenaer, D. Adons, R. Peeters, L. Cardon, F. Van Impe, F. Devlieghere, *Application of bioplastics for food packaging,* Trends in Food Science & Technology, 2013, **32** (2), p. 128-141.

[420] J. Jacobson, M. Keif, X. Rong, J. Singh, K. Vorst, *Flexography printing performance of PLA film,* Journal of Applied Packaging Research, 2009, **3** (2), p. 91-104.

[421] R. Auras, B. Harte, S. Selke, *An overview of polylactides as packaging materials,* Macromolecular Bioscience, 2004, **4** (9), p. 835-864.

[422] M. Jamshidian, E. Arab Tehrany, F. Cleymand, S. Leconte, T. Falher, S. Desobry, *Effects of synthetic phenolic antioxidants on physical, structural, mechanical and barrier properties of poly lactic acid film,* Carbohydrate Polymers, 2012, **87** (2), p. 1763-1773.

[423] M. Jamshidian, E. A. Tehrany, M. Imran, M. J. Akhtar, F. Cleymand, S. Desobry, *Structural, mechanical and barrier properties of active PLA–antioxidant films,* Journal of Food Engineering, 2012, **110** (3), p. 380-389.

[424] T. Hirvikorpi, M. Vähä-Nissi, A. Harlin, J. Marles, V. Miikkulainen, M. Karppinen, *Effect of corona pre-treatment on the performance of gas barrier layers applied by atomic layer deposition onto polymer-coated paperboard,* Applied Surface Science, 2010, **257** (3), p. 736-740.

[425] N. De Geyter, R. Morent, T. Desmet, M. Trentesaux, L. Gengembre, P. Dubruel, C. Leys, E. Payen, *Plasma modification of polylactic acid in a medium pressure DBD,* Surface and Coatings Technology, 2010, **204** (20), p. 3272-3279.

[426] J. Fahlteich, M. Fahland, S. Straach, S. Günther, N. Schiller, *Transparente Barriereschichten auf flexiblen Polymersubstraten,* Vakuum in Forschung und Praxis, 2011, **23** (4), p. 29-37.

[427] T. Hirvikorpi, M. Vähä-Nissi, T. Mustonen, E. Iiskola, M. Karppinen, *Atomic layer deposited aluminum oxide barrier coatings for packaging materials,* Thin Solid Films, 2010, **518** (10), p. 2654-2658.

[428] T. Hirvikorpi, M. Vähä-Nissi, T. Mustonen, A. Harlin, T. Hirvikorpi, M. Vähä-Nissi, T. Mustonen, A. Harlin, E. Iiskola, M. Karppinen, *Thin inorganic barrier coatings for packaging materials,* TAPPI PLACE Conference, 2010.

[429] T. Hirvikorpi, M. Vähä-Nissi, J. Nikkola, A. Harlin, M. Karppinen, *Thin Al_2O_3 barrier coatings onto temperature-sensitive packaging materials by atomic layer deposition,* Surface and Coatings Technology, 2011, **205** (21–22), p. 5088-5092.

[430] T. Hirvikorpi, M. Vähä-Nissi, A. Harlin, M. Karppinen, *Comparison of some coating techniques to fabricate barrier layers on packaging materials,* Thin Solid Films, 2010, **518** (19), p. 5463-5466.

[431] N. Schiller, S. Straach, M. Räbisch, M. Fahland, C. Charton, *Method of vapor-depositing strip-shaped substrates with a transparent barrier layer made of aluminum oxide*, 2009, Fraunhofer Gesellschaft Zur Foerderung Der Angewandten Forschung E.V., US patent US7541070 B2

[432] R. W. Phillips, L. R. Wendt, M. Tan-Johnson, D. W. Todd, C. T. Markantes, *Method for forming barrier film*, 2003, Flex Products, Inc., US patent US6576294 B1

[433] R. W. Phillips, L. R. Wendt, M. Tan-Johnson, D. W. Todd, *Barrier film having high colorless transparency and method*, 1998, Flex Products, Inc., US patent US5792550 A

[434] P. Markiewicz, M. C. Goh, *Simulation of atomic force microscope tip-sample/sample-tip reconstruction,* Journal of Vacuum Science & Technology B: Microelectronics and Nanometer Structures, 1995, **13** (3), p. 1115-1118.

[435] J. P. Luongo, *Infrared study of polypropylene,* Journal of Applied Polymer Science, 1960, **3** (9), p. 302-309.

[436] T. V. Karstang, A. Henriksen, *Infrared spectroscopy and multivariate calibration used in quantitative analysis of additives in high-density polyethylene,* Chemometrics and Intelligent Laboratory Systems, 1992, **14** (1–3), p. 331-339.

[437] E. Richaud, F. Farcas, B. Fayolle, L. Audouin, J. Verdu, *Accelerated ageing of polypropylene stabilized by phenolic antioxidants under high oxygen pressure,* Journal of Applied Polymer Science, 2008, **110** (6), p. 3313-3321.

[438] G. Geertz, R. Brüll, J. Wieser, R. Maria, M. Wenzel, K. Engelsing, J. Wüst, M. Bastian, M. Rudschuck, *Stabiliser diffusion in long-term pressure tested polypropylene pipes analysed by IR microscopy,* Polymer Degradation and Stability, 2009, **94** (7), p. 1092-1102.

[439] R. Spatafore, L. T. Pearson, *Migration and blooming of stabilizing antioxidants in polypropylene,* Polymer Engineering & Science, 1991, **31** (22), p. 1610-1617.

[440] N. C. Billingham, P. Garcia-Trabajo, *Physical chemistry of a phosphite processing stabilizer in polypropylene. Part 1: Solubility,* Polymer Engineering & Science, 2001, **41** (3), p. 417-425.

A APPENDIX

A1 Surface energy calculation

As mentioned and discussed in Chapters 5.6.3.1 and 6.1.3.1, the surface energy determined strongly depends on the calculation approach and test liquids used and, consequently, results originating from different methods should, in general, not be compared. Furthermore, also the surface energies of the test liquids (e.g. diiodomethane), which are needed for the calculation, may vary, depending on the reference data used in the individual publication. Therefore, this chapter examines the effect of two different calculation approaches, Owens-Wendt-Rabel-Kaelble and Wu, as well as the effect of a polar surface energy different from 0 mN/m for the test liquid diiodomethane.

For this investigation, three samples were selected in order to evaluate a broad range of surface energies (the non-treated side of a BOPP film, the corona treated side of a BOPP film and the AlO_x coating on a BOPP film) and the following methods were used to calculate the surface energy:

Owens-Wendt-Rabel-Kaelble, as described in Chapter 5.6.3.1, with three liquids (water, diiodomethane and ethylene glycol)

- (1) using the liquid surface energies stated in *Table 5-6*
- (2) with diiodomethane having a γ^p = 2.3 mN/m and γ^d = 48.5 mN/m [194]
- (3) with diiodomethane having a γ^p = 6.7 mN/m and γ^d = 44.1 mN/m [198]

Owens-Wendt-Rabel-Kaelble with two liquids (water and diiodomethane)

- (4) using the liquid surface energies stated in *Table 5-6*
- (5) with diiodomethane having a γ^p = 2.3 mN/m and γ^d = 48.5 mN/m
- (6) with diiodomethane having a γ^p = 6.7 mN/m and γ^d = 44.1 mN/m

Wu [198] (harmonic mean) with two liquids (water and diiodomethane)

- (7) using the liquid surface energies stated in *Table 5-6*
- (8) with diiodomethane γ^p = 2.3 mN/m and γ^d = 48.5 mN/m
- (9) with diiodomethane γ^p = 6.7 mN/m and γ^d = 44.1 mN/m

For the method according to Wu, only two liquids are used (water and diiodomethane have been suggested by Wu in reference [198]), whilst for the Owens-Wendt-Rabel-Kaelble approach several liquids can be used due to the linear regression applied. In this investigation, the Owens-Wendt-Rabel-Kaelble approach was applied using two liquids (water and diiodomethane) and three liquids (water, diiodomethane and ethylene glycol). The surface energy results for the three

samples investigated are summarised in *Table A-1* (non-treated BOPP), *Table A-2* (corona treated BOPP) and *Table A-3* (AlO_x coated BOPP), with the contact angles measured for each sample stated at the bottom of the corresponding table.

Table A-1: Surface energies determined for non-treated BOPP A (reverse side) using various calculation approaches

Method	Surface energy		
	Polar	Dispersive	Total
	mN/m	mN/m	mN/m
(1)	0.1	30.0	30.1
(2)	0.1	30.6	30.7
(3)	0.0	33.1	33.1
(4)	0.1	30.5	30.6
(5)	0.0	31.4	31.4
(6)	0.0	35.1	35.1
(7)	0.0	32.1	32.1
(8)	1.0	31.2	32.2
(9)	0.6	33.9	34.5

water 104.0° ± 1.1°, diiodomethane 56.7° ± 1.4°, ethylene glycol 72.5° ± 1.0°

As can be seen from examining the results in *Table A-1*, *Table A-2* and *Table A-3*, there are variations present when different techniques, as well as different polar/dispersive surface energy components for diiodomethane, are used. In the case of the non-treated BOPP, the data varies the least (total surface energies between 30.1 and 35.1 mN/m), with the polar surface energies being very similar for all nine calculations applied. It is, nevertheless, observable that within each calculation approach the increase of the polar part of diiodomethane increases the total surface energy calculated.

In the case of the corona treated BOPP, the calculated surface energies vary between 34.7 and 49.0 mN/m, a significantly broader range than for the non-treated BOPP. Furthermore, within each calculation approach, a rise of the polar surface energy fraction of diiodomethane results in an increase of the polar surface energy, a decrease of the dispersive surface energy and, overall, a decrease of the total surface energy calculated. The change of the dispersive surface energy within one calculation approach is around 10 mN/m, whilst the polar component varies a lot less.

Table A-2: Surface energies determined for corona treated BOPP A using various calculation approaches

Method	Surface energy		
	Polar	Dispersive	Total
	mN/m	mN/m	mN/m
(1)	7.7	31.2	38.9
(2)	10.1	25.9	36.0
(3)	11.9	22.8	34.7
(4)	7.6	35.4	43.0
(5)	9.6	29.3	38.9
(6)	11.0	26.0	37.0
(7)	12.6	36.4	49.0
(8)	13.7	31.9	45.6
(9)	15.3	26.5	41.8

water 72.3° ± 1.4°, diiodomethane 47.9° ± 2.9°, ethylene glycol 52.2° ± 0.5°

For the AlO_x coated BOPP, the results are similar to the corona treated BOPP, with total surface energy values distributed over quite a broad range from 50.0 to 63.5 mN/m. Also here, the increase of the polar surface energy fraction of diiodomethane results in an increase of the polar surface energy, a drop of the dispersive surface energy and the overall decrease of the total surface energy (of the coating) for each individual calculation approach. Nevertheless, for both Owens-Wendt-Rabel-Kaelble approaches, the polar surface energy increases by approximately 10 to 15 mN/m, whilst the dispersive surface energy drops by 15 to 20 mN/m (with increasing polar surface energy fraction of diiodomethane). Overall, the Owens-Wendt-Rabel-Kaelble approach using three test liquids yields nearly identical total surface energies despite the changes for diiodomethane, whilst with two liquids, the total surface energy changes from 58.9 mN/m to 52.5 mN/m. The calculation method according to Wu generally gives higher total surface energies than the Owens-Wendt-Rabel-Kaelble approach (for all three samples) and in the case of AlO_x coated BOPP, the total surface energy declines from 63.5 mN/m to 56.1 mN/m for the increasing polar surface energy fraction of diiodomethane. The calculated polar and dispersive surface energies for AlO_x coated BOPP vary to a lesser degree for Wu, in contrast to Owens-Wendt-Rabel-Kaelble.

Table A-3: Surface energies determined for AlO_x coated BOPP B using various calculation approaches

Method	Surface energy		
	Polar	Dispersive	Total
	mN/m	mN/m	mN/m
(1)	22.0	29.4	51.4
(2)	29.9	20.1	50.0
(3)	36.9	13.9	50.8
(4)	21.7	37.2	58.9
(5)	28.3	25.8	54.1
(6)	34.3	18.2	52.5
(7)	25.5	38.0	63.5
(8)	27.2	32.9	60.1
(9)	30.4	25.7	56.1

water 45.9° ± 1.9°, diiodomethane 44.6° ± 1.0°, ethylene glycol 40.2° ± 1.4°

A2 AFM investigation of craters/dimples on plain BOPP A

The defects found on plain BOPP A were further investigated, using cross-sections extracted from the 5 x 5 µm² AFM scans, in order to examine whether the AFM tip will image the craters correctly and is capable of reaching the 'bottom' of the crater-shaped defect. If this is the case, it can be assumed that the depth given by the AFM analysis reflects the true value.

For this investigation, the geometric parameters of the tip are required. The images investigated in the following section were acquired in tapping mode, using a rotated pyramidal-shaped tip with a nominal tip radius of 8 nm (maximum 12 nm). The tip height is between 15 and 20 µm and the angles of the pyramidal-shaped tip are given as follows; front angle: 15° ± 2°, back angle: 25° ± 2°, side angles: 17.5° ± 2°. These values have been taken from the tip specification given by the supplier. As slight variations are possible, the actual tip shape of the specific tip used for a scan is not known and has neither been investigated.

Figure A-1 shows the investigated AFM scan of uncoated BOPP A. Two crater-shaped defects have been chosen in this scan, one with a dimension along the x-axis of approximately 200 nm (y-axis 100 nm) and a smaller defect of roughly 60 nm in width along the x- and y-axis. The cross-sections (horizontal and vertical) for each dimple/crater were acquired so that they run through the deepest part of the defect.

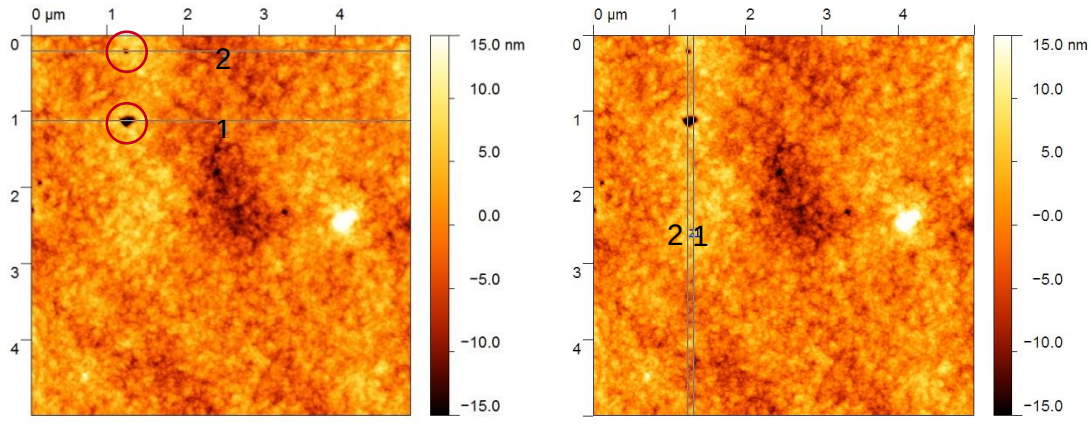

Figure A-1: 5 x 5 µm² AFM scan of uncoated BOPP A showing investigated craters and progression of horizontal (left) and vertical (right) cross-sections

The horizontal cross-sections[I] are illustrated in *Figure A-2*, together with two schematic AFM tips of different tip radius (light blue 10 nm, dark blue 20 nm). The two side angles of 17.5° were used for the tip shape, since the cross-sections run

[I] Note: *Figure A-2* and *Figure A-3* only show the part of the cross-sections that contain the craters.

parallel to the scanning motion. For the vertical cross-sections, which are proceeding perpendicular to the scan direction, the back angle of 25° and front angle of 15° were used to create the tip schematic. The corresponding cross-sections are shown in *Figure A-3*. A tip radius size of 10 nm was chosen since it is the midpoint between the nominal and maximum tip radius (as stated by the manufacturer), whilst a 20 nm tip radius can represent the situation after a tip has been used for several scans and is either contaminated or slightly worn, both resulting in an increased tip radius. The cross-sections (x-, y- and z-axis) and the AFM tip schematics have been scaled appropriately, in order to represent the actual scanning situation and proportions (regarding size) between sample surface and AFM tip.

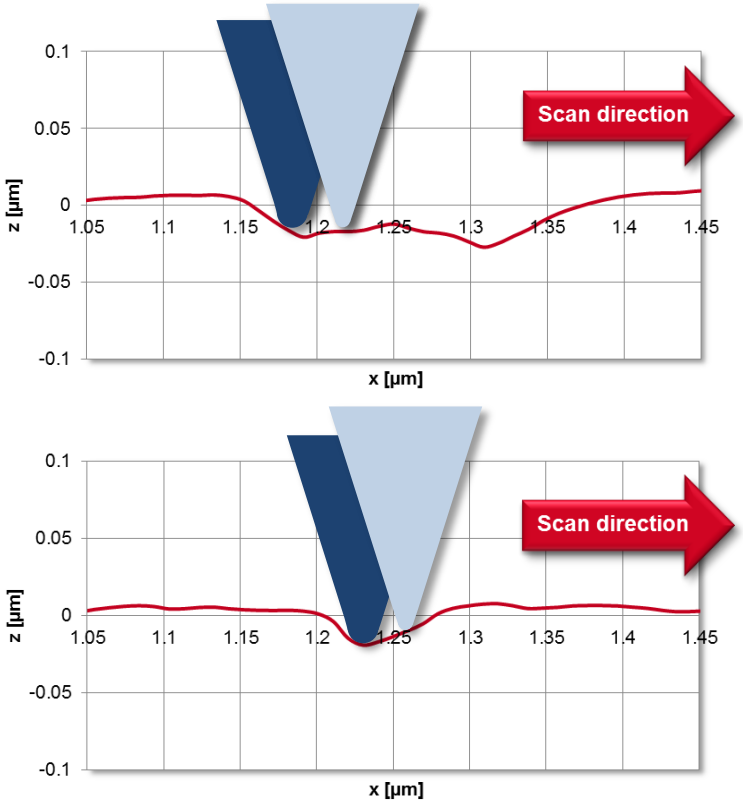

Figure A-2: AFM cross-sections (horizontal) of crater-shaped defects in uncoated BOPP A; top: 200 nm wide defect; bottom: 60 nm wide defect; dark blue AFM tip has 20 nm tip radius; light blue AFM tip has 10 nm tip radius

It can be seen that the 'normal' AFM images (refer to *Figure A-1*), with a vastly different z-range (scale bar in nm), compared to the investigated area (scale in µm), exaggerate the appearance and depth of the craters, in contrast to the scaling shown in *Figure A-2* and *Figure A-3*, whereby the x-, y- and z-axis have the same scale. For the larger size crater (refer to *Figure A-2*, top), it seems that the AFM tip can actually reach the bottom of the crater, as there appears a slightly raised area

within the crater itself. The maximum depth of the crater is approximately 30 nm. Also for the smaller crater (depth approximately 20 nm) depicted in *Figure A-2*, bottom image, it seems plausible that the AFM tip is capable of imaging the defect correctly. The crater would need to be a lot narrower in diameter (dimension along x-axis and y-axis), in order for the AFM tip to get trapped before reaching the crater bottom. It can also be concluded that a change in tip radius would not lead to the crater bottom not being detected, although a larger tip radius will affect the fine detail that can be imaged [330, 331].

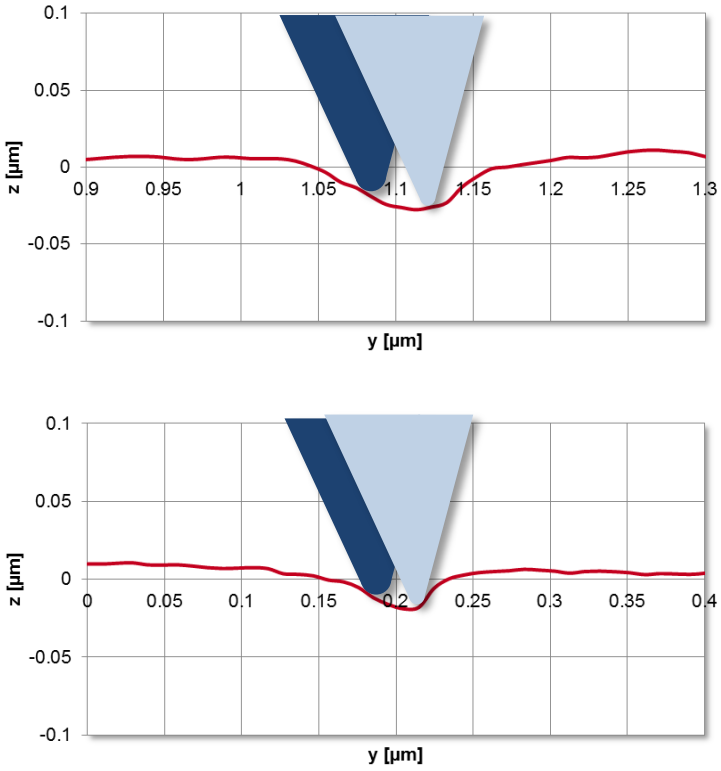

Figure A-3: AFM cross-sections (vertical) of crater-shaped defects in uncoated BOPP A; top: large defect; bottom: small defect; dark blue AFM tip has 20 nm tip radius; light blue AFM tip has 10 nm tip radius

Nevertheless, it can be assumed that the relatively shallow angles of the sides towards the centre of the defect do not represent the reality and that the actual side walls of the craters may be a lot steeper. This is due to the AFM image being a convolution of the sample surface and the tip shape [434], which is an AFM imaging artefact, and is schematically depicted in *Figure A-4*. For the vertical cross-sections (see *Figure A-3*), one can notice that the slope on the left-hand side of the crater is always flatter, compared to the slope on the right-hand side. This can be attributed to the specific shape of the pyramidal tip, with a larger back angle, compared to the front angle, as represented by the tip schematics in *Figure A-3*.

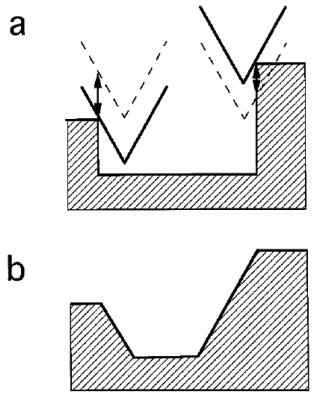

Figure A-4: AFM imaging artefact due to tip geometry; a: actual surface; b: surface as imaged by AFM (reproduced from [434])

Based on the investigations carried out and summarised in this chapter, the conclusion is that the depth of the crater-shaped defect, as obtained via AFM measurements, is very likely to be a true representation. There are, though, imaging artefacts involved when the shape, i.e. sidewalls and their slope, is depicted in the AFM cross-sectional images.

A3 Correlation between wire feed rate and TEM film thickness

In addition to depositing AlO_x coatings with a standard thickness of approximately 10 nm (refer to Section 6.2.5), thicker coatings were deposited in order to investigate the effect of AlO_x coating thickness on barrier properties (refer to Section 6.2.1.4). The thickness is changed via the evaporation rate of aluminium and, hence, depends on the amount of wire fed onto the resistively heated boats. For this investigation, 19 different settings for the wire feed rate were used and selected samples were analysed for AlO_x thickness using TEM cross-sections, in order to establish a correlation between the on-machine parameter of wire feed rate and the off-line parameter of AlO_x thickness. The graph showing this correlation is depicted in *Figure A-5*. Additionally, a 2nd order polynomial trend line is fitted, which gave a coefficient of determination of 1.

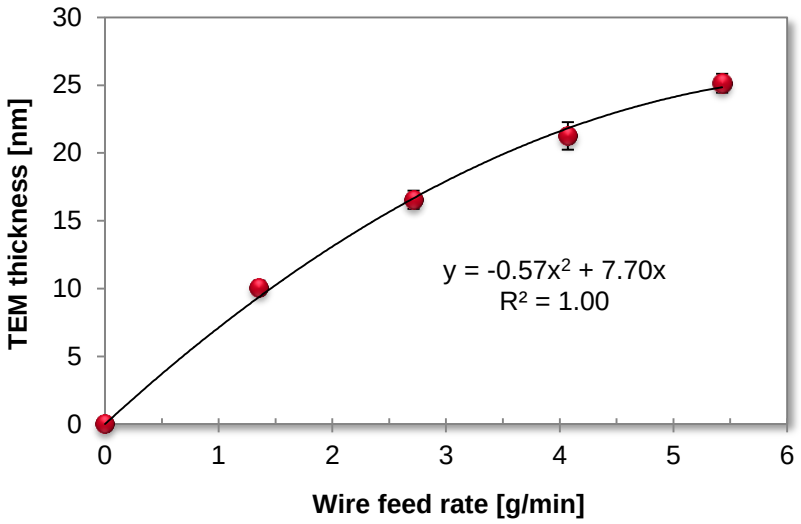

Figure A-5: Correlation between the on-machine parameter of wire feed rate and the off-line determined AlO_x coating thickness

As can be seen from *Figure A-5*, the correlation between wire feed rate and AlO_x thickness is not linear, as one would have expected. It can be noticed that with increasing the amount of aluminium evaporated, the slope of the graph starts to decrease. Nevertheless, with increasing the amount of aluminium evaporated, also the amount of oxygen added to produce AlO_x is increased. This resulted in an increase of the pressure during deposition (by a factor of approximately four when comparing the 'standard' AlO_x with the thickest AlO_x produced), as not all additional oxygen was gettered by the aluminium (i.e. incorporated into the coating) or pumped away. With the higher pressure, the mean free path is reduced and, hence, more scattering (collision of the evaporated aluminium and oxygen) takes place. This, in turn, will result in less aluminium reaching the substrate and, therefore, will affect the

coating thickness. Due to the increased evaporation rate of aluminium at higher AlO_x thickness, there may also be more aluminium lost to surfaces near the web and source, which also entails a reduction of collection efficiency.

Kobayashi and co-workers [294], who deposited AlO_x coatings of various transparencies/stoichiometries using reactive evaporation of aluminium (via induction heating), mention that the AlO_x thickness was reduced when the oxygen supply was increased. Nevertheless, it is not specified in their publication, whether/how the pressure changed with growing oxygen supply, but just a range of 9 to 12 x 10^{-2} Pa is given for the pressure during AlO_x deposition. They, furthermore, propose that with rising oxygen flow, the aluminium surface (i.e. of the aluminium pool in the crucible/boat) becomes increasingly oxidised, which causes a drop of the aluminium evaporation rate, due to a lower vapour pressure of the oxide, in comparison to the metal. Finally, also Yoon et al. [350] state that during plasma activated reactive electron beam evaporation of aluminium, the deposition rate decreases with rising oxygen pressure. They observed that the pool of molten aluminium decreased in its surface area at higher oxygen pressure, which led to less aluminium being evaporated. Furthermore, they (and also Kobayashi et al. [294]) state that the increased collision of aluminium atoms and oxygen molecules additionally reduces the arrival rate at the substrate.

A4 Soxhlet extraction of BOPP films and analysis of extracts

Based on the surface energy data obtained in Chapter 6.2.4, which showed differences in the time related surface energy decay for the various investigated AlO_x coated BOPP films, BOPP A, B and C were further examined using a Soxhlet extraction apparatus. The aim was to extract any material from the uncoated film that may have the capability of migrating or transferring onto the AlO_x layer and, hence, may cause the drop of its surface energy with storage time. Since it is assumed that the AlO_x surface energy decay is due to the transfer or migration of mobile polymeric material, i.e. material of predominantly nonpolar nature, a nonpolar solvent (n-hexane) was chosen for the extraction. Approximately 4 g of film (individual sheets wound up to a small roll; placed in extraction thimbles) were extracted for 26 hours under reflux at approximately 70 °C with roughly 125 ml of n-hexane. The amount of extract was determined from the solvent residue after evaporating the n-hexane off under reduced pressure (1), as well as from the weight difference pre- and post-extraction of the film sample (2). Per film type, five samples were extracted in parallel and the relative amounts of extractables for each film type are summarised in *Table A-4*. It is observable that both ways of determination yielded nearly identical results for the amount of extractables.

Table A-4: Relative amount of n-hexane extractables of various BOPP films

Film	Extractables	
	(1)	(2)
	%	%
BOPP A	1.82 ± 0.09	1.73 ± 0.16
BOPP B	2.44 ± 0.14	2.47 ± 0.10
BOPP C	2.56 ± 0.10	2.59 ± 0.10

From *Table A-4* it is clear that BOPP B and BOPP C appear to contain a larger amount of extractables, compared to BOPP A. However, based on the surface energy of the AlO_x coated films (refer to *Figure 6-39*, Chapter 6.2.4), one would expect a higher amount for BOPP A, as for this film the AlO_x surface energy was significantly lower than for the other two films. Consequently, with respect to the total amount of extractables, the extraction results would not agree with the surface energy data presented in Chapter 6.2.4. Nevertheless, it may not be the total amount of extractables that is of importance (since it is unknown whether all the extracted material will actually migrate), but rather its chemical composition and molecular weight distribution (more accurately: molar mass distribution). Therefore,

the extracts were further investigated using FTIR spectroscopy and gel permeation chromatography (GPC). FTIR spectra of the extracts of BOPP B and C are shown in *Figure A-6*, where they have been shifted along the y-axis in order to underline differences. Additionally, the wavenumber regions of interest (3645, 1744, 1492 and 1082 cm^{-1}) are marked with vertical lines. No spectrum for BOPP A is shown as it revealed identical features to BOPP B. For reference purposes, the spectrum of an atactic PP sample and the spectrum of a BOPP film are displayed.

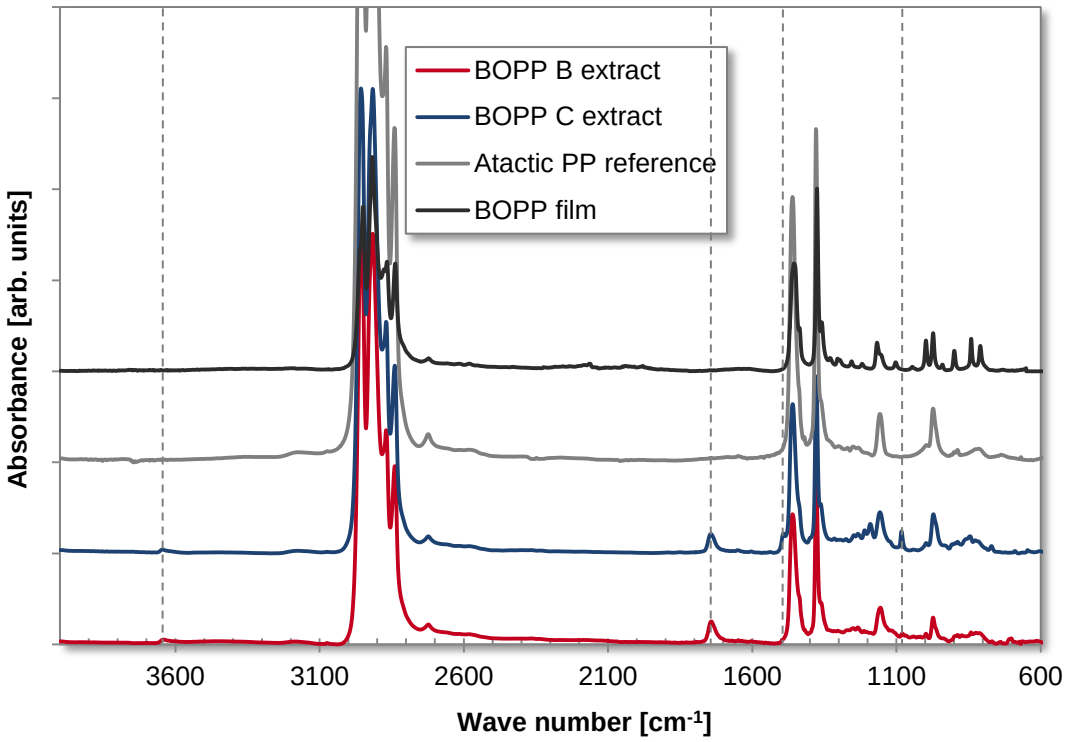

Figure A-6: FTIR spectra of n-hexane extracts of BOPP B and C (including reference spectra of atactic PP and BOPP film)

All extract spectra predominantly show atactic polypropylene, as can be seen distinctively from the region between 1000 cm^{-1} to 800 cm^{-1}, where the characteristic peak splitting (due to crystallinity, see also spectrum of BOPP film in *Figure A-6*) for isotactic PP is missing [435]. Additionally, this was also determined via a reference sample of atactic PP (obtained from Sigma Aldrich). There are, nevertheless, additional bands visible, around 3645 cm^{-1} (weak band for all extracts), 1744 cm^{-1} (relatively strong band for all extracts), 1492 cm^{-1} (band for BOPP C only) and 1082 cm^{-1} (stronger band for BOPP C extract, very weak and slightly shifted bands for BOPP A and B extracts). The former two peaks are assigned to the O-H and C=O stretching bands and presumably originate from the phenolic hydroxyl group and the ester group of the antioxidant Irganox 1010 [436-438], an additive frequently

used to stabilise PP. The latter band at around 1082 cm^{-1} is attributed the antioxidant Irgafos 168 [439, 440]. Billingham and Garcia-Trabajo [440] state that this stabiliser exhibits several absorption bands, with a peak (in their case) at 1083 cm^{-1}, assigned to the O-aryl vibration [436], being the most clearly defined. Furthermore, they mention additional characteristic bands at 1213, 1196, 854 and 776 cm^{-1}, which are resolvable from a spectrum of PP containing Irgafos 168. Spatafore and Pearson [439] also discuss absorption bands at 1194, 1084 and 851 cm^{-1} for Irgafos 168. They, additionally, mention peaks at 1364 and 1493 cm^{-1}, which are sharp bands for the antioxidant in its solid crystalline state. In the investigation carried out for this thesis, the extract of BOPP C revealed distinct peaks at 1492, 1210, 1190, 1082 and 770 cm^{-1} and a peak/shoulder at 857 cm^{-1} (apart from the peaks at 1492 and 1082 cm^{-1}, absorption bands are not observable in the survey spectrum of *Figure A-6*, but shown in the high-resolution spectrum in *Figure A-7*). These are very close to the bands mentioned in the latter two references. Hence, it is assumed that the extract of BOPP C very likely contains Irgafos 168. For the extracts of BOPP A and B, only a few of the absorption bands mentioned above could be found, which were, however, rather weak and at slightly shifted wave numbers, compared to BOPP C.

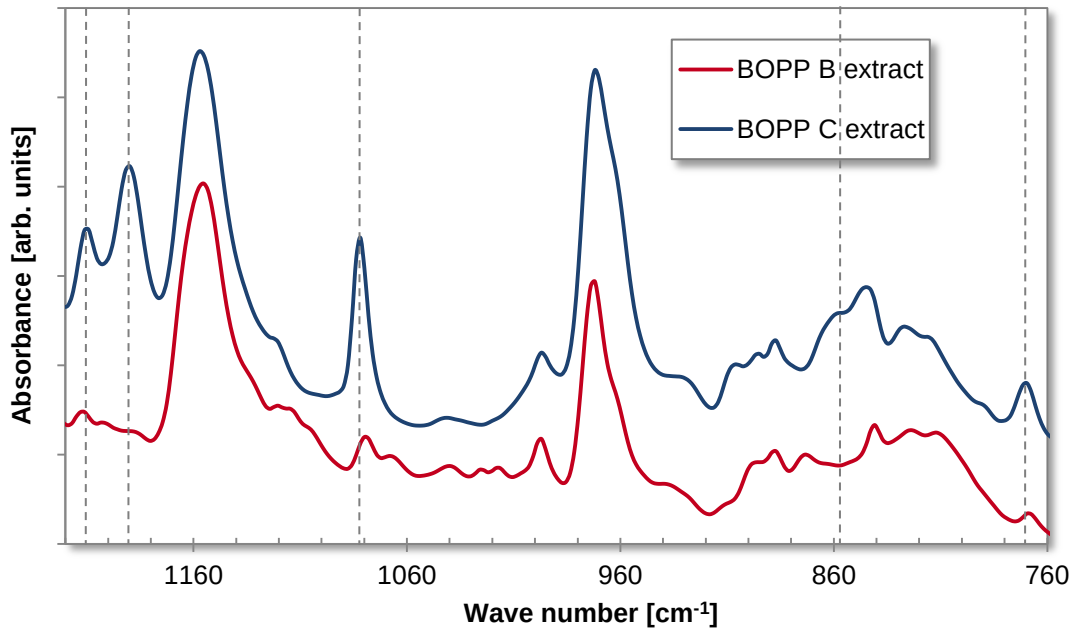

Figure A-7: High-resolution FTIR spectra of n-hexane extracts of BOPP B and C

As stated before, GPC was additionally carried out with the extracts of the three films. Therefore, approximately 6 mg/ml of the dried extracts were re-dissolved in trichlorobenzene (at 110 °C) and analysed using a high temperature GPC (Viscotek HT-GPC Module 350A) with multiple detectors (refractive index detector, low and

right angle light scattering detector). The column train consisted of two PLgel columns, which are based on a highly cross-linked polystyrene/divinylbenzene matrix of porous copolymer beads (here 10 µm particles). The GPC was performed at 160 °C with trichlorobenzene as eluent at a flow rate of 1 ml/min and was calibrated with a polystyrene standard of narrow molecular weight distribution. Two samples per extract were run and yielded comparable results.

The molecular weight distributions of the three extracts, as obtained via the GPC, are illustrated in *Figure A-8*.

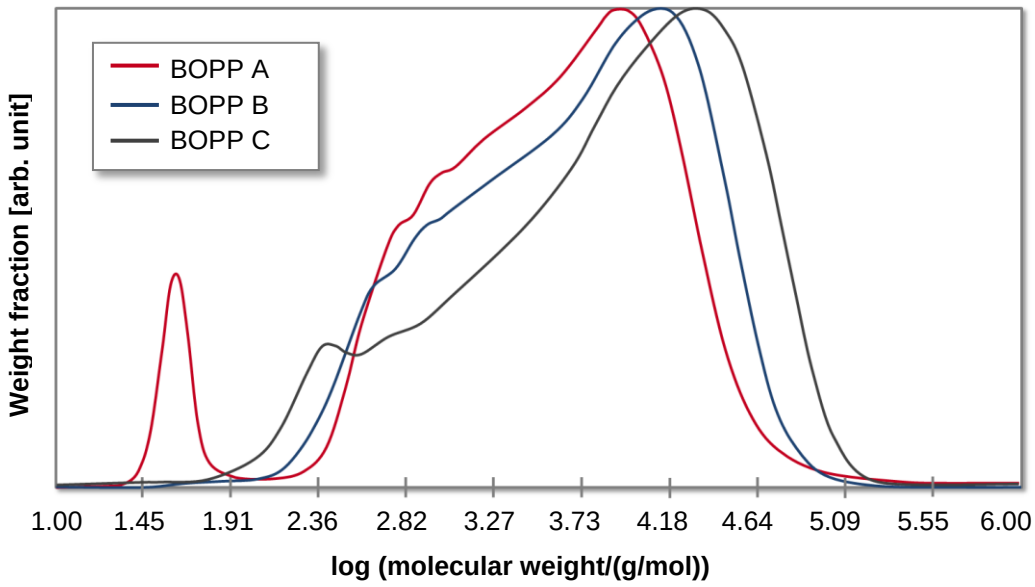

Figure A-8: Molecular weight distribution of n-hexane extracts obtained via GPC

From *Figure A-8*, it is highly evident that the extract of BOPP A reveals a clear peak corresponding to a low-molecular-weight fraction, which is not present in the other extracts. The extract of BOPP C exhibits a shoulder/hump in its molecular weight distribution also indicating low-molecular-weight material; nevertheless, of a higher molecular weight than the component found for BOPP A. BOPP B shows a distribution similar to BOPP A, but with the low-molecular-weight material missing. The low-molecular-weight materials could be caused by the additive package and possible additive fragments (e.g. from Irganox 1010). Overall, the GPC results are in very good agreement with the AlO_x surface energy data of Chapter 6.2.4. AlO_x coated BOPP B revealed the highest surface energy, closely followed by BOPP C, whilst AlO_x coated BOPP A showed the lowest surface energy level. This could be caused by the fact that BOPP A contains a low-molecular-weight component that may migrate easily and, hence, may contribute to the AlO_x surface energy decay. Furthermore, BOPP C also shows a low-molecular-weight fraction (with a higher

molecular weight than the component in BOPP A) and, consequently, the surface energy of AlO_x coated BOPP C is also lower than measured for BOPP B, but higher than for BOPP A.

It has to be mentioned here that the GPC column used had a specified molecular weight range from 500 to 10000000 g/mol, which means that the low-molecular-weight fractions found for BOPP A and C are not within the specification of the column. Nevertheless, as replicates were run, which revealed comparable results and always indicated the presence of low-molecular-weight material, it is assumed that these fractions are present, but that their molecular weight, as determined by the GPC analysis, may not be accurate.

In addition to GPC, the sample extracts were further analysed using liquid chromatography-mass spectrometry (LC-MS). An Agilent 6540 Q-TOF LC-MS using positive ionisation (electrospray ionisation source) and a mass range of 30 to 1000 Da was applied. The eluent used was acetonitrile with 0.1 % formic acid, which was run through a loop, i.e. no column was utilised. For each film type, two extracts were analysed using this technique. In the case of BOPP B and C, no low-molecular-weight fractions could be detected, whilst for BOPP A, one sample revealed low-molecular-weight material with the most intense peak for an m/z ratio of 182 (followed by further peaks of lower intensity at m/z 170 and 152). Attempts were made to elucidate the structure of the molecular ions, but none of the structures matched probable ion fragments of the possible film ingredients, such as antioxidants, acid scavengers or polymer fractions.

A5 Publications and conference presentations

Peer reviewed publications:

1. C. F. Struller, P. J. Kelly, N. J. Copeland, C. M. Liauw, *Characterization studies of aluminum oxide barrier coatings on polymeric substrates,* Journal of Vacuum Science & Technology A, 2012, **30** (4), p. 041502.
2. C. F. Struller, P. J. Kelly, N. J. Copeland, *Aluminum oxide barrier coatings on polymer films for food packaging applications,* Surface and Coatings Technology, 2013, **in press**
3. C. F. Struller, P. J. Kelly, N. J. Copeland, V. Tobin, H. E. Assender, C. W. Holliday, S. J. Read, *Aluminium oxide barrier films on polymeric web and their conversion for packaging applications*, Thin Solid Films, 2013, **in press**

Characterization studies of aluminum oxide barrier coatings on polymeric substrates

Carolin F. Struller and Peter J. Kelly[a)]
Surface Engineering Group, John Dalton Building, Manchester Metropolitan University, Manchester, M1 5GD, United Kingdom

Nick J. Copeland
General Vacuum Equipment Ltd., Pilsworth Road, Heywood, Lancashire OL10 2TL, United Kingdom

Christopher M. Liauw
School of Engineering, John Dalton Building, Manchester Metropolitan University, Manchester, M1 5GD, United Kingdom

(Received 9 November 2011; accepted 14 April 2012; published 27 April 2012)

Aluminum coatings are widely used as oxygen and water barrier layers on food packaging materials to protect the product from contamination and to extend its shelf life. Thin layers of aluminum, of the order of a few tens of nanometers, are thermally evaporated onto polymeric web in high speed roll-to-roll vacuum metallizers. More recently, transparent barrier layers, based on silica or aluminum oxide, have been introduced to allow product visibility and provide retortable, sterilizable, or microwaveable packaging. In all cases, though, the barrier characteristics are critically dependent on both the structure and properties of the coating and the nature and surface properties of the polymer film substrate. This paper, therefore, reports on characterization trials of aluminum oxide (AlO_x) coatings deposited onto polyethylene terephthalate (PET) and biaxially oriented polypropylene (BOPP) film substrates. Coating structures and properties have been investigated by scanning electron microscopy and atomic force microscopy; the influence of process parameters on barrier levels has been determined; surface energies have been determined through contact angle measurements; and coating-to-substrate adhesion has been assessed using "pull-off" tests. The main findings of this study are that the barrier performance of AlO_x coated PET and BOPP films strongly depends on the surface properties of the plain film and the aluminum oxide film growth. While AlO_x coated PET films deliver consistent barrier results, BOPP reveals considerable variations, depending on the individual substrate. © *2012 American Vacuum Society.* [http://dx.doi.org/10.1116/1.4709451]

I. INTRODUCTION

Thermal evaporation of thin aluminum layers onto commodity polymer films via roll-to-roll vacuum web coating represents a common technique in the field of food packaging materials and other applications. In regards to food stuffs, the packaging material needs to meet very high standards in order to be able to preserve the food products and ensure a long shelf life. Thus, barrier properties against water vapor, oxygen, and also aromas are key properties for successful food packaging. Transparent barrier coatings on polymer films not only provide a barrier against moisture and oxygen, but also offer further advantages, such as product visibility and microwaveability. Traditionally, the clear barrier flexible packaging market is held by products such as ethylene vinyl alcohol copolymer (EVOH) or polyvinyl alcohol (PVOH) coextruded barrier layer films and polyvinylidene chloride (PVdC) atmospheric coated polymer films. However, EVOH, and to a larger extent PVOH, are moisture sensitive and lose their barrier at high humidity,[1] while PVdC coated polymer films have fallen into disrepute due to the possible release of dioxins upon incineration.[2] In the last decades, a development toward the production of transparent ceramic barrier layers, i.e., aluminum oxide (referred to here as AlO_x as the stoichiometry is not confirmed), using standard "boat-type" roll-to-roll vacuum web coaters with high throughput has taken place.[3–8] Therefore, the standard aluminum metallization process is modified by the injection of oxygen into the aluminum vapor cloud; thus resulting in the deposition of a transparent aluminum oxide layer. Adapting a standard aluminum vacuum web coater for the deposition of transparent AlO_x coatings has been an aspiration for many years. A modification of this well established process will give the unique possibility of using standard high speed coating equipment for the production of transparent barrier films at low cost. Nevertheless, optimization and development leading to a commercially viable and fully productionized process is far from straightforward.

While the barrier levels obtained on polyethylene terephthalate (PET) with reactively evaporated aluminum oxide readily fulfill the requirements for food packaging applications, biaxially oriented polypropylene (BOPP) films, which offer cost advantages over PET, have proven to be a more difficult base material. The barrier properties of aluminum oxide coated BOPP greatly depend on the plain film surface and the growth conditions for the depositing film, which both can vary to a large extent. In this investigation, aluminum oxide coated BOPP and PET films were characterized

a)Electronic mail: peter.kelly@mmu.ac.uk

regarding their barrier properties, coating adhesion, surface topography, and surface energy.

II. EXPERIMENTAL SETUP AND METHODOLOGY

A. Materials, coating process, and plasma treatment

Standard packaging grade BOPP and PET base films from various suppliers have been coated using a General Vacuum Equipment (GVE) K4000 vacuum metallizer (with an AlO_x coating system installed). The standard packaging grade BOPP films comprise a three layer structure with a polypropylene homopolymer core and co- or ter-polymer skin layers. The PET film, by contrast, only consists of a single layer. In addition to the polymer, the films contain various additives in order to confer stabilization and optimize processing and end-use properties. The individual film formulations, however, are commercially sensitive information and therefore not disclosed by the manufacturer. Furthermore, the authors have not attempted to conduct their own analysis of the base films. The K4000 roll-to-roll metallizer can handle webs up to 2450 mm wide, but for these experiments the BOPP films had web widths between 1000 and 1250 mm, while the PET film used was 1650 mm wide. The specimens analyzed were taken from the center section of each web. The vacuum metallizer uses resistively heated evaporation boats onto which aluminum wire is continuously fed. Additionally, oxygen is introduced into the aluminum vapor in order to deposit a transparent oxide. The pressure in the evaporation chamber during deposition is of the order of 0.1 Pa. All films were coated at a web speed of 420 m/min under the same deposition conditions and a control loop, which constantly monitored the optical properties of the coated polymer film, was used to achieve reliable and consistent coating performance. Thus, the AlO_x deposition process was the same in each case in terms of coating stoichiometry and thickness. Additionally, various in-line plasma pre- and post-treatments with different gases (Ar, O_2, N_2; details given in Table I) were also conducted using a plasma source with magnetically enhanced water cooled electrodes. In order to minimize any unintentional sputtering from these sources, the pressure at the plasma treatment units was kept between 2 and 4 Pa.

TABLE I. Barrier properties of plain and AlO_x coated BOPP and PET films, all samples produced under the same deposition conditions apart from the plasma treatment variations listed.

AlO_x coated film	Plasma treatment	OTR ($cm^3/(m^2$ days))	WVTR ($g/(m^2$ days))
BOPP A	Ar/O_2 pre	224.39 ± 34.83	3.98 ± 0.40
	N_2/O_2 pre	183.85 ± 1.98	3.09 ± 0.22
	O_2 pre + O_2 post	249.47 ± 36.35	4.00 ± 0.13
BOPP B	—	47.00 ± 5.35	5.89 ± 0.23
	N_2/O_2 pre	35.33 ± 3.05	6.08 ± 0.17
	N_2/O_2 pre + O_2 post	26.06 ± 1.03	4.73 ± 0.07
BOPP C	O_2 pre + O_2 post	63.28 ± 9.67	4.46 ± 1.06
PET	Ar/O_2 pre + Ar/O_2 post	0.54 ± 0.05	0.80 ± 0.04
Plain film	Thickness (μm)	OTR ($cm^3/(m^2$ days))	WVTR ($g/(m^2$ days))
BOPP A	30	1600	4
BOPP B	20	2400	6
BOPP C	20	2600	6
PET	12	100	45

B. Analytical methods

Oxygen and water vapor transmission rates (OTR/WVTR) of the aluminum oxide coated and plain films were analyzed according to ASTM F 1927 and F 1249 using a Mocon Oxtran 2/20 and a Mocon Permatran-W 33/3 permeation instrument, respectively. Test conditions for OTR were 23 °C and 50% relative humidity (RH), while WVTR is stated for 38 °C and a gradient of 90% RH. The tested sample area was 50 cm^2 for OTR and WVTR measurements. In the case of OTR values greater than 100 $cm^3/(m^2$ days) and WVTR greater than 10 $g/(m^2$ days), the samples were masked with aluminum foil to a 5 cm^2 permeation area.

A Zeiss Supra 40VP field emission gun scanning electron microscope (SEM) was used to obtain images of the plain film and aluminum oxide coated surfaces. Coatings were examined with a 0.5 kV acceleration voltage and without applying any conductive layer to avoid masking surface detail.

The plain film and coating surfaces were additionally analyzed with a WiTec alpha500 atomic force microscope (AFM). Pulsed force mode was used to acquire roughness data and topography images. Images were corrected by linewise leveling.

Measurement of coating adhesion was performed using a peel test as described in Refs. 9 and 10. For this industrial based test, which is normally applied to assess the adhesion of aluminum metallized films, an ethylene acrylic acid (EAA) film is bonded to the coated surface of the polymer film (sealing at 105 °C, 4 bar, 20 s). After conditioning, the EAA/coating is peeled-off with a constant speed of 50 mm/min at a peel-off angle of 180° using a Mecmesin VersaTest tensile tester. (This peel test procedure is also available at the European Metallizers Association, The Hague, The Netherlands.) Infrared spectra were recorded with a Thermo Scientific Nicolet 380 Fourier transform infrared (FTIR) spectrometer using a single bounce diamond attenuated total reflectance (ATR) accessory.

The change of coating surface energy as a function of time was investigated by means of contact angle measurement via the sessile drop method. A Krüss MobileDrop contact angle measuring system was used. Based on the measured contact angles of three test fluids (water, diiodomethane, and ethylene glycol), the surface energies were calculated according to the Owens–Wendt–Rabel–Kaelble approach.[11–13] Sample swatches were stored under ambient conditions and analyzed periodically over time.

III. RESULTS AND DISCUSSION

A. Barrier performance

In Table I barrier results for the different BOPP films and several plasma treatment variations are displayed. For

comparison, Table I also contains barrier levels obtained on standard grade PET film and the plain film barrier performance. As can be seen, the OTR and WVTR measured for AlO_x coated PET are both below 1 $cm^3/(m^2$ days) and 1 $g/(m^2$ days), respectively. With the GVE AlO_x system, values around 1 $cm^3/(m^2$ days) and 1 $g/(m^2$ days) are achieved on standard packaging grade PET film independently of the plasma treatment applied and without the need for sophisticated and expensive plasma densification processes. However, for the AlO_x coated BOPP films, the barrier performance strongly depends on the base material itself. For example, the barrier results obtained for BOPP A, shown in Table I, were fairly inconsistent and none of the trials performed resulted in a clear improvement of the oxygen barrier down to levels below 100 $cm^3/(m^2$ days), i.e., comparable to aluminum metallized BOPP. On BOPP B, by contrast, very good oxygen barrier performance was obtained with an average OTR of 26.06 ± 1.03 $cm^3/(m^2$ days) for plasma pre- and post- treated samples. These values clearly reveal an improvement in barrier levels through the additional application of plasma pre- and post-treatment. Pretreatment improves barrier by chemical modification of the plain film surface; thus improving coating film growth. The bombardment of the coating during post-treatment can result in a densification of the outermost atomic layers of the coating, which may protect the AlO_x layer and reduce oxygen permeation. AlO_x coated BOPP C also exhibited oxygen barrier levels comparable to metallized BOPP, however, not to the level achieved for BOPP B. These results show that whether a good barrier performance on BOPP is obtained or not is very much film dependent, which clearly makes this a film and not a process related issue. Possible reasons for the barrier differences between BOPP films A and B will be discussed Sec. III B with the results of the SEM and AFM investigations. Despite the good oxygen barrier obtained for BOPP film type B, the moisture barrier achieved was not comparable to metallized BOPP, i.e., the barrier improvement factor was negligible. This fact confirms that oxygen and moisture permeation through inorganic barrier layers are based on different mechanisms. However, plain BOPP film already has an inherently good water barrier.

As the AlO_x coated polymer films will be in a multilayer structure (laminate) in their final packaging application, it is important that these barrier layers can endure further downstream processing, such as laminating, printing, or slitting. Therefore, the retention of barrier properties on being subjected to straining action was investigated (test for stretch durability/resistance as suggested by Felts[14]). The AlO_x coated polymer films were subjected to a certain strain between 0.5% and 5% with a Hounsfield H10KS tensile tester, relaxed and then measured for barrier. Results are shown in Fig. 1 for AlO_x coated PET and in Fig. 2 for AlO_x coated BOPP B. For PET, these investigations clearly show that WVTR starts to deteriorate at an earlier strain level than OTR. Furthermore, the shape of the two curves is completely different. While WVTR starts increasing between 1% and 1.5% strain with a decreasing slope, OTR starts to deteriorate slowly between 3% and 4% strain and then increases

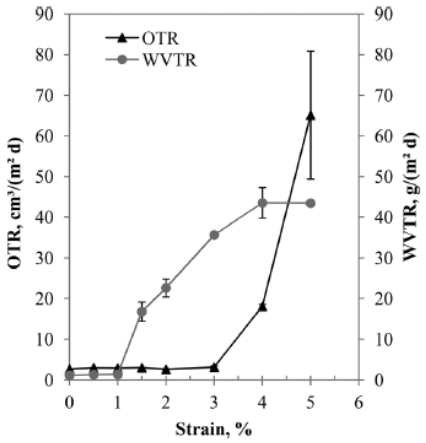

FIG. 1. Variation in oxygen and water vapor transmission rate with applied strain for AlO_x coated 12 μm PET (measured after strain was released).

rapidly. As the elastic limit of the PET film has been determined to be about 1%, the results indicate that WVTR is affected when plastic deformation of the polymer takes place. The WVTR behavior shown for AlO_x coated PET is in good agreement with results shown by Schiller *et al.*[15] Their reactively evaporated AlO_x coating starts to deteriorate between 1.25% and 1.5% strain when no plasma assistance was applied during deposition. The OTR deterioration that starts between 3% and 4% strain agrees with results published by Kelly[4] and Skinner.[16] In comparison to PET, AlO_x coated BOPP already starts losing its oxygen barrier at a lower strain between 1.5% and 2.0%, whereas WVTR is unaffected by the amount of strain. The latter point confirms the good inherent moisture barrier of plain BOPP film and also indicates that the AlO_x coating did not provide any barrier improvement. It is postulated that the two different behaviors for AlO_x on BOPP and PET may be due to the

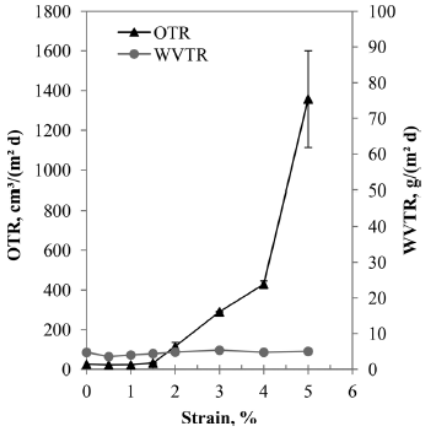

FIG. 2. Variation in oxygen and water vapor transmission rate with applied strain for AlO_x coated BOPP B (measured after strain was released).

AlO_x growing in a different way on the BOPP film surface compared to the PET surface; thus resulting in a different structure of the coating itself.

B. Surface topography (AFM, SEM)

The plain BOPP and PET films and AlO_x coated samples have been investigated further by SEM and AFM analysis. The SEM images of the plain BOPP film surfaces show "antiblock" particles of various sizes, with an average diameter of a few microns, protruding from the film surface (see Fig. 3). Antiblock particles, commonly consisting of silica, are additives incorporated into the film in order to ease film handling during processing by modifying surface roughness and acting as spacers between adjacent surfaces in the rolls of film.[17] However, a major difference between BOPP A and B/C was observed, in that BOPP A featured "dimples" (small recessed areas) with diameters of 100 nm to several hundred nanometers. The origin of these defects is unknown, but the authors assume they may be caused be microarcs occurring during in-house corona treatment by the film manufacturer. The PET film surface was visibly different to the BOPP films and revealed a large surface coverage of antiblock particles; however, these particles gave the appearance of being more incorporated into the PET film surface than was the case for the BOPP films. In all cases, the AlO_x coated film surfaces looked very similar to the plain film surfaces, with the AlO_x coating reproducing the plain film surface topography, as shown in Fig. 4. AFM analysis of the plain film and AlO_x coated surfaces confirmed the results of the SEM investigations and revealed the same "grainy" structure (Fig. 5). However, on comparing the SEM images of AlO_x coated BOPP A with B and C, major differences can again be seen. While on BOPP B and C the AlO_x surface is very regular and has a smooth surface appearance, the coating on BOPP A exhibits pores and what appear to be variations in thickness, as shown in Fig. 6. These pores and thickness irregularities are already visible at 10 000 x magnification and were, additionally, detected by the AFM examinations of AlO_x coated BOPP film A (see Fig. 7). As pores could neither be found on AlO_x coated BOPP B or C, it is assumed that these pores are major pathways for oxygen molecules, which result in the high OTR values for AlO_x coated BOPP A (see Table I). AFM and SEM analysis already showed the presence of dimples in the plain film surface of BOPP A, which were of similar dimensions to the pores in the AlO_x coating and, therefore, may have caused these pores. Clearly, the plain film surface seems to be of great importance in regard to the barrier levels of the AlO_x coated film, and differences in the surfaces of the plain BOPP films seem to account for the large differences measured in OTR for BOPP A compared to B and C.

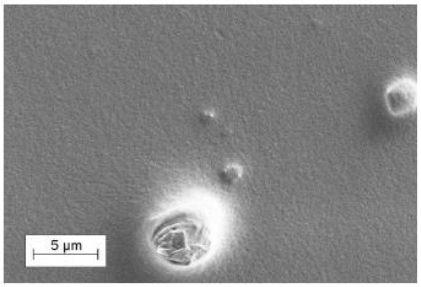

FIG. 3. SEM image of antiblock particles in plain BOPP B film surface.

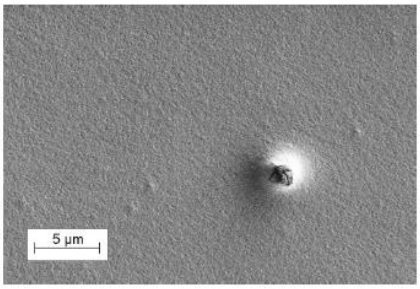

FIG. 4. SEM image of antiblock particle protruding from AlO_x coated BOPP B film surface.

For AFM surface roughness evaluation, root mean square (rms) and roughness average values were calculated from scans of $5 \times 5\,\mu m^2$ size and all scans were acquired in areas that did not include antiblock particles. Results of this investigation are summarized in Table II. The lowest values were obtained on plain and AlO_x coated PET with average rms values of 1.6/1.7 nm, while BOPP C gave the highest roughness values with an rms of 6.0 ± 0.3 nm for the plain film and 6.9 ± 0.4 nm for the AlO_x coated film. But despite having the highest surface roughness, BOPP C still shows acceptable OTR values, which supports the idea that nanoscale surface roughness of the plain film is not the main factor regarding oxygen barrier performance after AlO_x coating. Plain BOPP A and B show approximately the same surface roughness (rms about 4 nm), but very different OTR values. The plain film roughness values measured are in good agreement with results obtained by Benmalek and Dunlop[18] and

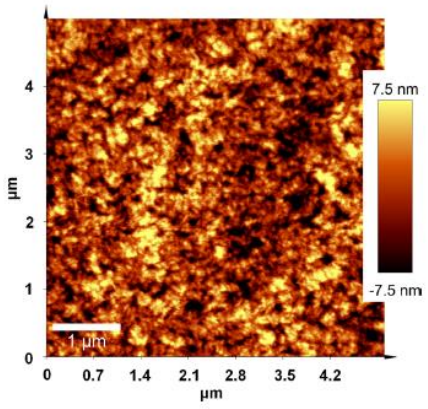

FIG. 5. (Color online) $5 \times 5\,\mu m^2$ AFM topography image of AlO_x coating on BOPP B.

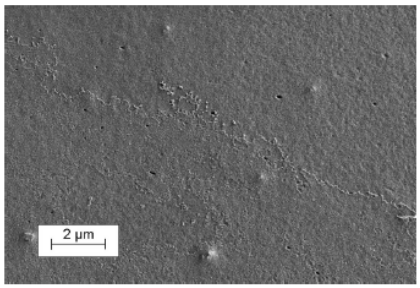

FIG. 6. SEM image of AlO_x coated BOPP A film surface showing coating defects.

Deng *et al.*[19] despite small differences in the AFM scan size used for roughness evaluation. Additionally, the AFM investigation shows that for each film type the plain film and AlO_x coating roughness are approximately in the same range as found by other researchers.[19–21] Comparison of rms values of post-treated AlO_x coated BOPP A and B with non-post-treated samples suggests that plasma post-treatment smoothens the AlO_x surface, which may result in a densification of the outermost atomic layers of the coating; thus explaining the barrier improvement with post-treatment (for BOPP B, see Table I). As mentioned previously, for BOPP A barrier results appeared to be fairly inconsistent and no improvement tendencies with the various parameter changes were discernible.

C. Coating adhesion: Peel-test results

Since vacuum coated films are further converted by laminating another polymer on top of the coating to protect the barrier layer, a good coating to substrate adhesion is an important criterion in preventing delamination during the final packaging application of the composite material. The adhesion of the reactively evaporated AlO_x coating to the BOPP films was assessed using a peel test normally used for the determination of the adhesion of metal (i.e., aluminum)

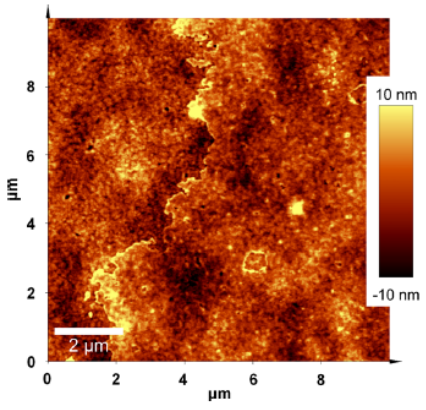

FIG. 7. (Color online) $10 \times 10\ \mu m^2$ AFM topography image of AlO_x coated BOPP A film surface showing coating defects.

TABLE II. AFM surface roughness results (average and standard deviations) for plain and AlO_x coated (see type of plasma treatment) polymer films, obtained from $5 \times 5\ \mu m^2$ AFM scans.

Film	Plasma treatment	Root mean square (nm)	Roughness average (nm)
BOPP A	Plain film	4.1 ± 0.8	3.2 ± 0.6
	Ar/O_2 pre	3.5 ± 0.3	2.7 ± 0.3
	N_2/O_2 Pre	3.8 ± 0.5	3.0 ± 0.4
	O_2 pre + O_2 post	2.9 ± 0.1	2.3 ± 0.1
BOPP B	Plain film	3.8 ± 0.4	3.0 ± 0.3
	N_2/O_2 pre	4.6 ± 0.2	3.6 ± 0.2
	N_2/O_2 pre + O_2 post	4.2 ± 0.3	3.3 ± 0.2
BOPP C	Plain film	6.0 ± 0.3	4.7 ± 0.3
	O_2 pre + O_2 post	6.9 ± 0.4	5.5 ± 0.3
PET	Plain film	1.6 ± 0.3	1.2 ± 0.2
	Ar/O_2 pre + Ar/O_2 post	1.7 ± 0.4	1.3 ± 0.3

coatings on polymer films. A main requirement for the validity of this test is the achievement of full coating, i.e., metal, removal. Earlier investigations of AlO_x adhesion to BOPP films have shown that this peel test can be applied in the case of AlO_x coated polymer films. Full coating removal was possible and visible to the naked eye, despite the transparency of the coating. In general, the AlO_x coated BOPP films show a visible transparency of 91%–93%, with the plain BOPP film transparency being slightly higher. The peel strength values obtained and the corresponding standard deviations are summarized in Table III for the three BOPP films investigated and the various plasma pre- and post-treatments. In all cases, very high peel strength values were obtained. These values far exceed the adhesion values obtained for aluminum metallized standard packaging grade BOPP film [peel strength values for metallized BOPP are generally below 1.5 N/(15 mm) according to peel tests carried out at General Vacuum Equipment]. Additionally, it is obvious from Table III that the adhesion strength values obtained for BOPP film types A and B are independent of the applied plasma pre- and post-treatment. While for BOPP B and C the average peel forces are around 5 N/(15 mm), BOPP A showed a slightly lower peel force of about 3.7–3.9 N/(15 mm). The high peel strength values and also the apparent independence from the plasma pretreatment suggest that, in addition to the AlO_x coating, polymeric material, such as the skin layer of the BOPP film, was also removed during the peel test. Consequently, the EAA films

TABLE III. Measured peel-force values (average and standard deviations) for various plasma treatments using a 180° EAA peel test on 15 mm wide strips.

Film	Plasma treatment	Peel force N/(15 mm)
BOPP A	Ar/O_2 Pre	3.88 ± 0.09
	N_2/O_2 Pre	3.68 ± 0.14
	O_2 Pre + O_2 post	3.80 ± 0.09
BOPP B	—	5.05 ± 0.17
	N_2/O_2 Pre	5.07 ± 0.12
	N_2/O_2 Pre + O_2 post	5.04 ± 0.14
BOPP C	O_2 Pre + O_2 post	4.98 ± 0.21

that had been peeled-off were further analyzed by FTIR spectroscopy to see if the presence of polypropylene could be detected. ATR FTIR spectroscopy has a wavelength dependent penetration depth that is in the region of a few micrometers and consequently will not show small residues of polymeric origin on the peeled-off region. However, if a layer with a thickness of a few 100 nm of polymer is removed, this will be visible in the FTIR spectra. For all three BOPP film types, FTIR confirmed that polymeric material, presumably the BOPP skin layer, was present on the peeled-off EAA film region. Figure 8 shows the FTIR spectra obtained for the EAA film (top), BOPP A (middle), and the EAA film peeled-off region (bottom). The bottom spectrum represents a mixed spectrum, showing peaks that can clearly be attributed to the BOPP film only (peaks around 2954 and 1373 cm^{-1}) and to the EAA film only (peaks around 1699 and 711 cm^{-1}). Additionally, peel-force values for the EEA film sealed to the plain BOPP film surface under the same conditions were determined in order to rule out the possibility of the EAA melting through the thin AlO_x layer onto the BOPP surface; thus resulting in the high peel forces. In all cases, the values obtained were around 0.1–0.9 N/(15 mm), clearly well below the peel-force values measured for the AlO_x coated BOPP films. Furthermore, FTIR analysis did not show polypropylene on the EAA film peeled-off region.

This investigation shows that a cohesive failure occurred during the peel tests, i.e., the locus of failure is not at the interface between coating and substrate but within the substrate. Nevertheless, as the failure in a multilayer structure generally initiates at the weakest point of the system,[22] it can be assumed the adhesion of the AlO_x coating to the BOPP film exceeds the values measured, which most likely represent the adhesion between the skin layer and the core layer of the BOPP film.

D. Surface energy

Further conversion of vacuum coated films, such as printing or laminating on top of the barrier layer, requires a high surface energy as this generally results in better adhesion of inks or the laminated polymers. Therefore, the AlO_x coated BOPP films were analyzed at regular time intervals by contact angle measurement to investigate any ageing process (change of surface energy) that may take place. Surface energy results including standard deviations for AlO_x coated BOPP A and B are depicted as a function of time in Fig. 9. BOPP film A started off with a total surface energy of 57.0 ± 0.9 mN/m, measured a few hours after the coating process, which then dropped down rapidly to approximately 46 mN/m within the first 30 days. Following this initial very strong decrease, the surface energy continued to decay, but at a much slower rate. After 104 days, the surface energy reached a value of approximately 44–45 mN/m; still revealing a tendency to decrease further. BOPP B showed a similar behavior, though with the average AlO_x surface energy being somewhat higher than for BOPP A. On dividing the total surface energy into its polar and dispersive parts, it can be seen that the decrease in total surface energy over time is predominantly due to a fall in the polar fraction. While the dispersive surface energy remains approximately constant, with average values around 29–31 mN/m, the polar surface energy decreases from approximately 25 to 15 mN/m within the 104 days of investigation (for BOPP A, refer to Fig. 10).

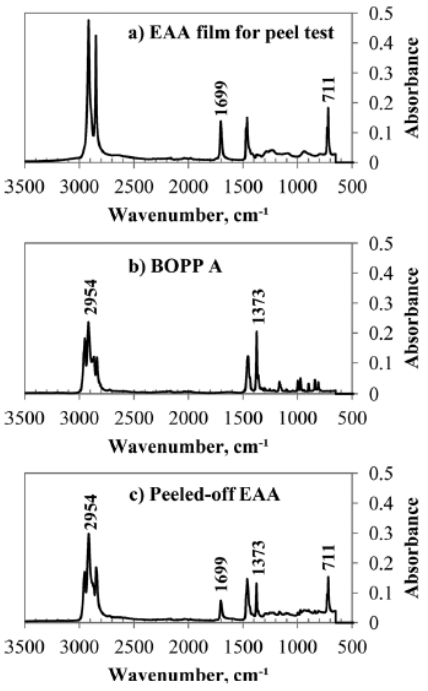

FIG. 8. FTIR spectra of the EAA film used for peel tests (a), BOPP film A (b), and the EAA film peeled-off region (c).

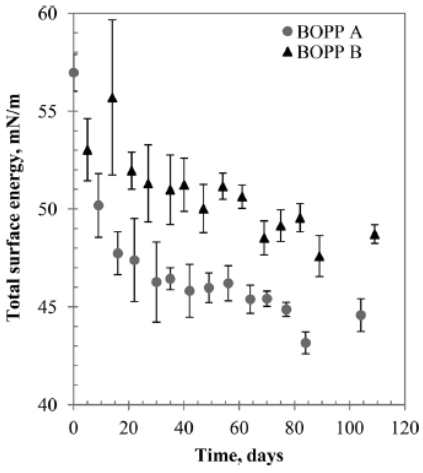

FIG. 9. Variation of total surface energy of AlO_x coated BOPP films with storage time (in days after coating process).

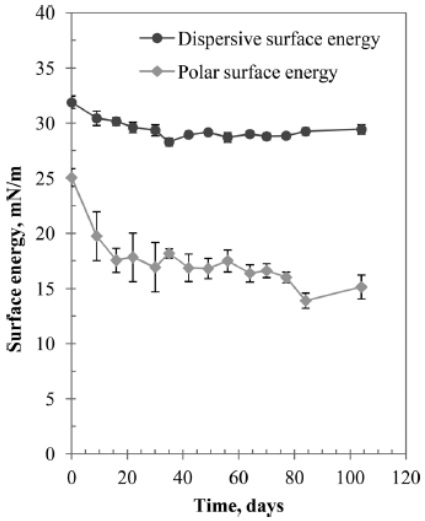

FIG. 10. Variation of polar and dispersive surface energy of AlO_x coated BOPP A with storage time.

The decrease in surface energy of vacuum coated films with time is a well known phenomenon within the metallizing and converting industries.[23–25] This ageing effect is believed to be due to the transfer of polymeric material (oligomers) and migratory additives from the reverse side of the coated film onto the coating, and also migration from the bulk polymer through the coating onto its surface via defects. BOPP film surfaces freshly coated with either aluminum or aluminum oxide exhibit a very high surface energy (several 100 mN/m) and are therefore extremely reactive. Consequently, the surface can attract low-energy mobile materials and contaminates quickly. This happens as soon as the film is wound into roll form after the coating process and the fresh coating surface is in direct contact with the polymer back surface.[26,27]

This hypothesis would explain the reduction in surface energy, and also the relatively low surface energy measured on the day of the coating, due to the immediate contact (after deposition) with the reverse side of the BOPP film, which for all BOPP film types had a surface energy of below 30 mN/m. Also, during this investigation the samples were stored in swatches, which means the AlO_x coating was always touching the reverse side of the BOPP film. Taking the previously described SEM images of AlO_x coated BOPP A and B into account, it may well be that mobile polymeric material migrates through the pores present in the AlO_x coating on BOPP A, resulting in the lower surface energy for AlO_x on BOPP A, compared to BOPP B. An additional fact supporting the idea of transfer of polymeric material from the BOPP reverse side is the dispersive surface energy of the AlO_x coating, which is 29–31 mN/m, and therefore virtually identical to the surface energy of the reverse side of the BOPP films (polar component of the reverse is about 0 mN/m).

IV. SUMMARY AND CONCLUSIONS

The barrier performance of packaging grade PET and BOPP films, coated with reactively evaporated aluminum oxide, strongly depends on the surface properties of the plain film and the aluminum oxide film growth. While AlO_x coated PET films deliver consistent barrier results, BOPP reveals considerable variations, depending on the individual substrate. The general rule of thumb that a higher surface energy of the plain film results in better growth and, therefore, greater barrier of the coated film, may well explain the differences in barrier levels between AlO_x coated PET and BOPP. In the case of PET, the higher surface energy is due to a completely different surface chemistry compared to BOPP. However, the drastic differences between AlO_x coated BOPP films A and B cannot be due to the polymer surface energy (38 ± 0.5 mN/m for BOPP A, 36.4 ± 0.6 mN/m for BOPP B) as both films were corona treated by the supplier and, additionally, were subjected to the same low-pressure in-line plasma pretreatment. Furthermore, the nanoscale surface roughness of the plain and AlO_x coated BOPP films A and B is very similar and therefore cannot be the determining factor regarding oxygen barrier performance after coating. Nevertheless, the smoother PET film (plain and AlO_x coated) compared to all BOPP film types may explain why no water vapor barrier improvement was obtained on BOPP, since according to other researchers a smooth substrate surface is an important requirement for good moisture barrier performance.[20] The poor barrier performance of AlO_x coated BOPP A does also not seem to be related to a low coating to substrate adhesion, since, during peel tests, failure occurred within the polymer film and not at the coating–film interface. However, AFM and SEM analysis of plain BOPP A revealed dimples (small recessed areas) that may have caused the pores found in the AlO_x coating; thus impairing the oxygen barrier properties of AlO_x coated BOPP A. Consequently, the barrier performance of AlO_x coated BOPP is mainly dependent on the plain film surface characteristics and thus the nucleation and growth behavior of the coating, which needs to be investigated further. With respect to future work, possible differences in the chemical composition of BOPP A and B will be studied using x-ray photoelectron spectroscopy in addition to the surface energy determination of the polymer films, which has already been performed. Furthermore, the origin of the defects (dimples) in plain BOPP A will be investigated.

ACKNOWLEDGMENTS

The authors would like to thank General Vacuum Equipment for providing an industrial trial platform. Additionally, the authors are grateful to the Fraunhofer Institute for Process Engineering and Packaging IVV, Freising, for giving access to their AFM.

[1]R. Catalá and R. Gavara, Food Sci. Technol. Int. **2**, 281 (1996).
[2]A. Yasuhara, T. Katami, and T. Shibamoto, Chemosphere **62**, 1899 (2006).
[3]R. S. A. Kelly, *Society of Vacuum Coaters 36th Annual Technical Conference Proceedings*, Dallas, TX, 25–30 April 1993 (Society of Vacuum Coaters, Albuquerque, NM, 1993), pp. 312–316.

[4]R. S. A. Kelly, *Society of Vacuum Coaters 37th Annual Technical Conference Proceedings*, Boston, MA, 8–13 May 1994 (Society of Vacuum Coaters, Albuquerque, NM, 1994), pp. 144–148.
[5]S. Schiller, M. Neumann, H. Morgner, and N. Schiller, *Proceedings of the 7th International Conference on Vacuum Web Coating*, Miami, FL, 10–12 November 1993 (Bakish Materials, Englewood, NJ, 1993), pp. 194–219.
[6]S. Schiller, M. Neumann, H. Morgner, and N. Schiller, *Society of Vacuum Coaters 37th Annual Technical Conference Proceedings*, Boston, MA, 8–13 May 1994 (Society of Vacuum Coaters, Albuquerque, NM, 1994), pp. 203–210.
[7]N. Schiller, S. Straach, S. Günther, A. L. Quiceno, A. G. Contreras, R. Ludwig, and G. Hoffmann, *Association of Industrial Metallizers, Coaters and Laminators (AIMCAL) Fall Technical Conference Proceedings*, Myrtle Beach, SC, 19–22 October 2008 (AIMCAL, Fort Mill, SC, 2008).
[8]S. Günther, S. Straach, N. Schiller, A. L. Quiceno, A. G. Contreras, R. Ludwig, and G. Hoffmann, *Society of Vacuum Coaters 52nd Annual Technical Conference Proceedings*, Santa Clara, CA, 9–14 May 2009 (Society of Vacuum Coaters, Albuquerque, NM, 2009), pp. 727–729.
[9]C. Bichler, H.-C. Langowski, U. Moosheimer, and B. Seifert, J. Adhes. Sci. Technol. **11**, 233 (1997).
[10]H.-C. Langowski, J. Adhes. Sci. Technol. **25**, 223 (2011).
[11]D. K. Owens and R. C. Wendt, J. Appl. Polym. Sci. **13**, 1741 (1969).
[12]W. Rabel, Farbe Lack **77**, 997 (1971).
[13]D. H. Kaelble, J. Adhes. **2**, 66 (1970).
[14]J. T. Felts, J. Plast. Film Sheeting **9**, 139 (1993).
[15]N. Schiller, H. Morgner, M. Fahland, S. Straach, M. Räbisch, and C. Charton, *Society of Vacuum Coaters 42nd Annual Technical Conference Proceedings*, Chicago, IL, 17–22 April 1999 (Society of Vacuum Coaters, Albuquerque, NM, 1999), pp. 392–396.
[16]A. Skinner, *Association of Industrial Metallizers, Coaters and Laminators (AIMCAL) Fall Technical Conference Proceedings*, Reno, NV, 22–25 October 2006 (AIMCAL, Fort Mill, SC, 2006).
[17]T. Kromminga and G. Van Esche, in *Plastic Additives Handbook*, edited by H. Zweifel, R. D. Maier, and M. Schiller (Carl Hanser, Munich, 2008), pp. 613–628.
[18]M. Benmalek and H. M. Dunlop, Surf. Coat. Technol. **76–77**, 821 (1995).
[19]C. S. Deng, H. E. Assender, F. Dinelli, O. V. Kolosov, G. A. D. Briggs, T. Miyamoto, and Y. Tsukahara, J. Polym. Sci. Part B: Polym. Phys. **38**, 3151 (2000).
[20]H. Low and Y. Xu, Appl. Surf. Sci. **250**, 135 (2005).
[21]B. M. Henry, H. E. Assender, A. G. Erlat, C. R. M. Grovenor, G. A. D. Briggs, T. Miyamoto, and Y. Tsukahara, *Society of Vacuum Coaters 47th Annual Technical Conference Proceedings*, Dallas, TX, 24–29 April 2004 (Society of Vacuum Coaters, Albuquerque, NM, 2004), pp. 609–614.
[22]K. L. Mittal, in *Adhesion Measurements of Films and Coatings*, edited by K. L. Mittal (VSP, Utrecht, 1995), Vol. 1, pp. 1–13.
[23]C. A. Bishop, http://www.convertingquarterly.com/blogs/vacuum-web-coating/id/1588/question-re-decline-in-metal-coating-surface-energy.aspx (accessed August 9, 2011).
[24]E. Mount, http://www.convertingquarterly.com/blogs/substrate-secrets/id/2190/aluminum-layer-contamination-in-wound-rolls-of-metallized-films.aspx (accessed August 9, 2011).
[25]E. Mount, http://www.convertingquarterly.com/blogs/substrate-secrets/id/2661/pet-film-coatings-for-maintaining-the-surface-energy-of-the-films.aspx (accessed August 9, 2011).
[26]J. V. Marra, J. Plast. Film Sheeting **4**, 27 (1988).
[27]C. A. Bishop, *Roll-to-Roll Vacuum Deposition of Barrier Coatings* (Scrivener, Salem, 2010).

ARTICLE IN PRESS
SCT-18795; No of Pages 8
Surface & Coatings Technology xxx (2013) xxx–xxx
Contents lists available at ScienceDirect
Surface & Coatings Technology
journal homepage: www.elsevier.com/locate/surfcoat

Aluminum oxide barrier coatings on polymer films for food packaging applications

C.F. Struller [a,b,*], P.J. Kelly [a], N.J. Copeland [b]

[a] Surface Engineering Group, Manchester Metropolitan University, Manchester, M1 5GD, UK
[b] Bobst Manchester Ltd., Pilsworth Road, Heywood, Lancashire OL10 2TL, UK

ARTICLE INFO

Article history:
Received 12 June 2013
Accepted in revised form 9 August 2013
Available online xxxx

Keywords:
Aluminum oxide
BOPP
Barrier coatings
Reactive evaporation
Adhesion
Surface energy

ABSTRACT

In the field of packaging, barrier layers are functional films, which can be applied to polymeric substrates with the objective of enhancing their end-use properties. For food packaging applications, the packaging material is required to preserve packaged food stuffs and protect them from a variety of environmental influences, particularly moisture and oxygen ingress and UV radiation. Aluminum metallized films are widely used for this purpose. More recently, transparent barrier coatings based on aluminum oxide or silicon oxide have been introduced in order to fulfill requirements such as product visibility, microwaveability or retortability. With the demand for transparent barrier films for low-cost packaging applications growing, the use of high-speed vacuum deposition techniques, such as roll-to-roll metallizers, has become a favorable and powerful tool. In this study, aluminum oxide barrier coatings have been deposited onto biaxially oriented polypropylene and polyethylene terephthalate film substrates via reactive evaporation using an industrial 'boat-type' roll-to-roll metallizer. The coated films have been investigated and compared to uncoated films in terms of barrier properties, surface topography, roughness and surface energy using scanning electron microscopy, atomic force microscopy and contact angle measurement. Coating to substrate adhesion and coating thickness have been examined via peel tests and transmission electron microscopy, respectively.

1. Introduction

Polymer films vacuum coated with a thin layer of evaporated aluminum are a standard component in the composite structure of flexible packaging materials for a variety of food stuffs. These thin coatings with a thickness of a few tens of nanometers [1] are produced on industrial roll-to-roll vacuum web coaters, generally referred to as metallizers. The machines predominantly use resistively heated evaporation boats and can coat films of a width of 4.45 m at speeds up to 1000 m/min [2,3]. The main purpose of applying these thin layers is to confer barrier properties to the polymer films, which on their own generally do not act as good barriers, and thus create a functional packaging material. The impermeability of the packaging material to vapors and gases such as water, oxygen, carbon dioxide and aromas (either going into or coming from the product) is an essential design consideration for the longevity of the packaged food product and hence key to successful food packaging. In recent years, transparent barrier coatings, such as aluminum oxide or silicon oxide (usually referred to as AlO_x and SiO_x as the exact stoichiometry is not generally measured) have been gaining interest. When applied onto polymer films, these barrier coatings bring additional advantages over opaque metallized films in that they offer product visibility, microwaveability/retortability and are also suitable for passing through metal detectors, whilst still providing the barrier levels required. With the transparent barrier flexible packaging market growing worldwide at a rate of 10 to 15% per year [2], the use of vacuum deposition techniques to produce transparent barrier layers has become very attractive. Products such as ethylene vinyl alcohol copolymer (EVOH) coated and coextruded barrier films and polyvinylidene chloride (PVdC) atmospheric coated polymer films conventionally tend to dominate this market [4]. However, vacuum deposited thin barrier coatings only require a small fraction of the thickness of these polymer based barrier layers, i.e. their thickness is three orders of magnitude less, whilst still producing similar barrier properties. This can potentially provide vast economic and environmental benefits in terms of raw material consumption and the associated costs. Using and modifying a standard 'boat type' roll-to-roll metallizer to deposit transparent barrier coatings has been an aspiration for many years [5–10]. The injection of oxygen into the aluminum vapor stream in the evaporation zone results in the deposition of a transparent aluminum oxide layer, which can give good barrier properties, when the process and its conditions are controlled appropriately. When using polyethylene terephthalate (PET) base film, this process produces consistent barrier performance with the reactively evaporated aluminum oxide. However, considering the low profit margins within the packaging market, the associated cost of the base substrate also plays a major part and commodity biaxially oriented polypropylene (BOPP) films still remain at a lower cost level than PET.

* Corresponding author at: Surface Engineering Group, Manchester Metropolitan University, Manchester, M1 5GD, UK. Tel.: +44 161 2474643; fax: +44 161 247 4693.
E-mail address: carolin.struller@stu.mmu.ac.uk (C.F. Struller).

0257-8972/$ – see front matter © 2013 Elsevier B.V. All rights reserved.
http://dx.doi.org/10.1016/j.surfcoat.2013.08.011

Please cite this article as: C.F. Struller, et al., Surf. Coat. Technol. (2013), http://dx.doi.org/10.1016/j.surfcoat.2013.08.011

The barrier levels of aluminum oxide coated BOPP, though, are heavily affected by the plain film surface characteristics and thus the growth conditions created for the depositing thin film. As will be shown, the surface characteristics of standard packaging grade BOPP films can vary significantly. Therefore, this paper reports the characterization of plain film surface properties, such as surface energy, roughness and topography and relates the findings to the barrier levels obtained after AlO_x coating. Additionally, coating adhesion and coating surface energy, important parameters for further conversion of vacuum coated films, and coating thickness have been assessed using peel tests, contact angle measurement and transmission electron microscopy, respectively.

2. Experimental

2.1. Substrate materials

Various packaging grade BOPP films and a PET base film (all corona treated in-house by the film producers), as well as a BOPP film coextruded with a special high surface energy polymer as a skin layer ('UHB', produced by Brückner Maschinenbau GmbH & Co. KG, Siegsdorf, Germany) were coated with an aluminum oxide barrier layer. The coatings were applied to the corona treated side of each film and the high surface energy polymer skin layer, respectively. All standard packaging grade BOPP films used consist of a three layer coextruded structure with a homopolymer core and either co- or terpolymer skin layers on each side in order to obtain a heat-sealable film. These skin layers also contain additives such as antiblock particles (up to several μm in diameter, typically consisting of silica), which ensure good film processing and converting characteristics. However, they are also known to negatively impact the barrier properties of vacuum deposited coatings. In contrast to the standard packaging grade BOPP films, the BOPP film with the special polymer skin layer consists of a five layer coextruded structure, with no antiblock particles added to the high surface energy polymer skin layer [11]. The PET film coated as a reference material is a monolayer film, with antiblock particles dispersed throughout the single layer. Furthermore, all films contain a variety of additives to stabilize the polymer film and guarantee optimized film handling and end-use properties. Exact film compositions are, however, commercially sensitive information not made available by the individual film producers.

2.2. Coating process

The polymer films were coated via reactive thermal evaporation using a Bobst Manchester Ltd. (formerly General Vacuum Equipment Ltd.) General K4000 vacuum metallizer with an AlO_x coating system installed. The K4000 roll-to-roll metallizer can handle webs up to 2450 mm wide and the AlO_x coating process was performed at web speeds up to 840 m/min. For the films coated here, the web width varied between 1000 mm and 1650 mm and samples were generally taken from the center of the web. The vacuum coater has a deposition source consisting of resistively heated evaporation boats (standard intermetallic composite) onto which aluminum is continuously fed in the form of a wire. Oxygen is introduced into the aluminum vapor stream in order to produce a transparent aluminum oxide coating and a special optical monitor beam and closed loop control system is used to achieve consistent optical properties of the coated film across the web width and length. The pressure during aluminum oxide deposition is of the order of 0.05 Pa. For development purposes, in-line plasma pre- and post-treatments were performed using a plasma source with magnetically enhanced water cooled electrodes. The pressure at the plasma treatment units is kept between 2 and 4 Pa, in order to minimize unintended sputtering from the electrodes. The plasma treatment was performed using power settings and gas recipes previously optimized at Bobst. For this study, other than the plasma treatment conditions, all coating parameters were kept constant to ensure coatings of comparable thickness and stoichiometry.

2.3. Analytical techniques

Barrier properties, in terms of oxygen and water vapor transmission rates (OTR/WVTR), were determined in accordance with ASTM F 1927 and ASTM F 1249/ISO 15106-3 using a Mocon Oxtran 2/20 and Systech Illinois 8001 for oxygen permeation and a Mocon Permatran-W 3/33 and Systech Illinois 7001 for water vapor permeation. Test conditions for OTR were 23 °C and 50% relative humidity (RH), whilst WVTR is stated for 37.8 °C and a gradient of 90% RH.

Furthermore, a Zeiss Supra 40VP field emission gun scanning electron microscope (SEM) was used to acquire images of the uncoated and aluminum oxide coated film surfaces at an acceleration voltage of 0.4/0.5 kV. In order to avoid masking any surface detail, no conductive layer was applied to these insulating samples prior to analysis.

The plain film and coating surfaces were additionally analyzed with a WiTec alpha500 and a Veeco DI CP II atomic force microscope (AFM). Pulsed force mode and tapping mode, respectively, were used to acquire roughness data and topography images. All images were corrected by first order line-wise leveling. Root mean square (RMS) and roughness average (R_A) values were calculated from 5×5 μm^2 size scans. Therefore, several scans were performed from different areas that did not exhibit antiblock particles in order to obtain an average value and the standard deviation.

The coating to substrate adhesion was assessed using a peel test, as described in further detail in Ref. [12,13]. This industrial based test is normally applied to examine the adhesion of aluminum metallized films. For this test, an ethylene acrylic acid (EAA) film is bonded to the coated surface of the polymer film and, after conditioning, the EAA/coating is peeled off at a peel-off angle of 180°.

The surface energy of the uncoated films and the AlO_x coating surface energy were investigated by means of contact angle measurement via the sessile drop method. Contact angles for three different test fluids (water, diiodomethane and ethylene glycol) were measured with a Krüss MobileDrop system and DSAII software. When curve fitting and measurement of contact angles were not possible with the Krüss system, the acquired images were analyzed using a drop shape analysis plugin for ImageJ [14]. These angles were then used to calculate the surface energies according to the Owens–Wendt–Rabel–Kaelble approach [15–17]. Throughout this investigation, sample swatches were stored under ambient conditions.

A FEI Tecnai 12 Biotwin transmission electron microscope (TEM) at a 100 kV acceleration voltage was used to acquire images of the AlO_x layer for coating thickness evaluation after embedding and ultra-microtome sectioning.

3. Results and discussion

3.1. Barrier performance

The barrier performance obtained for the plain BOPP films and the AlO_x coated films is summarized in Table 1. Also listed in this table are the results for a PET reference film and the results following different plasma treatments. These values were used to determine the barrier improvement factor (BIF) for each transmission rate (i.e. transmission rate ratio of uncoated to coated film), which is a quality indicator commonly used to characterize the effect of vacuum deposited barrier coatings. The results presented in Table 1 allow the BOPP films to be rated with respect to their barrier performance after AlO_x coating:

- BOPP A — poor performing polymer
- BOPP B — standard performing polymer
- BOPP C — standard performing polymer with improved oxygen barrier
- BOPP D — BOPP with special polymer skin layer.

As mentioned in Section 1, AlO_x coated standard packaging grade PET delivers consistent barrier properties, typically around or less than

Please cite this article as: C.F. Struller, et al., Surf. Coat. Technol. (2013), http://dx.doi.org/10.1016/j.surfcoat.2013.08.011

ARTICLE IN PRESS

C.F. Struller et al. / Surface & Coatings Technology xxx (2013) xxx–xxx 3

1 cm^3 (STP)/(m^2 d bar) and 1 g/(m^2 d). This can be seen from the OTR and WVTR values in Table 1, which are both around 0.5 cm^3 (STP)/(m^2 d bar) and 0.5 g/(m^2 d), respectively, for the PET reference sample. However, when coating standard packaging grade BOPP films with reactively evaporated AlO_x, the barrier performance can vary to a large extent and appears to be strongly affected by the individual base material itself. BOPP, in contrast to PET, is a non-polar polymer with a completely different surface chemistry, which can have a large impact on coating nucleation and growth [18]. For AlO_x coated BOPP A for example, the OTR was very inconsistent and the application of plasma treatment did not appear to bring improvement. None of the trials performed resulted in a clear enhancement of the oxygen barrier down to levels below 100 cm^3 (STP)/(m^2 d bar), which would be comparable to aluminum metallized BOPP (see for example barrier performance of metallized BOPP B in Table 1, an OTR value <100 cm^3 (STP)/(m^2 d bar) is generally guaranteed in a datasheet for metallized standard BOPP film). BOPP C, in contrast, delivered acceptable (e.g. <100 cm^3 (STP)/(m^2 d bar)) oxygen barrier performance even without any in-line plasma treatment. With the application of pre- and post-treatments an OTR of 26.68 ± 3.07 cm^3 (STP)/(m^2 d bar) was achieved for this film. In the case of BOPP D, which is coextruded with a special high surface energy polymer skin layer in order to enhance barrier performance after coating, remarkable barrier improvement for OTR (and WVTR) could be obtained by applying the AlO_x layer (refer to Table 1). Even without any in-line treatment the OTR improved significantly, due to the different surface chemistry of the skin layer, which enhances AlO_x nucleation/growth and consequently the coating structure.

The OTR values for both BOPP B and C clearly revealed an improvement in barrier levels obtained when in-line plasma pre- and post-treatments were applied. Pre-treatment improves barrier by chemical modification of the plain film surface, which enhances coating nucleation/growth conditions and hence affects the final coating structure in terms of coating density/porosity [19]. During this chemical modification, functional groups are incorporated into the film surface, which can act as nucleation sites for the depositing coating [12,20]. Furthermore, plasma treatment is generally accompanied by a cleaning effect, during which low molecular weight species loosely bonded to the film surface are removed through bombardment with energetic plasma species [2]. Bichler and coworkers [21] showed an improvement of the oxygen barrier properties of AlO_x coated BOPP film (electron beam evaporation) following oxygen plasma pre-treatment. They attributed this, though, to the smoothing of the polymer surface induced by the plasma treatment, resulting in the homogeneous growth of the coating. However, as will be shown in Section 3.2, we did not find any difference in surface roughness between the plain and AlO_x coated film and hence exclude a smoothing effect of the plasma pre-treatment. The bombardment of the coating during post-treatment can result in a densification of the outermost atomic layers of the coating, which may protect the AlO_x layer and reduce oxygen permeation. Overall, though, these barrier results suggest that barrier performance of AlO_x coated BOPP is very much base film dependent. Possible reasons for the barrier differences between the standard packaging grade BOPP films A, B and C will be discussed along with the results of the SEM and AFM investigations in Section 3.2.

Table 1
Barrier performance (oxygen and water vapor transmission rates) of plain and AlO_x coated BOPP films and PET reference film including barrier improvement factors.

Film type/base film thickness	In-line plasma treatment	OTR		WVTR	
		cm^3 (STP)/(m^2 d bar)	BIF	g/(m^2 d)	BIF
BOPP A	Plain film	≈1600	–	≈4	–
30 μm	No	270.50 ± 34.65	6	3.99 ± 0.06	1
	PRE	201.55 ± 24.45	8	3.43 ± 0.35	1.2
	PRE + POST	258.00 ± 18.57	6	3.98 ± 0.30	1
BOPP B	Plain film	≈2700	–	≈7	–
15 μm	No	475.88 ± 27.45	6	5.78 ± 0.01	1.2
	PRE	118.42 ± 21.70	23	5.47 ± 0.35	1.3
	PRE + POST	79.49 ± 19.58	34	5.89 ± 0.18	1.2
	[a]Metallized PRE	24.65 ± 3.61	110	0.34 ± 0.03	21
BOPP C	Plain film	≈2400	–	≈6	–
20 μm	No	47.00 ± 5.35	51	5.89 ± 0.23	1
	PRE	35.33 ± 3.05	68	6.08 ± 0.17	1
	PRE + POST	26.68 ± 3.07	90	4.73 ± 0.07	1.3
BOPP D	Plain film	≈500	–	≈4.5	–
18 μm	No	0.89 ± 0.01	562	2.19 ± 0.06	2
	PRE	0.83 ± 0.30	602	0.56 ± 0.07	8
	PRE + POST	0.60 ± 0.14	833	0.45 ± 0.11	10
PET	Plain film	≈120	–	≈40	–
12 μm	PRE + POST	0.54 ± 0.05	222	0.56 ± 0.03	71

[a] Aluminum coating, no AlO_x.

For BOPP D, the improvement of OTR by the AlO_x coating (compared to the AlO_x coating on the 'standard' BOPP films) is additionally due to the fact that the high surface energy skin layer itself has a better oxygen barrier than BOPP, as can be seen from the enhanced plain film oxygen barrier performance (refer to Table 1). As described by Jamieson and Windle [22] and also Beu and Mercea [23], applying a thin and less permeable coating (e.g. polymer layer) to the polymer film prior to metallization (or in our case AlO_x coating) can improve barrier performance in the case of a defect driven permeation through the inorganic coating due to a reduction of the concentration gradient in the polymer in the vicinity of the defects. This has also been further discussed and explored by Langowski [24].

When investigating the WVTR of the AlO_x coated BOPP films, it is clear that, with the exception of BOPP D, no true moisture barrier improvement was obtained in the trials conducted, i.e. the BIF values are around ≈1. An acceptable water barrier level would be less than 1 g/(m^2 d), i.e. similar to AlO_x coated PET. That good oxygen barrier has been achieved whilst still lacking water barrier improvement indicates that oxygen and moisture permeation through inorganic barrier layers are dominated by different mechanisms [25–28]. However, plain BOPP film already has an inherently good water barrier compared to plain PET (see Table 1). For BOPP D, the data in Table 1 also shows the importance of in-line plasma pre-treatment for obtaining a water barrier performance of less than 1 g/(m^2 d) for the AlO_x coated film. Once again, the improvement of WVTR with plasma pre-treatment is attributed to the chemical modification and cleaning induced by the plasma treatment. It is assumed that any low molecular weight material on top of the high surface energy polymer skin layer (presumably transferred from the reverse side of the film) is removed by the plasma and thus cannot compromise the depositing coating. This presumably results, along with the functional groups created on the treated film surface, in a better nucleation of the coating and therefore a denser structure exhibiting less defects with a size of a few nm down to the sub-nm range (referred to as microscopic defects [24] or nano-defects [29]) that would predominantly affect water vapor permeation.

3.2. Surface topography and roughness

Due to the large variation of barrier properties obtained for AlO_x coated standard packaging grade BOPP films, the surface topography of the plain BOPP films and AlO_x coated samples was investigated further at a range of resolutions, using optical microscopy, SEM imaging and finally AFM analysis on 5 × 5 μm^2 scans.

Light microscopy analysis (no images shown) and SEM analysis (see Fig. 1) revealed major differences between BOPP A, B and C, particularly in terms of the size and density distribution of the antiblock particles present on the film surface. Antiblock particles normally consist of inorganic materials, typically silica, and are added to the outer layers of the coextruded BOPP film in order to ease film handling during processing. They protrude from the film surface and thus reduce contact area by separating the individual film layers in the rolls of film [30]. Whilst BOPP A and B showed a large number of small (sub μm size) antiblock particles, BOPP C featured fewer but substantially larger antiblock particles

Please cite this article as: C.F. Struller, et al., Surf. Coat. Technol. (2013), http://dx.doi.org/10.1016/j.surfcoat.2013.08.011

(diameter >1 μm). The damage seen on BOPP A (Fig. 1, left image, center) was created by an antiblock particle dislocating from the film surface. This is a common phenomenon for BOPP films, where the antiblock particles are added to the outer skin layers only and thus are less incorporated into the film, and frequently happens during film conversion and winding. In contrast to all these standard BOPP films, BOPP D does not contain any antiblock particles in its special polymer skin layer. All three standard BOPP films exhibited a 'granular' or 'orange-peel' surface structure, which is a typical characteristic of BOPP films, however, with major individual differences. On BOPP B the grains were a lot larger and more pronounced than on BOPP A and C. In addition to that, another key difference between BOPP A and B/C was seen, in that plain BOPP A was covered in defects shaped like small craters or 'dimples' (see Fig. 1, left image) with diameters of 50 nm to several 100 nm (measured via AFM). These defects were originally assumed to be caused by micro-arcs appearing during corona treatment at the film production site [31]. However, with our more recent investigations we could exclude corona treatment as a potential source of the defects and now focus on the heat setting/thermofixation applied to BOPP films after the orientation process in order to stabilize the film and prevent unintentional shrinkage. The authors suspect that during this re-heating process, volatile components within the film surface flash evaporate off and consequently leave crater shaped defects.

When analyzing the AlO_x coated films, it was found that in all cases (BOPP films and also PET reference) the AlO_x coating reproduced the underlying plain film surface topography and showed a similar 'grainy' structure with the individual film characteristics as discussed for the plain BOPP film surfaces. For BOPP A, the AlO_x coating also seemed to recreate the described dimples/craters as pores in the coating and, furthermore, showed irregularities in coating thickness (see Fig. 2). In contrast to that, AlO_x coated BOPP B and C had a very 'regular' surface appearance and did not reveal variations in coating thickness or pores. Based on this observation, the pores in the coating on BOPP A are assumed to act as pathways of unhindered permeation for oxygen, therefore inducing the low oxygen barrier performance of this film after AlO_x coating (refer to Table 1). For BOPP D (no SEM images shown), the plain as well as the AlO_x coated film surface showed a very smooth surface appearance with no antiblock particles.

The AFM analysis of the plain films and AlO_x coated surfaces confirmed the results of the SEM investigations and revealed the same 'grainy' structures and other surface features (refer to Fig. 3 for AFM images of plain BOPP films). For example, craters/dimples and pores were again detected by the AFM examinations of plain and AlO_x coated BOPP film A, respectively. The SEM and AFM investigations show that the plain film surface and its specific characteristics, such as defects, play an important role in determining the barrier levels obtained after AlO_x coating. For the samples investigated here, the plain film surface defects (dimples/craters) appear to be the main cause for the vast differences in OTR values obtained for BOPP A in contrast to B and C. The AFM analysis was used to collect further information about the surface

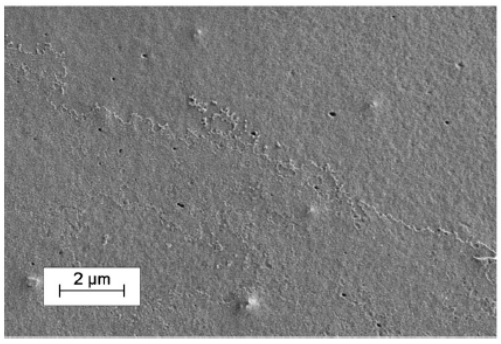

Fig. 2. SEM image of AlO_x coated BOPP A showing pores in the coating and thickness variations.

roughness of the uncoated and coated polymer films in terms of root mean square and roughness average, which have been summarized in Table 2. Plain and AlO_x coated PET showed the lowest surface roughness, with average RMS values of 1.6 nm and 1.8 nm, respectively, whilst BOPP B gave the highest roughness values. BOPP D with its special polymer skin layer showed a slightly higher surface roughness than PET, but was still smoother than all the analyzed standard packaging grade BOPP films. BOPP A and C revealed the same surface roughness values, despite the dimples/craters present in the surface of BOPP A. For the plain PET and BOPP films, the surface roughness values measured in this study are in agreement with results obtained by Benmalek and Dunlop [32] and Deng et al. [18]. When investigating the AlO_x coated samples, the roughness data obtained was very similar to the plain films and no impact of pre- or post-treatment on the roughness of the AlO_x layer was observed. For each film type, plain and AlO_x coated film exhibited virtually identical surface roughness values, which again indicate that the thin AlO_x layer reproduces the underlying surface roughness and structure as seen in the SEM investigation. Deng et al. [18], who used electron beam evaporation to deposit AlO_x layers onto PET and polypropylene, found that this was only the case for PET, whilst for polypropylene the 10 nm AlO_x layer showed an increased roughness compared to the plain film (the thickness of the coatings investigated in our study is identical, see Section 3.4, however a lower scan size of 1×1 μm^2 was used by Deng et al. [18]). Therefore, they hypothesized an island growth mechanism for the AlO_x layer on polypropylene and a layer-by-layer growth mechanism on PET. The work presented here, however, suggests that there is no difference for BOPP compared to PET, as for each BOPP film type, the plain and AlO_x coated films showed similar/identical surface roughness. Nevertheless, the authors still assume that the AlO_x layer grows in a different manner (nanostructure of the coating) on BOPP than it does on PET, due to the

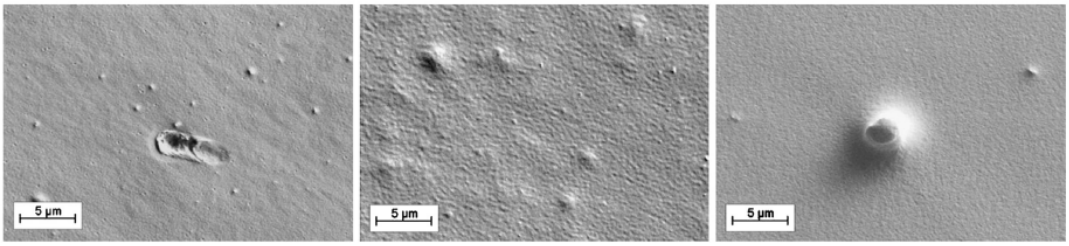

Fig. 1. SEM images of plain film surfaces — left to right: BOPP A, BOPP B, and BOPP C.

Please cite this article as: C.F. Struller, et al., Surf. Coat. Technol. (2013), http://dx.doi.org/10.1016/j.surfcoat.2013.08.011

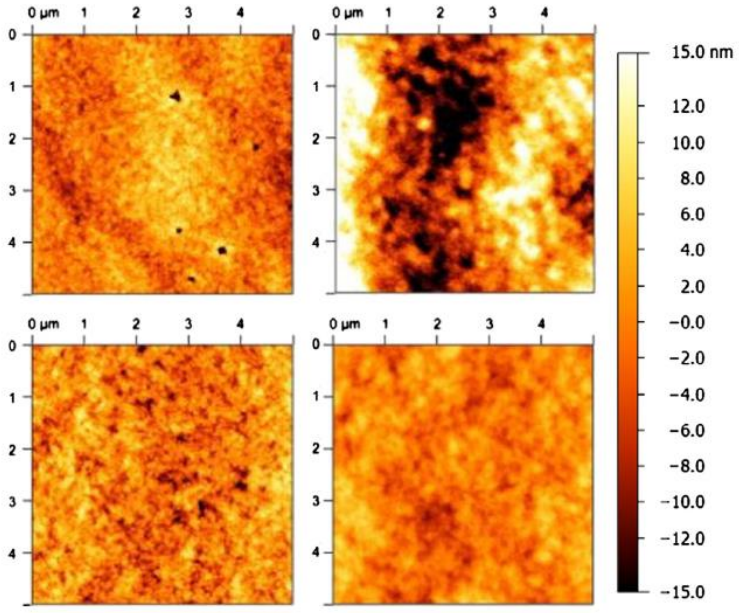

Fig. 3. 5 × 5 µm² AFM scans of plain film surfaces — from left to right: BOPP A, BOPP B, BOPP C, and BOPP D.

different surface chemistry, and this contributes to the different barrier properties. This nanostructure of the coating does, however not affect the roughness of the AlO_x coating, as measured by AFM, i.e. it is beyond the resolution of this analytical technique at the chosen scan size.

Not taking BOPP A into account, the roughness data may suggest that a smoother surface results in better barrier properties after AlO_x coating. In the case of BOPP D and PET, we however assume that the barrier improvement is caused by the change in surface chemistry (see Section 3.3) whilst for BOPP B and C there are further differences (such as the antiblock particle size and distribution density) that are known to have an impact on barrier properties. Antiblock particles protruding up to several microns from the film surface will quite likely result in defects in the coating. BOPP B showed a larger number of micron and submicron size antiblock particles, whilst BOPP C showed substantially larger particles and a lesser amount of smaller particles. This may potentially have a large impact on the barrier properties after AlO_x coating, as other researchers state that "many small holes in a barrier layer are much more effective in compromising the system barrier properties than a few large holes with the same total area" [33].

Table 2
Surface roughness of plain and AlO_x coated BOPP films and PET reference film (calculated from 5 × 5 µm² AFM scans).

Film	Plasma treatment	RMS	R_A
		nm	nm
BOPP A	Plain film	4.1 ± 0.7	3.3 ± 0.5
	PRE	3.7 ± 0.5	2.9 ± 0.4
	PRE + POST	4.1 ± 0.6	3.2 ± 0.5
BOPP B	Plain film	5.7 ± 1.8	4.5 ± 1.5
	PRE	5.8 ± 0.9	4.6 ± 0.7
	PRE + POST	6.0 ± 0.7	4.8 ± 0.6
BOPP C	Plain film	4.1 ± 0.3	3.2 ± 0.2
	PRE	4.6 ± 0.2	3.6 ± 0.2
	PRE + POST	4.3 ± 0.3	3.4 ± 0.2
BOPP D	Plain film	2.8 ± 0.2	2.2 ± 0.1
	PRE	2.9 ± 0.2	2.3 ± 0.2
	PRE + POST	3.0 ± 0.2	2.4 ± 0.1
PET	Plain film	1.6 ± 0.2	1.2 ± 0.2
	PRE + POST	1.8 ± 0.3	1.4 ± 0.3

3.3. Surface chemistry

The plain polymer films were further characterized in terms of surface chemistry via contact angle measurement for surface energy determination. This technique can be regarded as an indirect method to assess information about the chemical composition of the different substrate film surfaces. As can be seen from the results presented in Table 3, the total surface energies of BOPP B and C with values around 36.5 mN/m are slightly lower than for BOPP A, which shows an average surface energy of 38.0 mN/m. All surface energies of the corona treated standard packaging grade BOPP films are, though, typical levels to be expected for industrially corona treated BOPP film [34,35]. It is, however, well known that corona treated polypropylene film undergoes an aging process [34,36]. This thermodynamically driven process causes the polymer surface to revert towards its initial more hydrophobic state and is explained by mechanisms including reorientation of the functional groups created towards the bulk polymer; migration of mobile short polymer chains (low molecular weight material created by the treatment) to the polymer surface; or diffusion of additives to the film surface, and its extent depends strongly on ambient conditions [20,37]. It may, therefore, well be that differences in the polarity of the film surfaces are present, but are not detected due to the nature of the contact angle measurement, which only probes the outermost atomic layers. Furthermore, the films are coated in vacuum and in this environment volatile components may desorb from and leave the film surface more readily due to the lower vapor pressure. Thus, these components may interfere with the contact angle measurements conducted under atmospheric conditions, but have less impact for the depositing coating in vacuum. In order to further characterize the

Please cite this article as: C.F. Struller, et al., Surf. Coat. Technol. (2013), http://dx.doi.org/10.1016/j.surfcoat.2013.08.011

Table 3
Surface energy results for plain BOPP films and PET reference film. The total surface energy has been split into its polar and dispersive components.

Film	Surface energy		
	mN/m		
	Polar	Dispersive	Total
BOPP A	8.9 ± 0.6	29.1 ± 0.4	38.0 ± 0.4
BOPP B	7.8 ± 0.6	28.6 ± 0.3	36.4 ± 0.4
BOPP C	7.9 ± 0.2	28.7 ± 0.1	36.6 ± 0.2
BOPP D	6.2 ± 1.3	36.2 ± 1.4	42.4 ± 0.3
PET	9.6 ± 0.9	38.6 ± 0.9	48.2 ± 1.3

films and detect possible differences, the exact chemical composition of the plain BOPP films needs to be studied using X-ray photoelectron spectroscopy (XPS) analysis.

The total surface energies of BOPP D, the film with the modified skin layer, and PET are higher compared to the standard BOPP films, which is due to a higher dispersive surface energy component. This difference is caused by the different chemical surface compositions of these films and it is assumed that this surface chemistry creates better nucleation conditions for the depositing AlO_x layer, therefore improving growth and structure/density of the coating, which in turn enhances the barrier properties. The surface energy of BOPP D measured in this study is lower than expected, based on published data [38]. However, it has to be noted that the high surface energy polymer skin layer is in contact with the low surface energy reverse side of BOPP D (a polypropylene copolymer) when stored in roll form and material may be transferred from the reverse onto the special skin layer, thus reducing the surface energy measured. It is also worthwhile mentioning that, whilst the surface energy measured using dyne pens according to ASTM D-2578 was in good agreement with the results obtained via contact angle measurement and the calculation approach used for BOPP A to D, there was a strong discrepancy for the surface of the corona treated PET film. However, different techniques (i.e. test fluids, calculation methods) will result in different surface energies [39].

3.4. Coating thickness

In order to determine the thickness of the reactively evaporated AlO_x layers, film samples were embedded in an epoxy resin, cross-sectioned with an ultramicrotome and subsequently examined using TEM. Fig. 4 shows the representative TEM cross-section images for AlO_x coated BOPP C at two different magnification levels. For standard BOPP films, TEM revealed the typical three layer structure with a core layer surrounded by a skin layer on each side. One of the skin layers, i.e. the skin layer that is coated with AlO_x, can be clearly seen in the lower magnification TEM image (Fig. 4A) and reveals a thickness of less than 0.5 µm. Here, it is also observable that the AlO_x layer fractures during TEM sample preparation, caused by the compression of the microtoming process and the different elastic properties of the BOPP polymer, the embedding medium and the ceramic AlO_x layer. In all cases, the thickness of the AlO_x barrier layer was determined to be between 9 and 11 nm (refer to Fig. 4B) independent of the barrier performance. This thickness is approximately only one fourth of the thickness of an aluminum barrier layer on a standard metallized film with an optical density of 2.5 [1], which is used in food packaging applications. It was also attempted to investigate the structure of the coating using the TEM cross-section images. However, no structural differences were visible between the AlO_x coating on the various BOPP films and the PET reference film at the resolution level provided by TEM analysis. It is therefore concluded that the nanostructure and potential differences of the approximately 10 nm thin AlO_x coatings cannot be resolved using TEM analysis of cross-sections. The thickness in our study is similar to aluminum oxide barrier layers deposited by other researchers using PVD processes [40,41], who found that effective barrier properties can be obtained at such a coating thickness. However, it disagrees with Kelly [6], who stated that below 15 nm coating thickness the reactively evaporated AlO_x layer is discontinuous and barrier properties are impaired.

3.5. Coating adhesion

The AlO_x coated samples were further investigated to gain information about coating to substrate adhesion, which is an important aspect for the conversion of vacuum coated films. A 180 degree peel test was used in this investigation and the peel force values obtained are summarized in Table 4. In our previous work [31] we have shown that for AlO_x coated BOPP very high peel force values were obtained, independent of the plasma treatment applied and also independent of the barrier performance, thus indicating that insufficient barrier properties are not related to poor adhesion. This was also found for the additional BOPP films investigated in this study. In all cases, infra-red spectroscopy of the peeled-off EAA layer proved that cohesive failure had occurred within the polymer substrate during the peel test. Based on the probing depth of the analytical technique used for polymer identification, it was concluded that in addition to the AlO_x coating, the skin layer of the coextruded BOPP films was also peeled off with the EAA film. Since adhesion failure in a multilayer system generally occurs at the

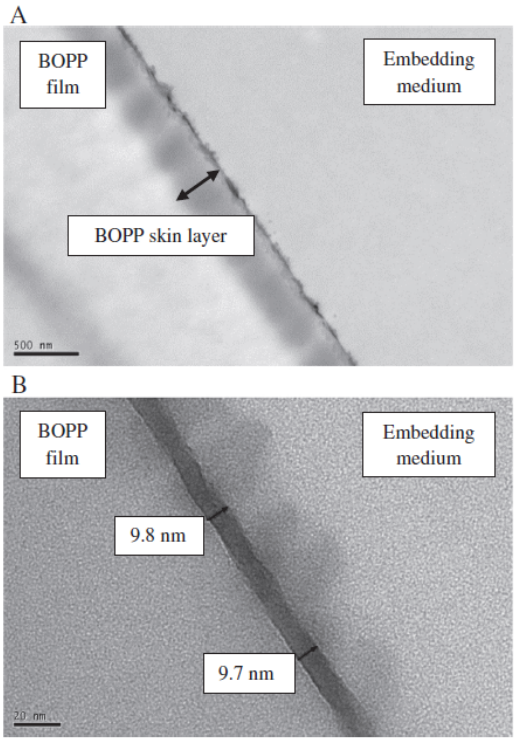

Fig. 4. TEM cross-section images of AlO_x coated BOPP C; A: lower magnification level showing the BOPP skin layer; B: higher magnification level for coating thickness determination.

Please cite this article as: C.F. Struller, et al., Surf. Coat. Technol. (2013), http://dx.doi.org/10.1016/j.surfcoat.2013.08.011

ARTICLE IN PRESS

C.F. Struller et al. / Surface & Coatings Technology xxx (2013) xxx–xxx 7

weakest point [42], it can be assumed that the adhesion of the AlO_x coating to the BOPP film exceeds the values measured. Table 4 also contains the reference values for metallized BOPP A and B, which are a lot lower than the forces obtained for their AlO_x coated opponents and, furthermore, did not show removal of the BOPP skin layer along with the metal coating. Peel tests were additionally carried out for the AlO_x coated PET and the AlO_x coated 5 layer BOPP film coextruded with a different polymer as skin layer. Also, for the latter film, the skin layer was removed during all peel tests. For AlO_x coated PET, it was, though, not possible to peel off the AlO_x layer. Here the EAA film stretched until it tore at values around 6 to 7 N/(15 mm) without removing any AlO_x or parts of the PET film. This is attributed to the PET substrate being a single layer and not a coextruded film. Due to the high intrinsic strength of this single layer material, no cohesive failure within the PET film can occur. Indeed, in the case of PET, the EAA peel test is known to be reaching its limits [13].

3.6. AlO_x surface energy

In addition to coating to substrate adhesion, coating surface energy is a further important factor to be considered for conversion processes of the vacuum coated films, such as printing or laminating on top of the barrier layer. These process steps require a high surface energy as this usually results in better wetting of inks or the adhesives used for lamination. Good wetting, in general, is the first step towards good adhesion. The AlO_x coated films were investigated using contact angle measurement to calculate their surface energy. Samples were stored under ambient conditions without precise control of environmental parameters as this is seen as a more realistic approximation to the storage conditions of industrial film rolls. We have previously published the initial results of this investigation [31] and are now presenting the long term behavior of the samples examined. The measurements were carried out over an extended period of approximately 700 days and results are depicted as a function of time in Fig. 5. For AlO_x coated BOPP A, which was initially analyzed on the day of coating, a rapid decrease of the total surface energy from a start value of 57.0 ± 0.9 mN/m is visible for the first few days after coating, followed by a further decay at a lower rate until around 175 days of age. From this time onwards, there was still a measurable, but very slow, decline with current values at around 40 mN/m. BOPP D behaved nearly identically to BOPP A and also BOPP C showed similar behavior, although the average AlO_x surface energy was somewhat higher than for the other films. However, over extended time periods, AlO_x coated BOPP C appears to approach surface energy values similar to the other two AlO_x coated BOPP films. For comparison, Fig. 5 also contains the surface energies obtained on AlO_x coated PET. These values are considerably higher (63 to 66 mN/m) and also only reveal a marginal decrease with time. As discussed in more detail in our earlier work [31] this drop of coating surface energy is caused by the transfer of polymeric material and film additives from the reverse of the polymer film onto the fresh coating and also the migration through the coating via defects. This happens as soon as the coated film is wound into a roll and a contact is established between the fresh coating and the reverse side of the polymer film. Consequently, it is inevitable for roll to roll coating processes. In the case of all BOPP films, including BOPP D with a different polymer as skin layer, the reverse side is a polypropylene surface, either a co- or terpolymer. Hence, the three BOPP films behave very similarly, in contrast to the AlO_x coated PET. Differences between PET and BOPP in terms of the surface energy decay characteristics of the AlO_x coated side can be explained by the difference in glass transition temperature (T_g) of the two polymers. BOPP at ambient temperature will be above its T_g (in the range of 0 to 10 °C [43] for isotactic PP) and consequently all amorphous parts will be in a rubbery state. In this state, polymer chains and fragments are more flexible and mobile. In contrast, PET has a higher T_g (69 to 115 °C [43]). Thus, in PET the oligomers and polymer chains in the amorphous regions are in the glassy state at ambient temperature and are less mobile; it is therefore argued that less migration will occur. In addition to that, fewer film additives are required during PET film production. XPS surface analysis of the AlO_x coated BOPP and PET films in this study confirmed the presence of carbon based material as well as residues of film additives, such as acid scavengers (for BOPP), on the AlO_x coating, assumed to have come from contact with the reverse side of the film. Furthermore, there was a larger amount of carbon based contamination on AlO_x coated BOPP than on AlO_x coated PET, which is in good agreement with the surface energy being higher for the AlO_x coating on PET compared to any type of BOPP.

Table 4
Peel forces obtained for AlO_x coated standard packaging BOPP films (180° peel test, with EAA film).

Film	Plasma treatment	Peel force
		N/(15 mm)
BOPP A	No	3.16 ± 0.11
	PRE	3.15 ± 0.12
	PRE + POST	3.13 ± 0.08
	[a]Metallized (PRE)	0.82 ± 0.04
BOPP B	No	3.46 ± 0.08
	PRE	3.51 ± 0.10
	PRE + POST	3.50 ± 0.16
	[a]Metallized (PRE)	0.78 ± 0.03
BOPP C	No	5.05 ± 0.17
	PRE	5.07 ± 0.12
	PRE + POST	5.04 ± 0.14

[a] Aluminum coating, no AlO_x

4. Summary and conclusions

Barrier properties of packaging grade PET and BOPP films, coated with aluminum oxide via reactive thermal evaporation, are strongly affected by the surface characteristics of the plain film, such as surface defects and surface chemistry. These parameters have a large impact onto the aluminum oxide coating nucleation, growth and structure and not only vary to a large extent between the different polymer film types, but can also change significantly within one substrate type, as has been shown here for standard packaging grade BOPP films. The barrier levels obtained for PET films coated with reactively evaporated aluminum oxide are consistent and reliably achieved. In contrast to that, though, AlO_x coated BOPP films exhibit significant differences in their barrier performance, depending on the individual substrate. Substrate surface defects, such as the craters/dimples found on BOPP A, appeared to play an important role

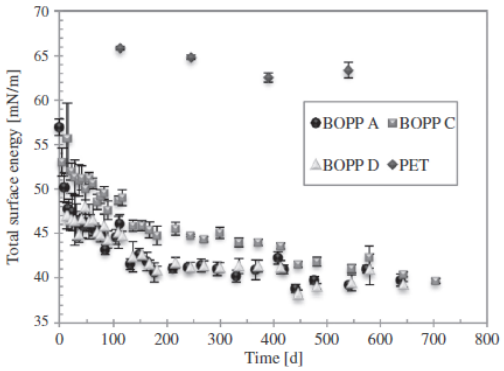

Fig. 5. Change of AlO_x surface energy with storage time for various AlO_x coated BOPP films and PET reference film.

Please cite this article as: C.F. Struller, et al., Surf. Coat. Technol. (2013), http://dx.doi.org/10.1016/j.surfcoat.2013.08.011

in compromising barrier properties. These defects were found to be reproduced as pores in the AlO_x coating, thus acting as permeation pathway for oxygen and increasing the measured transmission rates for BOPP A compared to B and C. Furthermore, the standard packaging grade BOPP films also featured considerable differences in the antiblock particle size and density, which can potentially affect the size and number of defects in the AlO_x layer, and therefore is of great importance to the barrier levels that can be achieved. The surface energy determination for the plain standard BOPP films could not explain the differences seen in barrier performance after AlO_x coating, as all corona treated standard packaging grade BOPP films showed a similar value. For the PET film, as well as the BOPP film coextruded with a special skin layer, the surface energy was higher than for the corona treated BOPP films, due to the different surface chemistry. With respect to surface chemistry, XPS analysis of all plain films is needed in order to investigate compositional differences, which, in the case of the corona treated BOPP films, were potentially not detected using contact angle measurement. TEM analysis indicated an average thickness of 10 nm for all AlO_x coatings, but could, unfortunately, not reveal any structural differences between the individual coatings on the BOPP films and PET reference film. For all films a very high coating to substrate adhesion was observed, which resulted in cohesive failure of the substrate occurring during peel tests of the AlO_x coated BOPP films. Therefore, poor barrier performance is not related to insufficient adhesion. An important result is that the use of a high surface energy polymer skin layer, which can be coextruded with the BOPP film, significantly helps to improve the oxygen as well as water vapor barrier performance of AlO_x coated BOPP film and thus to obtain barrier levels comparable to AlO_x coated PET.

Acknowledgments

The authors would like to thank Bobst Manchester Ltd. (Heywood, United Kingdom) for providing an industrial trial platform and, moreover, film producers and customers including Brückner Maschinenbau GmbH & Co.KG (Siegsdorf, Germany) for supplying base films. Additionally, we are grateful to Innovia Films Ltd. (Wigton, United Kingdom) for being able to use their analytical facilities, the Fraunhofer Institute for Process Engineering and Packaging IVV (Freising, Germany) for giving access to their AFM and Dr. Aleksandr Mironov of the electron microscope facility in the Faculty of Life Sciences of the University of Manchester (Manchester, United Kingdom) for his assistance in performing TEM analysis. Furthermore, we thankfully acknowledge Dr. Charles Bishop for his valued comments and input.

References

[1] D.J. McClure, N. Copeland, AIMCAL 2010 Fall Technical Conference, AIMCAL, 2010.
[2] C.A. Bishop, Roll-to-roll Vacuum Deposition of Barrier Coatings, Scrivener, Salem, 2010.
[3] R. Ludwig, R. Kulka, E. Josephson, Proc. IEEE 93 (2005) 1483–1490.
[4] The future of transparent barrier films to 2011, Pira International Ltd., Leatherhead, 2006.
[5] R.S.A. Kelly, Proceedings of the 36th Annual Technical Conference of the Society of Vacuum Coaters, 1993, pp. 312–316.
[6] R.S.A. Kelly, Proceedings of the 37th Annual Technical Conference of the Society of Vacuum Coaters, 1994, pp. 144–148.
[7] S. Schiller, M. Neumann, H. Morgner, N. Schiller, Proceedings of 7th International Conference on Vacuum Web, Coating, 1993, pp. 194–219.
[8] S. Schiller, M. Neumann, H. Morgner, N. Schiller, Proceedings of the 37th Annual Technical Conference of the Society of Vacuum Coaters, 1994, pp. 203–210.
[9] N. Schiller, S. Straach, S. Günther, A.L. Quiceno, A.G. Contreras, R. Ludwig, G. Hoffmann, AIMCAL 2008 Fall Technical Conference, AIMCAL, 2008.
[10] S. Günther, S. Straach, N. Schiller, A.L. Quiceno, A.G. Contreras, R. Ludwig, G. Hoffmann, Proceedings of the 52nd Annual Technical Conference of the Society of Vacuum Coaters, 2009, pp. 727–729.
[11] J. Breil, in: J.R. Wagner Jr. (Ed.), Multilayer Flexible Packaging: Technology and Applications for The Food, Personal Care and Over-the-counter Pharmaceutical Industries, Elsevier, Amsterdam, 2010, pp. 231–237.
[12] H.-C. Langowski, J. Adhes. Sci. Technol. 25 (2011) 223–243.
[13] M. Jesdinszki, C. Struller, N. Rodler, D. Blondin, V. Cassio, E. Kucukpinar, H.-C. Langowski, J. Adhes. Sci. Technol. 26 (2012) 2357–2380.
[14] A.F. Stalder, G. Kulik, D. Sage, L. Barbieri, P. Hoffmann, Colloids Surf., A Physicochem. Eng. Asp. 286 (2006) 92–103.
[15] D.K. Owens, R.C. Wendt, J. Appl. Polym. Sci. 13 (1969) 1741–1747.
[16] W. Rabel, Farbe Lack 77 (1971) 997–1005.
[17] D.H. Kaelble, J. Adhes. 2 (1970) 66–81.
[18] C.S. Deng, H.E. Assender, F. Dinelli, O.V. Kolosov, G.A.D. Briggs, T. Miyamoto, Y. Tsukahara, J. Polym. Sci. B Polym. Phys. 38 (2000) 3151–3162.
[19] W. Decker, B. Henry, Proceedings of the 45th Annual Technical Conference of the Society of Vacuum Coaters, 2002, pp. 492–502.
[20] E.M. Liston, L. Martinu, M.R. Wertheimer, J. Adhes. Sci. Technol. 7 (1993) 1091–1127.
[21] C. Bichler, T. Kerbstadt, H.C. Langowski, U. Moosheimer, Surf. Coat. Technol. 112 (1999) 373–378.
[22] E.H.H. Jamieson, A.H. Windle, J. Mater. Sci. 18 (1983) 64–80.
[23] T.A. Beu, P.V. Mercea, Mater. Chem. Phys. 26 (1990) 309–322.
[24] H.-C. Langowski, in: O.G. Piringer, A.L. Baner (Eds.), Plastic Packaging — Interactions with Food and Pharmaceuticals, Wiley-VCH, Weinheim, 2008, pp. 297–347.
[25] O. Miesbauer, M. Schmidt, H.-C. Langowski, Vak. Forsch. Prax. 20 (2008) 32–40.
[26] M. Hanika, H.-C. Langowski, W. Peukert, Proceedings of the 46th Annual Technical Conference of the Society of Vacuum Coaters, 2003, pp. 592–599.
[27] A.G. Erlat, B.M. Henry, C.R.M. Grovenor, A.G.D. Briggs, R.J. Chater, Y. Tsukahara, J. Phys. Chem. B 108 (2004) 883–890.
[28] Y.G. Tropsha, N.G. Harvey, J. Phys. Chem. B 101 (1997) 2259–2266.
[29] A.P. Roberts, B.M. Henry, A.P. Sutton, C.R.M. Grovenor, G.A.D. Briggs, T. Miyamoto, M. Kano, Y. Tsukahara, M. Yanaka, J. Membr. Sci. 208 (2002) 75–88.
[30] T. Kromminga, G. Van Esche, in: H. Zweifel, R.D. Maier, M. Schiller (Eds.), Plastic Additives Handbook, Carl Hanser, Munich, 2008, pp. 613–628.
[31] C.F. Struller, P.J. Kelly, N.J. Copeland, C.M. Liauw, J. Vac. Sci. Technol. A 30 (2012) 041502.
[32] M. Benmalek, H.M. Dunlop, Surf. Coat. Technol. 76–77 (1995) 821–826.
[33] G. Rossi, M. Nulman, J. Appl. Phys. 74 (1993) 5471–5475.
[34] J.M. Strobel, M. Strobel, C.S. Lyons, C. Dunatov, S.J. Perron, J. Adhes, Part. Sci. Technol. 5 (1991) 119–130.
[35] R. Wolf, A.C. Sparavigna, Engineering 2 (2010) 397–402.
[36] M. Strobel, C.S. Lyons, J.M. Strobel, R.S. Kapaun, J. Adhes. Sci. Technol. 6 (1992) 429–443.
[37] F. Garbassi, M. Morra, E. Occhiello, Polymer Surfaces — From Physics to Technology, John Wiley & Sons, Chichester, 1994.
[38] M. Wolf, J. Breil, R. Lund, TAPPI 2008 PLACE Conference, TAPPI, 2008.
[39] M. Zenkiewicz, J. Adhes. Sci. Technol. 15 (2001) 1769–1785.
[40] N. Schiller, H. Morgner, M. Fahland, S. Straach, M. Räbisch, C. Charton, Proceedings of the 42nd Annual Technical Conference of the Society of Vacuum Coaters, 1999, pp. 392–396.
[41] R.W. Phillips, T. Markantes, C. LeGallee, Proceedings of the 36th Annual Technical Conference of the Society of Vacuum Coaters, 1993, pp. 293–301.
[42] K.L. Mittal, in: K.L. Mittal (Ed.), Adhesion Measurements of Films and Coatings, VSP, Utrecht, 1995, pp. 1–13.
[43] J.E. Mark, Polymer Data Handbook, second ed., Oxford University Press, New York, 2009.

Please cite this article as: C.F. Struller, et al., Surf. Coat. Technol. (2013), http://dx.doi.org/10.1016/j.surfcoat.2013.08.011

ARTICLE IN PRESS
TSF-32745; No of Pages 4
Thin Solid Films xxx (2013) xxx–xxx
Contents lists available at ScienceDirect
Thin Solid Films
journal homepage: www.elsevier.com/locate/tsf

Aluminium oxide barrier films on polymeric web and their conversion for packaging applications

C.F. Struller [a,b,*], P.J. Kelly [a], N.J. Copeland [b], V. Tobin [c], H.E. Assender [c], C.W. Holliday [d], S.J. Read [d]

[a] Surface Engineering Group, Manchester Metropolitan University, Manchester M1 5GD, UK
[b] Bobst Manchester Ltd., Pilsworth Road, Heywood, Lancashire OL10 2TL, UK
[c] Department of Materials, University of Oxford, Begbroke Science Park, Oxford OX5 1PF, UK
[d] Innovia Films Ltd., Lowther R&D Building, West Road, Wigton, Cumbria CA7 9XX, UK

ARTICLE INFO

Available online xxxx

Keywords:
Aluminium oxide
Biaxially oriented polypropylene
Barrier coatings
Reactive evaporation
Lamination
Acrylate
Coatings

ABSTRACT

In recent years, inorganic transparent barrier layers such as aluminium oxide or silicon oxide deposited onto polymer films have emerged as an attractive alternative to polymer based transparent barrier layers for flexible food packaging materials. For this application, barrier properties against water vapour and oxygen are critical. Aluminium oxide coatings can provide good barrier levels at thicknesses in the nanometre range, compared to several micrometres for polymer-based barrier layers. These ceramic barrier coatings are now being produced on a large scale using industrial high speed vacuum deposition techniques, here, reactive evaporation on a 'boat-type' roll-to-roll metalliser. For the thin barrier layer to be useful in its final packaging application, it needs to be protected. This can be either via lamination or via an additional topcoat. This study reports on acrylate topcoats, but also undercoats, on aluminium oxide coated biaxially oriented polypropylene films. The effect of the acrylate layer on barrier levels and surface topography and roughness was investigated. The acrylate was found to smooth the substrate surface and improve barrier properties. Furthermore, the activation energy for water vapour and oxygen permeation was determined in order to investigate barrier mechanisms. The oxide coated film was, additionally, converted via adhesive lamination, which also provided improvement in barrier levels.

1. Introduction

Transparent barrier films have been attracting increasing interest in recent years. Applications range from moderate barrier levels required for food packaging to very high barrier levels for encapsulating electronic devices. With the transparent barrier flexible packaging market growing worldwide at a rate of 10 to 15% per year [1], the use of vacuum deposition techniques to produce transparent barrier layers such as aluminium oxide (AlO_x) or silicon oxide has become a favourable and powerful tool. For food packaging, this market is traditionally dominated by ethylene vinyl alcohol copolymer co-extruded barrier layer films and polyvinylidene chloride coated films [2]. However, vacuum-deposited barrier coatings only require a small fraction of the thickness of these barrier layers, i.e. their thickness is three orders of magnitude smaller, whilst still producing comparable barrier properties. The standard aluminium metallisation process, usually carried out in a roll-to-roll coater, can be modified by the injection of oxygen into the aluminium vapour in order to deposit a transparent aluminium oxide barrier layer; a process that has been developed over the last few decades [3–7]. The use of such large scale and high speed coating equipment can potentially provide vast economic and environmental benefits, which is of great importance for the cost sensitive food packaging market, where profit margins generally are small. Considering the low profit margins within the packaging market, the associated cost of the base substrate also plays an important role. On this point, biaxially oriented polypropylene (BOPP) base film still remains at a lower cost level than polyethylene terephthalate (PET) film, which causes it to be the material of choice regarding commodity clear barrier films. Nevertheless, whilst PET films coated with reactively evaporated AlO_x give reliable barrier properties against water vapour and oxygen, BOPP films have proven to be a more difficult substrate material. Here, the barrier levels strongly depend on the film surface characteristics and the resulting growth conditions for the AlO_x layer, as discussed in more detail in our earlier paper [7]. After coating with the thin barrier layer, there is, though, a further conversion step required in order to obtain the final packaging structure. This is either achieved by laminating the vacuum coated films (adhesive lamination, extrusion lamination) or via application of an additional polymer coating on top of the inorganic layer, both serving the purpose of protecting the thin barrier layer during its final packaging application. Hence, it is

* Corresponding author. Bobst Manchester Ltd, Pilsworth Road, Pennine Business Park, OL10 2TL Heywood, United Kingdom. Tel.: +44 1706 622 442; fax: +44 1706 622 772.
E-mail address: Carolin.Struller@bobst.com (C.F. Struller).

0040-6090/$ – see front matter © 2013 Elsevier B.V. All rights reserved.
http://dx.doi.org/10.1016/j.tsf.2013.10.091

essential that barrier loss upon conversion due to damage of the coating is avoided. In the course of this investigation, the effects of adhesive lamination as well as acrylate coatings on AlO_x coated polymer film were examined.

2. Experimental details

2.1. Substrate material, coating and conversion processes

The film used in this study was a 20 μm thick three layer coextruded biaxially oriented polypropylene film with a homopolymer core and either a co- or terpolymer skin layer on each side. The film was also corona treated in-house by the film manufacturer. The corona treated side was coated with a 10 nm thin AlO_x layer via reactive thermal evaporation on an industrial roll-to-roll metalliser using a Bobst Manchester (formerly General Vacuum Equipment) General K4000 vacuum metalliser. This vacuum coater has a source consisting of resistively heated evaporation boats, onto which aluminium wire is continuously fed. Oxygen is introduced into the aluminium vapour cloud to produce a transparent aluminium oxide coating and an optical monitoring beam and closed loop control system are used to achieve consistent optical properties of the coated film across the web width and length. The pressure during aluminium oxide deposition is of the order of 0.05 Pa. AlO_x layers were deposited onto rolls of film (for acrylate topcoats and lamination) and A4 samples mounted onto a carrier web (for acrylate undercoats). In the development work carried out, all coated film samples exhibit a transparency between 90 and 92% visible light transmission, which is approximately equivalent to the light transmission of the uncoated BOPP substrate used. The transparency level is also maintained during the subsequent conversion processes of acrylate topcoating and lamination.

The acrylate deposition was achieved via flash evaporation of a monomer liquid in vacuum. These monomers condense as a liquid film on the substrate surface and are subsequently cured using electron beam radiation (with a current of 400 mA) to obtain a cross-linked layer. Acrylate deposition was carried out on a system licensed by Sigma Technologies International Inc. (USA). Tripropylene glycol diacrylate was chosen as a monomer and an acrylate thickness of 0.75 μm was deposited. Acrylate layers were coated onto A4 samples as undercoats and topcoats prior and after AlO_x deposition as an off-line process.

Lamination of the AlO_x coated film was performed on an industrial laminator (Bobst Rotomec CL850) via solvent-based adhesive lamination. A high performance two component polyurethane adhesive was used and the AlO_x coated BOPP was laminated against another plain 20 μm BOPP film.

2.2. Analytical methods

Oxygen and water vapour transmission rates (OTR/WVTR) were determined in compliance with ASTM F 1927 and ASTM F 1249/ISO 15106-3 using a Mocon Oxtran 2/20 and Systech Illinois 8001 for oxygen permeation and a Mocon Permatran-W 3/33 and Systech Illinois 7001 for water vapour permeation. Test conditions for OTR were 23 °C and 50% relative humidity (RH), whilst WVTR is stated for 37.8 °C and a gradient of 90% RH. During WVTR measurement of coated samples, the coated side was always facing the 0% RH. For the determination of the apparent activation energy of oxygen/moisture permeation, barrier measurements were carried out at 4 different temperatures (20 °C, 30 °C, 40 °C in addition to the respective temperature for a standard measurement).

A Veeco DI CP II atomic force microscope (AFM) in tapping mode was used to acquire roughness data and topography images. All images were corrected by first order line-wise levelling. Root mean square (RMS) values were calculated from 5 × 5 μm^2 size scans.

Table 1
Barrier performance of AlO_x coated BOPP in combination with acrylate top- and undercoats.

Description	OTR	WVTR
	$cm^3/(m^2\ d)$	$g/(m^2\ d)$
BOPP (uncoated)	≈2100	6–7
BOPP + *Acrylate undercoat*	1675.50 ± 129.40	6.59 ± 0.08
BOPP + *Acrylate undercoat* + AlO_x	15.83 ± 1.94	1.93 ± 0.21
BOPP + AlO_x	26.68 ± 3.07	4.73 ± 0.07
BOPP + AlO_x + *Acrylate topcoat*	13.65 ± 0.49	0.46 ± 0.07

3. Results and discussion

3.1. Acrylate coated films

3.1.1. Barrier performance

The barrier performance of AlO_x coated BOPP with and without the application of acrylate top- and undercoats is summarised in Table 1. Additionally, the barrier properties of the plain BOPP film and the acrylate coated BOPP film prior to AlO_x deposition are listed. As can be seen, the OTR of the plain film can be significantly reduced by the application of the inorganic AlO_x layer. Nevertheless, the improvement of WVTR is only marginal. These differences have been attributed to the film surface properties affecting coating nucleation and growth and thus the final structure of the thin AlO_x barrier layer [7,8]. Furthermore, the use of an acrylate undercoat prior to AlO_x deposition can additionally enhance the oxygen as well as water vapour barrier, though the acrylate on its own only slightly improves the plain film OTR and leaves the WVTR unchanged. This has also been reported by other research groups for AlO_x layers on polypropylene [9] and polyethylene terephthalate [10–13] and is assigned to a variety of changes the acrylate confers to the polymer film. Acrylate layers have the capability to smoothen the substrate surface, eliminate surface features and thus decouple its defects from the subsequently deposited inorganic barrier layer [10,12–15]. Furthermore, the barrier properties of the acrylate itself, which has a better oxygen barrier than BOPP [16], play a role, as these can affect and reduce the concentration gradient of the permeating substances in the polymer layer adjacent to the defects in the inorganic barrier layer [17,18]. Finally, the acrylate represents a change of surface chemistry, which may offer more nucleation sites to the depositing inorganic coating thus resulting in a denser coating structure [9,12]. The improvement seen when applying an acrylate topcoat, especially the significant enhancement of WVTR to less than 1 $g/(m^2\ d)$, could be attributed to the protection of the barrier layer by the topcoat from damage during winding and handling, which is generally argued to be the reason for the barrier improvement [9,10]. However, it is possible that infiltration of the acrylate into the defects of the AlO_x layer ('pore-filling') could lead to a reduction of the permeation coefficient within the defects from that of air to that of the acrylate [19]. A reduction in permeation has previously been reported for a post-winding laminated barrier film [20], and, more recently, a post-production chemical vapour deposition layer has also been reported to fill defects [21]. In our case, the samples were rewound in vacuum after AlO_x deposition as well as being handled prior to depositing the topcoat. Subsequently, an acrylate coat was applied. So in our experiments, we were able to test whether the acrylate topcoat gave an inherent improvement in barrier due to pore-filling, rather than acting as a protection layer during winding and handling. Once again, the barrier properties of the acrylate should be mentioned here. Acrylate has a better oxygen barrier than BOPP, nevertheless, it does not enhance the moisture barrier of BOPP (see Table 1), i.e. its water vapour barrier is inferior. Hence, we conclude that to some degree the oxygen barrier improvement seen by the application of the topcoat may also be caused by the better oxygen barrier of the acrylate (and therefore the resulting lower concentration gradient in the direct vicinity of defects). For the water vapour barrier improvement seen, we assume, though, that the pore-filling plays a major role.

Please cite this article as: C.F. Struller, et al., Thin Solid Films (2013), http://dx.doi.org/10.1016/j.tsf.2013.10.091

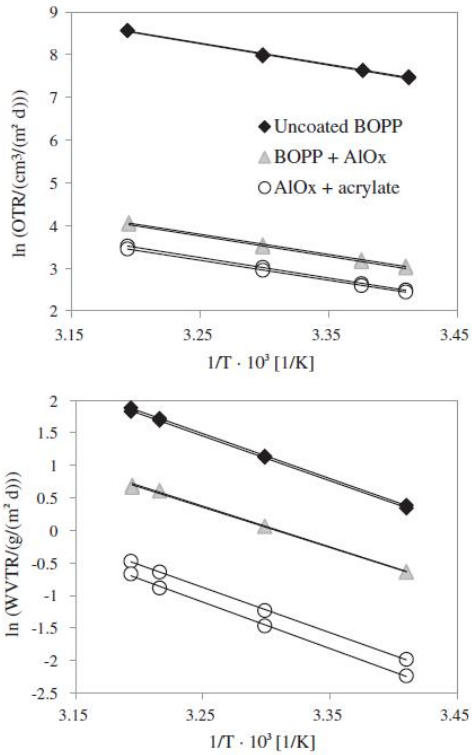

Fig. 1. Arrhenius plots of ln(OTR), top, and ln(WVTR), bottom, as a function of 1/T for uncoated, AlO_x coated and acrylate topcoated BOPP.

3.1.2. Apparent activation energy

To further investigate the permeation mechanisms of oxygen and moisture through AlO_x coated and AlO_x/acrylate topcoated films, the activated rate theory was applied in order to calculate apparent activation energies of permeation [22–24]. The Arrhenius plots of this investigation and the activation energies obtained are summarised in Fig. 1 and Table 2, respectively. As can be seen, the activation energy of oxygen permeation remains largely unchanged by the application of the AlO_x layer as well as the acrylate topcoat, which indicates a macro-defect dominated permeation of oxygen through the coated film with the permeation through the BOPP polymer being the rate limiting step [25]. Furthermore, the activation energies obtained for oxygen are in agreement with values given in the literature [25–27]. For water vapour, the AlO_x layer apparently slightly decreases the activation energy, whilst the application of the acrylate topcoat results in an increase back to the level of plain BOPP. It is, however, assumed that this change is not significant given the relatively small number of samples tested; in this case two (compare also the high standard deviations of activation energies obtained by Tropsha and Harvey [22]). The lack of significant change in activation energy is attributed to a macro-defect driven mechanism, as stated previously for oxygen permeation. This means that the vast majority of the permeating molecules passes through defects of the size of a few nanometres to several micrometres, whilst the rest of the coating can be assumed to be virtually impermeable. Consequently, the AlO_x layer primarily acts as a hurdle containing macroscopic defects, which the permeating molecules have to negotiate in order to enter/leave the polymer. There are, however, also a few cases published where despite the unchanged activation energy of water vapour permeation additional investigations suggested a chemical interaction rather than a defect dominated permeation [22,28]. The activation energy for water vapour permeation through uncoated BOPP falls within the broad range of values reported in literature (Deng et al. [25] 64.6 ± 2.0 kJ/mol, Tropsha and Harvey [22] 38.9 ± 2.1 kJ/mol).

Table 2
Apparent activation energy E_A of oxygen and water vapour permeation through uncoated BOPP, AlO_x coated BOPP and acrylate topcoated AlO_x coated BOPP.

Description	E_A (OTR) kJ/mol	E_A (WVTR) kJ/mol
BOPP (uncoated)	41.5 ± 0.3	57.3 ± 0.2
BOPP + AlO_x	39.4 ± 0.3	51.8 ± 0.4
BOPP + AlO_x + *Acrylate topcoat*	39.2 ± 0.7	58.6 ± 1.1

3.1.3. Surface topography

The surface topographies of the uncoated and acrylate undercoated films were additionally investigated. Differential interference contrast light microscopy (no images shown) revealed major changes induced by the acrylate with smaller filler particles being masked by the acrylate layer as well as the typical BOPP film texture ('orange-peel') being

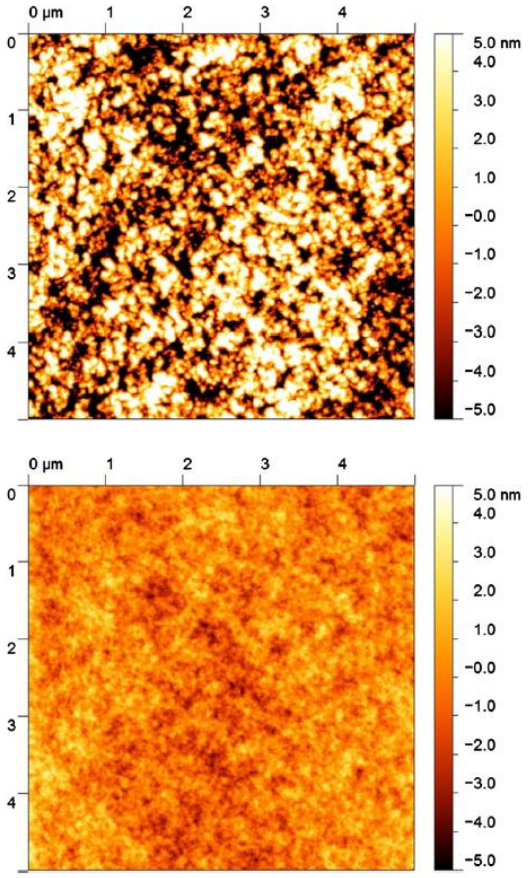

Fig. 2. Representative 5 × 5 µm² AFM scans of uncoated BOPP (top) and acrylate coated BOPP, undercoat, no AlO_x (bottom).

Please cite this article as: C.F. Struller, et al., Thin Solid Films (2013), http://dx.doi.org/10.1016/j.tsf.2013.10.091

Table 3
Barrier performance of AlO_x coated BOPP before and after adhesive lamination.

Description	OTR	WVTR
	$cm^3/(m^2\ d)$	$g/(m^2\ d)$
BOPP + AlO_x (before lamination)	48.62 ± 8.18	4.76 ± 0.35
BOPP + AlO_x + adhesive + BOPP (laminated)	11.92 ± 0.61	2.63 ± 0.17

eliminated, which is in agreement with results published by other researchers [10,14,29]. AFM investigation of the uncoated and acrylate coated BOPP revealed a substantial decline of surface roughness with RMS values decreasing from 4.1 ± 0.3 nm to 1.1 ± 0.1 nm by the application of the acrylate layer, accompanied by a considerable change in surface structure, as can be seen in Fig. 2. The acrylate RMS roughness compares well with a range of 0.8 to 1.5 nm as stated by Affinito et al. [11]. This smoother surface could reduce the number of defects in the subsequently deposited AlO_x layer, and thus account for the improved barrier of the film with an acrylate undercoat, as reported in Table 1.

3.2. Lamination

For the industrial scale lamination, the AlO_x coated BOPP film was combined with an uncoated 20 μm BOPP film using a two component polyurethane adhesive. Thus, the thin AlO_x barrier layer is embedded between and protected by the BOPP films and is adjacent to the adhesive layer. As can be seen from the barrier performance pre and post-lamination stated in Table 3, the OTR could be significantly decreased, whilst WVTR was approximately halved. The latter could be attributed to the doubling of the film thickness by adding another 20 μm thick BOPP film. The improvement of OTR is predominantly assigned to the barrier properties of the adhesive, which has a lower oxygen permeability compared to BOPP. This results in a reduction of the concentration gradient in the adhesive layer adjacent to the defects (in the AlO_x coating) and therefore improves the overall oxygen barrier of the laminated structure containing the AlO_x barrier layer [30]. Furthermore, the infiltration of the adhesive into defects in the AlO_x layer, as discussed for the acrylate topcoat, has also been suggested by other researchers [31] to play an important role for the barrier improvement obtained by the adhesive lamination of vacuum coated polymer films.

4. Summary and conclusions

Acrylate top- and undercoats as well as adhesive lamination can significantly enhance the barrier performance of reactively evaporated AlO_x barrier layers on BOPP film. The change of surface chemistry and the smoothing of the BOPP film surface induced by the acrylate undercoat are thought to be of major importance for this barrier enhancement. During topcoating and presumably also lamination, the infiltration of the acrylate and adhesive into defects of the inorganic AlO_x layer, such as cracks, pinholes or pores, and the better oxygen barrier properties of the acrylate/adhesive can account for the obtained improvement of barrier levels. The investigation of apparent activation energy revealed a macro-defect driven permeation process through the AlO_x coated as well as AlO_x/acrylate topcoated film for both, oxygen and water vapour.

References

[1] C.A. Bishop, Roll-to-Roll Vacuum Deposition of Barrier Coatings, Scrivener, Salem, 2010.
[2] The Future of Transparent Barrier Films to 2011, Pira International Ltd., Leatherhead, 2006.
[3] R.S.A. Kelly, 36th Annual Technical Conference Proceedings of the Society of Vacuum Coaters, 1993, p. 312.
[4] R.S.A. Kelly, 37th Annual Technical Conference Proceedings of the Society of Vacuum Coaters, 1994, p. 144.
[5] S. Schiller, M. Neumann, H. Morgner, N. Schiller, 37th Annual Technical Conference Proceedings of the Society of Vacuum Coaters, 1994, p. 203.
[6] S. Günther, S. Straach, N. Schiller, A.L. Quiceno, A.G. Contreras, R. Ludwig, G. Hoffmann, 52nd Annual Technical Conference Proceedings of the Society of Vacuum Coaters, 2009, p. 727.
[7] C.F. Struller, P.J. Kelly, N.J. Copeland, C.M. Liauw, J. Vac. Sci. Technol. A 30 (4) (2012) 041502.
[8] C.F. Struller, P.J. Kelly, N.J. Copeland, Surf. Coat. Technol. (2013) http://dx.doi.org/10.1016/j.surfcoat.2013.08.011 (in press).
[9] A. Yializis, 38th Annual Technical Conference Proceedings of the Society of Vacuum Coaters, 1995, p. 95.
[10] J.D. Affinito, M.E. Gross, C.A. Coronado, G.L. Graff, E.N. Greenwell, P.M. Martin, Thin Solid Films 290–291 (1996) 63.
[11] J.D. Affinito, S. Eufinger, M.E. Gross, G.L. Graff, P.M. Martin, Thin Solid Films 308–309 (1997) 19.
[12] T. Miyamoto, K. Mizuno, N. Noguchi, T. Niijima, 44th Annual Technical Conference Proceedings of the Society of Vacuum Coaters, 2001, p. 166.
[13] G.L. Graff, R.E. Williford, P.E. Burrows, J. Appl. Phys. 96 (4) (2004) 1840.
[14] A. Yializis, M.G. Mikhael, R.E. Ellwanger, 43rd Annual Technical Conference Proceedings of the Society of Vacuum Coaters, 2000, p. 404.
[15] A.G. Erlat, B.M. Henry, C.R.M. Grovenor, A.G.D. Briggs, R.J. Chater, Y. Tsukahara, J. Phys. Chem. B 108 (3) (2004) 883.
[16] M. Hanika, H.-C. Langowski, U. Moosheimer, 45th Annual Technical Conference Proceedings of the Society of Vacuum Coaters, 2002, p. 519.
[17] E.H.H. Jamieson, A.H. Windle, J. Mater. Sci. 18 (1) (1983) 64.
[18] T.A. Beu, P.V. Mercea, Mater. Chem. Phys. 26 (3–4) (1990) 309.
[19] J.D. Affinito, D. Hilliard, 47th Annual Technical Conference Proceedings of the Society of Vacuum Coaters, 2004, p. 563.
[20] B.M. Henry, A.G. Erlat, C.R.M. Grovenor, C.-S. Deng, G.A.D. Briggs, T. Miyamoto, N. Noguchi, T. Niijima, Y. Tsukahara, 44th Annual Technical Conference Proceedings of the Society of Vacuum Coaters, 2001, p. 469.
[21] G. Aresta, J. Palmans, M.C.M. van de Sanden, M. Creatore, Microporous Mesoporous Mater. 151 (2012) 434.
[22] Y.G. Tropsha, N.G. Harvey, J. Phys. Chem. B 101 (13) (1997) 2259.
[23] A.G. Erlat, R.J. Spontak, R.P. Clarke, T.C. Robinson, P.D. Haaland, Y. Tropsha, N.G. Harvey, E.A. Vogler, J. Phys. Chem. B 103 (29) (1999) 6047.
[24] A.P. Roberts, B.M. Henry, A.P. Sutton, C.R.M. Grovenor, G.A.D. Briggs, T. Miyamoto, M. Kano, Y. Tsukahara, M. Yanaka, J. Membr. Sci. 208 (1–2) (2002) 75.
[25] C.S. Deng, H.E. Assender, F. Dinelli, O.V. Kolosov, G.A.D. Briggs, T. Miyamoto, Y. Tsukahara, J. Polym. Sci. B Polym. Phys. 38 (23) (2000) 3151.
[26] S.-I. Hong, J.M. Krochta, J. Food Eng. 77 (3) (2006) 739.
[27] M. Kurek, D. Klepac, M. Šćetar, K. Galić, S. Valić, Y. Liu, W. Yang, Polym. Bull. 67 (7) (2011) 1293.
[28] B.M. Henry, F. Dinelli, K.Y. Zhao, C.R.M. Grovenor, O.V. Kolosov, G.A.D. Briggs, A.P. Roberts, R.S. Kumar, R.P. Howson, Thin Solid Films 355–356 (1999) 500.
[29] B.M. Henry, D. Howells, J.A. Topping, H.E. Assender, C.R.M. Grovenor, L. Marras, 49th Annual Technical Conference Proceedings of the Society of Vacuum Coaters, 2006, p. 654.
[30] H.-C. Langowski, in: O.G. Piringer, A.L. Baner (Eds.), Plastic Packaging – Interactions with Food and Pharmaceuticals, Wiley-VCH, Weinheim, 2008, p. 297.
[31] O. Miesbauer, M. Schmidt, H.-C. Langowski, Vak. Forsch. Prax. 20 (2008) 32.

Please cite this article as: C.F. Struller, et al., Thin Solid Films (2013), http://dx.doi.org/10.1016/j.tsf.2013.10.091

Non-peer reviewed publications:

1. Struller, C.F., et al., *Aluminum oxide barrier layers on polymer web.* Converting Quarterly, 2013, Quarter 1, p. 50
2. Struller, C.F., et al., *Aluminum oxide barrier layers on polymer web.* Vacuum and Coating Technology, 2013, August, p. 28

Conference presentations:

1. *Aluminum oxide barrier coatings on polymeric substrates*, Carolin Struller, CCR 18th New Industrial Chemistry & Engineering workshop "Barrier Technologies", 2012, Arlington, VA, USA
2. *Aluminium oxide clear barrier coatings on polymeric substrates for food packaging applications,* poster presentation, Carolin Struller, Nanostructured Metal Oxide Thin Films Conference (Vacuum Symposium UK), 2012, Coventry, UK
3. *Aluminum oxide barrier layers on polymer web*, Carolin Struller, AIMCAL Web Coating & Handling Conference, 2012, Myrtle Beach, SC, USA
4. *Aluminium oxide barrier films on polymeric web and their conversion for packaging applications*, poster presentation, Carolin Struller, EMRS Spring Meeting, 2013, Strasbourg, France
5. *Aluminum oxide barrier coatings on polymer films for food packaging applications*, Carolin Struller, SVC Technical Conference, 2013, Providence, RI, USA
6. *Aluminium oxide barrier layers on Bopp film*, Carolin Struller, BOPP Film Conference, 2013, Singapore
7. *Characterization and conversion of aluminum oxide coated flexible barrier films*, Carolin Struller, AIMCAL Web Coating & Handling Conference, 2013, Charleston, SC, USA